Experimental and Theoretical Analysis of the Luminescence Spectroscopy of atomic Mercury and atomic Manganese isolated in Rare Gas Solids

A Thesis submitted by

Martin A. Collier, B.Sc. (Hons.)

to the **National University of Ireland** in fulfilment of the requirements for the Degree of Doctor of Philosophy

NUI MAYNOOTH

Ollscoil na hÉireann Má Nuad

Based on research carried out in the

Low Temperature Laboratory,

Department of Chemistry,

National University of Ireland, Maynooth.

Research Supervisor: Dr. John G. McCaffrey

Head of Department: Prof. Charles M. Quinn

Maynooth,
Co. Kildare,
Eire.

August, 2004

Table of contents

Page

Abstract **XI**

Chapter I

The optical spectroscopy of metal atoms isolated in rare gas solids
Introduction

I.1 Overview 1

I.2 Matrix-isolation; History and development 1

I.3 Rare Gas solids, (RG) 4

I.4 Matrix Effects 7
I.4.I Multiple metal atom trapping sites 8
I.4.II Gas Phase – Matrix transition frequency shifts 9
I.4.III Dynamic Jahn-Teller effect 11

I.5 Luminescence spectroscopy of Hg/RG and Mn/RG solids 13
I.5.I Hg/RG 13
I.5.I Mn/RG 14

References 17

Chapter II

Experimental

II.1 Introduction 20

II.2 Matrix – isolation apparatus 20

II.3 Gas handling system, (GHS) 23

II.4 M/RG sample preparation 24
II.4.I Metal vapour generation, Mercury 24
II.4.II Metal vapour generation, Manganese 25

II.5 Luminescence measurements 28
II.5.I Steady-state spectroscopy (continuous lamp excitation) 28
II.5.II Time-resolved spectroscopy 31
II.5.III Excited state lifetime measurements 37

References 39

Chapter III

Luminescence spectroscopy of $^3P_1$ and $^3P_0$ state atomic mercury isolated in solid Ar, Kr and Xe

III.1 Introduction 41

III.2 Results 42

III.2.I Hg $^3P_1 \leftarrow {}^1S_0$ absorption spectra 42
III.2.II Hg $^3P_1 \leftrightarrow {}^1S_0$ excitation and emission spectra 43
III.2.III Hg $^3P_0 \rightarrow {}^1S_0$ emission spectra 57

III.3 Discussion 63

III.3.I Hg $^3P_1 \rightarrow {}^1S_0$ emission 63
III.3.II Hg $^3P_0 \rightarrow {}^1S_0$ emission 64

III.4 Conclusion 67

References 68

Chapter IV

A pair-potentials analysis of the optical spectroscopy of $^3P_1$ state atomic mercury isolated in solid Ar, Kr and Xe

IV.1 Introduction 70

IV.2 Methods and Results 72

IV.2.I Ground $^1S_0$ state 74
IV.2.II Excited $^3P_1$ state 75
IV.2.II.I Tetragonal (4-atom) symmetry modes 79
IV.2.II.II Trigonal (6-atom) symmetry modes 85
IV.2.II.III Two-fold (2-atom) symmetry modes 91

IV.3 Discussion 94

IV.3.I Absorption Energies 96
IV.3.II Emission Energies 97

IV.4 Conclusions 101

References 102

Chapter V

A pair-potentials analysis of I) the $Hg(^3P_1 \leftrightarrow {}^1S_0)$/Ne luminescence and II) $Hg(^3P_0 \leftrightarrow {}^1S_0)$/RG (RG = Ar, Kr and Xe) emission spectroscopy

V.I A pair potentials analysis of the $Hg(^3P_1 \leftrightarrow {}^1S_0)$/Ne luminescence 104

V.I.1 Introduction 104

V.I.2 Methods and Results 107
- **V.I.2.I** Ground State Site occupancy 107
- **V.I.2.II** Excited $^3P_1$ state 111

V.I.3 Absorption and Emission Energies 118

V.I.4 Discussion 119

V.I.5 Conclusion 122

V.II $Hg(^3P_0 \rightarrow {}^1S_0)$/RG emission spectroscopy (Ar, Kr and Xe) 123

V.II.1 Introduction 123

V.II.2 Method and Results 125
- **V.II.2.I** Ground $^1S_0$ and Excited $^3P_0$ states 125
- **V.II.2.II** $Hg(^3P_0 \leftrightarrow {}^1S_0)/RG_{18}$ Absorption and Emission Energies 128

V.II.3 Discussion 129

V.II.4 Conclusion 130

References 131

Chapter VI

The absorption spectroscopy of atomic manganese isolated in solid Ar, Kr and Xe.

VI.1 Introduction 132

VI.2 Results – Mn/RG UV/Vis absorption spectroscopy 134
- **VI.2.I** Mn/Ar 134
- **VI.2.II** Discussion Mn/Ar absorption spectroscopy 138
- **VI.2.III** Mn/Kr 141
- **VI.2.IV** Discussion Mn/Kr absorption spectroscopy 145
- **VI.2.V** Mn/Xe 146
- **VI.2.VI** Discussion Mn/Xe absorption spectroscopy 149

VI.3 Discussion Mn/RG UV/Vis absorption spectroscopy 150

VI.4 Conclusion 154

References 155

Chapter VII

Luminescence spectroscopy of the z^6P state of atomic manganese isolated in rare gas solids, (RG = Ar, Kr and Xe)

VII.1 Introduction 156

VII.2 Results Mn(z^6P)/RG luminescence 158
VII.2.I Mn(z^6P)/Xe 159
VII.2.I.I Discussion Mn(z^6P)/Xe 167

VII.2.II Mn(z^6P)/Ar 168
VII.2.II.I Mn(z^6P)/Ar Site Specific Emission spectroscopy 174
VII.2.II.II Mn(z^6P)/Ar – Red (1°) site luminescence 175
VII.2.II.III Mn(z^6P)/Ar – Blue (2°) site luminescence 190
VII.2.II.IV Discussion Mn(z^6P)/Ar 199

VII.2.III Mn(z^6P)/Kr 202
VII.2.III.I Mn(z^6P)/Kr Site Specific Emission spectroscopy 207
VII.2.III.II Mn(z^6P)/Kr – Blue (1°) site luminescence 208
VII.2.III.III Mn(z^6P)/Kr – Red (2°) site luminescence 218
VII.2.III.IV Discussion Mn(z^6P)/Kr 226

VII.3 Discussion Mn(z^6P)/RG luminescence 229

VII.4 Conclusion 232

References 234

Chapter VIII

Direct laser excitation of the 'forbidden' z^8P ↔ a^6S and a^6D ↔ a^6S transitions of atomic Mn/RG solids, (RG = Ar, Kr and Xe)

VIII.1 Introduction 235

VIII.2 Results Mn(a^6D)/RG luminescence 238
VIII.2.I Mn(a^6D)/Xe 239
VIII.2.II Mn(a^6D)/Kr 246
VIII.2.III Mn(a^6D)/Ar 257

VIII.3 Discussion Mn(a^6D)/RG luminescence 264
VIII.3.I Mn(a^6D)/RG Excitation spectroscopy 264
VIII.3.II Mn(a^6D)/RG Emission spectroscopy 266

VIII.4 Conclusion Mn(a^6D)/RG luminescence 267

VIII.5 Results Mn(z^8P)/RG luminescence 268
VIII.5.I Mn(z^8P)/Xe 269

VIII.5.II Mn(z^8P)/Kr 273
VIII.5.II.I Mn(z^8P)/Kr – Blue (1°) site luminescence 276

VIII.5.III Mn(z^8P)/Ar 280
VIII.5.III.I Mn(z^8P)/Ar – Red (1°) site luminescence 282
VIII.5.III.II Mn(z^8P)/Ar – Blue (2°) site luminescence 284

VIII.6 Discussion Mn(z^8P)/RG luminescence 287
VIII.6.I Mn(z^8P)/RG Excitation spectroscopy 287
VIII.6.II Mn(z^8P)/RG Emission spectroscopy 288

VIII.7 Conclusion Mn(z^8P)/RG luminescence 290

VIII.8 Mn/RG Discussion – Blue site-specific luminescence 290

VIII.9 Conclusion Mn(a^6D and z^8P $\leftrightarrow$ a^6S)/RG 294

References 296

Chapter IX

Sites of manganese atom isolation in RG solids, RG = Ar, Kr and Xe

IX.1 Introduction 297

IX.2 Site Analysis Mn(z^6P $\leftarrow$ a^6S)/RG 299

IX.3 Site Analysis Mn(y^6P and z^8P $\leftarrow$ a^6S)/RG 303
IX.3.I Mn y^6P $\leftarrow$ a^6S Excitation spectroscopy 303
IX.3.II Mn z^8P $\leftarrow$ a^6S Excitation spectroscopy 305

IX.4 Discussion 307

IX.5 Conclusion 311

References 312

Chapter X

Conclusion

IX.1 Hg/RG 313

IX.2 Mn/RG 316

IX.3 Summary 320

Summary

Experimental and Theoretical analysis of the Luminescence Spectroscopy of atomic Mercury and atomic Manganese isolated in solid Rare Gases

The work presented in this thesis is primarily experimental but also contains an important theoretical extension to gain further insight into the optical spectroscopy of atomic ns^2 metal atoms, mercury and manganese isolated in cryogenic thin films of rare gases argon, krypton and xenon. The luminescence spectroscopy of solid-state M/RG (M = Hg and Mn; RG = Ar, Kr and Xe) samples has been recorded employing both time-integrated (steady-state) and time-resolved methods. The impetus for the selection of the Hg/RG systems being the availability of solid-state spectroscopic and gas phase pair-potentials data that allowed the development of a theoretical model. The theoretical analysis conducted on the Hg/RG systems, yielded a qualitative interpretation of the recorded experimental data, providing information on the vibronic modes leading to the observed luminescence. In contrast, the investigation of Mn/RG solids was motivated by the absorption similarities between this transition metal atom and the simpler Hg/RG system, as both exhibit a ground ns^2 electronic configuration and excited states derived from the ns^1np^1 configuration. However, the existence of low lying excited states in Mn, originating from electronic configurations other than the $[Ar]3d^5 4s4p$ configuration accessed in absorption, provides multiple radiative and non-radiative relaxation channels for excited state populations. The luminescence spectroscopy of Hg and Mn atoms isolated in rare gas matrices has shown that the solid state environment provides an ideal environment to study the solvation of ground and excited state metal atoms. It allows the extraction of information on long-lived electronic transitions (> 100 μsec) that cannot be observed in gas phase experiments. The experimental results obtained for the Mn/RG systems have shown that the site of isolation governs the excited state interactions with the host. This observation therefore would allow the extension of this work to investigate site selective excited state reactions with reagents such as CH_4, CH_3F, NH_3 and H_2-doped rare gas matrices.

Chapter I

The optical spectroscopy of metal atoms isolated in rare gas solids – *Introduction*

I.1 Overview

The following provides a synopsis of the 'matrix-isolation' technique with particular emphasis on its application to the spectroscopic interrogation of metal atoms isolated in rare gas solids (RG). First, a brief history of the development of the technique since its inception in the 1920's is outlined. Second, some general remarks regarding the requirements of the apparatus necessary to realise a matrix-isolation experiment are given. Third, the structure of rare gas solids and the effect of the matrix environment on the dopant species are discussed in detail. Finally, a brief outline of the experimental and theoretical research conducted in this study is presented to provide a guide to the results which are presented in the Chapters following. This includes specific details of the metal atom systems, mercury and manganese, investigated.

I.2 Matrix-isolation; History and development

Matrix-isolation is a term, according to IUPAC, which refers to the isolation of a reactive or unstable species by dilution in a solid matrix such as argon, nitrogen or any other inert material. The matrix is usually condensed on a window or in an optical cell at low temperature, to preserve the structure of the reactive or unstable species for identification by spectroscopic means[1]. However, the expression is most commonly used in a narrower sense to refer to the technique of trapping atomic and molecular species in the solid rare gases. Occasionally reactive solids are used to investigate low temperature photochemistry.

L. Vegard[2,3,4] preformed the earliest reported experiments using low temperature matrix materials in the 1920's and observed the luminescence resulting from the electron bombardment of rare gas and nitrogen solids prepared at liquid helium temperatures. In the 1940's the first report of the isolation of molecular species in an optically transparent material for the purpose of spectroscopic investigation appeared. G. N. Lewis and co-workers[5] in Berkeley studied the

phosphorescence of aromatic molecules in low temperature organic glasses. In the 1950's two groups further developed the 'matrix-isolation' technique. Norman and Porter[6,7] reported the optical spectra of free radicals trapped in organic solvents while Pimentel and co-workers[8,9,10] adopted the solid rare gases as host materials for the study of free radicals using infrared spectroscopy. Pimentel's group are also credited with coining the phrase 'matrix-isolation'. Following the early development of the technique[11] and the adoption of rare gas solids as host materials, low temperature 'matrix' studies have blossomed from the investigation of unstable molecular species and reaction intermediates to encompass several other fields of spectroscopic investigation[12,13,14,15]. These fields include the analysis of matrix-isolated atoms and molecules using UV/Vis, IR, Raman, ESR, Mössbauer, MCD and electronic/time-resolved spectroscopy. These areas of research allow I) the identification and characterisation of new chemicals prepared in the solid, II) analysis of the interaction of the ground and excited states of the dopant species with the host matrix and III) determination of local matrix effects on the guest atom/molecule and the perturbation caused by the dopant species to the rare gas crystal.

In general 'matrix-isolation' experiments are preformed by condensing a gas phase vapour containing an excess of matrix material (a rare gas solid) with a small amount of the guest atom or molecule of interest onto a cold spectroscopic substrate. The matrix to guest ratio is usually between 10^4 and 10^5 in order to achieve complete isolation of the guest species and prevent guest-guest (metal-metal) interactions. Some practical requirements must be considered before attempting matrix-isolation experiments. The sample substrate (spectroscopic window) and host material must be transparent over a wide spectral range. One advantage of using rare gas solids is their transparency from the vacuum UV to the far-infrared spectral regions. However, the choice of spectroscopic window is dependent on the type of spectroscopy to be carried out. Duncan[16] provides details of the suitability of spectroscopic windows for different measurements. The guest species (metal atoms) must be volatile or a gaseous vapour must be produced. A stable method of guest vaporisation is required to ensure uniform matrix ratios are maintained throughout the sample deposition. Experiments involving the isolation of low vapour pressure molecular species must ensure that factors such as the thermal generation of the guest species does not cause decomposition before matrix condensation. Metal atom vapours can be achieved in a number of ways such as resistive heating, pulsed laser vaporisation and 'sputtering'

by electron bombardment of the bulk. Sample purity is a priority given the small amounts of dopant species used. This can be ensured for matrix gases by employing a high vacuum gas handling system. A vacuum shroud serves to protect the sample chamber from radiative and physical sources of heat. High vacuum (typically 10^{-6} mbar or better) must be maintained in the chamber to allow the refrigeration system achieve the low temperatures (4 to 40 K) required for sample deposition.

The use of low temperatures and rare gas solids in matrix-isolation are two of the advantages of the technique, as the low temperature ensures simpler molecular spectroscopy than that achievable in the gas phase, since only the lowest electronic and vibrational states are populated. The deposition and sample temperature also play important roles in simplifying the observed spectroscopy as the rigid matrix environment prevents molecular rotation. Therefore, rotational progressions corresponding to the P and R branches observed for molecular species in the gas phase are removed and only the vibrational transitions are observed. However the deposition temperature should be approximately one third the melting point of the host material (Ar, Kr and Xe) to produce samples with high crystallinity. To achieve isolation and avoid guest-guest interactions resulting from diffusion processes deposition temperatures less than this are sometimes used. The effect of the deposition temperature on the crystallinity of the solid rare gases is discussed later in this Chapter.

This thesis centres on an investigation of the luminescence spectroscopy of metal atoms isolated in solid Ar, Kr and Xe and therefore a brief overview of the development of this narrower subject area is provided. The investigation of the electronic spectroscopy of metal atoms in rare gas solids has paralleled, and in some cases, preceded the growth in understanding molecular interactions in matrices. This synergism was necessitated by preparative transition metal atom Cryochemistry[13] as the analysis of matrix-isolated metal atom reactions required an understanding of the atomic spectroscopy of the precursor metal atoms in rare gas solids. This is of great advantage in determining the reaction mechanisms involved in the preparation and characterisation of new species. The extensive study of matrix-isolated metal atoms began in 1959 when McCarthy and Robinson[17] reported optical absorption studies of Na and Hg in solid Ar, Kr and Xe deposited at 4.2 K. Since then, the optical absorption spectroscopy of many refractory metals have been reported and reviewed in the literature[11,18,19]. Only in the past decade, has the luminescence spectroscopy of

metal atoms isolated in rare gas solids been used as a sensitive probe of some aspects of the solid-state environment[20]. This role was afforded by the development of cold supersonic jets to study the interaction of the ground and excited states of a single metal atom interacting with rare gases in 1:1 M·RG complexes or in larger $M{\cdot}RG_n$ clusters[21]. The interaction of metal atoms in matrices can be seen as an infinite RG_n cluster and therefore information on energetics and dynamics extracted from gas phase experiments can be used to probe the matrix environment using theoretical simulations.

In the last ten years the Maynooth group have concentrated on the luminescence spectroscopy of $nsnp \leftarrow ns$ type electronic transitions of group I (Na)[22], group II (Mg)[23,24] and group IIA (Zn[25], Cd[26] and Hg[27]) metal atoms isolated in solid rare gases. These systems exhibit either ^2S or ^1S spherically symmetric ground states resulting from ns^1 and ns^2 ground state electronic configurations respectively. The excited np^1 and ns^1np^1 states reached in absorption are spatially very different to the ground states, leading to very different interaction with the host than the ground state. The high ground state symmetry and the availability of accurate ground and excited state diatomic pair-potentials allowed the development of a simple theoretical method[28] to model the local matrix cage interactions leading to the observed M/RG luminescence. The localised $M{\cdot}RG_{18}$ model employs pair-potentials from gas phase 1·1 M·RG complexes to simulate the interaction of the metal atom in the RG solid.

I.3 Rare Gas solids, (RG)

Solid rare gases make ideal matrix hosts, as they are chemically inert and transparent over a very wide spectral range, from the far-infrared to the vacuum UV. The RG's (Ne, Ar, Kr and Xe) all exhibit spherical ground states and adopt a simple packing structure in the solid state. The formation of simple solids on condensation owes its origin to the van der Waals nature of the RG-RG interactions, as forming close packed structures maximises the van der Waals forces between the RG atoms by achieving the highest coordination, that is the largest number of nearest neighbour atoms[15]. The structure adopted is the simple close packed, face centered cubic (*fcc*) arrangement. Figure I.1 presents an *fcc* unit cell, which when expanded in three dimensions *n* times generates the RG matrix. The *fcc* unit cell represented in Figure

I.1 shows fourteen lattice points, eight of which are positioned at the corners of the unit cell with the remaining six occupying the centre of the cubic faces. Each of these points corresponds to the centre of mass of a RG atom. The lattice parameter (*a*) and the next nearest neighbour distance (R) are depicted in Figure I.1. In an *fcc* lattice[29] each RG atom has twelve nearest neighbours at a distance of $R = a/\sqrt{2}$ and six next nearest neighbour atoms located at a distance of the lattice parameter, *a*. The lattice parameters for the solid rare gases Ne to Xe are presented in Table I.1 at 4 K[15].

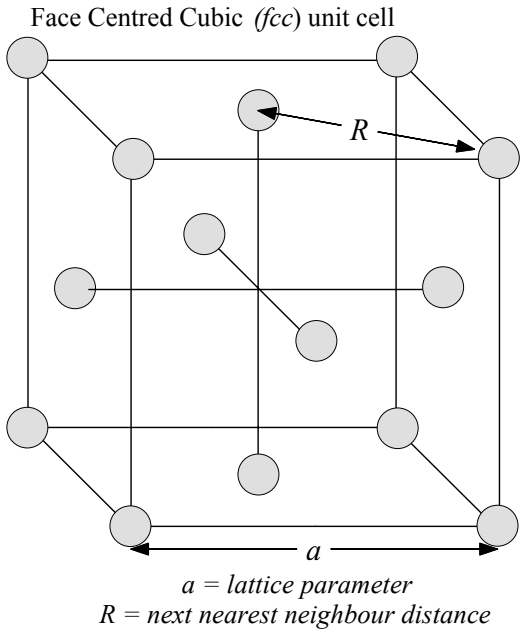

Figure I.1 **A representation of a face centered cubic unit cell showing the fourteen lattice points, the lattice parameter (*a*) and the nearest neighbour distance, R. The nearest neighbour distance can be calculated using simple algebra as $R = 0.707a = a/\sqrt{2}$.**

Table I.1 **Lattice parameter (*a*) and site sizes in angstrom units (Å) for specific spherically symmetric site types in the solid rare gases. The site sizes presented were calculated with respect to the lattice parameter using the simple algebraic expressions provided in the text and in the legend of Figure I.2.**

RG Solid	*Lat. Parm. (a,* Å)	T_d (Å)	I_{oh} (Å)	*ss* (Å)	T_{Vac} (Å)
Ne	4.462	0.709	1.307	3.155	3.699
Ar	5.312	0.844	1.556	3.756	4.404
Kr	5.644	0.897	1.653	3.991	4.679
Xe	6.131	0.974	1.796	4.335	5.083

The ordered *fcc* packing structure exhibited by solid Ne, Ar, Kr and Xe upon deposition allows the identification of the possible sites of isolation for spherical

ground state metal atoms. These 'S'-state metal atoms therefore show a preference for a spherically symmetric site within the host matrix. The site diameters (Å) of four of these sites as listed in Table I.1. The two-layer space filled representation of an *fcc* unit, shown in Figure I.2, allows a visual assessment of the relative site diameters of the four site types. The sites are:

(I) Substitutional Site (*ss*): A *ss* is the vacancy left in the host RG lattice following the removal of a single RG atom. The substitutional site diameter is calculated with respect to the lattice parameter (a) of the RG as $ss = a/\sqrt{2}$. The *fcc* unit cell in Figure I.2 shows that these sites are centered at the unit cell lattice points as indicated by the large circles.

(II) Octahedral Interstitial Site (I_{oh}): This site is located at the centre of the *fcc* unit cell as shown in Figure I.1 and encompassed by six host RG atoms. The site size and its position in the unit cell is shown (dashed circle) at the centre of Figure I.2. The largest guest species it can accommodate without disruption of the lattice is 70.7% of the size of the host (rare gas) atom radius. The site size is calculated from the lattice parameter using the expression $I_{oh} = (a - ss)$.

(III) Tetrahedral Interstitial Site (T_d): There are eight of these sites per *fcc* unit cell, four of these are represented by the smallest circles in Figure I.2. These sites are also referred to as tetrahedral holes as the vacancy is located at the centre of four rare gas atoms forming a regular tetrahedron. The centre of this site is located at a distance $\sqrt{3}(a/4)$ away from the corner of the cubic *fcc* cell. A tetrahedral interstitial site can accommodate a spherical dopant species of radius less than a fifth of the radius of the host RG atom[15].

(IV) Tetravacancy Site (T_{Vac}): This site, like the substitutional site, is generated by the removal of a tetrahedron of four adjacent host atoms surrounding a tetrahedral interstitial site and its replacement by the guest species. Therefore, the centre of a T_{Vac} coincides with the centre of a tetrahedral interstitial site, T_d. Although this site is not shown explicitly, its size can be assessed by inspection of Figure I.1.

The simple *fcc* unit cell therefore allows the identification of possible sites of atomic isolation in the rare gas lattice. This aids in the analysis of the solid-state luminescence spectroscopy of M/RG's. For example the Hg atom exhibits a $^1S_0$ ground state and a comparison of the ground state bond length[30], for the $Hg(^1S_0)\cdot Xe$

1:1 complex known from the gas phase to be 4.25 Å, with the site size available in solid Xe (*ss* = 4.334 Å) reveals that the Hg·Xe bond length is less than *ss*, and therefore substitutional site occupancy is expected for Hg atoms in solid Xe.

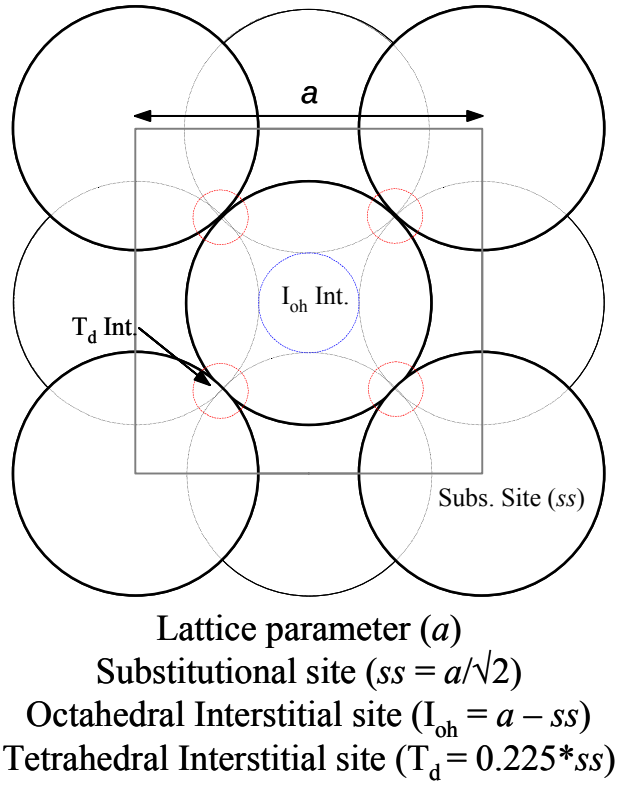

Figure I.2 **A space filling representation of the face centered cubic (*fcc*) unit cell showing two layers AB of the repeating structure ABCABC that describes the layer-packing characteristic of RG solids. The circles represent the spherical sites sizes and the legend provides the simple expressions used to calculate the site sizes available from the lattice parameter (*a*) for a given solid.**

I.4 Matrix Effects

In the following section some effects of the rare gas solid host matrix on the luminescence spectroscopy of metal atoms, are presented. These include the formation of multiple trapping sites, a topic discussed with respect to identification and removal of thermally labile sites. In addition a general comparison of the RG solids is made to allow an assessment of their relative preference for multiple site formation. The origin of gas phase to matrix frequency shifts for transitions is discussed with respect to the role of electron-phonon coupling for luminescent F-

centres in solids. The origin of Jahn-Teller effect which gives rise to structured broadband profiles observed for P ← S type electronic transitions is also discussed.

I.4.I Multiple metal atom trapping sites

As the M/RG solid condensation proceeds at low temperatures (4 to 35 K) metal atoms exhibit a preference for certain sites of isolation within the RG host as controlled by the M·RG ground state bond length. The Hg/Xe case mentioned in Section I.3 represents the ideal situation where the $Hg(^1S_0)$·Xe bond length is less than the *ss* site diameter of solid xenon. This is not always the case. If the ground state bond length is slightly larger than the substitutional site size available in the solid, isolation may occur in multiple sites. Thus isolation may occur in a larger site such as a tetravacancy but also in a substitutional site following an expansion. In addition, where the solid formation occurs at the lower end of the temperature range ($T < 12$ K) isolation in thermally unstable sites that contain defects such as lattice vacancies may result. These sites are subsequently removed by the formation of a more crystalline lattice by annealing, where the solid is gently heated and re-cooled to allow organisation of the lattice into its regular packing structure. Matrix annealing or high deposition temperatures are therefore required to assess the thermal stability of the sites of isolation occupied by dopant species in RG solids.

Due to the larger site sizes available but also for rigidity reasons, solid Xe is known to be most efficient rare gas matrix for the isolation of atomic species. The rigidity is directly related to the magnitude of the RG·RG diatomic dissociation energy (D_e). Table I.2 presents the dissociation/binding energies for the rare gas dimers. A comparison of the D_e values for the Xe_2 and Ne_2 reveals the Xe·Xe binding energy is almost seven times larger than that of Ne·Ne. The difference in the RG dimer dissociation energies is manifest in how solid Xe achieves and maintains the crystalline *fcc* packing easier than Ne.

Table I.2 **Lattice parameters (*a*) for the RG solids and the ground state bond lengths for the RG dimers presented in angstrom units. The binding / dissociation energies (D_e) for the RG dimers are presented in wavenumber units.**

RG Solid	*Lat. Parm. (a,* Å)[15]	RG·RG	R_e (Å)	D_e (cm^{-1})
Ne	4.462	Ne·Ne[31]	3.091	29.4
Ar	5.312	Ar·Ar[32]	3.756	99.5
Kr	5.644	Kr·Kr[31]	4.017	138.4
Xe	6.131	Xe·Xe[31]	4.363	196.2

I.4.II Gas Phase – Matrix transition frequency shifts

It has been observed for several metal atom systems undergoing P ← S type electronic transitions, that the solid host strongly influences the spectroscopy. The differences from the free atom in the gas phase include the observation of a shift between absorption and emission energies. The magnitude of this shift is calculated as the difference in energy between the absorption and emission band maxima. It is generally referred to as the Stokes' shift. In the gas phase absorption occurs from the ground state E_0 to the excited state E_1 corresponding to a transition energy $\Delta E_{1,0} = E_1 - E_0$ and the emission occurs between the same levels. Therefore, as depicted on the left of Figure I.3 $\Delta E_{1,0}$ (Abs.) = $\Delta E_{1,0}$(Em.) in the gas phase. The introduction of the luminescent centre (the atom) to a crystalline solid (RG) results in a Stokes' shift as $\Delta E_{1,0}$ (Abs.) > $\Delta E_{1,0}$(Em.). This is due to interaction with lattice phonons in both the ground E_0 and excited E_1 states. Electron-phonon coupling results in the population of $E_1(v_n)$ from $E_0(v_0)$ in absorption as shown in the middle panel (Atom A) of Figure I.3. Then fast non-radiative relaxation occurs from the excited state phonon levels accessed $E_1(v_n)$ to $E_1(v_0)$ followed by the radiative transition to the ground state phonon level $E_0(v_n)$ where a second non-radiative relaxation occurs to $E_0(v_0)$. As a result, the radiative transition energy is $\Delta E_{1,0}$ (Em.) = $E_1(v_0) - E_0(v_n)$, and the Stokes' shift observed is the sum of the non-radiative energies occurring in both the ground and excited states. This process is shown in Figure I.3, where the solid and dashed arrows represent radiative and non-radiative processes respectively.

In Figure I.3 $E_1 \leftarrow E_0$ represents the electronic transition for metal atoms undergoing P ← S type transitions in solid RG matrices. The matrix absorption energies are normally observed to blue shift by approximately 1% of the gas phase transition energy[11] $\Delta E_{1,0}$. This effect is due, in part, to the electron-phonon coupling

and is dominated by the interaction of the excited state with the rare gas solid, occurring in the Frank-Condon region of the ground state potential energy surface. The gas-phase to matrix shift of electronic transition energies of M/RG solids arises from contributions from both the ground and excited state interactions. This is revealed by the linear correlation between the matrix shifts and the RG polarizability. This was shown by the analysis of the Zn/RG, Cd/RG and Hg/RG systems by Laursen and Cartland[33]. However, another factor leads to the observation of broad absorption features for P ← S transitions in RG solids. This results from the dynamic Jahn-Teller effect, which is discussed in the next section.

In emission the relative positions of the ground and excited state potential energy curves are of great importance in determining the observed Stokes' shift as the transition energies are restricted by the Frank-Condon approximation. If a large difference exists between the excited and the ground state minima (for the same configuration of the atoms), a large Stokes' shift will be observed. If the excited state is stabilised greatly, the ground state may be very repulsive at the excited state minimum. However, the overall emission bandshape is determined by the electron-phonon coupling strength, of which the Huang and Rhys factor[34], S is a measure. The larger the value of S, the more Gaussian the observed emission band will be. In cases where interactions in the excited and ground states leads to a coincidence in the minima of both potential energy surfaces, radiative relaxation from $E_1(v_0)$ to $E_0(v_0)$, as shown on the right hand side of Figure I.3, allows the electronic transition to occur with minimal electron-phonon coupling ($S \approx 0$). In this case the observed emission feature corresponds to the band origin, ($v_{0,0}$) and a narrow zero-phonon line (ZPL) is observed. These effects are of reference to Chapter III where the first evidence of ZPL's for matrix-isolated metal atoms is presented for the $^3P_0 \rightarrow {}^1S_0$ transition of atomic mercury. ZPL's have, however been observed in the spectroscopy of matrix-isolated molecules. Bondybey and Brus[35] have discussed in detail the physical origin of electron-phonon lineshapes observed for matrix-isolated molecules such as Cl_2 and C_2.

The material presented above indicates the profound changes that can occur on placing a metal atom into a solid-state environment. Therefore knowledge of M·RG systems in the gas and condensed (M/RG) phases provide powerful methods to

examine the interactions occurring in the condensed phase which contribute to the observed spectral band shapes.

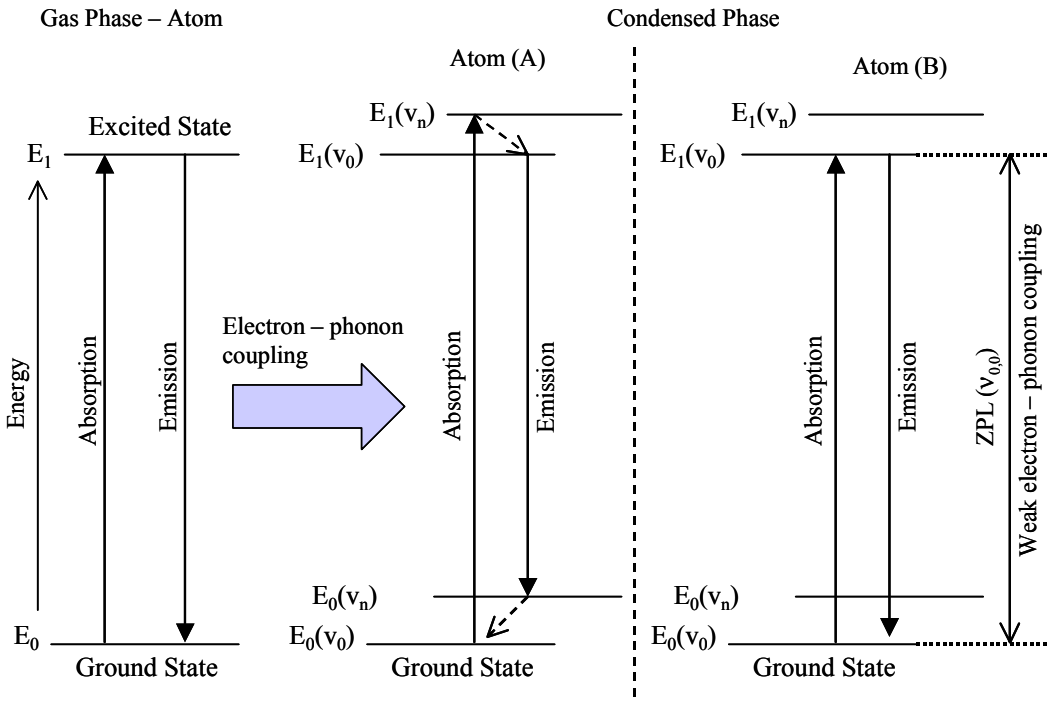

Figure I.3 **A comparison between the interactions of luminescent metal atoms in the gas and condensed phase. E_0 and E_1 represent the ground and excited electronic states of the atom and v represent the vibronic interactions in the ground and excited states induced by electron-phonon coupling. The right hand panel in this figure depicts the case of a luminescent centre in the solid where weak electron-phonon coupling ($S \approx 0$) exists.**

I.4.III Dynamic Jahn-Teller effect

The optical absorption spectroscopy of matrix-isolated metal atoms undergoing P ← S transitions in the rare gas matrices often show a threefold split pattern[13,18]. Jahn and Teller[36,37] showed that an electronically degenerate state of a non-linear complex is unstable with respect to some asymmetric nuclear displacement that lowers its energy by lowering the symmetry and thereby removing the electronic degeneracy. In the early literature, the presence of the structured absorption features on matrix-isolated atoms was attributed to effects such as multiple site occupancy[38], crystal field splittings[39] and non-nearest neighbour M-M[40,] interactions in the solid. In the 1950's, the JT effect was first detected in EPR spectra of paramagnetic ions isolated in crystals[41]. In the late 1970's moment analyses using magnetic circular dichroism (MCD) studies of matrix-isolated Mg atoms[42] in rare gas solids and comparison to the

observed absorption spectra, revealed for the first time substantial evidence that the threefold splitting observed for M(P ← S)/RG transitions was a consequence of the dynamic Jahn-Teller effect. It was concluded that the threefold absorption pattern resulted from a splitting of the Mg ^{1}P excited state due to a quenching of the excited state orbital angular momentum for Mg atoms isolated in single site type in solid Ne, Ar, Kr and Xe. The quenching was believed to be as a result of mixing of the 3p Mg orbitals with orbitals from neighbouring host rare gas atoms. An analysis of higher MCD moments and absorption spectra, assuming octahedral site symmetry for the Mg atom showed a dominant non-cubic (JT active) vibronic mode contributed to the observed bandwidth in the rare gas hosts (Ar, Kr and Xe) where the threefold pattern was observed. A Jahn-Teller explanation of this splitting, via $T_1 \times t_{2g}$ coupling, was thus proposed for Mg/RG and assigned as the origin of other triplet splitting patterns observed for P ← S type transitions of matrix-isolated atoms.

Analysis of the ^{2}P ← ^{2}S transition of matrix-isolated Li atoms[43] in rare gas matrices using the MCD technique showed that strong Jahn-Teller coupling in the ^{2}P state contributes to the absorption bands recorded in solid Kr and Xe. In addition, the application of simple crystal field models to these systems were unable to account for the threefold pattern. A theoretical analysis[44] of the MCD and absorption measurements made for the Li/Xe system showed good agreement between simulation and experiment when the JT active modes, (e_g and t_{2g}) had equivalent frequencies and coupling strengths. The e_g and t_{2g} designations are the non-cubic vibronic modes of the rare gas lattice. The Na/Xe and Li/Xe systems were further investigated[45] using a temperature dependent moment and theoretical lineshape analysis of the MCD spectra. This study conclusively assigned the threefold splitting pattern observed for the P ← S type electronic transition to the dynamic Jahn-Teller effect. Information on the actual site occupied by the guest metal atom in the rare gas solid was not available in the early ‘80’s. Since this time, accurate experimental and theoretical work has been presented on the 1:1 M·RG diatomics. This is particularly true of the Hg·RG diatomics and it is this system which is analysed first in the present work.

I.5 Luminescence spectroscopy of Hg/RG and Mn/RG solids

The following sections provide a general outline of the experimental and theoretical (Hg only) analyses of the luminescence spectroscopy of atomic mercury and manganese isolated in rare gas solids (Ar, Kr and Xe) presented in this thesis.

I.5.II Hg/RG

The metal atom whose spectroscopy has been most extensively studied, both in 1:1 van der Waals (Hg·RG) complexes[21] and isolated in solid rare gas matrices[20] (Hg/RG), is mercury. This is particularly true of the 6p $^3P_1 \leftrightarrow$ 6s $^1S_0$ transition[46] which occurs in the gas phase at 39412.3 cm^{-1}. Figure I.4 presents a schematic of the gas phase energy level diagram for atomic Hg[46]. As accurate Hg·RG pair-potentials, obtained from spectroscopy of the diatomic Hg·RG complexes stabilised in supersonic expansions are available in the literature[21], spectral simulations of the matrix absorption and emission spectroscopies are undertaken in this study. The simulations completed are an extension of the pair-potentials approach the Maynooth group has implemented in the Zn/RG[28] and Cd/RG[47] matrix systems. The results of these calculations are presented in Chapter IV.

Following the theoretical work, it was necessary to extend the experimental analysis of the emission spectroscopy to provide sufficient information for comparison with predictions. The aspects relating to the spectroscopy of the 6p $^3P_1$ and 6p $^3P_0$ states will be addressed in the luminescence spectroscopy reported in Chapter III.

In Chapter V, the Hg/RG_{18} pair-potentials calculations, presented in Chapter IV for RG = Ar, Kr and Xe, are extended to model the luminescence of the atomic Hg 6p $^3P_1 \leftrightarrow$ 6s $^1S_0$ transition in solid neon, reported by Chergui and co-workers[48,49]. In addition, the localised Hg/RG_{18} model was extended to simulate the emission spectroscopy of the atomic Hg 6p $^3P_0 \rightarrow$ 6s $^1S_0$ transition reported in Chapter III.

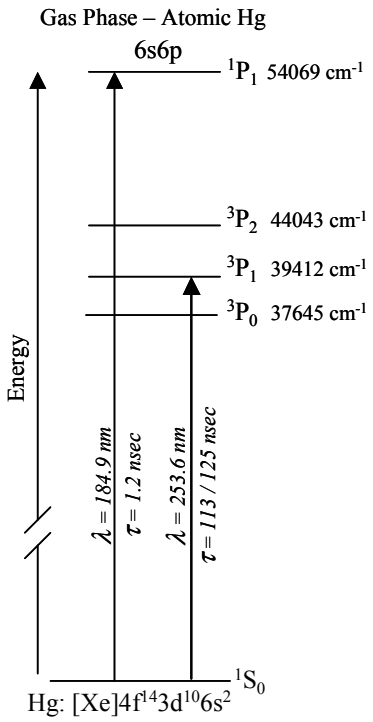

Figure I.4 **Schematic of the energy levels of atomic Hg[46] the arrows indicate the allowed transitions and there energies in wavenumber units above the ground $^1S_0$ state of atomic Hg. The gas phase lifetimes[50,51,52] of the transitions are also presented.**

I.5.II Mn/RG

Like mercury[17], manganese[53] was one of the earliest metal atom systems to be investigated with the matrix-isolation technique. Since the first report by Schnepp[53] on the absorption spectroscopy of atomic Mn/RG solids, further work has appeared in the literature, including a review of the UV/Vis absorption spectroscopy of Mn/RG solids[18,54,55]. In contrast, no reports of the Mn/RG luminescence spectroscopy of atomic manganese have appeared to date. Therefore, the experimental work presented in Chapters VI – IX report both the UV/Vis absorption and luminescence spectroscopy of Mn isolated in solid Ar, Kr and Xe. The motivation for this being the similarities between atomic manganese, which exhibits an ns^2 ground state electronic configuration and M/RG systems such as Mg[23,24] where the solid-state spectroscopy has been studied in detail. The similarities in the gas phase spectroscopy of Mg and Mn is evident on inspection of Figure I.5.

The lowest energy electronic configuration of atomic Mn is [Ar]3d^{5}4s^2 giving rise to the spherically symmetric $a^6S_{5/2}$ ground state. Chapter VI presents the UV/Vis

absorption spectroscopy of Mn/RG (RG = Ar, Kr and Xe) solids. The aim of this being to assign the of s → p electronic type transitions of Mn atoms from the ground $a^6S_{5/2}$ state to the excited Mn [Ar]$3d^5$4s4p states. The excited states are the 'singlet-like' [$3d^5(^6S)$4s4p($^1P°$)] y^6P and 'triplet-like' [$3d^5(^6S)$4s4p($^3P°$)] z^6P states occurring in the gas phase[56] at 35,725.85 cm^{-1} (279.91 nm) and 24,788.05 cm^{-1} (403.42 nm), as shown in Figure I.5. Following the identification of the fully allowed $y^6P \leftarrow a^6S$ and $z^6P \leftarrow a^6S$ transitions in Chapter VI, the subsequent Chapter presents the luminescence spectroscopy of Mn/RG solids following resonant ($z^6P_{5/2} \leftarrow a^6S_{5/2}$) excitation with continuous and pulsed light sources. Excitation spectra are recorded to resolve multiple site occupancies, which are, convoluted in the absorption spectra and determine the matrix shifts of $z^6P_{5/2} \leftarrow a^6S_{5/2}$ transition in each solid. High-resolution time-integrated and time-resolved emission spectra are recorded following resonance excitation to assign the observed emission features to radiative transitions from excited states of the Mn atom that occur to lower energy than the z^6P state. Excited state lifetime measurements are reported to identify the excited state dynamics, inter-system crossing and inter-multiplet relaxation processes leading to the observed emission bands.

Although the absorption spectra of atomic manganese and magnesium share many characteristics, the existence of several atomic states (a^4D, z^8P and a^6D) that occur to lower energy than the z^6P state means that the emission spectra of the former is complex. The spectral regions of the 'forbidden' $3d^5$4s4p $z^8P_{5/2} \leftrightarrow 3d^5$4$s^2$ $a^6S_{5/2}$ and $3d^6$4s $a^6D_{5/2} \leftrightarrow 3d^5$4$s^2$ $a^6S_{5/2}$ atomic transitions at 543.4 and 573.0 nm, (18402.46 and 17451.52 cm^{-1}) were investigated with direct dye laser excitation. The intrinsic high-resolution of the laser coupled with the high intensity, allows excitation spectra for both of these forbidden transitions to be recorded. These spectra also provide a comparison of the absorption characteristics of Mn atoms undergoing P ← S or D ← S transitions. The emission spectroscopy recorded following direct laser excitation of the z^8P and $a^6D \leftarrow a^6S$ transitions provides more definitive state assignments of the emitting levels.

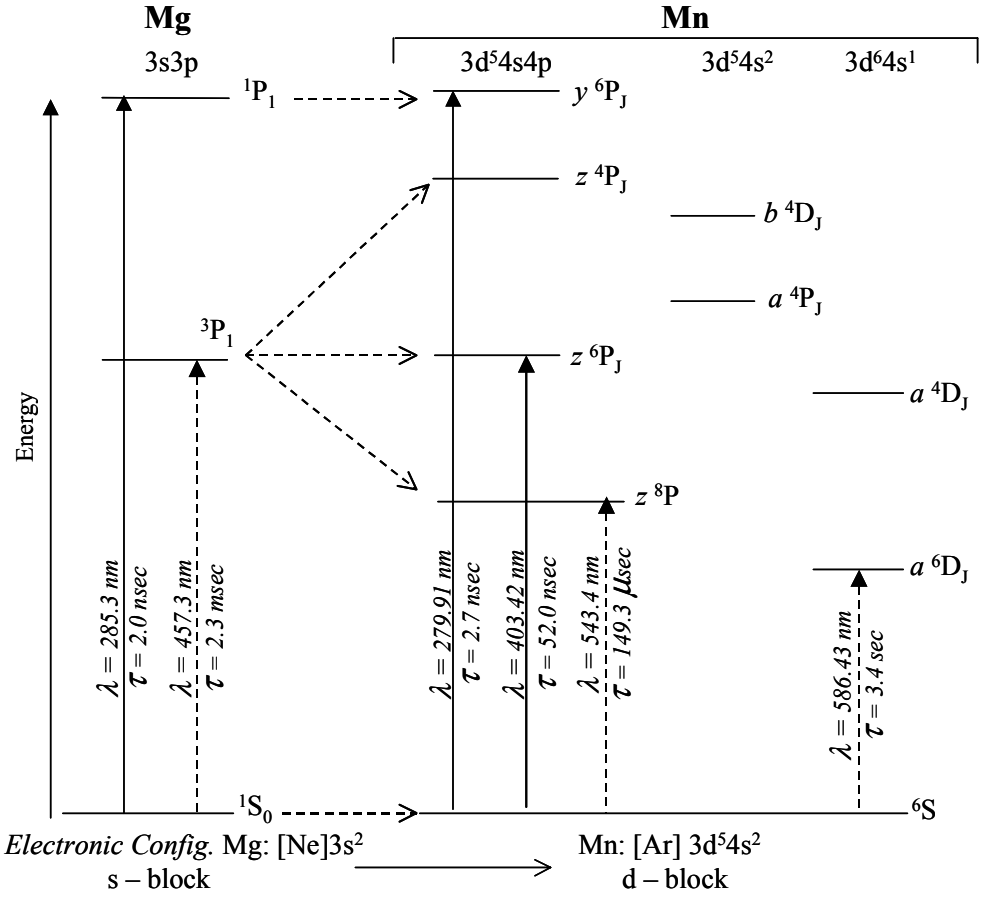

Figure I.5 **Schematic representation of the energy levels of gas phase atomic manganese[56] The allowed $y^6P_{5/2} \leftarrow a^6S_{5/2}$ and $z^6P_{5/2} \leftarrow a^6S_{5/2}$ transitions occur at 35726 cm^{-1} (279.91 nm) and 24788 cm^{-1} (403.42 nm) respectively, are indicated by arrows.**

Chapter IX provides a comparison of the excitation spectroscopy recorded for the y^6P, z^6P and z^8P $\leftarrow a^6$S transitions of atomic Mn. Allied with the similarities of the Mn/RG systems and those of Mg/RG systems, an attempt is made to identify the site or sites of Mn atom isolation in each RG system employing the polarizability model of Laursen and Cartland[33].

All of the experimental data reported in this thesis was recorded in the Low Temperature Laboratory in the Department of Chemistry, National University of Ireland – Maynooth, with the exception of the Hg($^3P_1$)/Ne luminescence data which was provided by M. Chergui and co-workers[48,49]. The specifics of the experimental apparatus and spectroscopic techniques used to achieve these results are presented in Chapter II.

References

[1] IUPAC Compendium of Chemical Terminology; 2nd Edition, (1997). Free text search for 'matrix-isolation' http://www.chemsoc.org/cgi-shell/empower.exe (Last accessed 7th June 2004)

[2] L. Vegard, *C. R. Acad. Sci.*, **176**, 941 (1923).

[3] L. Vegard, H. Kamerlingh-Onnes and W. H. Keesom, *C. R. Acad. Sci.*, **180**, 1084 (1925).

[4] L. Vegard, *Ann. Phys.*, **6**, 487 (1930).

[5] G. N. Lewis and D. Lipkin, *J. Am. Chem. Soc.*, **64**, 2801 (1942).

[6] I. Norman and G. Porter, *Nature*, **174**, 508 (1954).

[7] I. Norman and G. Porter, *Proc. Roy. Soc.*, **A230**, 399 (1955).

[8] E. Whittle, D. A. Dows and G. C. Pimentel, *J. Chem. Phys.*, **22**, 1943 (1954).

[9] E. D. Becker and G. C. Pimentel, *J. Chem. Phys.*, **25**, 224 (1956).

[10] E. D. Becker, G. C. Pimentel and M. Van Thiel, *J. Chem. Phys.*, **26**, 195 (1957).

[11] B. Meyer, *Low Temperature Spectroscopy*, American Elsevier Publishing Company Inc., New York, 1971.

[12] D. W. Ball, Z. H. Kafafi, L. Fredin, R. H. Huage and J. L. Margrave, Rice University Houston, *A Bibliography of Matrix Isolation Spectroscopy*, 1954 – 1985, 1988.

[13] M. Moskovits and G. A. Ozin, *Cryochemistry*, Wiley – Interscience, New York, 1976.

[14] L. Andrews and M. Moskovits, *Chemistry and Physics of Matrix – Isolated Species*, North – Holland, Amsterdam, 1989.

[15] H. E. Hallam, *Vibrational Spectroscopy of Trapped Species*, Wiley – Interscience, New York, 1973.

[16] I. Dunkin, *Matrix - Isolation Techniques*, (A Practical Approach), Oxford University Press, 1998.

[17] M. McCarthy and G. W. Robinson, *Mol. Phys*., **2**, 415 (1959).

[18] D. M. Gruen, Spectroscopic Identification and Characterization of Matrix Isolated Atoms in *Cryochemistry*, edited by M. Moskovits and G. A. Ozin, Wiley – Interscience, New York, 1976.

[19] B. Meyer, *Ber. Bunsenges. Phys. Chem*., **82**, 24 (1978).

[20] C. Crepin-Gilbert and A. Tramer, *Intl. Rev. Phys. Chem*., **18**, 485 (1999).

[21] W.H. Breckenridge, C. Jouvet, B. Soep, in: M. Duncan (Ed.), *Advances in Metal and Semiconductor Clusters*, Vol. 3, JIA Press, Greenwich, CT, 1995.

[22] M. Quigley, *M.Sc. Thesis*, National University of Ireland – Maynooth, Maynooth, Co. Kildare, Ireland, 2002, (*unpublished results*).

[23] J.G. McCaffrey and G. A. Ozin, *J. Chem. Phys.*, **101**, 10354 (1994).

[24] P. Kerins, B. Healy and J.G. McCaffrey, *Low. Temp. Phys.*, **26**, 756 (2000).

[25] V. A. Bracken, P. Gürtler and J.G. McCaffrey, *J. Chem. Phys.*, **107**, 5290 (1997).

[26] B. Healy and J.G. McCaffrey, *J. Chem. Phys.*, **110**, 3903 (1998).

[27] M. A. Collier and J. G. McCaffrey, *J. Chem. Phys.*, **119**, 11878, (2003).

[28] J.G. McCaffrey and P. N. Kerins, *J. Chem. Phys.*, **106**, 7885 (1997).

[29] C. Kittel, *Introduction to Solid State Physics*, 6th Edition, Wiley and Co, New York, 1986, p. 12.

[30] K. Fuke, S. Takayuki and K. Kaya, *J. Chem. Phys.*, **81**, 2591 (1984).

[31] R. A. Aziz and M. J. Slaman, *Chem. Phys.*, **130**, 187, (1989).

[32] J.G. Kaup and W.H. Breckenridge, *J. Phys. Chem.*, **99**, 13701 (1995).

[33] S. L. Laursen and H. E. Cartland, *J. Chem. Phys.*, **95**, 4751 (1991).

[34] K. Huang and A. Rhys, Proc. Roy. Soc. (London) **204A**, 406 (1950), reprinted in *Selected papers on Photoluminscence of Inorganic Solids*, edited by M.J. Weber, SPIE-The International Society of Optical Engineering, Washington, 1998.

[35] V. E. Bondybey and L. E. Brus, *Adv. Chem. Phys.*, **41**, 269 (1980).

[36] H. A. Jahn and E. Teller, *Phys. Rev.*, **49**, 874 (1936).

[37] H. A. Jahn and E. Teller, *Proc. Roc. Soc.*, (London) **A161**, 220 (1937).

[38] W. W. Duley and J. Ryan, *Chem. Phys. Letts.*, **21**, 208 (1973).

[39] M. Brith and O. Schnepp, *J. Chem. Phys.*, **39**, 2714 (1963).

[40] L. A. Andrews and G. C. Pimentel, *J. Chem. Phys.*, **47**, 2905 (1967).

[41] B. Bleaney and D. J. E. Ingram, Proc. Phys. Soc. (London), **A63**, 408 (1950); F. Ham, *Electron Paramagnetic Resonance*, S. Geschwind, Plenum, New York, 1972; M. C. M O'Brien, *Vibrational Spectra and Structure*, Vol. 10, J. R. Durig, Chapter 5, Elsevier, 1981.

[42] R. L. Mowery, J. C. Miller, E. R. Krausz, P. N. Schatz, S. M. Jacobs and L. Andrews, *J. Chem. Phys.*, **70**, 3920 (1979).

[43] P. A. Lund, D. Smith, S. M. Jacobs and P. N. Schatz, *J. Phys. Chem.*, **88**, 31 (1984).

[44] M. C. M. O'Brien, *J. Chem. Phys.*, **82**, 3870 (1995).

[45] J. Rose, D. Smith, B. E. Williamson, P. N. Schatz and M. C. M. O'Brien, *J. Phys. Chem.*, **90**, 2608 (1986).

[46] Atomic Energy Levels, Volume 3, Circular 467, *Department of Commerce United* States of America.

[47] B. Healy and J. G. McCaffrey, *J. Phys. Chem. A*, **104**, 3553 (2000).

[48] J. Helbing, A. Haydar and M. Chergui, *Chem. Phys. Letts.*, **310**, 43, (1999).

[49] J. Helbing, A. Haydar and M. Chergui, *J. Chem. Phys.*, **113**, 3621, (2000).

[50] E. H. Pinnington, W. Ansbacher, J. A. Kernahan, T. Ahmad and Z. Q. Ge, *Can. J. Phys.*, **66**, 960 (1988).

[51] K. A. Mohamed, *J. Quant. Spectrosc. Radiat. Transfer*, **30**, 225, (1982).

[52] NIST, Physics Laboratory, Physical Reference Data, *www.physics.nist.gov*

[53] O. Schnepp, *J. Phys. Chem. Solids,* **17**, 188 (1960).

[54] E. L. Lee and R. G. Gutmacher, *J. Phys. Chem. Solids*, **23**, 1823 (1962).

[55] D. M. Mann and H. P. Broida, *J. Chem. Phys.,* **13**, 84 (1971).

[56] N.I.S.T. Atomic Spectra Database, Website: http://physics.nist.gov/cgi-bin/AtData/display.ksh?/XXE0qMnqIXXP-15XXT2XXS, (Last accessed 4th February 2004).

Chapter II

Experimental

II.1 Introduction

The experimental work involved the production and spectroscopic interrogation of low temperature solids doped with metal atoms. The sections which follow, develop the general remarks made in Chapter I on the matrix–isolation technique to provide specific details of the equipment and methods employed to achieve the results reported.

Solid M/RG (M = Mn and Hg, RG = Rare gases Ar, Kr and Xe) samples were prepared by co-condensing manganese or mercury vapour with the host gas onto a calcium fluoride (CaF_2) window at temperatures ranging from 12 to 35 K. The M/RG thin-films were characterised spectroscopically using both steady-state and time-resolved methods. This section is arranged in the following format, firstly the physical components comprising the matrix-isolation apparatus (MIA) used to achieve the deposition temperatures are described. Secondly, an account of the gas handling system (GHS) and the precautions taken to ensure sample purity is provided. Thirdly, the procedure of M/RG sample preparation and deposition on the cryogenic substrate is outlined, including two methods of metal vapour generation based on the physical properties of the bulk metals, Hg and Mn. Finally, a comprehensive description of the luminescence spectrometer used in the steady-state and time-resolved measurements is provided in addition to the continuous lamp and pulsed laser excitation sources.

II.2 Matrix – isolation apparatus

A typical matrix-isolation apparatus like that described by Ozin and Moskovits[1,2] was used during the course of this work as shown in Figure II.1. Vacuum, typically in the low 10^{-7} mbar range, was maintained in the sample chamber at room temperature using an Edwards *Speedivac* oil diffusion pump, model E02 backed by an Edwards Rotary Pump, model RV3. The vacuum was monitored using an Alcatel CF2P penning gauge. An Edwards cold trap filled with liquid N_2 (77 K) also minimised contamination of the deposition substrate from the diffusion pump oil. Following ‘cool–down’ to 12 K and prior to sample deposition the vacuum dropped to

approximately $9x10^{-8}$ mbar. A quarter swing butterfly valve, Edwards QSBR allowed isolation of the sample chamber from the pumping system for venting. Table II.1 outlines the individual components of the pumping system used to attain the high vacuum in the sample chamber[3].

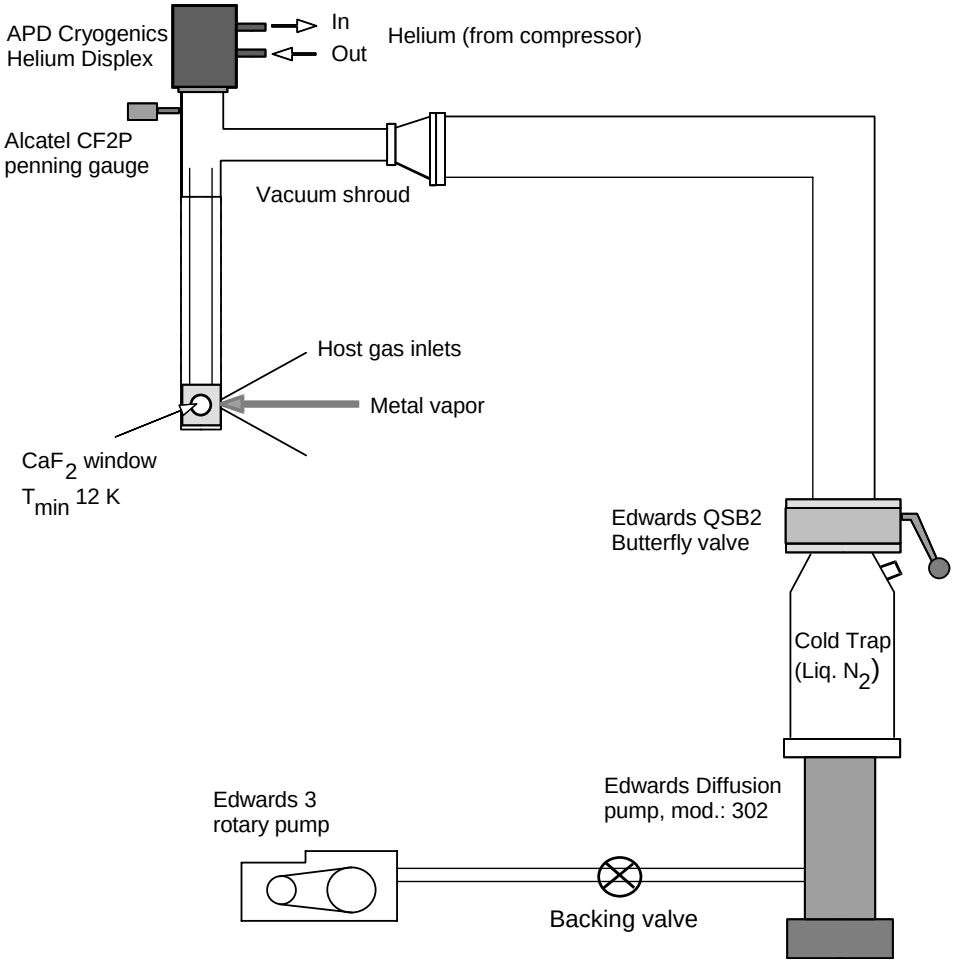

Figure II.1 **A representation of the matrix-isolation apparatus showing the pumping systems employed.**

Table II.1 **Equipment employed to achieve and monitor the vacuum in the sample chamber prior to and during sample deposition.**

Component	Manufacturer	Model/Part Number
Rotary pump	Edwards	RV3
Diffusion pump	Edwards	E02
Butterfly valve ($^1/_4$ swing)	Edwards	QSB2
Penning gauge	Alcatel	CF2P

A minimum temperature of 12 K was achieved at the CaF_2 window with an APD Cryogenics closed–cycle helium displex system, shown in Figure II.2. High-pressure

helium (270 psi) was admitted to the refrigeration unit via gas lines from an APD Cryogenics compressor[4], model HC-2. The two–stage refrigeration unit (expander) APD Cryogenics model DE-202 operates on the Gilford-McMahon refrigeration cycle at 50 Hz[5]. 'Cool-down' to 12 K was typically achieved in 70–80 minutes. Temperature was monitored and controlled with a Scientific Instruments 9600–1 silicon diode[6] and heater mounted on the copper holder of the CaF_2 window. Good thermal contact is achieved between the window and copper holder using an indium wire seal[7]. The refrigeration components and manufacturers are listed in Table II.2.

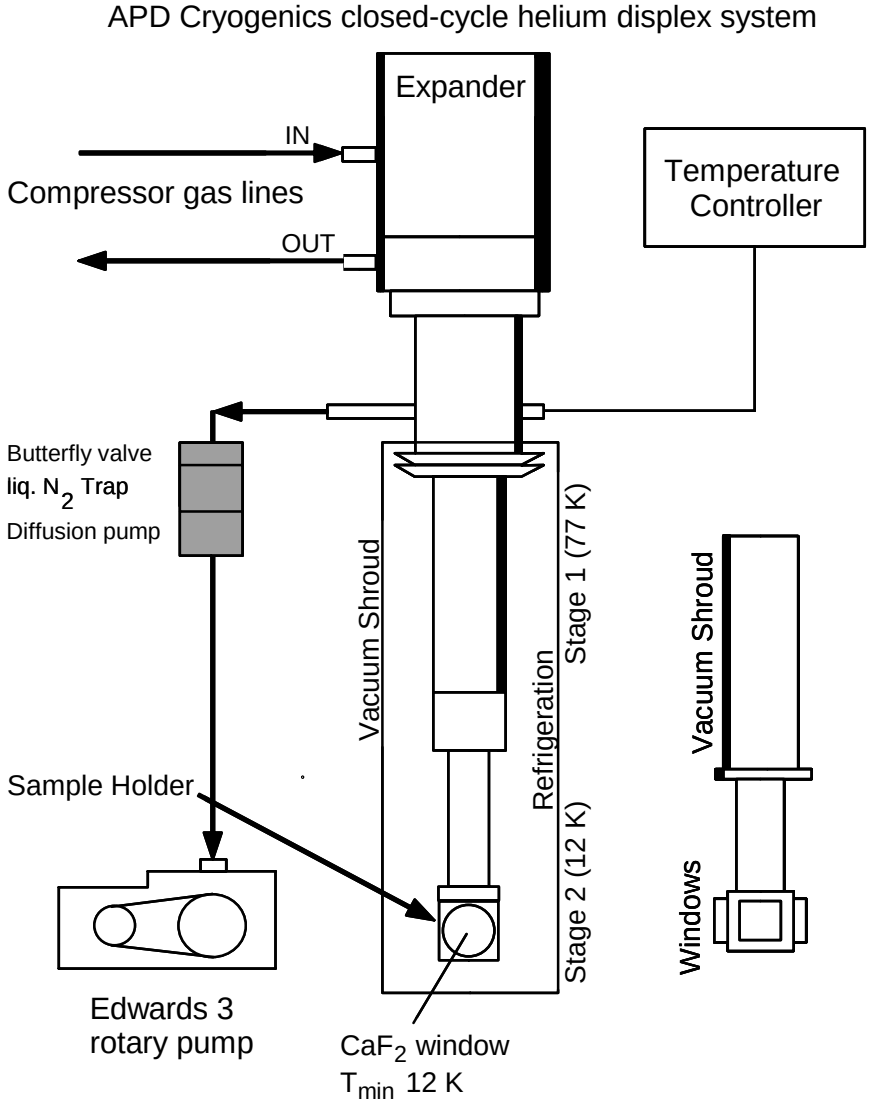

Figure II.2 **A representation of the APD Cryogenics closed-cycle helium displex system used to achieve the deposition temperatures required to for M/RG matrices showing the two – stage refrigeration system operated by the DE-303 expander[4].**

Table II.2 **Experimental apparatus used to attain cryogenic conditions (minimum temperature 12 K) at the CaF_2 window required to deposit M/RG thin films.**

Component	Manufacturer	Model/Part Number
Helium compressor[5]	APD Cryogenics	HC-2
Two – stage refrigerator[4]	APD Cryogenics	DE-202

II.3 Gas handling system, (GHS)

The matrix gases were handled using a dedicated gas handling system, (see Figure II.3) maintained at vacuum in the low 10^{-8} mBar range by a Pfeiffer Balzers turbo-molecular (TPU–180H) pump,[8] backed by a diaphragm pump[9]. An ionization gauge[10], combined with a Granville–Phillips (GP) vacuum gauge controller[11] (model 307), was used to monitor the vacuum in the GHS. The amounts of host gas in the gas handling system before and after sample deposition was monitored by two baratron gauges (Tylan General CDLD-11 and 31) sensitive in the ranges 0 – 10 and 0 – 1000 Torr respectively[12]. This allowed the rate of gas deposition to be determined. The RG was admitted to the sample chamber via a Granville–Phillips variable leak valve, (Type 203)[10]. It allowed isolation of the gas handling system from the matrix rig at all times except during sample deposition. The individual components comprising the GHS are listed in Table II.3.

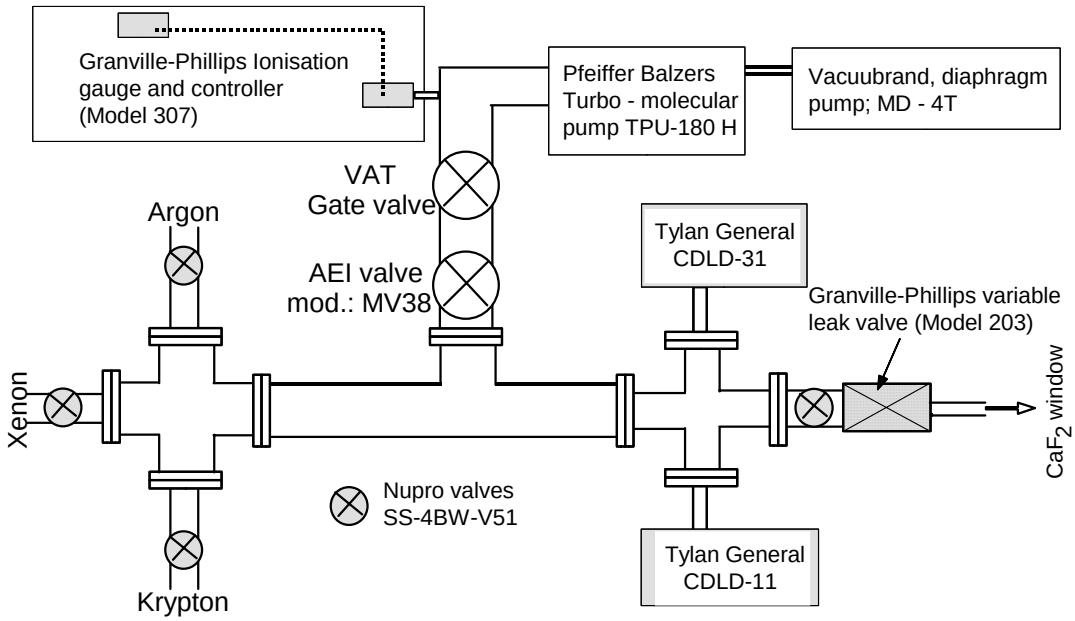

Figure II.3 **A schematic of the gas handling system.**

Table II.3 **Experimental apparatus used to maintain and monitor the vacuum in the gas handling system.**

Component	Manufacturer	Model/Part Number
Turbo – molecular pump[8]	Pfeiffer Balzers	TPU-180H
Diaphragm pump[9]	Vacuubrand	MD-4T
Ionisation gauge[11]	Granville – Phillips	307

II.4 M/RG sample preparation

Solid M/RG samples were prepared by co-condensing metal vapour with the host gases listed in Table II.4 onto a CaF_2 window at temperatures ranging up to approximately one quarter the melting point of the host gas depending on the sample characteristics under investigation. The method of metal vapour generation selected was specific to the physical properties of the metal. The two different techniques employed are discussed individually.

Table II.4 **Matrix host gases, purity and suppliers. The melting point of the host gases (M_p) in Kelvin.**

Host Gas	Purity	Supplier	M_p (K)[7]
Argon, (Ar)	99.998 %	BOC Gases	83.9
Krypton, (Kr)	99.998 %	Linde Gas UK	116.6
Xenon, (Xe)	99.998 %	Linde Gas UK	161.2

II.4.I Metal vapour generation, Mercury

The deposition method used for mercury, exploits its high vapour pressure whereby metal 'pick-up' by the matrix gases flowing over a Hg reservoir at room temperature, (296 K) entrains sufficient Hg vapour to produce moderately absorbing samples (OD = 0.9). Mercury has a vapour pressure (v.p.) of 1 x 10^{-3} Torr[14] at 16 °C. The reservoir consisted of a 15 cm long stainless steel tube, 1.5 cm in diameter containing 1 cm^3 of mercury, connected by one quarter inch tubing to the gas inlet of the matrix shroud. Pick-up is controlled by the three-way valve arrangement shown in Figure II.4, where two valves isolate the reservoir from the matrix rig, except during Hg/RG sample formation, when they are opened and a third valve, directly connecting the

GHS to the matrix, is closed. Freeze-pump-thaw cycles were used to remove air from the reservoir after the initial fill with mercury.

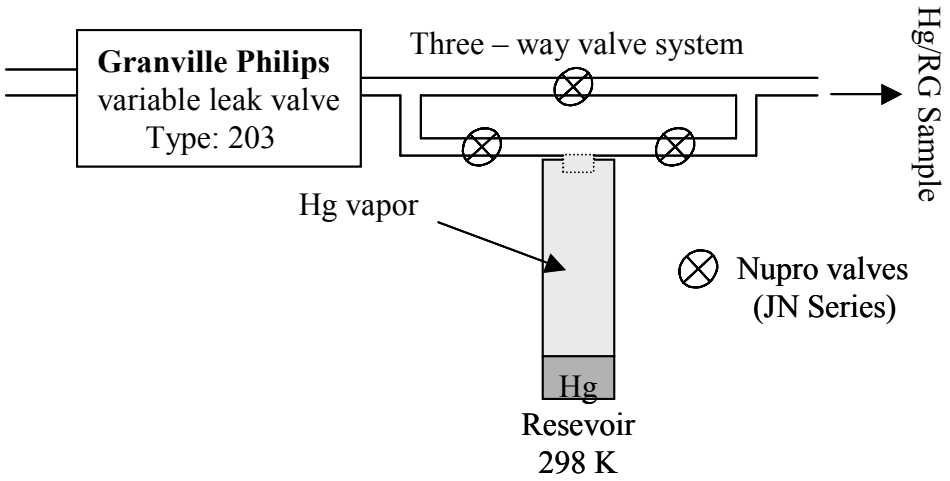

Figure II.4 A schematic of the three-way valve system used in the Hg 'pick–up' deposition.

II.4.II Metal vapour generation, Manganese

Manganese vapour was generated by electron bombardment (sputtering) of the bulk metal using an ultra-high vacuum Omicron evaporator, Model EFM3 (Evaporator with integral Flux Monitor)[13] shown in Figure II.5. Manganese is a high temperature metal with a melting point of 1244 K and a vapour pressure 1 $x10^{-3}$ torr[14] at 1108 K. The electron beam from a tungsten filament is as shown in Figure II.6 focused on irregular manganese pieces[15,16] (Goodfellow, Johnson Matthey; purity >99.5%) contained in a molybdenum crucible. The bombardment induces localised heating in the metal resulting in evaporation. The integrated flux monitor indicated the metal flux generated with this vaporisation. However, the absolute quantity of metal deposited in samples was ascertained from absorption spectroscopy, as irregular size Mn pieces were used the flux observed was dependent on the packing and subject to change as consistent loading of the crucible was not possible. Therefore, the flux monitored during sample deposition served only as a guide. The specifications of the EFM3, Mo crucible and the bulk metal are presented in Table II.5.

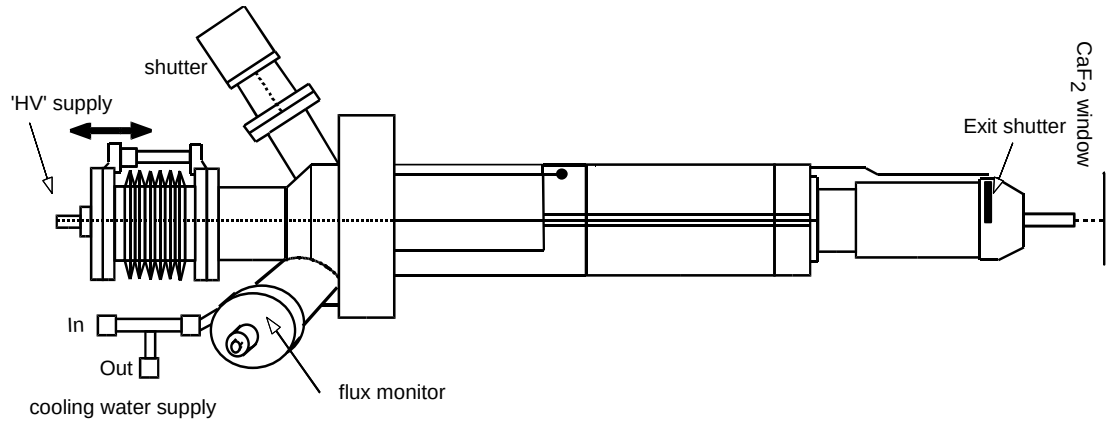

Figure II.5 **A representation of the metal atom source Omnicron UHV EFM3 evaporator showing the orientation of the source with respect to the sample substrate CaF_2 and the electrical and physical connections required for operation.**

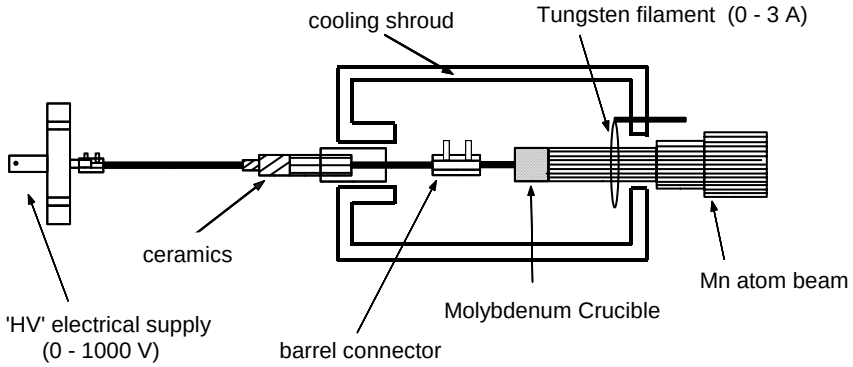

Figure II.6 **An illustration of the molybdenum crucible (containing the bulk manganese) and its immediate environs showing the relative positions of the filament and the exit path of the metal atom vapour within the Omnicron UHV EFM3 evaporator.**

This study centres on the atomic spectroscopy of metal atoms, therefore, low metal atom fluxes were used with an excess of the host gas to ensure atomic isolation dominated. Typically, for manganese, 700 V was applied to the EFM3 and filament currents (I_{Fil}) ranging from 1.3 to 1.5 A were used to achieve Mn/RG samples containing the maximum amount of isolated metal atoms while limiting the content of higher metal atom aggregates formed from metal nucleation during deposition.

To ensure sample purity and limit the effect of contaminations from the evaporation, such as MnO_2 adsorbed on the metal surface, the evaporant was degassed prior to depositing samples. This was done following each fill of the crucible. This procedure was completed in two stages. First, the filament was degassed by slowly increasing the filament current ($I_{Fil.}$) without high voltage. Second, the bulk metal was evaporated under the normal conditions (see above) with

the exit shutter (Figure II.5) closed until a stable flux could be maintained without any noticeable pressure rise in the sample chamber. This procedure was employed to remove the adsorbed species as the flux arising from these contaminants reduces over time whereas the remaining stable flux is due to the vaporisation of the bulk metal.

Table II.5 **Manufacturers of the equipment and the specific dimensions where appropriate for the UHV evaporator, molybdenum crucible and bulk manganese.**

Apparatus	Manufacturer	Model	Specifications
Evaporator	Omicron[13]	UHV EFM3	I_{Fil}: 0 – 2.5 A
			Voltage: 0 – 1000 V
Crucible	Omicron	Molybdenum	Outer diameter: 5.0 mm
			Inner diameter: 3.5 mm
			Capacity: 75 mm^3
			Temperature (max): 2200 K
Manganese	Goodfellow[15]	-	Condition: Irregular pieces
			Purity: 99.5 %
	Johnson Matthey[16]	-	Condition: Irregular pieces
			Purity: 99.99 %

Although the method by which the mercury and manganese vapours were produced are different, both present specific difficulties with respect to purification. However, once the vapour was achieved, the co-condensation with the host gas was completed as follows. Firstly, a layer of pure host gas (RG) was allowed to deposit on the CaF_2 window to minimise metal nucleation and contaminant build up at the sample window. This precaution limited the amount of sample-to-sample cross contamination. Secondly, the metal vapour was admitted and co-condensed with the rare gas of interest. In the case of Hg, this was achieved by allowing metal 'pick–up' to proceed. Opening the EFM-3 exit shutter allowed the co-condensation of Mn/RG samples to begin. The samples reported here were deposited at a rate of 8-10 mmol/hr for a period of 30 minutes. The same M:RG ratios and sample thickness were achieved by varying the two factors which govern the deposition rate; a) the backing pressure (P_{bk}) in the GHS and b) the flow rate selected for the Granville – Phillips variable leak valve.

II.5 Luminescence measurements

Following deposition of the M/RG thin films, the spectroscopic measurements reported in the following chapters were conducted using three optical arrangements, which can be considered in two classes depending on the excitation source employed. A) *Continuous Lamp Excitation* yielding steady–state excitation and emission spectra and B) *Pulsed Laser Excitation* allowing excitation and emission spectra and temporal measurements of the emission to be made.

II.5.I Steady-state spectroscopy (continuous lamp excitation)

A deuterium[17] (Hamamatsu L6310 and a Cathodeon C713 power supply[18]) and/or tungsten lamp (30 W, GE Model DZA) were used as the light sources for the ultra-violet (UV, 180–500 nm) and UV/Vis (350–600 nm)[19] spectral regions respectively to record both absorption and excitation spectra. An Acton Research Corporation (ARC) 0.30 m SpectraPro–300i monochromator[20] fitted with a 1200 grooves/mm diffraction grating, blazed at 300 nm was used for wavelength selection. The absorption, excitation and emission spectra reported later employed the highest resolution gratings (1200 grooves/mm) fitted in both ARC SpectraPro monochromators. However, both monochromators were fitted with additional diffraction gratings, the specifications of which are listed in Table II.6. Figure II.7 presents a schematic of the spectrometer employed for continuous lamp absorption and luminescence spectroscopies. The monochromatic light transmitted through the thin film M/RG matrix samples, located on a vertical CaF_2 window[21], was focused onto a photomultiplier tube (Hamamatsu, 1P28[22]) by means of a quartz focusing lens (Fl1) (Figure II.7) mounted with the PMT on the sample chamber. Absorption spectra of the M/RG samples were obtained in the usual manner by rationing sample transmittance spectra with their corresponding blanks, i.e., pure RG films, (RG_{bl}). The absorbance[23] quantified in terms of the optical density (O.D.) is calculated using the Equation II.1,

$$O.D. = - \log_{10} (I/I_0) \qquad \text{Equation. (II.1)}$$

Assuming the same sample thickness for the M/RG sample and the corresponding rare gas blank RG_{bl}, the absorbance was calculated using the following substitutions, $I = I(M/RG)$ and $I_0 = I(RG_{bl})$.

An important consideration for optical measurements is the choice of the deposition substrate in this case calcium fluoride, CaF_2. The substrate should be transparent in the regions of the electromagnetic spectrum where the measurements are preformed. Calcium fluoride is transparent over the range 129–1176 nm[7]. Also the matrix material, must be optically transparent in the region of interest. The rare gases are ideal as they are transparent over a very wide spectral range from the far infrared to the vacuum UV. The far IR absorptions are due to phonon absorptions, lattice vibrations of the atoms within the solid matrix crystal. The vacuum UV absorptions of the rare gas crystals correspond to Frenkel excitons, the lowest energy transition occurring for solid xenon at 150 nm[23].

Emission from the M/RG samples was monitored perpendicular to the excitation axis by focussing emitted light onto the entrance slits of an ARC 0.5 m SpectraPro-500i monochromator[24] fitted with a 1200 g/mm grating, blazed at 300 nm. Photon detection was achieved using a Hamamatsu R928-P PMT[25] maintained at –20 °C in a Products for Research cooled-housing (Photocool S600)[26]. This PMT was operated in photon counting mode by relaying its signal via an amplifier/ discriminator module[27] (Electron Tubes Ltd, type AD6) to the ARC NCL data acquisition and controller unit. The specifications of the photo-multiplier tubes used are presented in Table II.7. The SpectraPro-500i emission monochromator was calibrated using the sodium D lines from a hollow cathode Na lamp, UV lines of molecular oxygen were used to calibrate the excitation monochromator SpectraPro-300i.

Table II.6 **The specifications of the Acton Research Corporation (ARC) monochromators used during the course of this work. Note * indicates the specifications refer to the 1200 grooves/mm gratings.**

ARC Monochromator	SpectraPro-300i[20]	SpectraPro-500i[24]
Focal length (mm)	300	500
Wavelength range (nm)	180 nm – far infrared	180 nm – far infrared
Gratings (grooves/mm) / Blaze (nm)	1200 / 300 300 / 300	1200 / 300 600 / 600 150 / 300
Resolution (nm)*	0.1 @ 435.8 nm	0.05 @ 435.8 nm
Dispersion (nm/mm)*	2.7	1.7
Accuracy (nm)*	± 0.2	± 0.2

Table II.7 **The specifications of the Hamamatsu photo-multiplier tubes (PMT's) employed during the course of this work. Note the IP28 was mounted on the sample chamber and used to monitor the radiation transmitted by the M/RG samples.**

Hamamatsu PMT	IP28[22]	R928-P[25]
Range (nm)	185 – 650	185 – 900
Peak wavelength (nm)	340	400
Photo-cathode material	Sb-Cs	Multialkali
Window material	UV glass	UV glass
Cathode sensitivity (μA/lm)	40	200
Anode sensitivity (A/lm)	200	2000
Response times – Rise time (ns)	2.2	2.2
Electron transit time (ns)	22	22

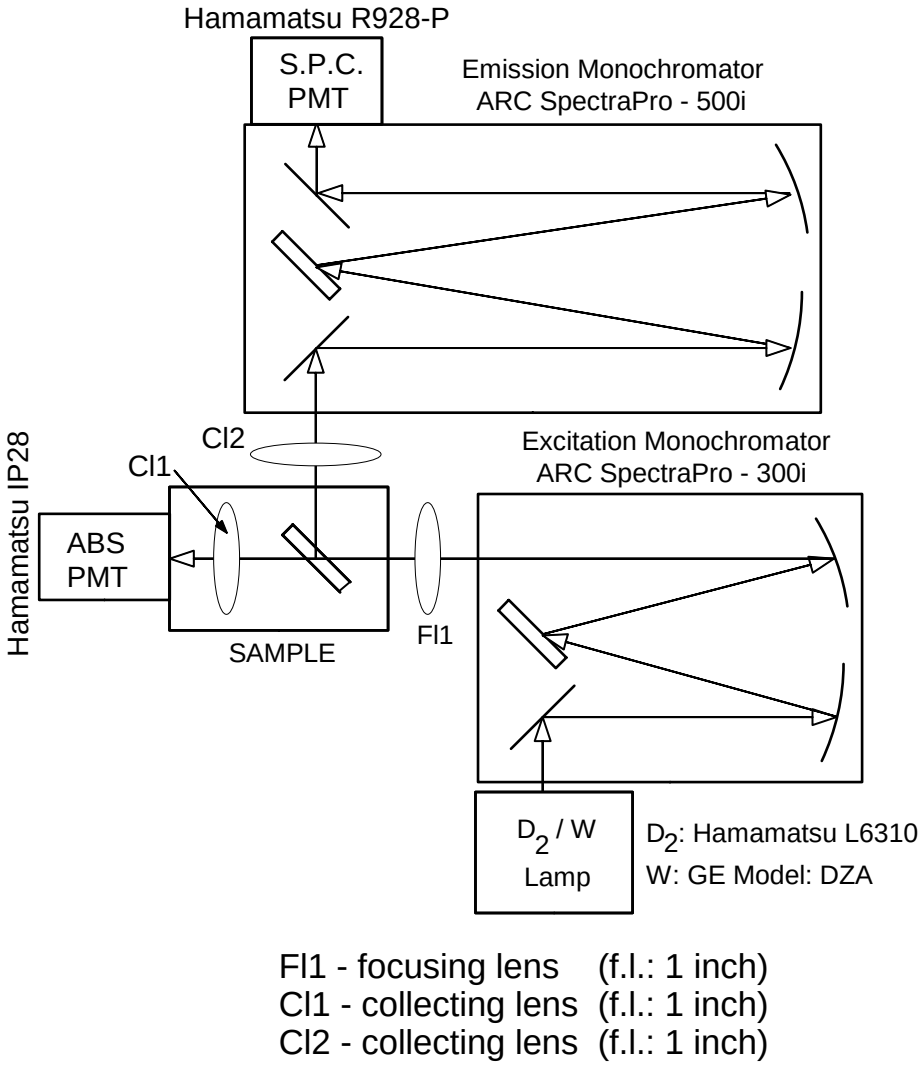

Figure II.7 **A Schematic of the luminescence spectrometer set–up used to record the steady–state (time–integrated) spectra.**

II.5.II Time-resolved spectroscopy

Emission spectra were also recorded with pulsed excitation using a Nd:YAG (Quantel YG 980E-10)[28] laser normally operating at a repetition frequency of 10 Hz. A dye laser[29] (Quantel TDL–90), pumped by either the second or third harmonics of the YAG, were used to produce tuneable laser radiation. The characteristics of the Quantel laser systems are presented in Table II.8.

Table II.8 The specifications of the Quantel laser systems.

Pump Laser System	**Nd:YAG, Quantel YG 980E**
Gain Medium	Neodymium-doped crystal (Yttrium – Aluminium – Garnet)
Repetition rate (Hz)	10, 5, 2,1
Energy (mJ) @ 1064, 532, 355 nm	850, 400, 165
Pulse duration (ns) @ 1064 nm	6
Flash-lamps	SFL 611.09N/RX
Flash-lamp Voltage (V)	1600
Q – Switch pre-pulse (ns)	500
Flash-lamp / Q – Switch delay (μs)	242
Dye Laser System	**Quantel TDL-90**
Tuning range (nm)	220 – 750
Linewidth (cm^{-1}) @ 560 nm	0.08

The wavelengths required for mercury atom excitation around 250 nm were achieved by mixing the residual Nd: YAG fundamental at 1064 nm with the doubled output of the dye laser using DCM (4-Dicyanmethylene-2-methyl-6-(p-dimethylaminostyryl)-4*H*-pyran) as the dye material. Manganese atom excitation in the UV at 280 nm was achieved by frequency doubling Rhodamine 590 (Benzoic Acid, 2-[6-(ethylamino)-3-(ethylimino)-2,7-dimethyl-3H-xanthen-9-yl]-ethyl ester, monohydrochloride). Manganese atom excitation in the 360-420 nm spectral region was produced by mixing the dye laser output with the Nd:YAG fundamental using DCM as the dye material. Table II.9 presents the details of the spectral characteristics of the dye materials used. KDP (Potassium Diphosphate) crystals, Quantel DCC2/3 and MCC1/2 were used to frequency double and mix respectively while quartz crystals, Quantel QCC1 and QCC2, were used to compensate for the walk of the resultant beams. The wavelength ranges accessible by frequency doubling and/or mixing the dye laser output are presented in Table II.10. Wavelength separation of

the final beam from residual beams was achieved with a Pellin-Broca prism, the UV output of which was trained onto the matrix sample (on a CaF_2 window) without focusing optics. The experimental arrangement of the laser is shown in Figure II.8.

The direct dye laser output was employed for pumping the forbidden a^6D and z^8P transitions Mn atom using Rhodamine 590 and Coumarin 500 as dye materials respectively. The former and the latter involved pumping with 2ω and 3ω of the Nd^{3+}:YAG at 532 and 355 nm respectively. Table II.9 presents the spectral characteristics of the dye materials. The use of the tuneable dye laser output allowed the acquisition of laser excitation spectra, using the arrangement shown in Figure II.8. Wavelength separation was not required using the direct dye output of the TDL-90 so the Pellin-Broca prism was replaced by a right-angled prism. Excitation spectra were recorded by scanning the dye laser wavelength monitoring a given emission band maximum. The excitation spectra recorded in this manner were not corrected for the intensity distribution of the dye material.

Table II.9 The specifications of the laser Dye materials employed for mercury and manganese atom excitation in RG solids.

Dye Material	Characteristic	Specification
DCM[30, 31]	Manufacturer	Exciton
(4-Dicyanmethylene-2-methyl-	Solvent	Ethanol
6-(p-dimethylaminostyryl)-4*H*-	Pump Source: Nd: YAG (nm)	532 (2ω)
pyran)	Absorption maximum, (nm)	472
$C_{19}H_{17}N_3$	Fluorescence maximum, (nm)	639
	Dye Laser Range, (nm)	615–666
Rhodamine 590[30, 31]	Manufacturer	Exciton
(Benzoic Acid, 2-[6-	Solvent	Ethanol
(ethylamino)-3-(ethylimino)-	Pump Source: Nd: YAG (nm)	532 (2ω)
2,7-dimethyl-3H-xanthen-9-yl]-	Absorption maximum, (nm)	530
ethyl ester, monohydrochloride)	Fluorescence maximum, (nm)	566
$C_{28}H_{31}N_2O_3Cl$	Dye Laser Range, (nm)	555–580
Coumarin 500[30, 31]	Manufacturer	Exciton
(7-Ethylamino-4-	Solvent	Ethanol
trifluormethycoumarin)	Pump Source: Nd: YAG (nm)	355 (3ω)
$C_{12}H_{10}NO_2F_3$	Absorption maximum, (nm)	395
	Fluorescence maximum, (nm)	495
	Dye Laser Range, (nm)	498–546

Table II.10 **Details of the technical processes used to achieve the laser frequencies[29] required for UV mercury and UV-Vis. Manganese atom excitation.**

M/RG System	Wavelength Range, nm	Technical Process	Crystals	Dye Material
Hg	231–272	Frequency Mixing after Doubling	MCC2/QCC2 DCC2/QCC1	DCM
Mn (UV)	267–325	Frequency Doubling	DCC3/QCC1	Rhodamine 590
Mn (Vis.)	360–420	Frequency Mixing	MCC1/QCC2	DCM

Typical laser fluence of 20 μJ/mm^2, measured with a Molectron power-max 500A meter and PM10V1 head, was achieved in the 250 nm spectral region using only the oscillator and pre–amplifier stages of the TDL-90 dye laser. The linewidth of the dye laser is 0.8 cm^{-1} at 560 nm.

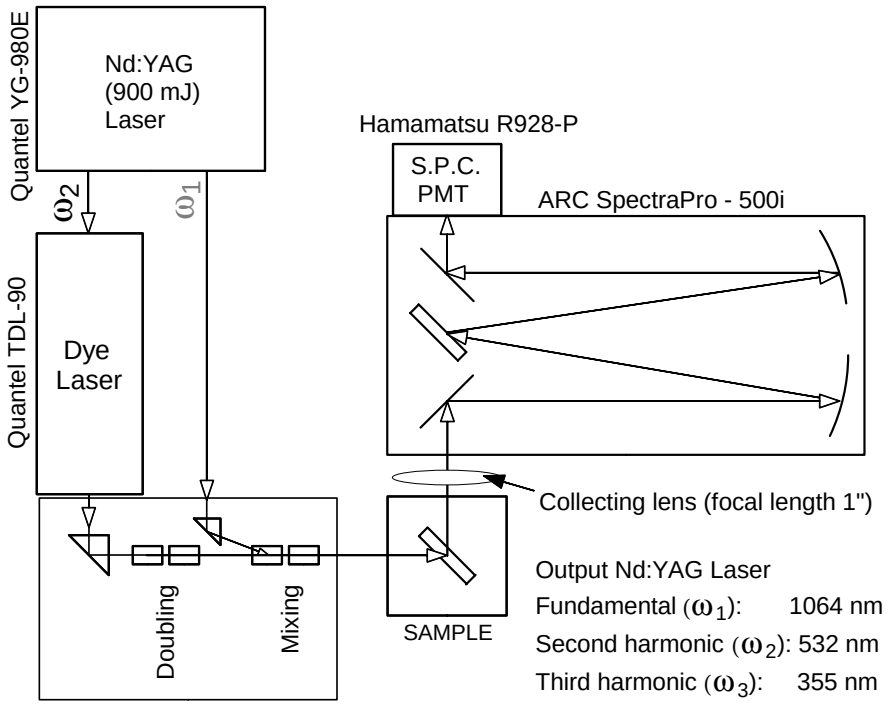

Figure II.8 **A representation of the luminescence spectrometer and the interaction with the Quantel Nd:YAG (YG-980E) pumped Dye laser (TDL-90) used to record the time-resolved luminescence of M/RG samples following UV/Vis excitation at a repetition frequencies of 1 to10 Hz.**

Emission was monitored perpendicular to the laser beam and recorded in the photon counting manner described previously for the steady-state measurements, except that each data point in the spectrum was obtained by averaging ten laser shots. Recording emission spectra in the manner described above provided temporal

resolution as coupling high intensity, low repetition excitation (Nd:YAG laser, 10 Hz) with single photon counting introduced a time–gating which favoured long lived emission over short-lived (nanosecond) fluorescence.

Time–resolved emission spectra were also recorded using an Andor Technologies iStar iCCD (Intensified Charge Coupled Device) camera mounted[32] on the ARC SpectraPro 500i as shown in Figure II.9. A swing mirror allowed the emitted radiation dispersed by the diffraction grating to fall directly on the iCCD camera.

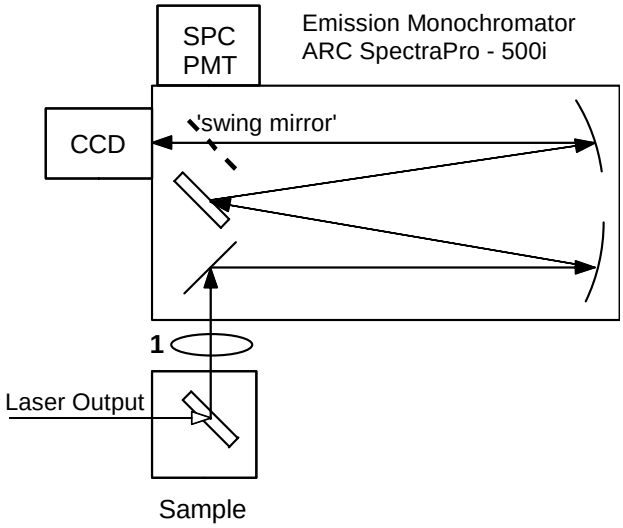

Figure II.9 **An illustration of the experimental set–up depicting the relative positions of the iCCD camera, swing mirror and single photon counting photomultiplier tube (SPC PMT) on the emission monochromator.**

A personal computer equipped with the Andor iStar software and controller card (CCI–010), allowed control of the iCCD unit and ARC SpectraPro 500i monochromator via the Remote Scan Controller Port, RS232. The intensified charge couple device comprises of a two–dimensional matrix of photo-sensors on a silicone based semiconductor chip. The iStar system employed contains 256 rows x 1024 columns of these photo-sensors. The iCCD was operated at -15°C maintained by an integrated fan cooling system. The specifications of the iCCD are listed in Table II.11. The main components of the iCCD camera in addition to the photosensitive pixel matrix are the photo-cathode, microchannel plate (MCP), output phosphor screen and a fibre optic bundle as shown in Figure II.10.

Table II.11 Specifications and performance of the Andor iStar CCD system

Component	Manufacturer	Model	Specifications
iStar System	Andor Technologies	DH 720-25F-03	Gating Speed:7 ns Photo-cathode: Wide Spectral Coverage Input Window: Quartz Spectral Range (nm): 180 –850 Phosphor: P43 Spatial Resolution: High Minimum Optical Gate: 4.6 ns Irising at Min. Optical Gate: 0.25 ns
iCCD	Marconi	CCD-30-11	Active Area: Φ25 mm Pixel: 1024 x 256 Active Pixels: 960 x 256 Eff. Pixel Size: 26 μm^2

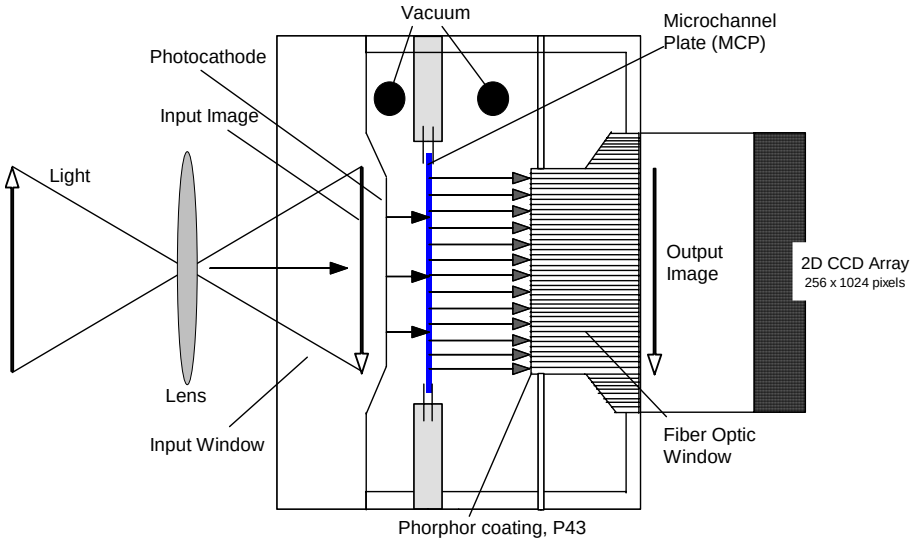

Figure II.10 A sectional view of the Andor iStar Image Intensifier

Briefly, the iCCD operates as follows; an incident photon of dispersed radiation falling on the input quartz window produce an electron from the photocathode. The emitted electron is drawn towards the microchannel plate by an electric field. The electrons cascade down the honeycomb channels of the MCP producing secondary electrons resulting in a net amplification of 10^4 per incident photon. The resultant electron shower is accelerated by means of a potential difference and focused onto a phosphor screen (P43) inside the fibre-optic exit window. Switching on/off the voltage to the photocathode allows time gating of the

device. The electrons strike the CCD producing an electrical signal proportional to their intensity. The final spectrum is generated with a "Vertical Binning" procedure where the charge (image) from each column of pixels is removed and summed vertically by a series of transparent horizontal electrode(s) to an 'on–chip' amplifier. The amplified signal is then transferred to the A/D converter on the CCI-010 controller card.

The spectral resolution of the iCCD is determined by the resolution of the dispersing element (diffraction grating) and limited by the number of pixels available to process the radiation. The wavelength range dispersed by each of the gratings mounted in the ARC SpectraPro 500i and the maximum resolution of each are listed in Table II.12.

Table II.12 Maximum resolution achievable employing the Andor iStar iCCD camera for each of the diffraction grating mounted in the ARC SpectraPro-500i monochromator.

Diffraction Grating – ARC SpectraPro–500i	Dispersal Range (nm)	Resolution (nm)
1200 g/mm; Blz: 300 nm	40	0.04
600 g/mm; Blz: 600 nm	80	0.08
150 g/mm; Blz: 300 nm	320	0.32

Time–gated and time–resolved emission spectra were recorded by turning on/off the voltage to the iCCD photocathode. Triggering the CCD was achieved using the fast external trigger obtained from the Q–switch pre-pulse of the YG 980 laser. Time–gated emission spectra are obtained by varying the delay in activation of the photocathode after laser excitation has occurred and/or recording the spectrum for a specific time duration, (gate width). These gated measurements and all the time resolved measurements were made within the total exposure time available (pulse to pulse time) limited by the repetition rate of the laser. Operating the YG 980 at 10 Hz allows a maximum exposure time of 100 msec. Time–resolved spectra were recorded by setting a small gate width and stepping this in time. Therefore, the time-resolved emission spectrum (TRES) is built from individual time-gated emission spectra recorded in known temporal slices.

II.5.III Excited state lifetime measurements

Emission lifetime measurements were completed using two different methods one direct and the second indirect by analysis of the time–resolved measurements made with the Andor iStar iCCD camera. The Andor software allowed the extraction of the emission intensities for a given emission feature (at a fixed wavelength) in the TRES allowing an examination of the temporal decay of individual features. Decay times were obtained by fitting single or multiple exponential functions to the decay curves extracted by applying a non-linear least squares analysis. The fits were completed over more than four orders of magnitude and convoluted with the temporal profile of the YG 980 excitation source (fwhm 6 nsec) where required to extracted the excited state decay times.

Emission decay measurements[33] were also conducted with photon counting detection of the emission produced with pulsed laser excitation (using repetition rates ranging from 1 to 10 Hz), and recorded with a multi-stop, multi-channel scalar (MCS). The signal from the photon counting (R928-P) emission PMT was amplified by an Ortec (Model VT120) fast-timing preamplifier[34] and relayed to an Ortec (Model 584) constant–fraction discriminator (CFD)[35] to limit electronic noise. The fast NIM-output of the CFD was passed simultaneously to an Ortec (Model 661) ratemeter[36] and to the stop-in on a 2 GHz multi-channel scalar (Fast ComTec, Model 7886), which has a minimum dwell time of 0.5 nsec per channel[37]. The start pulse for the MCS unit was obtained from the Q–switch pre-pulse of the YG 980 laser, see Figure II.11. The components used are listed in Table II.13. The temporal resolution of this arrangement has been determined to be approximately 500 nsec limited largely by the poor pulse-pair resolution of the R928-P PMT when high intensity, low repetition laser excitation is used. This characteristic allows the recording of only long-lived emission decay ($t \geq 1$ μsec) in the pulsed laser/MCS detection arrangement.

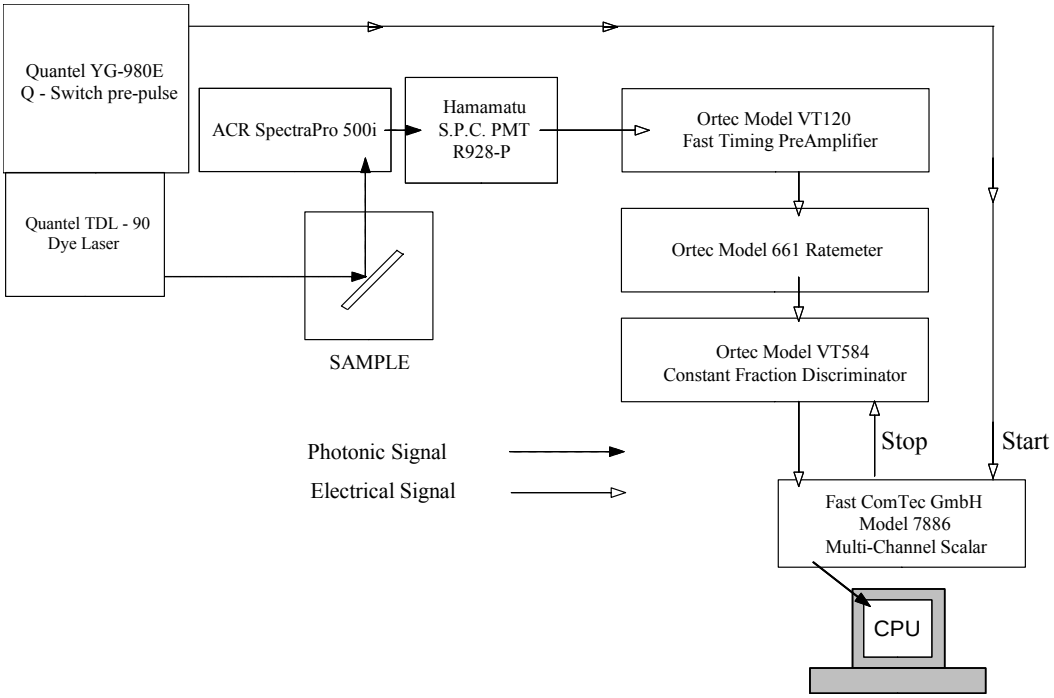

Figure II.11 **An illustration of the physical components used to record the decay characteristics of the luminescence of M/RG solids reported in this present work and there relative positions.**

Table II.13 **The components, manufacturers and model numbers of the experimental apparatus used to record the decay times of the atomic luminescence reported.**

Component	Manufacturer	Model/Part Number
Fast timing preamplifier[34]	Ortec	VT120
Ratemeter[36]	Ortec	661
Constant fraction discriminator[35]	Ortec	VT584
Multi Channel Scalar[37]	FAST ComTec GmbH	7886

References

[1] M. Moskovits and G. A. Ozin, Techniques of Matrix Cryochemistry in *Cryochemistry*, Wiley – Interscience, New York, 1976.

[2] L. Andrews and M. Moskovits, Introduction and Experimental Developments in *Chemistry and Physics of Matrix – Isolated Species*, North – Holland, Amsterdam, 1989.

[3] A. Kent, Experimental Low – Temperature Physics, Macmillan, London, 1983.

[4] APD Cryogenics Inc. (A subsidiary of Intermagnetics General Corporation) *DE-202 Expander Technical Manual*, May 1989 (257519A).

[5] APD Cryogenics Inc., *Helium Compressor HC-2D Technical Manual*, Jan 1992, (256685A)

[6] Scientific Instruments Inc. *Instruction Manual, Series 9600 microprocessor – based digital temperature indicators/controllers manual #A090-145*, March 6th, 1990.

[7] I. Dunkin, *Matrix - Isolation Techniques*, (A Practical Approach), Oxford University Press, 1998.

[8] Balzers *Operating Instructions, Turbo-molecular pump*, TPU 180H, Ed. 3.

[9] Balzers *Operating Instructions, Diaphragm Vacuum Pumps*, MD-4T Ed. 1.

[10] Granville-Phillips, *203 Variable Leak Valve, Technical Manual*, 1993.

[11] Granville-Phillips, *307 Vacuum Gauge Controller Technical Manual*, 1993.

[12] Tylan General, *Technical Sheets, Capacitance Diaphragm Gauges CDL Series*.

[13] Omicron, Instruments for Surface Science, Instruction Manual UHV Evaporator, EFM 3/4, Version. 2.0, May 1996, (reprinted Oct. 1996).

[14] T. L. Timms, Techniques of Preparative Cryochemistry in *Cryochemistry* edited by M. Moskovits and G. A. Ozin, Wiley – Interscience, New York, 1976.

[15] Manganese Rod, Goodfellow Catalogue 2000/01 Pt. No. MN007910 (p. 155).

[16] Irregular manganese pieces, Alfa Aesar Johnson Matthey Research Chemicals, Metals and Materials 2002-03 Catalogue, Stock. No. 36221 (p. 936).

[17] Hamamatsu, L2D2 Series Deuterium Lamps, Specifications, Aug. 1998, p. 4.

[18] Cathodeon, Deuterium Lamp Power Supply C713, Operation Notes, Specifications.

[19] Light sources mounted simultaneously using the Acton Research Corp., Dual Light Source Housing, Model TDS-429.

[20] Acton Research Corporation, *Operating Instructions SpectraPro – 300i*, SP – 300i Manual Rev. 997.1.

[21] PMT mounted on vacuum shroud using the Acton Research Corp. Model PD-471 PMT Detector Housing with Integral High Voltage Power Supply.

[22] Hamamatsu Data Sheet title '*Side-On Photomultiplier Tubes*'

[23] Mark Fox, *Optical Properties of Solids*, Oxford University Press, 2001.

[24] Acton Research Corporation SpectraPro – 500i, 500i Manual V1097.1.

[25] Hamamatsu Data Sheet title '*Photomultiplier Tubes R928, R955*'

[26] Products for Research, Inc., *Photocool Series Power Supply, Instruction Manual*, (Model PC177CE009 for R928).

[27] Electron Tubes Limited, Photomultiplier Amplifier-Discriminator Type AD 6, DS_AD6, Issue 1, 11.02.97

[28] Instruction Manual QUANTEL YG 980 Q-switched Nd:YAG laser, Doc. 980, Version #1, anglaise PM/DT (12.05.97).

[29] Quantel – TDL 90, Instruction Manual – Issue 1.

[30] Exciton, *Laser Dyes Catalogue*, 1992.

[31] Ulrick Brackmann, Lambda Physik, *Lambdachrome Laser Dyes Catalogue*, July 1985.

[32] The Andor iStar iCCD camera was mounted onto the ARC SpectraPro 500i using a monochromator specific flange, (Part Number: MFL-ARC-SPRO) to allow coincidence of the grating dispersed radiation and the detector focal plane.

[33] D. V. O'Connor and D. Philips, *Time – correlated Single Photon Counting*, Academic Press, London, 1984.

[34] Ortec, Model VT120 Fast Timing Pre-Amplifier, *Operating and Service Manual*, Part. No.760360, Revision B.

[35] Ortec, Model 584, Constant – Fraction Discriminator, *Operation and Service Manual*, Ortec, Pt. No. 733550, Revision B.

[36] Perkin Elmer Instruments, Model 661 Ratemeter, *Operation and Service Manual*, EG&G Ortec Pt. No. 740380, Revision B.

[37] Fast ComTec GmbH, Model 7886, 2 GHz Fast Multiscalar, *User Manual*, Version 2.1, Aug. 1998.

Chapter III

Luminescence spectroscopy of $^3P_1$ and $^3P_0$ state atomic mercury isolated in solid Ar, Kr and Xe.

III.1 Introduction

Historically Hg $^3P_1 \leftrightarrow {}^1S_0$ was one of the first atomic systems studied with the matrix-isolation technique[1,2,3,4]. Despite the existence, for more than a decade now, of accurate Hg·RG pair-potentials, obtained from the spectroscopy of the diatomic Hg·RG complexes stabilised in supersonic expansions, no calculations have appeared in the literature of the corresponding atomic absorption or emission spectra in rare gas matrices. With the availability of accurate interaction potentials for the Hg·RG diatomics, spectral simulations of the matrix absorption and emission spectroscopies were extended to the Hg/RG system using the pair-potentials approach our group has implemented in the Zn[5] and Cd[6] matrix systems. However, with several emission pathways identified in the theoretical work, it was necessary to extend experimental analysis of the emission spectroscopy to provide sufficient information for comparison with predictions. Specifically, the temperature dependence of the matrix emission is examined, lineshape analysis is performed and excitation spectra are recorded. Details of the pair-potentials simulations and a comparison with the experimental data are presented in Chapter IV.

The spectroscopy and reactivity of atomic mercury isolated in low temperature solids has been studied in greatest depth and scope by the Orsay group of Crepin and Tramer (C&T)[7]. As their work has been recently reviewed[8], only aspects relating to the spectroscopy of the 6p $^3P_1$ and 6p $^3P_0$ states will be addressed here. Absorption recorded by C&T with a deuterium lamp yielded spectra in agreement with the earlier work[9] showing a threefold split band for Hg/Xe in the vicinity of the gas phase 6p $^3P_1 \leftrightarrow$ 6s $^1S_0$ transition of atomic mercury at 253.6 nm. Featureless bands, progressively blue-shifted from the gas phase transition, were observed in Kr and Ar matrices. Dye laser excitation of the 6p $^3P_1$ state absorption produced multiple emission bands in the UV in all three rare gas matrices. Although excitation spectra were not presented in C&T's work[7], the most intense emission bands had the smallest Stokes'-shifts and were tentatively assigned to the occupancy of atomic mercury in substitutional sites. The Hg/Xe emission was quite different to that

recorded for Hg/Kr and Hg/Ar in that the Stokes' shift was very large and the emission bandwidth was much greater than the absorption bandwidth.

C&T also identified narrow "atomic-like" features in the matrix emission spectra which they assigned to the forbidden 6p $^3P_0 \rightarrow$ 6s $^1S_0$ transition. The linewidth of these transitions decreased in the order Ar to Xe but the shift of the band positions was irregular with the emission in Ar located between that in Kr and Xe. Other work by C&T on matrix-isolated atomic Hg has involved an examination of the relaxation of the excited atomic 6p $^1P_1$ state following resonance excitation with synchrotron radiation[10,11] and pulsed laser excitation[12,13]. Population of all three triplet spin-orbit states ($^3P_{2,1,0}$) was observed as a result of $^1P_1$ excitation. More recently, Chergui and co-workers[14] have conducted spectroscopic studies in neon matrices, work which will be compared with theoretical calculations presented in Chapter V.

This Chapter presents a study of the temperature dependence of the $^3P_1 \rightarrow {}^1S_0$ and $^3P_0 \rightarrow {}^1S_0$ transitions of atomic mercury isolated in the solid rare gases Ar, Kr and Xe, resulting from resonance excitation of the $^3P_1$ excited state. This state is accessed with continuous lamp and pulsed laser excitation, facilitating a clear distinction of the latter forbidden transition and the former, nearly fully allowed transition. Excitation spectra are presented for the first time allowing identification of the origin of the multiple emission features observed. Lineshape analysis of high-resolution $^3P_0 \rightarrow {}^1S_0$ emission spectra allow the strength of the electron-phonon coupling to be determined for this transition.

III.2 Results

III.2.I Hg $^3P_1 \leftarrow {}^1S_0$ absorption spectra

Following Hg/RG matrix deposition, as outlined in Chapter II, absorption spectra were recorded with a deuterium lamp in the vicinity of the $^3P_1 \leftrightarrow {}^1S_0$ transition[3] of atomic Hg at 253.6 nm. Figure III.1 shows the absorption spectra recorded at 12 K for atomic Hg isolated in Ar, Kr and Xe matrices deposited at 22, 25 and 35 K respectively. The Hg/RG samples were deposited at elevated temperatures to increase the matrix crystallinity and minimise thermally unstable sites of isolation. The spectra shown were obtained by rationing transmittance spectra recorded for

Hg/RG thin films with corresponding pure RG films. The spectra observed are in good agreement with those presented in the study by C&T.

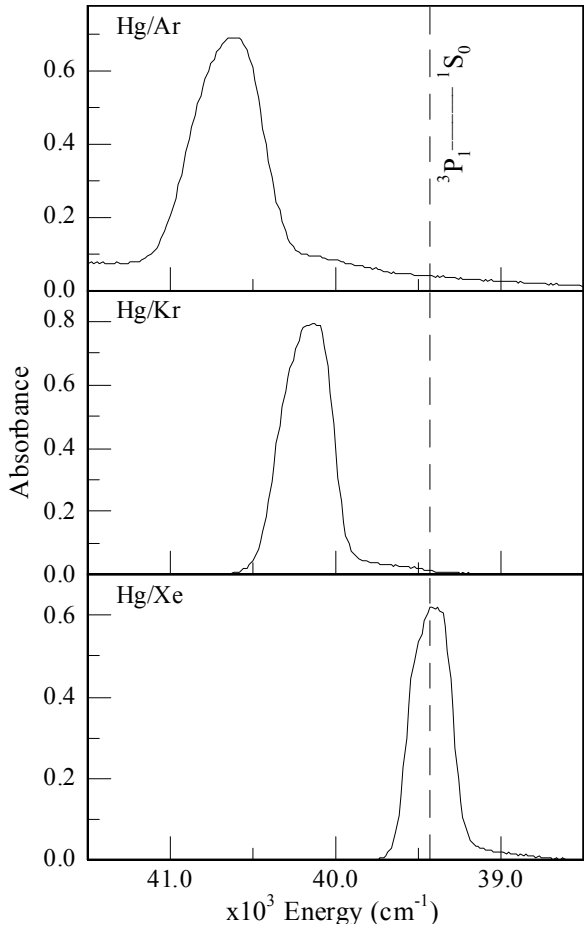

Figure III.1 Hg/RG absorption spectra recorded at 12 K in the vicinity of the atomic Hg $^3P_1 \leftrightarrow {}^1S_0$ transition[3] upon deposition at temperatures in excess of 12 K.

Thus, as observed by C&T[7] upon deposition at 14 K, a progressive red–shift of the Hg($^3P_1 \leftarrow {}^1S_0$)/RG band and decreasing linewidth of the matrix absorption band occurs from Ar to Xe. These spectra verified that the Hg/RG samples prepared by our group mirrored those reported in previous studies.

III.2.II Hg $^3P_1 \leftrightarrow {}^1S_0$ excitation and emission spectra

Emission spectra produced with continuous lamp excitation of the Hg $^3P_1$ state are presented in Figure III.2 for Ar, Kr and Xe samples. The overall features of the Hg/RG spectra agree well with the nanosecond, time-resolved spectra presented previously by Crepin and Tramer[7]. One difference is the presence of a weak, resolved feature at 265.1 nm in Hg/Xe that is due to the long-lived $^3P_0$ state emission of Hg. The main emission features are centered at 250.3, 254.1 and 273.0 nm in Ar, Kr and

Xe respectively as listed in Table III.1. Excitation spectra recorded for these emission wavelengths are shown on the left in Figure III.2 and correspond to the dominant features in the previously reported[7,9] absorption spectra.

Table III.1 **Photophysical characteristics of the triplet 6p $^3P_1 \leftrightarrow$ 6s $^1S_0$ transition[3] of matrix – isolated atomic mercury. λ_{Ex} indicates the position of the central component of the three–fold split excitation spectrum and λ_{Em} indicates the emission band-centre in nm units. The full-width at half-maximum intensity of the excitation/emission features is denoted by Δ and the Stokes shift by SS - both in wavenumber (cm^{-1}) units.**

Hg/RG System	Excitation		Emission		
	λ_{Ex} (nm)	Δ (cm^{-1})	λ_{Em} (nm)	Δ (cm^{-1})	SS (cm^{-1})
Ar	245.9	484	250.3	399	715
Kr	248.9	397	254.1	465	816
Xe	253.6	344	273.0	1472	2802

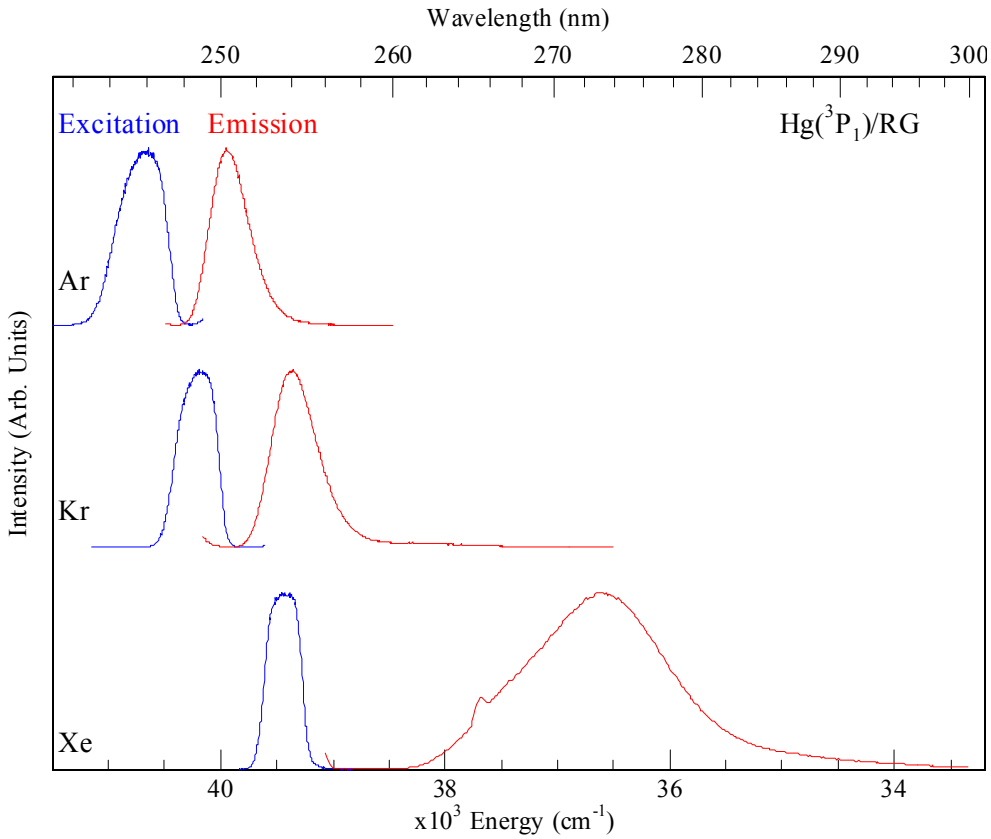

Figure III.2 **Emission spectra recorded at 12 K for the Hg/RG systems with lamp excitation of the Hg $^3P_1 \leftarrow {}^1S_0$ transition. The excitation spectra, recorded by monitoring emission at 250.4, 254.1 and 273.9 nm in Ar, Kr and Xe respectively, are shown on the left of the figure. Hg/Ar, Hg/Kr and Hg/Xe samples were deposited at 22, 25 and 35 K respectively.**

As observed by C&T, the emission band in Hg/Xe, centered at 273 nm, has a large bandwidth and Stokes' shift compared with those in the Hg/Ar and Hg/Kr systems. Moreover, the Hg/Xe emission band exhibits a clear asymmetry. To investigate the origin of this asymmetry we have examined the temperature dependence of the Hg/Xe emission and conducted lineshape analyses at 12 K and elevated temperatures.

The right hand panel in Figure III.3 provides a comparison of the Hg/Xe emission recorded at 12 and 42 K. As expected the emission bandwidth increases at elevated temperatures but contrary to expectation, the band-centre blue shifts. This effect is completely reversible because, although not shown in Figure III.3, the 12 K scan recorded after sample warming to 42 K is identical to the previous 12 K scan. Lineshape analysis of the time-integrated Hg/Xe emission spectrum is complicated by the presence of a small amount of $^3P_0$ state emission in addition to $^3P_1$ emission. The location of the former emission is revealed by overlaying, as shown on the left in Figure III.3, the $^3P_0$ emission spectrum produced with pulsed laser excitation. As indicated in this comparison, the emission bands of these two states are quite different - the $^3P_0$ state is very narrow while the $^3P_1$ state is broad.

The deconvolution of the fluorescent $^3P_1$ and phosphorescent $^3P_0$ components present in the time-integrated spectrum shown in the right panel Figure III.3 was also achieved temporally. The different lineshapes of the $^3P_1$ and $^3P_0$ excited state emission features were verified by time–gated emission spectra recorded with iCCD detection as shown in Figure III.4. It is evident from the time–gated spectra shown in Figure III.4 that employing no acquisition delay (t_d = 0 nsec) and a long gate width (95 msec) reproduced the time-integrated emission spectrum shown in the right panel of Figure III.3. Temporal separation of the $^3P_1$ and $^3P_0$ emission features was achieved using a delay time (t_d) of 1.0 μsec. As shown by the dotted trace in Figure III.4, this setting removes the broad $^3P_1$ fluorescence while maintaining the narrow $^3P_0$ emission. A long gate width of 95 msec was chosen to optimise the measurement time between excitation pulses from the Nd:YAG laser operating at 10 Hz.

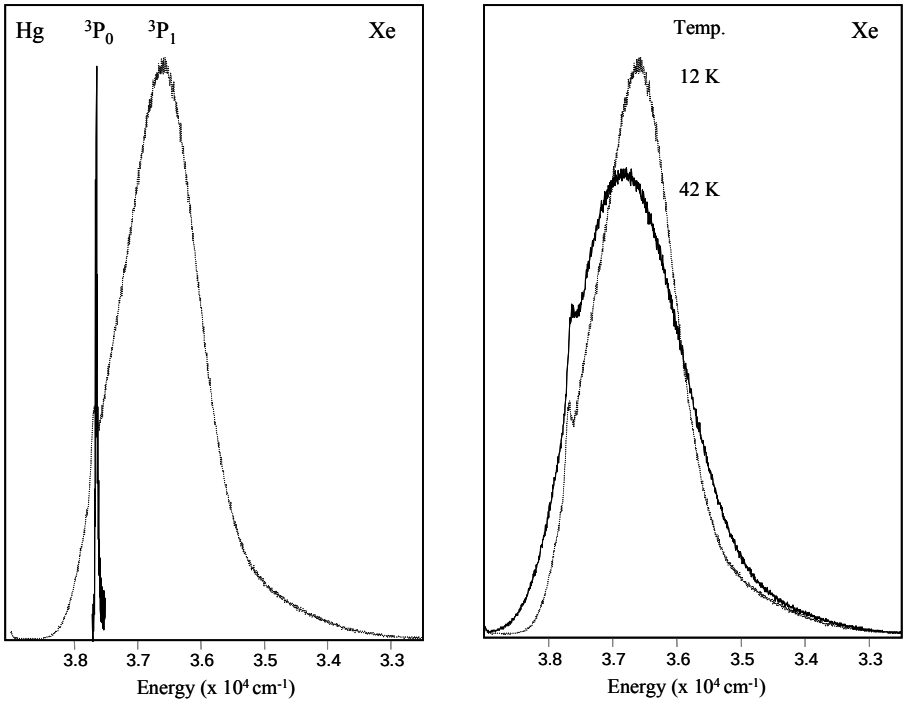

Figure III.3 **Details of Hg/Xe emission. The panel on the right shows a comparison of emission spectra recorded at 12 K and 42 K. In this comparison a reversible blue shift in the band maximum occurs with increasing temperature. The panel on the left shows a comparison of the emission spectra produced with pulsed and continuous excitation. The narrow feature at 265.1 nm was recorded with pulsed laser excitation and is gated to show only long-lived $^3P_0$ emission.**

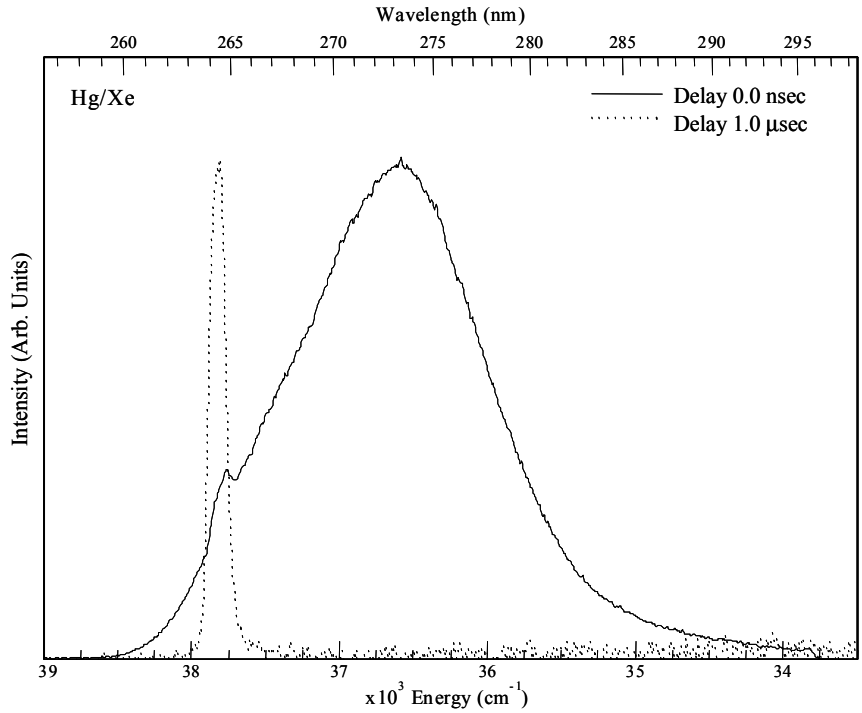

Figure III.4 **Hg/Xe time-gated emission spectra recorded at 12 K using iCCD detection following pulsed laser excitation, λ_{Ex} = 253.0 nm. The delay times (t_d) employed were 0 and 1.0 μsec with a constant gate width of 95 msec for the solid and dotted traces respectively.**

In the lineshape analysis conducted on the time-integrated Hg/Xe emission, provision was made for the presence of the narrow $^3P_0$ state emission band. A satisfactory fit of the 12 K emission band, shown on the bottom left in Figure III.5, is obtained with three Gaussian functions (not counting the narrow $^3P_0$ state emission). Details of the 12 K fits are presented in Table III.II, which gives the positions of the $^3P_1$ emission components as 37535, 36619 and 35729 cm^{-1}. Fitting the emission band profile to Gaussian functions is a realistic analysis for Hg/RG systems where the difference in the ground and excited state bond lengths ΔR is large. The excitation spectra recorded for all three emission components were identical. As the Hg/Xe samples were deposited at 35 K to minimize the formation of multiple trapping sites and annealed to approximately 60 K to remove any persistent unstable sites, we conclude the three components in the $^3P_1$ state emission centered at 273 nm arise from the occupancy of Hg in a single site in xenon.

The 42 K spectrum, shown on the right in Figure III.5, could also be fit adequately with three bands. An indication of the quality of the fits is provided in the upper panels, which show the residuals existing between data and fit. Also shown are the emission profiles generated in the fit. The comparison of the low and high temperature fits, shown on the bottom in Figure III.5, suggests that the origin of the unexpected blue shift occurring at higher temperatures in the emission band, arises from the increasing intensity of the unresolved blue component. However, when the spectra are plotted on absolute intensity, it becomes clear that it is the intensity of the central component, which is decreasing at higher temperatures.

Lineshape analyses of the emission bands in the Hg/Ar and Hg/Kr systems were also conducted, the results of which are shown in Figure III.6 and collected in Table III.2. As in the Hg/Xe system, allowance had to be made in the Hg/Kr system for the presence of a weak $^3P_0$ state emission. This component and a broad underlying feature, due to a thermally unstable site, occur to the red of the main $^3P_1$ state emission in Kr. Adequate fits in Hg/Ar were only obtained when three components were allowed for, as shown on the left in Figure III.6. The temperature dependence in the Hg/Ar and Hg/Kr systems is simpler than in the Hg/Xe system in so far as the emission bands broaden and red shift with increasing temperature.

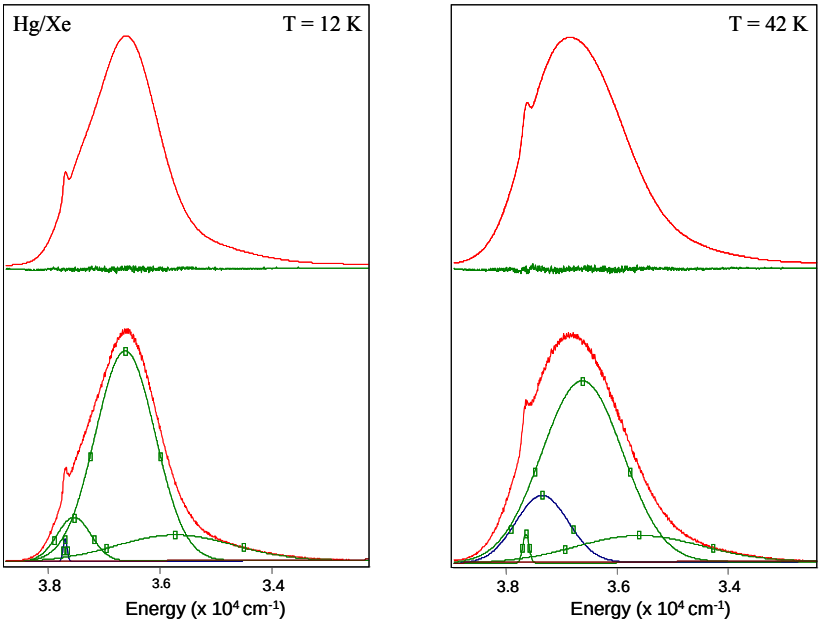

Figure III.5 **Lineshape analysis of $^3P_1$ emission in the Hg/Xe system. The panel on the left shows an acceptable fit of the spectra recorded at 12 K. In this fit, three broad Gaussian functions are required in addition to one, narrow function included for the $^3P_0$ state emission. The panel on the right shows a fit of the high temperature emission. As in the 12 K fits, three broad and one narrow Gaussian functions provide an adequate fit.**

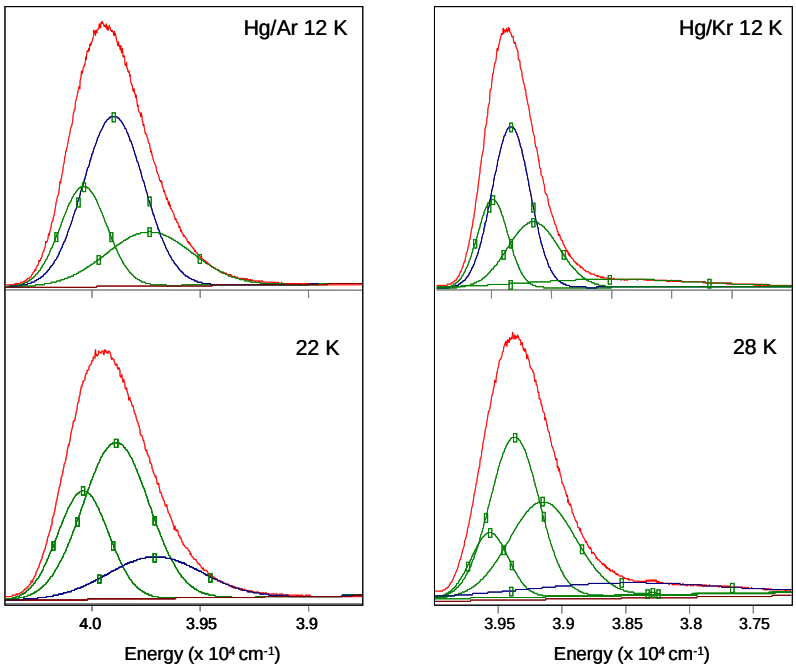

Figure III.6 **Lineshape analyses of $^3P_1$ state emission in the Hg/Ar and Hg/Kr systems. The panels on the top show acceptable fits of spectra recorded at 12 K, revealing the presence of multiple components in the Ar and Kr systems as observed in Hg/Xe. In contrast to the Hg/Xe system, little temperature dependence is exhibited as indicated in the panels on the bottom. The fourth Gaussian component used in the Hg/Kr system was required to account for a small amount of a red site present in this sample. Numerical values extracted in these fits are collected in Table III.2.**

Table III.2 **Parameters extracted in Gaussian fits of the Hg/RG 12 K emission spectra produced with continuous lamp excitation. The band areas were determined by numerical integration of the fitted curves.**

Hg/RG	Bandcentre ν_0 (cm^{-1})	Bandheight (counts)	Bandwidth Δ (cm^{-1})	Integrated area (counts)
Xe	37693.9	1658	84.3	1.488×10^5
	37534.9	3151	710.5	2.383×10^6
	36618.8	15229	1256.6	2.037×10^7
	35728.9	1924	2455.8	5.020×10^6
Kr	39486.9	6883	299.0	2.190×10^6
	39334.7	1249	371.7	4.944×10^6
	39149.0	5122	503.0	2.742×10^6
	38513.5[15]	619	1650	1.050×10^6
Ar	40038.0	5482	252.5	1.473×10^6
	39899.3	9309	329.4	3.263×10^6
	39734.6	2967	467.2	1.475×10^6

Time-resolved emission spectra (TRES) produced with pulsed laser excitation and iCCD detection are shown in Figure III.7 for Hg/Kr. Such scans yielded short lived (nanosecond) decay times for the Hg($^3P_1$)/RG emission features.

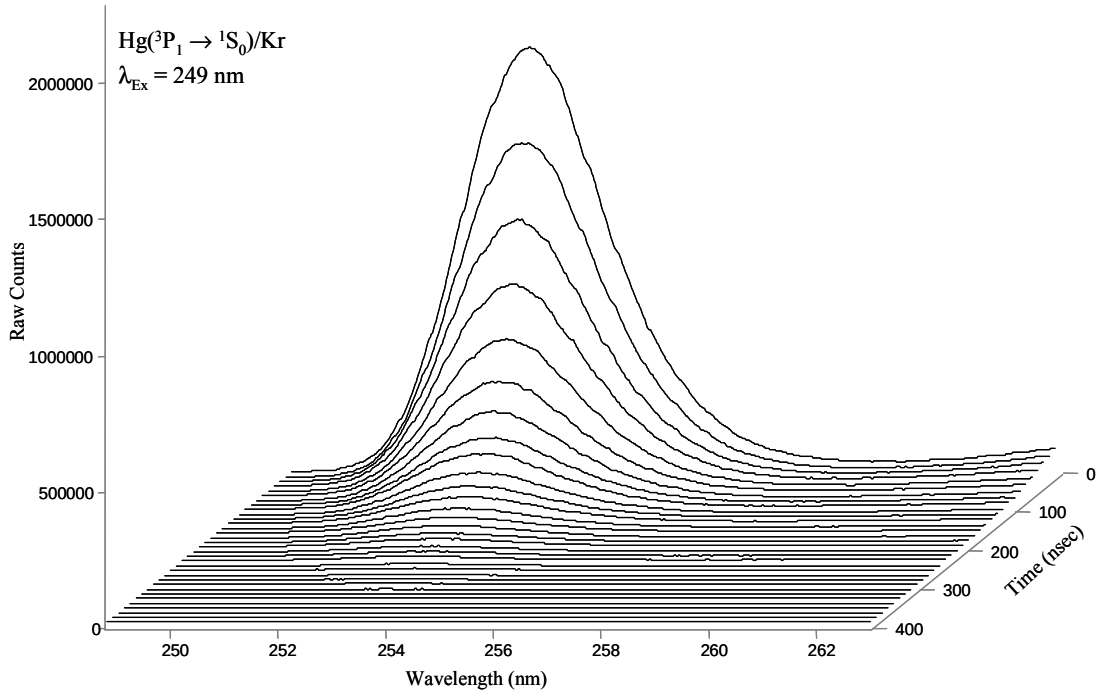

Figure III.7 **Hg/Kr time–resolved emission spectrum corresponding to the Hg $^3P_1 \rightarrow {}^1S_0$ nanosecond fluorescence recorded at 12 K produced with pulsed laser excitation and iCCD detection.**

Decay profiles were extracted from the time–resolved emission spectra as described in Chapter II. A representative plot of the Hg/Kr system is shown in Figure III.8. Adequate fits, generated with a single–exponential function convoluted with the temporal profile of the YG980 laser pulse, reproduced the overall decay profile of the emission feature well. Figure III.8 shows the result of this analysis for Hg/Kr, the upper panel showing the residuals - the deviation of the decay profile recorded from the fit completed. This analysis reveals the decay of the excited state population follows 1st order kinetics with a decay time τ = 39 nsec at 12 K.

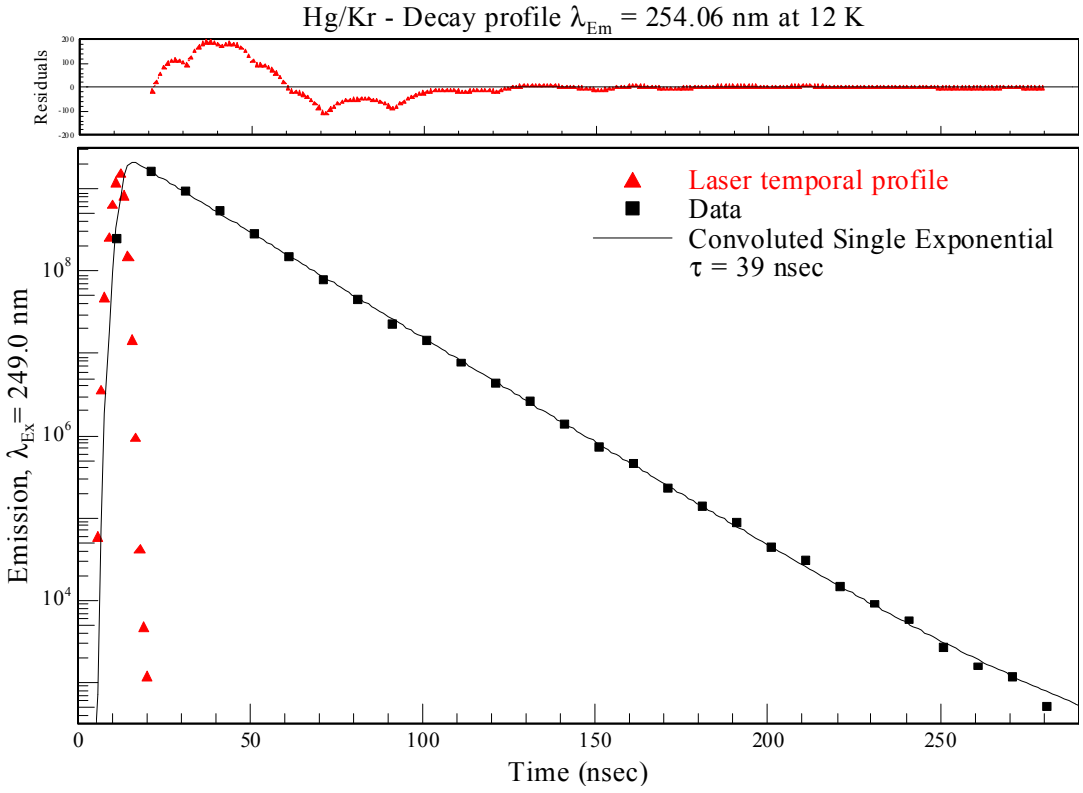

Figure III.8 **Decay profile of the Hg($^3P_1$)/Kr emission recorded at 12 K extracted from time–resolved emission spectrum, Figure III.7. The decay profile is convoluted with the temporal profile of the excitation laser source. The residual shown represents the difference between the decay recorded and the single-exponential fit.**

Single-exponential decays of τ = 46.5 and 37 nsec were extracted from similar fits of the time–resolved spectra recorded for Hg/Ar (250.3 nm) and Hg/Xe (273.0 nm). These nanosecond decay times confirm the assignment of the emission features to those of the Hg $^3P_1 \rightarrow {}^1S_0$ transition whose gas phase lifetime is reported to be in the range 113[16] to 125 nsec[17].

The temperature dependence of the decay profiles was investigated to assess the contributions of non-radiative components in the decay characteristics of the observed bands and thereby attempt and identify the true radiative decay times, (τ_{rad}) in the solid state. Figure III.9 presents the temperature dependence recorded for the Hg/Kr 254.06 nm emission at temperatures of 12, 27 and 35 K.

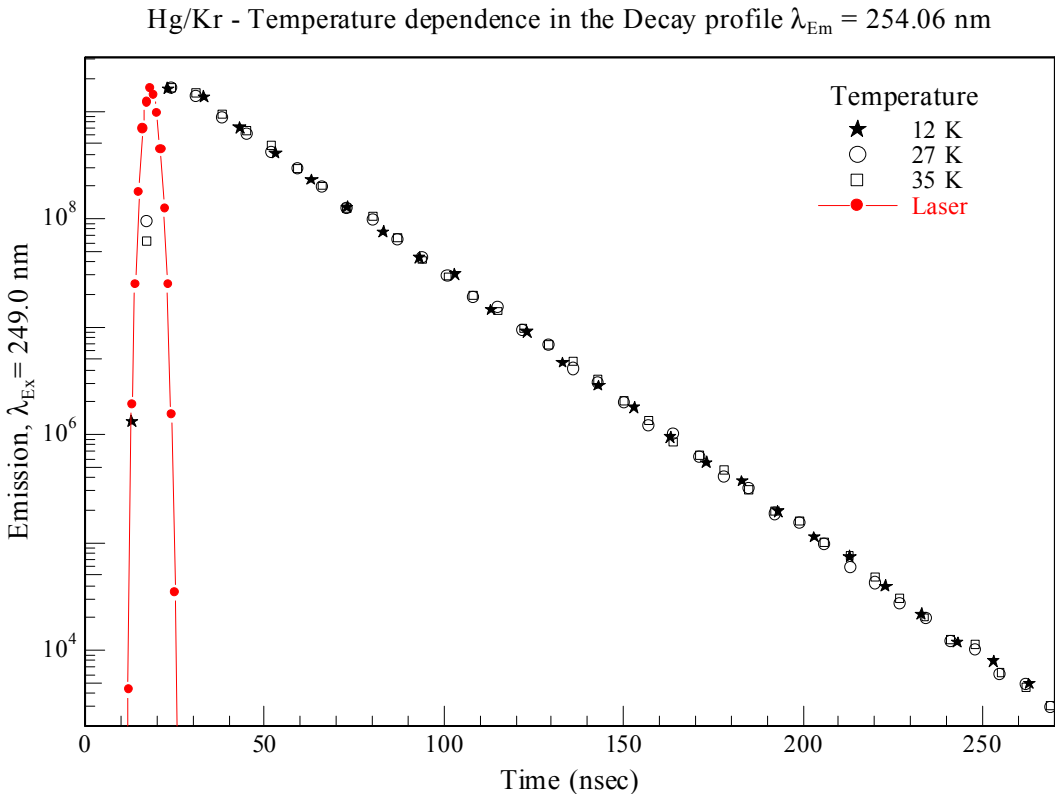

Figure III.9 **Decay profiles of the Hg($^3P_1$)/Kr emission at 254.06 nm recorded at 12, 27 and 35 K. The temporal profile of the YG 980 laser excitation source at 249 nm is also shown.**

It is evident from Figure III.9 that the decay profile for the Hg/Kr 254.06 nm emission feature does not exhibit any variation over the temperature range 12 to 35 K. This was also observed for the $^3P_1 \rightarrow {}^1S_0$ emission features in the Hg/Ar and Hg/Xe systems. This observation allowed the identification of the lifetimes extracted at 12 K, (τ_{obs}) as the radiative lifetimes (τ_{rad}) of the atomic Hg $^3P_1$ state emission for Hg/Ar, Hg/Kr and Hg/Xe, collected in Table III.3. The radiative decay times, τ_{rad}, presented in Table III.3 for the Hg($^3P_1$)/RG emission features are substantially less than the gas phase transition as the values quoted have not been corrected for the effective field of the host matrices. The effective field correction[18,19] is made with Equation III.1 using the index of refraction of the given rare gas host, n[20, 21].

$$\tau_{cor} = \tau_{obs}\, n[(n^2 + 2)/3]^2 \qquad \text{Equation (III.1)}$$

Application of the correction yields decay times of 95.52, 100.96 and 109.1 nsec for Hg($^3P_1$)/Ar, Kr and Xe respectively. Figure III.10 plots both the observed and corrected matrix lifetimes (τ_{obs} and τ_{cor}) as a function of emission wavelength. The gas phase lifetime τ_{gas} (open diamond) is also shown and the solid line intercepting this point represents a λ^3 extrapolation of the gas phase radiative lifetime. The observed lifetimes τ_{obs} at 12 K, the radiative τ_{rad} and the corrected matrix lifetimes τ_{cor} (nsec) are collected in Table III.3.

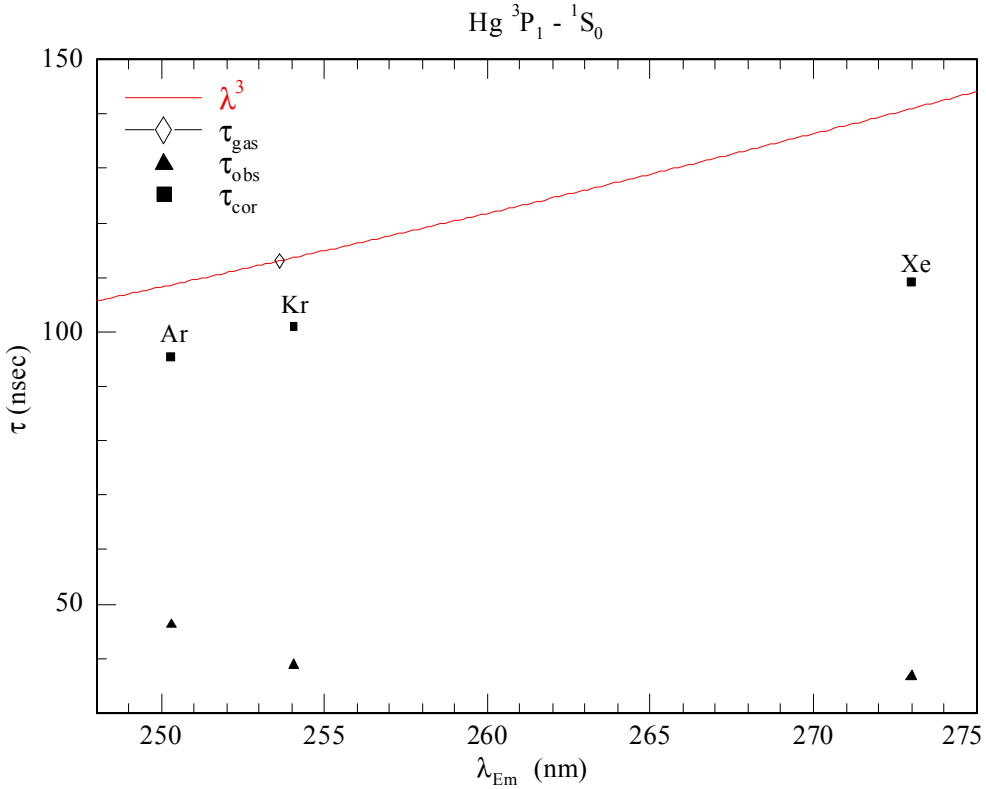

Figure III.10 **A comparison of the lifetimes recorded at 12 K for the Hg($^3P_1 \rightarrow {}^1S_0$) emission features in Ar, Kr and Xe and a λ^3 extrapolation of the gas phase lifetime of the $^3P_1$ state of atomic Hg. The uncorrected and the data corrected for the effective fields shown by closed triangles and closed squares respectively.**

Table III.3 **The lifetimes recorded at 12 K for the Hg($^3P_1 \rightarrow {}^1S_0$) emission features in Ar, Kr and Xe. The observed decay time (τ_{obs}) at 12 K, radiative lifetime (τ_{rad}) and the radiative lifetime corrected for the effective field of the RG solid using Equation III.1. The indices of refraction for the RG solids are also presented.**

Hg/RG System (λ_{Em}, nm)	τ_{obs} (nsec) @ 12 K	τ_{rad} (nsec)	τ_{cor} (nsec)	RG Refractive Index, n[20,21]
Ar	46.5	46.5	95.52	1.320
Kr	39.0	39.0	100.96	1.428
Xe	37.0	37.0	109.10	1.490

The λ^3 extrapolation presented in Figure III.10 is based on the relationship between the Einstein A coefficient for the emission decay rate $A_{m,n}$ and the radiative lifetime of a level *m* (τ_m). It is given by Equation III.2.

$$A_{m,n} = (64\,\pi^4/3h\lambda^3)\mu^2_{\ m,n} = {}^1/\tau_m \qquad \text{Equation (III.2)}$$

The trend of decreasing lifetimes observed from Ar to Xe in the uncorrected data τ_{obs} is reversed when the effective fields of the host matrices are taken into account, τ_{cor}. The trend in τ_{cor} suggests a λ^3 dependence as expected, shown by the solid line from Ar to Kr with slight deviation for Xe. This deviation in Xe may be as a result of the correction where the refractive index used was recorded at 60 K[20] unlike Ar and Kr[21] recorded at 6 K. C&T also presented lifetime measurements for the observed Hg $^3P_1$ emission features[7] and following effective field correction reported radiative lifetimes τ_{rad} = 45, 55 and 55 nsec for Ar, Kr and Xe host matrices. The radiative lifetimes reported by C&T are systematically less than the corrected values recorded in this study. However the nanosecond lifetimes recorded here allowed unambiguous assignment of the $^3P_1$ emission features using time-resolved methods.

Following the assignment of the radiative lifetimes (τ_{rad}) for the atomic Hg $^3P_1 \rightarrow {}^1S_0$ transition isolated in solid Ar, Kr and Xe, the decay profiles of the individual emission components identified in the lineshape analysis were investigated. The lineshape analysis of the Hg/Xe system revealed three fluorescence bandcentres at 12 K occurring at 266.42, 273.08 and 279.89 nm, shown bottom left of Figure III.5. These three emission components have the least spectral overlap so the Hg/Xe system was selected for this analysis. The decay profiles corresponding to these emission wavelengths were extracted from a single time-resolved emission spectrum at a given temperature. Because the emission features are temporally very similar, analysis with a single–exponential function provided adequate fits and allowed the extraction of the observed lifetimes, τ_{obs}. The Hg/Xe $^3P_1$ decay profiles corresponding to emission at 263, 273 and 280 nm are shown in Figure III.11. The band-centre of the high-energy emission feature was identified at 266.42 nm, however the decay profile of 263 nm was chosen to further reduce the spectral overlap between this band and the dominant, central 273 nm component.

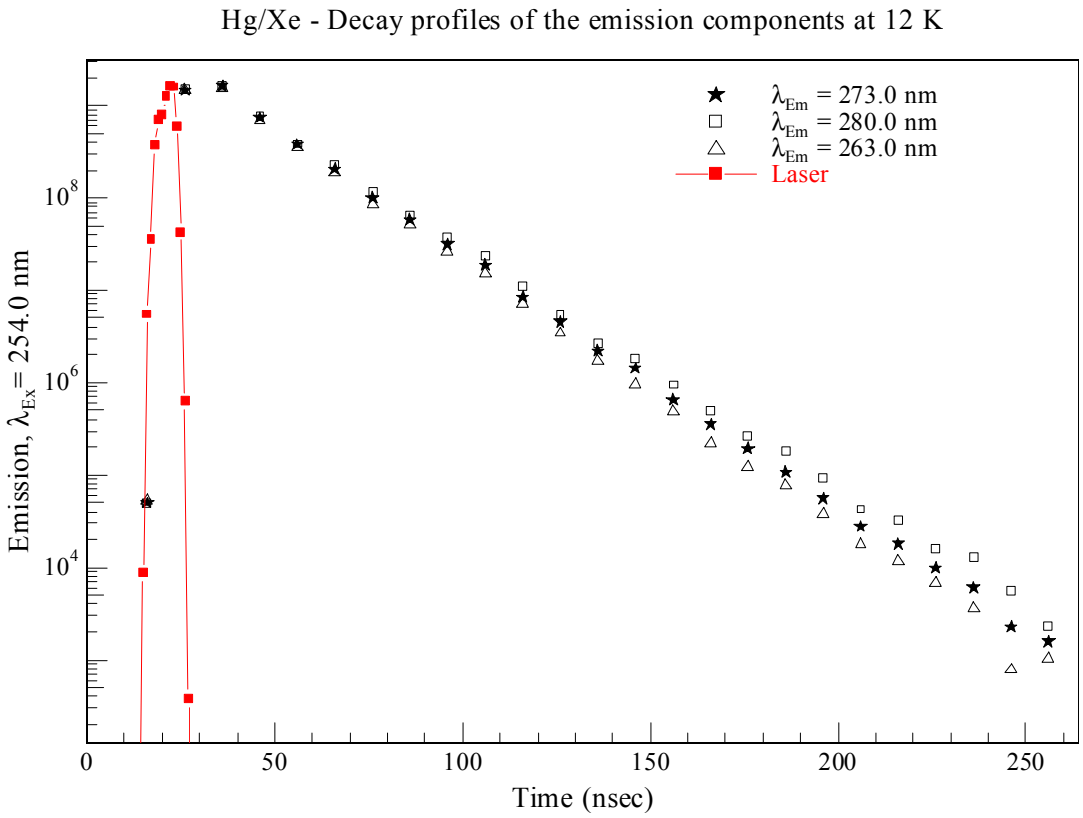

Figure III.11 **A comparison of the temporal decay profiles recorded for the three emission components identified in the lineshape analysis (Figure III.5) of the steady-state emission spectrum recorded for the Hg $^3P_1 \rightarrow {}^1S_0$ transition in solid Xe at 12 K.**

Inspection of the Hg/Xe decay profiles shown in Figure III.11 reveals slight differences in the profiles for the 263, 273 and 280 nm features at 12 K. Fits of the individual decay profiles with a single exponential function allowed the extraction of different lifetimes τ_{obs} (nsec) for each component. The observed lifetimes at 12 K, presented in Table III.4, show a progressive increase with increasing emission wavelength. When the decay times are corrected for the effective field, the corrected lifetimes τ_{cor} presented in Table III.4 are 103.05, 106.97 and 111.39 nsec for the 263, 273 and 280 nm features respectively. The plot of the corrected decay lifetimes versus λ^3 shown in Figure III.12 reveals this trend is not λ^3 dependent. Therefore the lifetimes extracted represent decay times for three different emission components corresponding to those identified using the Gaussian lineshape analysis of the Hg $^3P_1 \rightarrow {}^1S_0$ steady-state emission spectrum.

Table III.4 **The observed and corrected decay times (τ_{obs} and τ_{cor}, nsec) extracted from non-linear single exponential fits of the decay profiles recorded for the three components present in the Hg $^3P_1$ fluorescence in solid Xe at 12 and 46 K.**

Hg($^3P_1$)/Xe System λ_{Em}, (nm)	τ_{obs} (nsec)	τ_{cor} (nsec)
263.0 (12 K)	34.95	103.05
(46 K)	35.39	104.35
273.0 (12 K)	36.28	106.97
(46 K)	35.39	104.35
280.0 (12 K)	37.78	111.39
(46 K)	35.91	105.88

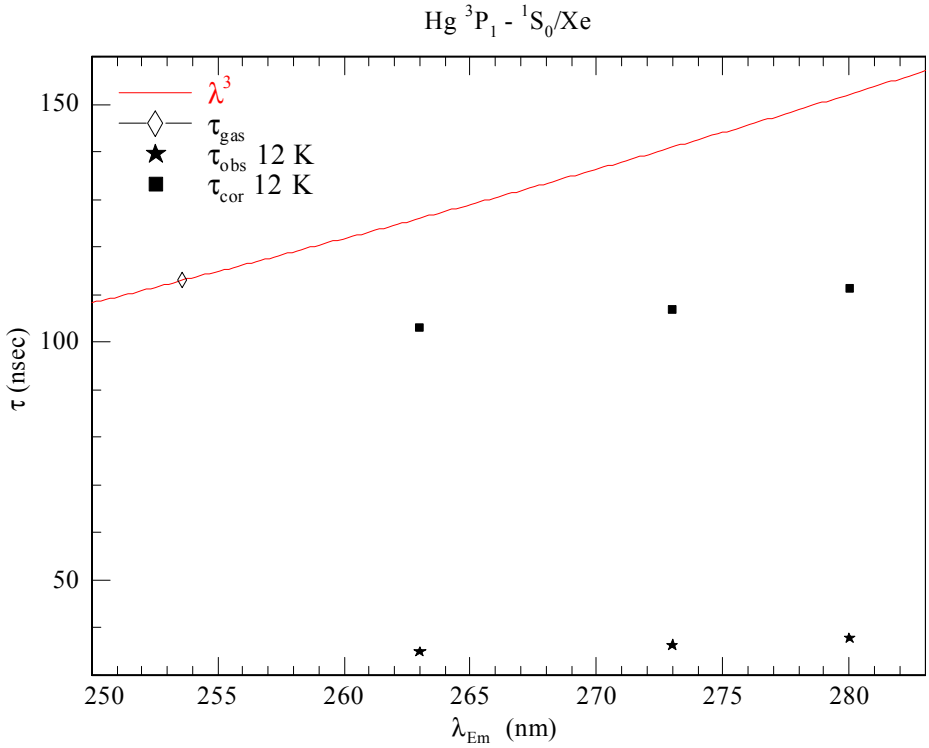

Figure III.12 **A comparison of the lifetimes recorded at 12 K for the emission features identified at 263.0, 273.0 and 280.0 nm using the lineshape analysis of the Hg($^3P_1 \rightarrow {}^1S_0$) emission feature in Xe. The solid line represents a λ^3 extrapolation of the gas phase lifetime of the $^3P_1$ state of atomic Hg.**

A similar analysis of the decay profiles recorded for the emission components identified in the lineshape analysis of the Hg($^3P_1$) emission spectra presented in Figure III.6 for Hg/Ar and Hg/Kr, showed no marked differences. This behaviour may stem from the lack of spectral resolution between the components identified and presented in Table III.2.

The temperature dependence of the decay profiles for the individual emission components identified in the lineshape analysis was investigated. The decay profiles

deviated from those recorded at 12 K for the Hg/Xe system only. Figure III.13 presents a comparison of the decay profiles recorded for the three emission features (263, 273 and 280 nm) at 42 K. It is evident in Figure III.13 that the decay profiles of the 263 and 273 nm features, represented by open triangles and stars respectively, are equivalent. This is reflected in the observed decay times (τ_{obs}) extracted at 46 K, collected in Table III.4, where the value of the emission (35.4 nsec) 263 nm is equal to that extracted for the 273 nm feature.

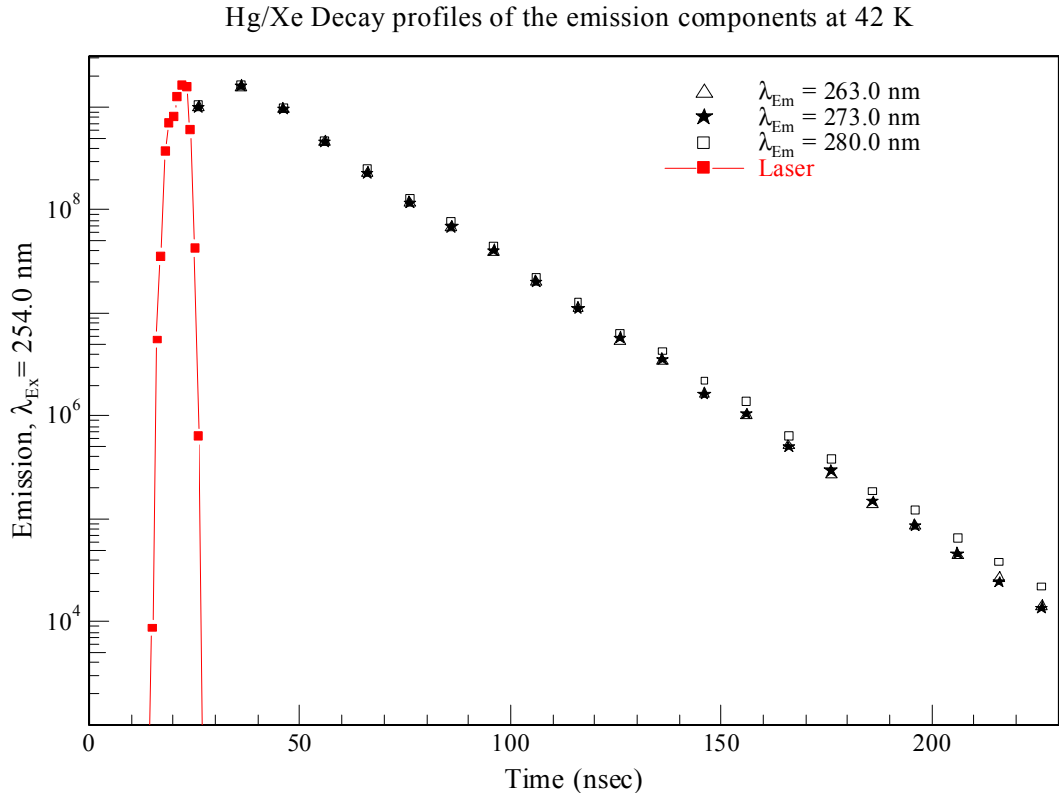

Figure III.13 **A comparison of the temporal decay profiles recorded for the three emission components identified in the lineshape analysis (Figure III.5) of the steady-state emission spectrum recorded for the Hg $^3P_1 \rightarrow {}^1S_0$ transition in solid Xenon at 42 K.**

This observation reveals the Hg/Xe decay profile is temperature dependent consistent with the lineshape analysis completed which showed that the 273 nm feature is diminished at temperatures in excess of 30 K. Therefore the temperature dependence in the decay time extracted is reflecting the behaviour of the 266 and 273 nm components identified in the lineshape analysis shown in Figure III.5.

III.2.III Hg $^3P_0 \rightarrow {}^1S_0$ emission spectra

In this section, details of the $^3P_0$ state emission of mercury atoms resulting from intermultiplet relaxation (IMR) following pulsed laser excitation of the $^3P_1$ level are presented. The combination of a high intensity, low-repetition excitation source (Nd:YAG laser) with photon counting detection is used for recording these spectra as it favours the long-lived $^3P_0$ emission over the nanosecond $^3P_1$ fluorescence. Hence the resulting spectra are free of the $^3P_1$ state emission bands described in the preceding section.

The excitation wavelengths chosen correspond to the Hg $^3P_1 \leftarrow {}^1S_0$ transition in solid Ar, Kr and Xe, at 245.9, 248.8 and 253.0 nm respectively. As shown in Figure III.14, the emission features resulting from pulsed laser excitation are centered at 258.9, 260.8 and 265.1 nm in Ar, Kr and Xe. The spectra shown in Figure III.14 exhibit a progressive red shift and decreasing linewidth from Ar to Xe. The red shift mirrors that of the $^3P_1$ emission but the linewidth behaviour is the reverse of that shown in Figure III.2 for the $^3P_1$ fluorescence. It should be noted that the progressive red shift evident in Figure III.14 was not present in C&T's data[7]. In their spectra, the position of the Hg/Ar emission was intermediate between that of Kr and Xe. It is thought that the $^3P_0$ data presented in the earlier Hg/Ar work, corresponds to Hg occupancy in a secondary site[13] of argon.

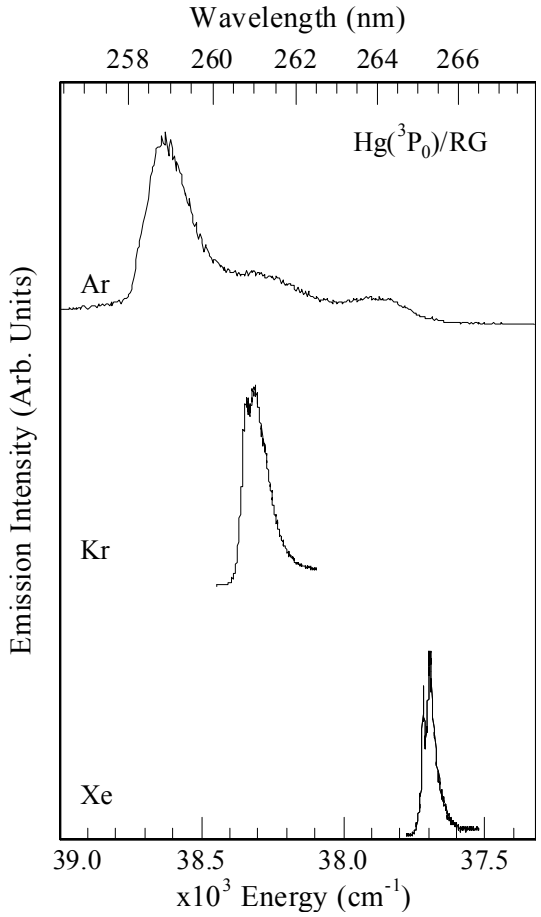

Figure III.14 **A summary of the long-lived emission features recorded in the Hg/RG systems at 12 K. These emission spectra were produced with pulsed laser excitation of the Hg atom $^3P_1 \leftarrow {}^1S_0$ transition and are gated to show only long-lived $^3P_0$ emission. Note the increasing red-shift in the emission bands on going from Ar to Xe but the decreasing linewidth.**

The emission features in Kr and Xe matrices reveal fine-structure splitting when recorded under high resolution. As shown in Figure III.15, Hg/Xe exhibits a narrow line (*fwhm* = 10.5 cm^{-1}) at 265.12 nm, (37718 cm^{-1}) and a broader red feature (*fwhm* = 70 cm^{-1} at 265.54 nm, (37658 cm^{-1}). High temperature scans, also shown in Figure III.15, indicate that the sharp feature is reversibly removed while the broad feature broadens and red-shifts. These lineshapes and their temperature dependence are characteristic of a zero phonon line (*ZPL*), for the narrow blue feature and a phonon sideband for the broader, red feature. Two features are also evident in the Hg/Kr system although not as well resolved as in Hg/Xe, but exhibiting the same temperature dependence. The main band of Hg/Ar at 258.9 nm exhibits little temperature dependence, except that the pair of weak side-bands at 261.0 and 263.7 nm are removed at high temperature.

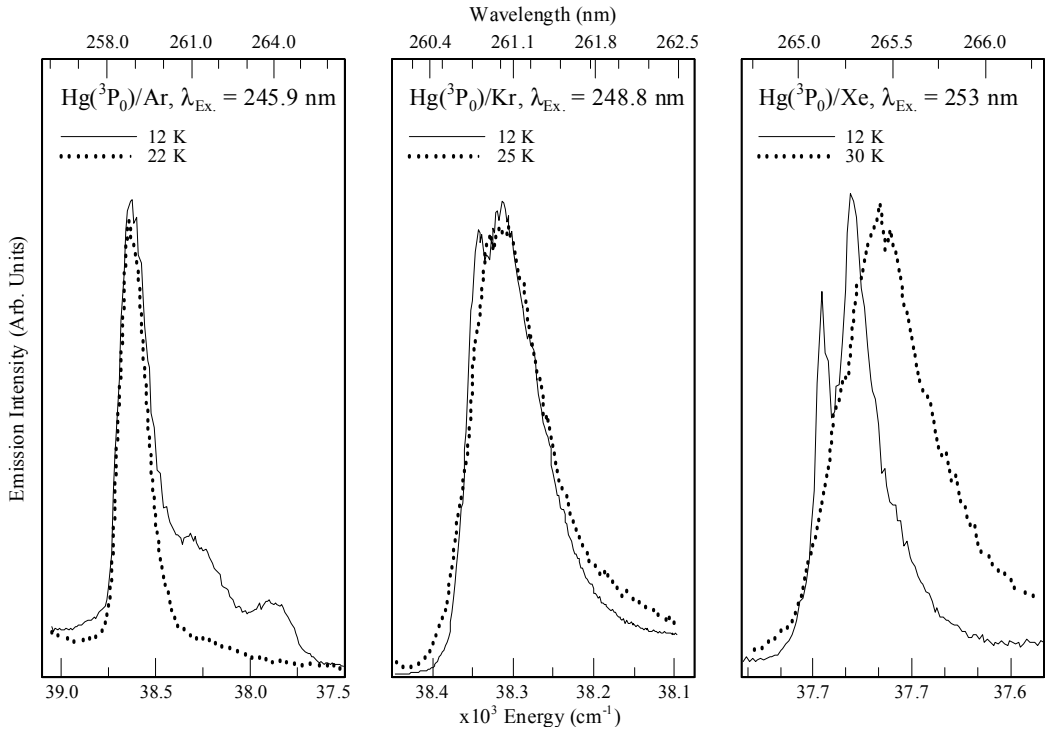

Figure III.15 **High resolution scans of the Hg $^3P_0$ state emission in Ar, Kr and Xe yielding resolved fine structure in the Hg/Kr and Hg/Xe systems. The solid traces were recorded at 12 K. High temperatures scans are shown by the dotted lines indicating reversible changes in the Hg/Kr and Hg/Xe spectra. The main band in the Hg/Ar system exhibits little temperature dependence but the weak pair of red bands, assigned to defect site occupancy, are quenched at elevated temperatures.**

To investigate the origin of the splitting observed at high resolution for the $^3P_0$ state emission in Hg/Xe, a lineshape analysis was conducted using the *Wp* optical function. This function was originally derived by Huang and Rhys[22]. It is described in detail by Struck and Fonger[23] and given by

Erreur ! Equation (III.3)

In this expression $r = \exp(-h,^{-}\omega/kT)$ and $Ip(x)$ is a modified Bessel function of variable order p and at a given temperature T, of fixed argument $\theta = 2Sr^{1/2}/(1 - r)$. The function W provides the distribution of intensity as a function of phonon number, p. It essentially provides Franck-Condon intensity factors for a single phonon mode of frequency $h,^{-}\omega$, coupling to the electronic transition with a strength S, a variable known as the Huang-Rhys factor. For large *S*, the *Wp* function approaches a Gaussian function. To maintain numerical accuracy in the weak electron-phonon characteristics of the Hg $^3P_0$ state emission spectra, the sum form of the Wp function was used in our programming. The sum form is

Erreur ! Equation (III.4)

and its evaluation is truncated at θ_m, the next integer greater than θ + 1. Clearly, the sum increases with the electron-phonon coupling strength S and the temperature.

A fit with the Wp function allows identification of the position of the zero-phonon line (*ZPL* or $\nu_{0,0}$), and the magnitude of the strength electron-phonon coupling S once the recorded spectrum has been transformed into phonon units, p. This initially involves estimating the magnitude of the phonon frequency, $h,^{-}\omega$, a task which was direct in the 12 K Hg/Xe spectrum due to the *ZPL* being resolved. A satisfactory fit, obtained with S = 1.3 and $h,^{-}\omega$ = 21.0 cm^{-1}, is shown on the left in Figure III.16. The fit verifies the *ZPL* is located at 37718 cm^{-1}, the phonon side-band is, as expected, to the red of this. In addition it reveals the presence of weak, 'hot' emission at 37739 cm^{-1} to the blue of the *ZPL*. Using the 12 K fit parameters (S, $h,^{-}\omega$ and $\nu_{0,0}$) the lineshape calculated with T = 30 K is compared on the right in Figure III.16 with the emission spectrum recorded at this temperature. Evident in this plot is the diminished intensity of the *ZPL* and the gain in the intensity of the phonon sideband now showing a maximum at 37673 cm^{-1}.

Similar fits were performed on the $^3P_0$ emission in Hg/Kr and Hg/Ar. A satisfactory fit was obtained in Hg/Kr with S = 2.2, $h,^{-}\omega$ = 28.0 cm^{-1} and $\nu_{0,0}$ = 38366 cm^{-1}. The comparison shown on the right in Figure III.17 indicates that the *ZPL* is not resolved in Hg/Kr but is located as a blue shoulder on the partially resolved feature. The fits conducted in Hg/Ar are not as definitive as those in Hg/Xe or Hg/Kr because fine-structure splitting has not been resolved to provide an initial estimate of the phonon frequency, $h,^{-}\omega$. However, the lineshape generated with S = 3.3, $h,^{-}\omega$ = 41.0 cm^{-1} and $\nu_{0,0}$ = 38740 cm^{-1} compares well, as shown on the left in Figure III.17 with the observed emission band. This fit indicates the *ZPL* is too weak to be resolved in the emission spectrum. The results of the Wp lineshape analyses are presented in Table III.5.

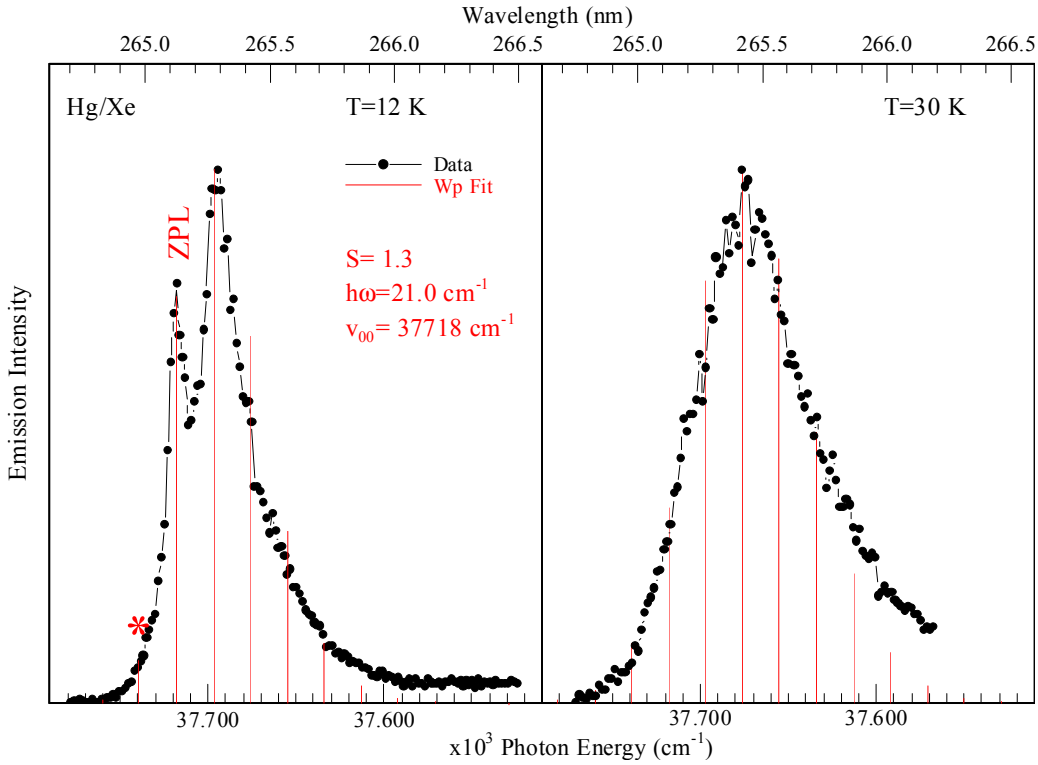

Figure III.16 **The Wp lineshapes calculated with Equation III.4 for the $^3P_0$ state emission in Hg/Xe recorded at 12 and 30 K and produced with pulsed laser excitation at 253 nm. The location of the zero-phonon line in the spectrum is indicated as *ZPL* and numerically as $\nu_{0,0}$. The presence of 'hot' emission in the 12 K spectrum indicated by the asterix is made evident in the comparison of fit and data, which reveals the existence of a line to the blue of the *ZPL*.**

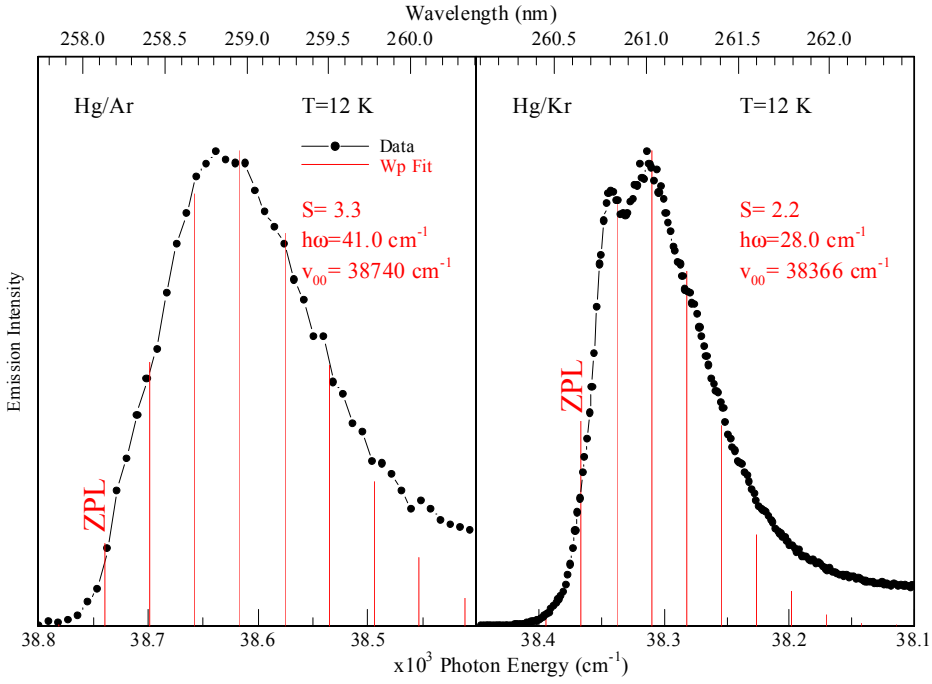

Figure III.17 **The Wp lineshapes calculated for the $^3P_0$ state emission in the Hg/Ar and Hg/Kr systems. The Hg/Ar emission was produced with laser excitation at 245.9 nm, the Hg/Kr spectrum with 248.8 nm excitation.**

Table III.5 **The location of the *ZPL* extracted in the Wp lineshape function analysis conducted on the recorded atomic Hg $^3P_0 \leftrightarrow {}^1S_0$ emission in solid Ar, Kr and Xe. For comparison purposes, the results of a similar analysis on the central component in the Hg/Xe $^3P_1 \leftrightarrow {}^1S_0$ emission are also given.**

Hg/RG	Transition	*ZPL*, $\nu_{0,0}$ (cm^{-1})	*S*	$\hbar\omega$ (cm^{-1})
Hg/Ar	$^3P_0 \leftrightarrow {}^1S_0$	38740	3.3	41
Hg/Kr	$^3P_0 \leftrightarrow {}^1S_0$	38366	2.2	28
Hg/Xe	$^3P_0 \leftrightarrow {}^1S_0$	37718	1.3	21
Hg/Xe	$^3P_1 \leftrightarrow {}^1S_0$	~39000	105	21

The two weak features in the Hg($^3P_0$)/Ar emission spectrum at 261.17 and 263.75 nm (see Figure III.14 and Figure III.15), have always been present in the samples we have prepared. As shown in Figure III.15, both of these low energy features are absent in the high temperature scans but re-appear at 12 K. It has also been observed that the intensities of these two features are increased dramatically by the introduction of a third species to the Hg/Ar matrix. This is most evident in Ar samples containing less than 0.1% Xe, where the intensities of the red-pair increase together relative to the 258.9 nm band. Crepin *et al.*[7] previously assigned the 263.75 nm feature to an Hg:H_2O complex in the Ar matrix, however, we find this band always accompanies the 261.17 nm feature and both are present in Ar samples free of water. Thus, we assign this pair of bands to mercury atom occupancy in imperfect sites in the Ar lattice, for example, a substitutional site with one of the 12 nearest neighbour atoms missing.

Long decay times, ranging from 8 – 530 ms, were recorded for the emission bands of Ar, Kr and Xe shown in Figure III.14 and Figure III.15, verifying that they correspond to the strongly forbidden Hg $^3P_0 \rightarrow {}^1S_0$ transition. Least squares fits with a triple–exponential function were required to obtain adequate fits, as shown in Figure III.18 for the Hg/Xe system. This is indicative of complex decay kinetics, behaviour already reported[7] by Crepin *et al*. It should be noted however, that by far the largest component in the decay curve has the shortest decay time (τ = 8.8 ms) while the longest decay (τ = 541 ms) is found only on the phonon sideband band and is the weakest component. An investigation of the temperature dependence in the decay times extracted monitoring the 265.3 nm emission up to 30 K allowed the assignment of the 8.8 ms component as the radiative lifetime for the $^3P_0 \rightarrow {}^1S_0$ transition in solid Xe.

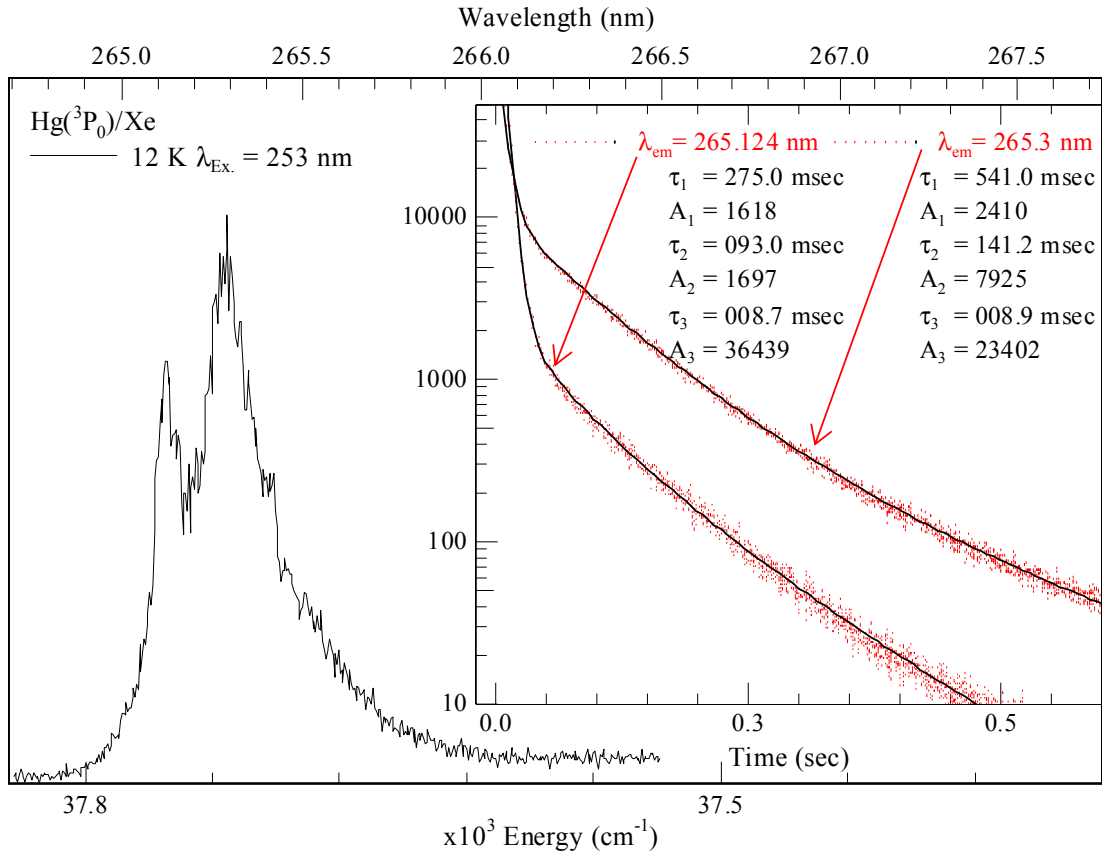

Figure III.18 **Hg/Xe high-resolution time-gated emission spectra produced with laser excitation at 253 nm. Inset results of the non-linear least squares analysis completed and the decay characteristics extracted for the resolved emission features at 265.124 and 265.3 nm respectively.**

III.3 Discussion

III.3.I Hg $^3P_1 \rightarrow {}^1S_0$ emission

The gross spectral features recorded for the Hg $^3P_1 \rightarrow {}^1S_0$ transition in the present study are in very good agreement with Crepin and Tramer's[7] earlier work. High resolution scans of the emission bands reveal complex profiles, requiring multiple emission components to yield adequate lineshape fits. Of the Hg/RG systems, the most complex behaviour is exhibited by the emission in Hg/Xe, which shows a blue shift with increasing temperature. Calculation of the Wp optical function for the $^3P_1$ state emission in xenon yields a Gaussian curve with an electron-phonon coupling strength S of 105. This is almost two orders of magnitude greater than the value of 1.3 extracted for the $^3P_0$ state emission and closely replicates the central Gaussian in the lineshape analysis of the 273 nm band. Gaussian fits done as a function of temperature reveal that the intensity of the central component is diminishing at high

temperature. The origin of the multiple emission components in the Hg/RG systems is known from excitation scans not to be due to multiple site occupancy. Pair-potential simulations described in Chapter IV, present a model, which explains the origin of multiple emission features for atomic mercury isolated at a single site. These calculations also suggest a mechanism for the quenching of the central emission component in the 273 nm emission in the Hg/Xe system.

Time-resolved emission spectra recorded allowed the assignment of the nanosecond radiative lifetimes τ_{rad} of the emission features corresponding to atomic Hg $^3P_1 \rightarrow {}^1S_0$ relaxation in solid Ar, Kr and Xe. The decay profiles extracted from the time-resolved emission spectra exhibited different decay characteristics for the emission components identified in the lineshape analysis completed for Hg/Xe system, providing further evidence for the multi-component nature of the Hg($^3P_1 \rightarrow {}^1S_0$)/Xe emission.

III.3.II Hg $^3P_0 \rightarrow {}^1S_0$ emission

The spectral and temporal characteristics of the Hg atom $^3P_1$ and $^3P_0$ excited state emissions are very different making them, as the comparison presented in Figure III.4 for Hg/Xe illustrates, easy to differentiate. Although the $^3P_0$ state was easily observed with laser excitation in the three rare gas hosts used, the actual amount of it produced with $^3P_1$ state excitation is rather small relative to emission of the $^3P_1$ state. The inefficiency of the $^3P_1 \rightarrow {}^3P_0$ intramultiplet relaxation is made clear in Figure III.2, where the only Hg/RG system showing a clear sign of the $^3P_0$ state in continuous (time-integrated) emission is Hg/Xe. Even in Hg/Xe, the ratio of the $^3P_1$ state radiative decay to the $^3P_1 \rightarrow {}^3P_0$ intramultiplet relaxation is estimated as 200:1 from the lineshape analysis presented in Figure III.5 and the corresponding numerical data collected. Moreover, the efficiency of the intramultiplet relaxation is not enhanced with increasing temperature up to 42 K as shown in Figure III.5.

Optical lineshapes generated with the Wp function indicate the $^3P_0$ emission in the solid rare gases involves weak electron-phonon coupling. The S values extracted are 1.3, 2.2 and 3.3 for Xe, Kr and Ar respectively. In solid-state spectroscopy, weak electron-phonon coupling is indicative of unshifted potentials for the two states involved in the optical transition. While the ground and many of the excited state potentials of the Hg·RG complexes are accurately known, the $\tilde{a}^3 0(^3\Sigma)$ states of the

Hg($^3P_0$)·RG diatomics cannot be determined directly be spectroscopic means. However, in the limit of Hund's case-c coupling, it can be extracted from the $A^3 1(^3\Pi)$ and $B^3 0(^3\Sigma)$ states[24,25] of the Hg($^3P_1$)·RG diatomics with Equation III.5

$$V(^3P_0)\ \tilde{a}^3 0 = 1/3[(V_\Sigma^e + V_\Pi^e) + V_\Pi] \qquad \text{Equation (III.5)}$$

presented by Duval *et al*[26]. In this expression V_Π is the spectroscopic A state, while V_Σ is determined from the A and B states from the relationship $V_\Sigma = 2V_B - V_A$.

The potential energy curves extracted for the $\tilde{a}^3 0(^3\Sigma)$ states of the Hg($^3P_0$)·RG diatomics from the spectroscopic A and B states are shown in Figure III.19 and their key parameters are collected in Table III.6. It is evident on inspection of the curves shown in Figure III.19 that the ground Hg($^1S_0$)·RG $X\ ^1 0(^1\Sigma)$ and excited Hg($^3P_0$)·RG $\tilde{a}\ ^3 0(^3\Sigma)$ state potential energy curves are very similar. Conversely the form of the excited Hg($^3P_1$)·RG $A^3 1(^3\Pi)$ state potentials are very different to the ground states. This explains the very strong electron-phonon exhibited on the Hg($^3P_1$) state emissions (e.g., Hg/Xe, S = 105) and the very weak coupling on the Hg($^3P_0$) state emission (S = 1.3).

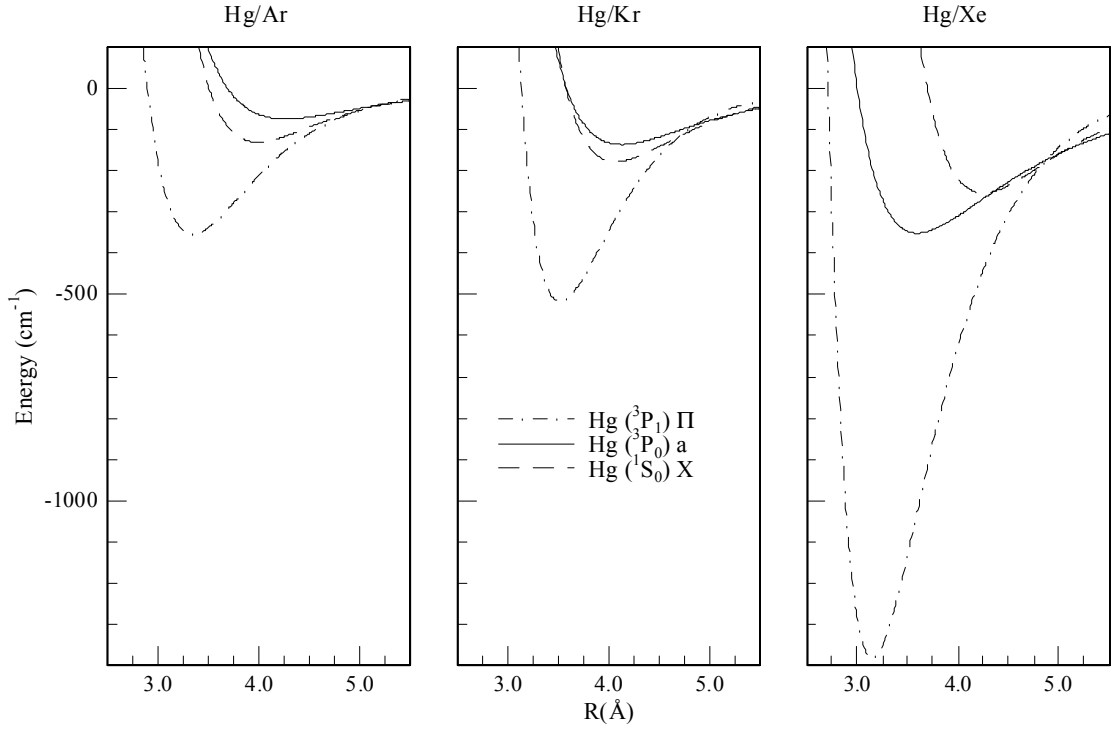

Figure III.19 **Potentials of the Hg·RG diatomics of relevance to the Hg($^3P_0$)/RG matrix emission spectra. The X and the A(Π) state potentials are obtained directly from spectroscopic data of the Hg·RG diatomics given in Ref.26 while the $\tilde{a}^3 0^-$ state potential was obtained with Equation III.5 which assumes case-(c) coupling.**

Table III.6 **Comparison of the key molecular parameters of the ground X $^1\mathbf{0}^+(^1\mathbf{\Sigma})$ and excited ã $^3\mathbf{0}^-(^3\mathbf{\Sigma})$ states of the Hg·RG diatomics. The ã(^{3}0$^-$) state was obtained from Equation III.3 using the spectroscopic potentials presented in Ref. 26 for the Hg($^3P_1$)·RG [A $^3\Pi$ (^{3}0$^+$)] and [B $^3\Sigma$ (^{3}1)] states. Also shown are the bond lengths of the rare gas dimers.**

State	Parameter	Hg·Ar	Hg·Kr	Hg·Xe
ã ^{3}0$^-$($^3\Sigma$)	D_e(cm^{-1})	92	136	351
	R_e(Å)	4.26	4.13	3.6
X ^{1}0$^+$($^1\Sigma$)	D_e(cm^{-1})	130.25	178	254
	R_e(Å)	3.98	4.07	4.25
X RG·RG	D_e(cm^{-1})	99.5	138.4	196
	R_e(Å)	3.756	4.017	4.363

Closer scrutiny of the bond lengths collected in Table III.6, reveals that another parameter plays a role in determining the electron-phonon coupling strengths. Specifically, the ã ^{3}0($^3\Sigma$) and X ^{1}0($^1\Sigma$) state bond lengths are almost identical in Hg·Kr and differ by larger amounts in the Hg·Ar and Hg·Xe cases. It will be remembered that the weakest electron-phonon coupling strength was identified in Xe, not in Kr. Application of Equation III.5, in the extraction of the ã^{3}0($^3\Sigma$) states, assumes case-(c) coupling but as this is expected to be reasonable in the case of the Hg·RG diatomics, some other factor must be partly determining the S value. Another parameter that plays a role in this regard is the site size presented by the solid. From the comparison made in Table III.6 of the substitutional site sizes of the solid rare gases with the Hg·RG ground state bond lengths, it is clear that Xe is the only system where the site size of the solid is larger than the bond length of any Hg·Xe state. Thus, in the case of Hg·Xe, emission will terminate in a state whose bond length is less than that the Xe-Xe distances in the lattice. Hence, little or no coupling will occur between the optically active Hg·(Xe)$_n$ "quasi-molecule" and the delocalised phonons of solid xenon. On this basis, stronger (but still weak) coupling is anticipated in Kr where the Hg·Kr ground state bond length (4.07 Å) only slightly exceeds that of Kr-Kr (4.017 Å). In solid Ar, the nearest neighbour distance (3.756 Å) is considerably shorter than the ground state bond length (3.98 Å) of Hg·Ar. In this case, emission will return a ground state configuration almost 0.25 Å more extended that the equilibrium Ar lattice positions. This will necessarily result in stronger coupling with the lattice phonons.

III.4 Conclusions

The sharp, weak feature centered at 37693.9 cm^{-1} in Hg/Xe is the 6p $^3P_0 \rightarrow$ 6s $^1S_0$ transition and arises from of intramultiplet $^3P_1 \rightarrow {}^3P_0$ relaxation. The contribution of this band to the time integrated emission intensity is only 0.5% indicating the inefficiency of intramultiplet $^3P_1 \rightarrow {}^3P_0$ relaxation compared with radiative decay of the $^3P_1$ excited state. The efficiency of the intramultiplet relaxation increases, but only very slightly, at higher temperatures. The presence of resolved fine structure on the Hg $^3P_0 \rightarrow {}^1S_0$ emission bands in Xe (and partly in Kr) matrices and the temperature dependence exhibited, allowed the identification of a zero phonon line and a phonon side band. This assignment is confirmed in the lineshape simulation conducted with the Wp function yielding small S values (1.3 and 2.2 in Xe and Kr respectively), which represent weak electron-phonon coupling. The close match between the excited Hg·RG($^3P_0$) $\tilde{a}^3 0^-(^3\Sigma)$ and ground X Hg·RG($^1S_0$) $^1 0^+(^1\Sigma)$ state bond lengths is the origin of the very weak electron-phonon coupling in the Hg($^3P_0$)/RG matrix system. Conversely the dissimilarity in the bond lengths in the excited A Hg·RG($^3P_1$) $^3 1(^3\Pi)$ state and ground X Hg·RG($^1S_0$) $^1 0^+(^1\Sigma)$ state potentials explains the large linewidths on the Hg($^3P_1$)/RG matrix bands. The multi-component nature of the $^3P_1$ state emission is shown not to arise from solid-state effects such as multiple site trapping. Its origin is examined in Chapter IV where the energetics of excited state vibronic modes are calculated with pair-potential methods for Hg($^3P_1$)/RG_{18} clusters.

References

1 W.H. Breckenridge, C. Jouvet, B. Soep, in: M. Duncan (Ed.), *Advances in Metal and Semiconductor Clusters*, Vol. 3, JIA Press, Greenwich, CT, 1995.

2 C. Crepin-Gilbert and A. Tramer, *Intl. Rev. Phys. Chem.*, **18**, 485 (1999).

3 Atomic Energy Levels, Volume 3, Circular 467, *Department of Commerce United* States of America.

4 M. McCarty and G.W. Robinson, *Mol. Phys.*, **2**, 415 (1959).

5 J. G. McCaffrey and P. N. Kerins, *J. Chem. Phys*., **106**, 7885 (1997).

6 B. Healy and J. G. McCaffrey, *J. Phys. Chem. A*, **104**, 3553 (2000).

7 C. Crepin and A. Tramer, *J. Chem. Phys*., **97**, 4772 (1992)

8 C. Crepin, F. Legay, N. Legay-Sommaire and A. Tramer, *Trends in Chem. Phys*., **7**, 111 (1999).

9 S.L. Laursen and H.E. Cartland, *J. Chem. Phys*., **95**, 4751 (1991).

10 M. Chergui, C. Crepin, T. Hebert and A. Tramer, *Chem. Phys. Letts*. **197**, 467 (1992).

11 C. Crepin, M. Chergui, T. Hebert, L. Konig, P. Martin and A. Tramer, *J. Phys. Chem.,* **98**, 3280 (1994).

12 C. Crepin and A. Tramer, *J. Chem. Phys*., **100**, 5467 (1994).

13 C. Crepin and A. Tramer, *J. Chem. Phys*., **107**, 2205 (1997).

14 J. Helbing, A. Haydar and M. Chergui, *J. Chem. Phys*., **113**, 3621 (2000).

15 This broad feature originates from the remnants of a thermally unstable site that still existed in this annealed Hg/Kr sample.

16 K. A. Mohamed, *J. Quant. Spectrosc. Radiat. Transfer*, **30**, 225, (1982).

17 NIST, Physics Laboratory, Physical Reference Data, *www.physics.nist.gov*

18 R. L. Fulton, *J. Chem. Phys*., **61**, 4141, (1974).

19 T. Shibuya, *J. Chem. Phys.*, **78**, 5175, (1983).

20 The refractive indices of Ar, Kr and Xe are 1.29, 1.28 and 1.49 recorded at 60 K and λ = 488 nm from H. J. Jodl, Solid-state Aspects of Matrices in *The Chemistry and Physics of Matrix-Isolated Species*, North-Holland, 1989.

21 The index of refractive used for solid Ar at 233 nm is 1.32 at 6 K. That of Kr is 1.428 at 241 nm at 12 K. (P. Gürtler, unpublished results, 1996).

22 K. Huang and A. Rhys, Proc. Roy. Soc. (London) **204A**, 406 (1950), reprinted in *Selected papers on Photoluminscence of Inorganic Solids*, edited by M.J. Weber, SPIE-The International Society of Optical Engineering, Washington, 1998.

23 C.W. Struck and W.H. Fonger, Understanding Luminscence Spectra and Efficiency *Using Wp and Related Functions*, Springer-Verlag, Berlin, 1991.

[24] J. Zuniga, A. Bastida, A. Requena, N. Halberstadt and J. Beswick, *J. Chem. Phys*., **98**, 1007 (1993).

[25] M. Okunishi, H. Nakazawa, K. Yamanouchi and S. Tsuchiya, *J. Chem. Phys*., **93**, 7526 (1990).

[26] M. C. Duval, O. B. D'Azy, W. H. Breckenridge, C. Jouvet and B. Soep, *J. Chem. Phys*., **85**, 6324 (1986).

Chapter IV

A pair-potentials analysis of the optical spectroscopy of $^3P_1$ state atomic mercury isolated in solid Ar, Kr and Xe.

IV.1 Introduction

In the sections which follow, a method of simulating the optical (absorption and emission) spectroscopy of metal atoms isolated in solid rare gases is outlined. This theoretical approach was developed by the Maynooth Group[1] for metal atoms with ns^2 ground states and utilises known Metal (M)·Rare Gas (RG) diatomic pair–potentials available from spectroscopic studies and *ab initio* calculations of interaction potentials for M·RG 1:1 van der Waals complexes. A pair–wise sum of these known M·RG potentials is used to construct a M/RG_{18} cluster and simulate the solid matrix, where the matrix can be considered as an infinite cluster RG_n. Allied with the availability of known interaction potentials is the particularly simple face centered cubic (fcc) packing structure exhibited by all the solid rare gases. These factors allowed the localized M/RG_{18} cluster model to be applied successfully in investigating the absorption and emission spectroscopy of atomic zinc[1] in rare gas matrices.

Here the localised, pair-potentials approach[1] is used to investigate the characteristics of the absorption and emission spectroscopy of the atomic mercury $^3P_1 \leftrightarrow {}^1S_0$ transition isolated in solid Ar, Kr and Xe. The validity of the pair potentials approach has been examined by Beswick *et al.*[2] for the triatomic Hg($^3P_1$)·Ar_2 complex by simulating the vibronic structure in the resonance two-photonionization (R2PI) spectra recorded for this cluster by Jouvet and co-workers[3]. A similar theoretical approach has also been used by Alexander and coworkers[4] on the ground state B(^2P_J)·Ar_2 system. McCaffrey and Kerins adapted Beswick's cluster method for the solid state in a simulation of the spectroscopy of atomic zinc[1] in the solid rare gases. The calculations originally employed for zinc were recently extended to cover atomic cadmium[5] and sodium[6] isolated in rare gas solids.

The most detailed spectroscopic study of matrix-isolated[7] atomic mercury (Hg/RG) has focused on the 6p $^3P_1 \leftrightarrow$ 6s $^1S_0$ transition and was conducted a decade ago by the Orsay group[8]. The present work has extended the experimental

information because of the need to examine aspects of the Hg/RG matrix emission revealed in Hg·RG pair-potentials[9] simulations. The new experimental work presented in Chapter III has shown that the $^3P_1$ emission bands are multi-component, requiring the use of three broad Gaussian functions to obtain satisfactory fits. Excitation spectra recorded for these emission components were all identical, indicating that the effect arises from single site occupancy. In this Chapter details of the pair-potential calculations are presented and highlight aspects of the luminescence not evident in the original experimental work, in particular the quenching of very strongly bound excited states in the Hg/Xe system.

In the following sections, an examination of the Hg atom $^3P_1 \leftrightarrow {}^1S_0$ matrix spectroscopy is presented using experimental Hg·RG pair potentials for the ground X and excited A and B states[2,10,11] in Hg·RG_{18} cluster calculations. In addition to the tetragonal (4-fold symmetry) "body" (Q_2) and "waist" (Q_3) modes described in earlier work[1,5], calculations of trigonal (3-fold symmetry) 6-atom "body" (Q_4) and "waist" (Q_5), modes are performed on the Hg/RG systems. Details of the two–fold symmetry 'body' (Q_6), and 'waist' (Q_7), modes are also presented for each of the excited state *p*–orbital orientations. The new calculations presented in this contribution cover the three symmetry poles of a cubo-octahedral point group[12] to which the substitutional site occupancy (M·RG_{12} system) belongs. This high symmetry approach has been adopted as it provides the most extreme energetics, i.e., the attractive orbital orientations yield the most stabilised energies while the repulsive orientations are the most destabilised. All lower symmetry selections will provide intermediate energies between these extreme values. In the high symmetry approach insight can be gained especially into the stabilised modes, which determine the excited state relaxation and produce emission. Molecular dynamics or Monte Carlo simulations can yield more general dynamics information but requires detailed analysis of the nuclear co-ordinates to identify the symmetry of the active vibrational modes.

For the purpose of illustration, a full account of the interaction details is presented for Hg/Xe, while only a summary of results, showing stabilised modes, is provided for the Hg/Ar and Hg/Kr systems. Predictions made in the theoretical analysis are compared with matrix absorption and emission spectra presented in Chapter III, revealing information on the site occupancy and excited state dynamics.

IV.2 Methods and Results

The assumptions on which the localized cluster model is based are I) the photo-physical properties (absorption and emission energies) of the metal atom chromophore are governed by its immediate environment within the rare gas solid. II) The interactions between the metal atom and the surrounding RG atoms can be described completely by the sum of diatomic pair potentials[13]. III) The atomic electronic angular momentum, J_e, at the molecular asymptote is conserved within the cluster. The validity of the pair potentials approach has been examined by Beswick *et al.*[2] for the triatomic Hg($^3P_1$)·Ar_2 complex by simulating the vibronic structure in the resonance two-photonionization (R2PI) spectra recorded for this cluster by Jouvet and co-workers[3]. A similar theoretical approach has also been used by Alexander and coworkers[4] on the ground state B(^2P_J)·Ar_2 system. McCaffrey and Kerins[1] adapted Beswick's cluster method for the solid state in a simulation of the spectroscopy of $^1P_1 \leftrightarrow {}^1S_0$ transition of atomic zinc in the solid rare gases based on metal atom occupancy in a substitutional site.

The most fundamental aspect of the solid-state calculations is the site occupied by the ground state metal atom in the rare gas lattices. From the ground state bond length (R_e) data presented in Table IV.1 for the mercury atom-rare gas atom diatomics and the rare gas dimers, very good matches exist between the Xe_2 and Kr_2 systems and their Hg·RG counterparts. Very favourable matches also exist for the Hg·RG van der Waals bond lengths and the substitutional site (*ss*) sizes of the solid rare gases. Thus in solid Xe, *ss* is 4.334 Å, calculated from the lattice parameter[14] a = 6.13 Å, while the Hg·Xe bond length is 4.25 Å and in solid Kr, *ss* is 3.991 Å while R_e Hg·Kr is 4.07 Å. The match that exists for Hg in Ar is not quite as good, where *ss* is 3.756 Å and R_e Hg·Ar is 3.98 Å. However, even in Hg/Ar, substitutional site occupancy is also expected[15].

Following identification of the site of isolation, the energy of a guest metal atom (M) occupying a substitutional site in a solid rare gas (M/RG) system is calculated for an M·RG_{18} cluster. The rare gas atoms in this cluster fall, as shown in Figure IV.1, into two categories based on whether they are located in the first or second sphere of host atoms surrounding the guest atom M. The first category has a cubo-octahedral arrangement of 12 host atoms located at a nearest neighbour (*nn*) distance of $a/\sqrt{2}$ from M. The other set, consisting of 6 atoms are located at a next

nearest neighbour (*nnn*) distance of the lattice parameter, *a*, from the guest atom and are arranged as a regular octahedron on the X, Y and Z axes.

Table IV.1 **Spectroscopic constants used to generate the Morse potential energy curves for the Hg·RG and RG_2 diatomics. Data source are indicated by the references.**

Hg·RG State	**Morse Parameters**	**Hg·Ar[2]**	**Hg·Kr[10,11]**	**Hg·Xe[11]**
$X\ ^1\Sigma$	$\mu_{Hg\text{-}RG}$ (amu)	33.3614162	59.2819820	79.7926882
($^10^+$)	$D_e(cm^{-1})$	130.25	178	254
	$\omega_e(cm^{-1})$	23.5	20	18.3
	$\omega_e x_e(cm^{-1})$	1.1	0.54	0.33
	R_e(Å)	3.98	4.07	4.25
	$\beta(Å^{-1})$	1.448348	1.40557	1.249072
$A\ ^3\Pi$ ($^30^+$)	$D_e(cm^{-1})$	353.63	517, (628.7)	1380.9
	$\omega_e(cm^{-1})$	41.2	43.5, (40.63)	54.17
	$\omega_e x_e(cm^{-1})$	1.2	1.5, (0.691)	0.565
	R_e(Å)	3.34	3.52, (3.35)	3.15
	$\beta(Å^{-1})$	1.54104964	1.793813, (1.5193512)	1.585736
$B\ ^3\Sigma$ (^{31})	$D_e(cm^{-1})$	51.57	96, (104.8)	187.6
	$\omega_e(cm^{-1})$	11.4	11.3, (11.1)	9.71
	$\omega_e x_e(cm^{-1})$	0.6	0.32, (0.301)	0.215
	R_e(Å)	4.66	4.57, (4.58)	4.47
	$\beta(Å^{-1})$	1.1166067	1.081374, (1.0166592)	0.77118
		Ar·Ar[16]	**Kr·Kr[16]**	**Xe·Xe[16]**
$X\ ^1\Sigma$	$D_e(cm^{-1})$	99.545	138.4	196.24
	R_e(Å)[17]	3.7565	4.017	4.3634
	$\beta(Å^{-1})$	1.40218	1.604	1.509

The expectation of substitutional site occupancy of atomic Hg within solid Ar, Kr and Xe lattices is tested by comparison of the predicted and observed absorption energies. The absorption energy is calculated as the difference between the energy of the cluster in the ground and excited state within the Frank – Condon principle. The method of evaluating the cluster energies for the ground Hg($^1S_0$)/RG_{18} and excited Hg($^3P_1$)/RG_{18} states is outlined in the following sections.

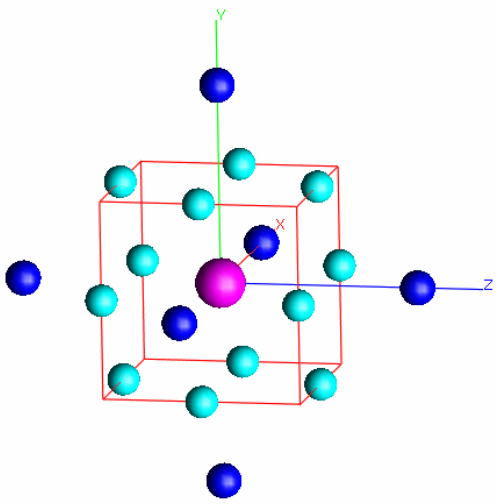

Figure IV.1 **The guest atom-based co-ordinate system used to calculate the energy of a metal atom, M in a substitutional site of an *fcc* lattice. The 12 nearest neighbour (*nn*) Rg atoms surrounding the guest atom located at the origin are shown as grey spheres on the edges of the cubic unit cell. The 6 next nearest neighbour (*nnn*) atoms in the second surrounding sphere are shown as the dark spheres on the X, Y, Z axes at the lattice parameter distance, *a*, from the guest metal atom. The axis system shown is co-incident with the three, fourfold (C_4) symmetry axes of the cubo-octahedral *fcc* unit cell and is referred to in the text as 4-atom mode calculations. The image was generated by the gOpenMol[18] programme.**

IV.2.I Ground $^1S_0$ state

The ground $^1S_0$ electronic state of a closed shell ns^2 metal atom within a M/RG_{18} cluster is simple to evaluate given the spherical symmetry of the atomic electronic angular momentum. The interactions between the ground $6s^2\ ^1S_0$ state mercury atom and the RG_{18} cluster is then simply a pair–wise sum of the interaction potentials at a specific distance (R_k). Because for $J_e = 0$, there is no angle dependence. This is evident in Equation IV.1, used to evaluate the ground state energy of the cluster, in which the energy is obtained as a sum of the Hg·RG and RG_2 pair-potentials.

$$W_X(R) = \textbf{Erreur !} \qquad \text{Equation (IV.1)}$$

Morse functions[19] are used for the ground state potentials for the Hg·RG diatomics and for the rare gas dimers, RG_2 (RG = Ar, Kr and Xe). The parameters used for these functions are listed in Table IV.1.

IV.2.II Excited $^3P_1$ state

In order to calculate the mercury atom $6p\ ^3P_1 \leftrightarrow 6s\ ^1S_0$ absorption and emission energies in the solid, it is necessary to obtain the energy of the electronically excited

$^3P_1$ state mercury atom in the Hg·RG_{18} cluster. This is more difficult than the ground X state due to the axial symmetry of the electronic angular momentum, $J_e = 1$. The method and notation used by Beswick and coworkers[2] was followed throughout. The Hg·RG molecular states arising from the approach of the Hg ($^3P_1$) to the closed shell rare gas atom with the internuclear axis defined as the *Z*–axis have pure Π and Σ arising from the projection of the atomic angular momentum onto the internuclear axis corresponding to p_x, p_y and p_z orbital occupancy. The cluster potentials are generated by applying the Wigner rotation matrices using Hund's case-(a) quantum numbers as the diatomic basis set. The general solution for $J_e = 1$ corresponding to the three 6p-orbitals of the excited $^3P_1$ state mercury atom give rise to the following cluster states, where *n* is number of metal-rare gas bonds in the cluster.

(p_z) $W_1(R)$ = **Erreur !** Equation (IV.2)

(p_x) $W_2(R)$ = **Erreur !** Equation (IV.3)

(p_y) $W_3(R)$ = **Erreur !** Equation (IV.4)

In contrast to the ground state potential, given by Equation IV.1, the excited state energy is not a simple sum of the $V_\Pi(R)$ and $V_\Sigma(R)$ pair potentials, but now depends on the angle variables[1] θ_k and ϕ_k. In a Cartesian co-ordinate system having the metal atom positioned at the origin, θ_k is the angle subtended between a rare gas atom *k* and the Z-axis, while ϕ_k is the angle obtained by projecting the vector connecting this atom and the origin onto the XY plane as shown in Figure IV.2.

The $V_\Pi(R)$ and $V_\Sigma(R)$ terms appearing in Equations IV.2-4 are the pure Π and pure Σ spatial state potentials and not the spectroscopic A and B states of the Hg·RG diatomics presented in Table IV.1. As the B($\Omega_A = \pm 1$) state is a linear combination of Π and Σ orientations, it is necessary to extract the pure Σ potential for use in Equations IV.2-4. This was achieved using the relationship[20] $V_B = \frac{1}{2}[V_\Sigma^e + V_\Pi^e]$ which yields the spatial Σ component of the original B state.

$$V_\Sigma(R) = 2V_B(R) - V_A(R) \qquad \text{Equation (IV.5)}$$

Since the A($\Omega_A = 0$) state is of pure Π symmetry ($V_A = V_\Pi^e$) this potential was used directly. The result of the deconvolution of the pure Σ component from the B state is shown in Figure IV.3 for the Hg·RG diatomics (RG = Ar, Kr and Xe).

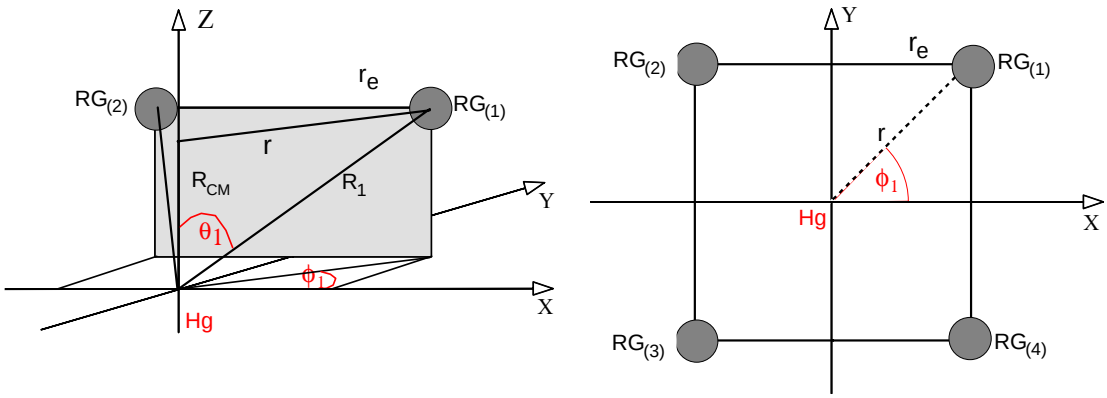

Figure IV.2 **Diagram of the metal atom based coordinate system illustrating the origin of the variables used in Equations (IV. 2-4) for the calculation of the excited state energies.**

It is clear from Figure IV.3 (dashed line) that the Σ states deconvoluted with Equation IV.5 are not completely repulsive as they all show weakly bound regions at long range. This behaviour is consistent with a slightly attractive van der Waals interaction which exists between the metal atom Hg(p_z) orbital and the rare gas atoms at long range. At short range, however, it was observed for all the Hg·RG systems, that the deconvoluted Σ state curves exhibited a non-physical minimum, instead of increasing exponentially like the B State. Fortunately, this non-physical behaviour of the Σ state (not shown in the plot) does not occur in the range of distances involved in the solid-state simulations. Even in Hg·Xe (the worst case of the Hg·RG diatomics) the Σ state becomes non-physical at distances less than 2.8 Å. As this is less than the shortest distance encountered for substitutional site occupancy (3.065 Å, half the lattice parameter of Xe), the raw deconvoluted Σ potential was used in all the excited state calculations.

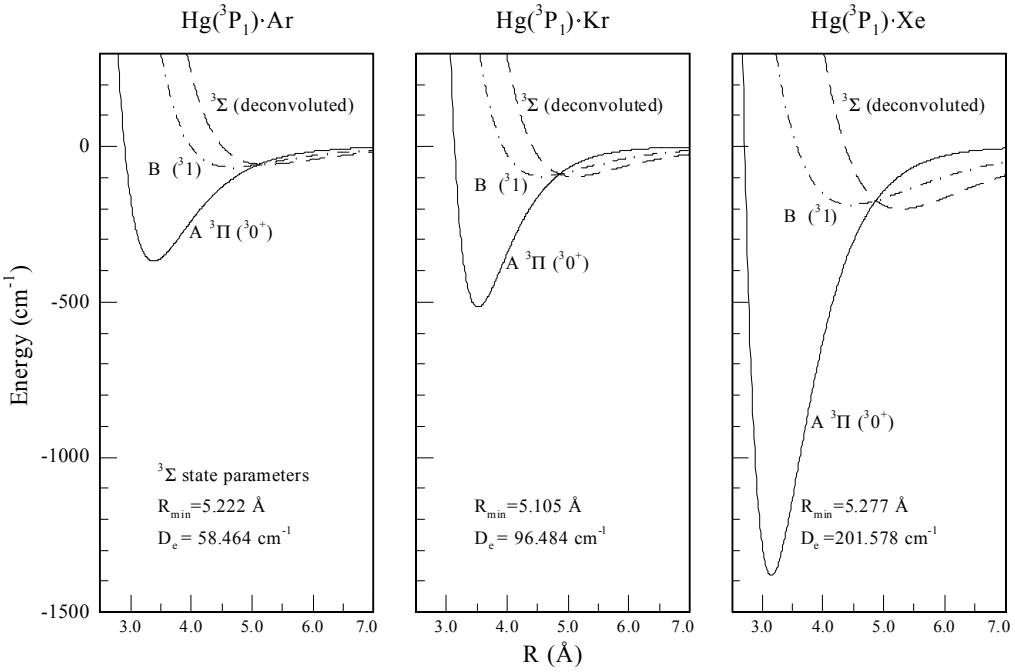

Figure IV.3 **The Hg($^3P_1$)·RG $^3\Sigma$ states extracted with Equation IV.5 from the spectroscopic [A ^{3}0$^+$ ($^3\Pi$)] and [B ^{3}1] states whose constants are presented in Table IV.1. All of these states share the Hg atom 6p $^3P_1$ asymptote at 39424.1 cm^{-1} but are shown dissociating to zero-energy for the purpose of comparison. Note that all the deconvoluted Hg·RG $^3\Sigma$ states show a weakly bound region at long internuclear distance. These distances are listed as R_{min} in the plots while the binding energies are indicated by D_e.**

Excited $^3P_1$ state energies were calculated for the body and waist vibronic (2) modes for the three p-orbital (3) orientations. The energetics of the two modes and the three orbital orientations were determined for three co-ordinate systems based on the three symmetry poles (3) of the cubo-octahedron. The symmetry poles[12] are fourfold, threefold and twofold symmetric and their calculations are referred to in this presentation as 4-atom, 6-atom and 2-atom modes respectively. The co-ordinate systems of the cubo-octahedron based on the three symmetry poles are shown in Figure IV.4.

Thus for a given rare gas host, a total of 18 excited state potential energy curves were calculated for an Hg·RG$_{18}$ cluster. Energies of the co-ordinate displacements were calculated at 0.001 Å intervals. As a check of the correctness of our code, absorption energies were compared for the three co-ordinate systems calculated. This can be used as a check since the three p-orbitals are degenerate at the centre of the cubo-octahedral substitutional site. Hence at R = 0, all modes must

produce identical absorption values irrespective of the vibronic mode, the symmetry co-ordinate system used or the orbital selected.

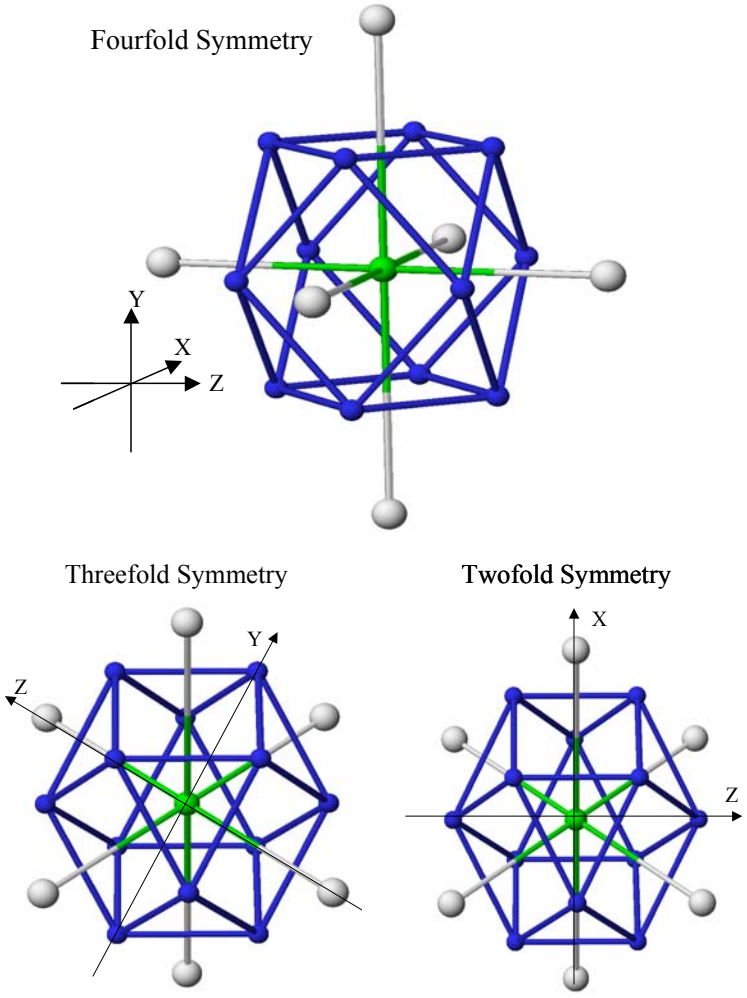

Figure IV.4 **Three co-ordinate systems based on the three symmetry poles of the cubo-octahedron with the metal Hg atom positioned in a substitutional site within the RG_{18} cluster. In fourfold symmetry the *Z*-axis is aligned with one of the six fourfold symmetry poles of the cubo-octahedron (the centre of the cubic faces). In the threefold and twofold symmetries, the *Z*-axis is aligned with one of the eight threefold symmetry poles (eight vertices of the cube) and the twelve twofold symmetry poles (one of the twelve edges of the cube) respectively.**

In generating the solid state localized model, individual calculations were preformed for smaller clusters and the resulting energies were used to obtain the energy of the Hg($^3P_1$)/RG_{18}. These calculations simulated the motion of the excited state Hg atom along the symmetry poles of the cubo-octahedron and provided information on interactions involved in 'body' mode calculations, where the $^3P_1$ Hg undergoes large amplitude motions within the rare gas lattice. The specific details of

the high symmetry cluster calculations completed are now presented. The results obtained and the connection between these smaller clusters (RG_n, $n \leq 6$) and the RG_{18} model are highlighted in the sections that follow.

IV.2.II.I Tetragonal (4-atom) symmetry modes

a. ***Q_2*** is the 4-atom 'body' mode presented in earlier work[1] on the Zn/RG systems. In this contribution, the energetics of this mode are given not only for the p_z orientation but also for the degenerate p_x/p_y set. These orientations correspond to the ^3A and ^3E states respectively of the excited Hg atom in a substitutional site. Details of the Hg·RG interactions considered in the calculation of the 4–atom 'body' mode are presented in Figure IV.5. The energetics of the Q_2 mode i.e., motion of the metal atom along the *Z*-axis in the four-fold symmetry system (Figure IV.4 top panel), is constructed from the interaction of the excited state Hg atom with four smaller clusters, all of fourfold symmetry. The smaller clusters are shown in Figure IV.5, in which S.site1 and S.site2 represent two planar arrangements of four RG atoms positioned at the nearest neighbour distance ($a/\sqrt{2}$) and next nearest neighbour distance of the lattice parameter *a* respectively from the Hg atom positioned at the centre of the substitutional site. The second set of fourfold symmetry clusters $I_{oh}1$ and $I_{oh}2$ are two RG_5 clusters forming square pyramids, whose base is located at the centre of the octahedral interstitial sites, at a distance of half the lattice parameter ($a/2$) from the centre of the substitutional site. Prior to completing the 4-atom 'body' mode calculations, the interaction of the excited Hg atom with these RG_4 and RG_5 clusters was examined.

The highest symmetry motion modelled by these cluster calculations was that of the C_{4V} approach of the Hg ($^3P_1$) atom towards a planar arrangement of four RG atoms[1]. This motion is representative of the motion of the metal atom from the centre of the substitutional site towards an octahedral interstitial site. This motion was restricted to the *Z*-axis perpendicular to the plane of the four RG atoms, (Figure IV.5)

By choosing, the Cartesian co-ordinate system to coincide with the three 4-fold symmetry axes of the cubo-octahedron (Figure IV.4, top panel), the general sum expressions given by Equations IV.2-4, reduce[1] to the simpler product expressions which provide the energies of the $^3A(p_z)$ and doubly degenerate $^3E(p_x, p_y)$ states of an excited $^3P_1$ state metal atom in a substitutional site.

$$W_{3A1}(R) = 4\left[\cos^2\theta\, V_{3\Sigma}(R) + \sin^2\theta\, V_{3\Pi}(R)\right] \qquad \text{Equation (IV.6)}$$

$$W_{3E}(R) = 2\left[\sin^2\theta V_{3\Sigma}(R) + (\cos^2\theta + 1)V_{3\Pi}(R)\right] \qquad \text{Equation (IV.7)}$$

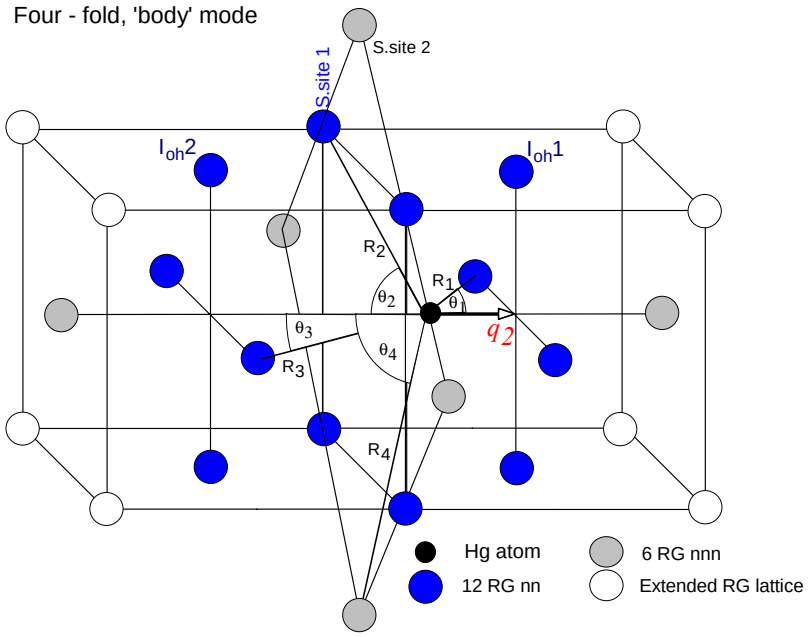

Figure IV.5 **A diagram representing the distance and angle parameters used in the calculation of the Tetragonal fourfold symmetry, 'body' mode, Q_2. The motion of the metal atom from the substitutional site towards the octahedral interstitial site $I_{oh}1$ along in the fourfold symmetry *Z*-axis is represented as q_2. Shown are the 12 nearest neighbour (*nn*) RG atoms arranged as three RG_4 square planar clusters in the XY plane. The six next nearest neighbour (*nnn*) atoms are also shown, four of these identified as S.site2 are positioned as a RG_4 cluster in the XY plane with each RG atom at the lattice parameter distance from the Hg atom at the centre of the substitutional site. The final two *nnn* atoms are positioned on the Z-axis positioned in the apical position of RG_5 square pyramidal clusters, the base of which corresponds to the octahedral interstitial site.**

Equations IV.6 and 7 were obtained upon summation of the expressions resulting after substituting values of $\phi_k = k\pi/4$, k=1, 2, 3 and 4 in Equations IV.3 and 4. Plots of the $^3A(p_z)$ and $^3E(p_x, p_y)$ states as a function of distance from the centre of mass R_{cm} of the Xe_4 cluster are shown in Figure IV.6. The variables, R and θ in Equations IV.6 and 7 are obtained from the relations $R = \sqrt{(R_{cm}^2 + r^2)}$ and $\theta = \sin^{-1}(r/R)$ where r = $r_e/\sqrt{2}$ is the distance of each Xe atom from the centre-of-mass of the Xe_4 cluster. The distance between the Xe atoms arranged in the Xe_4 (Figure IV.2) cluster is set at the equilibrium internuclear separation (r_e) of the ground state Xe dimer (see Table IV.1).

It is observed in Figure IV.6 that the $Hg(p_z)$ $^3A_1$ state is stabilised upon approaching the planar Xe_4 cluster exhibiting a dissociation energy D_e = 5459.3 cm^{-1} at R_{cm} = 0 Å, corresponding to the centre of mass of the cluster. The doubly

degenerate ^3E (p_x, p_y) states are also stabilized up to 2.38 Å from the centre of the cluster. However, further approach results in destabilisation.

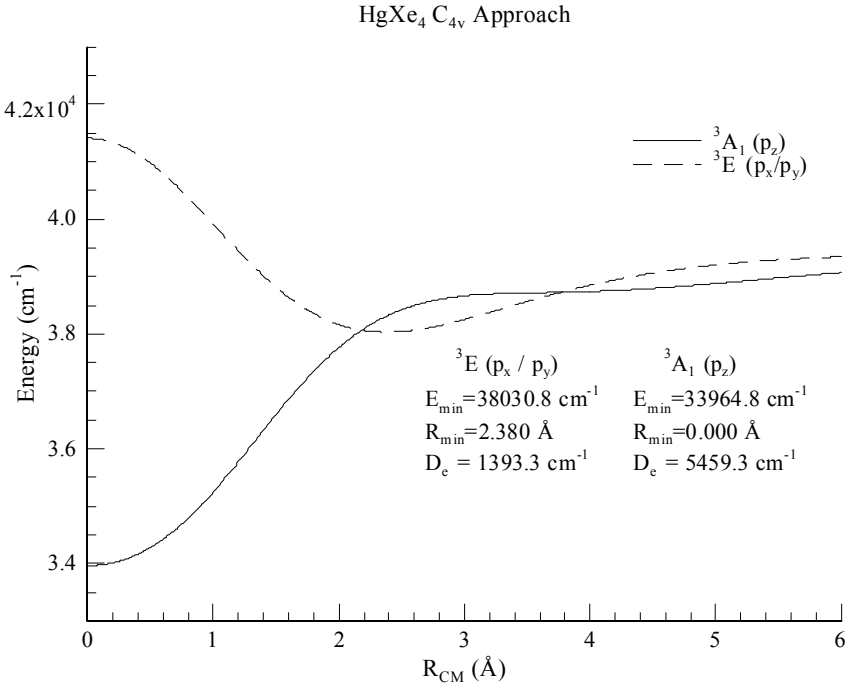

Figure IV.6 **Potential energy curves of the $^3A_1$ and doubly degenerate ^3E states calculated using Equations IV.6 and 7 as a function of distance of the Hg atom from the centre of mass (R_{cm}) of the Xe_4 cluster. The approach of the atomic Hg occurs along *Z*-axis perpendicular to the planar Xe_4 cluster.**

The 4-atom 'body' mode, Q_2 involves motion of the excited state metal atom along the *Z*-axis from the centre of the substitutional site towards the octahedral interstitial site located on the face of the unit cell as shown in the fourfold co-ordination system Figure IV.4, top panel. The octahedral interstitial site (I_{oh}) is positioned at the base of a square pyramid of RG atoms. Therefore, in simulating the approach of the excited state Hg atom to this site, an extension of the Xe_4 cluster calculation to a C_{4v} square pyramid of Xe_5 atoms is required. This is achieved with the addition to the Hg·Xe_4 expressions of a $V_\Sigma(R + r)$ for the $^3A_1$ electronic state (Equation IV.6) and a $V_\Pi(R + r)$ for the ^3E state (Equation IV.7) as shown in Equations IV.8 and IV.9 respectively.

$$W_{3A1}(R) = 4\left[\cos^2\theta V_{3\Sigma}(R) + \sin^2\theta V_{3\Pi}(R)\right] + V_\Sigma(R + r) \qquad \text{Equation (IV.8)}$$

$$W_{3E}(R) = 2\left[\sin^2\theta V_{3\Sigma}(R) + (\cos^2\theta + 1)V_{3\Pi}(R)\right] + V_\Pi(R + r) \qquad \text{Equation (IV.9)}$$

In these equations *r* is the distance from the apical rare gas atom to the base of the square pyramid RG_5 structure. The exact value of *r* is calculated for the equilibrium geometries of the rare gas clusters as $r = r_e/\sqrt{2}$, where r_e is the equilibrium separation of the gas phase rare gas dimers quoted in Table IV.1. R is now the distance from the Hg atom to the base of the square pyramid of five Xe atoms. The potential energy curves calculated for the C_{4v} approach of the Hg $^3A_1$ and degenerate ^3E states to the Xe_5 cluster are shown in Figure IV.7.

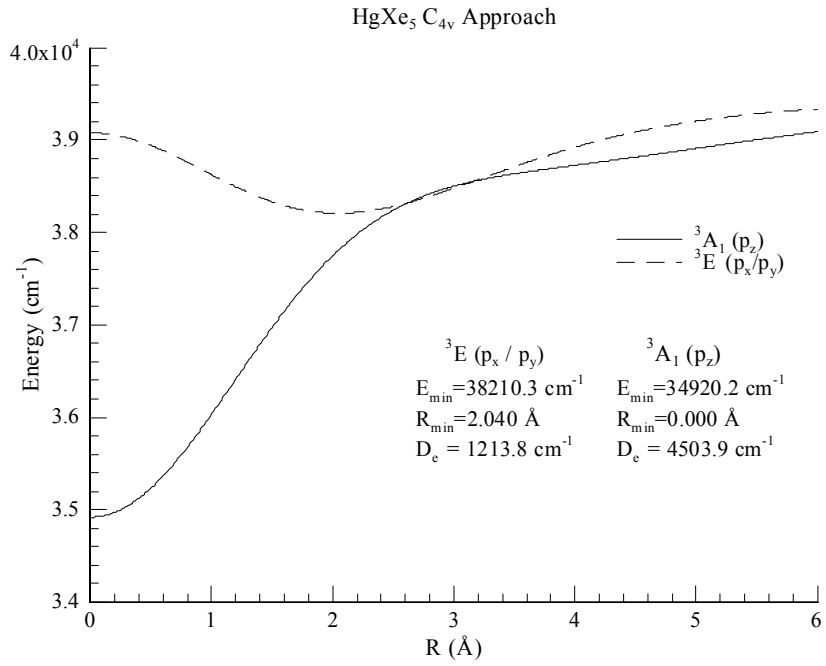

Figure IV.7 **Potential energy curves calculated for the C_{4v} approach of the atomic Hg $^3A_1$ and ^3E states to the Xe_5 cluster calculated using Equations IV.8 and 9.**

The approach of the Hg(p_z) orbital towards the Xe_5 cluster results in stabilisation of the $^3A_1$ state by 4503.9 cm^{-1} at the centre of the base of the square pyramid of Xe atoms. A comparison between the energetics of the approach to the Xe_4 and Xe_5 clusters (Figure IV.6 and Figure IV.7 respectively) reveals the addition of the V_Σ interaction arising from the apical Xe atom, reduces the stabilisation of the $^3A_1$ state. However the addition of the V_Π term to the ^3E electronic state leads to increased stabilisation, a decrease in the position of the shallow minimum for the state is also calculated due to the interaction with the apical atom. The cluster models calculated are extended for the $Hg{\cdot}RG_{18}$ cluster species, the details of which are now presented.

The individual interactions are calculated using Equations IV.6 and 7 for the 'body' mode as follows; I) $I_{oh}1$ / W(R_1, θ_1) + $V_\Sigma(a - q)$; motion towards the centre of the octahedral interstitial site equivalent to the C_{4v} approach to the RG_5 cluster presented earlier. II) *S.site1* / W(R_2, θ_2); Motion of the Hg atom from the centre of the planar arrangement of four nearest neighbour RG atoms forming *S.site* 1. III) $I_{oh}2$ / W(R_3, θ_3) + $V_\Sigma(a + q)$; Motion of the metal atom away from the five RG atoms forming $I_{oh}2$. IV) *S.site* 2 / W(R_4, θ_4); motion away from the four next nearest neighbour RG atoms in the XY plane *S.site*2 initially at the lattice parameter distance (a) from the Hg atom in the substitutional site. The calculations are preformed linear in q with the four specific R_n and θ_n variables calculated from the trigonometric relationships presented earlier for the Hg·Xe_4 cluster.

The results of the individual interactions comprising Q_2 are indicated by the legend and the solid line indicates the overall sum in the upper half of Figure IV.8 for the Hg/Xe system.

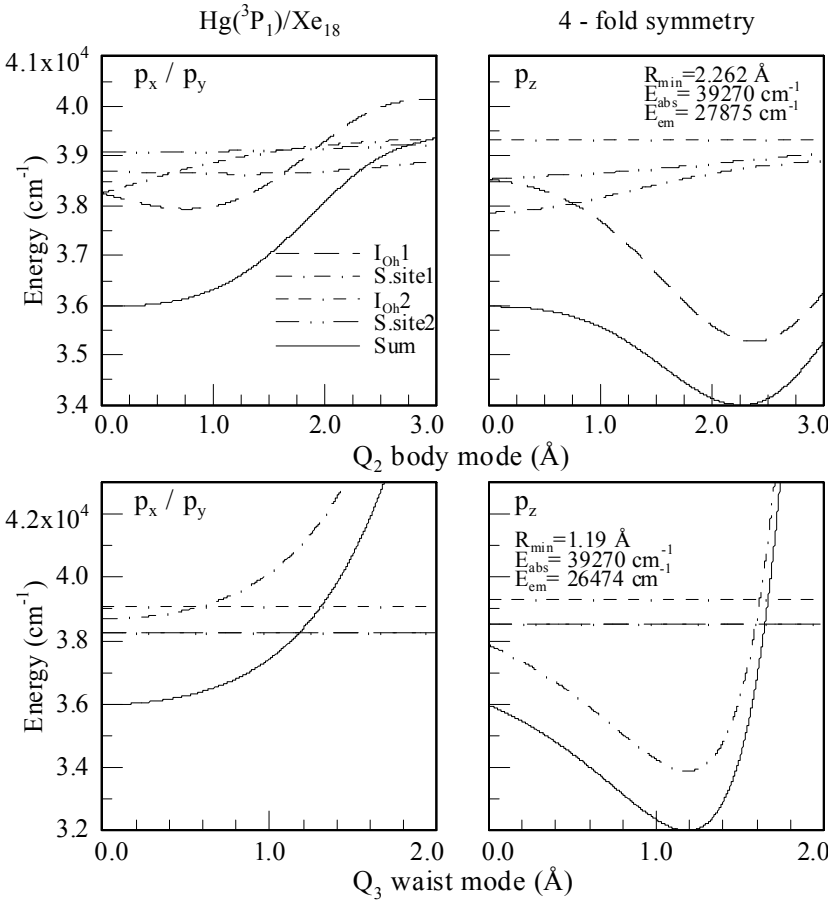

Figure IV.8 **Potential energy curves calculated for the 4-atom (tetragonal, Q_2 and Q_3) modes based on substitutional site (*ss*) occupancy of the Hg atom in the Hg/Xe system.**

Clearly the p_z orbital orientation is the only one exhibiting stabilization for the 4-atom body-mode, Q_2. It is evident upon inspection of Figure IV.8 that stabilisation is due to the approach of Hg(p_z) atom to the octahedral interstitial site ($I_{oh}1$, dashed line). This result reflects that calculated for the C_{4v} approach of the Hg $^3A_1$ (p_z) and doubly degenerate ^3E (p_x, p_y) Xe_4 and Xe_5 clusters where only the $^3A_1$ state arising from the Hg(p_z) orbital orientation was stabilized on approaching the clusters.

b. The 'waist' mode, (Q_3) involves contraction of 4 host atoms on a non-close packed plane towards the central metal atom. The 4-atom 'waist' mode is simpler to evaluate than the corresponding 'body' mode, Q_2 since the calculation involves, as shown in Figure IV.9, a single variable arising from the motion of the four RG atoms (S.site1) surrounding the Hg fixed at the centre of the substitutional site.

The overall energy of this vibronic mode for the M·RG_{18} cluster is obtained as a sum of the four 4-fold symmetry moieties making up what are the first and second spheres surrounding the metal atom in a substitutional site and the lattice contribution. Results calculated for the Q_3 mode of Hg/Xe are presented in the lower half of Figure IV.8. As shown by the solid curves in the lower right panel of Figure IV.8, this mode leads to excited state stabilisation only for the p_z orbital orientation.

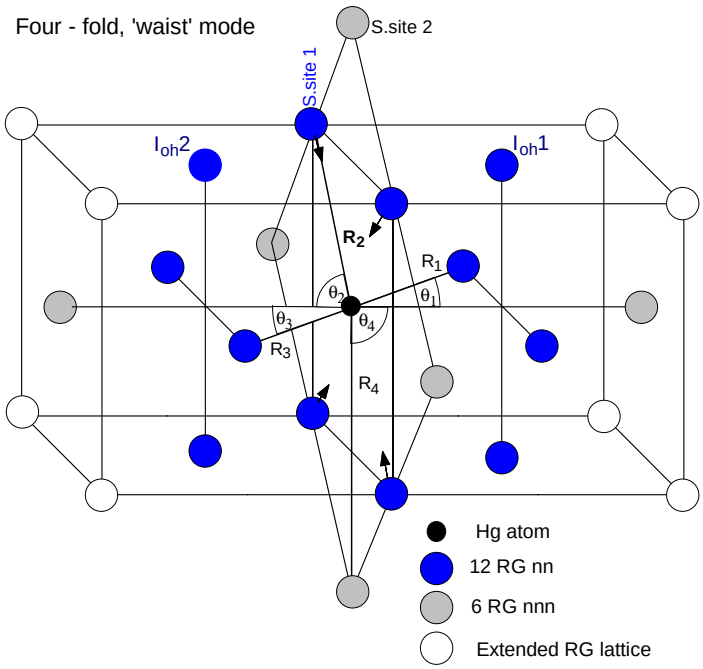

Figure IV.9 **A diagram representing the distance and angle parameters used in the calculation of the Tetragonal fourfold symmetry, 'waist' mode, Q_3. The motion as indicated by the solid arrows (R_2) is the in-phase contraction of the four nearest neighbour RG atoms in the XY plane forming S.site1 towards the fixed Hg atom.**

IV.2.II.II Trigonal (6-atom) symmetry modes

Calculation of the 6-atom modes involves a 45° rotation of all three axes used for the 4-atom modes, such that the *Z*-axis is co-incident with one of the four, threefold symmetry axes of the Hg·RG_{12} cubo-octahedron. As shown in Figure IV.4, this co-ordinate system results in a perpendicular intersection of the *Z*-axis through the centres of the two 'end' triangles and the central hexagon of rare gas atoms with the X and Y axes in the plane of the regular hexagon. In this arrangement, the 12 nearest neighbour atoms surrounding the metal atom are positioned as 3, 6 and 3 atoms on planes perpendicular to the *Z*-axis. The associated two triangles and hexagon are located on the close-packed A, B and C planes of the *fcc* structure.

To achieve the required p-orbital degeneracy in the substitutional site, the 6 next nearest neighbour (*nnn*) atoms in the second sphere surrounding the guest metal atom must be included. The six additional atoms are arranged, as shown in Figure IV.10, in the larger triangles on the A and C planes at a distance of the lattice parameter, *a*, from the guest metal atom.

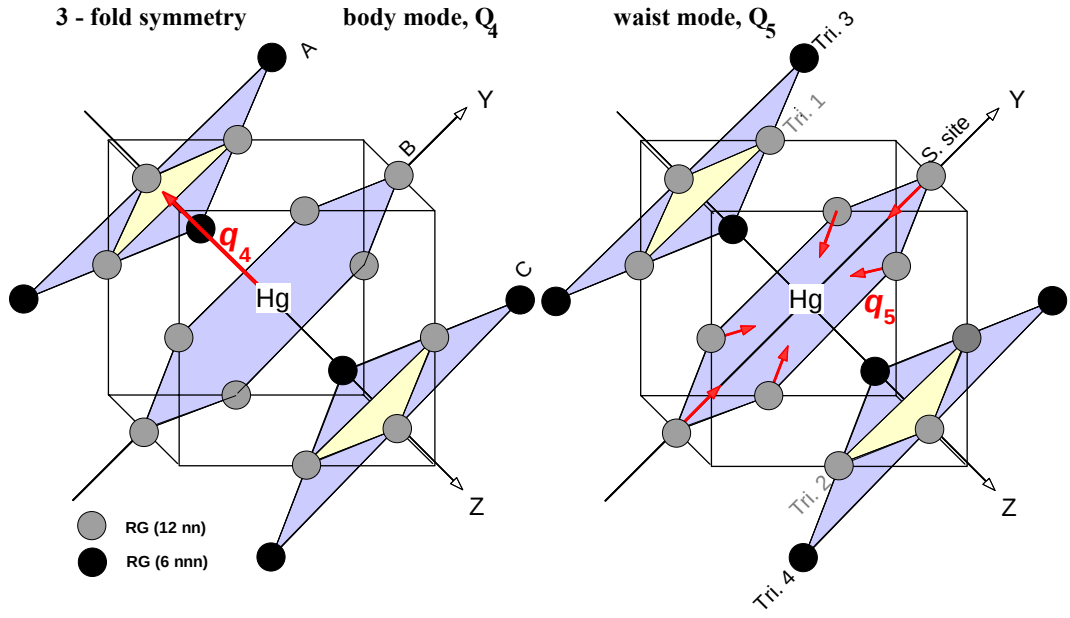

Figure IV.10 **The alternative guest atom-based co-ordinate system used to calculate the 6-atom vibronic modes occurring for substitutional site occupancy. The *Z* axis is chosen co-incident with one of the four threefold symmetry axes of the cubo-octahedral *fcc* unit cell. The *X* and *Y* axes are then located on the central hexagonal plane. The atoms located on the close packed A, B and C planes are shown on the shaded background. In the 6-atom 'body' mode (Q_4), depicted on the left, the metal p_z-orbital atom moves along the *Z*-axis perpendicular to the close-packed planes. For the 6-atom waist mode, shown on the right, the 6 nn atoms move in phase on Plane B, towards the guest metal atom.**

Two types of 6-atom modes are identified in the excited state. One involves the in-phase contraction of the 6 rare gas atoms on the X / Y plane towards the central metal atom. The other is motion of the metal atom along the *Z*-axis.

a. The 6–atom 'body' mode, Q_4, as illustrated on the left hand side of Figure IV.10, involves perpendicular motion of the excited state Hg atom from the centre of the hexagon of rare gas atoms on plane B to either plane A or C. The motion of the excited Hg atom towards the triangles of RG atoms was calculated using the smaller cluster model where the energetics of the Hg $^3A_1$ and doubly degenerate ^3E states were calculated for the C_{3v} perpendicular approach to the centre of mass of a planar RG_3 cluster. Equations IV.2-4 were used to evaluate the energetics of the system. Applying the metal-atom-based coordinate system shown in Figure IV.2 to the RG_3 cluster where the distance to the centre of mass of the planar RG_3 cluster is $R_{cm} = r_e/\sqrt{3}$ and $\phi_k = \pi/6$, $5\pi/6$ and $2\pi/3$ and $R = \sqrt{((R_{cm})^2+r^2)}$ and $\theta = \sin^{-1}(r/R)$. The expressions for the $^3A_1$ (p_z) and ^3E (p_x, p_y) presented in Equations IV.10 and IV.11 were obtained from Equations IV.2-4 upon substitution of the values of ϕ_k for the RG_3 planar cluster.

$$W_{3A1}(R) = 3[\cos^2\theta V_{3\Sigma}(R) + \sin^2\theta V_{3\Pi}(R)] \qquad \text{Equation (IV.10)}$$

$$W_{3E}(R) = (^3/_2)[\sin^2\theta V_{3\Sigma}(R) + (\cos^2\theta + 1) V_{3\Pi}(R)] \qquad \text{Equation (IV.11)}$$

Figure IV.11 shows the result of the calculation for the C_{3v} approach of the Hg atom towards the centre of the Xe_3 cluster. The $^3A_1$ state does not result in overall stabilisation however a local minimum is crossed upon approaching the Xe_3 cluster. It is also evident from Figure IV.11 that ^3E states arising from the approach of the Hg p_x and p_y orbitals are stabilized approaching the Xe_3 cluster, however this stabilisation of 1588 cm^{-1} occurs at 2.56 Å from the centre of mass of the xenon cluster.

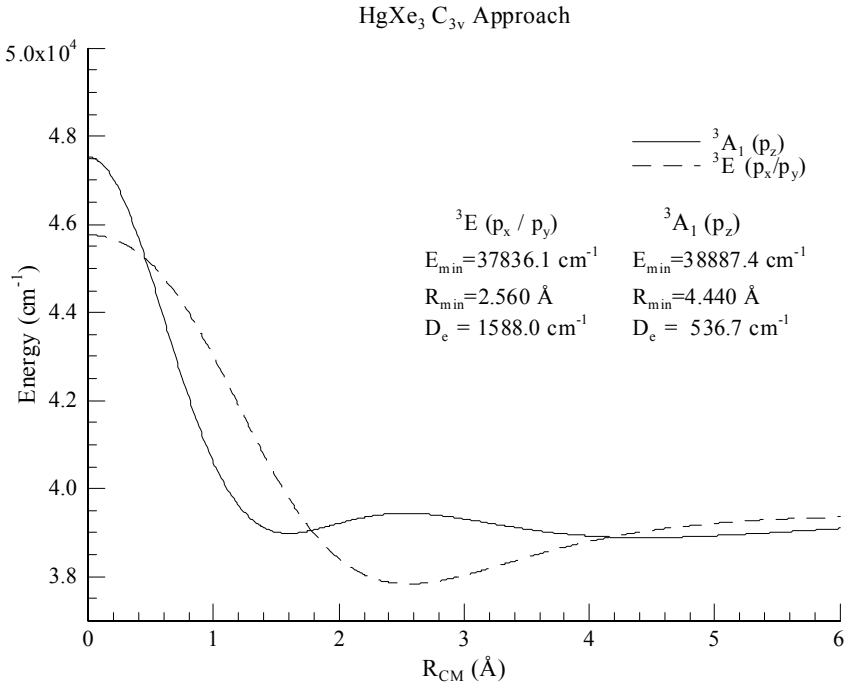

Figure IV.11 **Hg $^3A_1$ and doubly degenerate ^3E potential energy curves calculated for the C_{3v} approach to a planar arrangement of three Xe atoms.**

The energetics of the Hg $^3A_1$ and doubly degenerate ^3E states were also calculated for the C_{6v} perpendicular approach to the centre of mass of a planar RG_6 cluster. The approach to the RG_6 cluster is the opposite of the motion occurring for the 6-atom 'body' mode, (Q_4). Equations IV.2-4 were used to evaluate the energetics of the C_{6v} approach where $R = \sqrt{((R_{cm})^2+r^2)}$ and $\theta = \sin^{-1}(r/R)$ given $R_{cm} = r_e$ and ϕ_k = 0, $\pi/3$, π, $4\pi/3$ and $5\pi/3$ for the planar arrangement of six RG atoms[1]. Equations IV.12 and IV.13 were obtained from Equations IV.2-4 upon substitution of the values of ϕ_k for the RG_6 planar cluster.

$$W_{3A1}(R) = 6[\cos^2\theta\, V_{3\Sigma}(R) + \sin^2\theta\, V_{3\Pi}(R)] \qquad \text{Equation (IV.12)}$$

$$W_{3E}(R) = 3[\sin^2\theta\, V_{3\Sigma}(R) + (\cos^2\theta + 1)\, V_{3\Pi}(R)] \qquad \text{Equation (IV.13)}$$

Figure IV.12 shows the potential energy curves calculated for the Hg $^3A_1$ and ^3E states for the C_{6v} approach to the planar Xe_6 cluster. Upon inspection of Figure IV.12 it is evident that the $^3A_1$ (p_z) and ^3E (p_x, p_y) states are both stabilised at the centre of mass R_{cm} = 0 Å of the Xe_6 cluster. The $^3A_1$ state exhibits a stabilisation of D_e = 2242.8 cm^{-1} at R_{cm} = 0 Å. However, even though the ^3E state is stabilised at the centre of the cluster, the potential minimum of 1168.8 cm^{-1} actually occurs at a distance of 1.22 Å from the centre of the cluster.

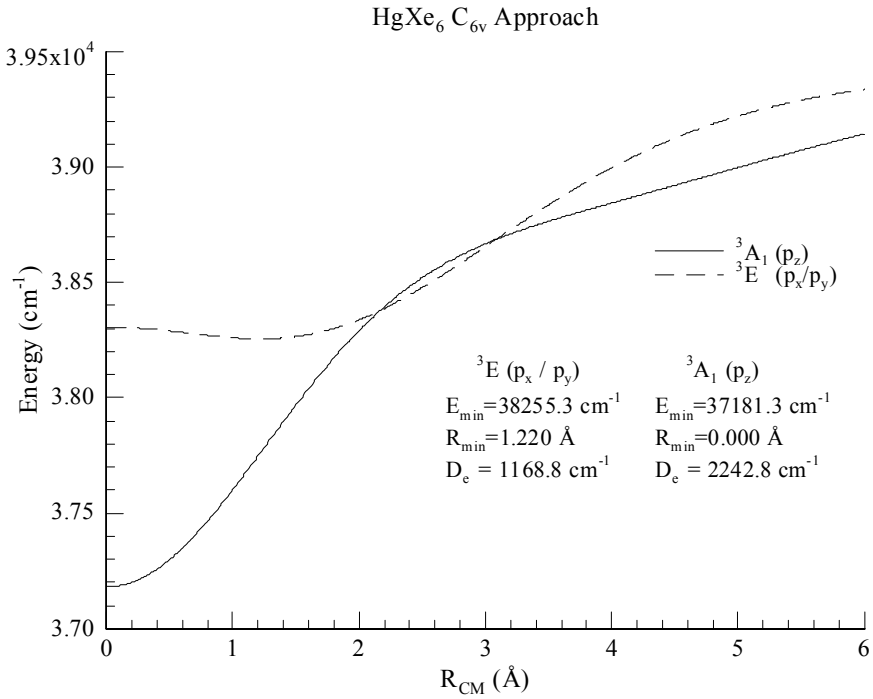

Figure IV.12 **Hg $^3A_1$ and doubly degenerate ^3E potential energy curves calculated for the C_{6v} approach to a planar arrangement of six Xe atoms.**

Five categories of Hg·RG interactions are identified for the Q_4 mode, the geometric details of which are illustrated in Figure IV.10. (I) S.site/W(R_1, θ_1), motion of the Hg atom away from the hexagon of 6 *nn* atoms on Plane B. (II) Tri.1/W(R_2, θ_2), motion towards the centre of the 3 *nn* atoms on Plane A (small, light shaded triangle). The separation between the close packed A, B and C planes, *b*, is $\sqrt{(2/3)}ss$. (III) Tri.2/W(R_3, θ_3), motion away from the 3 *nn* atoms on Plane C, (small, light triangle), i.e. the opposite of (II). (IV) Tri.3/W(R_4, θ_4), motion towards the 3 *nnn* atoms indicated by the large, dark shaded triangle on Plane A. These atoms are initially at a lattice parameter distance, *a*, from the guest metal atom in the substitutional site. (V) Tri.4/W(R_5, θ_5), motion away from 3 *nnn* atoms on Plane C, the opposite of (IV). The potential energy for each of the interactions was evaluated using Equations IV.2-4.

The potential energy curves obtained by summing the five interactions, are shown by the solid traces in the top of Figure IV.13 for the Hg/Xe system. In contrast to the 4-atom body mode, the $^3A_1(p_z)$ state in the 6-atom 'body' mode is not stabilised. The lack of stabilisation evident in Figure IV.13, arises from strong destabilisation occurring with movement of the metal (p_z) orbital away from the hexagon (S.site) on Plane B and the initially repulsive interaction it experiences as it

approaches the 3 *nn* Xe atoms positioned as a triangle on planes A or C. The latter repulsive interaction is shown by the dash-dot line (Tri.1) in Figure IV.13, the former destabilisation by the dashed line (S.site). However, the ^3E state of this mode, corresponding to the degenerate p_x/p_y orbital orientations of the excited $^3P_1$ Hg atom, is slightly stabilised. The stabilisation arises from the approach of the Hg p_x/p_y orbital to the 3*nn* atoms arranged as a triangle (Tri. 1) on Plane A. This is nearly counteracted by the destabilisation incurred by movement away from the other *nn* triangle (Tri. 2) on Plane C, resulting in only a small net stabilisation. The slight stabilisation calculated for the Hg ^3E state is that indicated by the C_{3v} approach to the RG_3 cluster shown earlier. The dominant interaction leading to the destabilisation of the 6-atom 'body' mode, (Q_4) for the excited state Hg p_z orbital orientation is the motion from the centre of the hexagon of Xe atoms forming S.site. This excited state destabilisation was predicted by the Xe_6 cluster calculation, inspection of Figure IV.12 reveals that motion of the Hg $^3A_1$ (p_z) state from R_{cm} = 0 Å is a repulsive interaction.

b. The 6-atom "waist" mode, Q_5 involves, as shown on the right in Figure IV.10, in-phase contraction of 6 *nn* lattice atoms on the close-packed B plane towards the central metal atom. The total energies of the excited $^3A_1(p_z)$ and $^3E(p_x/p_y)$ states in the waist mode of the Hg($^3P_1$)·RG_{18} cluster obtained from Equations IV.2-4 are given by the expressions

$$\mathbf{W_{3A1}}(\boldsymbol{R}) = 6[\cos^2\theta_A V_{3\Sigma}(R_1) + \sin^2\theta_A V_{3\Pi}(R_1)] + 6[\cos^2\theta_B V_{3\Sigma}(R_2) + \sin^2\theta_B V_{3\Pi}(R_2)] + 6[\cos^2\theta_C V_{3\Sigma}(R_3) + \sin^2\theta_C V_{3\Pi}(R_3)] + \mathbf{Erreur\ !} \qquad \text{Equation (IV.14)}$$

$$\mathbf{W_{3E}}(\boldsymbol{R}) = 3[\sin^2\theta_A V_{3\Sigma}(R_1) + [\cos^2\theta_A + 1]V_{3\Pi}(R_1)] + 3[\sin^2\theta_A V_{3\Sigma}(R_2) + [\cos^2\theta_A + 1]V_{3\Pi}(R_2)] + 3[\sin^2\theta_A V_{3\Sigma}(R_3) + [\cos^2\theta_A + 1]V_{3\Pi}(R_3)] + \mathbf{Erreur\ !} \qquad \text{Equation (IV.15)}$$

in which the angles θ_A, θ_B and θ_C are defined with respect to the *Z*-axis and have values of $\pi/5.104299$, $\pi/2$ and $\pi/3.288535$ radians. R_1 and R_2 refer to the nearest neighbour distance ($a/\sqrt{2}$) and R_3 refers to the next nearest neighbour (a) distance.

In the calculation of the energetics of the 6-atom 'waist' mode, only the distance of the 6 Hg-RG interactions on Plane B (R_1) is decreased, as shown on the right in Figure IV.10. Although the cluster size is restricted to an M·RG_{18} species, 24

additional on-plane RG-RG interactions arising inside the 4th surrounding sphere are included. This term (m = 24 in Equation IV.14 and 15) is required[21] to account for the strong lattice destabilisation that occurs on the close packed Plane B from contraction of the equilibrium rare gas distances. The results of the 6-atom "waist" mode calculations are shown on the bottom of Figure IV.13 for the Hg/Xe system. As indicated by the dashed lines in this figure, stabilization arises only for the p_z orbital orientation with the contraction of the 6 Hg-RG bonds on Plane B. Strong destabilisation, shown by the broken grey line, comes from disruption of the *nn* Rg-Rg distances on the close packed B plane of the lattice, greatly reducing the overall stabilisation (solid trace) of this mode.

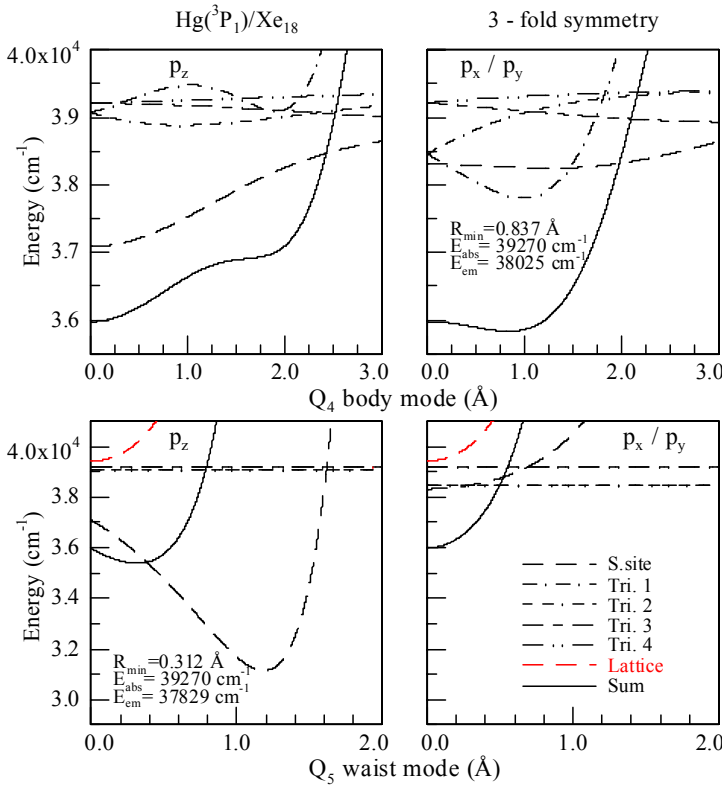

Figure IV.13 **Energetics calculated for the five specific interactions involved in the 6–atom 'body' (Q_4) and 'waist' (Q_5) mode for the Hg/Xe system are shown by the legend used. The total potential energy curves obtained by summing these five interactions and the lattice contribution are shown by the solid line.**

IV.2.II.III Two-fold (2-atom) symmetry modes

Calculation of the 2–atom modes involves a 45° rotation of the *Z* and *Y* axes about the *X*–axis from the coordinate system used[1] for the 4-atom modes, where the Cartesian axes were coincident with the three, four–fold symmetry axes. Figures IV.14 and IV.2 show the resulting arrangement of the 12 nearest neighbour (*nn*) RG atoms

around the guest metal atom in the substitutional site, (*ss*). When counted along the *Z*–axis, there is a 1, 4, 2, 4, 1 arrangement of the 12 *nn* RG atoms on this axis with the metal atom at the origin. It can be seen in Figure IV.14 that there are 2 *nn* on both the *Z* and *Y* axes with the remaining 8 *nn* atoms located in two rectangles at right angles to the *Z*-axis. Two types of 2-atom modes are identified in the excited state. One involves the in-phase contraction of the 2 *nn* rare gas atoms on the *Y* axis towards the central metal atom. The other is motion of the metal atom along the *Z*-axis directly towards one *nn* atom.

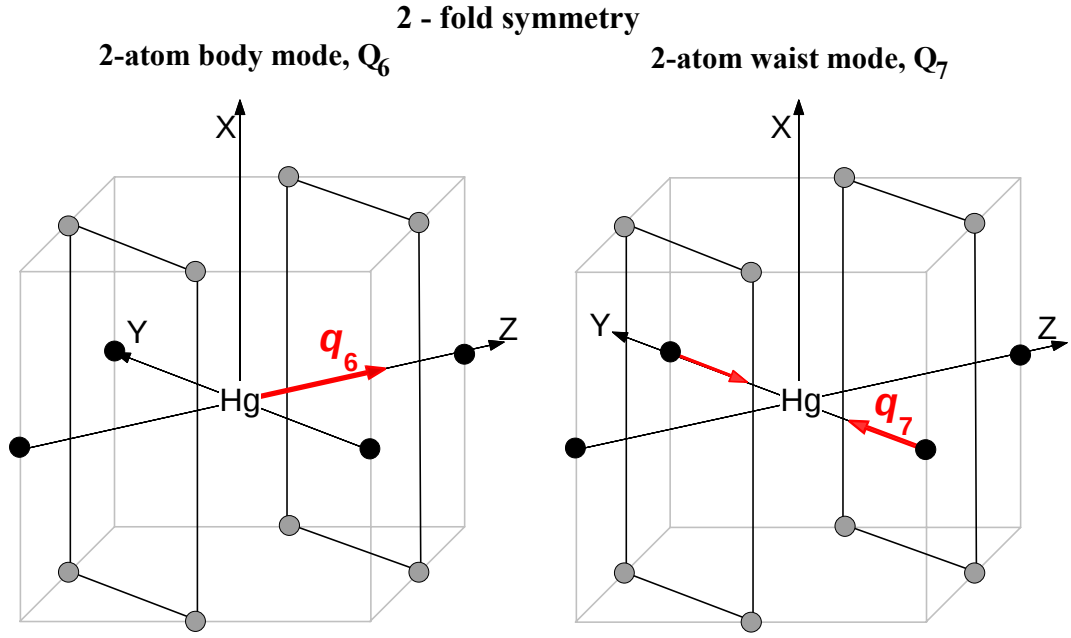

Figure IV.14 **A representation of the co-ordinate system used for the 2–atom 'body' and 'waist' mode Q_6 and Q_7 calculations respectively. The co-ordinate system has been chosen to coincide with the one of the twofold symmetry axes of the cubo-octahedron.**

a). 2–atom 'body' mode, Q_6, involves motion of the excited state metal atom on the *Z*–axis towards one of the 12 *nn* RG atoms positioned on this axis. It is illustrated on the left in Figure IV.14 and involves passage of the excited state metal atom through the 4 *nn* RG atoms arranged as a rectangle perpendicular to the *Z*-axis. With the length of the sides of this rectangle, the lattice parameter (*a*) and substitutional site size (*ss*), the distance of each of the four rare gas atoms to the centre of the rectangle is then $R_{cm} = \sqrt{3}/8(a)$. Using the associated values of ϕ_k in Equations IV.3 and 4, $\phi_1 = (\frac{1}{2})\cos^{-1}(\frac{1}{3})$, $\phi_2 = \pi - [(\frac{1}{2})\cos^{-1}(-\frac{1}{3})]$, $\phi_3 = [(\frac{1}{2})\cos^{-1}(\frac{1}{3})] + \pi$ and $\phi_4 = 2\pi - [(\frac{1}{2})\cos^{-1}(\frac{1}{3})]$ the following expressions were obtained for the $^3B_1(p_x)$ and $^3B_2(p_y)$ states,

$$p_y \Rightarrow W_{B2}(R) = {}^4/_3[V_\Sigma(R)\sin^2\theta_k + V_\Pi(R)(\cos^2\theta_k + 2)] \quad \text{Equation (IV.16)}$$

$$p_x \Rightarrow W_{B1}(R) = {}^8/_3[V_\Sigma(R)\sin^2\theta_k + V_\Pi(R)(\cos^2\theta_k + {}^1/_2)] \quad \text{Equation (IV.17)}$$

The following expression for the $^3A_1(p_z)$ electronic state was obtained from Equation (IV.2).

$$p_z \Rightarrow W_{A1}(R) = 4[V_\Sigma(R)\cos^2\theta_k + V_\Pi(R)\sin^2\theta_k] \quad \text{Equation (IV.18)}$$

Calculation of the 2-atom modes for a Hg/RG_{18} cluster involves consideration of the eight interactions illustrated in Figure IV.14. They are as follows; (1) End 1/W(R_1,θ_1), motion of the Hg atom from the substitutional site towards one of the nearest neighbour *nn* atom on the *Z*–axis. $R_1 = ss - x$ where *x* represents displacement along the *Z* – axis. (2) End 2/W(R_2,θ_2), the motion of the metal atom away from the other *nn* on the *Z*–axis. This is the opposite of interaction (1) and the distance is $R_2 = ss + x$. (3) Rect. 1/W(R_3,θ_3), this interaction involves approach to the rectangle of 4 *nn* atoms. Initially the Hg(p_z) atom is at a distance *ss*/2 from the centre of mass of the rectangle. During the motion this distance becomes *ss*/2 – *x*. The distance from each of the RG atoms to the centre of mass of the rectangle is $r = \sqrt{3}/8(a)$, so this interaction occurs at a distance $R_3 = [(ss/2 - x)^2 + (3/8\ a)^2]^{1/2}$ and the angle θ_3 = asin (r/R_3). (4) Rect. 2/W(R_4,θ_4), this interaction is the motion of the excited state guest atom away from the rectangle of 4 *nn*. It is the opposite of interaction (3), therefore $R_4 = [(ss/2 + x)^2 + (3/8\ a)^2]^{1/2}$ and θ_4 = asin (r/R_4). (5) 2 *nn* Y/W(R_5,θ_5), motion of the metal atom away from the 2 *nn* rare gas atoms on the *Y*–axis. This interaction takes place at $R_5 = [(ss)^2 + (x)^2]^{1/2}$ where θ_5 = asin (ss/R_5). (6) 2 *nnn* X/W(R_6,θ_6), involves the interaction between the metal atom and the 2 *nnn* on the X–axis. Initially these 2 rare gas atoms are at the next nearest neighbour, (*nnn*) distance of the lattice parameter *a* from the metal atom. During the motion the distance becomes $R_6 = [(a)^2 + (x)^2]^{1/2}$ where θ_6 = asin (a/R_6). (7) 2 *nnn* YZ/W(R_7,θ_7), this motion involves approach of the Hg atom to the 2 *nnn* RG atoms positioned on the YZ-plane on the diagonal initially at a distance *a*. $R_7 = [(ss - x)^2 + (ss)^2]^{1/2}$ where θ_7 = asin (ss/R_7). (8) 2 *nnn* YZ/W(R_8,θ_8), this interaction is the opposite of (VII) and $R_8 = [(ss + x)^2 + (ss)^2]^{(1/2)}$ and θ_8= asin (ss/R_8).

The potential energy curves calculated for the interactions 1 to 8 involved in the 2-atom body mode, Q_6 are shown for the Hg/Xe system in Figure IV.15. The potential energy curves for Q_6 are obtained by the summation of the eight

interactions, and are shown by the solid traces in Figure IV.15. Only the p_y orbital orientation leads to stabilization[22] for the Q_6 mode in Hg/Xe.

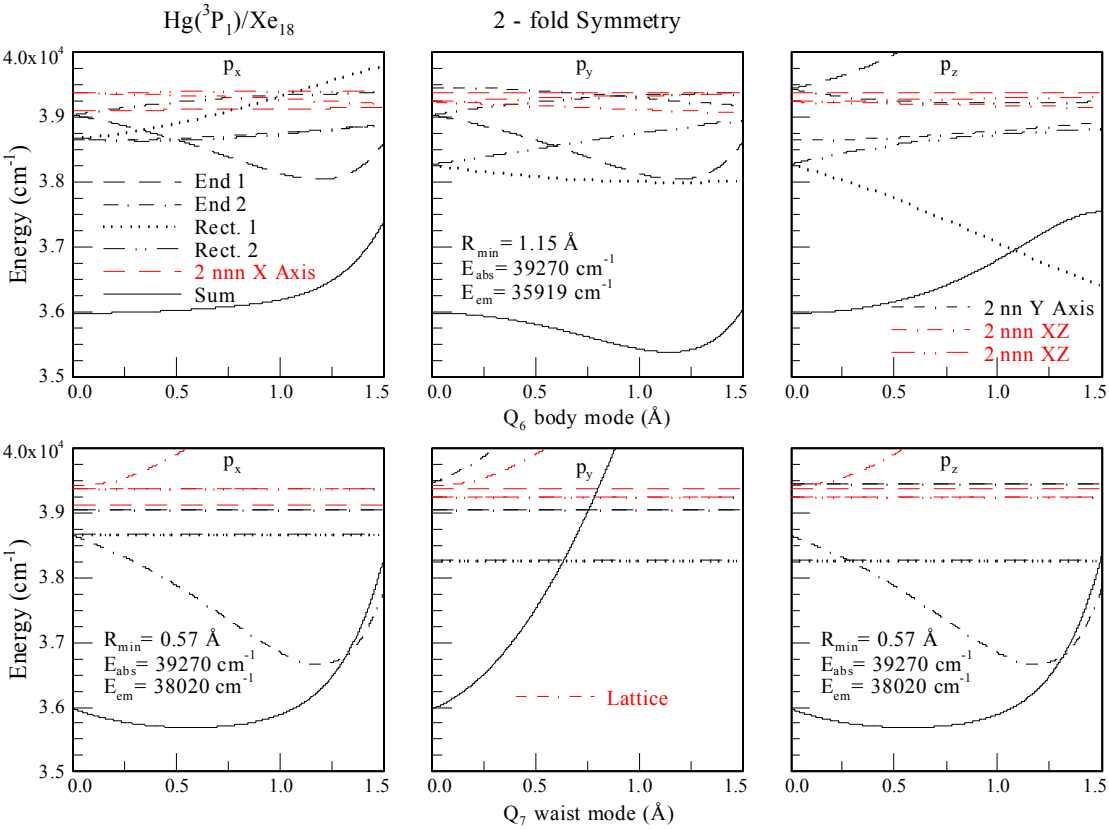

Figure IV.15 **Energetics calculated for the eight specific interactions involved in the 2–atom 'body' (Q_6) and 'waist' (Q_7) modes depicted in Figure IV.14. The potential energy curves obtained by summing these eight interactions for the three p-orbital orientation are shown by the solid lines for Hg/Xe.**

b). 2-atom 'waist' mode, Q_7, involves, as shown on the right of Figure IV.14, the in–phase contraction of 2 nearest neighbour rare gas atoms on the Y-axis to the central metal atom. The overall energies of the excited $^3A_1(p_z)$, $^3B_1(p_x)$ and $^3B_2(p_y)$ $^3P_1$ states of the mercury atom in the M·RG$_{18}$ cluster are obtained from Equations. IV.2-4. For the $^3A_1(p_z)$ state the following expression is used

$$\mathbf{W_{3A1}(R)} = 2[\cos^2\theta_A V_{3\Sigma}(R_1) + \sin^2\theta_A V_{3\Pi}(R_1)] + 8[\cos^2\theta_B V_{3\Sigma}(R_1) + \sin^2\theta_B V_{3\Pi}(R_1)] + 2[\cos^2\theta_C V_{3\Sigma}(R_1) + \sin^2\theta_C V_{3\Pi}(R_1)] + 4[\cos^2\theta_D V_{3\Sigma}(R_2) + \sin^2\theta_D V_{3\Pi}(R_2)] + 2[\cos^2\theta_E V_{3\Sigma}(R_2) + \sin^2\theta_E V_{3\Pi}(R_2)] + \mathbf{Erreur\ !} \qquad \text{Equation (IV.18)}$$

In this equation the angles θ_A, θ_B, θ_C, θ_D and θ_E are defined with respect to the Z–axis and have values of 0, $\pi/3$, $\pi/2$, $2\pi/3$ and π radians respectively. R_1 and R_2 refer to the nearest neighbour distance and the next nearest neighbour distances respectively.

Results calculated for the Q_7 mode are shown on the bottom in Figure IV.15 for Hg/Xe. Excited state stabilization occurs for both the p_x and p_z orbital orientations, whereas p_y is strongly repulsive due to the pure Σ interaction with the two approaching rare gas atoms on the *Y*-axis. The p_x and p_z orbitals, although arising from different electronic states of the excited state Hg $^3P_1$ atom, show the same excited state minimum due to symmetry.

Lattice destabilization must also be included in these calculations as the waist mode Q_7 involves motion of two rare gas atoms with respect to their nearest neighbours. Since the RG atoms initially occupy equilibrium positions in the lattice, any displacement from these positions will destabilize the host lattice. 22 RG-RG interactions were considered, of which the motion of the two RG atoms on the *Y*–axis towards a rectangle of its nearest neighbours is the most important. This repulsive lattice interaction is represented by the grey line in the bottom panels in Figure IV.15, and reduces considerably the stabilization of these modes for the p_x and p_z orbital orientations.

IV.3 Discussion

A summary of the excited state calculations conducted on the three Hg/RG systems is presented in Figure IV.16. In constructing this figure, identical calculations to those shown in detail for the Hg/Xe system were performed on the Hg/Ar and Hg/Kr systems. However, only the modes exhibiting stabilisation are shown, as they are the only ones that will lead to Stokes'-shifted emission.

As indicated by the solid curves in Figure IV.16, the 4-atom waist mode, Q_3, leads to excited state stabilisation for all the Hg/RG systems but only for the p_z orbital orientation. In contrast, the 4-atom body mode, Q_2, exhibits stabilisation only in the Hg/Xe system. The $^3A_1(p_z)$ state in the 6-atom 'body' mode, Q_4, is not stabilised in any of the solid rare gases. It is evident in the detailed Hg/Xe plot shown in Figure IV.13, that the reason for the lack of stabilisation is the repulsive interaction the metal (p_z) orbital experiences as it approaches the 3 *nn* Xe atoms positioned as a triangle on planes A or C. This repulsive interaction (shown for Hg/Xe in Figure IV.13 by the dash-dot line, Tri.1), is much stronger in Hg/Kr and stronger still in Hg/Ar as the lattice parameters get smaller. The $^3E(p_x,p_y)$ state of this mode shows a shallow

minimum in Hg/Xe. The 6-atom 'waist' mode, Q_5, exhibits excited state minima in the p_z orbital orientation for all the Hg/RG systems.

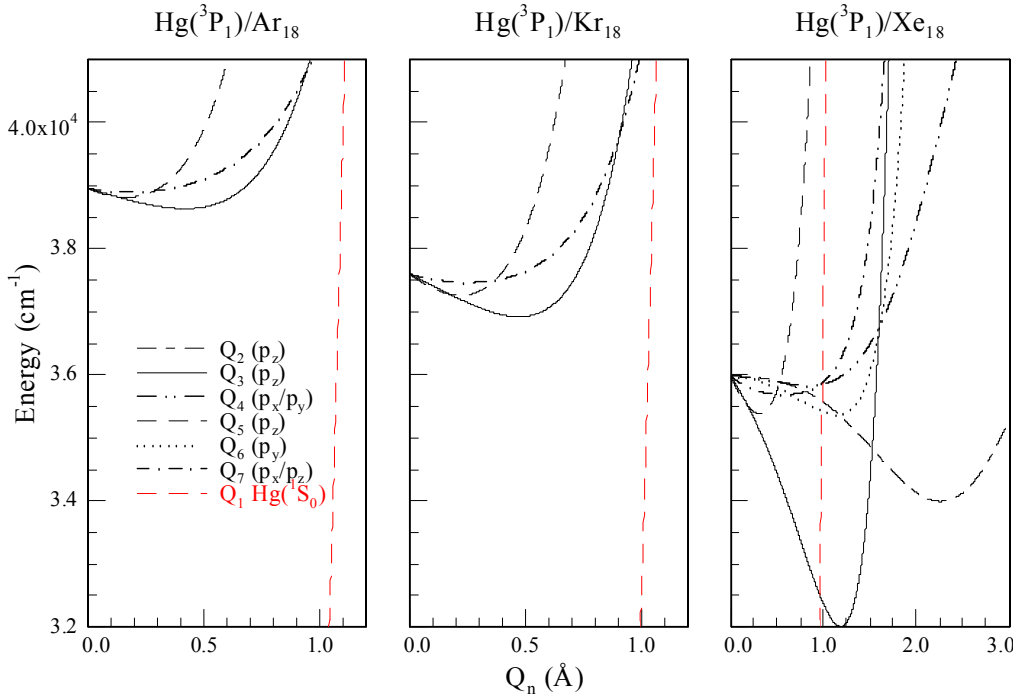

Figure IV.16 **A comparison of the excited Hg($^3P_1$) state potential energy curves of the vibronic modes exhibiting stabilisation in the Hg/RG systems. Shown also is the ground Hg($^1S_0$) state potential energy curves calculated for the breathing mode, Q_1. Particularly noteworthy is the crossing of this curve with the very strongly stabilized 4-atom modes in the Hg/Xe system.**

Stabilisation is not found for the 2-atom 'body' mode, Q_6, in any of the orbital orientation for Hg isolated in Ar and Kr. However, the p_y orbital orientation exhibits a stabilisation for the body mode, Q_6, in Hg/Xe. In contrast, the 'waist' mode of this symmetry, Q_7, is stabilised for the p_x,p_y orbital orientations in all three rare gas systems. In the next section a comparison of the predicted absorption and emission energies is made with recorded matrix spectra presented in Chapter III.

IV.3.I Absorption Energies

The absorption energy of the guest mercury atom isolated in a solid rare gas lattice is calculated as the difference between the ground Hg($^1S_0$)·RG$_{18}$ and the excited state Hg($^3P_1$)·RG$_{18}$ cluster energies at the centre of a substitutional site, R = 0 Å. Within the Frank-Condon approximation no movement will occur between the Hg and the cluster atoms during the electronic transition, so the absorption energy is given by

$$E_{abs} = E[Hg(^3P_1)\cdot RG_{18}]_{Q(R=0)} - E[Hg(^1S_0)\cdot RG_{18}]_{Q(R=0)} \qquad \text{Equation (IV.19)}$$

where Q(R = 0) represents zero displacement for a vibronic mode, Q_n (corresponding to the centre of a substitutional site). Accordingly, for a given site occupancy, the calculated absorption energies must be identical for all vibronic modes. The level of agreement between the 4-atom modes and the new 6-atom and 2-atom mode calculations is evident for Hg/Xe in Figure IV.8, Figure IV.13 and Figure IV.15 by the identical 'E_{abs}' values (39270 cm^{-1}) obtained for the Q_3, Q_5 and Q_7 modes. Table IV.2 shows a comparison of the observed absorption wavelengths with those calculated for substitutional site occupancy.

Table IV.2 **A comparison of the observed absorption wavelengths (*nm* units) for the $^3P_1 \leftarrow {}^1S_0$ transition of matrix-isolated atomic mercury with the calculated absorption values. The difference between the observed band maxima and the predicted values are quoted as $\delta_{Obs-Cal}$ in cm^{-1}. For a given Hg/RG system, the quoted predicted value was found for the three symmetry systems used, the three p-orbital orientations and the body and waist vibronic modes.**

Hg/RG	E_{Cal}	λ_{Calc}	λ_{Obs}	$\delta_{Obs-Cal}$
Hg/Ar	40495	246.94	246.0	+155
Hg/Kr	39922	250.49	249.1	+227
Hg/Xe	39270	254.65	253.4	+192

The 246.94 nm absorption wavelength calculated for Hg/Ar, compares very well with the observed band centre at 246 nm. The recorded[8] absorption band centre for Hg isolated in solid Kr is at 249.1 nm while the calculated value is 250.49 nm. Better agreement with observed data is achieved in Hg/Xe where the calculated value of 254.64 nm compares favourably with the observed absorption centered at 253.4 nm. From the comparison presented in Table IV.2, it is clear that the calculated absorptions match the red component of the threefold-split bands for all three Hg/RG systems. It thereby supports the assumption of substitutional site occupancy inherent in the pair-potential calculations conducted. It is not within the scope of the present calculations to examine the threefold absorption splitting effect because as indicated by Equation IV.19, the absorption values are determined only at the centre of the substitutional site i.e., at R = 0. Simulation[23] of the Jahn-Teller structure on the absorption profiles requires displacement of the ground state metal atom from the centre of the substitutional site, a task difficult to implement in the code developed for the calculations presented.

IV.3.II Emission Energies

The Hg($^3P_1 \rightarrow {}^1S_0$) emission energies are calculated with the formula

$$E_{em} = E\left[Hg(^3P_1)\cdot RG_{18}\right]_{Q(Rmin')} - E\left[Hg(^1S_0)\cdot RG_{18}\right]_{Q(Rmin')} \qquad \text{Equation (IV.20)}$$

where $R_{min'}$ represents the nuclear configuration of a given excited state vibronic mode, Q, at its energy minimum. In accordance with the Franck-Condon approximation, the energy of this vibronic mode on the ground state is obtained at the $R_{min'}$ value identified in the excited state. The results calculated in this way for the vibronic modes exhibiting excited state stabilisation (shown in Figure IV.16) in the Hg/RG systems are collected in Table IV.3.

Hg/Ar: The 4-atom (p_z), 6-atom (p_z) and 2-atom (p_x and p_z) 'waist' modes exhibit excited state stabilisation in solid argon. The emission wavelengths calculated for these Q_3, Q_5 and Q_7 modes are 256.14, 250.51 and 248.29 nm respectively. From the comparison made in Figure IV.16 of the three excited state vibronic modes, it is expected that Hg/Ar emission is dominated by the 6–atom 'waist'mode, (Q_5) as it exhibits more rapid stabilisation (i.e., a steeper gradient) than the more deeply bound 4–atom 'waist', (Q_3) or the 2-atom 'waist' mode. As shown in Figure IV.17, the 250.51 nm emission calculated for the Q_5 mode closely matches the deconvoluted central component at 250.69 nm in the observed band. The two other predicted emission bands lie to the blue and red of the two remaining deconvoluted emission components.

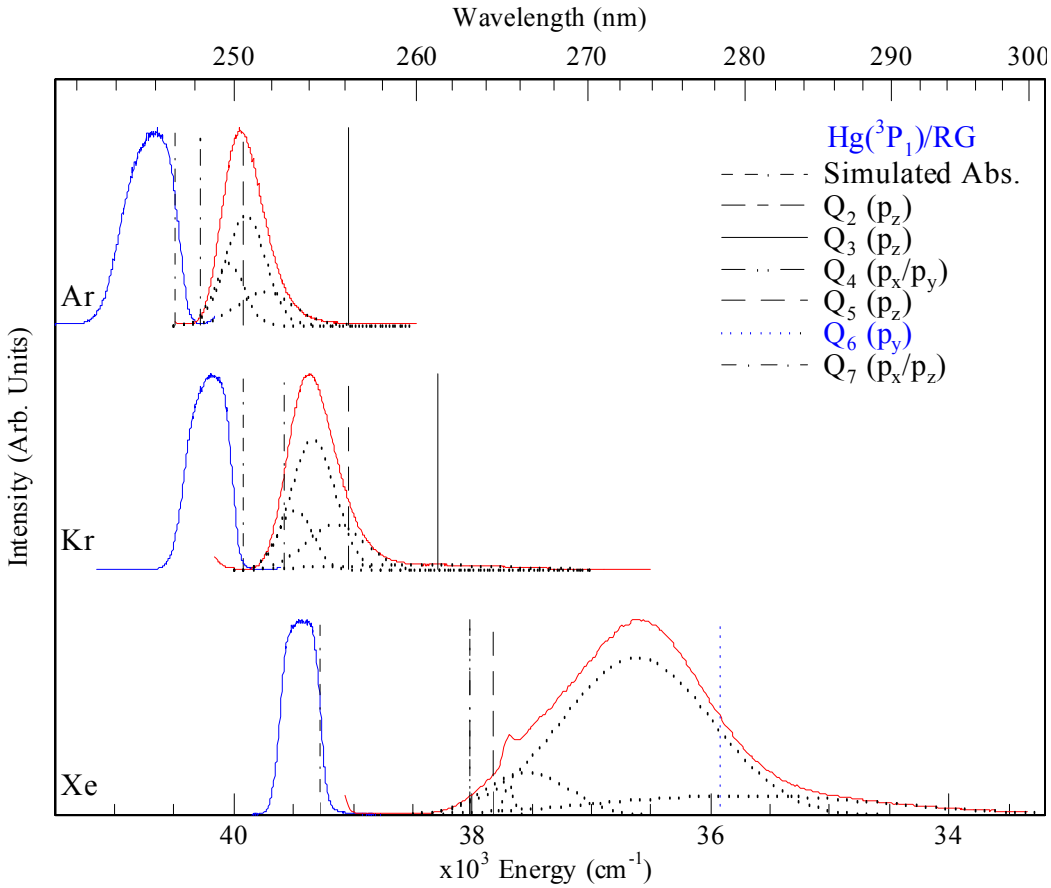

Figure IV.17 **A comparison of the observed and calculated atomic Hg ($^3P_1 \leftrightarrow {}^1S_0$) spectroscopy. The experimental emission spectra shown were recorded at 12 K and the underlying dotted lines show the deconvoluted components extracted in the Gaussian lineshape fits shown in Chapter III.**

Hg/Kr: As found in Hg/Ar, only the $Q_3(p_z)$, $Q_5(p_z)$ and $Q_7(p_x, p_y)$ modes exhibit excited state stabilisation in Hg/Kr leading to predicted emission at 261.16, 256.12 and 252.71 nm respectively. The 6-atom 'waist' mode Q_5 in this system also exhibits the steepest stabilization gradient (middle plot of Figure IV.16) and is therefore expected to dominate the emission. The associated predicted emission at 256.12 nm is red of the deconvoluted central component at 254.22 nm. The 2-atom waist mode at 252.7 nm agrees well with the blue component at 253.25 nm. As in the Hg/Ar system, the 4-atom waist mode (261 nm) is red of the deconvoluted red component (255 nm).

Table IV.3 **A comparison of the calculated Hg atom $^3P_1 \rightarrow {}^1S_0$ emission wavelengths with the experimental data reported in Chapter III and Ref. 8 for the Hg/Ar, Hg/Kr and Hg/Xe systems. All the vibronic modes of $Hg{\cdot}RG_{18}$ clusters which lead to excited state stabilisation are presented and compared with the bands deconvoluted in Gaussian fits of the emission bands centered at 250.3, 254.1 and 273 nm in Ar, Kr and Xe respectively.**

Hg/RG	Mode	Motion	Calculated $E(cm^{-1})$ / λ(nm)	Observed $E(cm^{-1})$ / λ(nm)
Hg/Ar	Q_3 (p_z)	4-waist	39041 / 256.14	39719 / 251.77
	Q_5 (p_z)	6-waist	39919 / 250.51	39890 / 250.69
	Q_7 (p_x, p_z)	2-waist	40275 / 248.29	40034 / 249.78
Hg/Kr	Q_3 (p_z)	4-waist	38290 / 261.16	39149 / 255.43
	Q_5 (p_z)	6-waist	39044 / 256.12	39335 / 254.22
	Q_7 (p_x, p_z)	2-waist	39571 / 252.71	39487 / 253.25
Hg/Xe	Q_2 (p_z)	4-body	27875 / 358.74	N/A
	Q_3 (p_z)	4-waist	26474 / 377.73	N/A
	Q_4 (p_x, p_y)	6-body	38025 / 262.98	-
	Q_5 (p_z)	6-waist	37829 / 264.34	36619 / 273.08
	Q_6 (p_y)	2–body	35919 / 278.40	35729 / 279.88
	Q_7 (p_x,p_z)	2-waist	38020 / 263.02	37535 / 266.42

Hg/Xe: Stabilisation was found in Hg/Xe for the six excited state vibronic modes shown on the right in Figure IV.16. In addition to the three modes stabilised in the Hg/Ar and Hg/Kr systems, the Q_2 (4-fold symmetry, p_z), Q_4 (3-fold symmetry p_x, p_y) and the Q_6 (2-fold symmetry p_y) modes are stabilised in Hg/Xe.

The calculated emission wavelengths for the Hg/Xe system, collected in Table IV.3, occur at 358.74, 377.73, 262.98, 264.34, 278.4 and 263.02 nm for the $Q_2(p_z)$, $Q_3(p_z)$, $Q_4(p_x/p_y)$, $Q_5(p_z)$, $Q_6(p_y)$ and $Q_7(p_x, p_z)$ modes respectively. The predicted $Q_6(p_y)$ value at 278.4 nm provides the best match with the red emission component at 279.88 nm. Stabilisation of this mode, the 2-atom body mode, is due to the favourable interaction between the Hg atom p_y orbital and a single Xe atom. This attractive interaction with one Xe atom is possible only for the $\Pi(p_y)$ orbital as the metal atom in this orientation can pass through the long side of the rectangle of *nn* Xe atoms, whose length is the lattice parameter, *a*, without experiencing strong repulsive interactions. In contrast, motion in the $\Pi(p_x)$ orbital orientation involves, as shown on the left in Figure IV.14, passage through the short side of the rectangle which, a

substitutional site size in length, and experiences repulsive interaction as indicated by the dotted lines in Figure IV.15. The 6-atom waist mode yields emission at 264.34 nm to the blue of the deconvoluted blue component at 273.08 nm. The remaining two modes in Hg/Xe (Q_4 and Q_7) are located at 263 nm in the vicinity of the blue deconvoluted component at 266 nm.

Conspicuous in Figure IV.16 is the fact that the 4-atom body Q_2 and waist Q_3 modes of Hg/Xe exhibit much larger excited state stabilisation energies than the 2- and 6-atom modes. Thus, an obvious question arises as to the role these modes play in emission as it is very likely that the former modes will lead to some relaxation of the excited state population. This is especially so for the 377 nm, 4-atom 'waist' mode, Q_3, as it exhibits a steep stabilisation gradient, so that even at low temperatures, excited state relaxation must occur along this vibronic mode. At higher temperatures, the branching ratios should favour the strongly stabilised modes leading to a reversible enhancement of the Q_2 and Q_3 modes (358 and 377 nm, near-UV bands) at the expense of the 6-atom waist mode Q_5 (273 nm, UV band) and the 2-atom body mode.

According to the present Hg/Xe_{18} calculations, the Q_2 and Q_3 modes are predicted to produce emission in the near-UV (350-400 nm) spectral region where mercury dimer and several unassigned emission bands have recently[24] been observed in Hg/Xe samples. Hg/Xe samples reported in Chapter III showed no atomic emission in the near-UV and no reversible temperature dependence was observed. However, the growth of Hg_2 bands was observed with prolonged atomic excitation, signalling that non–radiative processes must be considered which quench the atomic emission. The following quenching mechanism has become evident in our pair-potentials calculations of Hg/Xe and is illustrated in Figure IV.16.

It involves the deeply-bound, 4-atom excited state vibronic modes being crossed by the breathing mode of the electronic ground state. The 'breathing' mode, Q_1, presented in Chapter V involves in-phase motion of the 12 nearest neighbour atoms and the curves calculated with Equation IV.1 for the Hg/Ar, Hg/Kr and Hg/Xe systems are shown in Figure IV.16. It is clear in this figure that Hg/Xe is the only system exhibiting a crossing between stabilized excited state vibronic modes and the repulsive ground state. The origin of this difference lies in the much greater stabilization that the Hg/Xe 4-atom modes exhibit compared with the corresponding modes in the Hg/Ar and Hg/Kr systems. Quenching will then arise for the most

strongly stabilized excited state modes in Hg/Xe due to their crossing with the ground state. Because of the large spin-orbit coupling in atomic mercury, the crossing of these states of different spin will give rise to very efficient intersystem crossing and will quench the near–UV emission.

Although emission quantum yields have not been measured in the Hg/RG systems it is known that prolonged excitation of the atomic resonance in Hg/Xe produces mercury dimer. Thus the quenching mechanism presented would also rationalize this surprising observation of photo-clustering in a solid whose substitutional sites ideally accommodate atomic mercury. Thus the atomic quenching mechanism will dispose up to 30,000 cm^{-1} energy into the host lattice, providing sufficient energy for the migration of the atomic mercury in the solid.

IV.4 Conclusions

From the close agreement found with observed absorption energies[8], pair-potentials calculations indicate that atomic mercury occupies essentially undistorted substitutional sites in solid Ar, Kr and Xe. Calculation of the excited state energies for Hg/Ar and Hg/Kr show that three vibronic modes lead to emission in these matrices. Of these, the 6-atom 'waist' mode, Q_5, is expected to dominate the low temperature spectra as it has the steeper stabilization gradient. In Hg/Ar matrices, this mode predicts emission in close agreement with the observed bands but in Hg/Kr it is slightly to the red of the observed band[8]. Hg/Xe calculations indicate that emission can arise from six modes. The 2–atom 'body' $Q_6(p_y)$ mode leads to emission which most closely matches the observed band centre at 273 nm. This mode involves motion of the Hg(p_y) atom to one of the 12 nn Xe atoms and corresponds to the proposal made by C&T, that excimer type behaviour was responsible for the emission in Hg/Xe. However, the results presented here indicate that this motion must occur in a specific orbital orientation (p_y) to achieve stabilization and produce emission.

Calculations conducted on the 4–atom 'waist' (Q_3) and the 4–atom 'body' modes (Q_2) predict emission in the 350-400 nm region in Hg/Xe which has never been detected in the spectra recorded. A quenching mechanism of these modes is identified in the calculations, involving the crossing of these strongly bound, excited state vibronic states by the repulsive ground state potential. This crossing does not occur in the Hg/Ar and Hg/Kr systems.

References

1 J.G. McCaffrey and P. N. Kerins, *J. Chem. Phys.*, **106**, 7885 (1997).

2 J. Zuniga, A. Bastida, A. Requena, N. Halberstadt and J. Beswick, *J. Chem. Phys.*, **98**, 1007 (1993).

3 S. Martrenchard-Barra, C. Jouvet, C. Lardeux-Dedonder and D. Solgadi, *J. Chem. Phys.*, **98**, 5281 (1993).

4 M.H. Alexander, A.R. Walton, M. Yang, Y. Yang. E. Hwang and P.J. Dagdigian, *J. Chem. Phys.*, **106**, 6320 (1997).

5 B. Healy and J. G. McCaffrey, *J. Phys. Chem.* A*,* **104**, 3553 (2000).

6 M. Quigley, *M.Sc. Thesis*, National University of Ireland – Maynooth, Maynooth, Co. Kildare, Ireland, 2002, (unpublished results).

7 M. McCarty and G.W. Robinson, *Mol. Phys.*, **2**, 415 (1959).

8 C. Crepin and A. Tramer, *J. Chem. Phys*., **97**, 4772 (1992).

9 W.H. Breckenridge, C. Jouvet, B. Soep, in: M. Duncan (Ed.), *Advances in Metal and Semiconductor Clusters*, Vol. 3, JIA Press, Greenwich, CT, 1995.

10 M. Okunishi, H. Nakazawa, K. Yamanouchi and S. Tsuchiya, *J. Chem. Phys.*, **93**, 7526 (1990).

11 K. Fuke, S. Takayuki and K. Kaya, *J. Chem. Phys.*, **81**, 2591 (1984).

12 S.L. Altmann and P. Herzig, *Point-Group Theory Tables*, p. 595, Oxford Science Publications, 1994.

13 Assuming the complete energy of the M/RG_{18} can be described by M·RG interactions ignores multi – body interactions however these interactions are usually quite weak contributing less than 10% of the overall energy of the system.

14 C. Kittel, *Introduction to Solid State Physics*, 5th Edition, Wiley and Co, New York, 1976, p. 77.

15 Preliminary lattice relaxation calculations reveal substitutional site expansions of only 0.067 and 0.015 Å for Ar and Kr respectively while a contraction of 0.026 Å is calculated for the Hg/Xe system using the ground state, 'breathing' mode, (Q_1) presented in Chapter V.

16 J.G. Kaup and W.H. Breckenridge, *J. Phys. Chem.*, **99**, 13701 (1995).

17 Small differences which exist between the substitutional site sizes (calculated from the crystal lattice parameters) of rare gas atoms in the solid state and the equilibrium ground state bond lengths of the rare gas dimers in the gas phase arise from weak multi-body effects occurring in the solid state.

18 L Laaksonen, *J. Mol. Graph*, **10**, 33 (1992).

[19] The functional form of the Morse Potential; $V(R) = D_e[1-\exp(-\beta(R-R_e))^2]$ where $\beta = 1.2177881 \times 10^{-1}[(\mu_{AB}.(\omega_e)^2/ D_e]^{1/2}$ and $\mu_{AB} = (m_A.m_B/m_A+m_B)$ was employed to describe the interaction for the Hg·RG diatomics. Morse potential from I. G. Wallace, J. Ryter, W. H. Breckenridge; *J. Chem. Phys.*, **96**, 136, (1992).

[20] O. Roncero, J. Beswick, N. Halberstadt and B. Soep, p. 471, in *Dynamics of Poylatomic van der Waals complexes* eds. N. Halberstadt and K. Janda, NATO ASI Series Vol. 227 Plenum press 1990.

[21] The Q_5 mode contrasts with the 6-atom 'body' mode, Q_4, for which the rare gas potential term does not appear since the latter involves only the motion of the guest metal atom and does not result in any changes in the positions of the lattice atoms.

[22] Note that the energy maximum present in the p_z body-mode in the two-fold symmetry is a result of the non-physical behaviour of the deconvoluted Hg·Xe Σ potential at short range.

[23] An alternative Molecular dynamics approach which invokes a DIM method to probe vertical excitation energies of a very large number of ground state nuclear configurations is currently being applied to the mercury and other matrix-isolated metal atom systems. Initial results reveal the threefold absorption splitting assigned to the Jahn-Teller effect. P. dePujo, C. Crepin and J.G. McCaffrey, unpublished results 2003.

[24] J. Helbing, A. Haydar and M. Chergui, *J. Chem. Phys*., **113**, 3621 (2000).

Chapter V

A pair-potentials analysis of I) the Hg ($^3P_1 \leftrightarrow {}^1S_0$)/Ne luminescence and II) Hg ($^3P_0 \rightarrow {}^1S_0$)/RG (RG = Ar, Kr and Xe) emission spectroscopy.

V Introduction

This Chapter consists of two parts both of which employ the M/RG_{18} localised model to simulate the observed luminescence of atomic mercury isolated in solid rare gases. In Part I, the Hg/RG_{18} pair-potentials approach, presented in Chapter IV for the rare gases Ar, Kr and Xe, is extended to model the luminescence of the atomic Hg 6p $^3P_1 \leftrightarrow$ 6s $^1S_0$ transition isolated in solid neon. Part II focuses on Hg isolated in Ar, Kr and Xe in an attempt to simulate the emission spectroscopy of the Hg atom $^3P_0 \rightarrow {}^1S_0$ transition reported in Chapter III. These two sections provide insights into 1) ground and excited state metal atom solvation, 2) the effect of local lattice perturbations caused by the dopant and 3) the importance of the site of isolation occupied by the metal atom in determining the observed luminescence.

V.I A pair-potentials analysis of the Hg ($^3P_1 \leftrightarrow {}^1S_0$)/Ne luminescence

V.I.1 Introduction

The localised pair-potentials approach[1] is employed here to investigate the absorption and emission spectroscopy of the atomic $^3P_1$ state Hg in solid neon. The spectroscopic studies of matrix-isolated[2] atomic mercury focusing on the 6p $^3P_1 \leftrightarrow$ 6s $^1S_0$ transition reported by the Orsay group[3] and recently by our group at Maynooth[4] outlined the luminescence in solid Ar, Kr and Xe as 12 K. This was the minimum temperature available with those experiments but recently Chergui and co-workers[5,6] have conducted spectroscopic studies of atomic Hg in neon matrices at 4 K. The deposition temperature was achieved on a LiF window cooled by a liquid helium cryostat. The atomic Hg($^3P_1 \leftrightarrow {}^1S_0$)/Ne excitation and emission spectra reported by Chergui and co-workers[5] are presented in the top panel of Figure V.1. The emission spectrum and fluorescence-excitation reported by Chergui were produced with UV laser excitation. Emission was detected using a UV-enhanced CCD camera or photomultiplier tube following dispersion by an Acton Research UV-Vis monochromator equipped with a 150-grooves/mm diffraction grating. Table V.1 presents a comparison of the photo-physical characteristics of the Hg($^3P_1 \leftrightarrow {}^1S_0$)/Ne

results[5] and those recorded for Hg/Ar, Hg/Kr and Hg/Xe in this work and presented in Chapter III.

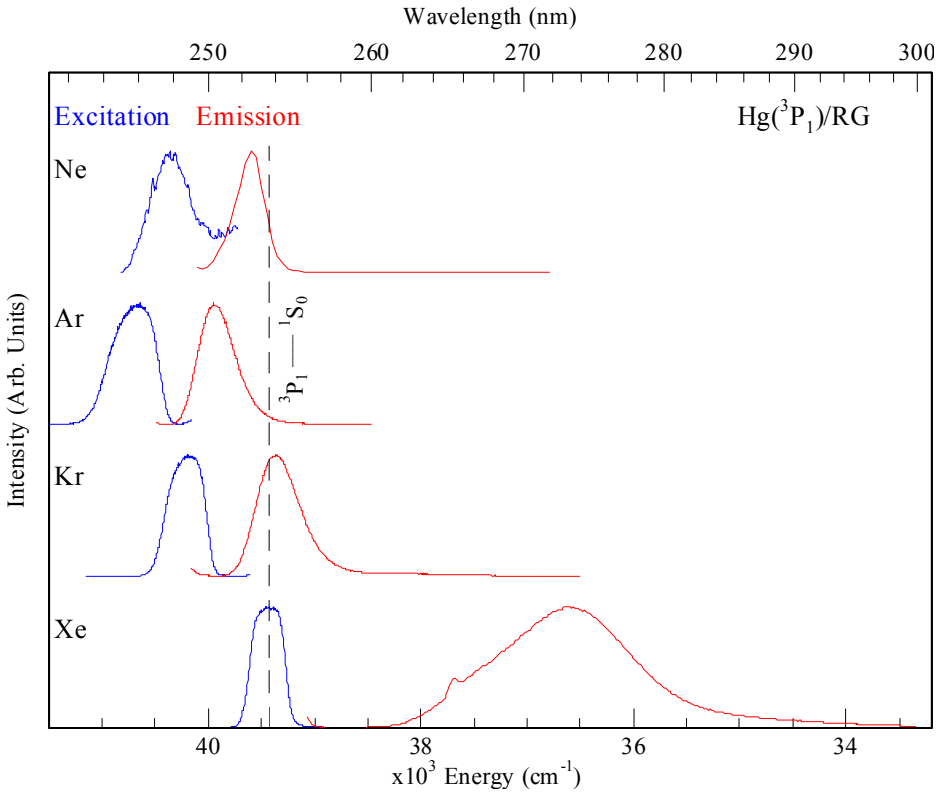

Figure V.1 **A comparison of the emission spectra recorded for Hg/Ne, Ar, Kr and Xe systems (shown right) produced with excitation of the Hg $^3P_1 \leftarrow {}^1S_0$ transition. The Hg/Ne emission spectrum shown (top right) was produced with laser excitation and recorded at 4 K using CCD detection, as reported by Chergui and co-workers[5]. The Hg/Ar, Kr and Xe data presented are time-integrated emission spectra recorded following deuterium lamp excitation at 12 K as outlined in Chapter III. The excitation spectra shown left were produced monitoring the Hg $^3P_1 \rightarrow {}^1S_0$ fluorescence emission maximum for each Hg/RG system.**

Table V.1 **Photophysical characteristics of the triplet 6p $^3P_1 \leftrightarrow$ 6s $^1S_0$ transition of matrix – isolated atomic mercury. λ_{Ex} indicates the position of the central component of the three–fold split excitation spectrum and λ_{Em} indicates the emission band-centre in nm units. The full-width at half-maximum intensity of the excitation/emission features is denoted by Δ and the Stokes' shift by SS - both in wavenumber (cm^{-1}) units.**

Hg/RG	Excitation		Emission		
System	λ_{Ex} (nm)	Δ (cm^{-1})	λ_{Em} (nm)	Δ (cm^{-1})	SS (cm^{-1})
Ne[5,7]	247.8	470	252.5 ± 0.5	300-500	668
Ar	245.9	484	250.3	399	715
Kr	248.9	397	254.1	465	816

It is evident from the comparison made in Figure V.1 and Table V.1 that the Hg($^3P_1$)/Ne excitation and emission spectra do not follow the overall trend exhibited by the other Hg/RG systems, where a progressive blue-shift in the excitation and emission band maxima (λ_{Ex} and λ_{Em}) is observed from Xe to Ar. However the Hg/Ne emission spectrum conforms to the trends evident for Hg/Ar and Kr where the Stokes' shift (SS) and the emission linewidth (Δ) increase from Ne to Xe. The expected blue-shift of the excitation band maximum (λ_{Ex}) with decreasing rare gas polarizability for a given site of isolation of the metal atom within the RG matrix is not exhibited by the Hg/Ne system. A linear correlation between the gas phase – matrix absorption/excitation band maximum and rare gas polarizability was presented by Laursen and Cartland[8] (L&C) for the M($^1P_1$ and $^3P_1 \leftarrow {}^1S_0$)/RG transitions of the metal atoms Zn, Cd and Hg in Ar, Kr and Xe matrices. The polarizability model held true for the Hg ($^3P_1 \leftarrow {}^1S_0$) transition in Ar, Kr and Xe matrices but until recently[5,6], Hg/Ne results were not available for comparison. The Hg($^3P_1 \leftrightarrow {}^1S_0$)/$Ne_{18}$ pair-potentials simulations presented in this Chapter allow an investigation of the deviations shown by the Hg($^3P_1$)/Ne excitation and emission spectra from the trends exhibited by the other Hg/RG systems.

The availability of the Hg($^3P_1$)/Ne matrix data[5] and diatomic Hg($^3P_1$)·Ne [X $^1{0}^+$ ($^1\Sigma$)], [A $^3{0}^+$ ($^3\Pi$)] and [B $^3{1}$] state potentials[9,10] allowed the application of the Hg·RG_{18} model to solid Ne. In the sections which follow, an examination of the Hg $^3P_1 \leftrightarrow {}^1S_0$ Ne matrix spectroscopy is conducted using the Hg·RG_{18} cluster calculations. The tetragonal (4-fold symmetry), trigonal (3-fold symmetry) and 2-fold symmetry calculations outlined in Chapter IV are performed for atomic Hg isolated in solid Ne matrices. The calculations presented in the previous Chapter are based on atomic mercury occupying unperturbed substitutional sites in solid Ar, Kr and Xe. The Hg/Ne simulations presented are based on substitutional site occupancy but allow the ground state Hg $6s^2\ {}^1S_0$ atom to deform its immediate neon matrix environment. The original and deformed matrix environments are referred to in the text as "rigid" and "relaxed" lattice calculations respectively. Therefore, in addition to the calculations outlined in Chapter IV, details of a lattice expanding symmetric 'breathing' mode, (Q_1) and modifications to the trigonal, 6-atom 'waist' mode, (Q_5) are presented. The 'breathing' mode Q_1 involves the symmetric expansion (or contraction) of the first solvation shell of Ne atoms surrounding the metal atom

thereby allowing relaxed substitutional site occupancy. Comparison of the calculated Hg($^3P_1 \leftarrow {}^1S_0$)/Ne absorption energies with the observed Hg/Ne spectroscopy allowed the assignment of relaxed substitutional site occupancy for atomic mercury in solid neon. The emission comparison allows an assessment of the effects of a ground state perturbation on the Hg($^3P_1$) excited state dynamics. In solid neon a significantly Stokes' shifted emission is predicted by the Hg/Ne_{18} cluster model only for relaxed lattice calculations. A combination of the re-establishment of the equilibrium neon lattice and stabilisation of the Hg·Ne interactions lead to energy values which compare well with observed emission. These conditions are fulfilled by 'waist' modes calculated where the Hg $^3P_1$ state is stabilised by the trigonal 6-atom 'waist + limited stretch' mode, (Q_8^*) - a modification of the 6-atom 'waist' mode (Q_5) presented in Chapter IV.

V.I.2 Method and Results

The pair-potentials analysis of the Hg($^3P_1 \leftrightarrow {}^1S_0$)/Ne luminescence spectroscopy outlined in this section employs the localized M/RG_{18} model[1] presented in Chapter IV. Therefore only the modifications required to simulate the Hg/Ne spectroscopy are presented here.

V.I.2.I Ground State Site occupancy

The starting point for the Hg/Ne_{18} simulations is the selection of the site occupied by the ground state Hg atom within the host neon matrix. This is achieved by comparison of the Hg·Ne X ($^1\Sigma$) ground state bond length with that of neon dimer Ne_2. As presented in Table V.2, the Hg·Ne ground state bond length is 3.89 Å whereas the neon dimer bond length is 3.091 Å.

The substitutional site (*ss*) size available in solid Ne is 3.155 Å[11], calculated from the lattice parameter[12] a = 4.462 Å, using the relationship $ss = a/\sqrt{2}$ Å. The comparison of the substitutional site size available and the Hg·Ne van der Waals bond length reveals a difference of 0.735 Å. This unfavourable comparison makes rigid substitutional site occupancy unlikely within solid neon. Therefore, an expansion of the substitutional site may be required to facilitate the isolation of the mercury atom. Whether Hg atom occupancy in a substitutional site leads to the deformation of the

original site can be determined by comparing the predicted and observed Hg($^3P_1 \leftarrow {}^1S_0$)/Ne absorption energies.

The ground state energy of the cluster is evaluated with the method presented in Chapter IV, Section IV.2.I. The Morse parameters used to describe the Hg·Ne and Ne·Ne interactions are provided in Table V.2.

Table V.2 **Spectroscopic constants used to generate the Morse potential energy curves for the Hg·Ne and Ne_2 diatomics. Data source are indicated by the references.**

Morse Parameters	Hg·Ne[10]			Ne·Ne[13]
	X $^1\Sigma$ ($^10^+$)	**A $^3\Pi$** ($^30^+$)	**B $^3\Sigma$** (^{31})	**X $^1\Sigma$**
$\mu_{Hg\text{-}RG}$ (amu)	18.191701	-	-	9.996219
$D_e(cm^{-1})$	42	79	13.3	29.4
$\omega_e(cm^{-1})$	17.2	26.9	7.7	29.1
$\omega_e x_e(cm^{-1})$	1.77	2.28	1.12	-
R_e(Å)	3.89	3.497	4.71	3.091
$\beta(Å^{-1})$	1.378517	1.57198	1.09666	2.0906[14]

Ground State 'breathing' mode, (Q_1)

Due to the unfavourable match between the substitutional site size available in solid Ne and the Hg·Ne ground state bond length, the 12 nearest neighbour (*nn*) Ne atoms surrounding the Hg atom undergo a radial expansion. The ground state 'breathing' mode, (Q_1) is akin to the previously described 'waist' mode as the motions of the lattice atoms are 'in-phase' relative to the fixed metal atom. Q_1 lowers the energy of the Hg·Ne_{12} cluster as the Hg-Ne interaction distance is increased by +X Å from *ss Ne* = 3.155 Å to *ss* + X Å allowing the Hg-Ne distance to approach the Hg·Ne ground state bond length listed in Table V.2. The interactions involved in Q_1 are shown in Figure V.2. The motion of the 12 *nn* Ne atoms results in a destabilisation of the Ne lattice as the Ne-Ne distances are displaced from their equilibrium value, (R_e). The lattice destabilisation caused by the motion of the 1st sphere limits the amount the Hg·RG_{12} cluster can be stabilised. Therefore, the extent of the expansion occurring in the 1st sphere surrounding the metal atom is identified as the point where the Hg·Ne stabilisation and the Ne lattice destabilisation energies are equal. To identify this point, the energies at the equilibrium positions of the Hg·Ne_{12} (the Hg·Ne ground state bond length) and Ne lattice (where all Ne·Ne interactions occur at the distance

of the Ne_2 equilibrium bond length) are both set to zero. Equation IV.I is applied with the number of Hg·Ne and Ne·Ne interactions occurring i.e., n = 12 and m = 120 respectively.

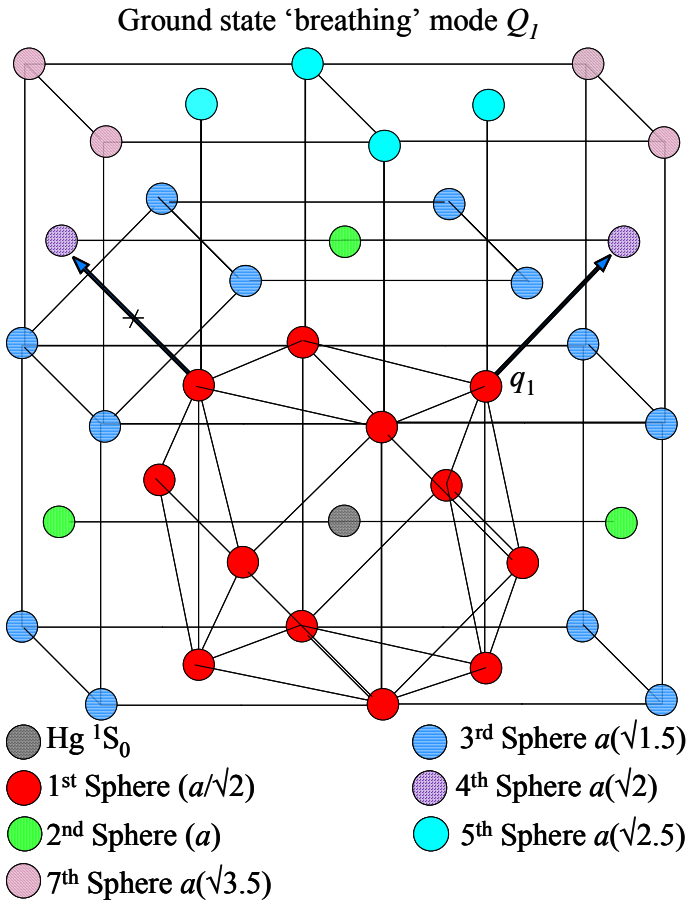

Figure V.2 **Representation of the interactions involved in the calculation of the energetics of the ground state 'breathing' mode (Q_1). The symmetric expansion of the 12 nearest neighbour (*nn*) Ne atoms forming the 1st co-ordination sphere of the Hg atom isolated in a substitutional site, shown by q_1. The relative positions of the 2nd and successive metal atom co-ordination spheres are indicated by shaded spheres and the radial distances to the Ne atoms forming the different shells are provided as a function of the lattice parameter of solid Ne (a = 4.462 Å).**

A total of 120 Ne·Ne interactions occurring within the 4th sphere are considered in the calculation of the lattice destabilisation due to the motion of the 12 *nn*. The Ne·Ne interactions considered are shown in Figure V.2 the geometric details of which are now presented, labelled I-V. I) The expansion of the 12 *nn* Ne atoms surrounding the Hg atom results in the contraction of the distance between the moving atoms and 12 RG atoms positioned in the 4th sphere (spotted circles), resulting in the contraction of 12 'on-axis' RG interactions from the initial

substitutional site distance $ss = a/\sqrt{2}$ Å to ss – x Å. II) Each of the moving 12 *nn* Ne atoms approach a rectangle of Ne atoms located in the 3rd sphere by a distance $\left(\sqrt{\frac{a}{\sqrt{2}}} - x\right)^2 + \frac{3}{8}a^2$. There are 48 of these Ne·Ne interactions. III) The 12 *nn* Ne atoms move away from the 6 next nearest neighbour (*nnn*) atoms located in the 2nd co-ordination sphere by the amount $\left(\sqrt{\frac{a}{\sqrt{2}}}\right)^2 + x^2$, contributing another 24 Ne·Ne interactions. IV) The radial expansion of the 12 nearest neighbour atoms on the surface of the cubo-octahedron results in the extension of 24 Ne·Ne distances from the substitutional site distance $ss = a/\sqrt{2}$ to ss + x. V) 12 Ne·Ne next nearest neighbour (nnn) interactions on the surface of the cubo-octahedron are extended from the lattice parameter, a to ($a+\sqrt{2}$x).

The potential energy curves calculated for the expansion of the 1st sphere atoms from the Hg atom isolated in a substitutional site in solid Ne are shown in Figure V.3. Upon inspection of Figure V.3 it is evident that a lattice expansion of 0.293 Å occurs representing an increase in the substitutional site diameter of 9.29%. With this expansion the Hg·Ne_{12} cluster is stabilised by 353.0 cm^{-1} (Ne lattice destabilisation is -ΔE cm^{-1}) from the initial value (E_{subs}) for Hg atom isolated in a rigid site within the Ne_{12} cluster. The relaxed substitutional site size [ss_{Rel} = (3.155 + ΔQ)] is 3.448 Å. The stabilisation observed for Hg·Ne_{12} can be understood in terms of the Hg($^1S_0$)·Ne ground X state potential shown in the right panel of Figure V.4, where the vertical lines crossing the potential energy curve indicate the rigid (Ne_{SS}) and relaxed (Ne_{SS} + ΔQ) substitutional site diameters. The ground state energy of the Hg($^1S_0$)/Ne_{18} cluster is calculated for both rigid and relaxed substitutional site occupancy following the method detailed in Chapter III.

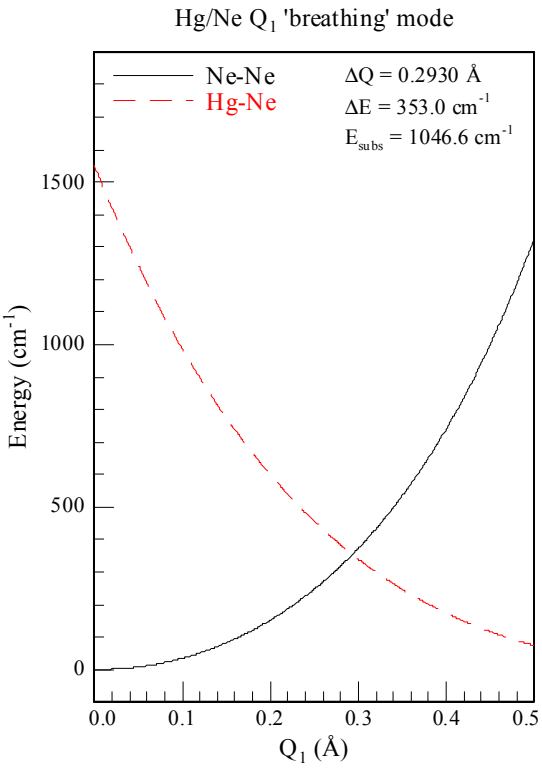

Figure V.3 **Potential energy curves for the Hg·Ne_{12} and 120 Ne·Ne interactions occurring for the symmetric ground state 'breathing' mode, (Q_1). R = 0 Å, for the mode Q_1 represents the undistorted substitutional site. The extent of the lattice expansion calculated is indicated as ΔQ = 0.293 Å.**

V.I.2.II Excited $^3P_1$ state

The excited state energy of the Hg($^3P_1$)/Ne_{18} cluster was calculated as outlined in Chapter IV; Section IV.2.II. The known diatomic Hg($^3P_1$)·Ne A [$^30^+$ ($^3\Pi$)] and B (^{31}) state potentials[10] are used to construct the excited state Hg/Ne_{18} cluster following deconvolution of the $^3\Sigma$ state from the experimentally observed B state using Equation IV.5. The A ($^3\Pi$), B and deconvoluted $^3\Sigma$ states for Hg·Ne are shown in the left panel of Figure V.4. The deconvoluted $^3\Sigma$ state exhibits a long range minimum as observed for Hg·Ar, Kr and Xe in Chapter IV.

Excited $^3P_1$ state energetics were calculated for the body and waist vibronic modes in the three orbital orientations (p_x, p_y and p_z) for the fourfold (4-atom), threefold (6-atom) and twofold (2-atom) co-ordinate systems shown Figure IV.4, Chapter IV. The calculations were completed for atomic mercury isolated in rigid and relaxed substitutional sites within the neon lattice. The absorption energies were compared for the three co-ordinate systems calculated and identical absorption energies were obtained for all modes given the condition of the site of isolation (rigid

or relaxed). As the absorption energy is calculated as the difference in the energy of the cluster in the ground and excited state within the Frank – Condon principle the absorption energies should be different for rigid and relaxed site occupancy.

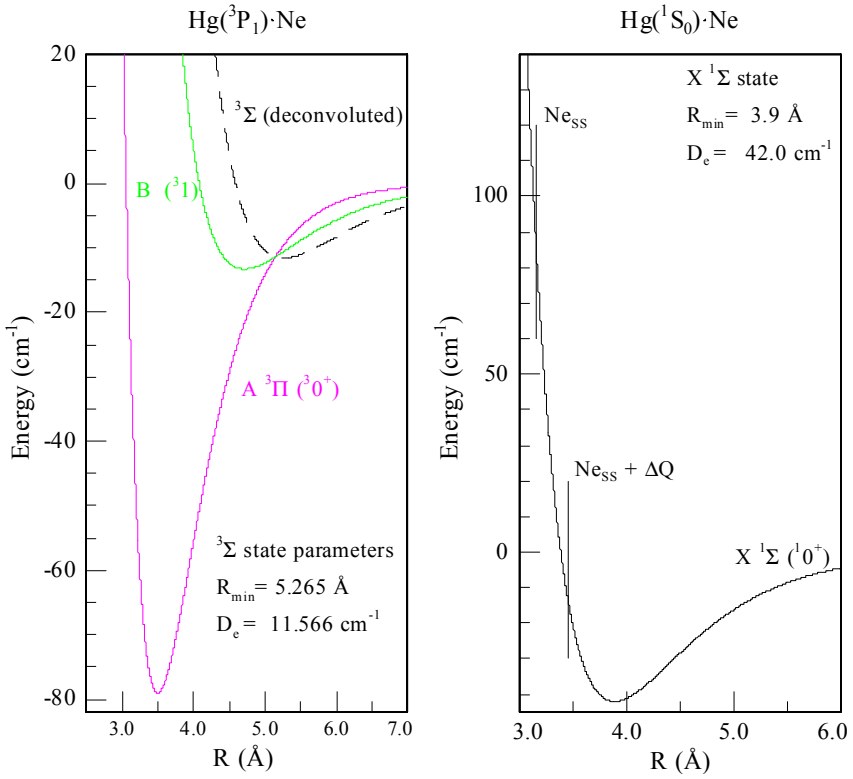

Figure V.4 **The Hg($^3P_1$)·Ne $^3\Sigma$ state extracted with Equation IV.5 from the spectroscopic [A ^{3}0$^+$ ($^3\Pi$)] and [B ^{3}1] states (left panel) whose constants are presented in Table V.2. Note: the most recent spectroscopic data on the Hg·Ne 1:1 van der Waals complex presented in Ref. 10 was used to generate the potential energy curves presented. The $^3\Sigma$ state shows a weakly bound region at long range corresponding to R_{min} and the binding energy is indicated by D_e. All of the states share the Hg atom 6p $^3P_1$ asymptote at 39424.1 cm^{-1} but are shown dissociating to zero-energy for the purpose of comparison with the potential energy curve for the Hg($^1S_0$)·Ne X ($^1\Sigma$) state shown right panel.**

Thus for Hg isolated in solid Ne, 18 excited state potential energy curves were calculated for both rigid and relaxed substitutional site occupancy. However, only the vibronic modes exhibiting stabilisation, are discussed as these are the only ones leading to emission. The tetragonal (4-atom) and the twofold (2-atom) 'body' and 'waist' modes Q_2, Q_3, Q_6 and Q_7 presented in the previous chapter were not stabilised for any p-orbital orientation. The trigonal (6-atom) 'body' mode Q_4 was not stabilised for Hg/Ne. However the 6-atom 'waist' mode was stabilised and the results are now presented. The details of two new vibronic modes (Q_8 and Q_8^*) based on the

6-atom 'waist' mode, (Q_5) presented in Chapter IV are discussed in the following section.

Hg/Ne$_{18}$ Trigonal (6-atom) symmetry modes

The co-ordinate system used to calculate the 6-atom 'body' (Q_4) and 'waist' (Q_5) vibronic modes is presented in Figure IV.4 where the Z-axis is co-incident with one of the four, threefold symmetry axes of the Hg·Ne$_{12}$ cubo-octahedron. The details of the modes and the calculation of the excited state energetics are presented in detail in Chapter IV; Section IV.2.II.II. The potential energy curves calculated for the 6-atom modes for rigid and relaxed neon lattice are shown in Figure V.5 and Figure V.6 respectively.

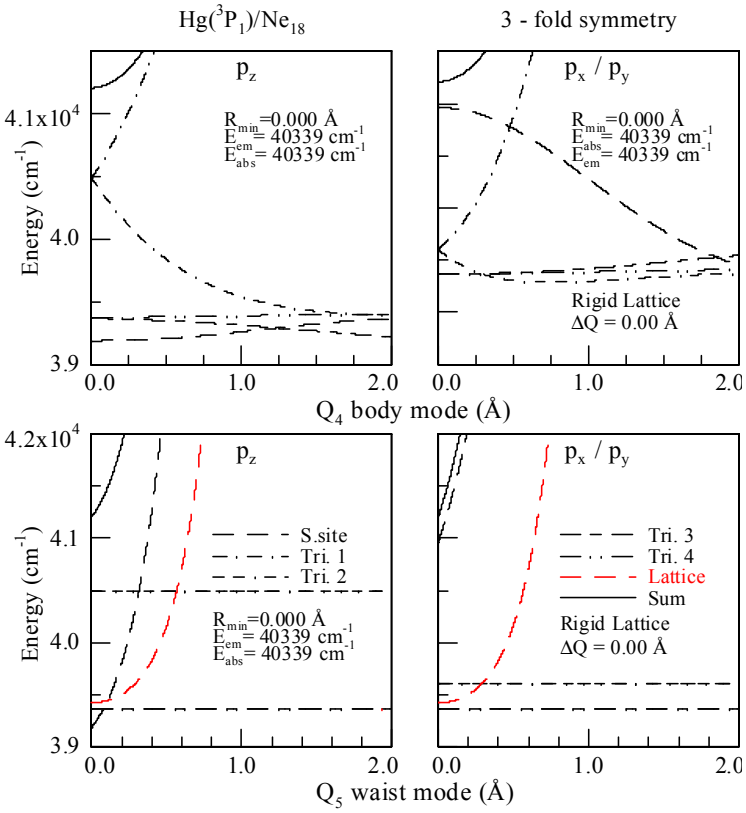

Figure V.5 **Energetics calculated for the Hg/Ne$_{18}$ trigonal (6-atom) 'body' and 'waist' modes, Q_4 and Q_5 respectively based on rigid substitutional site occupancy as indicated by ΔQ = 0.00 Å. The individual interactions (I–V) involved (the specific details of which are presented in Chapter IV) are shown by the legend. The total potential energy calculated for the mode is shown by the solid line obtained by summation of the individual interactions.**

Figure V.5 reveals that the excited state Hg($^3P_1$)/Ne$_{18}$ cluster is not stabilised by the 6-atom vibronic modes for Hg isolated in a rigid substitutional site in solid Ne. However the 6-atom 'waist' mode (Q_5) does lead to stabilisation for the p_z orbital

orientation upon relaxing the neon lattice by 0.293 Å. Closer inspection of Figure V.6 shows that although the in-phase contraction of the 6 Ne atoms forming S.site does not lead to an energy minimum, this coupled with the lattice stabilisation leads to an overall excited state minimum for the vibronic mode. The comparison between the rigid and relaxed threefold symmetry calculations reveals that the absorption energies calculated are different. The 6-atom 'body' mode Q_4 presented in the top panels of Figure V.5 and Figure V.6, although not stabilised, provided evidence of the cramped nature of the substitutional site occupancy in solid Ne as the only interactions producing minima for Q_4 are those where the Hg·Ne distance is increased, i.e., S.site and Tri. 3.

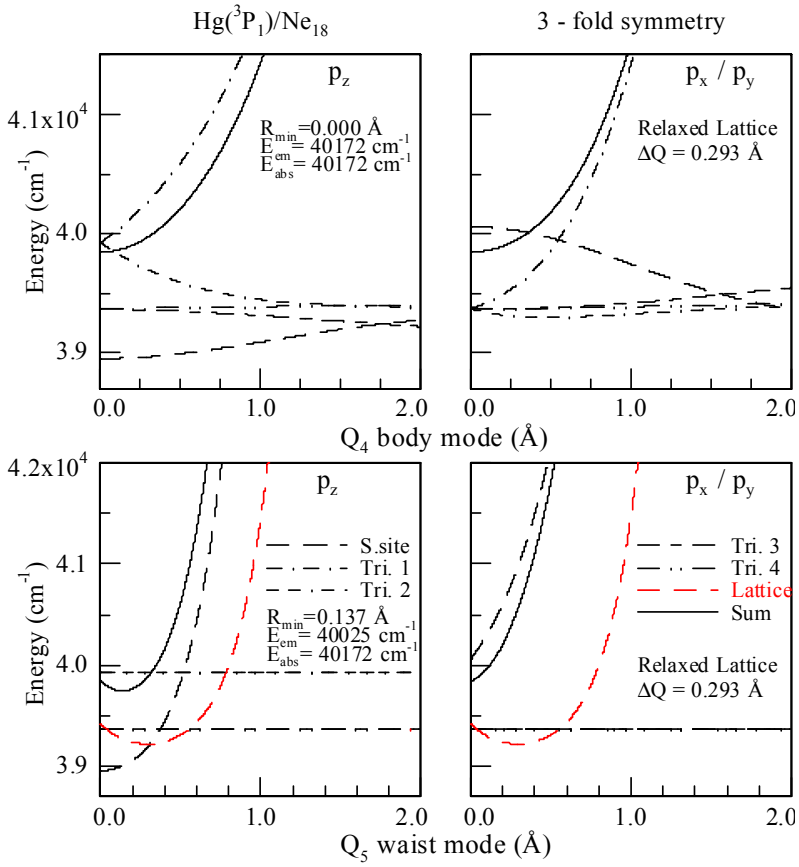

Figure V.6 **Energetics calculated for the Hg/Ne$_{18}$ trigonal (6-atom) 'body' and 'waist' modes, Q_4 and Q_5 respectively based on relaxed substitutional site occupancy as indicated by ΔQ = 0.293 Å.**

The excited state stabilisation exhibited by the relaxed lattice 6-atom 'waist' mode Q_5 (p_z) Figure V.6 (bottom left) is due to a combination of factors. Thus a) the Hg·Ne Π interaction is optimised as the 6 atoms involved in the 'in-phase' contraction (S.site) interact with the Hg $^3P_1$ p_z orbital orientation. b) The restoration

of the Ne lattice atoms on the close packed plane B (Figure IV.10) and c) The relaxation of the lattice reduces the repulsive Σ interaction between the excited state Hg atom the two triangles of nearest neighbour Ne atoms (Tri.1 and 2) and to a lesser extent the two triangles of next nearest neighbours (Tri.3 and 4.). Therefore the 6-atom 'waist' mode Q_5 is modified to minimise the repulsive Σ interactions.

The modification to the 6-atom 'waist' mode is the addition of a 6-atom stretch where the six nearest neighbour atoms forming Tri.1 and Tri.2 are allowed to move away by a distance +X Å from the excited state Hg atom. This excited state vibronic mode, the trigonal 6-atom 'waist + stretch' mode, (Q_8) is presented in Figure V.7, left panel. The original Q_5 mode is presented in the right panel for the purpose of comparison. The original Q_5 vibronic mode calculations, presented in Chapter IV, requires only slight modification to implement the 6-atom 'waist + stretch' mode, (Q_8). Equations IV.10 and IV.11 employed to calculate the total energetics of the excited $^3A_1(p_z)$ and $^3E(p_x/p_y)$ states in the waist mode are modified such that the interaction distance R_2 initially set at the nearest neighbour distance ($a/\sqrt{2}$) is increased to R_2 + X where +X represents the stretch.

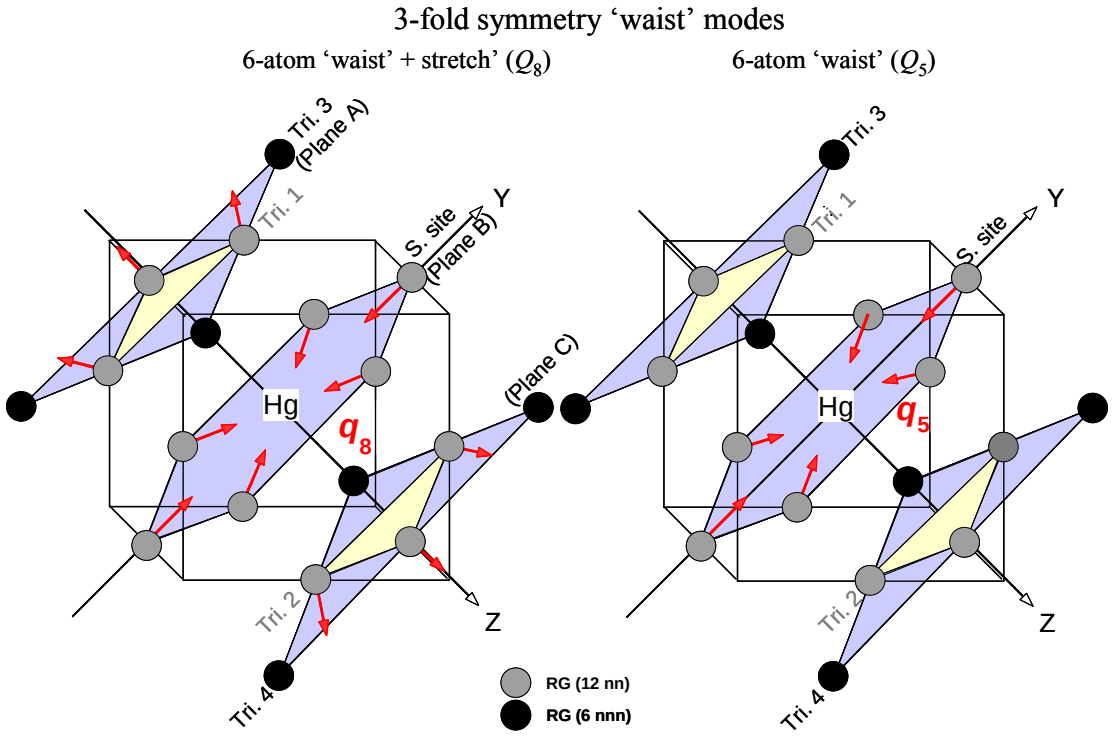

Figure V.7 **The threefold guest atom-based co-ordinate system used to calculate the 6-atom 'waist' modes occurring for substitutional site occupancy. The 6-atom 'waist + stretch' mode (Q_8) and the original 6-atom 'waist' mode (Q_5) are depicted.**

The energies calculated for the trigonal 6-atom 'waist + stretch' mode (Q_8) are presented in Figure V.8 and Figure V.9 for the rigid and relaxed substitutional site occupancy respectively.

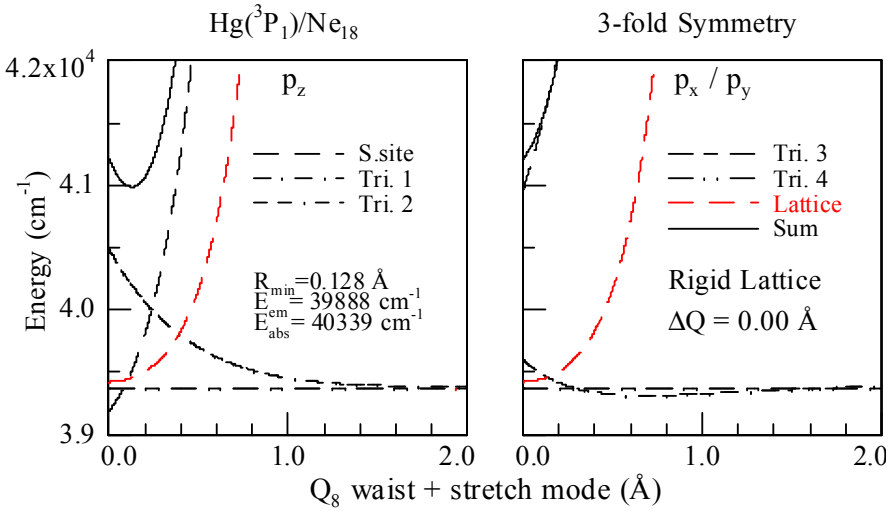

Figure V.8 **Potential energy curves calculated for the 6-atom 'waist + stretch' mode, (Q_8) based on rigid substitutional site occupancy of the Hg atom in solid Ne.**

Upon inspection of Figure V.8 it is evident that the modification of the 6-atom 'waist' calculation to include the 6-atom stretch, produces excited state stabilisation for a rigid lattice calculation. The absorption energy calculated for the Q_8 mode agrees with that achieved for the Hg($^3P_1 \leftarrow {}^1S_0$)/Ne$_{18}$ rigid lattice simulations.

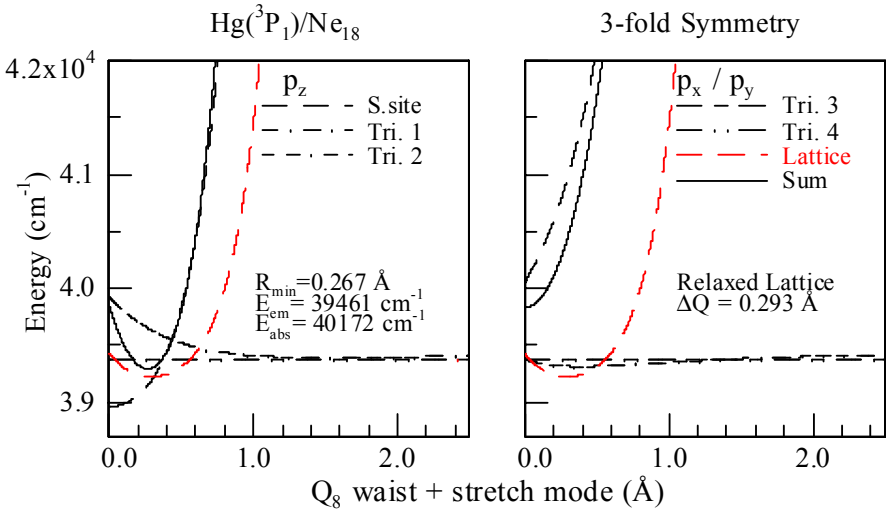

Figure V.9 **Potential energy curves calculated for the 6-atom 'waist + stretch' mode, (Q_8) based on relaxed substitutional site occupancy of the Hg atom in solid Ne.**

The addition of the 6-atom 'stretch' to the relaxed lattice calculation results in the increased stabilisation of the Hg $^3P_1$ excited state in solid neon. However the increased stabilisation introduced is believed to be over-estimated since the 6-atom 'stretch' calculated is not restrained by repulsive interactions for the neon lattice that would limit such a free expansion. A simple modification is suggested to limit the free 'stretch'. It involves the addition of a Ne·Ne nearest neighbour interactions occurring at an initial distance of $ss = a/\sqrt{2}$ (the nearest neighbour distance) from each of the moving Ne atoms. This will limit the free expansion of the 6-atoms forming Tri.1 and 2 and thereby represent the solid-state environment better. The modification is denoted 6-atom 'waist + limited stretch' mode (Q_8^*).

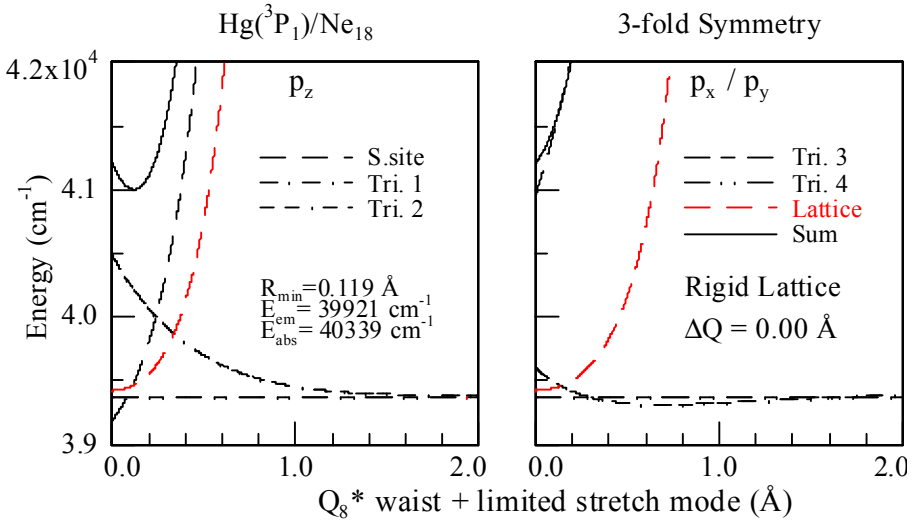

Figure V.10 **Potential energy curves calculated for the 6-atom 'waist + limited stretch' mode, (Q_8^*) based on rigid substitutional site occupancy of the Hg atom in solid Ne.**

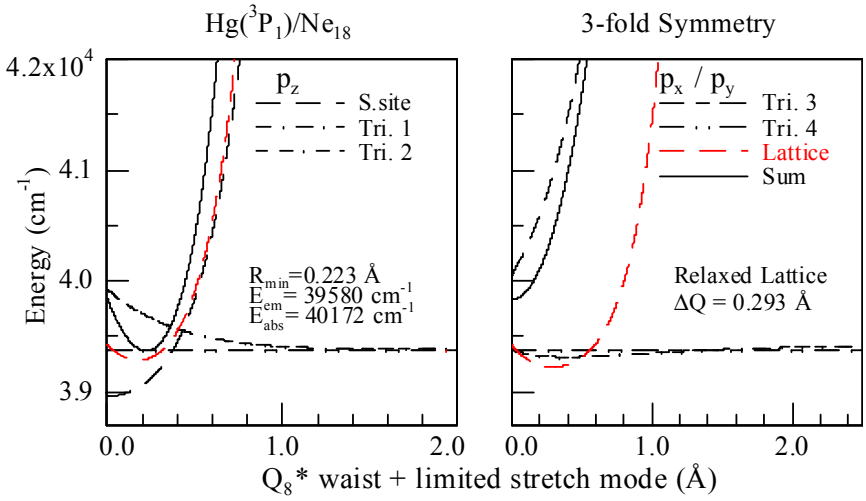

Figure V.11 **Potential energy curves calculated for the 6-atom 'waist + limited stretch' mode, (Q_8^*) based on relaxed substitutional site occupancy of the Hg atom in solid Ne.**

A comparison of the 6-atom 'waist + stretch' (Q_8) and the modified 6-atom 'waist + limited stretch' (Q_8^*) calculations for both the rigid and relaxed neon lattice reveals that the excited stabilisation calculated for Q_8 is as anticipated greater than that observed for the Q_8^* mode. In the following section the absorption and emission energies calculated for the Hg($^3P_1 \leftrightarrow {}^1S_0$)/$Ne_{18}$ are compared to the Hg/Ne matrix luminescence recorded by Chergui and co-workers[5,6].

V.I.3 Absorption and Emission Energies

The absorption energy of the guest mercury atom was calculated as the difference between the ground Hg($^1S_0$)/Ne_{18} and the excited Hg($^3P_1$)/Ne_{18} cluster energies using Equation IV.16. Within the Frank-Condon approximation no movement will occur between the Hg atom and the Ne cluster during the electronic transition. This implies two different absorption energies must be obtained for the Hg/Ne_{18} simulations presented in this chapter corresponding to the $^3P_1 \leftarrow {}^1S_0$ electronic transition of atomic mercury occurring within the rigid and relaxed substitutional site environments respectively. This requirement was used as a check of the validity of the calculations throughout, and the values of E_{abs} (rigid) and E_{abs} (relaxed) calculated although different, were identical for all the vibronic modes, Q_n calculated for the rigid and relaxed lattice calculations. The absorption energies calculated are compared to those observed for the $^3P_1 \leftarrow {}^1S_0$ transition of atomic mercury isolated in solid neon in Table V.3.

Table V.3 **A comparison of the observed[7] absorption wavelength (*nm* units) for the $^3P_1 \leftarrow {}^1S_0$ transition of matrix-isolated atomic mercury with the calculated absorption values for Hg isolated in a rigid and relaxed substitutional site in solid neon. The difference between the observed band maxima and the predicted values are quoted as $\delta_{Obs\text{-}Cal}$ in cm^{-1}.**

Hg/Ne_{18}	E_{Cal}	λ_{Calc}	λ_{Obs}	$\delta_{Obs\text{-}Cal}$
Rigid Lattice	40339	247.9	247.8	+16.1
Relaxed Lattice	40172	248.93	247.8	+183.1

The comparison of the absorption energies obtained for the rigid and relaxed lattice Hg·Ne_{18} show good agreement with the observed spectroscopy leading to the identification of substitutional site occupancy for atomic Hg in solid neon.

The Hg($^3P_1 \rightarrow {}^1S_0$)/Ne emission energies were calculated as outlined in Chapter IV. The results calculated for the vibronic modes exhibiting Hg $^3P_1$ excited state stabilisation are summarised in Table V.4 for both the rigid and relaxed lattice calculations. Overall the 6-atom 'waist' mode (Q_5) and the two modifications presented for this mode, Q_8 and Q_8^*, are the only vibronic modes calculated for Hg isolated in solid neon that are stabilised and will produce emission. The 4-atom and 2-atom waist modes are not stabilised and will thereby not produce emission. The 'body' modes, which simulate the internal motion of the excited state mercury atom within the solid, are not stabilised for any of the co-ordinate systems examined. The best agreement observed between the calculated and observed emission energies is achieved for the trigonal 6-atom 'waist + limited stretch' mode (Q_8^*) predicting the $^3P_1$ emission at 39580 cm^{-1} (252.65 nm) in neon.

Table V.4 **A comparison of the calculated Hg atom $^3P_1 \rightarrow {}^1S_0$ emission wavelengths with the experimental data reported by Chergui and co-workers[5,6,7] for the Hg/Ne system. All the vibronic modes of Hg·Ne$_{18}$ cluster that lead to excited state stabilisation are presented and compared with the observed emission feature reported.**

Hg/Ne$_{18}$ Motion	Mode	Calculated Rigid Lattice E(cm^{-1}) / λ(nm)	Calculated Relaxed Lattice E(cm^{-1}) / λ(nm)	Observed E(cm^{-1}) / λ(nm)
6-waist	Q_5 (p_z)	-	40025 / 249.84	
6-waist + stretch	Q_8 (p_z)	39888 / 250.70	39461 / 253.41	
6-waist + limited stretch	Q_8^* (p_z)	39921 / 250.49	39580 / 252.65	39682 / 252.0 (± 0.5)

V.I.4 Discussion

On first inspection the absorption comparison made in Table V.3 suggests that atomic Hg occupies undistorted substitutional sites in solid Neon. However the absorption energy predicted by the Hg/Ne$_{18}$ relaxed lattice calculations occurs on the red wing of the observed spectrum. This result is in line with those presented in Chapter IV for the Hg/Ar, Hg/Kr and Hg/Xe systems as shown in Figure V.12. The absorption calculations completed simulate the pure electronic transition (i.e. $\nu_{0,0}$ the position of the zero-phonon line, ZPL).

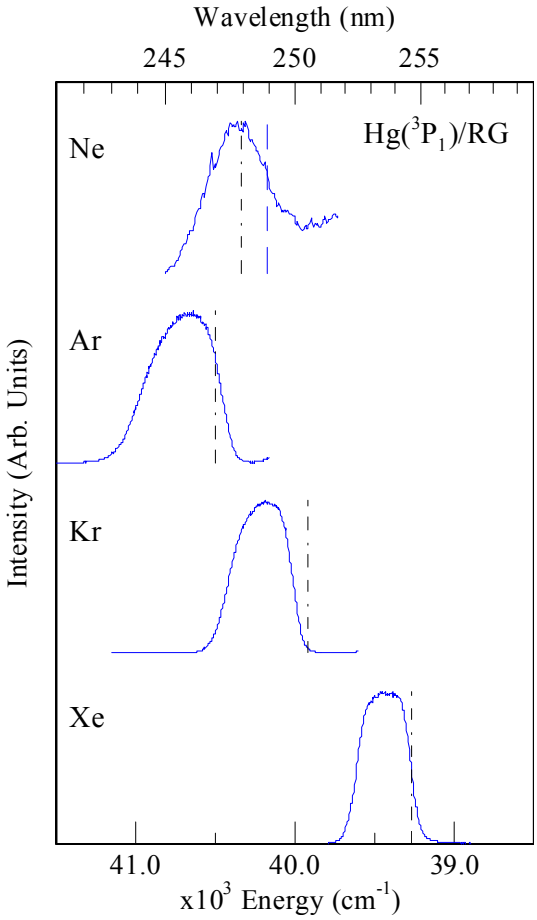

Figure V.12 **A comparison of the observed excitation spectra and calculated atomic Hg ($^3P_1 \leftarrow {}^1S_0$) absorption energies. The Hg/Ne spectrum (top) is that recorded at 4 K by Chergui and co-workers. The excitation spectra presented for Hg/Ar, Kr and Xe are those recorded at 12 K presented in Chapter III. The absorption energies calculated for atomic Hg isolated in rigid substitutional site in solid Ar, Kr and Xe reported in Chapter IV are indicated by the double dash dot (DD-D). The absorption energies calculated for Hg isolated in rigid and relaxed substitutional sites in solid Ne are indicated by DD-D and dashed lines respectively.**

Further evidence that atomic Hg occupies a relaxed substitutional site in solid neon is provided by the ground state lattice expansion of 9.29% required to accommodate the Hg atom and the observation that the shift of the excitation band maximum from the gas phase $^3P_1 \leftarrow {}^1S_0$ observed for Hg/Ne does not show the linear correlation with the rare gas polarizability[15]. Table V.5 presents the gas phase to matrix frequency shifts and the rare gas polarizabilities. A plot of the frequency shift (δ cm^{-1}) of the Hg $^3P_1 \leftarrow {}^1S_0$ transition from the gas phase position to the Hg/RG matrix position (λ_{Ex}) versus rare gas polarizability is shown in Figure V.13.

Table V.5 **Gas phase to matrix frequency shifts of the atomic Hg $^3P_1 \leftarrow {}^1S_0$ transition, δ in wavenumber units. The rare gas polarizabilities and λ_{Ex} the position of the Hg($^3P_1 \leftarrow {}^1S_0$) transition in the rare gas hosts.**

Hg/RG System	λ_{Ex} (nm)	δ (cm^{-1})	RG Polarization (Å^3)[15]
Ne	247.8	+ 942.83	0.400
Ar	245.9	+ 1254.64	1.640
Kr	248.9	+ 764.47	2.485
Xe	253.6	+ 19.88	4.050

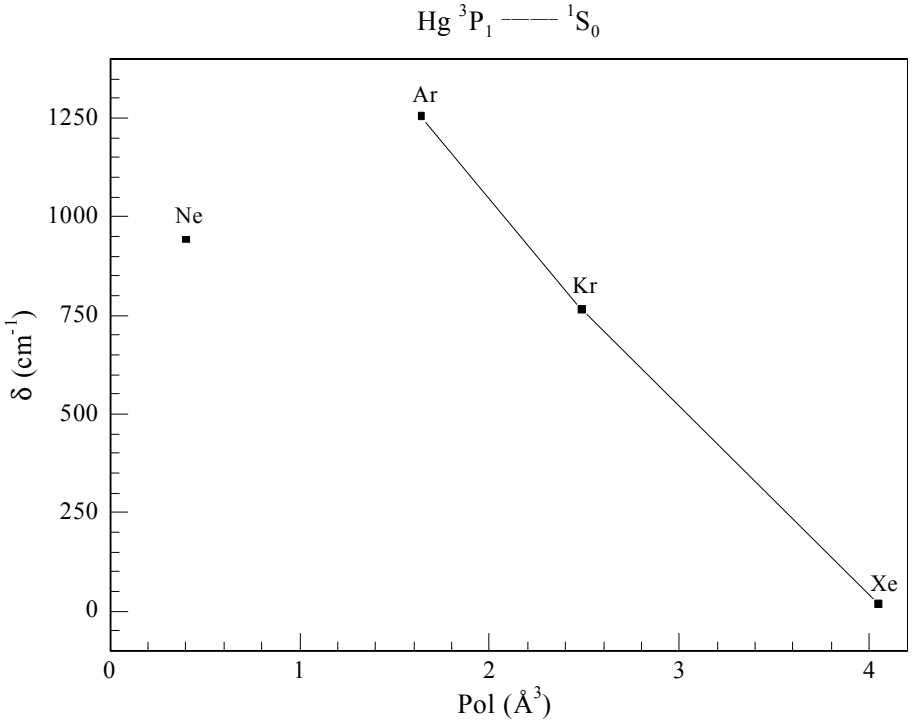

Figure V.13 **A plot of the gas phase to Hg/RG matrix frequency shifts (δ cm^{-1}) observed for the $^3P_1 \leftarrow {}^1S_0$ transition of atomic mercury versus the polarizabilities of the host rare gas solids. The solid line shown highlights the linear correlation between the frequency shifts and rare gas polarizability observed by the Hg $^3P_1 \leftarrow {}^1S_0$ transition in solid Ar, Kr and Xe.**

The calculated emission energies (E cm^{-1}) for atomic Hg isolated in an expanded substitutional site (i.e. relaxed lattice) are compared to the observed matrix emission spectra in Figure V.14. The best agreement is achieved using the 6-atom 'waist + limited stretch' mode, (Q_8^*) for the p_z orbital orientation. The stabilization arises from the 'in-phase' contraction of the six Ne atoms on the close packed plane B towards the metal atom and in so doing, these Ne·Ne interactions approach their equilibrium lattice positions. The role of the metal atom is revealed as Q_8^* is stabilised for the p_z orbital orientation thus maximising the pure Π Hg·Ne interaction.

The 6-atom 'stretch' contributes in reducing the overall energy of the Hg $^3P_1$ excited state by reducing the Σ interaction.

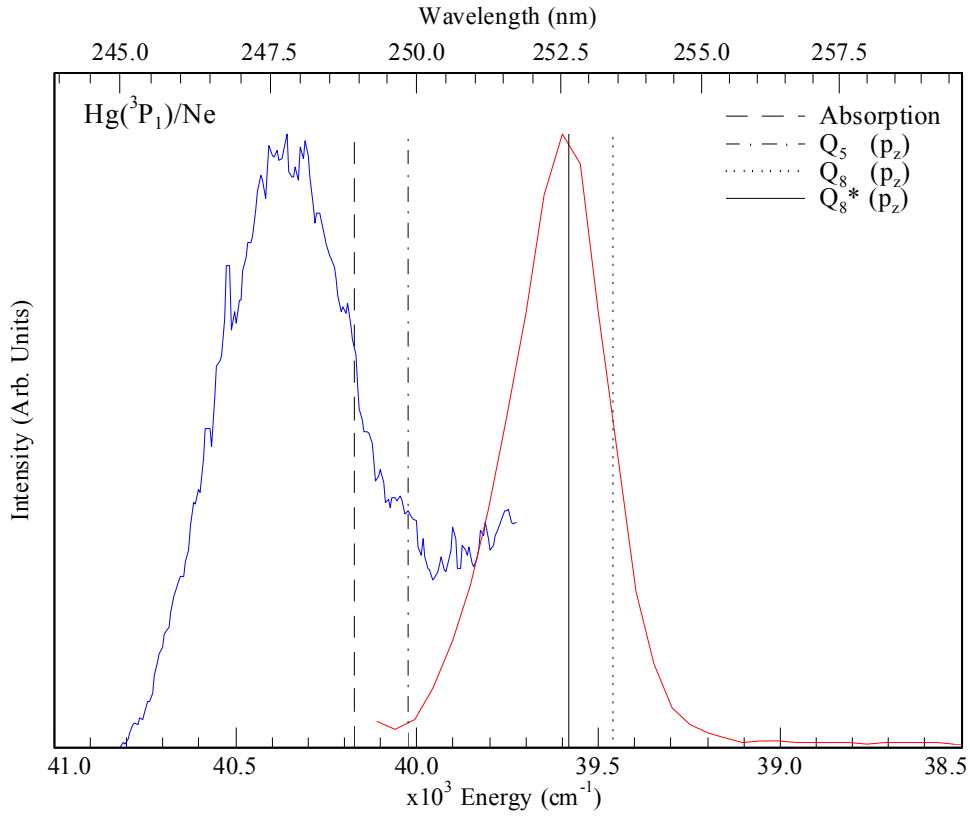

Figure V.14 **A comparison of the observed and calculated Hg($^3P_1 \leftrightarrow {}^1S_0$)/Ne spectroscopy. The experimental spectra shown reported by Chergui and co-workers[5,6,7] were recorded on deposition at 4 K. The vertical lines represent the absorption and emission energies calculated for Hg isolated in an expanded substitutional site in solid neon presented in Table V.3 and Table V.4 respectively. The vibronic modes leading to the stabilisation of the excited state are indicated in the legend.**

V.I.5 Conclusion

The agreement between the calculated and observed[5] absorption energies indicate that atomic Hg occupies distorted (relaxed) single substitutional sites in solid neon. This accounts for the observation that the Hg 6p $^3P_1 \leftarrow$ 6s $^1S_0$ transition occurs to lower energy than that predicted by an extrapolation of the polarizability model[8]. However, as the expansion of the substitutional site produces essentially a different matrix environment than the rigid substitutional sites occupied by atomic Hg isolated in solid Ar, Kr and Xe, Hg/Ne will deviate from the linear behaviour.

The observed emission spectroscopy is also best predicted by simulations based on relaxed substitutional site occupancy for Hg in neon. It is observed that the

excited state lattice reorganisation is both dependent on the lattice energy and the stabilisation of the metal atom excited state. Solid neon provided an ideal system to probe the effect of ground and excited state solvation as the cramped lattice site allowed an investigation of the lattice contribution to the overall excited state cluster stabilisation. This insight is not provided by the calculations presented in Chapter IV for atomic Hg isolated in rigid substitutional sites in solid Ar, Kr and Xe as the lattice interactions calculated for these systems, always showed a destabilising effect since these modes move the lattice atoms away from there equilibrium positions. Therefore the calculations presented for Hg/Ne show the importance of the equilibrium lattice restoration in producing the observed luminescence in cases where there is an unfavourable match between the site of isolation and the M·RG ground state bond length. They also show that for a cramped site of isolation, the 'waist' type vibronic modes are of greater importance than the 'body' modes in producing excited state stabilisation of a metal atom. This can be understood on the basis that the internal motion of the metal atom within such a cramped lattice is not feasible because of the immediate on-set of repulsive interactions.

V.II Hg ($^3P_0 \rightarrow {}^1S_0$)/RG emission spectroscopy (RG = Ar, Kr and Xe)

V.II.1 Introduction

The remaining sections of this Chapter present pair-potential simulations of the emission spectroscopy of the $^3P_0 \rightarrow {}^1S_0$ transition of atomic mercury isolated in solid Ar, Kr and Xe. The most recent experimental study of the Hg($^3P_0 \rightarrow {}^1S_0$)/RG (RG = Ar, Kr and Xe) emission spectroscopy was conducted in the present study[4]. Chapter III presents the observed emission spectroscopy of the $^3P_0$ state produced as a result of intermultiplet relaxation following pulsed laser excitation of the $^3P_1 \leftarrow {}^1S_0$ transition. The $^3P_0$ state emission spectra exhibited a progressive red shift and decreasing linewidth from Ar to Xe. Recording the emission spectra at higher temperatures than 12 K suggested the presence of zero phonon lines and phonon sidebands for the Hg($^3P_0 \rightarrow {}^1S_0$) emission in solid Kr and Xe. A lineshape analysis of the high-resolution emission spectra, using the *Wp* optical function allowing the identification of *ZPL* in Kr and Xe. Figure V.15 presents a summary of the Hg $^3P_0 \rightarrow$

$^1S_0$ emission spectroscopy reported in Chapter III. The spectral positions of the observed phonon sidebands and the calculated ZPL's ($\nu_{0,0}$) are provided in Table V.6.

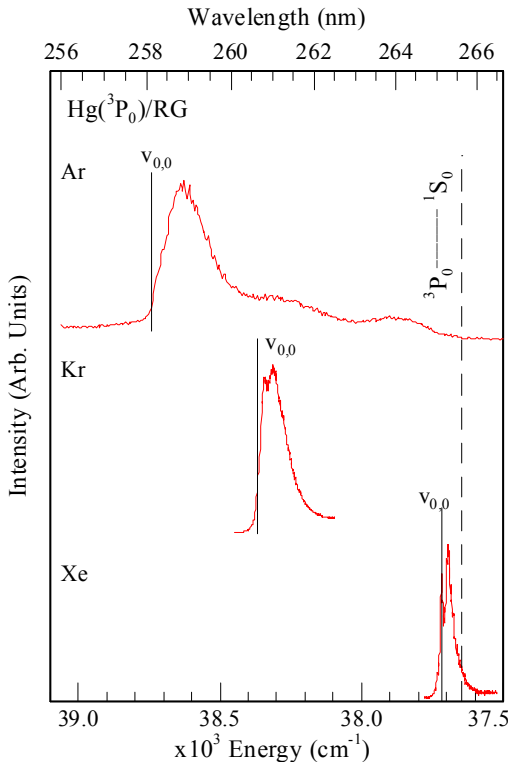

Figure V.15 **A summary of the emission features assigned in Chapter III to the 6p $^3P_0 \rightarrow$ 6s $^1S_0$ transition of atomic Hg recorded in Ar, Kr and Xe at 12 K. These emission spectra were produced with pulsed laser excitation of the Hg atom $^3P_1 \leftarrow {}^1S_0$ transition. The calculated positions of the zero-phonon lines $\nu_{(0,0)}$ are indicated by the solid lines.**

Table V.6 **The location of the ZPL for the atomic Hg $^3P_0 \leftrightarrow {}^1S_0$ emission in solid Ar, Kr and Xe. The location of the phonon sideband and the difference in energy between the ZPL and the phonon sideband denoted by Δ both of which are presented in wavenumber units.**

Hg/RG	**ZPL, $\nu_{(0,0)}$** E (cm^{-1}) / λ (nm)	**Phonon sideband** E_{PSB} (cm^{-1}) / λ (nm)	$\Delta = \nu_{(0,0)} - E_{PSB}$ (cm^{-1})
Hg/Ar	38740 / 258.13	38625 / 258.9	+ 115
Hg/Kr	38366 / 260.65	38314 / 261.0	+ 52
Hg/Xe	37718 / 265.13	37672 / 265.4	+ 46

The pair-potential calculations presented assume ground state rigid substitutional site occupancy for atomic mercury in Ar, Kr and Xe (identified in Chapter IV from a comparison of the calculated and observed Hg($^3P_1 \leftarrow {}^1S_0$) absorption energies). A pair-wise sum of the Hg($^3P_0$)·RG (0) $\tilde{a}$ state potentials extracted from the experimental Hg($^3P_1$)·RG [A $^3 0^+$ ($^3\Pi$)] and [B $^3 1$] states[16,17,18] is used to examine the vibronic mode coupling with the excited $^3P_0$ state metal atom

which lead to stabilization. Unlike the Hg $^3P_1$ excited state which has axial symmetry, the Hg $^3P_0$ state exhibits spherical symmetry as the atomic electronic angular momentum, J_e is 0. A comparison of the calculated and observed emission energies lead to the identification of the excited state 'breathing' mode (Q_1^*) as the vibronic mode coupling with this excited state. The theoretical model predicts excited state stabilisation for the 'breathing' mode in Hg/Ar, Hg/Kr and Hg/Xe systems. The Hg($^3P_0 \rightarrow {}^1S_0$) emission energies calculated are progressively red-shifted of the observed band maxima.

V.II.2 Method and Results

The localised pair-potential approach is applied to the simulation of the 6p $^3P_0 \rightarrow$ 6s $^1S_0$ transition of atomic Hg isolated in solid Ar, Kr and Xe. The simulations undertaken represent extensions to those presented in Part I of this chapter for the analysis of the Hg ($^3P_1 \leftrightarrow {}^1S_0$)/RG luminescence for solid Ne and outlined in Chapter IV in simulating the observed luminescence in solid Ar, Kr and Xe. Therefore only the modifications necessary to complete the Hg($^3P_0$)/RG calculations are presented.

V.II.2.I Ground $^1S_0$ and Excited $^3P_0$ states

Normally the simulated absorption energies are calculated and compared to the experimental data allowing the identification of site of occupancy. The Hg ($^3P_0 \leftarrow {}^1S_0$) absorption cannot be observed experimentally, due to the negligible oscillator strength of the transition, making this comparison impossible. However, the pair potentials simulations presented in Chapter IV for the Hg $^3P_1 \leftrightarrow {}^1S_0$ transition concluded that Hg occupies rigid (unperturbed) substitutional sites (*ss*) only in solid Ar, Kr and Xe. Assuming exclusive substitutional site occupancy, a comparison of the experimental and calculated emission energies is completed, which provide insight into the vibronic modes coupling with the excited $^3P_0$ state metal atom.

Calculation of the solid-state Hg ($^3P_0 \leftrightarrow {}^1S_0$) atom absorption and emission energies is achieved by calculating the energy for both the ground and excited states of the guest metal atom, (Hg) occupying a substitutional site in a Hg·RG_{18} cluster. The method employed to calculate the energy of the ground state for the Hg·RG_{18} cluster using a simple sum of the Hg($^1S_0$)·RG and RG·RG pair potentials was described in Chapter IV.

Due to the spherical symmetry of the $^3P_0$-excited state ($J_e = 0$) the energy of the excited state cluster is also a simple summation of the Hg($^3P_0$)·RG and RG·RG pair potentials, modifying Equation IV.1 for the excited state. The Hg($^3P_0$)·RG diatomic potentials are not available experimentally for all the Hg·RG pairs (except Ar[19]). However the Hg[$^3P_0$ (0) *ã*]·RG potential can be calculated from the known Hg($^3P_1$)·RG [A $^3\Pi$ ($^30^+$)] and [B $^3\Sigma$ (^{31})] state potentials presented. The A state is pure Π whereas the B state is a linear combination Π and Σ atomic orbitals. The pure Σ component was extracted from this B state, as outlined previously. The expressions for V_Π and V_Σ were then used to obtain an expression for the diatomic Hg($^3P_0$)·RG interaction using the following equation presented previously by Duval *et al*[19].

$$V(^3P_0)\ \tilde{a}^30 = 1/3[(V_\Sigma^e + V_\Pi^e) + V_\Pi] \qquad \text{Equation (V.1)}$$

The Morse function parameters and the energy curves calculated for the Hg($^3P_0$)·RG diatomics are presented in Figure V.16.

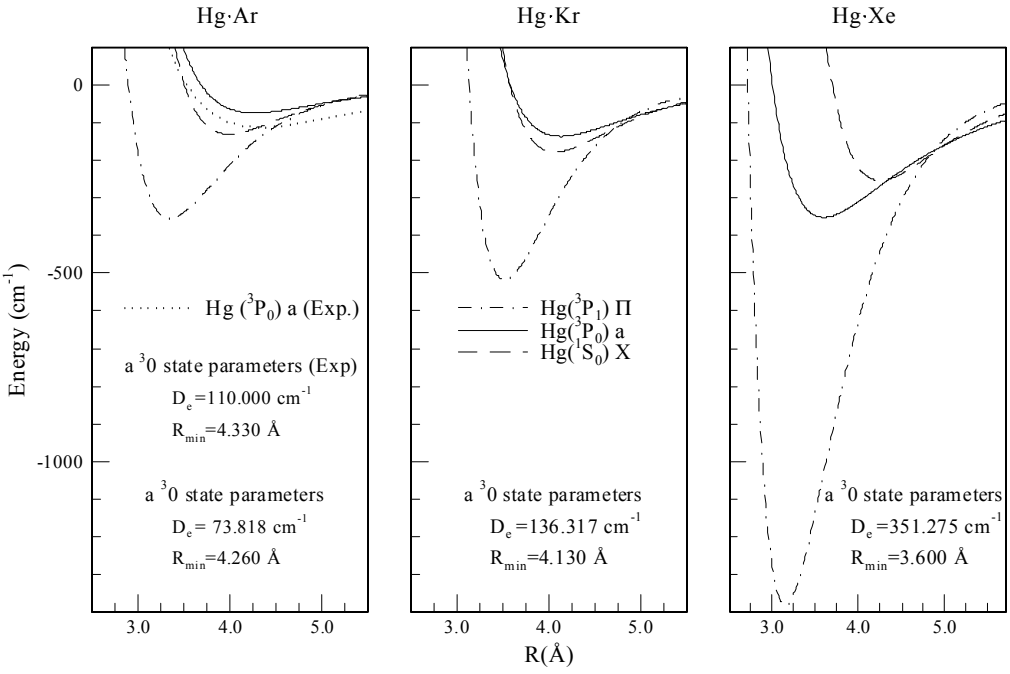

Figure V.16 **Potentials of the Hg·RG diatomic the X and the A(Π) state potentials are obtained directly from spectroscopic data of the Hg·RG diatomics presented in Table IV.1, Chapter IV while the $\tilde{a}^30^-$ state potential was obtained with Equation V.1 which assumes case-(c) coupling. The available spectroscopic data for the Hg($^3P_0$)·Ar system reported by Duval *et al*[19] is also presented.**

It is evident from the potential energy curves shown in Figure V.16 that the Hg ($^3P_0$) excited state is similar to the Hg·RG ground state interaction. By inspection

of Figure V.16, it is also clear that the Ar ground state bond length is less than that of the excited state, whereas in Xe, the reverse is the case. The ground and excited states for Hg·Kr show very little difference in bond length.

The zero total angular momentum of the $^3P_0$ state suggests that only a solid-state vibronic mode which conserves the spherical symmetry of the Hg($^3P_0$)·RG_{18} cluster will couple with this excited state. The details of the interactions involved for the lattice expansion or contraction ground state 'breathing' mode (Q_1) calculation are outlined in Section V.I.2.II. In this case the Q_1* calculation pertains to the excited state of the metal atom where the same lattice interactions considered for Q_1 are used to identify excited state stabilisation of the Hg $^3P_0$ metal atom. The results of the excited state 'breathing' mode (Q_1^*) calculations are shown in Figure V.17. Inspection of the potential energy curves calculated for the excited state Q_1^* reveals that the preference for an expansion or contraction of the 12 RG nearest neighbour atoms is in line with the trends observed for the Hg($^3P_0$)·RG and Hg($^1S_0$)·RG states for the 1:1 van der Waals complexes.

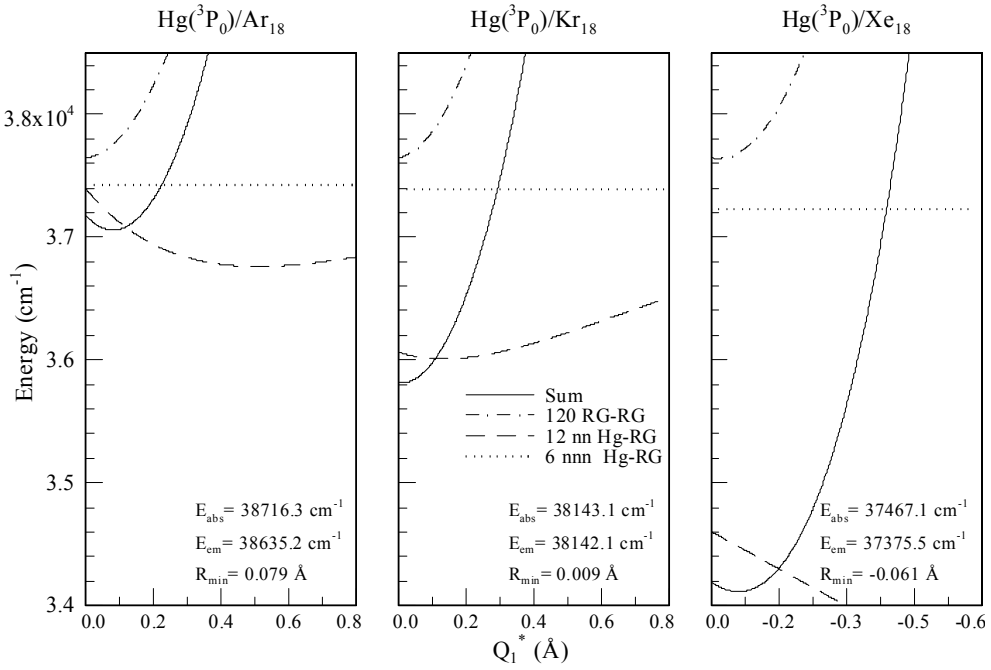

Figure V.17 **Energetics calculated for the Hg/RG_{18} (RG = Ar, Kr and Xe) symmetric excited state 'breathing' mode (Q_1^*) based on rigid substitutional site occupancy. The individual interactions involved are shown by the legend. The total potential energy calculated for the mode is shown by the solid line obtained by summation of the individual interactions.**

Q_1^* involves a contraction in solid Xe as the Hg·Xe excited ($^3P_0$) and ground state bond lengths are 3.6 Å and 4.25 Å respectively. The Hg/Ar and Kr systems exhibit an expansion due to Q_1^* as the Hg·Ar and Hg·Kr ground state bond lengths are less than the excited state bond lengths as shown in Figure V.16.

V.II.2.II Hg($^3P_0 \leftrightarrow {}^1S_0$)/RG$_{18}$ Absorption and Emission Energies

As stated earlier, neither absorption nor excitation spectra exist for the 'forbidden' $^3P_0 \leftrightarrow {}^1S_0$ transition of atomic Hg in solid Ar, Kr or Xe. However, assuming mirror symmetry between the $^3P_0$ absorption and emission (equivalent full width at half maximum, (*fwhm*) and intensity) allows the creation of an estimated 'best guess' absorption spectra. The estimated absorption spectra presented in Figure V.18 were achieved by assuming mirror symmetry about the *ZPL*'s identified in Chapter III for the Hg($^3P_0 \rightarrow {}^1S_0$)/RG, listed in Table V.6. Comparison of calculated absorption energies for the Hg $^3P_0 \leftarrow {}^1S_0$ transition in the RG solids are then made.

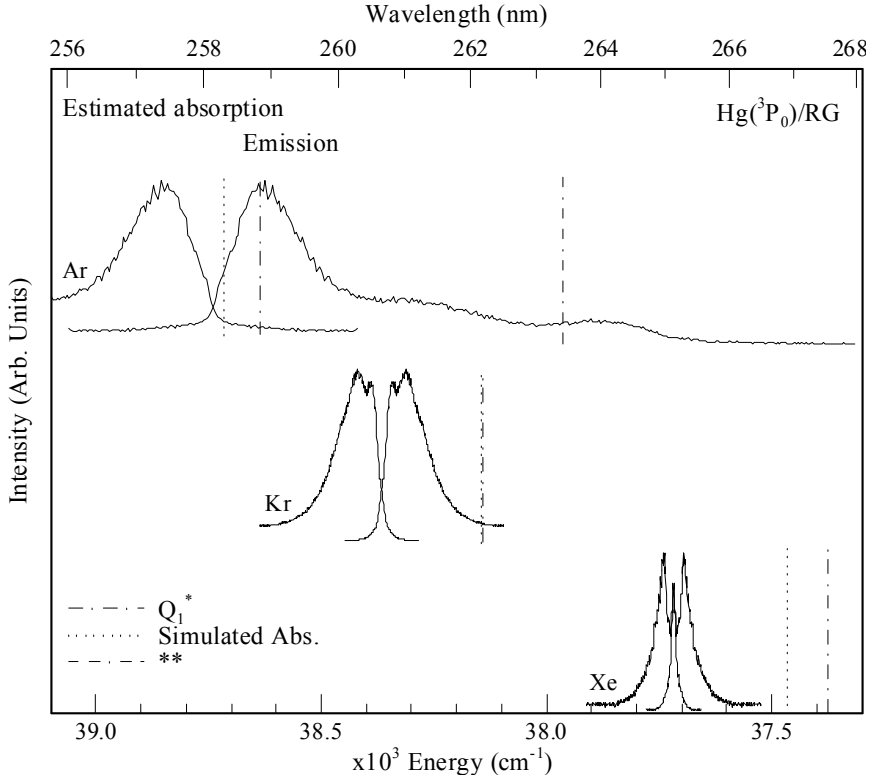

Figure V.18 **A comparison of the observed and calculated Hg($^3P_0 \rightarrow {}^1S_0$)/RG emission spectroscopy recorded at 12 K (reported Chapter III), and the estimated Hg($^3P_0 \leftarrow {}^1S_0$)/RG absorption spectra (shown left). The vertical lines represent the Q_1^* absorption and emission energies calculated (Table V.7) for Hg isolated in substitutional sites in the solid RG's. ** Indicates the calculated absorption energy for Q_1^* using the experimental Hg·Ar experimental data[19].**

Table V.7 **A comparison of the observed emission wavelength (*nm* units) for the $^3P_0 \rightarrow {}^1S_0$ transition of matrix-isolated atomic mercury with the calculated emission values for the excited state 'breathing' mode (Q_1^*) for Hg isolated in substitutional sites in solid Ar, Kr and Xe. The Hg/Ar** results presented were achieved using the spectroscopic available parameters[19] reported. The difference between the observed band maxima and the predicted values are quoted as $\delta_{Obs-Cal}$ in cm^{-1}.**

Hg/RG	E_{Cal}	λ_{Calc}	λ_{Obs}	$\delta_{Obs-Cal}$
Hg/Ar	38635.2	258.83	258.9	- 10.2
Hg/Ar**	37965.0	263.40	258.9	+ 660.0
Hg/Kr	38142.1	262.18	261.0	+ 172.0
Hg/Xe	37375.5	267.55	265.4	+ 296.5

The estimated absorption energy is obtained by subtraction of the difference in energy between the ZPL position and that of the phonon sideband labelled Δ cm^{-1} in Table V.6. The estimated Hg($^3P_0$)/RG absorption positions are 38855, 38418 and 37764 cm^{-1} for Ar Kr and Xe respectively, shown in Figure V.18 and collected in Table V.8.

Table V.8 **A comparison of the estimated experimental absorption wavelength (*nm* units) for the $^3P_0 \leftarrow {}^1S_0$ transition of atomic mercury with the calculated absorption values for Hg/Ar, Kr and Xe. The difference between the estimated band maxima and the calculated values are quoted as $\delta_{Obs-Cal}$ in cm^{-1}. ** Indicates the calculations were completed using the spectroscopic parameters for the Hg($^3P_0$)·Ar system reported by Duval *et al*[19].**

Hg/RG	E_{Abs} Cal	λ_{Calc}	λ_{Estm}	$\delta_{Estm-Cal}$
Hg/Ar	38716.3	258.29	257.37	+ 138.7
Hg/Ar**	37984.2	263.27	257.37	+ 870.8
Hg/Kr	38143.1	262.17	260.29	+ 274.9
Hg/Xe	37467.1	266.90	264.80	+ 296.9

V.II.3 Discussion

A comparison of the experimental data and the results of the pair potential simulations, shown in Figure V.18, reveals that the predicted emission is within the broad-band profile of the phonon sideband in solid Ar (using the extracted $^3P_0$ potential). The calculations outlined in this report predict the position of the *ZPL* in absorption as the calculation assumes a pure Frank Condon transition. Table V.7 presents the calculated emission energy for the excited state 'breathing' mode of atomic Hg $^3P_0$ excited state in solid Ar. Upon inspection it is observed that the

extracted $^3P_0$ ã^{3}0 potential for Hg·Ar provided better agreement with the observed matrix emission spectroscopy reported in Chapter III.

In Kr and Xe the pair potentials model however predicts emission energies red shifted from the observed band maxima see Table V.7. The Stokes' shift calculated for both of these systems is very small therefore predicting the presence of the observed *ZPL*. The red shift between the calculated and observed emission energies may suggest that the extracted potentials used are inaccurate for these systems. Two reasons are suggested for the inaccuracy 1) the potential used assumes that the pure case-c coupling ($^3P_0$) is maintained between the $^3P_0$ state Hg metal atom on interaction with the RG. This approximation becomes inaccurate, as the excited state interactions (well depths) increase from Ar to Xe. 2) The localised cluster approach employed assumes that the spherical symmetry of the Hg 6p $^3P_0$ state from the 1:1 van der Waals complex is preserved in the solid. This may be inaccurate as the p orbital which give rise to the excited state may interact with the RG host in the octahedral field of the substitutional site and lead to a symmetry breaking. These effects may account for the red shifted emissions calculated in solid Kr and Xe. However the increase in the importance of 1) may account for the good agreement observed in solid Ar. These possibilities must be taken into account when accessing the theoretical results reported here for the Hg $^3P_0 \leftrightarrow {}^1S_0$ luminescence spectroscopy.

V.II.4 Conclusion

The pair-potential simulations outlined in the previous sections to predict the spectroscopy of the 6s6p $^3P_0 \leftrightarrow 6s^2\ {}^1S_0$ transition of atomic mercury in Ar, Kr and Xe indicate that the excited state 'breathing' mode (Q_1^*) leads to emission for each system. The simulations predict excited state absorption and emission energies with small Stokes' shifts consistent with the observation (or calculated) of zero-phonon lines reported in Chapter III. The emission energies calculated are progressively red-shifted of the observed band maxima. The red shift discrepancy is attributed to a breakdown in the pure Hund's Case–*c* coupling of the Hg ($^3P_0$) state in the solid.

References

1 J.G. McCaffrey and P. N. Kerins, *J. Chem. Phys*., **106**, 7885 (1997).

2 M. McCarty and G.W. Robinson, *Mol. Phys.*, **2**, 415 (1959).

3 C. Crepin and A. Tramer, *J. Chem. Phys.*, **97**, 4772 (1992).

4 M. A. Collier and J. G. McCaffrey, *J. Chem. Phys.*, **119**, 11878, (2003).

5 J. Helbing, A. Haydar and M. Chergui, *Chem. Phys. Letts.*, **310**, 43, (1999).

6 J. Helbing, A. Haydar and M. Chergui, *J. Chem. Phys.*, **113**, 3621, (2000).

7 J. Helbing, A. Haydar and M. Chergui, *unpublished results*, (2001).

8 S. L. Laursen and H. E. Cartland, *J. Chem. Phys.*, **95**, 4751, (1991).

9 W.H. Breckenridge, C. Jouvet, B. Soep, in: M. Duncan (Ed.), *Advances in Metal and Semiconductor Clusters*, Vol. 3, JIA Press, Greenwich, CT, 1995.

10 J. Koperski, J.B. Atkinson and L. Krause, *Chem. Phys.*, **186**, 401, (1994).

11 Slight differences exist between the ground state bond length of the neon dimer R_e Ne_2 = 3.091 Å and the substitutional site diameter ss Ne = 3.155 Å as calculated from the lattice parameter of solid neon. This effect is a result of multi-body interactions in the solid.

12 C. Kittel, *Introduction to Solid State Physics*, 5th Edition, Wiley and Co., New York, 1976, p. 77.

13 R. A. Aziz and M. J. Slaman, *Chem. Phys.*, **130**, 187, (1989).

14 The β coefficient was obtained by fitting a Morse function to the short-range ($r < 4.6$ Å) form of Aziz and Slaman's empirical HFD-B potential given in Ref 13 for Ne_2. B. Healy and J. G. McCaffrey, (*unpublished results*).

15 T. M. Miller, *Handbook of Chemistry and Physics*, edited by D. R. Lide, 73rd ed. (CRC, Boca Raton, 1991-1993).

16 J. Zuniga, A. Bastida, A. Requena, N. Halberstadt and J. Beswick, *J. Chem. Phys.*, **98**, 1007 (1993).

17 M. Okunishi, H. Nakazawa, K. Yamanouchi and S. Tsuchiya, *J. Chem. Phys.*, **93**, 7526, (1990).

18 K. Fuke, S. Takayuki and K. Kaya, *J. Chem. Phys.*, **81**, 2591 (1984).

19 M. C. Duval, O. B. D'Azy, W. H. Breckenridge, C. Jouvet and B. Soep, *J. Chem. Phys.*, **85**, 6324, (1986).

Chapter VI

The absorption spectroscopy of atomic manganese isolated in solid Ar, Kr and Xe

VI.1 Introduction

The luminescence spectroscopy of matrix–isolated metal atoms with ns^2 ground state electronic configurations has lead to considerable insights into the behaviour of ground and excited electronic state atoms in condensed matter. The *Maynooth Group* have reported on the spectroscopy of Zn[1], Cd[2] and Hg[3] isolated in solid rare gases. Chapter III presented the luminescence spectroscopy of the $^3P_1$ and $^3P_0 \leftrightarrow {}^1S_0$ transitions of atomic mercury isolated in RG solids (RG = Ar, Kr and Xe). Chapter IV described the M·RG_{18} localised pair-potentials model used to investigate ground and excited state interactions of the guest metal atom within the solid. This analysis allowed identification of 1) the site occupancy and 2) the localised M-RG interactions leading to the excited state stabilisation which produce the observed solid-state luminescence. Therefore, luminescence work on metal atoms such as Hg[3,4] and Mg[5] in solid rare gases has provided insight into the link between the solid state and the behaviour of the corresponding diatomic M·RG van der Waals complexes[6] stabilized in cold supersonic expansions.

This Chapter presents the absorption spectroscopy of matrix-isolated atomic manganese. This experimental work was motivated by the similarities between atomic manganese, which exhibits an ns^2 ground state electronic configuration like the M/RG systems (M = Zn[1], Cd[2], Hg[3,4] and Mg[5]) where the solid-state spectroscopy has been studied in detail. The lowest energy electronic configuration of atomic Mn is $[Ar]3d^54s^2$ giving rise to the spherically symmetric $a^6S_{5/2}$ ground state. UV/Vis absorption spectra presented for each of the Mn/RG (RG = Ar, Kr and Xe) systems allowed the assignment of s $\rightarrow$ p type electronic transitions from the ground $a^6S_{5/2}$ state to the excited Mn $[Ar]3d^54s4p$ states. The electronic absorptions observed were those corresponding to the 'singlet-like' $[3d^5(^6S)4s4p(^1P°)]$ y^6P and 'triplet-like' $[3d^5(^6S)4s4p(^3P°)]$ z^6P states known to occur in the gas phase[7] at 35,725.85 cm^{-1} (279.91 nm) and 24,788.05 cm^{-1} (403.42 nm) respectively. The quoted energies correspond to the transition from the ground $a^6S_{5/2}$ state to the $J = {}^5/_2$ spin-orbit level of the y^6P and z^6P excited states.

Atomic Mn also exhibits a third more exotic x^6P excited state resulting from the $[Ar]3d^6(^5D)4p$ excited electronic configuration. The $x^6P_{5/2} \leftrightarrow a^6S_{5/2}$ transition occurs in the gas phase at 45,156.11 cm^{-1} (221.45 nm) and unlike the y^6P and z^6P states, involves a two-electron transition from the ground $3d^54s^2$ state configuration. Absorption features are assigned to the $x^6P_{5/2} \leftarrow a^6S_{5/2}$ transition of atomic Mn isolated in all the Mn/RG systems investigated.

Like mercury[8], manganese[9] was one of the earliest metal atom systems to be investigated with the matrix-isolation technique. Since the first report of the spectroscopy of atomic Mn/RG solids by Schnepp[9], Lee and Gutmacher[10] and Mann and Broida[11] completed further work focusing on the UV/Vis atomic absorption spectroscopy in solid argon matrices deposited at 4.2 K. A summary of these earlier results obtained from absorption spectroscopy has appeared in Gruens' review[12]. Mn/RG solids containing isolated Mn atoms and higher aggregates have been investigated using the Magnetic Circular Dichroism (MCD) technique in Ar, Kr and Xe[13]. Many reports of spectroscopic analysis of the van der Waals, antiferromagnetic manganese dimer[14,15,16], Mn_2 and bimetallic clusters (containing Mn) isolated in RG solids have appeared in the literature[17]. In contrast, no reports of the luminescence spectroscopy of atomic manganese have appeared to date. These new results are presented in Chapters VII to IX inclusive, while in this Chapter the absorption spectra are reported for samples prepared with controlled guest:host (Mn:RG) ratios. These concentration studies allowed the identification of Mn atom and dimer absorption bands and their distinction from higher Mn cluster species. Spectra recorded following matrix annealing and / or at different deposition temperatures (T_d) are presented which allow the identification of matrix site effects produced during condensation. Secondly, the absorption spectroscopy is discussed with reference to the previous reports for each Mn/RG system[9-11, 13-17].

The atomic Mn/RG absorption spectra reported in this Chapter showed good agreement with previous investigations. However, the Mn/RG samples prepared during the course of this work are more 'atomic' than those reported in previous studies[9-11, 13-17]. This is attributed to the increased control of the Mn vaporisation afforded by electron bombardment vaporisation of Mn over the bulk heating that results from resistive heating of Knudsen cells. The absorption spectra recorded

allowed the identification of multiple thermally stable sites of isolation for Mn isolated in solid Ar and Kr and single site of isolation in Xe.

VI.2 Results – Mn/RG UV/Vis absorption spectroscopy

The following sections presents the absorption spectra recorded for Mn/Ar, Mn/Kr and Mn/Xe in the UV/Vis spectral range (180–500 nm). The Mn/RG samples were prepared with the method described in Chapter II. Under low metal loading conditions the isolation of manganese atoms is favoured. The atomic manganese absorption features are assigned from their proximity to the gas phase positions, as the weak van der Waals interaction between the Mn atom and its immediate matrix environment results in a small change of the transition energy from that observed for the free atom. The assignment of Mn atomic absorptions may be simplified by the presence of resolved threefold splitting pattern indicative of the dynamic Jahn-Teller effect, (Chapter I, Introduction). This effect has been observed for several matrix-isolated metal atoms and in the present study, on the $^3P_1 \leftarrow {}^1S_0$ absorption of Hg in solid Xe, (Chapter III).

Absorption bands of manganese clusters are identified from concentration studies as increasing the metal flux allows the formation of Mn aggregates while the solid condenses. The metal aggregation occurs in the liquid phase (accretion layer) on the surface of the matrix host, before the condensation process is completed. Identification of the Mn_x ($x > 1$) absorption features is achieved by inspection, as the absorption strength of these features increase in intensity with respect to the atomic transitions, as the metal concentration is increased.

VI.2.I Mn/Ar

Absorption spectra recorded for manganese deposited in solid argon at 12 K are presented in Figure VI.1. The three panels, showing the effect of increasing the metal flux, provide a concentration study of Mn in solid Ar. The gas phase positions[7] of the $x^6P_{5/2}$, $y^6P_{5/2}$ and $z^6P_{5/2} \leftrightarrow {}^6S_{5/2}$ transitions are shown by the dashed vertical lines. Inspection of the bottom panel of Figure VI.1 reveals absorption features at 211.8, 278.1 and 397.4 nm under low Mn loading conditions with much weaker bands occurring at 254.4 and 311.6 nm. The spectra shown in Figure VI.1 are normalised with respect to the 278.1 nm feature.

The dominant absorption feature observed for Mn/Ar at 278.1 nm (35958 cm^{-1}) is assigned to the $y^6P_{5/2} \leftarrow {}^6S_{5/2}$ transition of atomic Mn. The 278.1 nm ($y^6P_{5/2} \leftarrow {}^6S_{5/2}$) absorption feature is shifted to higher energy from the gas phase (G.P.) position[7] by 232 cm^{-1} and exhibits a resolved threefold splitting pattern. A low-energy shoulder is present 281.5 nm while a more discernable high energy shoulder is located at 273 nm. The effect of annealing on these features is shown in Figure VI.2.

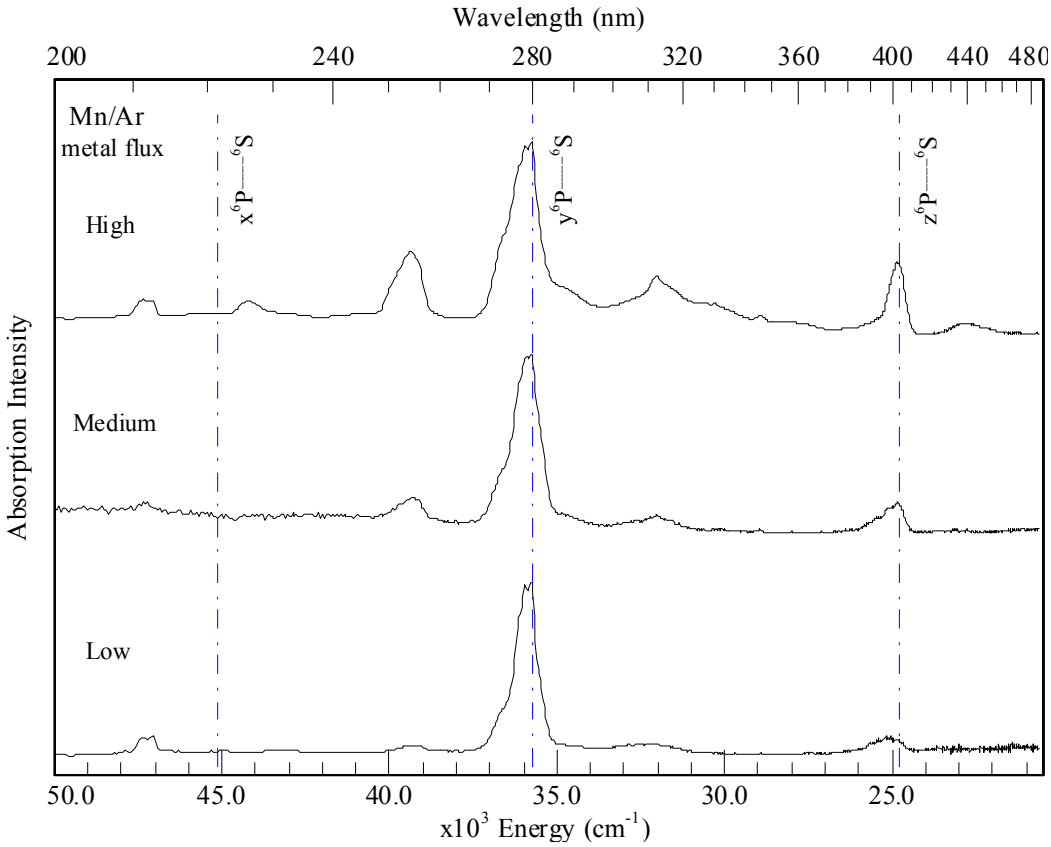

Figure VI.1 **Mn/Ar UV/Vis absorption spectra recorded at 12 K following sample deposition at 12 K. The three spectra shown indicate the changes in the relative intensities of the observed bands with increased metal flux, metal atom concentration.**

Annealing Mn/Ar matrices resulted in the removal of the red shoulder at 281.5 nm as presented in the right panel of Figure VI.2. In addition the annealing process had the effect of enhancing the structured features evident on the high-energy shoulder centered at 273 nm without reducing its intensity. These effects indicate the presence of two thermally stable sites centered at 278.1 and 273 nm labelled the red (1°) and blue (2°) sites respectively. The removal of the low-energy 281.5 nm shoulder reveals the presence of at least one thermally unstable site of atomic isolation present in Ar samples deposited at 12 K.

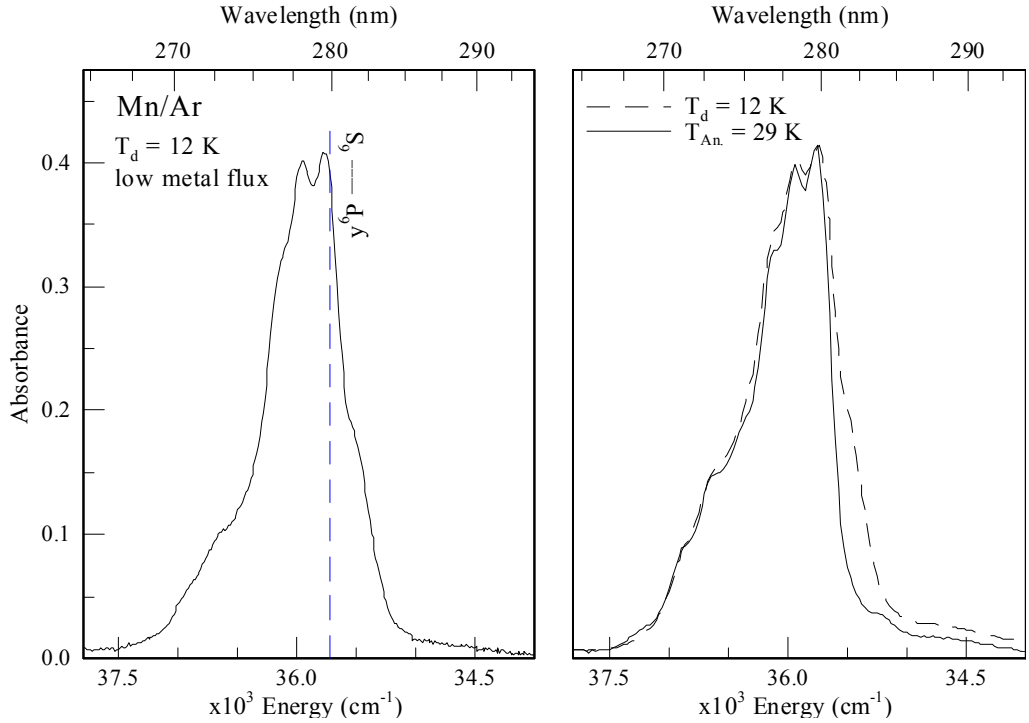

Figure VI.2 **Mn/Ar absorption spectrum recorded at 12 K upon deposition (T_d) at 12 K, in the vicinity of the atomic Mn $y^6P_{5/2} \leftrightarrow a^6S_{5/2}$ transition, shown left. Sample deposition was completed at 12 K using a low manganese flux, and indicates the presence of sites on both the blue and red sides of the dominant feature centered at 278.1 nm. A comparison of the absorption recorded on deposition and following matrix annealing to 29 K ($T_{An.}$) is shown right.**

The absorption feature observed at 397.4 nm in solid Ar is assigned to the $z^6P_{5/2} \leftarrow a^6S_{5/2}$ transition, based on its proximity to the location of this transition at 403.42 nm in the gas phase[7]. Inspection of the bottom panel of Figure VI.1 reveals the absorption band exhibits a progressive shift to lower energy with increased metal loading. This red-shift is attributed to the production of Mn_2. The band maximum of this feature occurs at 402.3 nm but the high-energy blue wing, assigned to the atomic transition, is also evident, as shown in the top panel of Figure VI.1. The atomic $z^6P_{5/2} \leftarrow a^6S_{5/2}$ transition of Mn is blue shifted in Ar by 375 cm^{-1} from its position in the gas phase. The very different intensities of the recorded y^6P and z^6P absorption bands of atomic Mn result from their singlet and triplet characteristics respectively of these two excited states. This is reflected in the reported Einstein A_{ki} coefficients[18], of the y^6P^o $3d^5(^6S)4s4p(^1P^o) \leftrightarrow 3d^54s^2$ a^6S and z^6P^o $3d^5(^6S)4s4p(^3P^o) \leftrightarrow 3d^54s^2$ a^6S transitions 3.7 x10^8 and 0.19 x10^8 sec^{-1} respectively.

Inspection of the UV region shown in Figure VI.1, close to the gas phase $x^6P_{5/2} \leftrightarrow a^6S_{5/2}$ transition energy reveals the presence of two features at 211.8 and

226.4 nm. The bottom panel shows that the 211.8 nm feature is present in very dilute Mn/Ar samples whereas the 226.4 nm[19] feature gains in intensity relative to the dominant 278.1 nm band with increased metal loading. Therefore the 211.8 nm feature is assigned to the $x^6P_{5/2} \leftarrow a^6S_{5/2}$ absorption in Ar, blue-shifted by 2058 cm^{-1} from the gas phase position at 221.45 nm, (45156 cm^{-1})[7]. The observed gas phase-Ar matrix shift is greatest for the x^6P atomic absorption. This may arise because the excited electronic configuration ([Ar]$3d^6$4p) is reached by a two electron transition from the [Ar]$3d^5$$4s^2$ ground configuration. Table VI.1 presents a summary of the absorption spectroscopy of atomic manganese isolated in solid Ar.

Table VI.1 **Spectral positions of the atomic absorption features assigned for atomic manganese isolated in solid Ar on deposition at 12 K. λ_{abs} indicates the position of the band centre or the central three-fold split component where possible. The gas phase transition energies for the Mn atom are also presented. The gas phase – Ar matrix shift is denoted by δ in wavenumber units.**

Transition	Mn/Ar		Mn atom – Gas Phase[7]		
	λ_{Abs} (nm)	E_{Abs} (cm^{-1})	λ (nm)	E (cm^{-1})	δ (cm^{-1})
$z\ ^6P_{5/2} \leftarrow a\ ^6S_{5/2}$	397.4	25163	403.42	24788	+375
$y\ ^6P_{5/2} \leftarrow a\ ^6S_{5/2}$	278.1 (1°)	35958	279.91	35725	+232
	273.0 (2°)	36630			+904
$x\ ^6P_{5/2} \leftarrow a\ ^6S_{5/2}$	211.8	47214	211.45	45156	+2058

The Mn/Ar samples prepared at 12 K using low metal fluxes show very weak absorption features at 254.4 and 311.6 nm. These features are observed to increase in intensity at medium metal fluxes, middle panel of Figure VI.1. Another 226.4 nm feature is present in the most concentrated samples[19]. In addition to the 226.4, 254.4 and 311.6 nm features, the red-shift of the band maximum of the 397.4 nm band to 402.3 nm is assigned to an increased contribution from a manganese dimer absorption. Therefore, the 254.4, 311.6 and 402.3 nm features are assigned to absorption transitions of manganese aggregates most probably Mn dimers in Ar matrices.

Inspection of the high metal flux deposition shown in the top panel of Figure VI.1, for the most concentrated Mn/Ar samples prepared, show an additional set of features at 226.4 and 345.7 nm. These bands are tentatively assigned to Mn_x where $x > 2$. The assignment to Mn_2 species is rejected as Mn_2 absorptions are identified even in the most dilute Mn/Ar samples at 254.4, 311.6 and 402.3 nm. The van der Waals

nature of Mn_2 can result in the efficient formation of larger cluster species Mn_x (x > 2) due to chemical bond formation in the higher metal aggregates. The 226.4 and 345.7 nm bands are assigned to absorptions of manganese aggregates with higher nuclearity than the dimer. This assignment is consistent with the trends evident in the concentration studies completed. The additional dimer features assigned from the concentration studies at 254.4, 311.6 and 402.3 nm showed no discernible temperature dependence.

It is also evident from the top panel of Figure VI.1 that increasing the Mn loading increases the complexity of the absorption spectra recorded. This spectral congestion is most pronounced from 300 to 360 nm, where two weak bands appear at 330 and 345.7 nm. Additional features are also observed in the vicinity of the $y^6P_{5/2}$ and $z^6P_{5/2} \leftarrow a^6S_{5/2}$ transitions at 290 and 438.5 nm respectively. The discussion and assignment of these features is postponed until the Mn/Kr absorption spectroscopy is presented.

VI.2.II Discussion Mn/Ar absorption spectroscopy

In the following section the absorption spectroscopy recorded for manganese isolated in solid Ar is discussed with reference to the previous Mn/Ar experimental work[9,10-13,17]. The first reports of the absorption spectroscopy of Mn/Ar are those of Schnepp[9] and Lee and Gutmacher[10] who employed photographic detection methods to observe the atomic y^6P and $z^6P \leftarrow a^6S$ transitions in matrices deposited at 4.2 K. Overall the earlier absorption spectra showed good agreement with those presented in this Chapter in that both studies assigned the $y^6P \leftarrow a^6S$ transition of atomic manganese in Ar as a triplet centered at 277.54 and 277.7 nm in Refs. 9 and 10 respectively. These results show close agreement with the centre of the threefold split absorption reported here, which occurs at 278.1 nm, Table VI.1. The weaker, absorption features to the blue of 278.1 nm were also observed and assigned[9,10] to multiple site occupancy of Mn atoms in solid Ar.

The $z^6P \leftarrow a^6S$ transition in Ar was reported at 396.6 and 403.06 nm by Schnepp[9] and at 392.77 and 402.25 nm by Lee and Gutmacher[10]. The higher energy features shows good agreement with the $z^6P \leftarrow a^6S$ absorption reported here at 397.4 nm. The absorption at 402.3 nm was assigned to Mn_2 in the previous section from

concentration study completed (Figure VI.1), as this feature is absent in dilute Mn/Ar samples. All the earlier samples[9,10] exhibited strong absorption at 402/403 nm and represents the larger metal fluxes which accompany Mn vaporisation by bulk resistive heating.

Shakhsemampour *et al*[13] assigned two sites of isolation for atomic manganese in solid argon. The primary site (s1) was centered at approximately 279.5 and 393.5 nm with the secondary site (s2) observed at 275.25 and 381 nm corresponding to the $y^6P \leftarrow a^6S$ and $z^6P \leftarrow a^6S$ atomic transitions respectively. The spectral positions of the two sites reported for the y^6P state are in good agreement with the red (1^o) 278.1 nm band and the blue shoulder (2^o) 273 nm identified in this Chapter. The report of the dominant site (s1) $z^6P \leftarrow a^6S$ absorption occurring at 393.5 nm agrees with that assigned here at 397.4 nm. The presence of a secondary site (s2) at 381 nm[13] is not immediately evident in the absorption spectra reported here. Its presence in Mn/Ar was identified however in luminescence excitation spectroscopy, the results of which are presented in Chapter VII.

Lee *et al*[10] reported an additional feature at 311.23 nm in solid Ar, which they assigned to the $z^4P \leftarrow a^6S$ atomic transition, commenting that the absorption band appeared after annealing to 30 K. Mann and Broida[11] also assigned the 311.5 nm band to the $z^4P \leftarrow a^6S$ transition of atomic Mn occurring as imperfectly isolated Mn atoms. Given the weak oscillator strength of the $z^4P_{3/2} \leftarrow a^6S_{5/2}$ transition (A_{ki} = 0.0027 x 10^8 sec^{-1}), observation of this spin-forbidden transition using absorption techniques seems unlikely. No evidence for this atomic absorption feature was observed upon deposition of dilute Mn/Ar samples (bottom panel Figure VI.1). However under medium/high metal loading conditions, absorption at 311.6 nm is observed. Consequently this band was assigned earlier in this Chapter to a Mn_2 absorption. The observations of Lee *et al*[10] that the intensity of the 311 nm absorption feature increased after matrix annealing and the assignment by Mann *et al*[11] of the $z^4P \leftarrow a^6S$ transition occurring within an imperfect matrix site are inconsistent, as annealing results in the production of a more crystalline matrix environment. Annealing should therefore weaken the $z^4P \leftarrow a^6S$ atomic absorption if it occurs from an imperfect lattice site. However, both observations are consistent with the assignment of the 311 nm feature to a Mn_2 absorption band whose presence on deposition is metal-loading-dependent and production after annealing resultant

from metal atom nucleation. Mn/Ar concentration studies reported by Ozin and co-worker[17] also lead to the assignment of the 311 nm feature to that of a manganese aggregate.

Ozin and co-workers[17] reported the absorption spectra for Mn/Ar in the vicinity of the $x^6P_{5/2} \leftrightarrow a^6S_{5/2}$ transition[7] of atomic manganese at 221.45 nm in the gas phase. They assign a band at 226 nm in solid Ar to the $x^6P_{5/2} \leftarrow a^6S_{5/2}$ transition. The concentration study for Mn/Ar shown in Figure VI.1 shows that only samples prepared using high metal fluxes contain the 226 nm band. This absorption intensity is enhanced relative to the dominant 278.1 nm ($y^6P_{5/2} \leftrightarrow a^6S_{5/2}$) atomic absorption feature under higher metal loading conditions. This behaviour is consistent with the assignment of the 226 nm feature to a Mn aggregate. In addition the absorption observed at 211.8 nm in dilute Mn/Ar samples (bottom, Figure VI.1) is in agreement with the assignment to the $x^6P_{5/2} \leftrightarrow a^6S_{5/2}$ transition, blue shifted of the gas phase transition by 2058 cm^{-1}. Ozin and co-workers[17] observed a similar absorption feature at 211 nm under low metal loading conditions and assigned the feature to the $w^6P_{5/2} \leftrightarrow a^6S_{5/2}$ transition. The assignment of the absorption feature to that of the $w^6P_{5/2}$ state produces an inconsistency in the observed matrix-shifts as this $w^6P_{5/2}$ absorption would exhibit a red-shift of 445 cm^{-1} from the gas phase position at 209.82 nm (47659 cm^{-1})[7], while both the $y^6P_{5/2}$ and $z^6P_{5/2} \leftarrow a^6S_{5/2}$ absorption features show blue-shifts. No data is available on the relative oscillator strengths of the $w^6P_{5/2}$ and $x^6P_{5/2} \leftrightarrow a^6S_{5/2}$ transitions so assignment cannot be made from the observed intensities. However, from the matrix shifts exhibited and the observation that higher Mn atom concentration lead to the increase in the 226 nm band relative to the dominant $y^6P_{5/2}$ absorption feature, the aggregate assignment made in this Chapter is reinforced.

In earlier work, the interpretation of the optical absorption spectroscopy of manganese species isolated in solid rare gases (especially Ar) has proven difficult due to the variety of species present on deposition. The concentration studies of Mn/Ar reported in this Chapter allowed the assignment of the features at 254.4, 311.6 and 402.3 nm to transitions of the manganese dimer. In the literature however, one definitive assignment of a Mn_2 transition appears corresponding to the A ← X absorption reported at 650 nm in solid Ar[14]. Ozin and co-workers[17] assigned two sets of small cluster species as Mn_x and Mn_y from concentration studies completed. Mn_x

they assigned to the binuclear molecule showing absorption features at 253, 312 and 400 nm. These conclusions are in good agreement with the Mn_2 absorption species assigned in this Chapter at 254.4, 311.6 and 402.3 nm. The 226.4 nm absorption feature was identified here to a manganese aggregate of higher nuclearity than the dimer, however assignment to Mn_2 cannot be rejected based on the absorption spectra reported earlier. In addition the persistence of this band in the most 'dilute' samples prepared by Ozin and co-workers[17] lead to their assignment of the 226 nm feature to the $x^6P_{5/2} \leftarrow a^6S_{5/2}$ atomic transition. However, from the concentration studies reported here this atomic assignment has been amended to an Mn_2 absorption.

VI.2.III Mn/Kr

A comparison of the UV/Vis absorption spectra recorded at 12 K for manganese isolated in solid krypton using different metal fluxes is presented in Figure VI.3. All the spectra shown were recorded at 12 K (T_s) for samples deposited at 12 K, (T_d). Examination of the concentration study presented for Mn/Kr in Figure VI.3 reveals that the dominant feature overlaps the gas phase[7] $y^6P_{5/2} \leftrightarrow a^6S_{5/2}$ transition of atomic manganese at 279.9 nm. The bottom panel of Figure VI.3 presents the absorption spectrum recorded for the most dilute Mn/Kr sample. Three pairs of bands are observed at 210 / 213.1, 279.3 / 284.9 and 385.5 / 401.9 nm. The dominant absorption feature occurring at 279.3 nm exhibits a threefold split pattern and is assigned to the $y^6P_{5/2} \leftarrow a^6S_{5/2}$ transition, blue-shifted from the gas phase position by only 79 cm^{-1}. The 279.3 nm absorption band in Mn/Kr exhibits a weak low-energy shoulder, shown Figure VI.4. This is the reverse of the Mn/Ar situation where the pronounced shoulder occurred to the blue of the threefold split absorption assigned to the $y^6P_{5/2} \leftarrow a^6S_{5/2}$ transition. The shoulder occurs at 284.9 nm and is assigned to the $y^6P_{5/2}$ absorption occurring from a second site of isolation in solid Kr, red-shifted from the gas phase position at 279.9 nm[7] by 626 cm^{-1}.

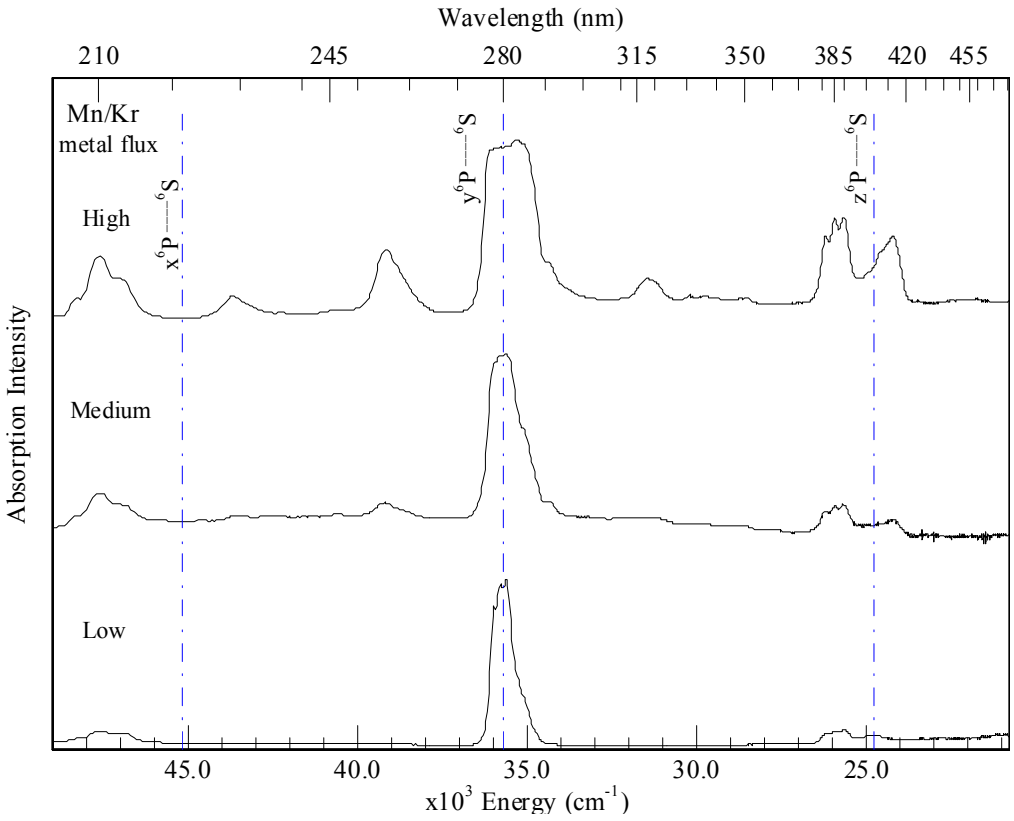

Figure VI.3 **Mn/Kr UV/Vis absorption spectra recorded at 12 K following sample deposition at 12 K. The three spectra shown indicate the changes in the relative intensities of the observed bands with increased metal flux. Note the top panel presents the most concentrated sample prepared the dominant absorption feature located at ≈280 nm is fully absorbing.**

Annealing Mn/Kr matrices to 37 K resulted, as presented in the right panel of Figure VI.4, in the formation of a high-energy shoulder at 276 nm, increased resolution of the 284.9 nm feature and producing an additional band at 291.2 nm. The stability of these features was investigated by irradiation at the band maxima 284.9 and 291.2 nm for 15 minutes. Irradiation of the 291.2 nm feature lead to its removal and also the loss of the high-energy shoulder. No additional absorption bands were produced by the removal of these features. The production of the 276 and 290.9 nm bands by the annealing process is assigned to the production of a thermally induced site of atomic isolation. Mn′ is used to denote Mn atoms isolated in 'thermally-induced' sites. The 276 and 290.9 nm bands are assigned to the $y^6P_{5/2}$ and $z^6P_{5/2} \leftarrow a^6S_{5/2}$ transitions occurring for Mn′. The annealing process had the effect of resolving the 284.9 nm feature resulting from the removal of a broad low energy component.

These effects indicate the presence of multiple thermally stable sites centered at 279.3 and 284.9 nm labelled blue (1°) and red (2°) sites respectively. The removal of the weak high-energy shoulder reveals the presence of at least one thermally unstable site of atomic isolation present in solid Kr on deposition at 13 K.

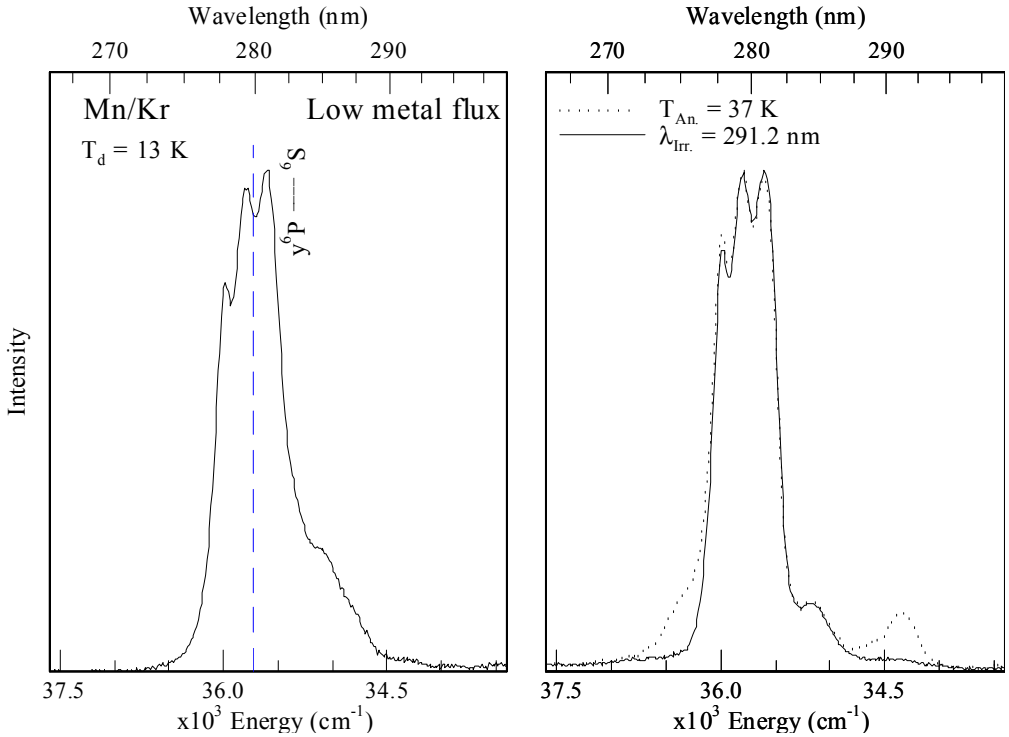

Figure VI.4 **Mn/Kr absorption spectra recorded in the vicinity of the $y^6P_{5/2} \leftrightarrow a^6S_{5/2}$ gas phase transitions of atomic manganese recorded at 12 K following sample deposition at T_d (Kelvin) using low manganese atom concentrations.**

The absorption feature centered at 385.5 nm shows a resolved threefold splitting pattern and is assigned to $z^6P_{5/2} \leftarrow a^6S_{5/2}$ transition exhibiting a blue matrix shift of 1152 cm^{-1}. The 385.5 nm absorption feature is overlapped by the lower energy 401.9 nm band. The 401.9 nm band, like the 397.4 nm feature assigned to the $z^6P_{5/2} \leftarrow a^6S_{5/2}$ transition in solid Ar, appears to red-shift at higher manganese concentrations. This occurs due to the appearance of a Mn_2 band at 413.2 nm, top panel Figure VI.3. Accordingly the 401.9 nm feature is assigned to the $z^6P_{5/2} \leftarrow a^6S_{5/2}$ transition of atomic Mn isolated in a secondary site (2^o) in solid Kr.

Table VI.2 **Spectral positions of the atomic absorption features assigned for atomic manganese isolated in solid Kr on deposition at 12 K. λ_{abs} indicates the position of the band centre or the central three-fold split component where possible. The dominant/primary (1^o) and secondary (2^o) site absorptions are labelled blue and red respectively to reflect their relative absorption energies. The gas phase transition energies for the Mn atom are also presented. The gas phase – Kr matrix shift is denoted by δ in wavenumber units.**

		Mn/Kr		Mn atom – Gas Phase		
Transition	Site	λ_{Abs} (nm)	E_{Abs} (cm^{-1})	λ (nm)	E (cm^{-1})	δ (cm^{-1})
$z\ ^6P_{5/2} \leftarrow a\ ^6S_{5/2}$	Blue (1^o)	385.5	25940	403.42	24788	+1152
	Red (2^o)	401.9	24882			+94
$y\ ^6P_{5/2} \leftarrow a\ ^6S_{5/2}$	Blue (1^o)	279.3	35804	279.91	35725	+79
	Red (2^o)	284.9	35100			-626
$x\ ^6P_{5/2} \leftarrow a\ ^6S_{5/2}$	Blue (1^o)	210.0	47619	211.45	45156	+2463
	Red (2^o)	213.1	46926			+1770

The UV absorptions occurring at 210 and 213.1 nm, shown in Figure VI.3 are assigned to $x^6P_{5/2} \leftarrow a^6S_{5/2}$ absorptions from a dominant blue (1^o) and secondary red (2^o) site blue-shifted by 2463 and 1770 cm^{-1} respectively from the gas phase position. Higher metal loading reveals a complex overlapping set of bands where the 210 nm feature dominates confirming its assignment as the primary site of Mn isolation. Table VI.2 presents a summary of the absorption spectroscopy of atomic manganese isolated in solid Kr matrices deposited at 12 K.

Absorption spectra recorded for concentrated Mn/Kr samples formed at 12 K contain additional absorption features at 255.3, 317.7 and 413.2 nm evident from a comparison of the top and middle panels of Figure VI.3 recorded for high and medium metal concentrations respectively. The isolation of atomic manganese in Kr is much more efficient than in Ar matrices. This was manifest in the observation that producing samples with detectable amounts of dimer bands resulted in fully absorbing atomic transitions. The 229.1, 255.3, 317.7 and 413.2 nm absorption features observed are assigned to the Mn_2 species. Further increasing the metal concentration in Kr results in additional absorption features at 330.7 and 349.1 nm, top panel of Figure VI.3. These features are also assigned to Mn_2 absorptions, similar to the bands identified under high metal loading conditions in the 300-350 nm region in solid Ar by Vala and co-workers[15].

VI.2.IV Discussion Mn/Kr absorption spectroscopy

In this section the spectroscopy of manganese atoms and aggregates isolated in solid Kr are discussed in relation to the results and band assignments reported in earlier studies[9,13,17]. The absorption features assigned to the atomic absorption transitions of manganese in solid Kr are presented in Table VI.2. The absorption spectra reported in this Chapter reveal the presence of multiple sites of isolation for dilute Mn/Kr samples deposited at 12 K.

Schnepp[9] reported strong triplets of atomic Mn absorptions corresponding to the $y^6P_{5/2}$ and $z^6P_{5/2} \leftarrow a^6S_{5/2}$ transitions centered at 279.1 and 395.1 nm respectively. Additional weaker absorption bands were observed at approximately 283.7 and 400.3 nm. The absorption features reported by Schnepp, using photographic detection methods, show good agreement with those identified during the course of this work (Table VI.2) leading to the assignment of multiple occupancy for Mn in solid Kr. The relative absorption strengths identified by Schnepp[9] on deposition at 4.2 K mirrored those achieved here with matrix deposition at 12 K. Ozin and co-workers[17] achieved similar absorption spectra for dilute Mn/Kr samples.

However, Shakhsemampour[13] observed absorption features only at 284.5 and 387 nm corresponding to the $y^6P_{5/2}$ and $z^6P_{5/2} \leftarrow a^6S_{5/2}$ transitions respectively in solid Kr. The observed features match the red (2^o) site for the $y^6P_{5/2}$ and blue (1^o) site for the $z^6P_{5/2}$ identified from the results of concentration studies of Mn/Kr collected in Table VI.2. The observation of atomic absorptions correlated to different sites of isolation for the $y^6P_{5/2}$ and $z^6P_{5/2} \leftarrow a^6S_{5/2}$ atomic transitions is difficult to resolve. In addition, as in solid Ar, Vala and co-workers[13] assigned the $z^4P_{3/2} \leftarrow a^6S_{5/2}$ transition of atomic Mn to occur at 310 nm from MCD measurements. This band was not present in the absorption spectra reported in the present study. Given the weak oscillator strength of the $z^4P_{3/2} \leftrightarrow a^6S_{5/2}$ transition ($A_{ki} = 0.0027 \times 10^8$ sec^{-1}), observation of this spin-forbidden using optical absorption techniques is unlikely.

As in Ar matrices, the absorption spectroscopy of Mn clusters in Kr is difficult to assess due to the number of absorption bands observed for concentrated Mn/Kr samples. Mn_2 absorption features at 229.1, 255.3, 317.7 and 413.2 nm were assigned from concentration studies of Mn deposited in solid Kr at 12 K, (Figure VI.3). These bands show good agreement with the 254, 317 and 410 nm absorption features assigned to Mn_x (where x is most probably two) by Ozin and co-workers[17].

Vala and co-workers[13] also assigned the 256.5 nm band to that of a Mn_2 absorption but the 414 nm feature was assigned to Mn_x where it is suggested that x = 5. The assignment of an absorption band due to an Mn_5 species was based on ESR measurements[20]. This assignment is rejected based on the growth patterns found in the concentration study presented in Figure VI.3, in which the 413.2 nm feature shows approximately the same dependence on the metal flux used as the 255.3 nm feature.

VI.2.V Mn/Xe

Figure VI.5 presents a comparison of the absorption spectra recorded on deposition at 12 K for manganese isolated in solid Xe at various metal concentrations. As shown in the bottom panel of Figure VI.5, absorption features are observed at 214.3, 288.2 and 395.5 nm for Mn/Xe samples produced using low metal fluxes. The dominant absorption feature, centered at 288.2 nm, is assigned to the $y^6P_{5/2} \leftarrow a^6S_{5/2}$ transition of atomic Mn red-shifted in solid Xe from the gas phase position by 1028 cm^{-1}. This absorption band exhibits, as shown in Figure VI.6 (left panel), high and low-energy shoulders and a well resolved threefold splitting pattern. The second threefold split band, centered at 395.5 nm, is assigned to the $z^6P_{5/2} \leftarrow a^6S_{5/2}$ transition of atomic Mn isolated in Xe. The $z^6P_{5/2} \leftarrow a^6S_{5/2}$ transition exhibits a blue-shift of 496 cm^{-1} from that of the free atom. The ratio of the oscillator strengths for the y^6P and z^6P transitions is approximately 19:1 in the gas phase. Fitting the integrated area for the y^6P and $z^6P \leftarrow a^6S$ matrix absorptions bands yielded a matrix intensity ratio $I_{Abs}(y^6P)$: $I_{Abs}(z^6P)$ of approximately 14:1. This numerical analysis was completed following Mn/Xe matrix deposition at 35 K under low metal loading conditions and provides further confirmation of the assignments made in solid Xe. The UV absorption at 214.3 nm is assigned to the $x^6P_{5/2} \leftarrow a^6S_{5/2}$ transition, blue-shifted by 1507 cm^{-1} from the gas phase transition energy. Table VI.3 presents the spectral positions of the electronic transitions assigned for atomic Mn isolated in Xe matrices.

As discussed in Chapter I, solid Xe is the most efficient rare gas host for the isolation of metal atoms, due to the increased site sizes available. The concentration study of Mn in solid Xe shown in Figure VI.5, reflects this characteristic where no additional absorption bands appear under medium metal fluxes. The most

concentrated Mn/Xe samples contain absorptions at 260.8 and 427 nm, features assigned to Mn_2 transitions.

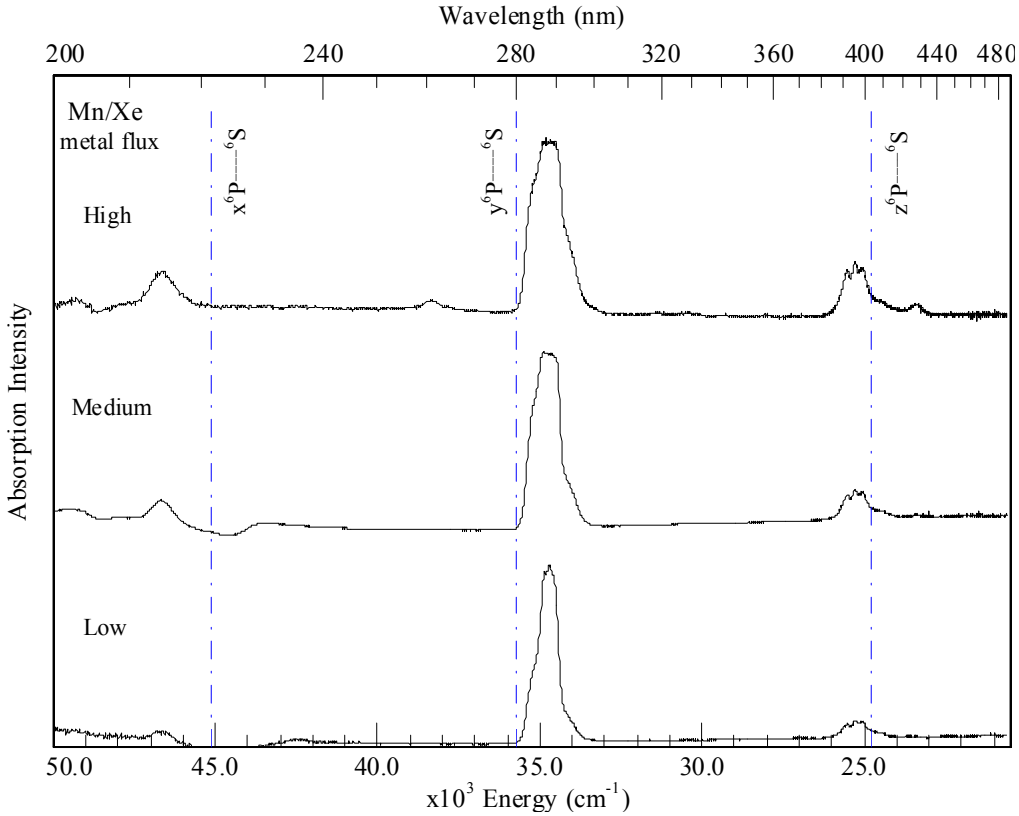

Figure VI.5 **Mn/Xe UV/Vis absorption spectra recorded at 12 K following sample deposition at 12 K. The three spectra shown indicate the changes in the relative intensities of the observed bands with increased metal flux.**

The dependence of the $y^6P_{5/2}$ and $z^6P_{5/2}$ absorption bands on the deposition temperature was investigated I) to assess the stability of the high and low-energy shoulders observed on the 288.2 nm band, II) to investigate the presence of such features on the 395.5 nm band and III) to confirm the assignment of the dimer species. Increasing the deposition temperature favours Mn dimer and smaller cluster formation as well as providing samples of greater crystallinity. Figure VI.6 presents a comparison of the absorption spectra recorded for samples deposited at 12 and 35 K. However, increasing the deposition temperature also favours the isolation of the guest metal atom in the most thermally stable sites. Therefore, the production of M/RG samples, with predominant atomic isolation, is achieved by employing the lowest metal concentration at a particular deposition temperature so as to avoid substantial metal aggregate formation and ensure matrix crystallinity.

Table VI.3 **Spectral positions of the atomic absorption features assigned for atomic manganese isolated in solid Xe on deposition at 12 K. λ_{abs} indicates the position of the band centre or the central three-fold split component where possible. The gas phase transition energies for the Mn atom are also presented. The gas phase – Xe matrix shift is denoted by δ in wavenumber units.**

Transition	Mn/Xe		Mn atom – Gas Phase		
	λ_{Abs} (nm)	E_{Abs} (cm^{-1})	λ (nm)	E (cm^{-1})	δ (cm^{-1})
$z\ ^6P_{5/2} \leftarrow a\ ^6S_{5/2}$	395.5	25284	403.42	24788	+496
$y\ ^6P_{5/2} \leftarrow a\ ^6S_{5/2}$	288.2	34698	279.91	35725	-1028
$x\ ^6P_{5/2} \leftarrow a\ ^6S_{5/2}$	214.3	46663	211.45	45156	+1507

It is evident from the left panel of Figure VI.6 that sample deposition at temperatures higher than 12 K reduces the intensities of the high and low-energy shoulders surrounding the main band centered at 288.2 nm. This corresponds to the normal effect of matrix annealing as the absorption profile (solid trace in Figure VI.6) assigned to the $y^6P_{5/2} \leftarrow a^6S_{5/2}$ transition, is simpler. Although deposition at 35 K did not remove all of the 283 and 293 nm absorptions, the overlapping band is reduced to such an extent that these features can be assigned to those of a thermally unstable site of isolation of Mn atoms in solid Xe. There is also an additional band present at 300 nm upon deposition at high temperatures. This absorption feature is assigned to the $y^6P_{5/2} \leftarrow a^6S_{5/2}$ transition of Mn atoms isolated in a high temperature thermally induced environment, (Mn′). The 300 nm band is assigned to the $y^6P_{5/2} \leftarrow a^6S_{5/2}$ transition of Mn′ indicating the production of an absorption feature dependent on the deposition temperature. The equivalent absorption feature was not identifiable for the $z^6P_{5/2} \leftarrow a^6S_{5/2}$ transition probably because of the lower oscillator strength.

The panel on the right of Figure VI.6 shows the effect of the deposition temperature on the atomic absorption feature assigned to the $z^6P_{5/2} \leftarrow a^6S_{5/2}$ transition of atomic Mn isolated in solid Xe. The low-energy absorption shoulder observed at 12 K is removed upon deposition at high temperature. Deposition at higher temperature also removes the high-energy shoulder of the $y^6P_{5/2} \leftarrow a^6S_{5/2}$ transition (shown left), an effect that is not observed for the $z^6P_{5/2}$ transition shown right. The loss of the high-energy shoulder on one transition only may indicate different site overlapping patterns for the different spectral regions. Therefore deposition at higher temperatures than 12 K results in simpler atomic absorption spectra for the $z^6P_{5/2} \leftarrow a^6S_{5/2}$ transition of Mn in Xe. However, the higher deposition temperature results in the increased production of the Mn_2 absorption at 427 nm relative to that of the atom

during the formation of dilute Mn/Xe samples. This is confirmed by the growth patterns observed for the 262 and 427 nm bands with respect to the atomic absorptions on deposition at 12 K shown in Figure VI.5.

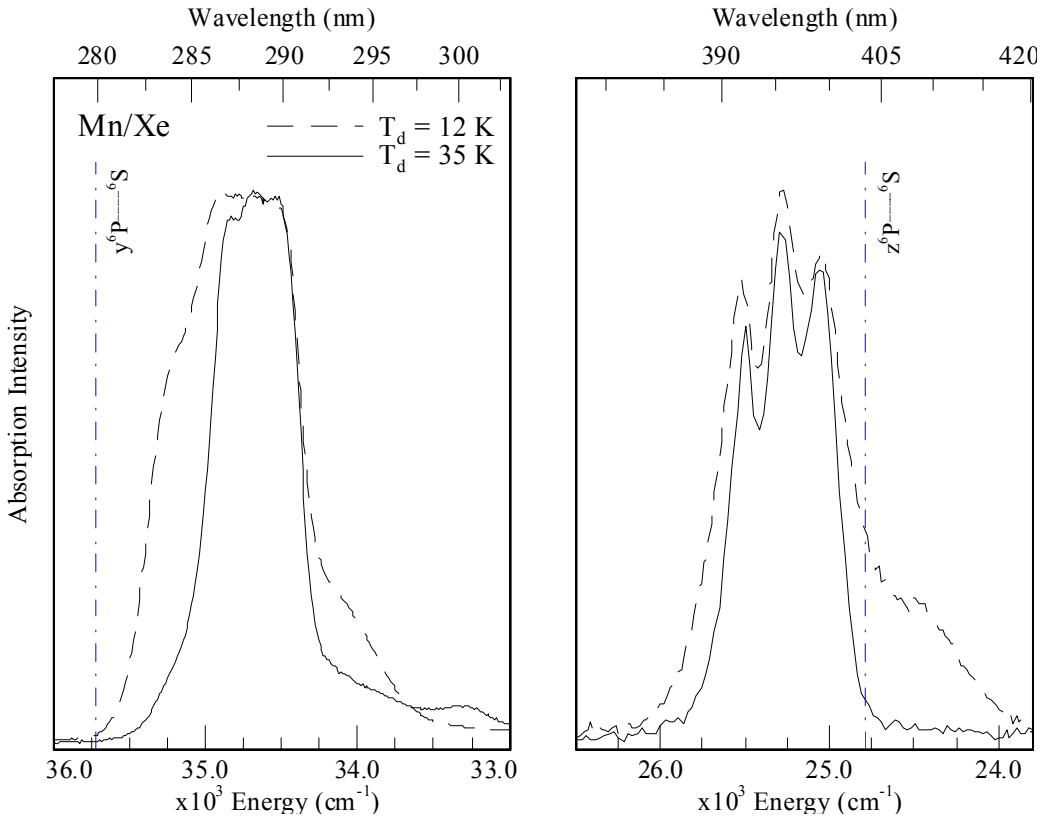

Figure VI.6 **Comparison Mn/Xe absorption spectra recorded in the region of the UV $y^6P_{5/2} \leftrightarrow a^6S_{5/2}$ (left panel) and visible $z^6P_{5/2} \leftrightarrow a^6S_{5/2}$ gas phase transitions of atomic manganese. Sample preparation was achieved using low (left) and medium (right) metal flux at different deposition temperatures (T_d, Kelvin).**

VI.2.VI Discussion Mn/Xe absorption spectroscopy

Previous work by Schnepp[9] on the absorption spectroscopy of atomic Mn isolated in solid Xe assigned the bands at 286.5 and 395.1 nm to the $y^6P_{5/2}$ and $z^6P_{5/2} \leftarrow a^6S_{5/2}$ transitions respectively. Three strong absorptions were observed using photographic detection corresponding to the threefold split pattern identified in the previous section for Mn/Xe atomic absorptions. In this work the $y^6P_{5/2}$ and $z^6P_{5/2} \leftarrow a^6S_{5/2}$ transitions of Mn in Xe are reported to occur at 288.2 and 395.5 nm respectively, see Table VI.3.

Vala and co-workers[13] reported the atomic Mn absorptions at 290 and 396.7 nm for concentrated Mn/Xe samples deposited at 20 K. This deposition temperature favours Mn cluster formation and two bands, like the dimer bands identified in this

Chapter (260.8 and 427 nm), are observed at 262 and 428 nm. Shakhsemampour[13] assigned the 428 nm feature to a possible Mn_5 species. In addition, the spectra presented [13] show multiple absorptions not observed during the course of the Mn/Xe experiments reported here. These absorption features are unassigned and occur at 237, 262, 302, 330, (broad) 350, 334 and 357 nm. The relative intensities of the 262 and 428 nm bands allow the assignment of these features to manganese dimer absorption. In line with the trend observed in Ar and Kr, the second set of absorptions at 237 and the broad band at 350 nm may result from Mn_2 species. This allows the assignment of the 237, 262, (broad) 350 and the 428 nm features to Mn_2.

Schnepp[9] also observed a broad, weak absorption located at 427.4 nm. Temperature dependent deposition and concentration studies presented in Figure VI.6 and Figure VI.5 confirm the assignment of the 427 nm absorption to that of the Mn dimer. The assignment of this band to a high cluster such as Mn_5 is rejected on the grounds that absorptions from the building blocks (smaller clusters) leading to the construction of such a high nuclearity species should also be present. None of these smaller clusters are observed in our Mn/Xe samples.

VI.3 Discussion Mn/RG UV/Vis absorption spectroscopy

In this section trends evident in the UV/Vis absorption spectra recorded for dilute Mn/RG (RG = Ar, Kr and Xe) samples are highlighted. The trends identified are discussed in order to extract some general conclusions on the sites of isolation occupied by atomic Mn in rare gas solids. Observations such as the differences in the absorption band profiles of the atomic transitions and gas phase-to-matrix shifts are discussed. Tables VI.1-3 provide summaries of the atomic absorption features present in Mn/Ar, Mn/Kr and Mn/Xe matrices.

The absorption spectra recorded on deposition in the most dilute Mn/RG samples at 12 K are shown in Figure VI.7. The vertical lines indicate the positions of the gas phase $x^6P_{5/2}$, $y^6P_{5/2}$ and $z^6P_{5/2} \leftrightarrow a^6S_{5/2}$ transitions of atomic Mn. The simplicity of the spectra and the location of the bands allow for easy assignment to the $x^6P_{5/2} \leftarrow a^6S_{5/2}$, $y^6P_{5/2} \leftarrow a^6S_{5/2}$ and $z^6P_{5/2} \leftarrow a^6S_{5/2}$ absorptions in RG matrices. High quality atomic isolation of Mn was achieved with the electron bombardment 'metal sputtering' technique, and indeed the absorption spectra reported in this Chapter are the most atomic recorded to date. Ozin and co-workers[17] refer to some of

the difficulties inherent in the vaporisation of Mn and the controlled production of Mn/RG samples that have clouded previous attempts at distinguishing Mn atom and cluster absorptions.

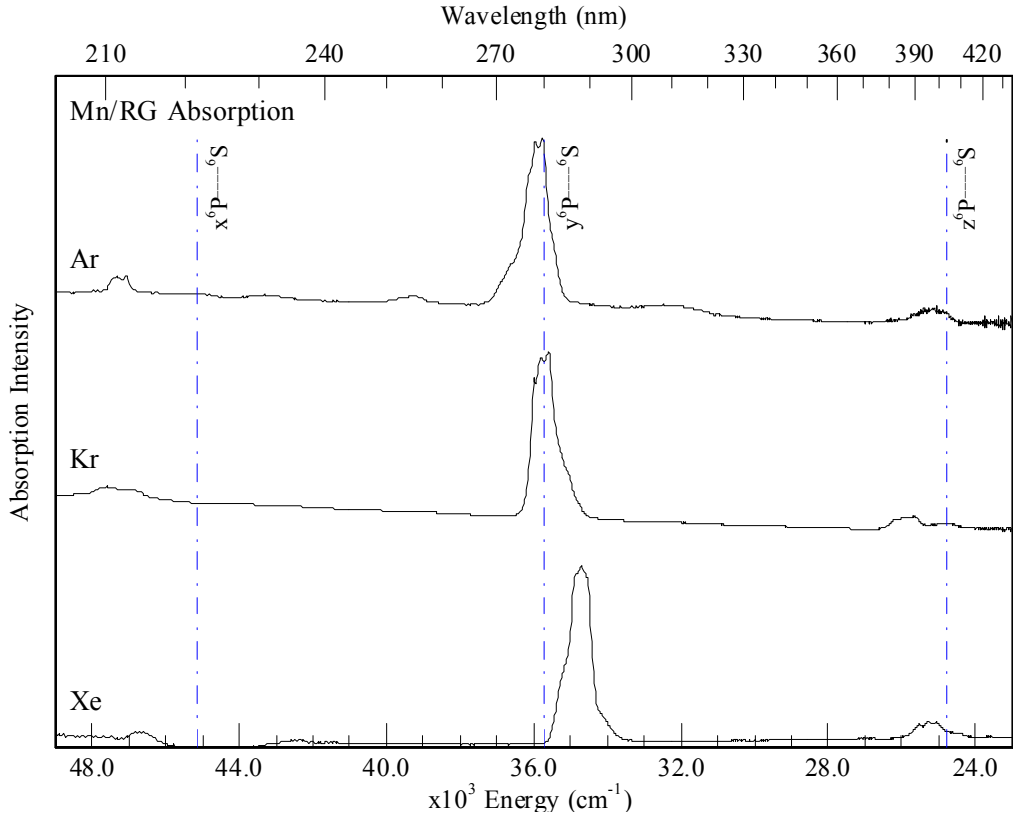

Figure VI.7 **Mn/RG UV/Vis absorption spectra recorded at 12 K following sample deposition at 12 K. The spectra shown correspond to the most dilute Mn/RG samples prepared. The gas phase positions of the $x^6P_{5/2}$, $y^6P_{5/2}$ and $z\ ^6P_{5/2} \leftarrow {}^6S_{5/2}$ transitions are shown by the dashed vertical lines.**

Analysis of the absorption features assigned to the $y^6P_{5/2} \leftarrow a^6S_{5/2}$ transition of atomic Mn isolated in RG solids reveals the red-shift of the band maximum from Ar to Kr to Xe deviates from linearity. Thus the shift from Ar to Kr is only 151 cm^{-1}, while that from Kr to Xe is 1109 cm^{-1}. This irregular behaviour can be analysed in relation to the dominant / minor sites of isolation. The dominant (1^o) Mn/Kr absorption feature at 279.91 overlaps the gas phase transition while the $y^6P_{5/2} \leftarrow a^6S_{5/2}$ absorption feature in solid Ar (278.1) shows a (blue) high-energy shoulder at 273 nm. The latter has been assigned by Vala and co-workers[13] to a secondary site of isolation of Mn atoms in Argon. However, the Mn/Kr $y^6P_{5/2} \leftarrow a^6S_{5/2}$ absorption centered at 279.91 nm shows a low energy shoulder at 284.9 nm. Comparison of the

Mn/Ar and Mn/Kr absorption features reveals a site reversal where the dominant red site (278.1 nm) in Ar corresponds to the minor, red (284.9 nm) feature in solid Kr. A better linear correlation between the matrix shifts is identified when the blue, minor (2°) site in Ar (273 nm) is selected for comparison with the band maxima in Kr and Xe. This provides more expected red matrix-shifts of 823 and 1109 cm^{-1} from Ar to Kr to Xe.

The extension of this argument to the $z^6P_{5/2} \leftrightarrow a^6S_{5/2}$ transition shown in Figure VI.8 suggests the presence of a secondary site of isolation in solid Ar to higher energy than the band maximum observed. However, inspection of the visible absorptions shows that a progressive red-shift from Ar to Xe is not observed, as the Mn/Kr $z^6P_{5/2} \leftarrow a^6S_{5/2}$ absorption appears to higher energy than the Mn/Ar band. This is largely due to the presence of Mn_2 absorption at 403 nm but the identification of a secondary site, blue-shifted from the assigned 1^o absorption in Ar, would rationalize the behaviour of the trends exhibited by the matrix shifts for the $z^6P_{5/2} \leftarrow a^6S_{5/2}$ absorption. Excitation spectroscopy of the z^6P excited state of atomic Mn isolated in solid Ar presented in Chapter VII, provides spectral evidence for the existence of a secondary high-energy site of atomic isolation, yielding the expected linear correlation between the gas phase-matrix shift and host polarizability.

The absence of a linear correlation between the matrix-shifts of the dominant bands observed indicates Mn atoms isolated in Ar and Kr occupy more than one thermally stable matrix environment. The absorption features recorded for the Mn/Xe system indicate the presence of a secondary site that is removed by high temperature deposition. Thus only one thermally stable site of isolation is identified for manganese atoms in solid Xe.

Figure VI.7 presents a comparison of the spectral positions for the matrix absorption bands assigned to the $y^6P_{5/2} \leftarrow a^6S_{5/2}$ and $z^6P_{5/2} \leftarrow a^6S_{5/2}$ transitions of Mn atoms. Inspection reveals the $z^6P_{5/2} \leftrightarrow a^6S_{5/2}$ transition occurs to higher energy than the gas phase position in all three hosts. In contrast, the $y^6P_{5/2} \leftarrow a^6S_{5/2}$ absorption features overlap the gas phase position for Mn/Kr, while the Mn/Ar and Mn/Xe bands occur at higher and lower energies respectively. As the ground state ($a^6S_{5/2}$) is common to both the $y^6P_{5/2}$ and $z^6P_{5/2}$ transitions, the overall interaction of the excited state (i.e. sum of both Σ and Π) with the matrix environment must be more repulsive for the $z^6P_{5/2}$ excited state than for the $y^6P_{5/2}$ state. This effect has its origin in the

spin 'triplet' and 'singlet' like properties of the two excited states involved, such that the pure $^1\Pi$ component exhibits a shorter excited state bond length than its $^3\Pi$ equivalent. This allows an increased excited state stabilization (also true of the Σ interactions) therefore lowering the observed 'singlet-like', $y^6P_{5/2}$ transition energy and inducing a red matrix shift in Xe.

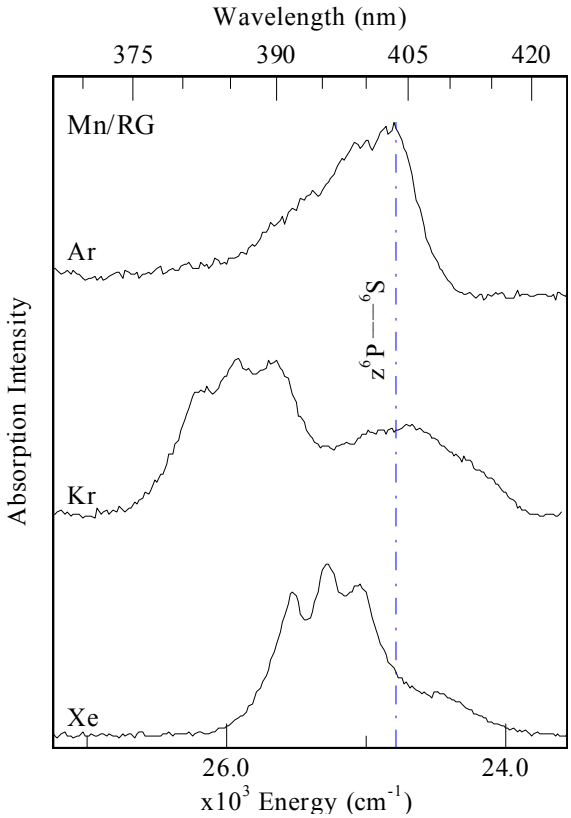

Figure VI.8 **Mn/RG Visible absorption spectra recorded at 12 K following sample deposition at 12 K. The spectra shown correspond to the most dilute Mn/RG samples prepared. The gas phase position of the $z\ ^6P_{5/2} \leftarrow\ ^6S_{5/2}$ transition is indicated.**

Discussion of the type of sites occupied by the Mn atoms is not attempted at this point. It is postponed until Chapter X, when a complete analysis of the luminescence excitation spectroscopy reported for the $y^6P_{5/2}$ and $z^6P_{5/2} \leftrightarrow a^6S_{5/2}$ transitions of Mn/RG solids have been presented. Excitation spectroscopy provides a much more sensitive method for site identification allowing the deconvolution of the observed absorption bands into individual site specific components. The spectroscopic analysis on which this is based is presented in the Chapters that now follow.

VI.4 Conclusion

The UV/Vis absorption spectroscopy reported for atomic manganese isolated in solid Ar, Kr and Xe allowed the assignment of the *x, y* and $z^6P_{5/2} \leftarrow a^6S_{5/2}$ transitions in each of the RG hosts. Multiple thermally stable sites of isolation were identified in solid Ar and Kr whereas single site occupancy is indicated in solid Xe. The additional absorption features identified are assigned to Mn_2 transitions only and the spectra recorded for the samples prepared in this study show no evidence for the production of higher Mn aggregates. Thus the production of manganese vapour by electron bombardment is seen to be an ideal method for preparing solid rare gas samples containing predominantly isolated metal atoms. This is a significant improvement over the resistive heating methods previously employed in Mn/RG sample formation.

References

[1] V. A. Braken, P. Gürtler and J. G. McCaffrey, *J. Chem. Phys.,* **107**, 5290 (1997).

[2] B. Healy and J. G. McCaffrey, *J. Chem. Phys.*, **110**, 3903 (1999).

[3] M. A. Collier and J. G. McCaffrey, *J. Chem. Phys.*, **119**, 11878, (2003).

[4] C. Crepin and A. Tramer, *J. Chem. Phys.*, **97**, 4772 (1992).

[5] J. G. McCaffrey and G. A. Ozin, *J. Chem. Phys.*, **101**, 10354 (1994).

[6] W. H. Breckenridge, C. Jouvet and B. Soep, *Advances in Metal and Semiconductor Clusters*, edited by M. A. Duncan (JAI, Greenwich, 1995), Vol. III.

[7] N.I.S.T. Atomic Spectra Database, Website: http://physics.nist.gov/cgi-bin/AtData/display.ksh?/XXE0qMnqIXXP-15XXT2XXS, (Last accessed 4th February 2004).

[8] M. McCarty and G.W. Robinson, *Mol. Phys.*, **2**, 415 (1959).

[9] O. Schnepp, *J. Phys. Chem. Solids*, **17**, 188 (1960).

[10] E. L Lee and R. G. Gutmacher, *J. Phys. Chem. Solids*, **23**, 1823 (1962).

[11] D. M. Mann and H. P. Broida, *J. Chem. Phys.*, **13**, 84 (1971).

[12] D. M. Gruen, Spectroscopic Identification and Characterization of Matrix Isolated Atoms in *Cryochemistry*, edited by M. Moskovits and G. A. Ozin, Wiley – Interscience, New York, 1976.

[13] J. Shakhsemampour, Ph.D. Thesis, University of Florida, 1983. (*unpublished results*)

[14] T. C. De Vore, A. Ewing, H. F. Franzen and V. Calder, *Chem. Phys. Letts.*, **35**, 78 (1975).

[15] J. C. Rivoal, J. Shakhsemampour, K. K. Zeringue and M. Vala, *Chem. Phys. Letts.*, **92**, 313 (1982).

[16] A. D. Kirkwood, K. D. Bier, J. K. Thompson, T. L. Haslett, A. S. Huber and M. Moskovits, *J. Phys. Chem.*, **95**, 2644 (1991).

[17] W. E. Klotzbücher and G. A. Ozin, *Inorg. Chem.*, **19**, 3776 (1979).

[18] S. M. Younger, J. R. Fuhr, G. A. Martin and W. L. Wiese, *J. Phys. Chem. Ref. Data* Vol. **7**, No. 2, 495, 1978.

[19] The apparent loss in intensity for the 211.8 and 226.4 nm features under medium metal loading conditions (middle panel, Figure VI.1) is as a result of employing a neutral density filter (ND3) between the sample and the transmittance PMT.

[20] C. A. Baumann, R. J. Van Zee, S. V. Bhat and W. Weltner Jr, *J. Chem. Phys.*, 78, 190, (1983).

Chapter VII

Luminescence spectroscopy of the z^6P state of atomic manganese isolated in rare gas solids, (RG = Ar, Kr and Xe).

VII.1 Introduction

The excitation and emission spectroscopy of atomic Mn isolated in solid Ar, Kr and Xe matrices resulting from excitation of the [Ar] $3d^5 4s4p$ z^6P ← a^6S [Ar] $3d^5 4s^2$ transition is reported in this Chapter. Although the absorption spectroscopy of atomic manganese has been extensively studied, no reports of the luminescence of Mn/RG solids have appeared in the literature. Absorption spectra presented in the previous Chapter identified multiple absorption features in the vicinity of the $z^6P_{5/2} \leftarrow a^6S_{5/2}$ transition of atomic Mn occurring in the gas phase[1] at 24788.05 cm^{-1} (403.42 nm). The analysis of concentration studies of manganese deposition in each of the RG host matrices, allowed the identification of experimental conditions ideal for atomic isolation. Matrix annealing and high temperature deposition lead to the identification of Mn atom 'trapping' in multiple thermally stable sites in Ar and Kr. The $z^6P_{5/2} \leftarrow a^6S_{5/2}$ transition was observed to occur from a single thermally stable site in solid Xe. The absorption band profiles recorded showed resolved threefold splitting patterns characteristic of Jahn-Teller interactions and indicating Mn atom isolation in high symmetry sites in Kr and Xe.

This chapter reports the luminescence of Mn atoms in RG solids the analysis of which is challenging for a number of reasons. I) The existence of multiple trapping sites of atomic isolation with each of these sites essentially presenting a different type of Mn atom capable of exhibiting individual excited state characteristics due to the guest – host interaction within the matrix cage. II) Atomic Mn exhibits several excited state electronic configurations, [Ar] $3d^6 4s^1$ and [Ar] $3d^5 4s^2$ like that of the ground state. These excited state electronic configurations and the [Ar] $3d^5 4s4p$ configuration accessed in absorption, give rise to many low lying excited states thereby providing multiple relaxation channels (both radiative and non-radiative) for excited state populations. The excited states energetically accessible with z^6P excitation are shown in Figure VII.1 by the region indicated by the broken box.

The luminescence reported in the following sections allowed definitive identification of multiple site occupancy suggested by the absorption spectroscopy reported in Chapter VI. Analysis of the emission-excitation bands allowed the assignment of the two distinct types of thermally stable Mn atom trapping sites in Ar and Kr and a single site in solid Xe.

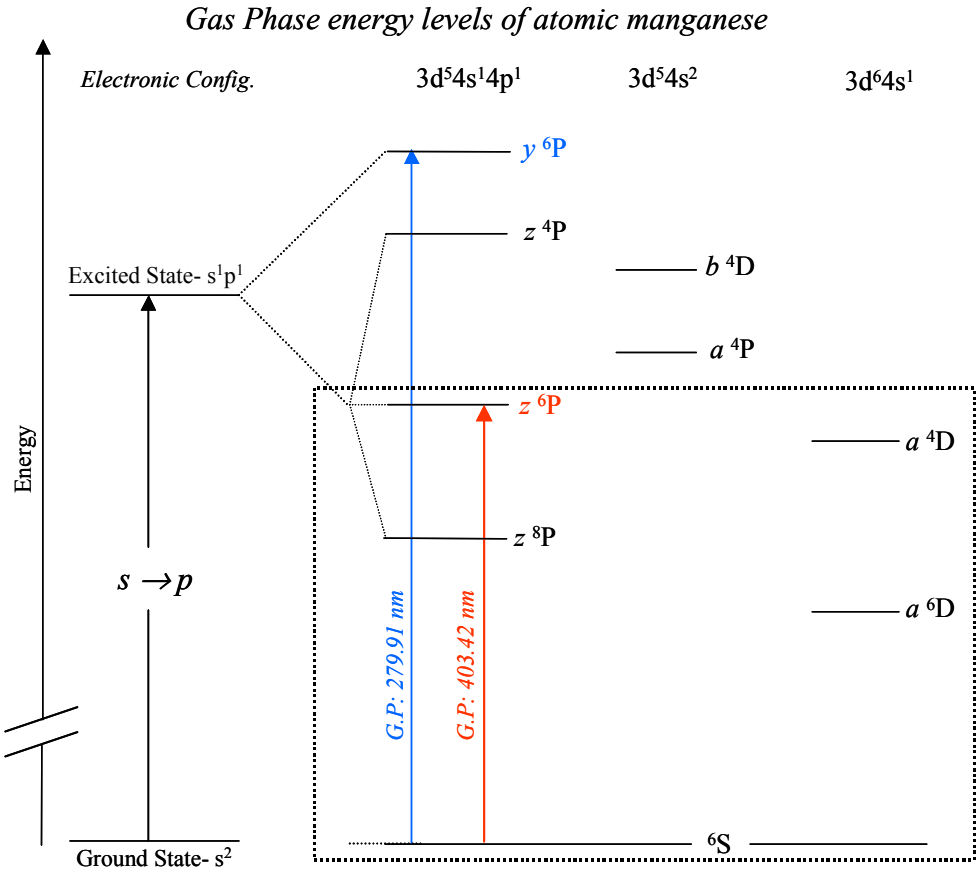

Figure VII.1 **Schematic representation of the energy levels of gas phase atomic manganese[1]. The allowed $y^6P_{5/2} \leftarrow a^6S_{5/2}$ and $z^6P_{5/2} \leftarrow a^6S_{5/2}$ transitions occur at 35726 cm^{-1} (279.91 nm) and 24788 cm^{-1} (403.42 nm) respectively, are indicated by arrows. The area of the diagram shown in the dotted box highlights the low lying excited states that exist below and are available to participate in the relaxation processes following the z^6P excitation.**

High–resolution emission spectra and excited state lifetime measurements recorded with $z^6P_{5/2} \leftarrow a^6S_{5/2}$ excitation, allowed the assignment of the atomic Mn fluorescent and phosphorescent transitions. Mn/RG luminescence was shown to be very site specific, where Mn atoms isolated in different sites of isolation lead to the production of specific excited states. Temperature dependent luminescence and lifetime measurements recorded for Mn isolated in Ar, Kr and Xe following site selective $z^6P_{5/2} \leftarrow a^6S_{5/2}$ excitation point to complex excited state dynamics, non-

radiative relaxation and inter-system crossing (ISC) processes that are both site and matrix host dependent.

This Chapter is structured as follows. Firstly, time-integrated (steady-state) emission spectra recorded with continuous lamp excitation of the absorption features assigned to the $z^6P_{5/2} \leftarrow a^6S_{5/2}$ transition of atomic Mn are presented separately for each of the Mn/RG systems. Excitation spectra recorded by monitoring the resulting emission features are then presented. These excitation spectra allowed the deconvolution of the broad, overlapped atomic absorption bands presented in Chapter VI, into individual site components. The excitation spectra also allowed the determination of the relative amounts of Mn atoms isolated in the different matrix environments. Primary (1°) and secondary (2°) sites of isolation are thereby established. Secondly, the results of high temperature deposition and/or matrix annealing experiments are presented to identify the thermal stability of the sites. Thirdly, following site identification, high resolution time-integrated and time-resolved emission spectra produced with continuous lamp and pulsed laser excitation of Mn atoms isolated in specific sites of isolation allow the assignment of excited states of atomic manganese producing the observed matrix emission features. Excited state lifetime measurements recorded at 12 K and lineshape analysis of the observed emission features are also used to assign the atomic transitions. The temperature-dependent, site-specific emission spectra and lifetime measurements are reported to provide insight into non-radiative excited state dynamics and ISC processes leading to the observed atomic emission. Where possible the radiative decay characteristics of the excited states assigned are presented. Finally, the results achieved for each Mn/RG are discussed and a comparison of the luminescence resulting from Mn $z^6P_{5/2} \leftarrow a^6S_{5/2}$ excitation in Ar, Kr and Xe solids is made.

VII.2 Results Mn(z^6P)/RG luminescence

Mn/RG matrix deposition was completed as outlined in Chapter II. The formation of dilute Mn/RG thin films using low metal fluxes ensured the production of samples containing predominately isolated Mn atoms. The majority of the Mn/Ar and Mn/Kr samples were prepared at 12 K, as substantial amounts of Mn dimer and higher aggregates were produced at higher deposition temperatures. As reported in Chapter

VI, metal nucleation is inefficient in solid Xe even at deposition temperatures up to 35 K. As solid Xe allowed the production of dilute samples containing Mn atoms isolated in one thermally stable site, solid Xe represents the simplest system with respect to site formation. As such, it provides the ideal starting point for the analysis of the Mn/RG luminescence.

VII.2.I Mn(z^6P)/Xe

The absorption spectra presented for Mn/Xe in Chapter VI indicated the $z^6P_{5/2} \leftarrow a^6S_{5/2}$ transition of atomic manganese occurs from a single thermally stable site of isolation centered at 395.5 nm (25284 cm^{-1}), Table VI.III. A comparison of the absorption spectra recorded close to the gas phase $z^6P_{5/2} \leftarrow a^6S_{5/2}$ transition at different deposition temperatures allowed the identification of an overlapping absorption feature formed at 12 K, shown on the top left of Figure VII.2. This broad feature was removed upon deposition at 35 K.

Figure VII.2 presents time-integrated emission spectra resulting from continuous lamp excitation of the $z^6P_{5/2} \leftarrow a^6S_{5/2}$ transition, following Mn/Xe sample deposition at 12 and 35 K. Inspection of the emission spectra shown on the right hand side of Figure VII.2 reveals only a single emission feature at 620.1 nm resulting from 395.45 nm excitation. However, excitation at 409.25 nm corresponding to the absorption of Mn atoms isolated in the thermally unstable site, produces emission centered at 650 nm. High-resolution excitation spectra recorded by monitoring the 620.1 and 650 nm emission features upon deposition at 12 K (bottom right Figure VII.2) confirm that these emission bands originate from the thermally stable and unstable sites respectively. The excitation spectrum recorded by monitoring the 620.1 nm emission shows a well resolved threefold split band, whose components are centered at 392.2, 395.5 and 399.2 nm. The threefold pattern indicates the isolation of Mn atoms within high symmetry sites in solid Xe. Gaussian lineshape analysis reveals an average linewidth (full width at half maximum, *fwhm*) of approximately 270 cm^{-1} for each component. The combination of the two recorded excitation spectra allow the reproduction of the absorption bands observed upon deposition at different temperatures as shown by the comparison of the upper and lower panels on the left of Figure VII.2.

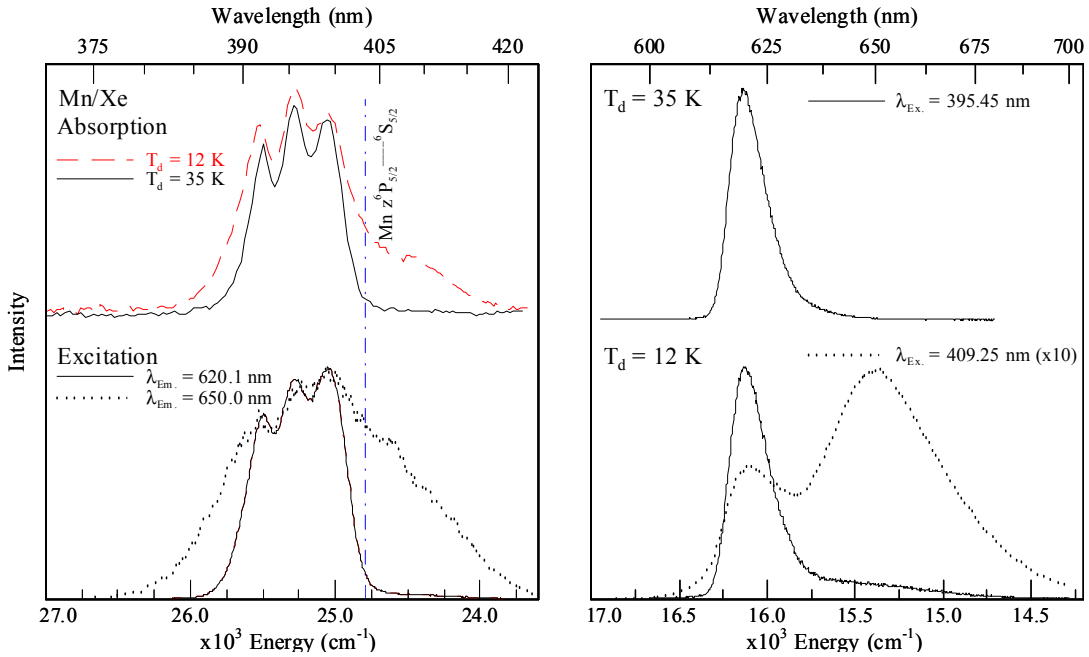

Figure VII.2 **Absorption spectra (top left) recorded for Mn/Xe in the vicinity of the gas phase $z^6P_{5/2} \leftarrow a^6S_{5/2}$ transition of atomic Mn at 403.42 nm upon sample deposition at T_d = 12 and 35 K. Time-integrated emission spectra recorded (shown right panel) upon excitation into the central threefold split component of the thermally stable absorption band assigned to the $z^6P_{5/2} \leftarrow a^6S_{5/2}$ transition at 395.45 nm following sample deposition at 12 and 35 K. The dashed line right panel represents the emission recorded with excitation into the thermally unstable site (λ_{Ex} = 409.25 nm) formed at 12 K. Excitation spectra recorded monitoring the observed emission band maxima at 620.1 and 650.0 nm upon deposition at 35 and 12 K respectively are shown bottom left. Note all the spectra have been normalized.**

It is concluded that only one thermally stable emission feature is produced at 620.1 nm (16126 cm^{-1}) upon excitation of the $z^6P_{5/2} \leftarrow a^6S_{5/2}$ transition in Xe. This broad band exhibits a linewidth of 240 cm^{-1} and a red matrix shift of 8662 cm^{-1} from the gas phase $z^6P_{5/2} \leftrightarrow a^6S_{5/2}$ transition. The large Stokes' shift of 9162 cm^{-1} excludes the assignment of the 620.1 nm feature to resonance fluorescence of the $z^6P_{5/2}$ state. The spectral position suggests an assignment of the emission band to either the $z^8P_{5/2} \rightarrow a^6S_{5/2}$ transition or the relaxation of the metastable $a^6D_{9/2}$ state of atomic Mn. The assignment to these states represents red matrix shifts of 2276 and 926 cm^{-1} from the gas phase[1] positions of the $z^8P_{5/2}$ and $a^6D_{9/2}$ states at 543.4 nm, (18402 cm^{-1}) and 586.43 nm (17052 cm^{-1}) respectively. The broad lineshape observed is indicative of a P $\rightarrow$ S type electronic transition, however the clear asymmetry of the observed emission band suggests a D $\rightarrow$ S type transition. Therefore, the assignment of the

emission feature based on the spectral characteristics (position and band-profile) is not possible.

The temperature dependence of the 620.1 nm emission was used to probe the behaviour of the excited state and identify the non-radiative relaxation processes involved. Steady-state emission spectra recorded at various temperatures showed a progressive red shift in the observed band maximum with increasing scan temperature, (T_s). The temperature dependent red shift is shown in Figure VII.3. Although not presented, the shift observed was completely reversible as the original spectrum was obtained upon returning to 12 K. This effect is consistent with the thermal population of phonon bands easily achieved from an excited state exhibiting a strong electron-phonon coupling. As an aid to the assignment of the emission feature, a Gaussian lineshape analysis of the 620.1 nm emission feature was completed at 12, 26 and 38 K, the results of which are presented in Figure VII.4. Inspection of the fitted spectra reveals that three Gaussian functions are required to effectively reproduce the observed bands at each temperature. Assessment of the relative intensities of the fitted curves reveals the growth of the central feature relative to the high and low energy components upon increasing temperature, thereby resulting in the observed red-shift of the band maximum. The origin of the red-shift and the relative growth of the central component located at approximately at 625 nm, was investigated as shown in Figure VII.4 over this temperature range. The Gaussian analysis presented in Figure VII.4 does not allow a precise identification of the origin of the observed emission lineshape, therefore, a Wp lineshape analysis was also completed as shown in Figure VII.5. Wp lineshape analysis allows, as shown in the Hg/RG work, identification of the band origin, $\nu_{0,0}$ (the zero phonon line, ZPL) and an assessment of the electron-phonon coupling strength from the Huang-Rhys Factor, S for the electronic transition involved. The starting point for the Wp lineshape analysis was the selection of a value for the vibrational frequency ($h,^{-}\omega$) a difficult task given that no resolved features are present on the emission band. For Mn/Xe, $h,^{-}\omega = 27$ cm^{-1} was selected, then the Wp function was calculated with Equation III.4. Lineshapes were generated at 12 K using various values for S until an adequate fit of the high-energy side of the asymmetric 620.1 nm emission profile was achieved. The same parameters ($h,^{-}\omega$, $\nu_{0,0}$ and S) were then employed at higher temperatures (28 K) to fit the observed emission.

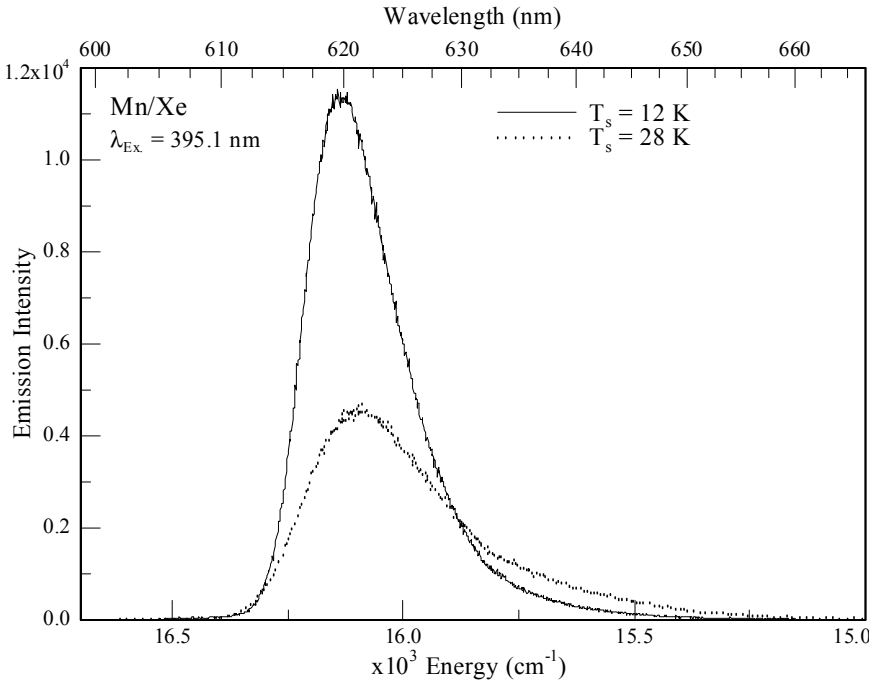

Figure VII.3 **Time-integrated emission spectra recorded at various temperatures (T_s) produced with $z^6P_{5/2} \leftarrow a^6S_{5/2}$ excitation.**

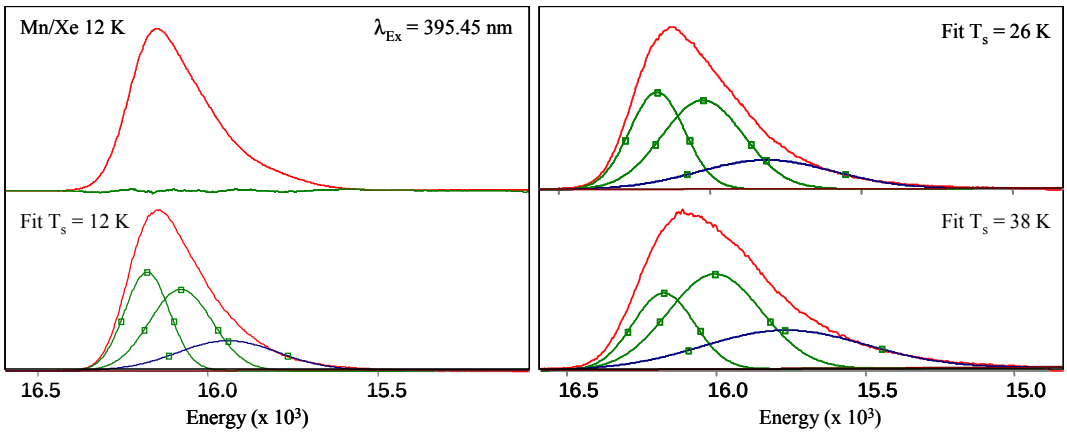

Figure VII.4 **Gaussian lineshape analysis of the 620.1 nm emission observed for Mn/Xe. The panel on the left shows an acceptable fit of the emission spectrum recorded at 12 K. Three broad Gaussian functions were required to completely represent the 12 K spectrum (bottom left). The result of the 12 K fit is shown top left where the simulated emission band and the residual is shown. The fits completed at 26 and 38 K are shown on the right.**

The Wp lineshape generated with $\nu_{0,0}$ = 16410 cm^{-1}, (609.38 nm), $h,^{-}\omega$ = 27 cm^{-1} and S = 11.0 compares well to the observed emission spectrum for T = 12 K as shown in Figure VII.5. At higher temperatures (T = 28 K) the Wp fit predicts the high-energy blue dominant component and the red-shift of the emission band maximum. However, the analysis is unable to reproduce the low energy wing observed, as the low energy wing may result from a minimum amount of the thermally unstable

emission feature produced on deposition at 12 K. The Wp analysis is therefore satisfactory but the growth of an additional emission component suggested by the Gaussian analysis must also be taken into account.

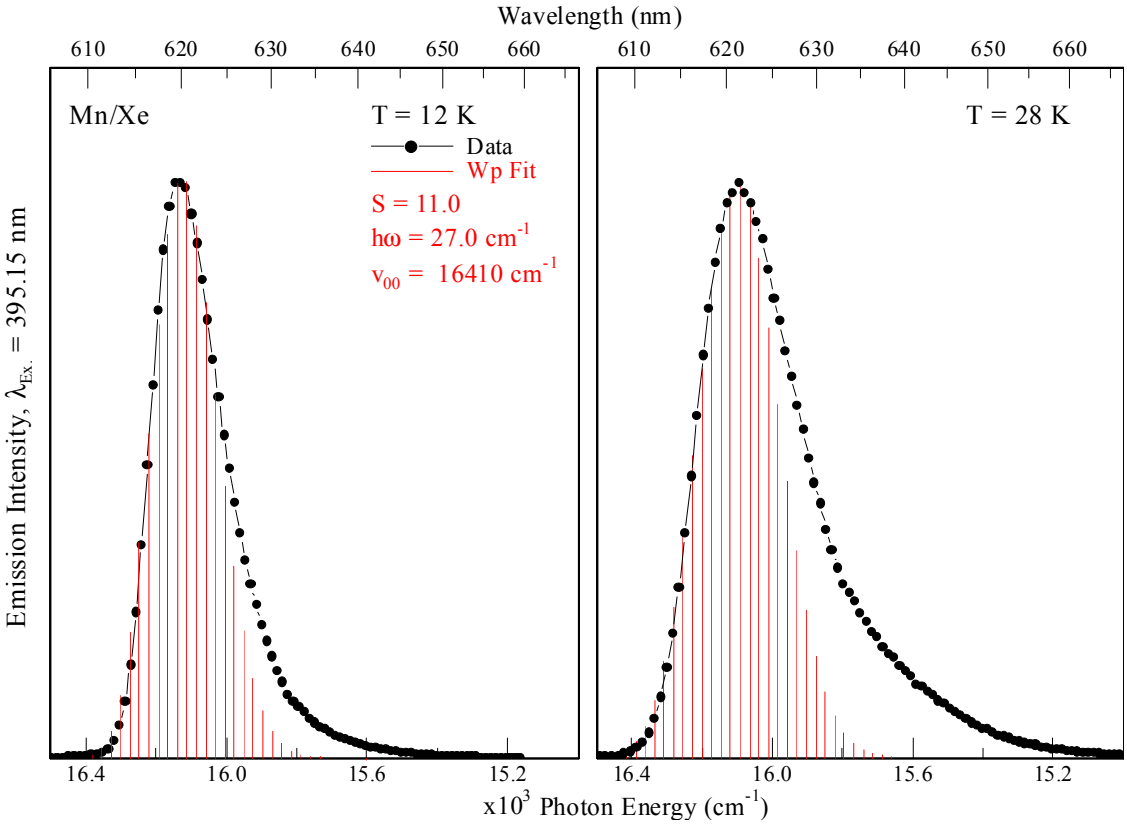

Figure VII.5 **The Wp lineshapes calculated with Equation III.4 for the 620 nm emission feature at 12 K (left) and 28 K (right) produced with pulsed laser excitation at 395.45 nm. The position of the ZPL is indicated by $\nu_{0,0}$ (cm^{-1}).**

Overall, the temperature dependent emission spectra presented in Figure VII.3 show that the progressive red-shift of the band maximum is explained by the growth of the central component (revealed in the Gaussian analysis shown in Figure VII.4). However, the Wp lineshape analysis is superior as it allows the identification of specific parameters such as the band origin and the electron-phonon coupling strength S for the electronic transition. The Wp analysis shown in Figure VII.5 predicts the high-energy rising portion and the overall asymmetry observed at 12 K and that the electronic transition involved in the production of the 620.1 nm feature is moderately coupled to the lattice phonon environment, suggesting that the $z^8P_{5/2} \rightarrow a^6S_{5/2}$ transition gives rise to the observed band. However, the band origin ($\nu_{0,0}$) is predicted to occur at 16410 cm^{-1} favouring the assignment to the relaxation of the a^6D excited state.

Further lineshape analysis of the temperature dependence of the observed time-integrated emission spectra is shown in Figure VII.6 and a comparison of the integrated area for the emission produced revealed the presence of a non-radiative component. The overall emission intensity was reduced to 94.5, 83.5, 72.7 and 68.2 % of the initial intensity I_0 at 12 K at temperatures of 20, 32, 44 and 48 K respectively.

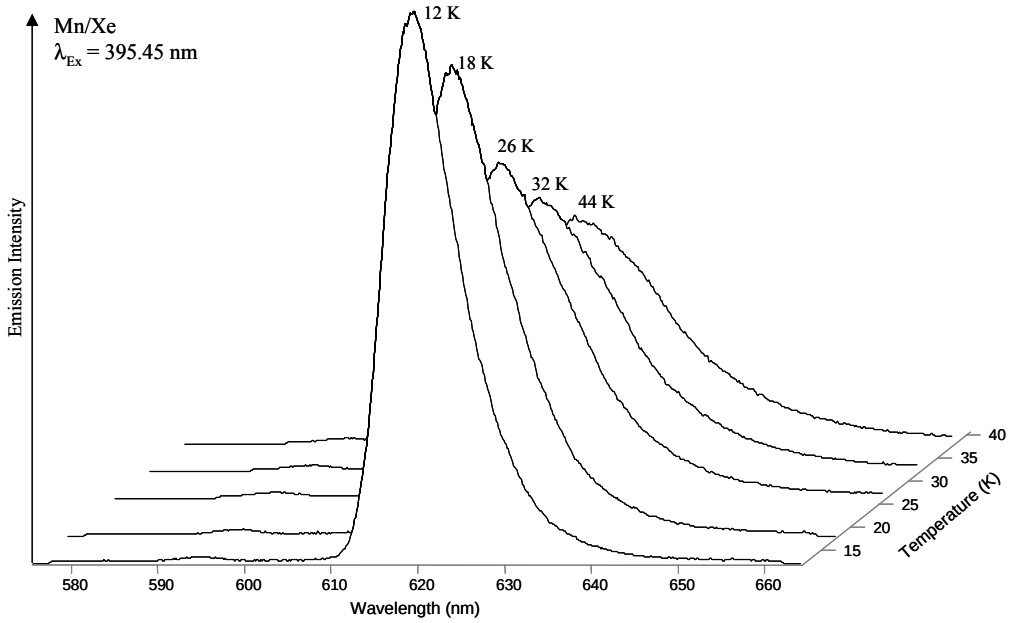

Figure VII.6 **Temperature dependent time-integrated emission spectra recorded with CCD detection following excitation of the $z^6P_{5/2} \leftarrow a^6S_{5/2}$ transition. Sample deposition was completed at 35 K and subsequently annealed to 50 K.**

Decay characteristics of the 620 nm emission feature were recorded using TCSPC following pulsed laser excitation at 395.45 nm corresponding to the central component of the threefold split $z^6P_{5/2} \leftarrow a^6S_{5/2}$ absorption band. Figure VII.7 presents the decay profile recorded at 12 K on a semi-log plot, following sample annealing to 62 K. A double exponential (non-linear least squares) fit was required to reproduce the decay profile. The result of the fit shown in Figure VII.7 allowed the extraction of two decay times τ_1 = 1.83 msec and τ_2 = 0.98 msec both with substantial amplitudes. The longer millisecond component (τ_1) dominates the decay profile at 12 K.

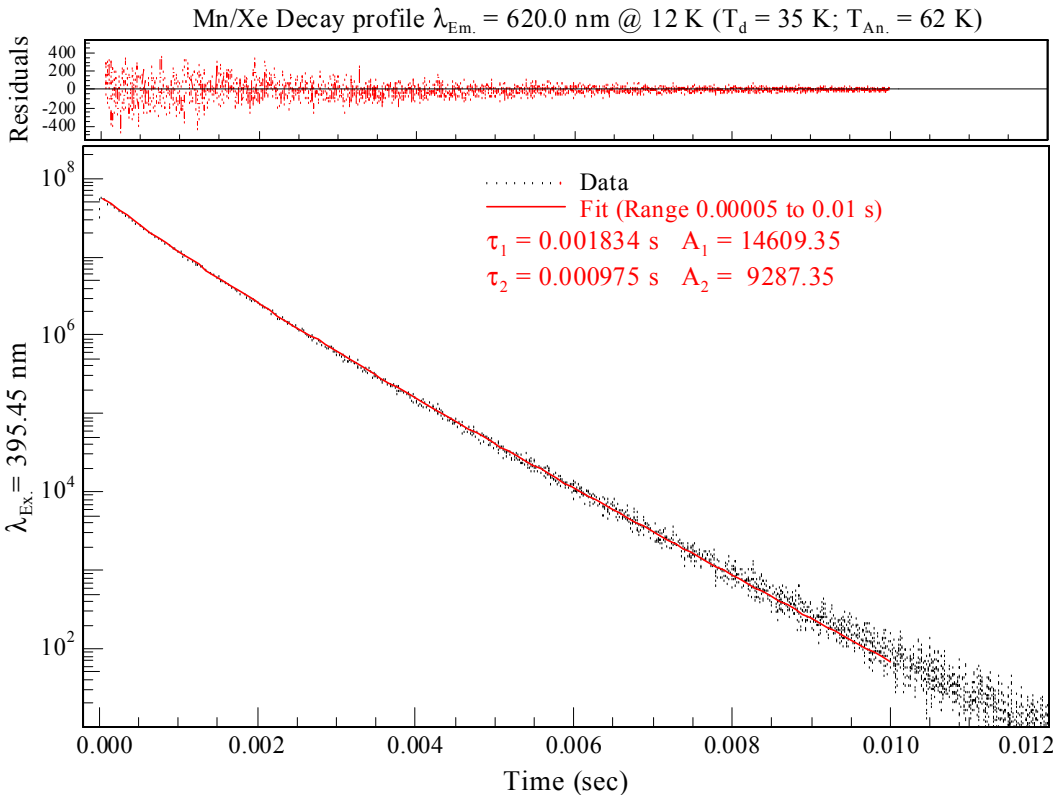

Figure VII.7 **Double exponential non-linear least squares fit of the decay profile recorded for the 620 nm Mn/Xe emission feature using the TCSPC technique following pulsed laser excitation at 393.45 nm corresponding to the $z^6P_{5/2} \leftarrow a^6S_{5/2}$ transition of atomic Mn isolated in Xenon.**

The decay characteristics of the 620 nm emission feature were also investigated at temperatures in excess of 12 K in an attempt to identify the radiative lifetime of the excited state involved in the transition. Figure VII.8 presents the temperature dependence of the decay profiles. It shows that the radiative decay time for the 620 nm emission feature has not been identified, as the both decay components extracted are temperature sensitive over the range 12 to 54 K. The longer msec component identified at 12 K, dominated the decay times extracted at all temperatures up to 54 K. At 54 K τ_1 and τ_2 were identified as 0.85 and 0.23 msec respectively. As the longer-lived component dominated at all temperatures, this is assigned as the observed lifetime τ_{obs}. The trends of decreasing emission intensity and shortening decay time (τ_{obs}) with increasing temperature for the 620 nm band is assigned to the presence a non-radiative process competing with the emitting level. This non-radiative step is active even in the temperature range 12 to 16 K (as shown in Figure VII.8) therefore, the true radiative lifetime of the excited state has not be identified.

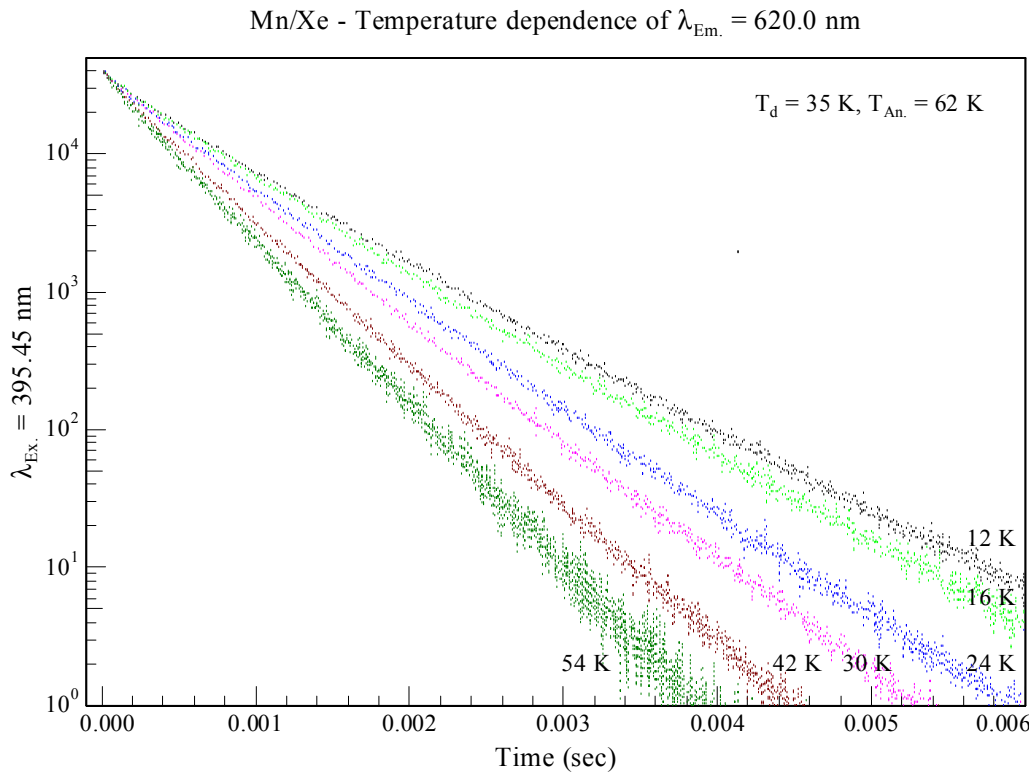

Figure VII.8 **Decay profile recorded for the 620.0 nm emission feature following pulsed laser excitation at 393.45 nm at various temperatures following sample deposition (T_d) at 35 K and matrix annealing $T_{An.}$ = 62 K.**

However, the long lifetime extracted at 12 K of 1.83 msec suggests that the emission is produced via a forbidden transition. The gas phase radiative lifetimes (τ_{Rad}) for the $z^8P_{5/2}$ and metastable $a^6D_{9/2}$ states are reported as 149.3 μsec[2] and 3.4 sec[3] respectively. Although the decay characteristics of the 620.1 nm feature are complicated, the long observed lifetime represents a substantial relaxation of the theoretically calculated a^6D gas phase lifetime by the effective field of the Xe matrix. However, it also suggests that the z^8P state is not responsible for the emission. Based on the results of direct a^6D excitation presented in Chapter VIII, the transition is assigned to $a^6D_{9/2}$ excited state relaxation, the photophysical characteristics of which are presented in Table VII.1.

Table VII.1 **Photophysical characteristics of excitation and emission bands assigned to the $3d^54s4p$ $z^6P_{5/2} \leftarrow 3d^54s^2$ $a^6S_{5/2}$ transition and emission features produced following $z^6P_{5/2} \leftarrow a^6S_{5/2}$ excitation of atomic manganese isolated in solid Xenon. λ_{Ex} (x; where x = 1, 2 or 3) indicates the position of each of the components of the three–fold split excitation spectrum. λ_{Em} indicates the emission band-centre in nm units. The full-width at half-maximum intensity of the excitation/emission features is denoted by Δ in wavenumber units. The gas phase to matrix frequency shifts for the assigned absorption and Stokes' shifts for emission are denoted δ and presented in wavenumber (cm^{-1}) units. The decay characteristics extracted for the observed emission feature are also presented.**

Mn Gas Phase	**Mn/Xe Matrix – *Excitation***			
Transition nm / cm^{-1}	Assignment	$\lambda_{Ex.}$ (x) (nm) / Δ (cm^{-1})		δ (cm^{-1})
$z^6P_{5/2} \leftrightarrow a^6S_{5/2}$ 403.42 / 24788	$Z^6P_{5/2} \leftarrow a^6S_{5/2}$	392.20; (x = 1) 395.45; (x = 2) / ≈ 270 399.15; (x = 3)		+500
	Mn/Xe Matrix – *Emission*			
		$\lambda_{Em.}$ (nm) / Δ (cm^{-1}) Wp Fit $\nu_{0,0}$ (cm^{-1})	Decay (msec)	δ (cm^{-1})
$a^6D_{9/2} \leftrightarrow a^6S_{5/2}$ 586.43 / 17052	$a^6D_{9/2} \rightarrow a^6S_{5/2}$	620.1 / ≈ 240 Fit; 16410	τ_{Obs} =1.83	-926

VII.2.I.I Discussion - Mn(z^6P)/Xe

Excitation of the $z^6P_{5/2}$ resonance transition of atomic Mn isolated in solid Xe results in a single thermally stable emission feature at 620.1 nm. High-resolution excitation spectra recorded in the vicinity of the $z^6P_{5/2} \leftrightarrow a^6S_{5/2}$ gas phase transition by monitoring the 620.1 nm band reproduce, as shown in Figure VII.2, the threefold split pattern evident in the absorption spectra reported in Chapter VI. Excitation spectra recorded following matrix annealing and/or high temperature deposition allowed the identification of a single thermally stable site of isolation of Mn in solid Xe centered at 395.45 nm, (25288 cm^{-1}).

The luminescence measurements reported thus far do not allow a definitive assignment of 620.1 nm emission feature to radiative transitions from either the $z^8P_{5/2}$ or the metastable $a^6D_{9/2}$ excited states to the ground state. However, the excited state producing this band is populated via a 100% efficient relaxation process from the $z^6P_{5/2}$ excited state accessed in excitation, as only this low energy emission feature is observed. The Wp lineshape analysis allowed identification of the electron-phonon coupling strength S for the electronic transition as S = 11.0 which is higher than expected for a D $\rightarrow$ S type transition. Although, identification of the radiative lifetime of the observed emission was not possible at 12 K – the lowest temperature range accessible in our experiment – an observed lifetime of 1.83 msec was extracted

at 12 K. This cannot be directly related to the gas phase lifetimes reported for either the z^8P and a^6D transitions of atomic Mn[2,3].

In addition, a non-radiative step that resulted in a completely reversible temperature dependence for the 620.1 emission feature, was identified in the emission spectra reported Figure VII.3. This non-radiative step was also apparent in the excited state lifetime measurements reported in Figure VII.8. A curve crossing process between the emitting state and the ground state $a^6S_{5/2}$ of atomic Mn is proposed as the origin of both of these temperature dependent observations.

VII.2.II Mn(z^6P)/Ar

The absorption feature observed at 397.4 nm (25136 cm^{-1}) under low metal loading conditions, Chapter VI (top panel Figure VI.8) was assigned to the $z^6P_{5/2} \leftarrow a^6S_{5/2}$ transition of atomic manganese isolated in Ar. Figure VII.9 presents the emission spectrum recorded with continuous tungsten lamp excitation of this absorption band. Inspection of Figure VII.9 reveals emission features centered at 428.3 nm (*fwhm* ≈ 120 cm^{-1}) and a much weaker band at 590.1 nm exhibiting a resolved red shoulder at 600 nm.

High-resolution excitation spectra recorded on deposition at 12 K for the 428.3 nm emission, yielded a threefold split band centered at 393.4 nm (25419 cm^{-1}) as shown in Figure VII.10. A Gaussian lineshape analysis of the excitation profile revealed three dominant components at 389.9, 393.4 and 397.2 nm each with an average linewidth of 253 cm^{-1}. The excitation spectrum recorded for the 590 nm emission shows the same bandwidth as that recorded for the 428.3 nm band but a less well resolved threefold split pattern. Recording a higher resolution excitation spectrum was not possible due to the weak emission intensity at 590 nm. The excitation spectrum recorded for the unresolved red wing at 625.0 nm revealed an additional threefold split band (shown Figure VII.10) centered at 380 nm (26316 cm^{-1}). A Gaussian lineshape analysis yielded three components at 375.5, 380 and 384.7 nm each with an average linewidth of 392 cm^{-1}. The occurrence of two excitation profiles, both exhibiting resolved threefold split patterns indicates the presence of two sites of Mn atom isolation on deposition of Ar at 12 K.

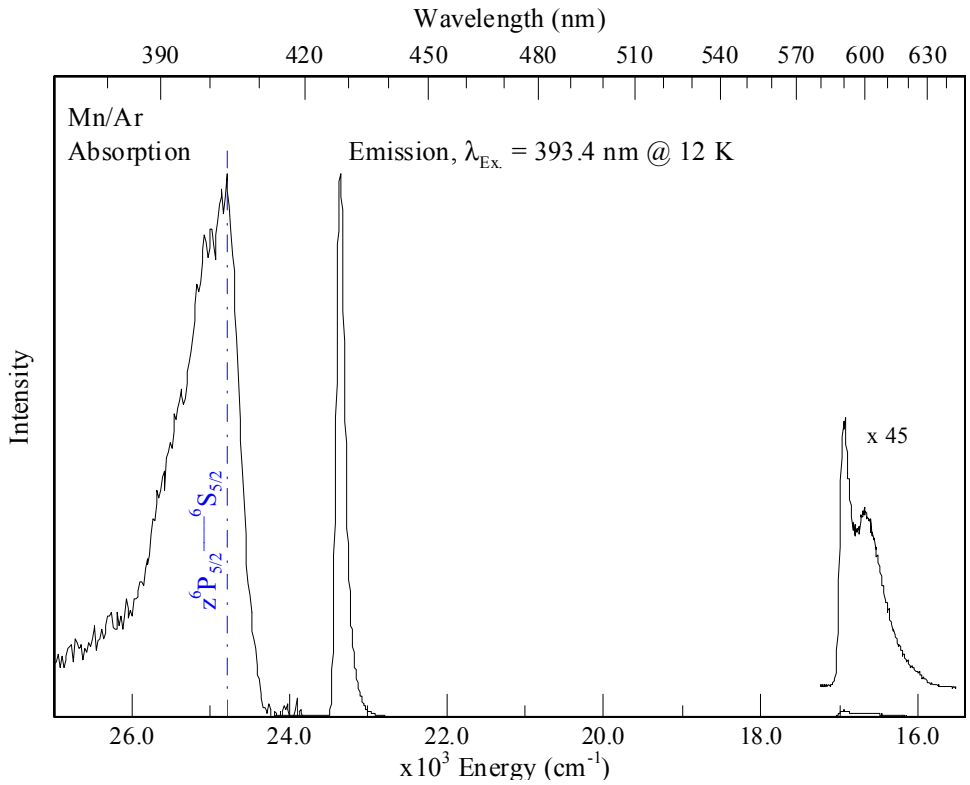

Figure VII.9 **Emission spectrum recorded at 12 K for Mn/Ar with lamp excitation of the Mn $z^6P_{5/2} \leftarrow a^6S_{5/2}$ transition. The absorption spectrum recorded on deposition at 12 K is shown left. The vertical line indicates the gas phase position of the $z^6P_{5/2} \leftrightarrow a^6S_{5/2}$ transition[1] at 403.42 nm (24788 cm^{-1}).**

The presence of a second site of isolation for Mn in Ar was identified in absorption of the $y^6P_{5/2}$ state in Chapter VI, in which the blue shoulder centered at 273.0 nm was assigned to the $y^6P_{5/2} \leftarrow a^6S_{5/2}$ transition occurring from a minor site. Subsequent annealing experiments showed the thermal stability of this site with respect to the high-energy shoulder at 281 nm. The trends evident in Figure VI.8 revealed that the relative matrix shifts for the $z^6P_{5/2} \leftarrow a^6S_{5/2}$ transition for Mn/Ar, Mn/Kr and Mn/Xe did not exhibit a linear correlation with the polarizability of the matrix host. These observations lead to the suggestion that a second minor site of Mn atom isolation existed in Ar. The excitation feature centered at 380 nm shown in Figure VII.10 is assigned to the minor secondary site.

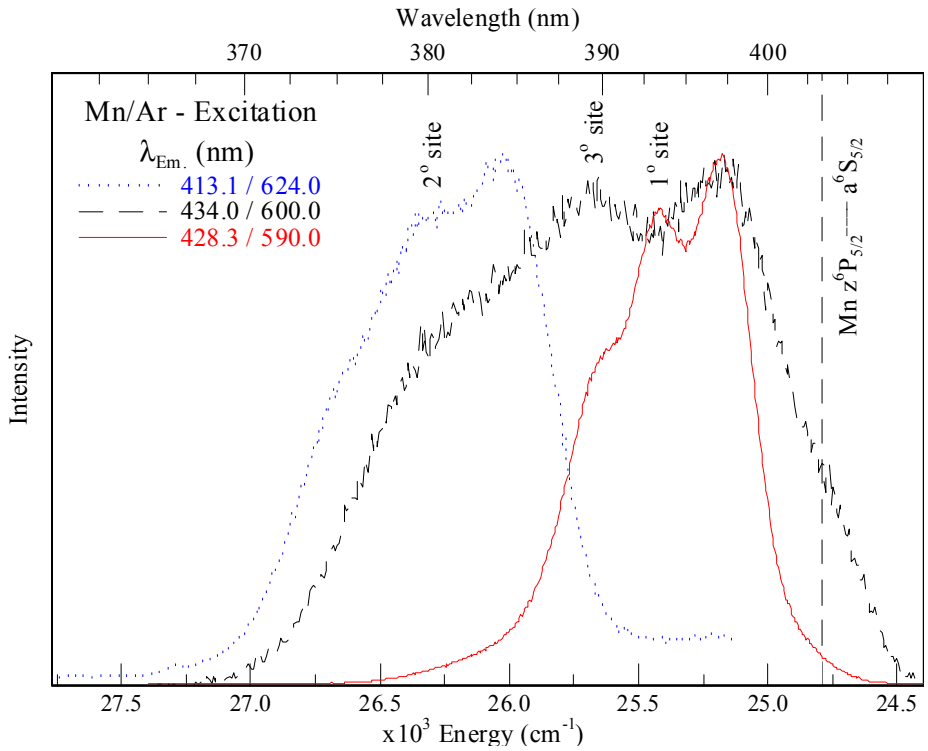

Figure VII.10 **High-resolution excitation spectra recorded monitoring the emission features produced with site selective $z^6P_{5/2} \leftarrow a^6S_{5/2}$ excitation at λ_{Ex} = 393.4 and 380 nm respectively. Note the bands shown have been normalised. The 1° feature is 6.0 times more intense than the 2° and 11.3 times more intense than the 3°.**

Emission spectra recorded with excitation at 393.4 and 380 nm, corresponding to the central threefold split component of the observed excitation features, are presented in Figure VII.11. It is evident in Figure VII.11 that site selective excitation produces spectrally different emission bands. Excitation of the red (1°) site at 393.4 nm) leads to narrow emission features centered at 428.3 and 590 nm, whereas, excitation of the blue (2°) site at 380 nm produces the broad emission features at 413, 431 and 624 nm. An additional unresolved red shoulder is observed at 437.0 nm with excitation at 380 nm. The 600 nm emission feature, produced with excitation into both the blue and red sites, indicates the presence of a third site, whose absorption overlaps the red (1°) and blue (2°) sites identified.

High-resolution excitation spectra recorded monitoring all the observed emission features are presented in Figure VII.10. Correlation of the excitation and the emission bands allows the identification of three sites of isolation labelled 1°, 2° and 3° in Figure VII.10. The photophysical characteristics of these sites are presented in Table VII.2. The red (1°) site centered at 393.4 nm leads to the emission features at 428.3 and 590 nm. The blue (2°) site at 380 nm produces the broad 413 and 624

nm features. Excitation of the 3° site at 389.5 nm leads to the 600 nm band[4]. The sites of isolation identified in solid Ar with deposition at 12 K all exhibit resolved threefold splitting patterns indicating the isolation of Mn atoms in high symmetry environments.

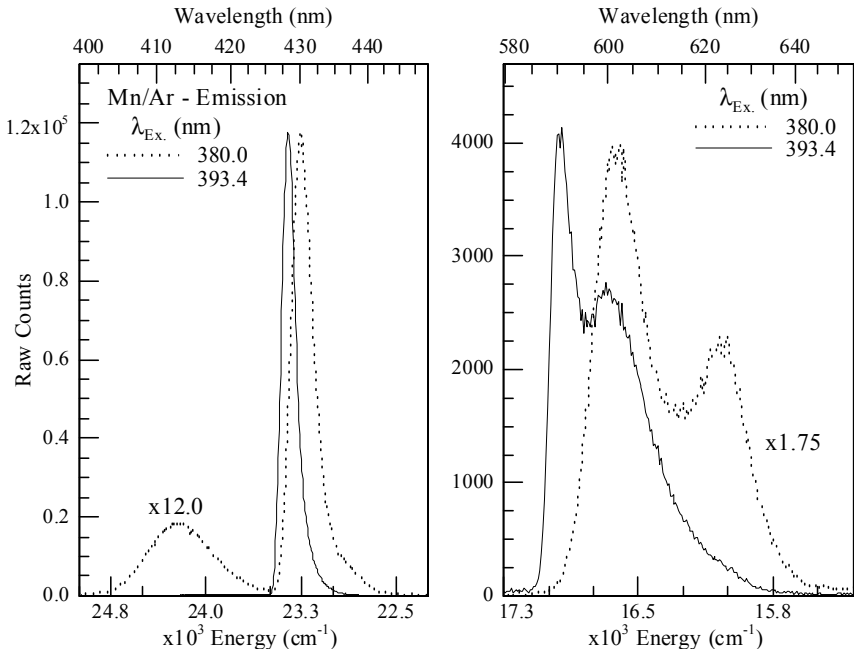

Figure VII.11 **Emission spectra produced with site selective excitation corresponding to the central threefold split component of the excitation spectra presented in Figure VII.10.**

Table VII.2 **Photophysical characteristics of the sites of isolation (1°, 2° and 3°) revealed in the excitation spectra of the $3d^54s4p\ z^6P_{5/2} \leftrightarrow 3d^54s^2\ a^6S_{5/2}$ transition of atomic manganese. The spectral position and average full width at half maximum (*fwhm*) denoted as Δ_{AV} of the three components identified in Gaussian lineshape analyses for the threefold split excitation spectra are presented in wavenumber units. Gas phase to matrix frequency shifts (δ) are presented for the atomic Mn $z^6P_{5/2} \leftarrow a^6S_{5/2}$ transition (G.P.: 24788 cm^{-1}), in wavenumber units. Note the frequency shifts are calculated with respect to the central feature of the observed threefold pattern.**

Mn/Ar Site	Component	E (cm^{-1})	Δ_{AV} (cm^{-1})	δ (cm^{-1})
1°	1	25644	≈ 253	+633
	2	25421		
	3	25174		
2°	1	26632	≈ 392	+1531
	2	26319		
	3	25992		
3°	1	26309	≈ 710	+859
	2	25647		
	3	25121		

The thermal stability of the three sites was investigated by comparison of the behaviour of the emission spectra on deposition at 12 K and following careful matrix annealing. Emission spectra produced with excitation at 393.4 nm allow the assessment of the relative intensities of the 1° and 3° sites where the spectral overlap between these two sites is greatest, (see Figure VII.10). Figure VII.12 presents the effect of matrix annealing on high-resolution emission spectra recorded in the 585-650 nm spectral region following red (1°) site excitation, revealing a large reduction of the 601 nm emission band. Therefore, matrix annealing reduces the 3° site of isolation which confirms its thermal instability. The thermally unstable 3° site also produced the 431 feature which is also removed by the annealing procedure. The apparent decrease in the emission intensity of the 590 nm band is due to the reduction of the underlying 601 nm band.

Emission spectra produced with blue (2°) site excitation at 380 nm also show the effect of matrix annealing on the relative intensities of the 2° and 3° sites as there is a substantial spectral overlap between these two sites, as shown in Figure VII.10 at this wavelength. Figure VII.13 presents the effect of matrix annealing on high-resolution emission spectra recorded for the spectral regions 440-455 nm (left) and 585-650 nm (right).

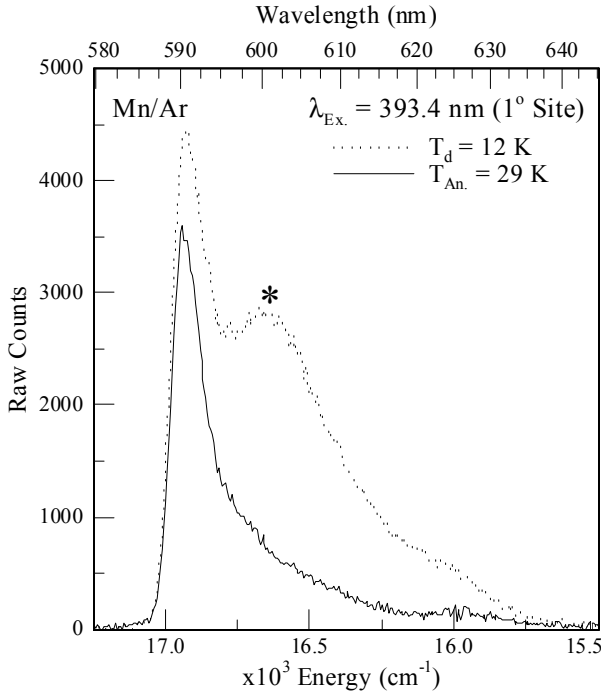

Figure VII.12 Time-integrated emission spectra produced with red (1°) site excitation at 393.4 nm on deposition at 12 K and following annealing to 29 K. Spectra recorded at 12 K. Note the asterisk indicates the emission feature is thermally labile.

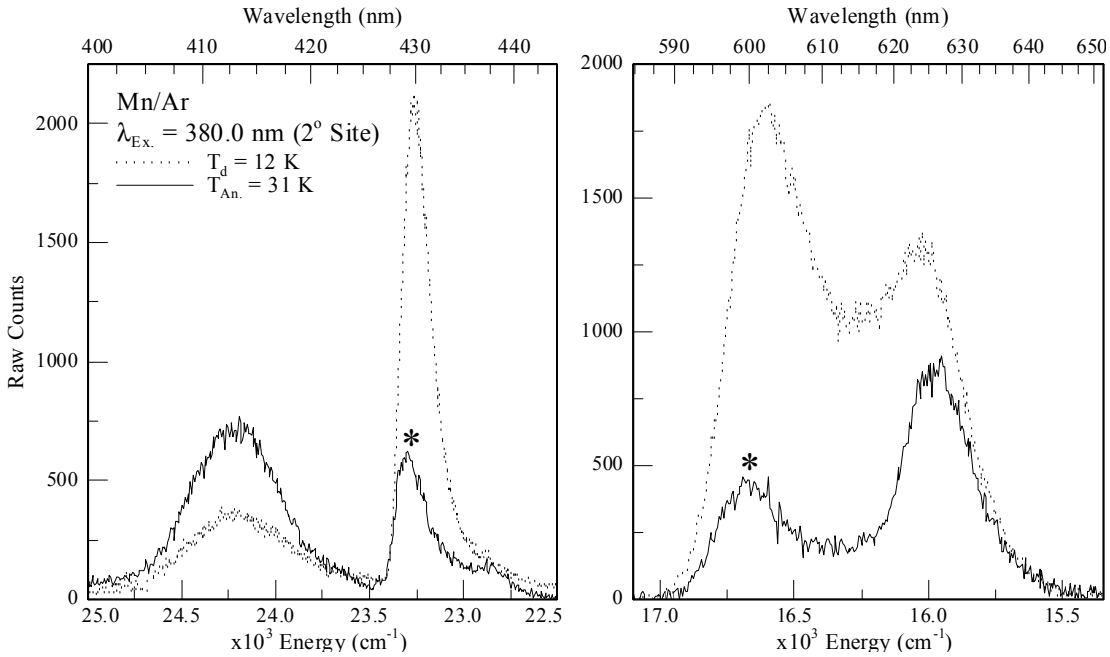

Figure VII.13 Time-integrated emission spectra produced with 2° site excitation at 380 nm on deposition at 12 K and following annealing to 31 K. Spectra recorded at 12 K. Note the relative intensities of the emission spectra shown left and right panels are not directly comparable as the spectrum shown right was recorded under lower resolution. The emission features reduced by the partial removal of the 3° site are highlighted using an asterisk.

Inspection of the left and right panels of Figure VII.13 reveals annealing results in the partial removal of the 431 nm and 601 nm emission bands. The thermally sensitive emission features (denoted by an asterisk) are not completely removed. The λ_{Em} (max) corresponds to the 428 nm feature resultant from spectral overlap between the 1° and 2° sites. It is also evident in the left panel of Figure VII.13 that the emission intensity observed at 413 nm increases. This effect represents the increased formation of the blue (2°) site occurring with the removal of the 3° site.

The recorded excitation spectra allow the extraction of features present but not resolved in the absorption spectrum. As shown in Figure VII.14, the dominant z^6P state feature at 397.4 nm in the low metal loading samples is identified as the major, 1° site of isolation. The 2° site, identified at 380 nm corresponds to the weak band observed in absorption. However, the low-energy side of the absorption band cannot be reproduced by the excitation spectra. This is due to the presence of a Mn_2 absorption band occurring at 403 nm as concluded by the Mn/Ar concentration studies presented in Figure VI.I. It is noteworthy that spectra recorded following excitation at 403 nm do not produce any emission features.

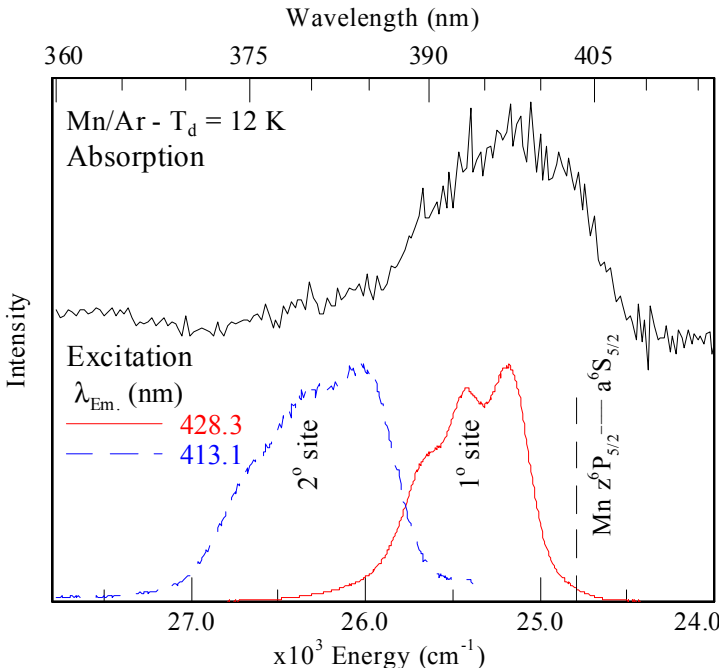

Figure VII.14 **Comparison of the band profiles identified from high-resolution excitation spectra recorded and absorption spectra recorded in the vicinity $z^6P_{5/2} \leftrightarrow a^6S_{5/2}$ transition of Mn for dilute Mn/Ar samples on deposition at 12 K.**

VII.2.II.I Mn(z^6P)/Ar Site-specific Emission Spectroscopy

Following the identification of two thermally stable Mn atom trapping sites, high-resolution emission spectra were recorded following site-specific excitation. Figure VII.15 presents the highest resolution spectra recorded with red (1°) and blue (2°) site excitation at 393.4 and 380 nm respectively. Upon inspection of the spectra recorded it is evident that the emission bands produced are very site specific. The red (1°) site gives rise to the very narrow emission centered at 427.5 nm and the asymmetric 590 nm[5] emission, while blue (2°) site excitation produces three broad emission bands located at 413, 438 and 625 nm. The additional features present at 431 and 601 nm have already been assigned to the excitation of the 3° thermally unstable site of isolation.

In the following two sections, the emission features produced with red and blue site excitation (shown in Figure VII.15) are treated separately. Excited state assignments are made based on I) comparisons of the spectral positions of the observed emission with respect to the gas phase transitions of atomic Mn (shown in Figure VII.1), and II) the results of time-resolved emission spectra produced with pulsed laser excitation and excited state lifetime measurements conducted using both

gated iCCD detection and TCSPC methods. Temperature dependence is also investigated to provide insight into the excited state dynamics leading the observed emission spectroscopy.

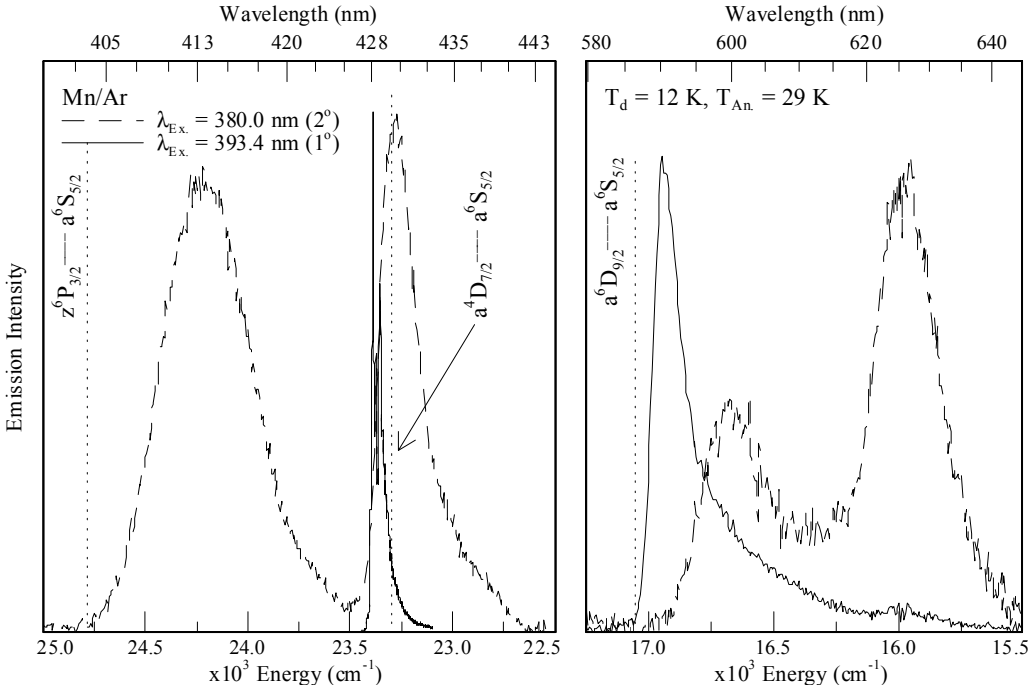

Figure VII.15 High resolution emission spectra recorded with site specific continuous lamp excitation at $\lambda_{Ex.}$ = 393.4 and 380 nm corresponding to the central threefold split component identified in the 1° and 2° site excitation spectra reported earlier in this Chapter. The locations of the gas phase $z^6P_{3/2} \leftrightarrow a^6S_{5/2}$, $a^4D_{7/2} \leftrightarrow a^6S_{5/2}$ and $a^6D_{9/2} \leftrightarrow a^6S_{5/2}$ transitions are indicated by the vertical lines.

VII.2.II.II Mn(z^6P)/Ar – Red (1°) site luminescence

Mn(z^6P)/Ar – Red Site - $\lambda_{Em.} \approx 427.5$ nm

High-resolution emission spectra produced with red site excitation at 393.4 nm produces multiple, narrow emission bands, the most intense of which is, as shown in Figure VII.16, located at 427.56 nm at 12 K. Two other resolved features are observed at 427.8 and 428.15 nm. The most intense 427.56 nm feature shows a linewidth of approximately 6.0 cm^{-1}. At higher temperatures, the splitting of the emission features is removed and a red shift of the band maximum to 427.65 nm is observed. However, the 428.2 nm shoulder persists to higher temperatures. The reduction of the intensity in the 427.56 nm feature at higher temperature is consistent with its identification as a zero phonon line (ZPL). The temperature dependence

observed for the 427.56 nm band was completely reversible with the original spectrum obtained on returning to 12 K.

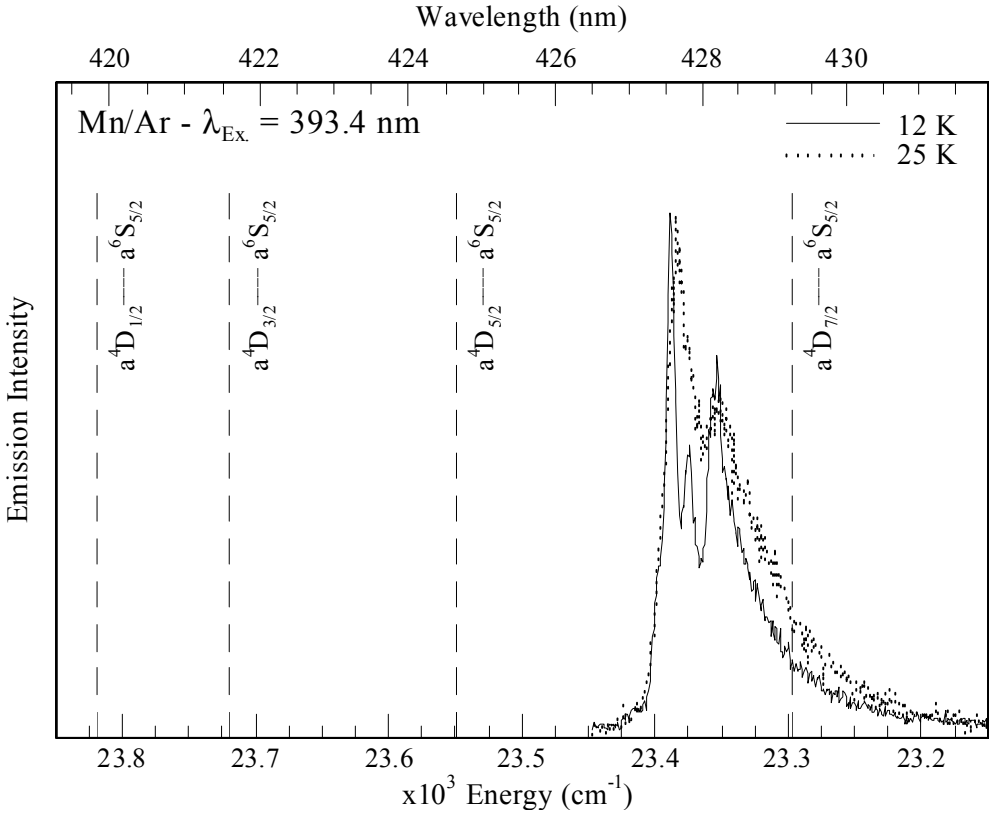

Figure VII.16 **Site specific high-resolution emission spectra produced with pulsed laser excitation at 393.4 nm at 12 K (solid) and 25 K (dashed) following Mn/Ar matrix deposition at 12 K and careful annealing to 30 K. The vertical lines indicate the location of the individual spin-orbit levels of the gas phase $a^4D_J \leftrightarrow a^6S_{5/2}$ transition.**

The location of the emission feature at approximately 427.56 nm (23388 cm^{-1}) and the narrow lines exhibited suggest an assignment to the $a^4D_{7/2} \rightarrow a^6S_{5/2}$ transition[1] of atomic manganese. With this assignment, the band at 427.56 nm is blue shifted from the gas phase position at 23297 cm^{-1} by only 92 cm^{-1}.

Time-resolved measurements allow the extraction of the decay characteristics of the resolved features at 427.56, 427.80 and 428.15 nm. Figure VII.17 presents a double exponential fit of the most intense 427.5(6) nm emission feature. This analysis revealed two decay times, 25.28 and 11.40 msec, the longer of which dominates by more than an order of magnitude. Temperature dependence measurements in the 427.5(6) nm decay profiles are shown in Figure VII.18. Inspection of the temporal profiles presented for temperatures from 12 K to 27 K (following deposition at 12 K and annealing to 28 K) reveals that the decay does not

remain constant over the range of temperatures selected. The decay times extracted at each temperature showed a decrease in both millisecond decay components with increasing temperatures (τ_1 ranged from 25.28 to 16.55 msec and τ_2 from 11.4 to 5.57 msec). The amplitude of the longer component remains an order of magnitude greater than that of the shorter component for temperatures from 12 K to 27 K. Plotting the τ_{obs} against temperature, as shown in Figure VII.18 (inset), reveals that the radiative lifetime (τ_{Rad}) has not been identified. Therefore, the radiative lifetime for the excited state giving rise to the 427.5(6) nm emission is longer than the 25.3 msec value measured at 12 K.

Analysis of the decay curves recorded for the 427.8 nm feature show the same behaviour as the dominant 427.5 nm feature. Double exponential functions were required to achieve an adequate fit of the decay profiles recorded at all temperatures accessible. The dominant decay component was found to have a lifetime of 25.23 msec and the minor had a value of 10.63 msec at 12 K. The relative amplitudes showed a marked deviation from those observed for the 427.5 nm feature insofar as the amplitude of the dominant feature was only a factor of four times that of the minor.

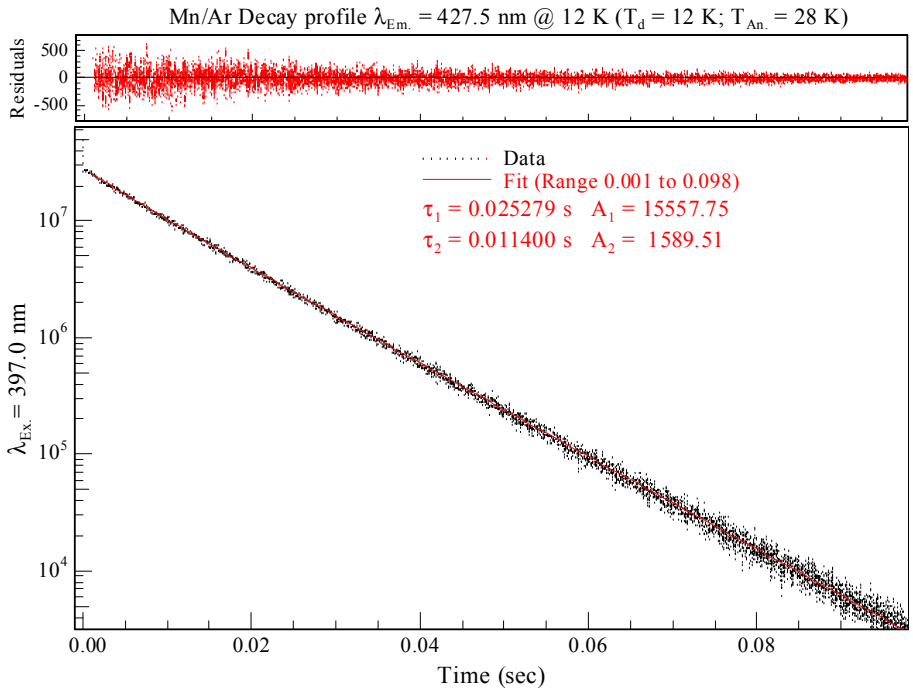

Figure VII.17 **Decay profile of the 427.5(6) nm emission recorded at 12 K using TCSPC following pulsed laser excitation at 397 nm, corresponding to the low energy threefold split component identified for the 1° site. The residuals present the difference between the double exponential fit completed and the decay recorded.**

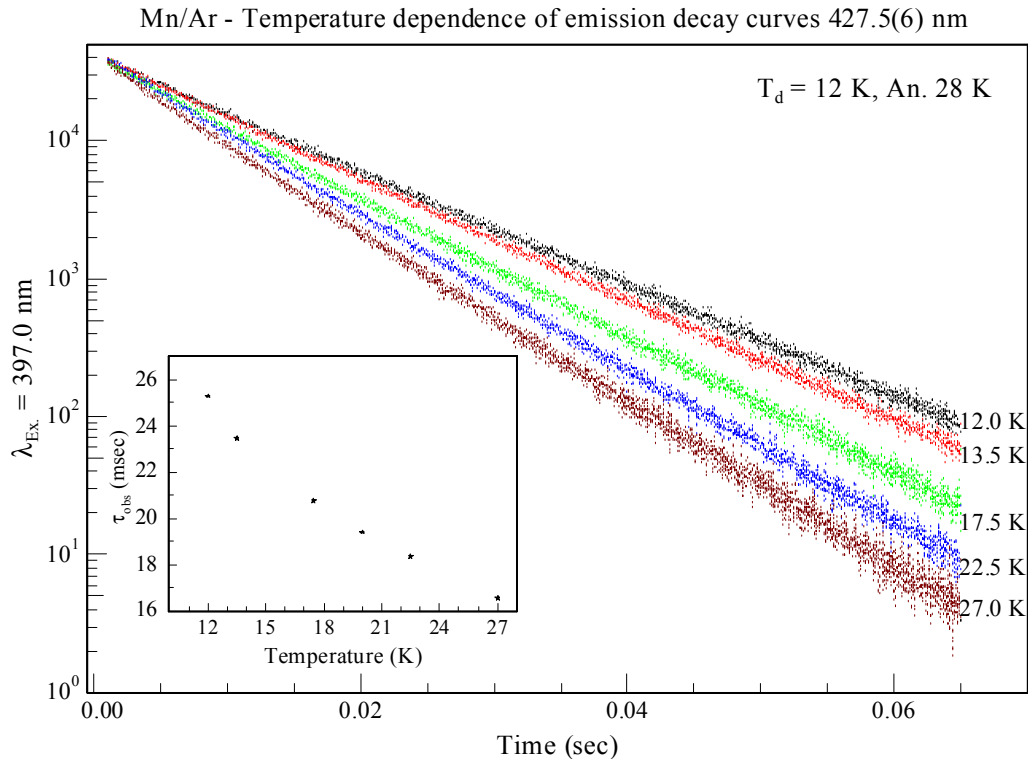

Figure VII.18 **Decay profiles recorded monitoring the 427.5(6) emission component produced with red site $z^6P_{5/2} \leftarrow a^6S_{5/2}$ excitation at 397 nm at various temperatures as indicated. Inset; temperature dependence of the observed excited state lifetime (τ_{obs}) extracted from double exponential fits of the decay profiles.**

Lifetime measurements of the resolved shoulder at 428.1 nm also required a double exponential fit with τ values of 23.4 and 10.43 msec at 12 K as shown in Figure VII.19. Both components were temperature dependent becoming shorter with increasing temperature as presented on the left hand side of Figure VII.20. It was observed that the shorter 10.43 msec component dominated the decay profiles of the 428.1 nm emission at all temperatures.

Overall the decay times of the 427.5 and 427.8 nm components are equivalent with observed matrix decay times of 25.28 and 25.23 msec respectively, whereas, the lifetime extracted for the 428.1 nm feature has a value of 10.43 msec. All the decay profiles exhibited a shortening of the extracted decay times with increasing temperature, as shown on the right of Figure VII.20. The decay times extracted at 12 K for the resolved emission features are collected in
Table VII.3 for comparison.

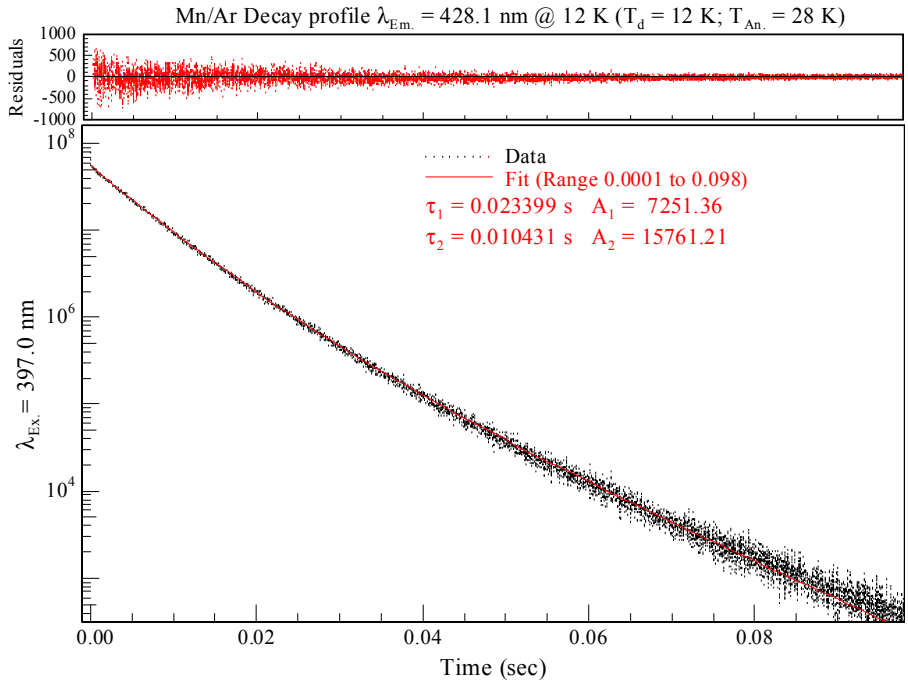

Figure VII.19 **Decay times recorded for the 428.1 nm emission at 12 K following site selective pulsed laser excitation of 1° site at 397 nm.**

Table VII.3 **Decay characteristics, components and amplitudes (A) extracted from double exponential fits of the three resolved features observed at ≈ 427.5 nm with red (1°) site excitation. Note the dominant decay time (τ_{Obs}) extracted at 12 K.**

$\lambda_{Em.}$ (nm)	A_1	τ_1 (msec)	A_2	τ_2 (msec)
427.5(6)	15558	**25.28**	1590	11.40
427.8	6849	**25.23**	2107	10.63
428.1	7251	23.40	15761	**10.43**

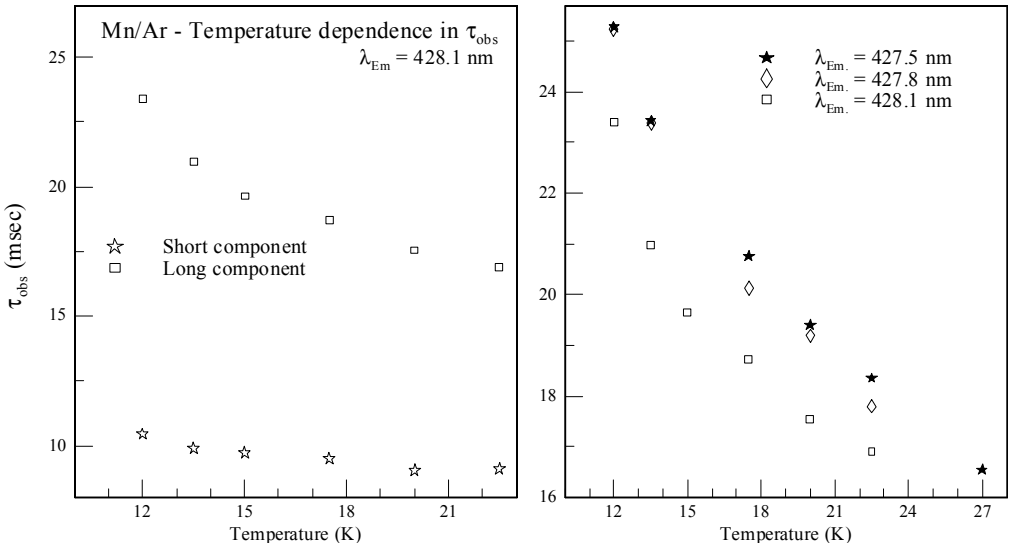

Figure VII.20 **Temperature dependence of the observed excited state lifetime (τ_{obs}) extracted from double exponential fits of the decay profiles recorded for $\lambda_{Em.}$ = 428.1 nm (shown left).**

Following the extraction of the decay characteristics of the resolved emission features observed at 427.5, 427.8 and 428.1 nm and the observation that the intensity of the narrow 427.5 nm band is reversibly reduced at higher temperatures, a Wp lineshape analysis was conducted using the resolved splitting between the observed features as a guide to the identification of the phonon frequency $\hbar\omega$, (cm^{-1}). The comparison between the predicted intensity distribution and the observed emission as a function of phonon number at 12 K and higher temperatures was used to access the quality of the analysis. As a first approximation, the emission band maximum at 427.56 nm (23388 cm^{-1}) was chosen as the band origin ($\nu_{0,0}$). The phonon frequency $\hbar\omega$ was selected as 32 cm^{-1} from the splitting observed between the most intense features at 12 K. The result of the Wp lineshape analysis is presented for temperatures of 12 and 25 K in Figure VII.21. The Wp lineshape provides an adequate fit of the intense features observed at 12 K and allows the identification of the zero phonon line as 23388 cm^{-1}. The 12 K fit, shown on the left of Figure VII.21, correctly predicts the relative intensities of the 427.56 nm (ZPL) and the 428.1 nm band assigned to the phonon side band using an electron-phonon coupling strength of S = 0.6 and a coupling frequency ($\hbar\omega$) of 32 cm^{-1}. Performing the analysis at a higher temperature (25 K) predicts a small increase in the intensity of the phonon side band with respect to the zero phonon line, both of which appear to the blue of the observed band maximum. The Wp analysis also reveals the presence of a 'hot' phonon emission band at 23420 cm^{-1} at 25 K. While the Wp lineshape analysis achieves good agreement at 12 K, not all of the resolved features are accounted for, most notably the feature at 427.8 nm. This is evident upon inspection of Figure VII.22, where Gaussian functions exhibiting linewidth of 6.6 cm^{-1}, corresponding to the *fwhm* of the ZPL identified at 23388 cm^{-1}, are shown. The fitted Gaussian functions have been substituted for the Wp positions and scaled to reflect the intensity distribution at 12 K. This was done by taking the Wp positions and intensities shown in the left panel of Figure VII.21, and broadening with a linewidth[6] of 6.6 cm^{-1}.

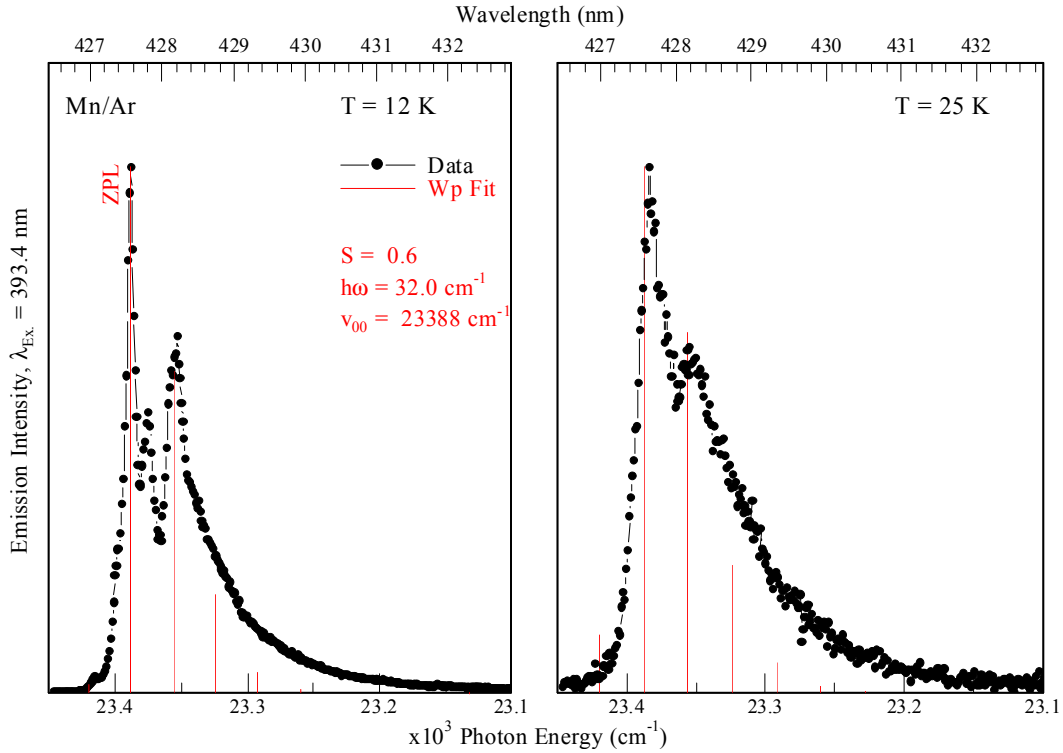

Figure VII.21 **The Wp lineshapes calculated with Equation III.4 for the resolved emission features observed in solid Ar at 12 K and 25 K produced with site specific pulsed laser excitation at 393.4 nm corresponding to the $z^6P_{5/2} \leftarrow a^6S_{5/2}$ transition from 1° site. The location of the zero phonon line is indicated as ZPL and $\nu_{0,0}$ in wavenumber units.**

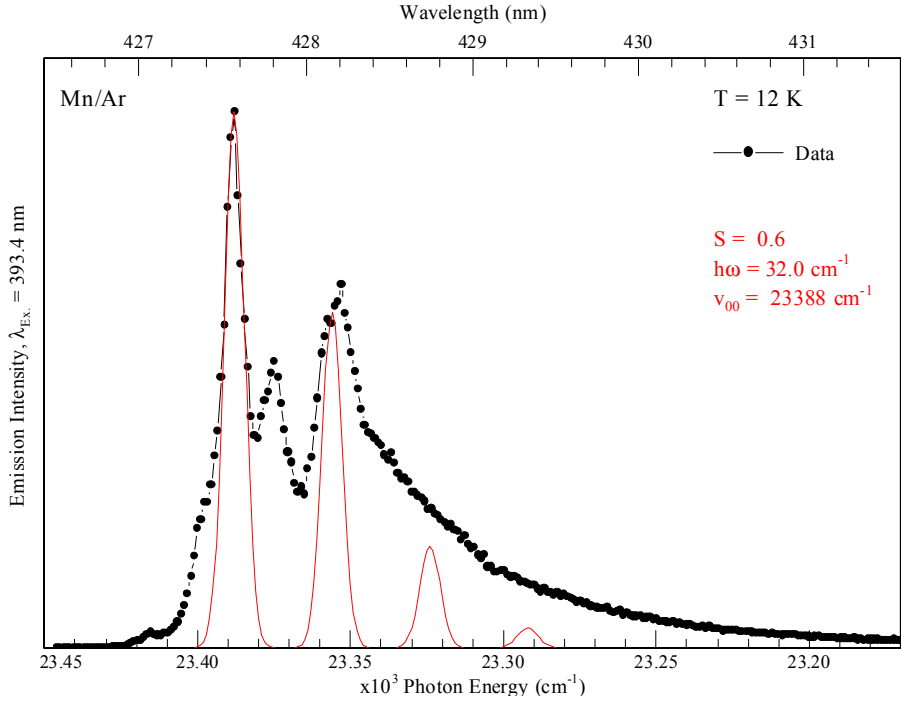

Figure VII.22 **Simulation of the emission band profile generated by the substitution of Gaussian functions for the Wp distribution as described in the text.**

A second Wp function was included for which $\nu_{0,0}$ = 23398 cm^{-1} was selected to coincide with the high-energy shoulder of the 12 K emission spectrum, (left, Figure VII.21). A phonon frequency of $\hbar\omega$ = 23 cm^{-1} was selected corresponding to the splitting between the new band origin and the 427.8 nm emission component. A satisfactory intensity distribution was achieved with S = 1.78 as shown in Figure VII.23. Table VII.4 presents the parameters used to achieve the Wp lineshape analyses (Wp Fit 1 and Wp Fit 2) shown in Figure VII.21 and Figure VII.23 respectively.

The second Wp lineshape analysis, the result of which is shown in Figure VII.23, provides an adequate fit of the observed intensity distribution observed in emission. The second ZPL is assigned at 23398 cm^{-1}, and the intensity distribution predicts the broad band profile and all but the resolved features identified in the first Wp analysis shown in Figure VII.21. However, the high temperature analysis presented in Figure VII.23 is superior as it allows the assignment of the phonon side band more accurately than in the previous attempt.

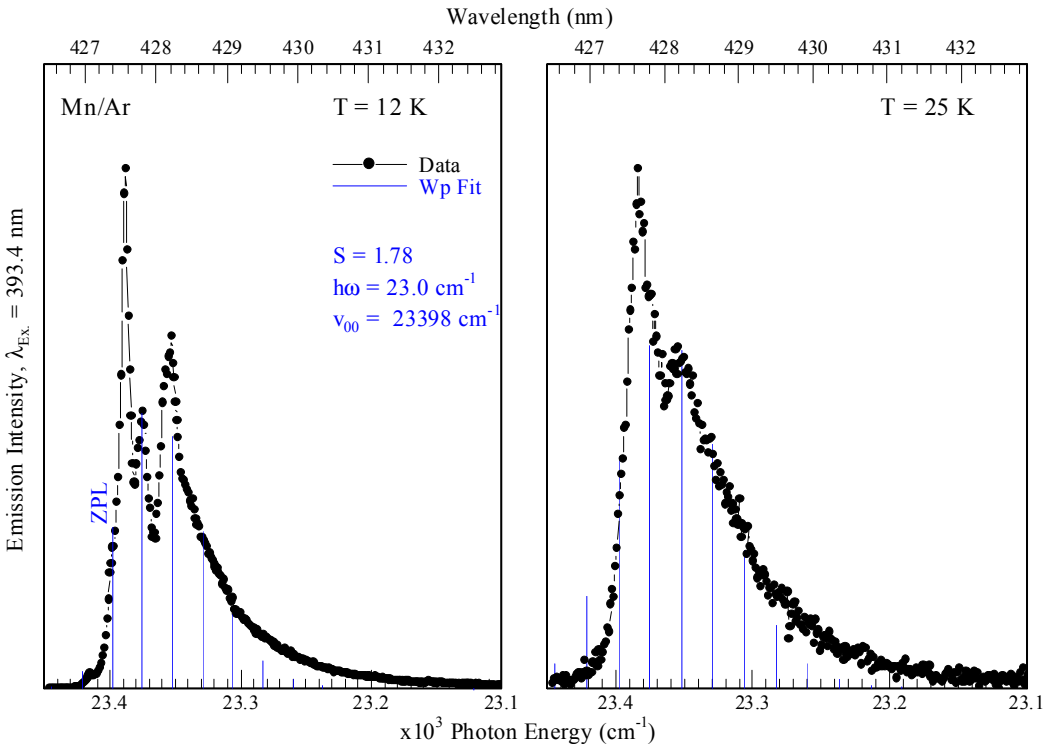

Figure VII.23 **The second Wp lineshapes calculated for the emission features observed in solid Ar but not accounted for in the original analysis shown in Figure VII.21 at 12 K and 25 K produced with site specific pulsed laser excitation at 393.4 nm corresponding to the $z^6P_{5/2} \leftarrow a^6S_{5/2}$ transition from the 1° site. The location of the second zero phonon line is indicated as ZPL. Note the intensity distribution predicted by the Wp analysis completed has been scaled to match the 427.8 nm feature at 12 K.**

Table VII.4 **The location of the ZPL's extracted in the Wp lineshape function analyses conducted on the atomic emission assigned to the $a^4D_{7/2} \rightarrow a^6S_{5/2}$ transition in solid Ar.**

Transition	*ZPL*, $\nu_{0,0}$ (cm^{-1})	*S*	$h,^{-}\omega$ (cm^{-1})
$a^4D_{7/2} \leftrightarrow a^6S_{5/2}$ - Wp Fit 1	23388	0.6	32
$a^4D_{7/2} \leftrightarrow a^6S_{5/2}$ - Wp Fit 2	23398	1.78	23

A summation of the intensity distributions broadened by a Gaussian function shows that two sets of Wp functions are required to generate the approximate emission band profile as shown in Figure VII.24. Inspection of the correspondence and the overlap of the Gaussian functions reveals a satisfactory fit of the high-energy side of the band profile. In addition, the presence of two sets of the Gaussian components, which are out of phase due to the different phonon frequencies, allows for explanation of the broad 428.1 nm feature. Therefore a combination of distinct electron–phonon interactions are assigned as the origin of the multiplet of resolved lines identified.

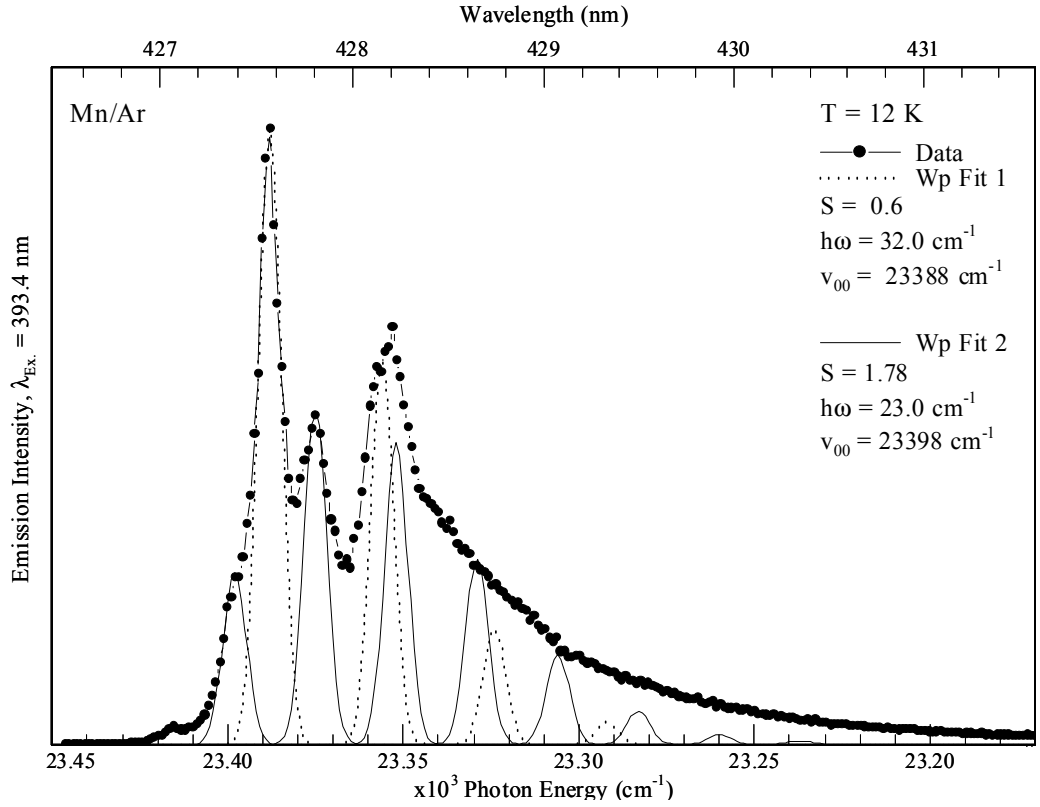

Figure VII.24 **Simulation of the emission band profile generated using Gaussian lineshapes (*fwhm* 6.6 cm^{-1}) for both of the Wp distributions identified as described in the text. The parameters and the positions of the two ZPL's ($\nu_{0,0}$) identified are indicated.**

The decay times extracted (shown in Table VII.3) for the 427.5 nm and 427.8 nm emission decay profiles are the same within the error of the present analysis. Identification of the radiative decay time was not possible due to a temperature dependence observed over the smallest increment at the lowest temperatures available, 12 K to 13.5 K, (Figure VII.20). The decay characteristics extracted show the observed excited state lifetime at 12 K is approximately 25 msec. This decay time is consistent with the assignment of the emission features to the spin and parity 'forbidden' $a^4D_{7/2} \rightarrow a^6S_{5/2}$ phosphorescent transition. In addition to these resolved features, the decay time of the 428.1 nm emission also exhibited marked temperature dependence where the observed lifetime was identified as 10.43 msec at 12 K. The temperature dependence in the decay profiles of the resolved features indicates the presence of an active, non-radiative decay component competing with the radiative decay of the excited state. Temperature dependence evident in the emission spectra allows the assignment of the 427.5 and 428.1 nm to a ZPL and phonon side band respectively. The 428.1 nm band persisted at higher temperatures, a characteristic indicative of a phonon side band, while the 427.5 nm band was removed at 25 K. The observation of a resolved feature at 427.65 nm at 25 K suggested the presence of a second ZPL and phonon sideband where the decay time extracted at higher temperatures showed an intermediate relationship between the relative amplitudes of the 25 and 10 msec decay components. The overlap of the ZPL and sideband is considered to be the origin of the double exponential decay profiles recorded.

The lineshape analysis of the emission band profile allowed the identification of a pair of ZPL's occurring at 23388 and 23398 cm^{-1}. The selection of two sets of oscillators for the transition allowed the simulation of the band profile as the sum of two intensity distributions exhibiting different electron-phonon coupling strengths. As presented in Figure VII.22 (and as summarised in Table VII.4) the combination of both intensity distributions per phonon allowed a good representation of the overall lineshape at 12 K.

Consideration of the decay characteristics presented in Table VII.3 in light of the Wp lineshape analysis, indicated the longer 25 msec component corresponds to that of a ZPL. Therefore, the decay time observed is a reflection of the radiative decay of the pure $a^4D \rightarrow a^6S$ electronic transition in the absence of phonon induced relaxation effects. In contrast, the 10 msec lifetime extracted from the decay profiles

of the 428.1 nm emission feature is representative of the decay of the excited state with the assistance of the local lattice environment, through phonon-induced excited state coupling. The relative electron-phonon coupling strengths and the spectral overlap of the individual Gaussian components (fitted to the Wp intensity distribution) are identified as the origin of the relative intensities of the bands assigned to the phonon sidebands at 427.65 and 428.1 nm. On inspection of Figure VII.21 and Figure VII.23, the Wp progression with the higher electron-phonon coupling (S = 1.78) dominated the low energy wing and the 428.1 nm feature at 25 K. The overlap between the ZPL of Wp Fit 1 at 23398 cm^{-1} with the phonon side band from the second Wp set may bias the relative intensities of the decay characteristics even at higher temperature. Therefore, double exponential functions were required to achieve adequate fits of the decay profiles recorded. The observation that the 10 msec decay component increases in importance monitoring the emission features from 427.65 to 428.1 nm is assigned to the effect of the increased overlap with the phonon sidebands.

The origin of two ZPL's and their associated phonon frequencies is not immediately obvious. Some possibilities are now suggested and the deficiencies of each are discussed. The observation of two sets of bands could result from atoms isolated in different sites, in which case the Wp fits would reflect the interaction of the excited state Mn atom and the site of isolation. However, the emission features are only produced from the red (1°) site with narrow line laser excitation. This rules the sites explanation out. The assignment of the transition to the relaxation of more than one spin-orbit level of the a^4D excited state of atomic manganese is unlikely given that the gas phase spin-orbit splittings[1] for the different states are 253.5, 170.3 and 99.0 cm^{-1} respectively between the $^7/_2$, $^5/_2$, $^3/_2$ and $^1/_2$ levels, as shown in Figure VII.16. These splittings are large when compared to the 10 cm^{-1} splitting between the observed bands. Assuming, the gas phase spin-orbit splitting is maintained within the matrix environment, thermal population of the J = $^5/_2$ level 253.5 cm^{-1} higher than the $a^4D_{7/2}$, is insignificant at temperatures of 12 K. In addition, the decay times recorded for the 427.5 and 427.8 nm emission lines at 12 K are equal confirming the same electronic transition gives rise to the observed features. The final option involves crystal field splitting of the J = $^7/_2$ level of the ^{4}D state by the site of isolation. Thus the crystal field splitting observed is small (10 cm^{-1}) corresponding to the difference

in energy between the two ZPL's identified. This effect may be manifested by the Mn atom in a 'D' state when isolated in either a site of octahedral or tetrahedral symmetry.

Mn(z^6P)/Ar - Red Site - $\lambda_{Em.} \approx 590.0$ nm

Emission spectra recorded with 393.4 nm excitation results in the production of the weak 590 nm (16949 cm^{-1}) feature shown Figure VII.15. The red shoulder observed upon sample deposition at 12 K was previously identified as resulting from isolation of Mn atoms in thermally unstable (3°) sites of isolation. The 590 nm emission feature exhibits an asymmetric lineshape that may be an intrinsic characteristic or a result of spectral overlap of the excitation of the 1° and 3° sites leading to the production of the 600 nm emission. However annealing allowed the removal of the 3° site. Therefore, the asymmetric lineshape is assigned to an intrinsic characteristic of the electronic transition involved. A Wp lineshape analysis of the 590 nm emission band profile was preformed using $\hbar\omega$ = 32 cm^{-1}, S = 3.3 and assigning the $\nu_{0,0}$ = 17020 cm^{-1} (587.54 nm). The result of this analysis is presented in Figure VII.25. As no narrow resolved emission features are observed to identify the phonon frequency ($\hbar\omega$), the result of the Wp fit (Fit 2) of the 427.5 nm emission feature (presented in Figure VII.23) was employed. Recording the emission spectrum at various temperatures showed no pronounced changes in the observed band profile. From a comparison of the Wp intensity distribution and the emission profile shown in Figure VII.25 it is evident that an adequate fit of the high-energy side of the observed band profile is provided.

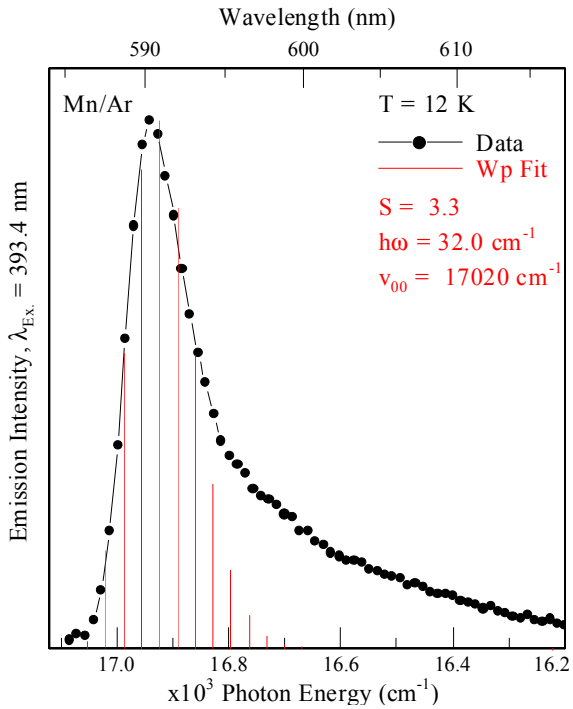

Figure VII.25 **The Wp lineshapes calculated for the 590 nm emission feature at 12 K, produced with steady state excitation at 393.4 nm corresponding to the $z^6P_{5/2} \leftarrow a^6S_{5/2}$ transition from red (1°) site. The location of the zero phonon line (ZPL) for the transition is indicated numerically as $\nu_{0,0}$ in wavenumber units.**

Decay profiles recorded for the 590 nm emission band following pulsed laser excitation at 397 nm, revealed complex multi-exponential decays. Excited state lifetimes were extracted using triple exponential functions to fit of the decay profiles. Figure VII.26 shows the decay profile recorded at 12 K, following annealing to 28 K. Three decay components are identified as 654 μsec, 21.895 and 6.841 msec at 12 K. A comparison of the amplitudes shown in Figure VII.26 identifies the microsecond lifetime as the dominant component in the decay profile.

At 12 K, the two smaller amplitudes A_1 and A_2, Figure VII.26, contribute 26 and 17 % of the overall temporal intensity of the emission. The decay times of these components show a match to the decay characteristics of the 427.5 nm emission presented in Table VII.3. The two msec components on the 427.5 nm band were identified as 25.28 and 11.4 msec somewhat longer than the 22 and 7 msec values identified in the 590 nm emission. The correlation of the two msec decay times extracted on these two emission bands suggests the presence of non-radiative relaxation from the $a^4D_{7/2}$ state to the terminal level producing the 590 nm emission[7]. The temperature dependence exhibited by the 427.5 nm band (Figure VII.18) is also

observed for both the msec components in the 590 nm band. The decay profiles recorded in the temperature range 12 to 22.5 K are presented in Figure VII.27.

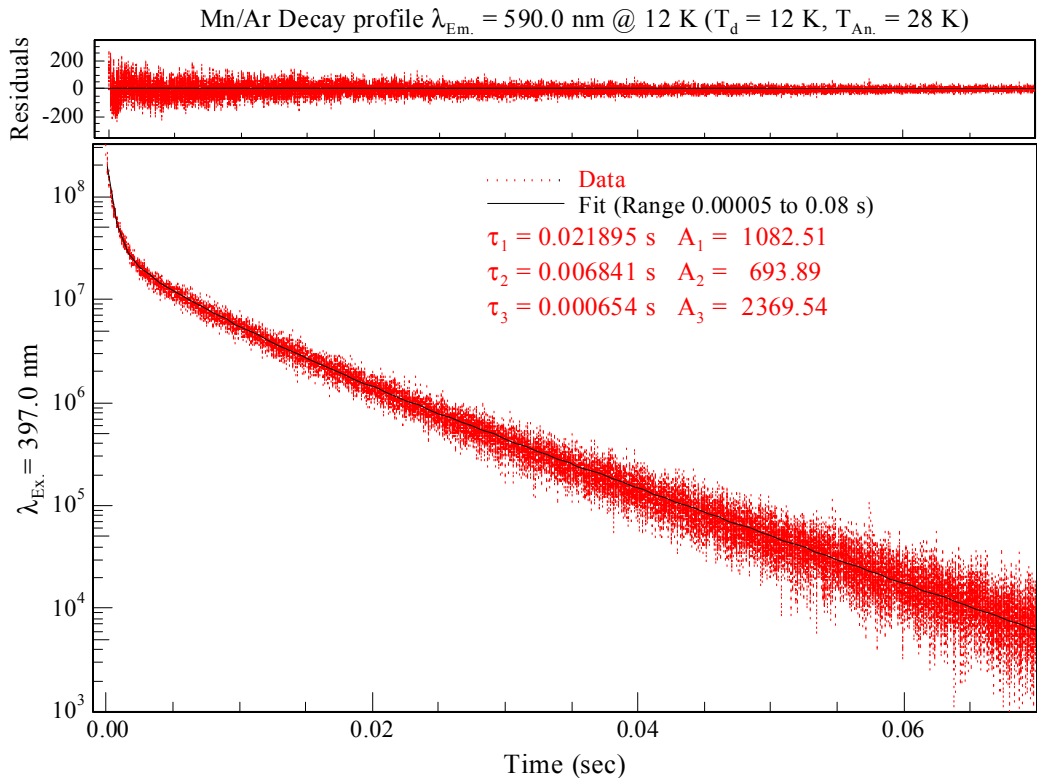

Figure VII.26 **Decay profile recorded for the 590 nm emission feature at 12 K following site selective pulsed laser excitation of red (1°) site at 397 nm.**

Table VII.5 **Decay characteristics, components and amplitudes (A) extracted from non-linear least squares analysis of the temporal profiles recorded monitoring emission at 590 nm at different temperatures, (T_s) following pulsed laser excitation at 397 nm. Note the dominant decay contribution is presented in bold.**

T_s. (K)	Fit Range (sec)	A_1	τ_1 (msec)	A_2	τ_2 (msec)	A_3	τ_3 (μsec)
12.0	5 x10^{-5} – 0.080	1083	21.895	694	6.841	**2370**	**654**
12.0	5 x10^{-5} – 0.045	1309	19.574	562	4.369	**2306**	**613**
13.5		2283	16.664	1378	2.380	**4302**	**534**
17.5		272	16.764	226	1.843	**537**	**509**
20.0	5 x10^{-5} – 0.030	7093	14.864	**12985**	**1.096**	11473	343
22.5	5 x10^{-5} – 0.032	1449	13.895	**4605**	**0.941**	2876	283

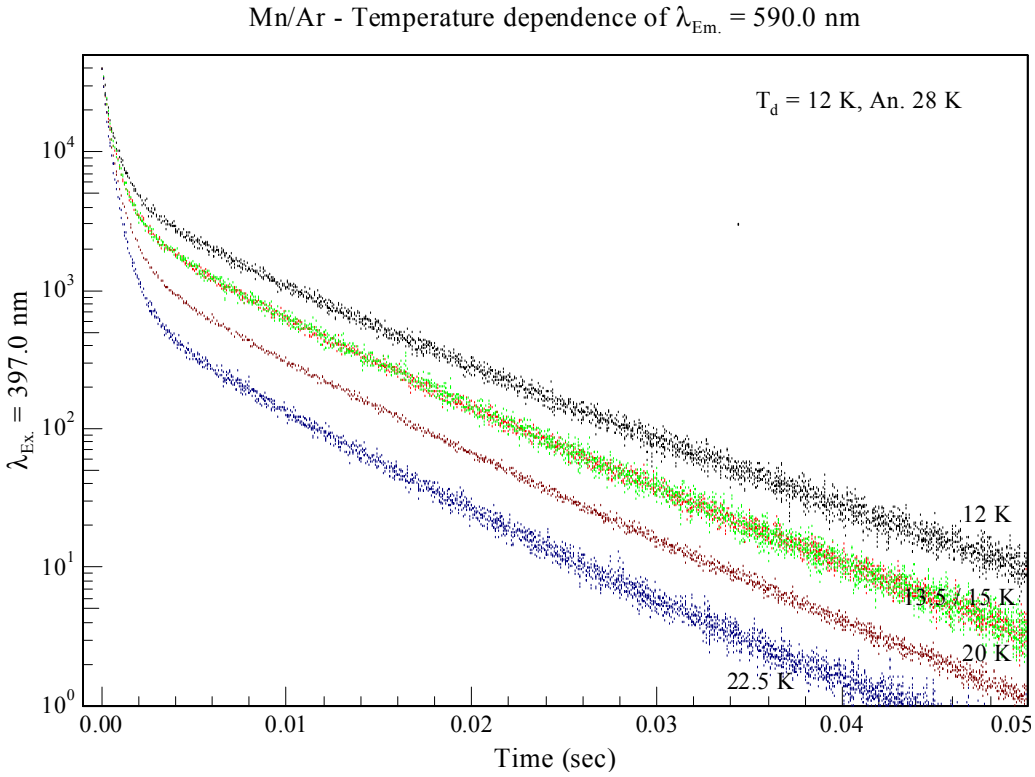

Figure VII.27 **Comparison of the excited state decay profiles produced monitoring 590 nm emission following pulsed laser excitation at 397 nm. $\lambda_{Ex.}$ corresponds to the red threefold split component of the excitation spectrum corresponding to the $z^6P_{5/2} \leftarrow a^6S_{5/2}$ transition occurring for atomic manganese isolated in the 1° site in solid Ar.**

The 590 nm emission is exhibits a red matrix shift of 1453 cm^{-1} and 103 cm^{-1} from the $z^8P_{5/2} \leftrightarrow a^6S_{5/2}$ and $a^6D_{9/2} \leftrightarrow a^6S_{5/2}$ transitions which occur at 543.4 nm (18402 cm^{-1}) and 586.43 nm (17052 cm^{-1}) respectively in the gas phase[1]. The Wp lineshape analysis preformed, (Figure VII.25) succeeded in predicting the asymmetric bandshape using an electron-phonon coupling strength of S = 3.3. The small S value suggests a weak electron-phonon coupling, indicative of a D $\rightarrow$ S type electronic transition. The Wp fit calculated the band origin for the transition to occur at $\nu_{0,0}$ = 17020 cm^{-1}, blue-shifted by only 32.0 cm^{-1} from the gas phase $a^6D_{9/2} \leftrightarrow a^6S_{5/2}$ transition at 586.53 nm (17052.29 cm^{-1}). Therefore, the spectral position and the asymmetry of the observed emission lineshape and the weak electron-phonon coupling provide strong evidence for the assignment of the 590 nm emission feature to that of the radiative relaxation of the metastable a^6D state.

However, the complicated decay characteristics of the 590 nm feature do not allow a definitive assignment to that of the $a^6D_{9/2} \rightarrow a^6S_{5/2}$ transition which has a theoretically predicted gas phase lifetime of 3.4 sec[3]. The decay components

observed at 12 K presented in Table VII.5 are all substantially longer than the gas phase lifetime for the $z^8P_{5/2} \leftrightarrow a^6S_{5/2}$ transition reported to be 165.5 μsec[8]. All of the decay components extracted for the excited state relaxation are in excess of this value strengthening the assignment to the metastable emission, which has been shortened dramatically by the matrix environment.

Although complicated by multiple feeding processes the assignment of the 590 nm emission to the $a^6D_{9/2} \rightarrow a^6S_{5/2}$ transition produced by relaxation from the a^4D state following resonance $z^6P_{5/2}$ excitation in solid Ar is preferred. Following direct a^6D excitation, the results of which are presented in Chapter VIII, the 590 nm emission feature has been assigned to the $a^6D_{9/2} \rightarrow a^6S_{5/2}$ transition.

VII.2.II.III Mn(z^6P)/Ar – Blue (2°) site luminescence

Atomic manganese occupies another high symmetry, thermally stable site of isolation that was identified in optical excitation spectra (Figure VII.13) at 380 nm. In this section the observed steady-state and time-resolved emission spectroscopy and excited state decay measurements are presented to assign the observed features. Temperature dependent emission spectra and lifetime measurements made with site-specific lamp and laser excitation are employed to assign the excited states as conducted in the previous section for the red (1°) site. The emission features produced with blue (2°) site excitation are located at 413, 438 and 625 nm as shown earlier in Figure VII.13. The experimental data recorded for each of these emission bands are presented separately in the following sections.

Mn(z^6P)/Ar - Blue Site - $\lambda_{Em.}$ = 413.0 nm

Figure VII.28 presents a comparison of time-integrated vs. time-gated emission spectra recorded with excitation at 380 nm corresponding to the central threefold split component identified in high-resolution excitation spectra shown Figure VII.14. The 413 nm feature exhibits a broad lineshape as shown by the dashed trace, Figure VII.28. Features centered at 431 and 438 nm are also present in the emission spectrum recorded in the 400 – 460 nm region. The 431 nm feature is present due to residue of the 3° site of isolation, some of which remains after matrix annealing to 30 K. The 438 nm feature is resultant from manganese atoms isolated in the 2° site and

is discussed at length in the section which directly follows. The time-gated emission spectra show the 432 (red shifted slightly) and 438 nm features but with the notable absence of the 413 nm feature. Time gating is intrinsic in emission spectra recorded with pulsed laser excitation and monitored with the photon counting PMT. It was used in Chapter III to enhance the weak Hg $^3P_0 \rightarrow {}^1S_0$ emission from the strong background $^3P_1 \rightarrow {}^1S_0$ fluorescence. Therefore, the absence of the 413 nm emission feature in Figure VII.28 reveals the short lived nature of this band and suggests its assignment to the z^6P state. The gas phase[1] $z^6P_{3/2} \leftrightarrow a^6S_{5/2}$ transition occurs at 403.56 nm (24779.32 cm^{-1}) and exhibits a nanosecond lifetime in the range 63.29 nsec[8] to 66.1 ± 1.4 nsec[9] depending on the literature cited.

Time-integrated emission spectra recorded at higher temperatures than 12 K following matrix annealing (although not presented) revealed that the emission intensity of the 413 nm feature decreased progressively with increasing temperature. This effect was completely reversible indicating the presence of a non-radiative step competing with the radiative process at temperatures above 16 K.

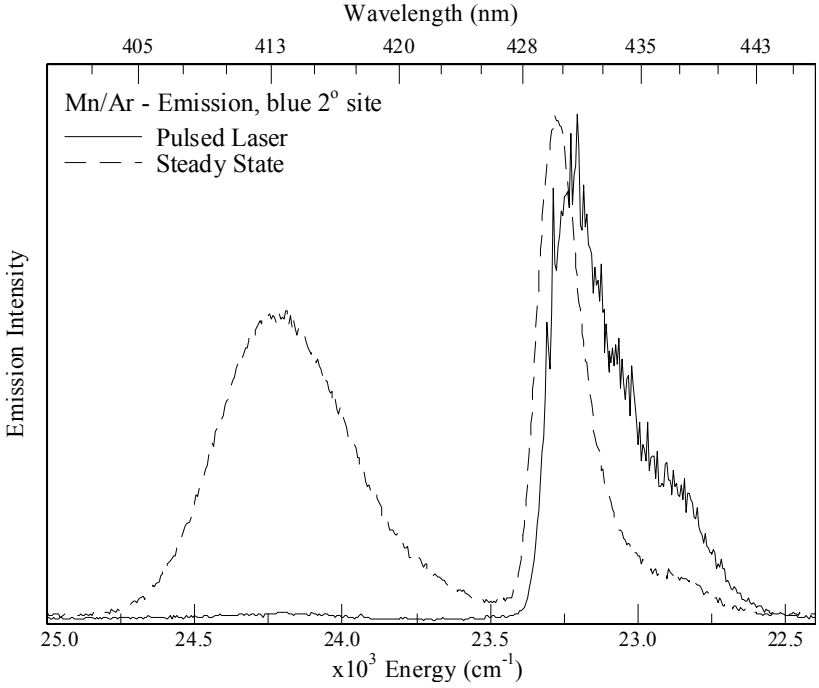

Figure VII.28 **Time-integrated and time-gated emission spectra recorded following site specific continuous W lamp and pulsed laser excitation at 380 nm. The excitation wavelength corresponds to the central threefold split component identified in Figure VII.10. Note the time gating is achieved using a single photon counting PMT as the outlined in Chapter II, Experimental.**

Figure VII.29 presents time-resolved emission spectra recorded using iCCD detection with pulsed laser excitation showing the behaviour of the emission intensity as a function of time on a nanosecond scale. The intensity of the 413 nm band maximum drops to approximately zero over the range 0 to 100 nsec as shown in Figure VII.29 consistent with the time-gated spectra shown in Figure VII.28. The temporal decay characteristics of the 413 nm emission band were extracted from the time-resolved emission spectra using the method outlined in Chapter II, Experimental. This analysis yielded the decay profile shown in Figure VII.30 at 12 K. A double exponential function was used to fit the emission decay curve. Two components of 28 and 10.5 nsec of equal weighting were identified. The temperature dependence in the decay profiles recorded for the 413 nm emission band is shown in Figure VII.31. The 12 and 15 K decay curves in Figure VII.31 are identical as are the extracted lifetime values, listed in Table VII.6. This observation allows the identification of the matrix radiative lifetime (τ_{Rad}) for the $z^6P_{3/2} \rightarrow a^6S_{5/2}$ transition to τ = 28 and 10.5 nsec.

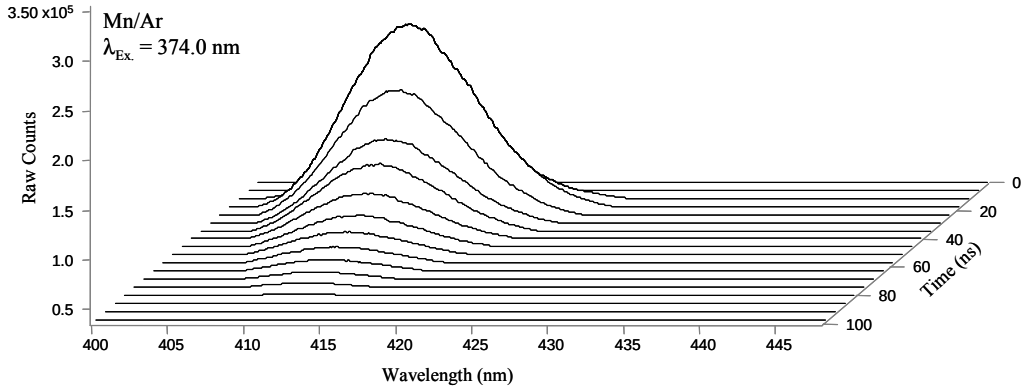

Figure VII.29 Time-resolved emission spectrum recorded monitoring $\lambda_{Em.}$ = 413 nm (at 12 K) following pulsed laser excitation at $\lambda_{Ex.}$ = 374 nm. The temporal step and gate width used was 10 nsec with a delay time of t_d = 0.0 nsec.

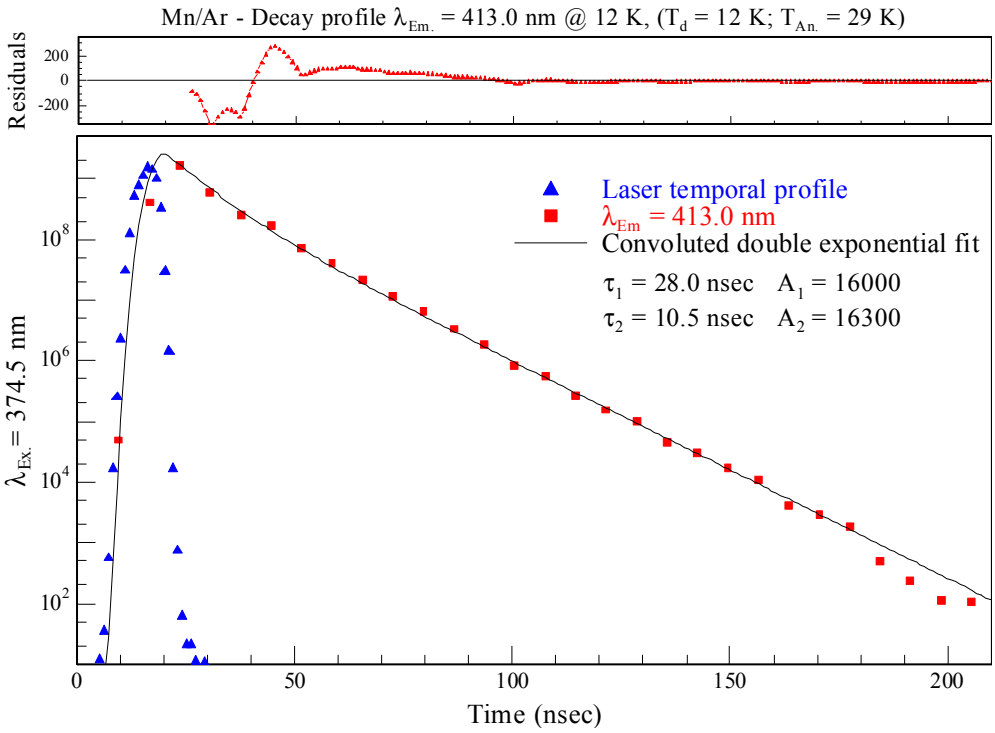

Figure VII.30 **Decay profile of the 413 emission feature recorded at 12 K extracted from time–resolved emission spectrum, Figure VII.29. The decay profile is convoluted with the temporal profile of the excitation laser source at 374.5 nm. The residual shown represents the difference between the decay recorded and the double exponential fit.**

Double exponential functions were required to provide adequate fits of all the decay profiles recorded in the temperature range from 12 K to 24 K. The lifetimes extracted from these decay profiles at all of the temperatures recorded are presented in Table VII.6. Upon inspection of Table VII.6 it is evident that the amplitudes of the nanosecond lifetimes (τ_1 and τ_2) are within 95% of each other at temperatures up to 19 K where a large deviation is observed and the shorter component dominates.

Table VII.6 **Excited state lifetimes (τ_{obs}) and amplitudes (A) extracted using a double exponential function convoluted with the laser temporal profile to fit the decay curves recorded monitoring the 413 nm emission at different temperatures, (T_s) following pulsed laser excitation at 374.5 nm. Note the dominant decay contribution is presented in bold.**

T_s. (K)	Fit Range (nsec)	A_1	τ_1 (nsec)	A_2	τ_2 (nsec)
12.0	0 – 210	16000	28.0	**16300**	**10.5**
15.0	0 – 210	16000	28.0	**16300**	**10.5**
19.0	0 – 190	13500	22.0	**14000**	**08.0**
24.0	0 – 090	09500	14.5	**14000**	**07.5**

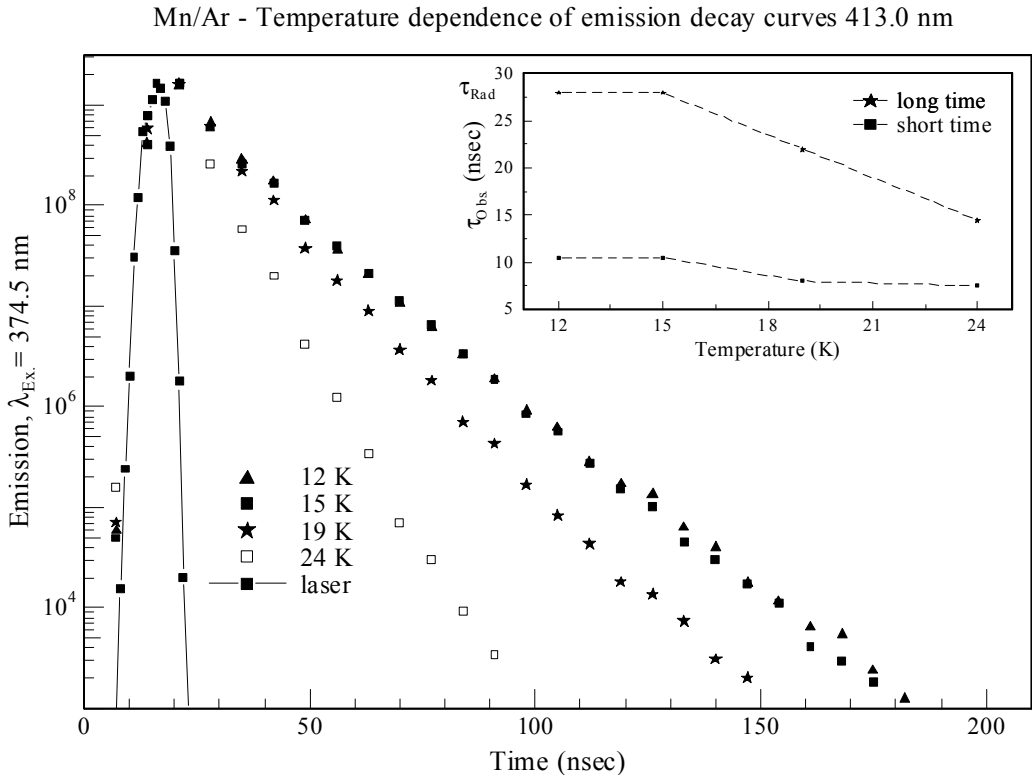

Figure VII.31 **Comparison of the excited state decay profiles produced monitoring the 413 nm emission following pulsed laser excitation at 374.5 nm at various temperatures as indicated. The temporal profile of the excitation source at 374.5 nm is also shown. The Temperature dependence of the observed excited state lifetimes (τ_{obs}) extracted using a double exponential analysis of the decay profiles recorded is shown; Inset.**

The excited state lifetime measurements are consistent with the assignment of the 413 nm emission feature to the $z^6P_{3/2} \rightarrow a^6S_{5/2}$ transition, insofar as the decay occurs on a nanosecond timescale corresponding to the fully allowed transition. However, the presence of two components is difficult to resolve. Figure VII.31 inset shows a plot of the observed lifetimes against scan temperature, the intercept with the y-axis represents the radiative lifetime uncorrected for the effective field of solid Ar. Applying the effective field correction using Equation III.1 to the observed matrix radiative decays at 12 K requires the refractive index of solid Ar known to be 1.32[10]. Therefore, τ_{Rad} for the $z^6P_{3/2} \rightarrow a^6S_{5/2}$ transition is 57.5 and 21.6 nsec in solid Ar. The longer decay component (57.5 nsec) compares well to the known gas phase value of 66.1 ± 1.4 nsec[9].

Lineshape analyses of the 413 nm emission resulting from $z^6P_{5/2} \leftarrow a^6S_{5/2}$ continuous lamp excitation at 12 and 22 K are presented in Figure VII.32. Using a phonon frequency of $\hbar\omega$ = 44 cm^{-1}, a satisfactory fit of the lineshape was achieved

using a high electron-phonon coupling S term of 23. This allowed the identification of $\nu_{0,0}$ = 25200 cm^{-1}, (396.8 nm). The position identified for the zero-phonon line ($\nu_{0,0}$) shows good agreement with the blue (2°) site absorption of the $z^6P_{5/2} \leftarrow a^6S_{5/2}$ transition shown in Figure VII.10.

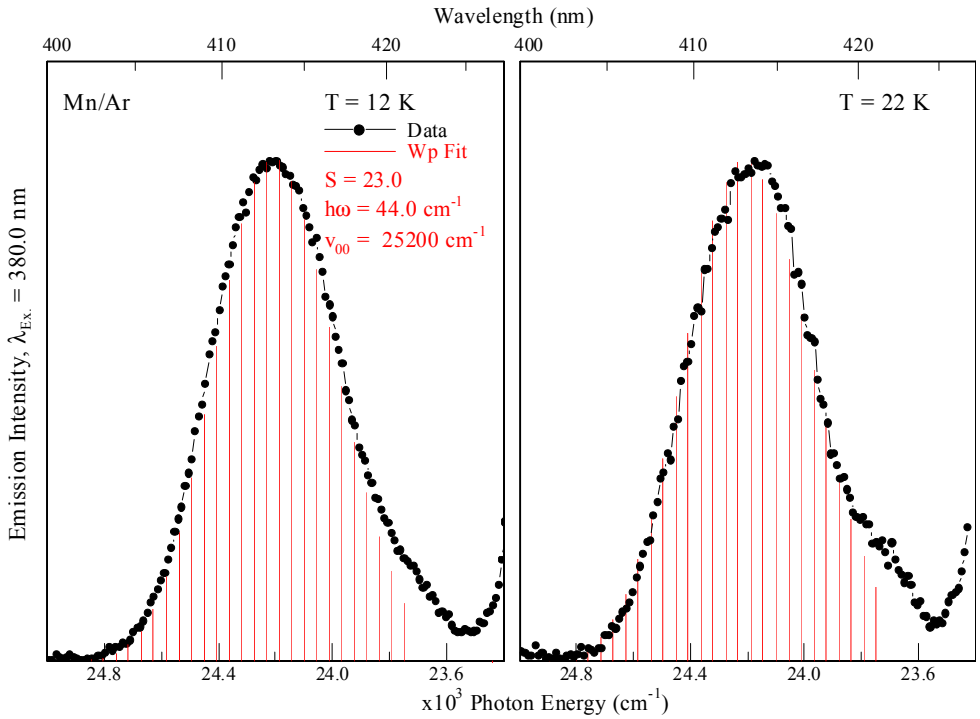

Figure VII.32 The Wp lineshapes calculated for the emission feature assigned to the $z^6P_{3/2} \rightarrow a^6S_{5/2}$ transition of atomic Mn isolated in solid Ar at 12 K and 22 K.

Mn(z^6P)/Ar - 2° Site - $\lambda_{Em.}$ = 438.0 nm

A time-resolved emission spectrum, shown in Figure VII.33, recorded with pulsed laser excitation of the $z^6P_{5/2} \leftarrow a^6S_{5/2}$ transition at 374.4 nm revealed the broad 438 nm emission to be long lived, persisting up to 95 msec. Inspection of the time-integrated emission spectrum presented in Figure VII.33 shows the weak emission intensity of the 438 nm band. The broad emission linewidth (*fwhm*) of ≈230 cm^{-1}, coupled with the lack of resolved structure suggests a P → S type electronic transition. However, the 413 nm emission has already been identified as the $z^6P_{3/2}$ state fluorescence, so it is proposed that the 438 nm emission results from the relaxation of the $a^4D_{7/2}$ state red shifted from the gas phase position by 466 cm^{-1}. This assignment also poses difficulties as no resolved narrow lines are evident in the emission band profile, in contrast to the 427.5 nm feature, assigned to the $a^4D_{7/2} \rightarrow$

$a^6S_{5/2}$ transition. The latter occurs for Mn atoms isolated in the red (1°) site and showed resolved features. Also, the large gas phase to matrix red-shift exhibited by the 438 nm emission is difficult to reconcile for a D → S type electronic transition.

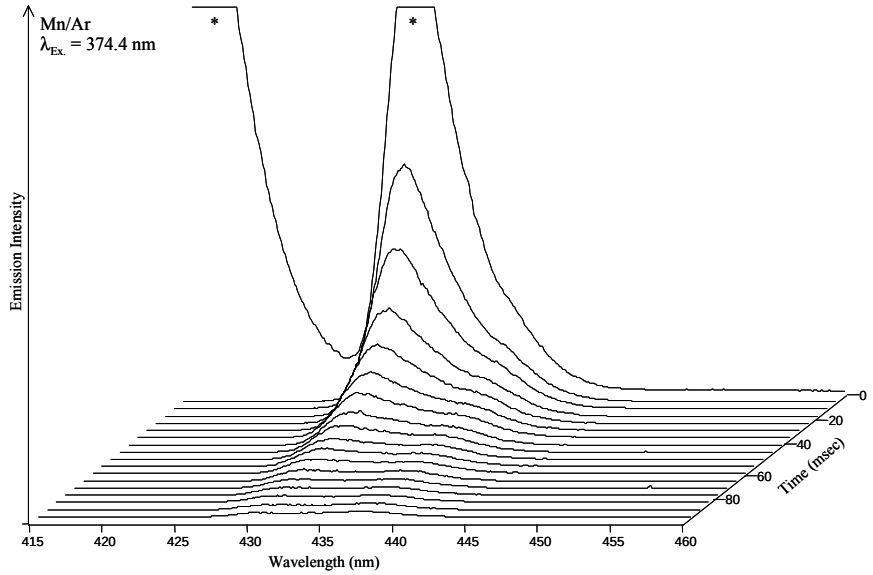

Figure VII.33 Time resolved emission spectrum recorded following pulsed laser excitation into the blue (2°) site $z^6P_{5/2} \leftarrow a^6S_{5/2}$ absorption at 374.5 nm, using iCCD detection. Note the asterisk represents the positions of the emission band maxima at 413 and 431 nm which have been removed for presentation purposes.

The long-lived nature of the 438 nm emission supports its assignment to the $a^4D_{7/2} \rightarrow a^6S_{5/2}$ transition but, a conclusive assignment of this emission feature to either the $z^6P_{3/2} \rightarrow a^6S_{5/2}$ or $a^4D_{7/2} \rightarrow a^6S_{5/2}$ transitions is not possible, at present.

Mn(z^6P)/Ar - 2° Site - $\lambda_{Em.}$ = 625.0 nm

Figure VII.34 presents emission spectra in the 600 nm region produced with red (1°) and blue (2°) site excitation. Three emission features are observed at 590, 601 and 625 nm, of which the 601 nm feature is thermally unstable as revealed by matrix annealing, see Figure VII.13. The high-resolution excitation spectra recorded near the $z^6P_{5/2} \leftrightarrow a^6S_{5/2}$ gas phase transition (see Figure VII.10) indicated that each emission feature is produced by excitation of Mn atoms in different sites of isolation. The 625 nm band is produced by blue (2°) site excitation and exhibits a broad linewidth (*fwhm*) of 285 cm^{-1}. The band profile observed is indicative of an P → S type electronic transition consistent with the assignment of the emission feature to the $z^8P_{5/2} \rightarrow a^6S_{5/2}$ transition of atomic manganese. With this assignment the 625 nm

band is red shifted from the gas phase position (543.4 nm)[1] by 2402 cm^{-1} – a rather large amount for Ar matrices.

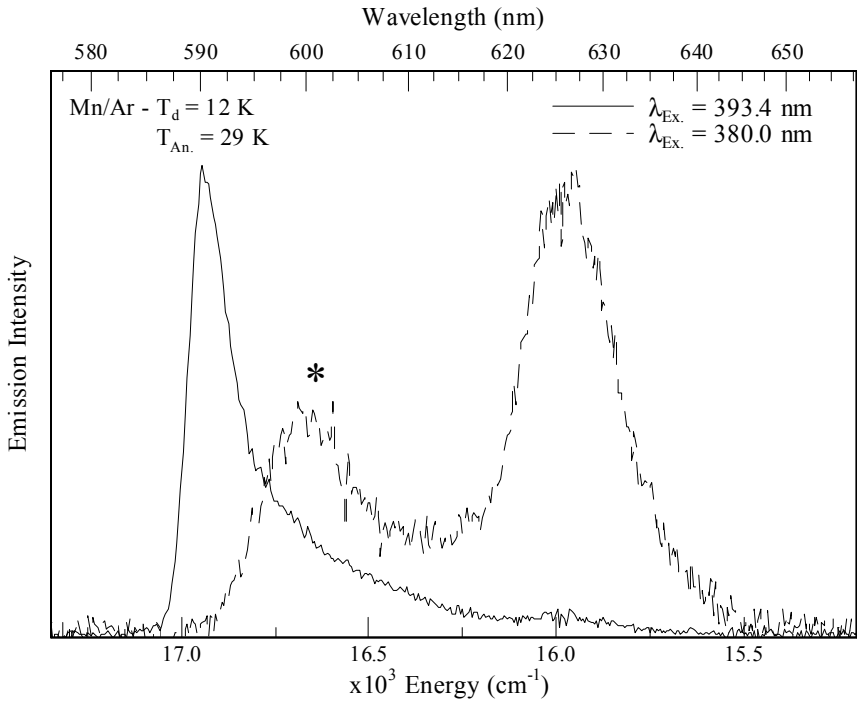

Figure VII.34 Time-integrated emission spectra recorded with red (1°) and blue (2°) site excitation at 393.4 and 380 nm respectively. Spectral overlap of the thermally stable red and blue sites with the thermally labile third site results in the production of the 601 nm emission with both excitation wavelengths chosen. The thermally unstable emission feature is denoted by the asterisk.

Applying the Wp lineshape analysis with the phonon frequency of $\hbar\omega$ = 44 cm^{-1}, used to model the 413 nm band assigned to the $z^6P_{3/2} \rightarrow a^6S_{5/2}$, a satisfactory fit of the intensity distribution of the observed band profile was achieved using a moderate electron-phonon coupling strength of S = 10. The band origin identified 16400 cm-1 is considerably to the red of the $z^8P_{3/2} \leftrightarrow a^6S_{5/2}$ transition, which occurs in the gas phase at 18402 cm^{-1}.

Figure VII.36 presents a decay profile recorded monitoring the emission at 625 nm employing the TCSPC technique. A triple exponential function was required to obtain an adequate fit of the decay profile. The decay times extracted are 168, 36 and 662 μsec all with substantial amplitudes. With the exception of the short 36 μsec component, all the decay times are longer than the gas phase lifetime for the $z^8P_{5/2} \rightarrow a^6S_{5/2}$ transition of atomic Mn of 149.3 μsec[8]. The temperature dependence in the 625 nm feature was not recorded.

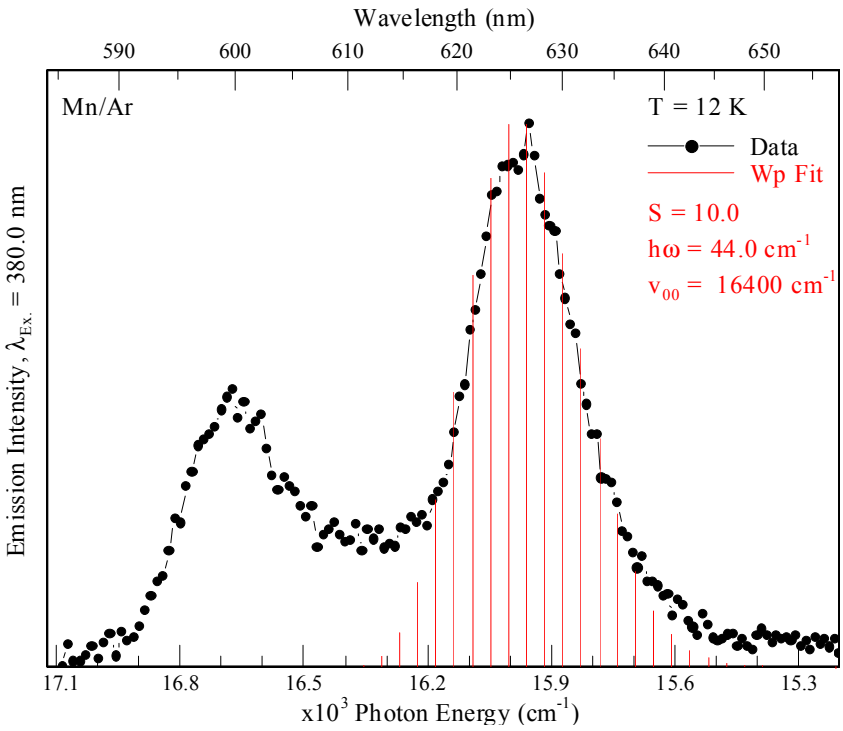

Figure VII.35 **The Wp lineshape calculated for the 625 nm emission feature in solid Ar at 12 K. The phonon frequency ($h,^{-}\omega$ = 44 cm^{-1}) was selected to match that used to fit the resonance $z^6P_{3/2} \rightarrow a^6S_{5/2}$ transition, Figure VII.32.**

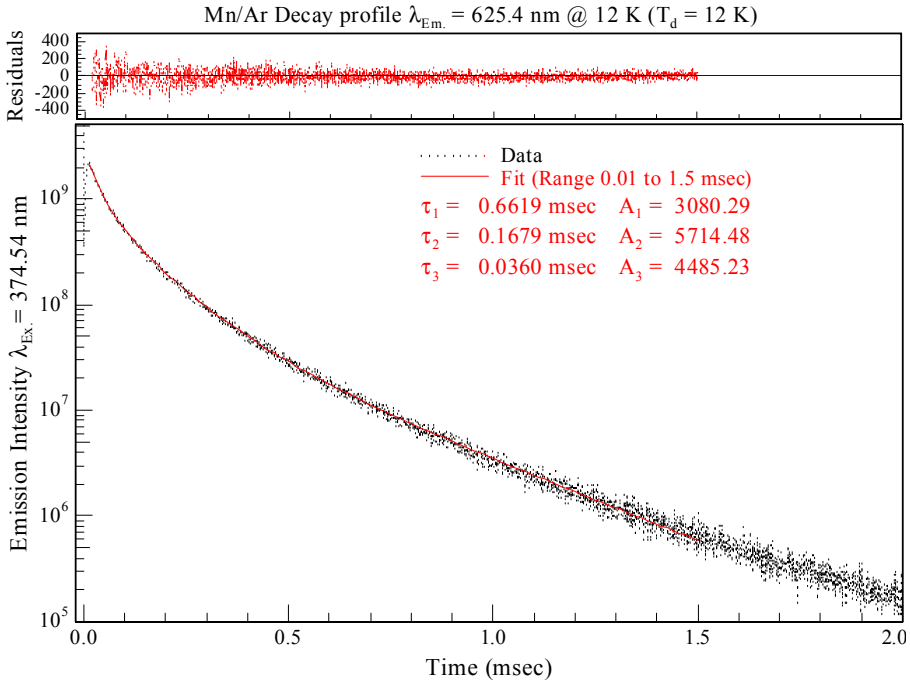

Figure VII.36 **Decay profile of the 625.0 nm feature recorded using TCSPC following pulsed laser excitation into the 2° thermally stable site of isolation at 374.54 nm. Note the decay profile was recorded following fresh Mn/Ar matrix deposition at 12 K.**

VII.2.II.IV Discussion - Mn(z^6P)/Ar

The luminescence resulting from excitation of the $z^6P \leftrightarrow a^6S$ transition of atomic Mn isolated in solid Ar is extremely rich spectroscopically. This is highlighted by the identification in excitation spectroscopy of two high symmetry sites of atomic isolation blue-shifted of the $z^6P_{5/2} \leftrightarrow a^6S_{5/2}$ gas phase transition[1]. These sites, centered at 393.4 (25419 cm^{-1}) and 380 nm (26316 cm^{-1}) allowed deconvolution of the complex absorption spectra recorded for Mn in solid Ar. The comparison between the absorption and excitation spectra presented in Figure VII.14 provides an indication of the relative amounts of Mn atoms isolated in each matrix environment assuming the oscillator strength of the $z^6P_{5/2} \leftrightarrow a^6S_{5/2}$ transition is independent of the site of isolation. The ratio of the red site to blue site is approximately 10:1. The excitation spectra (bottom panel, Figure VII.14) recorded for both of these sites showed resolved Jahn-Teller threefold splitting patterns. This structure was not evident in the absorption spectroscopy presented in Chapter VI, which was further complicated by the presence of Mn dimer absorption band at 403 nm.

The emission spectra recorded following site-specific excitation of the 1° and 2° (393.4 and 380 nm) sites are summarised in Figure VII.37 relative to the gas phase transitions of atomic Mn. The spectral assignments made in the previous section are also presented for both sites of atomic isolation. Inspection of the state assigned Mn/Ar matrix emission reveals that the site of isolation has a very strong influence on the relaxation of the z^6P excited state of atomic Mn. Table VII.7 presents the photophysical characteristics of the observed atomic emission features produced with resonance $z^6P_{5/2} \leftarrow a^6S_{5/2}$ excitation of Mn atoms occupying the 1° site in solid Ar. Selective excitation of the red (1°) site results in emission features assigned to the relaxation of the $a^4D_{7/2} \rightarrow a^6S_{5/2}$ at 427.5 nm and $a^6D_{9/2} \rightarrow a^6S_{5/2}$ at 590 nm. The assignment of the 590 nm emission to the radiative relaxation of the $a^6D_{9/2}$ is not definitive and investigated further in Chapter VIII following direct a^6D excitation. However, no resonance fluorescence corresponding to the $z^6P_{3/2} \rightarrow a^6S_{5/2}$ transition is observed following z^6P excitation of the atom in this, the red and dominant site.

The observation of the $a^4D_{7/2} \rightarrow a^6S_{5/2}$ phosphorescence centered at 427.5 nm without any evidence for the $z^6P_{3/2} \rightarrow a^6S_{5/2}$ fluorescence indicates a $z^6P \Rightarrow a^4D$ curve crossing with 100% efficiency. This crossing efficiency may originate from the freedom of the excited state Mn atom to move over large distances on the excited

state potential energy surface in the dominant, red site of isolation. This is further discussed in Chapter IX where site occupancy is discussed at length. The second feature observed at 590 nm is tentatively assigned to the emission of the metastable $a^6D_{9/2}$ level. This feature exhibits an asymmetric lineshape and linewidth of approximately 100 cm^{-1}. The observed matrix lifetime of 654 μsec, presented in Table VII.7, conceals the complex kinetics leading to the observed band. Figure VII.27 and Table VII.5 indicate the multiple features that occur between the z^6P and the terminal $a^6D_{9/2}$ level. The presence of two millisecond components in the 590 nm emission provides compelling evidence for cascade kinetics from the $a^4D \Rightarrow a^6D$ where this slower feeding step appears as a component in the final decay. These mechanisms are discussed fully in Chapter VIII following the presentation of the luminescence of the z^8P and a^6D excited states of atomic Mn accessed by direct laser excitation.

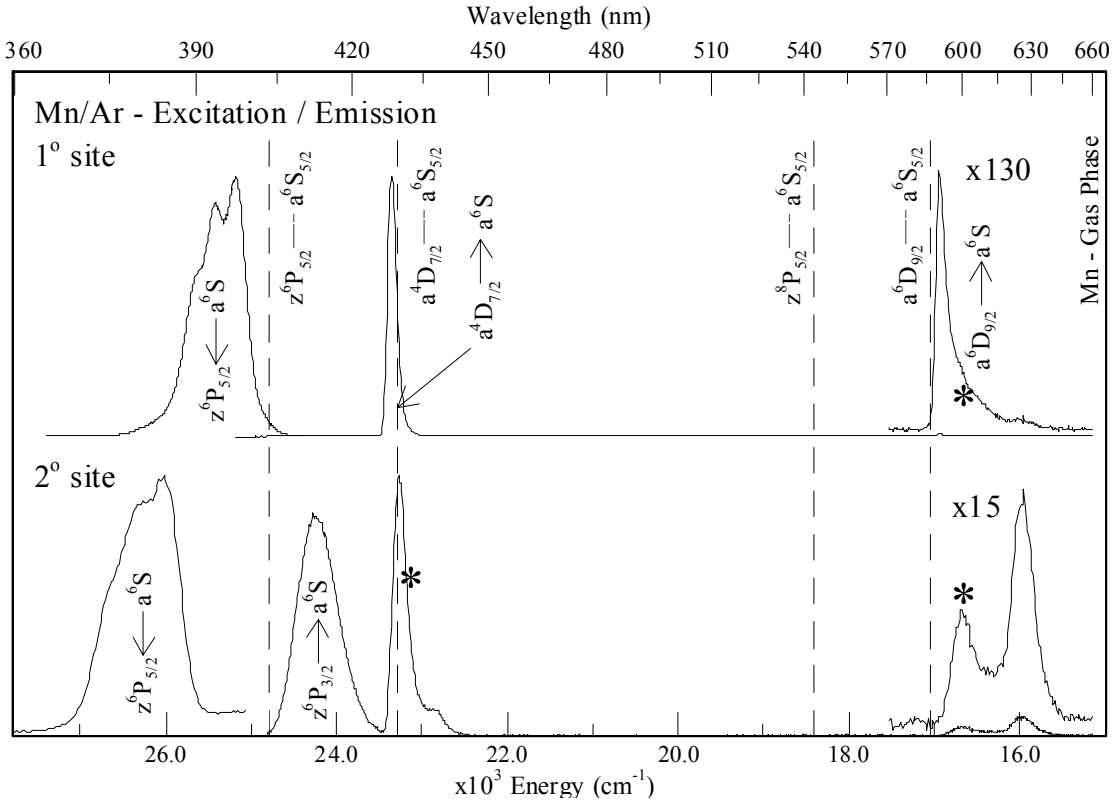

Figure VII.37 Emission spectra recorded at 12 K for the Mn/Ar system with site-selective lamp excitation of the Mn $z^6P_{5/2} \leftarrow a^6S_{5/2}$ transition, shown right. The excitation spectra (1° and 2° site), were recorded by monitoring emission at 428 / 590 and 413 / 625 nm (shown left). These spectra were recorded following Mn/Ar sample deposition at 12 K and matrix annealing to 28 K. The spectral positions of the gas phase transitions of atomic Mn are shown by the vertical lines. The observed Mn/Ar matrix absorption and emission bands assigned are indicated. Note * indicates the emission band is thermally unstable.

The lower panel in Figure VII.37 presents the emission features produced with $z^6P_{5/2}$ excitation of Mn atoms isolated in the blue (2°) site of isolation. Table VII.8 presents the photophysical characteristics and the assignments of the excited state emission features made in the previous sections. The dramatic differences in the emission resulting from 1° and 2° site excitation is evident by comparing the band profiles of the observed emission features presented in Figure VII.37. As the lower panel shows, blue (2°) site excitation produces emission features centered at 413, 431, 438 and 625 nm all of which show broad symmetric lineshapes indicative of strong electron phonon coupling and a high degree of excited state stabilisation.

Table VII.7 **Photophysical characteristics and excited state assignments of the emission features produced following excitation of the $3d^54s4p\ z^6P_{5/2} \leftarrow 3d^54s^2\ a^6S_{5/2}$ transition of matrix – isolated atomic manganese isolated in the low energy 1° site centered at 393.4 nm (25419 cm^{-1}). λ_{Em}, indicates the emission band-centre in nm units. The full-width at half-maximum intensity of the emission features is denoted by Δ and the matrix shift by δ - both in wavenumber (cm^{-1}) units. The excited state lifetimes (decay characteristics) are presented $\tau_{Obs.}$ indicates the dominant decay characteristic at 12 K.**

Mn Gas Phase	**Mn/Ar Matrix (1° site)**			
Transition nm / cm^{-1}	Assignment	$\lambda_{Em.}$ (nm) / Δ (cm^{-1})	δ (cm^{-1})	Decay time
$a^4D_{7/2} \leftrightarrow a^6S_{5/2}$ 429.25 / 23297	$a^4D_{7/2} \rightarrow a^6S_{5/2}$	≈ 427.5 / ≈ 7.0	+ 92	25.28 msec
$a^6D_{9/2} \leftrightarrow a^6S_{5/2}$ 586.43 / 17052	$a^6D_{9/2} \rightarrow a^6S_{5/2}$	590.0 / ≈ 100	-103	654 μsec

The 431 nm emission feature evident in Figure VII.37 is thermally unstable. The 413 nm emission feature is assigned to the $z^6P_{3/2}$ state fluorescence. The decay characteristics of the 625 nm feature reveal complex kinetics requiring a triple exponential fitting function. Of the three decay components only the short decay extracted (see Table VII.8) is in line with the known gas phase value of 149.3 μsec[8] for the $z^8P_{5/2} \leftrightarrow a^6S_{5/2}$ transition. However, the spectral location of the emission band does not support this assignment. The final emission feature exhibiting a broad band profile produced with blue (2°) site excitation occurs at 438 nm. This feature is unassigned as the spectral location and the broad linewidth observed indicate a large Stokes' shifted P → S type transition but, the long decay time recorded (> 0.1 sec) of the 438 nm band is at variance with a resonance emission unless an interaction with a trapping level (a^4D) is involved. Clearly, due to the conflicting spectral and kinetic data recorded the 438 nm emission in Mn/Ar, the band cannot be definitively

assigned to the relaxation of an excited state of atomic Mn. Further discussion of this feature is presented in Chapter VIII.

Overall, the Mn/Ar emission spectroscopy is strongly site specific. The most pronounced example being the presence of the $z^6P_{3/2}$ fluorescence from the blue (2°) site and its complete absence from the red (1°) site. The preference of the Mn atoms isolated in the red (1°) site to relax via a more complex curve crossing process from the $z^6P \Rightarrow a^4D$ is also evident. In the following section, the luminescence of Mn atoms isolated in solid Kr is presented.

Table VII.8 **Photophysical characteristics and excited state assignments of the emission features produced following excitation of the $3d^54s4p\ z^6P_{5/2} \leftarrow 3d^54s^2\ a^6S_{5/2}$ transition of matrix – isolated atomic manganese isolated in the high energy 2° site centered at 380 nm (26316 cm^{-1}). λ_{Em} indicates the emission band-centre in nm units. The full-width at half-maximum intensity of the emission features is denoted by Δ and the matrix shift by δ - both in wavenumber (cm^{-1}) units. The excited state lifetimes (decay characteristics, τ) are presented, the subscripts Rad. and Cor indicate the radiative lifetime of the excited state and the lifetimes corrected for the effective field. $\tau_{Obs.}$ indicates the dominant decay characteristic at 12 K.**

Mn Gas Phase	**Mn/Ar Matrix (2° site)**			
Transition nm / cm^{-1}	Assignment	$\lambda_{Em.}$ (nm) / Δ (cm^{-1})	δ (cm^{-1})	Decay time
$z^6P_{3/2} \leftrightarrow a^6S_{5/2}$ 403.56 / 24779	$z^6P_{3/2} \rightarrow a^6S_{5/2}$	413.0 / ≈ 465	-566	$\tau_{Rad\ /\ Cor}$ = 28.0/ 57.5 nsec $\tau_{Rad\ /\ Cor}$ = 10.5 / 21.6 nsec
$z^6P_{3/2} \leftrightarrow a^6S_{5/2}$ 403.56 / 24779 $a^4D_{7/2} \leftrightarrow a^6S_{5/2}$ 429.25 / 23297	(?)	438.0 / ≈ 230	-1948 -466	$\tau_{obs.}$ > 0.1 sec
$z^8P_{5/2} \leftrightarrow a^6S_{5/2}$ 543.40 / 18402 $a^6D_{9/2} \leftrightarrow a^6S_{5/2}$ 586.43 / 17052	(?)	625.0 / ≈ 260	-2402 -1052	$\tau_{1\ Obs.}$= 662 μsec $\tau_{2\ Obs.}$= 165 μsec $\tau_{3\ Obs.}$= 36 μsec

VII.2.III Mn(z^6P)/Kr

In Chapter VI, the absorption features observed at 385.5 nm (25940 cm^{-1}) and 401.9 nm (24881 cm^{-1}), shown in the middle panel of Figure VI.8, were both assigned to the $z^6P_{5/2} \leftarrow a^6S_{5/2}$ transition of atomic Mn isolated in Kr. Mn/Kr was the only system where analysis of the absorption spectroscopy lead to the identification of two sites of atomic isolation following matrix deposition. The sites identified were labelled blue (1°) at 385.5 nm and red (2°) at 401.9 nm. Given their relative abundance and

spectral positions, these labels are used throughout the following sections. It should be noted that the labels are not interchangeable with the labelling used for the sites identified for Mn/Ar where the 1° and 2° corresponded to the red and blue sites respectively.

Figure VII.38 presents a time-integrated emission spectrum recorded for Mn/Kr with continuous tungsten lamp excitation of the blue (1°) and red (2°) sites at 385.5 and 400 nm respectively. The top panel of Figure VII.38 shows the emission spectrum produced with excitation at 385.5 nm into the central component of the threefold split blue (1°) absorption band. Resolved, broad emission features are recorded at 416, 433.5, 440 and 626.8 nm exhibiting linewidths of 510, 285, 305 and 290 cm^{-1} respectively. Excitation into to the red (2°) site at 400 nm produces emission bands at 432.4, 603.8 and 626.5 nm with linewidths of 203, 320 and 300 cm^{-1} respectively. The dominant emission feature shows evidence of an unresolved blue shoulder at 428.9 nm. Like Mn/Ar, the emission features produced with site selective excitation of the $z^6P \leftarrow a^6S$ transition of atomic Mn in solid Kr are spectrally distinct.

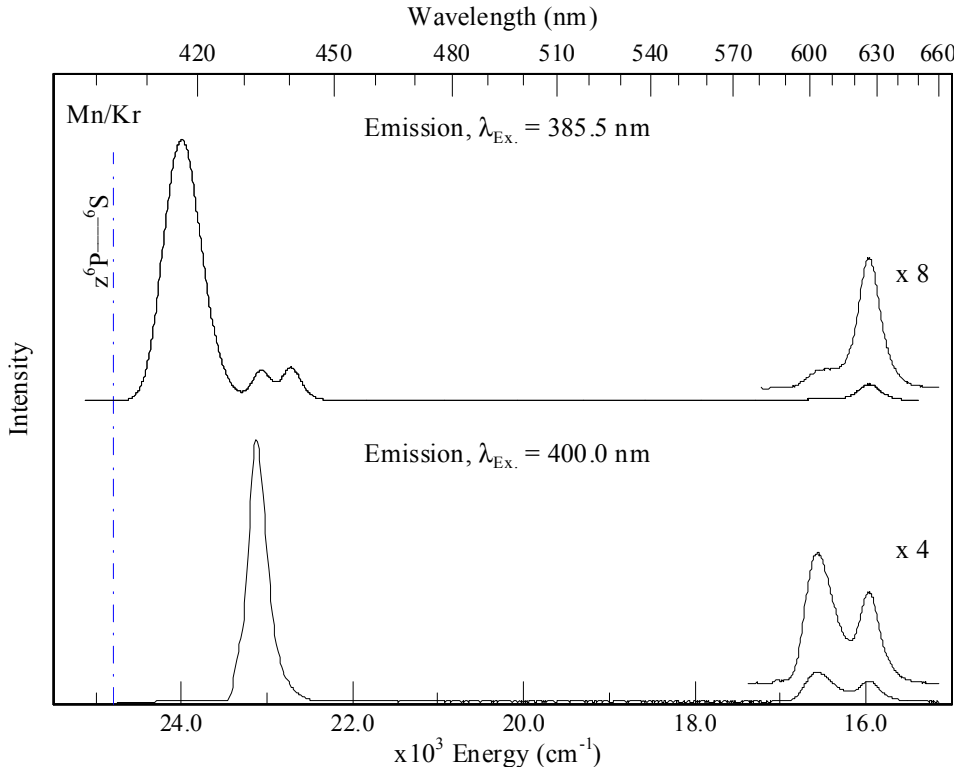

Figure VII.38 Emission spectra recorded at 12 K for Mn/Kr with lamp excitation of the 1° (385.5 nm) and 2° (400 nm) sites assigned to the Mn $z^6P_{5/2} \leftarrow a^6S_{5/2}$ transition.

High-resolution excitation spectra recorded monitoring the dominant emission features at approximately 417.1 and 432.4 nm produced with blue (1°) and red (2°) site excitation are presented in Figure VII.39. The excitation spectrum recorded monitoring the unresolved shoulder identified at 428.4 nm is also presented. Each of the three excitation spectra presented exhibit well-resolved threefold split patterns corresponding to three high symmetry sites of isolation of Mn atoms. The sites of isolation are labelled 1°, 2° and 3° and are centered at 385, 398.3 and 393.7 nm respectively. The blue (1°) site shows resolved components at 381.4, 385 and 388.8 nm each exhibiting an average linewidth of 295 cm^{-1}. Gaussian fits of the excitation spectra corresponding to the 2° and 3° bands revealed average linewidths of 203 and 484 cm^{-1} respectively. The photophysical characteristics of the three sites are presented in Table VII.9

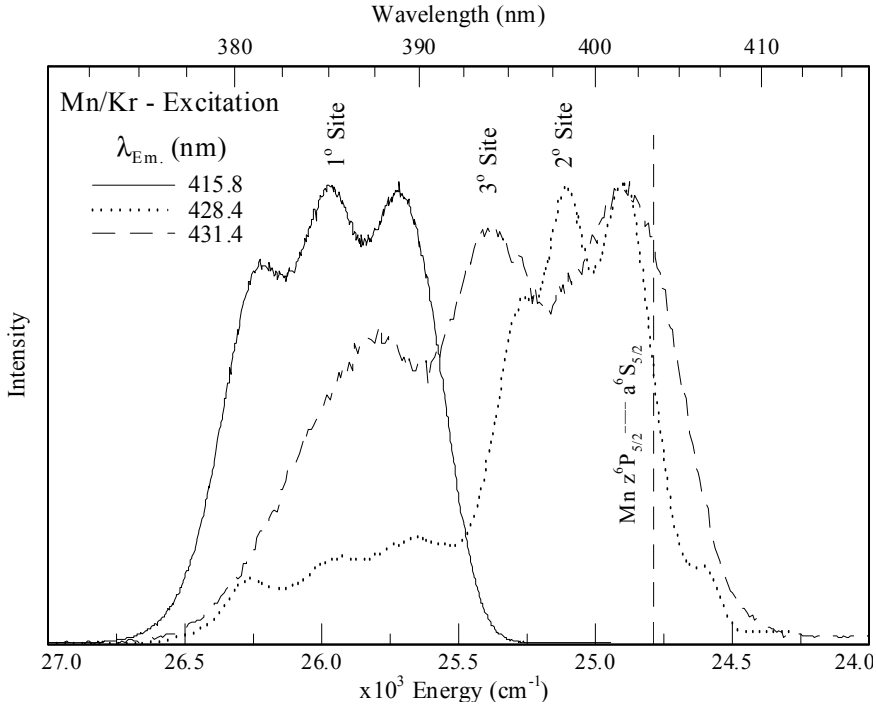

Figure VII.39 High-resolution excitation spectra recorded near the gas phase $z^6P_{5/2} \leftrightarrow a^6S_{5/2}$ transition of atomic Mn occurring at 403.42 nm monitoring the dominant emission features produced with 1° and 2° site excitation at 415.8 and 431.4 nm and the unresolved 428.4 nm shoulder observed on deposition at 12 K. The relative amounts of each site can be accessed from the emission spectra presented in Figure VII.38.

Table VII.9 **Photophysical characteristics of the sites of isolation (1°, 2° and 3°) revealed in excitation spectra of the $3d^54s4p\ z^6P_{5/2} \leftrightarrow 3d^54s^2\ a^6S_{5/2}$ transition of atomic manganese. The spectral position and average full width at half maximum (*fwhm*) denoted as Δ_{AV} of the three components identified in Gaussian lineshape analyses of the three–fold split excitation spectra are presented in wavenumber units. Gas phase to matrix frequency shifts (δ) are presented for the atomic Mn $z^6P_{5/2} \leftarrow a^6S_{5/2}$ transition (G.P.: 24,788.05 cm^{-1}) in wavenumber units. Note the frequency shifts are calculated with respect to the central feature of the observed threefold pattern.**

Mn/Kr Site	Component	E (cm^{-1})	Δ_{AV} (cm^{-1})	δ (cm^{-1})
1°	1	26219	≈295	+ 1187
	2	25974		
	3	25720		
2°	1	25259	≈203	+ 319
	2	25107		
	3	24900		
3°	1	25800	≈484	+ 612
	2	25400		
	3	24900		

High-resolution excitation spectra allowed the correlation of the emission features resulting from $z^6P_{5/2} \leftarrow a^6S_{5/2}$ excitation with Mn atoms in the three matrix sites. The blue (1°) site centered at 385 nm resolved in excitation, is identified as the major contribution to the observed absorption band. It leads to the emission features centered at 415.8, 440.2 and 626.4 nm. The red (2°) site centered at 398 nm produces the emission bands observed at 428.4 and 585.8 nm on deposition at 12 K. The 3° site whose absorption overlaps those of the 1° and 2° sites leads to both the 432.4 (433.5) and 603.8 nm features. The relative stability of these sites was assessed from emission spectra recorded following careful matrix annealing of Mn/Kr samples to 38 K.

Time-integrated emission spectra recorded following annealing to 38 K are presented in Figure VII.40. Comparison of the relative emission intensities before (Figure VII.38) and after annealing (Figure VII.40) for a specific site excitation reveals the thermal instability of the 3° site. It is evident from a comparison of the emission resultant from red (2°) site excitation at 400 nm, that the emission features located at 428.4 and 626.8 nm dominate those at 431.7 and 603 nm. This represents the reduction of the 3° site of isolation, therefore confirming its identification as a thermally labile site of atomic isolation. It is also apparent from the comparison that an additional asymmetric emission band at 585.8 nm is enhanced by the annealing procedure for red (2°) site excitation. Moreover, the 428.4 nm band has sharpened.

The emission spectra produced by blue (1°) site excitation at 385.5 nm before and after annealing revealed no dramatic changes in the relative emission intensities of the bands observed.

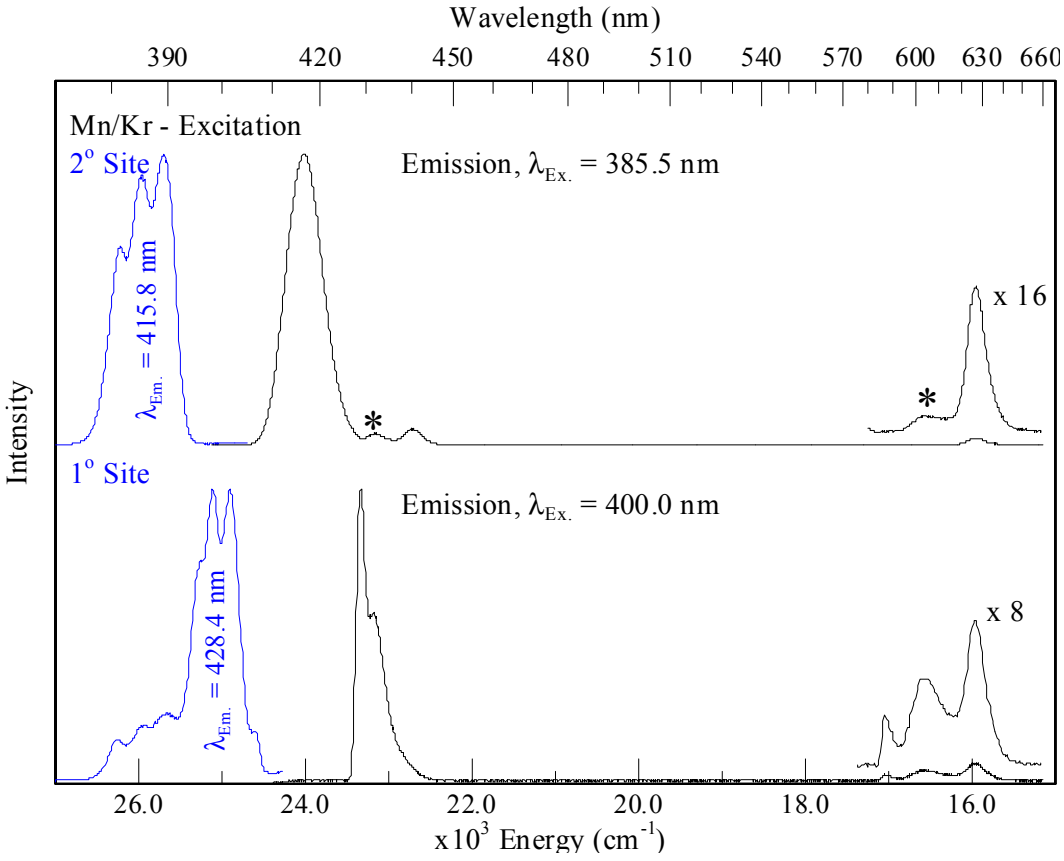

Figure VII.40 **Time-integrated emission spectra recorded at 12 K produced with lamp selective excitation of the 1° (385.5 nm) and 2° (400 nm) sites assigned to the Mn $z^6P_{5/2} \leftarrow a^6S_{5/2}$ transition following annealing to 38 K. The high-resolution excitation spectra recorded on deposition at 12 K are shown left. The emission features resulting from 3° excitation reduced by the annealing procedure are indicated by the asterisk.**

The annealing experiments allowed the identification of the blue (1°) and red (2°) sites centered at 385.5 nm and 398.3 nm as the thermally stable sites of Mn atom isolation in solid Kr. As revealed in Figure VII.41 by the comparison of the excitation spectra of the 1° and 2° sites with the absorption spectrum recorded at 12 K, it is evident that the absorption spectrum results from the presence of two thermally stable sites of isolation. It is concluded that absorption spectra recorded on deposition provide an accurate reflection of the site occupancy for atomic Mn isolated in solid Kr, insofar as the blue (1°) and red (2°) site components are observed in a 3:1

ratio. In the next section, the emission spectroscopy of atomic Mn isolated in solid Kr produced with site-specific $z^6P_{5/2} \leftarrow a^6S_{5/2}$ excitation is analysed.

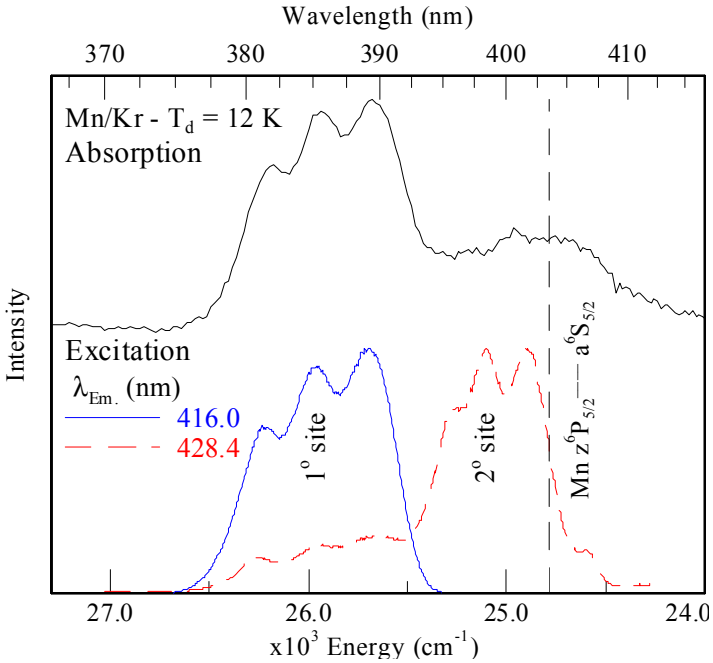

Figure VII.41 Comparison of the high-resolution excitation spectra recorded and absorption spectra recorded in the vicinity $z^6P_{5/2} \leftrightarrow a^6S_{5/2}$ transition of Mn for dilute Mn/Kr samples on deposition at 12 K.

VII.2.III.I Mn(z^6P)/Kr Site-specific Emission Spectroscopy

Figure VII.42 presents a summary of the emission spectra recorded in the 405 – 450 nm range, following selective excitation of the z^6P state of atomic Mn isolated in the blue and red sites in Kr. Inspection of Figure VII.42 highlights the difference in the emission features produced with excitation into the two sites. Thus, broad emission features at 416 and 440 nm are produced with excitation into the blue (1°) site. In contrast, red (2°) site excitation produces narrow linewidth emission at 428 nm. The weak side band observed at 432 nm is due to a residual amount of the thermally labile 3° site. As shown in Figure VII.42 this band is produced in the entire 380 – 405 nm excitation range. In the next section, the photophysical and temporal decay characteristics of each of the observed bands are used to assign the emission features to atomic transitions.

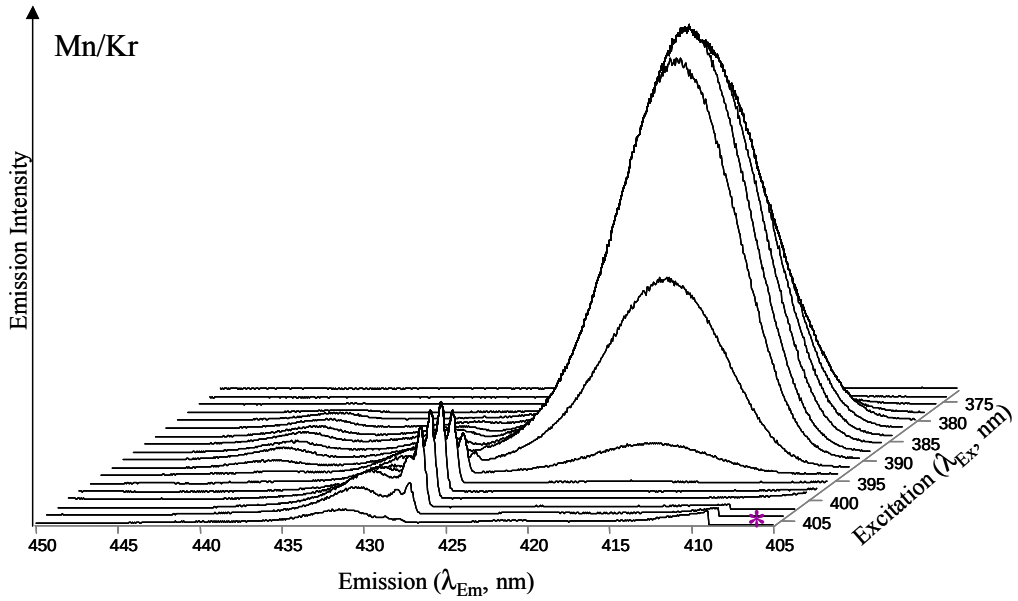

Figure VII.42 **A 3d plot of time-integrated Mn/Kr emission spectra (X-axis) produced with lamp excitation of the Mn $z^6P_{5/2}$ state (Y-axis) recorded at 12 K following annealing to 38 K. The asterisk indicated where scattered light was removed for presentational reasons.**

VII.2.III.II Mn(z^6P)/Kr - 1° site luminescence

Mn(z^6P)/Kr - 1° Site - $\lambda_{Em.}$ = 416.0 nm

The dominant emission feature produced with blue (1°) site excitation at 385 nm occurs at 416 nm exhibiting, as shown in Figure VII.38, a linewidth of 505 cm^{-1}. The observed broad band profile is indicative of a P $\rightarrow$ S type electronic transition and is reminiscent of the 413 nm emission feature assigned to the resonance $z^6P_{3/2}$ state fluorescence in solid Ar. In attempting to assign the emission band, the temporal decay characteristics of the emission were analysed. Figure VII.43 presents 'on a nanosecond scale' time-resolved emission spectra recorded for the 416 nm feature. It is apparent that the emission intensity decays on a nanosecond timescale.

Figure VII.44 presents, on a semi-log plot, the temporal decay profile extracted from the 416 nm intensity distribution shown in the time-resolved emission spectrum in Figure VII.43. Fitting the emission decay profile required the use of a double exponential function, convoluted with the temporal profile of the excitation laser. The two nanosecond decay components extracted are 46.4 and 30.5 nsec. A comparison of the relative amplitudes A_1 and A_2 indicates the dominance of the

shorter component and its identification as the observed excited state lifetime, $\tau_{Obs.}$ = 30.5 nsec.

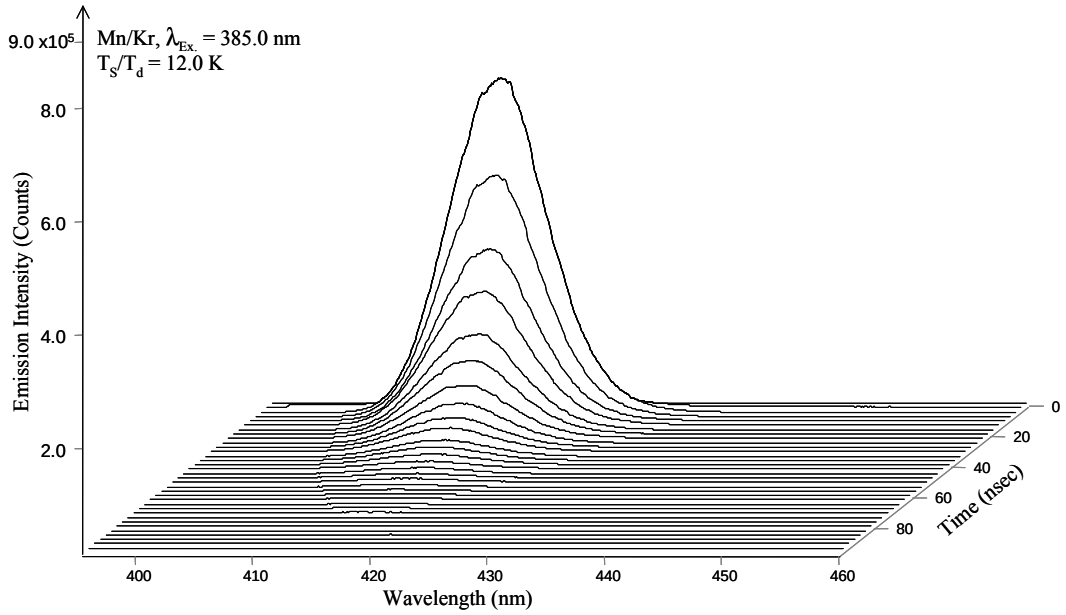

Figure VII.43 **Time-resolved emission spectra recorded for the 416 nm band (at 12 K) following pulsed laser excitation at 385 nm. The temporal step and width used was 10 nsec with a delay time of t_d = 0.0 nsec.**

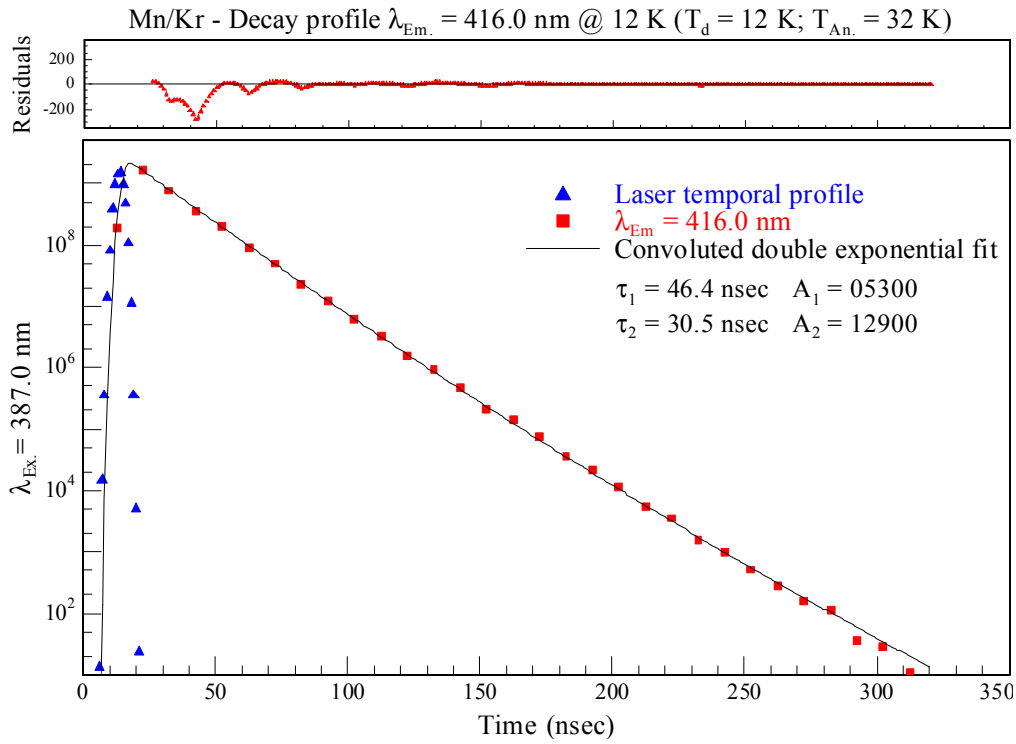

Figure VII.44 **Decay profile of the 416 nm emission feature recorded at 12 K extracted from time–resolved emission spectrum, Figure VII.43. The decay profile is convoluted with the temporal profile of the excitation laser source at 387 nm.**

The temperature dependence of the 416 nm decay profile was recorded. This allowed the identification of the observed emission lifetime ($\tau_{Obs.}$) as that of the radiative decay of the excited state (τ_{Rad}), because as shown in Figure VII.45, no change in the temporal profile was observed over the temperature range 12 to 18 K. Double exponential trial functions were required to provide an adequate model of the decay profiles at all temperatures from 12 to 31 K as shown in Figure VII.45.

Table VII.10 **Excited state lifetimes (τ_{obs}) and amplitudes (A) extracted by applying a double exponential function convoluted with the laser temporal profile to the decay curves recorded monitoring $\lambda_{Em.}$ = 416 nm at different temperatures, (T_s) following pulsed laser excitation at 387 nm. Note the dominant decay contribution is presented in bold.**

T_s. (K)	Fit Range (nsec)	A_1	τ_1 (nsec)	A_2	τ_2 (nsec)
12.0	0 – 320	5300	46.4	**12900**	**30.5**
15.0	0 – 260	6000	46.5	**16531**	**30.3**
18.0	0 – 300	6000	46.5	**16531**	**30.3**
21.0	0 – 260	7200	44.0	**16800**	**27.5**
24.0	0 – 260	9600	37.6	**16000**	**23.2**
28.0	0 – 240	8800	32.0	**14500**	**19.0**
30.0	0 – 200	**21500**	**24.0**	20500	12.5
31.0	0 – 190	22000	22.0	**22500**	**12.0**

Application of the effective field correction (Equation III.1), using the refractive index of solid Kr as 1.428[11], leads to a corrected decay time of 55.3 nsec. The gas phase lifetime for the fluorescent transition is reported as 66.1 ± 1.4 nsec[9]. Although, the corrected matrix lifetime ($\tau_{Cor.}$) is shorter than the reported gas phase value, it allows the assignment of the emission feature to the resonance fluorescence. The emission band is therefore red shifted by 740 cm^{-1} from the gas phase position[1] of the $z^6P_{3/2} \leftrightarrow a^6S_{5/2}$ transition at 403.56 nm (24779 cm^{-1}).

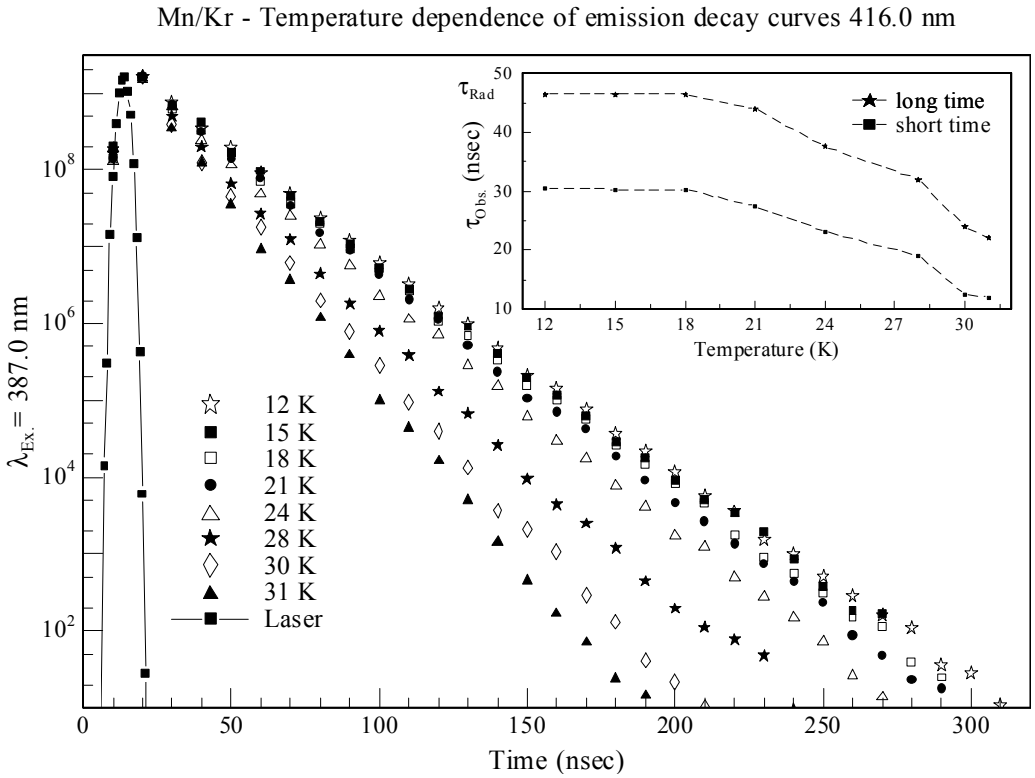

Figure VII.45 **Comparison of the excited state decay profiles produced monitoring the 416 nm emission feature following pulsed laser excitation at 385 nm at various temperatures as indicated. The temporal profile of the excitation source is also shown.**

Mn(z^6P)/Kr - 1° Site - $\lambda_{Em.}$ = 440.0 nm

Blue site excitation produces the emission feature at 440 nm which exhibits a linewidth of approximately 280 cm^{-1}. This broad emission accompanies the 416 nm band (see left panel of Figure VII.42) and suggests an assignment of resonance $z^6P_{3/2}$ fluorescence, blue-shifted from the gas phase[1] position (403.56 nm; 24779 cm^{-1}) by 2052 cm^{-1}. However, the broad 416 nm (24038 cm^{-1}) feature also observed with blue (1°) site excitation is already assigned to the $z^6P_{5/2} \rightarrow a^6S_{5/2}$ transition in the previous section.

Figure VII.46 presents a time-resolved emission spectrum monitoring emission bands in the vicinity of the $z^6P_{5/2} \rightarrow a^6S_{5/2}$ transition. Inspection of Figure VII.46 shows very long excited state decay characteristics for the 440 nm band in comparison to the nanosecond 416 nm fluorescence. Each temporal segment represents 5.0 msec and the 440 nm band is observed with significant intensity even at 100 msec, as shown by the inset of Figure VII.46.

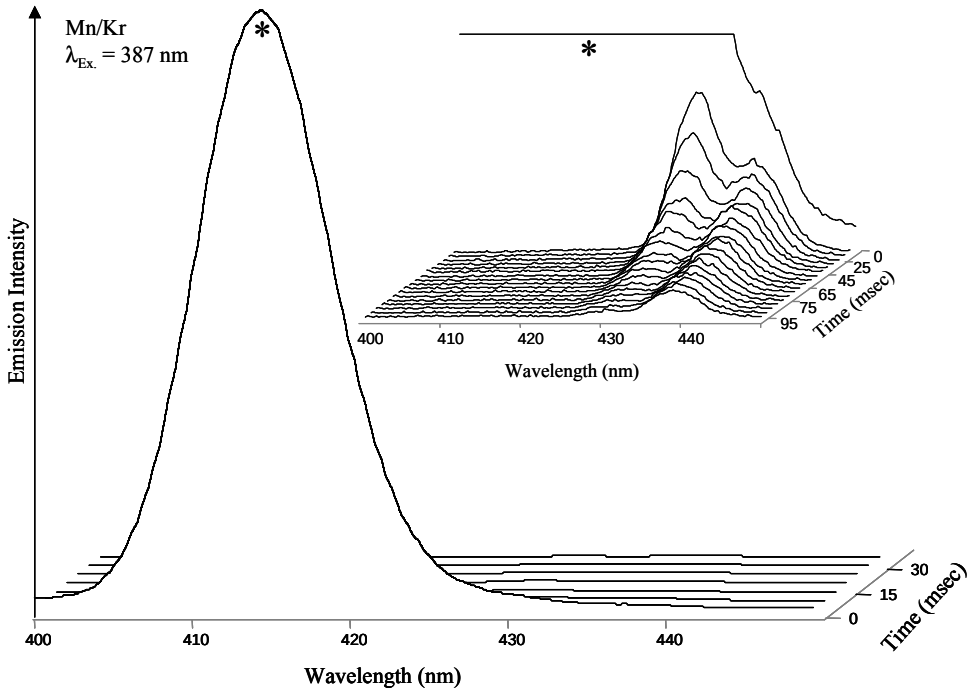

Figure VII.46 Time-resolved emission spectrum recorded monitoring $\lambda_{Em.}$ = 440 nm (at 12 K) following pulsed laser excitation at $\lambda_{Ex.}$ = 385 nm. The temporal step and width used was 10 nsec with a delay time of t_d = 0.0 nsec. Note the 431 nm feature observed is produced by excitation of the 3° thermally unstable site.

Decay profiles of the 440 nm emission were also recorded using the TCSPC technique. One such measurement made at 12 K following matrix annealing is shown in Figure VII.47. Least squares analysis of the decay profile required three exponential functions to achieve an adequate fit and extract the excited state decay characteristics. It is apparent from the complicated decay profile containing a rise time portion, that the 440 nm emission band is produced by complex excited state kinetics. The three decay times extracted, range from the shortest component τ_3 = 2.4 msec (identified as the rise time) to the dominant decay time τ_1 = 0.1 sec.

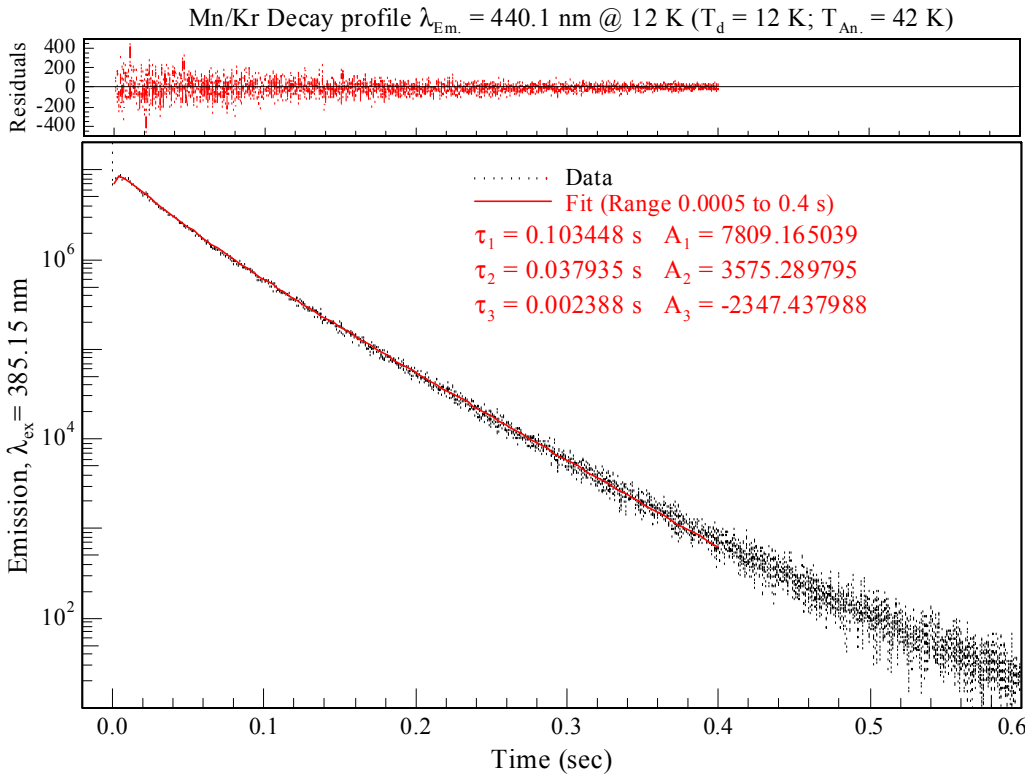

Figure VII.47 **Decay profile of the 440.1 nm emission recorded at 12 K using TCSPC following pulsed laser excitation at 385.15 nm. The residuals present the difference between the triple exponential non-linear least squares fit completed and the decay recorded.**

Decay profiles recorded at temperatures in excess of 12 K are presented in Figure VII.48. It is clear from the marked changes shown, that the excited state decay curves are extremely sensitive to temperature. Of particular note is the removal of the rise time component at temperatures greater that 25 K, shown inset in Figure VII.48. A double exponential fit of the decay profile recorded at 32 K showed two msec components. The strong temperature dependence and the multi-exponential nature of the decay profiles recorded do not allow a conclusive assignment of the excited state producing the 440 nm emission band.

Inspection of the spectra presented in Figure VII.49 shows the steady decrease in the emission intensity of the 416 nm band with increasing temperature. This observation indicates the presence of a non-radiative step which becomes active between 18 and 20 K and increased phonon relaxation at higher temperatures. However, the inset shows that in the temperature range 12 to 18 K, where the 440 nm emission showed a rise time component (Figure VII.48), there is an increase in its emission intensity. At temperatures greater than 20 K the intensities of both 416 and 440 nm features decreases.

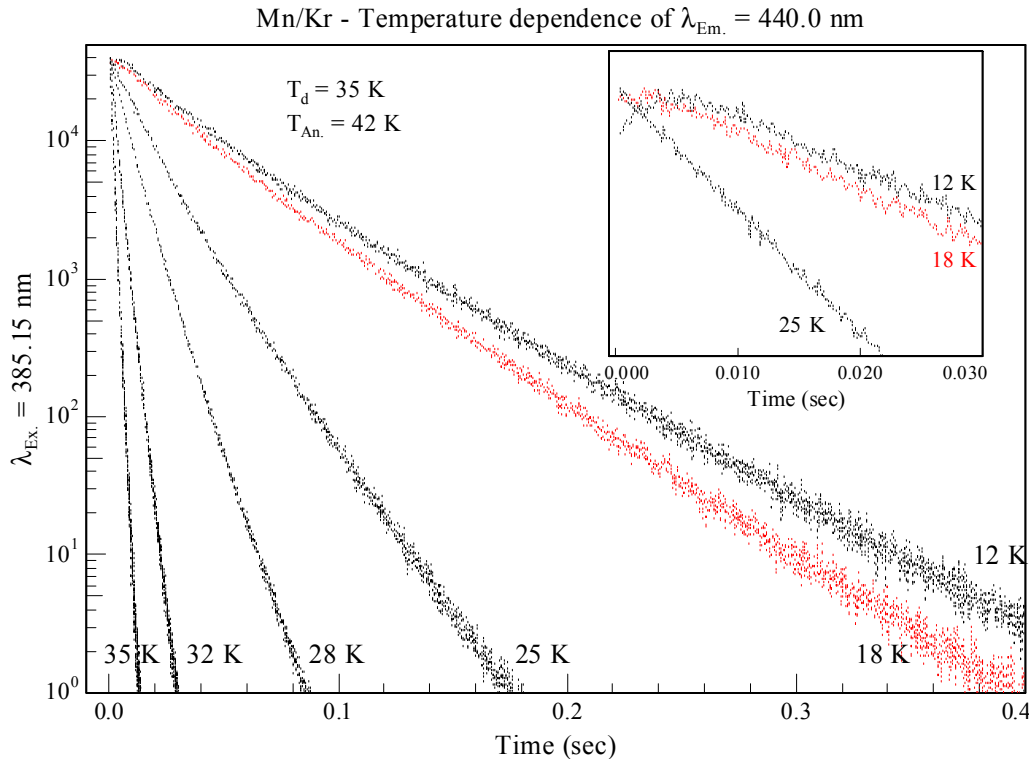

Figure VII.48 **Decay profiles recorded monitoring the 440 nm emission feature produced with 1° site $z^6P_{5/2} \leftarrow a^6S_{5/2}$ excitation at 385.15 nm at various temperatures as indicated. The behaviour of the rise time component at various temperatures is shown inset.**

These observations suggest that non-radiative steps are active in removing the population from the excited states leading to both the 416 and 440 nm bands at all temperatures above 20 K. The increase in the emission intensity at 440 nm up to 20 K is accompanied by the decrease in the intensity of the $z^6P_{3/2}$ fluorescence (416 nm) indicating a feeding step from the z^6P excited state leads to the population of the emitting level which gives rise to the 440 nm band. Unfortunately, the presence of a rise time and multiple long decay time components cannot be reconciled with this model as a direct feeding mechanism requires the appearance of the nanosecond decay time of the donor (the $z^6P_{3/2}$ excited state) as the rise time of the acceptor. The rise time observed is much longer.

Because of the conflicting spectral and temporal data recorded for the 440 nm emission, this feature, like the 438 nm band in solid Ar, cannot be definitively assigned to an electronic transition of atomic Mn in solid Kr. The assignment of this broad spectral feature to the $z^6P \rightarrow a^6S$ transition would require the stabilisation of the excited state via a second mechanism and is not consistent with the very long

decay times measured. The only alternative is the assignment of the emission feature to that of the relaxation of the a^4D excited state. However, the emission lineshape observed and the large matrix shift of 570 cm^{-1} observed from the gas phase position of the $a^4D_{7/2} \rightarrow a^6S_{5/2}$ transition make this assignment problematic as it is so different to the 428 nm band to be presented ahead.

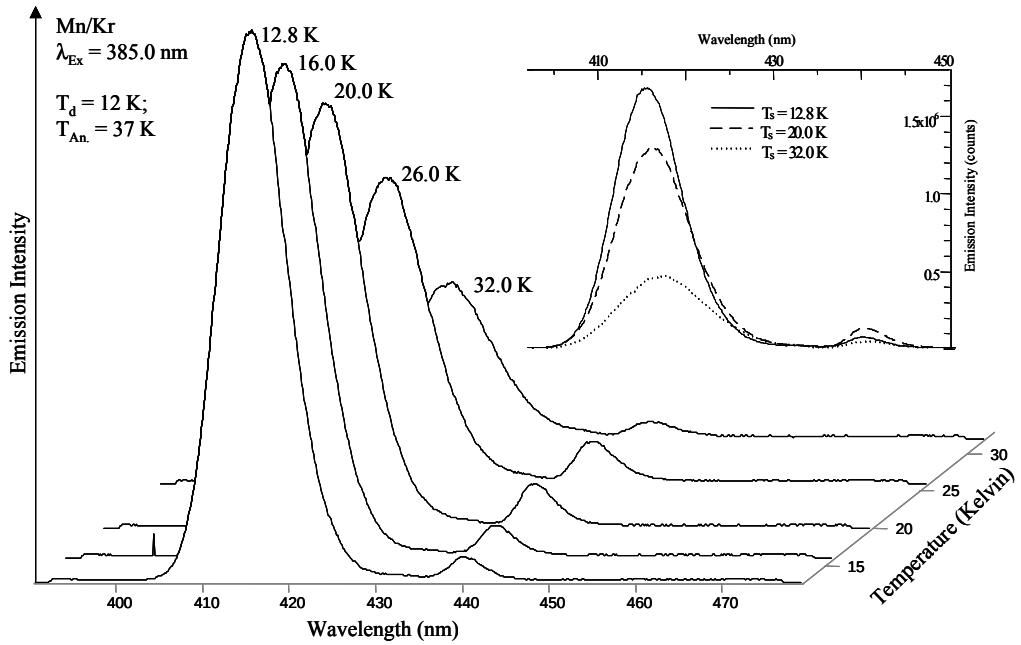

Figure VII.49 Time-integrated emission spectra recorded following $z^6P_{5/2} \leftarrow a^6S_{5/2}$ 1° site specific continuous W-lamp excitation at 385 nm at various temperatures.

Mn(z^6P)/Kr - 1° Site - $\lambda_{Em.}$ = 626.8 nm

The broad emission band centered at 626.8 nm (15954 cm^{-1}) resulting from blue (1°) site excitation of the z^6P excited state is shown in the upper panel of Figure VII.40. A decay profile recorded monitoring the 626.8 nm feature produced with z^6P excitation at 12 K is shown in Figure VII.50. Inspection of the decay profile reveals the complex kinetics leading to the observed emission, confirmed by the multi-exponential fit completed. The fit allowed the extraction of three decay components 1.67 msec, 564 and 101 μsec. The dominant 564 μsec decay component is assigned to the observed excited state lifetime at 12 K. The observed decay time is longer than the gas phase lifetime of the $z^8P_{5/2} \rightarrow a^6S_{5/2}$ transition 149.3 μsec[2] and shorter than the theoretically calculated lifetime for the $a^6D_{9/2}$ metastable state of 3.4 sec[3]. However, the short-lived minor 101 μsec component extracted is comparable to the gas phase

lifetime of the z^8P state. Decay profiles recorded at higher temperatures showed increased complexity as shown in Figure VII.51. Lifetimes extracted at elevated temperatures confirmed the temperature sensitivity of all the decay components.

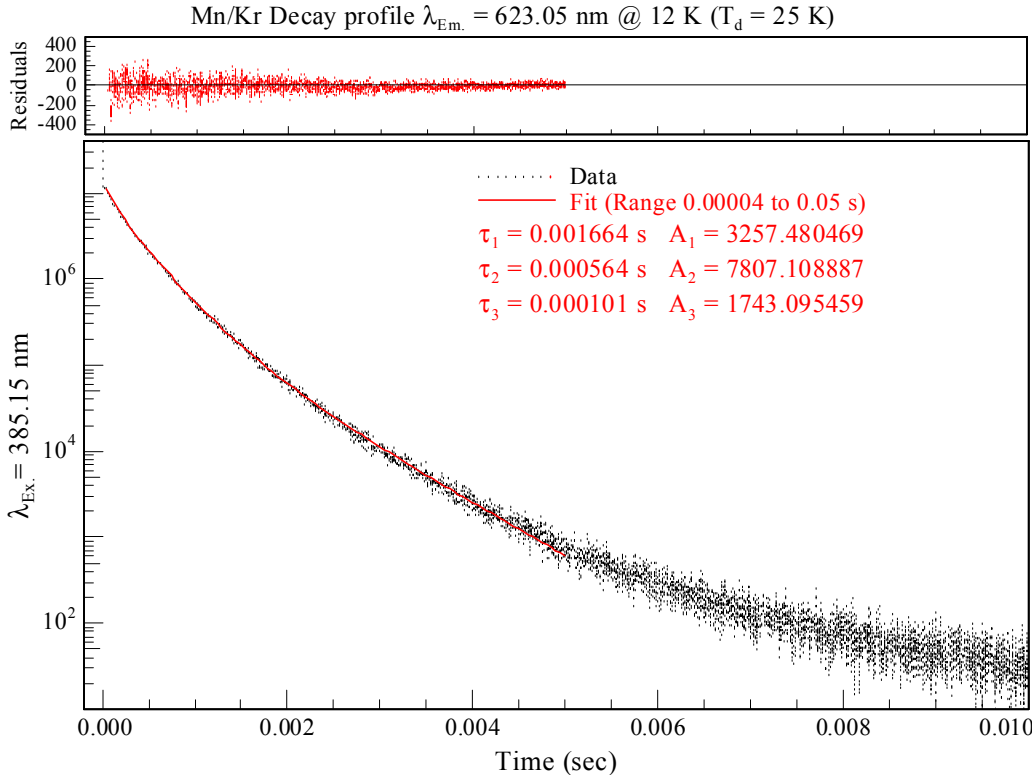

Figure VII.50 Decay profile of the 626.0 nm (623.05 nm) emission recorded at 12 K using TCSPC following deposition at 25 K pulsed laser excitation at 385.15 nm.

Temperature dependent time-integrated emission spectra recorded following excitation at 385 nm are shown in Figure VII.52. Comparison of these spectra reveals that increasing the temperature above 20 K enhances the 626.4 nm feature. This coincides with the removal of the emission intensity at 440 nm above 20 K. The decay profiles shown in Figure VII.51 reveal the decay time shortens up to 22 K, but at temperatures in excess of this value, the decay profiles appear longer and increase in complexity. The proposal that the relaxation occurs via the excited state leading to the 440 nm emission is reinforced by the dominance of the 2.23 msec component in the decay time extracted for the 626.4 nm band at 35 K. The rise time observed for the 440 nm feature at 12 K (2.4 msec, shown in Figure VII.47) matches the decay time (2.23 msec) observed of the 626.4 nm emission indicating a feeding of the emitting level by the state producing the 440 nm band at 35 K.

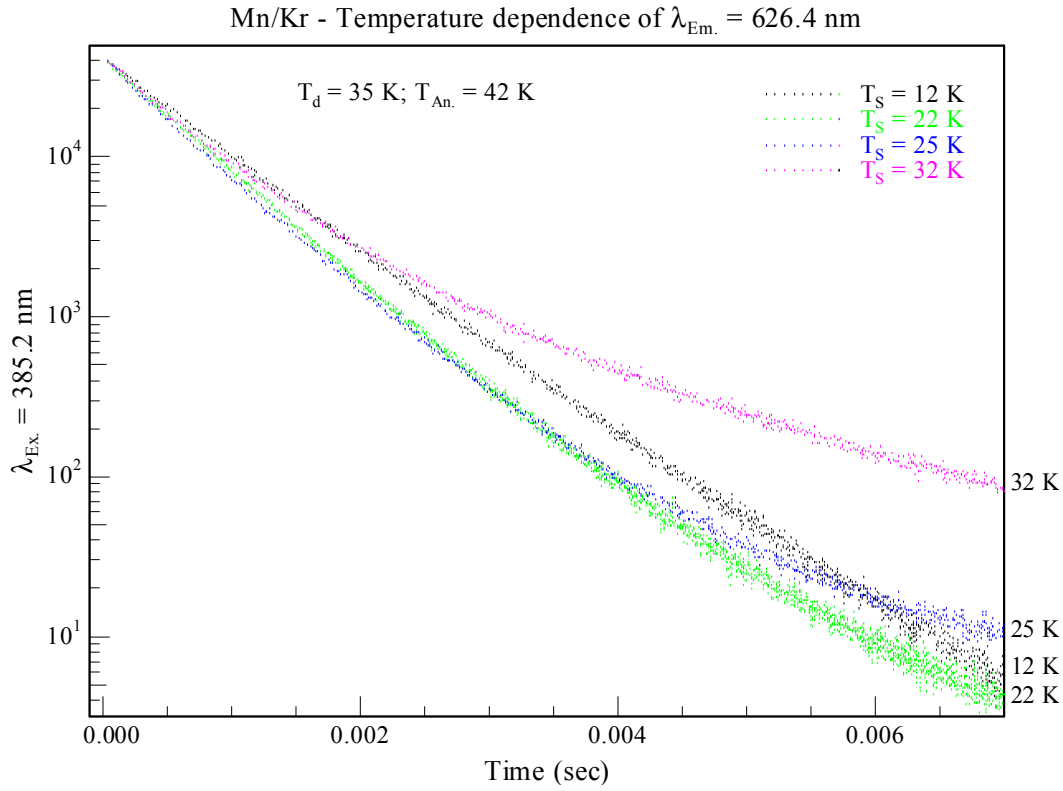

Figure VII.51 **Decay profiles recorded monitoring the 626.4 emission feature produced with 1° site $z^6P_{5/2} \leftarrow a^6S_{5/2}$ excitation at 385.15 nm at the temperatures indicated.**

The conflicting characteristics of the broad Gaussian lineshape, the spectral location and the complex emission kinetics do not allow the definitive assignment of the 626.4 nm emission feature to either the $z^8P_{5/2}$ or the $a^6D_{9/2}$ states of atomic Mn in solid Kr.

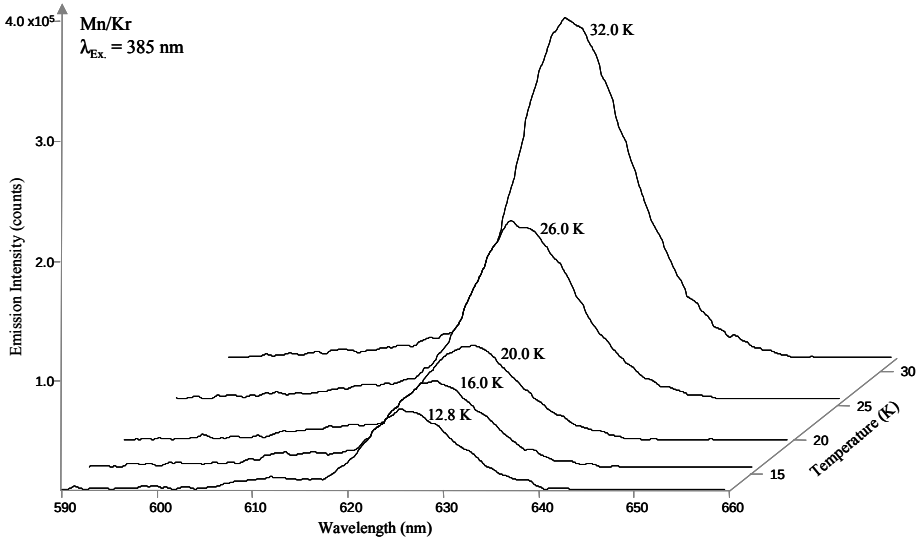

Figure VII.52 **Time-integrated emission spectra recorded following $z^6P_{5/2} \leftarrow a^6S_{5/2}$ blue (1°) site specific continuous W-lamp excitation at 385 nm at various temperatures.**

VII.2.III.III Mn(z^6P)/Kr - 2° site luminescence

In the following section, the narrow emission features located at 428.4 and 585.3 nm are assigned to electronic transitions of atomic Mn produced with red (2°) site resonance $z^6P_{5/2} \leftarrow a^6S_{5/2}$ excitation. Excitation spectra shown in Figure VII.39 reveal the presence of the 2° site centered at 398.3 nm (25107 cm^{-1}). Subsequent matrix annealing showed the thermal stability of the emissions at 428.4 and 585.3 nm over the 3° site that resulted in the labile 431.7 nm emission, (see Figure VII.38 and Figure VII.40).

Mn(z^6P)/Kr - 2° Site - $\lambda_{Em.} \approx 428.4$ nm

The left panel of Figure VII.53 presents a high-resolution emission spectrum recorded with laser excitation at 400 nm. Deposition was completed at 12 K and the sample was subsequently annealed to 38 K. Inspection of Figure VII.53 reveals five resolved emission components located at 427.68, 427.82, 427.88, 428.01 and 428.65 nm at 12 K. The spectral location and the narrow linewidth of the emission features are suggestive of a D → S type transition. At higher temperatures, the overall emission intensity decreased and the emission lineshape broadened substantially as evident in Figure VII.53.

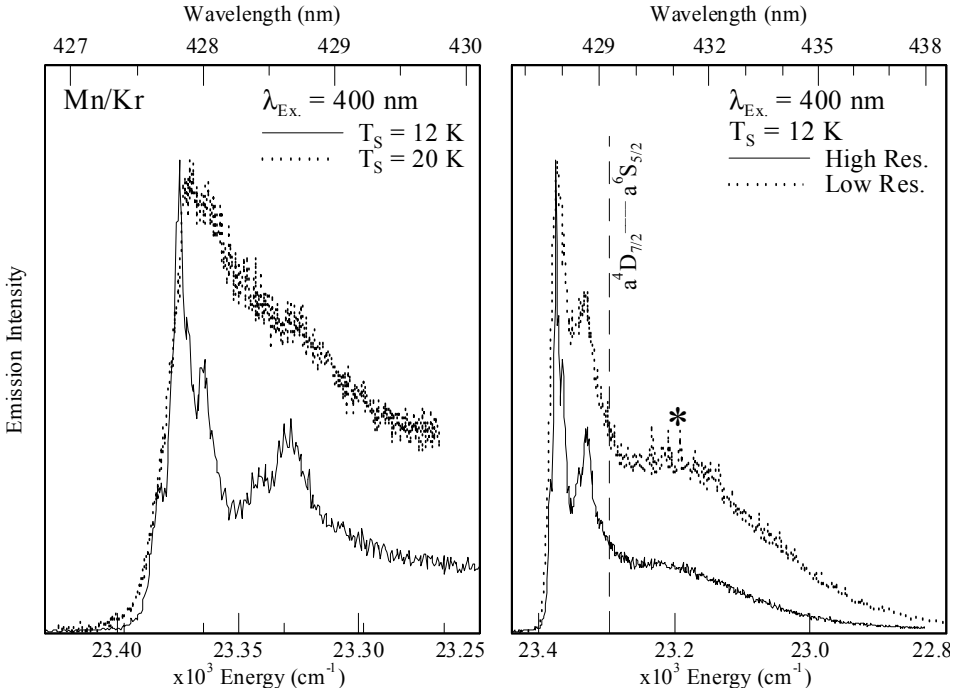

Figure VII.53 Site specific high-resolution emission spectra produced with pulsed laser excitation at 400 nm at 12 K (solid) and 25 K (dotted) shown left. The right panel depicts the effect of increased spectral resolution as indicated.

The narrow emission bands near 427.8 nm in Kr are reminiscent of those observed in Mn/Ar at 427.5 nm. This latter emission resulted from red (1°) site $z^6P_{5/2}$ state excitation in solid Ar shown in Figure VII.16. Wp lineshape analyses of the Mn/Ar emission assigned to the $a^4D_{7/2} \rightarrow a^6S_{5/2}$ transition, required the use of two sets of oscillators and allowed the identification of two band origins ($\nu_{0,0}$) shown in Figure VII.21 and Figure VII.23 respectively. The Mn/Ar Wp analysis also showed that the high temperature emission band profile was dominated by the component with the larger phonon frequency ($\hbar\omega$ = 35 cm^{-1}). The same analysis was conducted on the resolved emission features in the 427.8 nm band of the Mn/Kr system. The initial step in the Wp analysis, was estimating the phonon frequency of $\hbar\omega$ = 42 cm^{-1}. This allowed a fit, shown in Figure VII.54, of three of the emission features employing an electron-phonon coupling strength of S = 0.4. This S value was selected from the relative intensities of the two resolved high energy emission components, as the low energy portion shows an increased emission intensity due to the spectral overlap with the 431.7 nm emission not fully removed by the annealing process. As shown on the right hand side of Figure VII.53, the contribution of the thermally labile emission to the 428 nm lineshape is reduced by recording the emission using the highest resolution possible. The effect of the increased resolution is shown on the right of Figure VII.53. The Wp lineshape analyses presented in Figure VII.54 was successful in fitting the dominant emission features at 12 and 20 K. It is evident from the number of resolved features unaccounted for by the Wp Fit 1, that a second Wp function is required to complete the analysis at 12 K. The blue shoulder band located at 427.66 nm (23383 cm^{-1}) was selected as the second ZPL. Using a phonon frequency of $\hbar\omega$ = 19 cm^{-1} allowed an adequate fit of the remaining resolved features observed at 12 K, shown in Figure VII.55. The second Wp function also allowed a fit of the emission linewidth and the intensity distribution observed at 20 K, but is unable to fit the asymmetry observed at high energy as shown on the right panel of Figure VII.55.

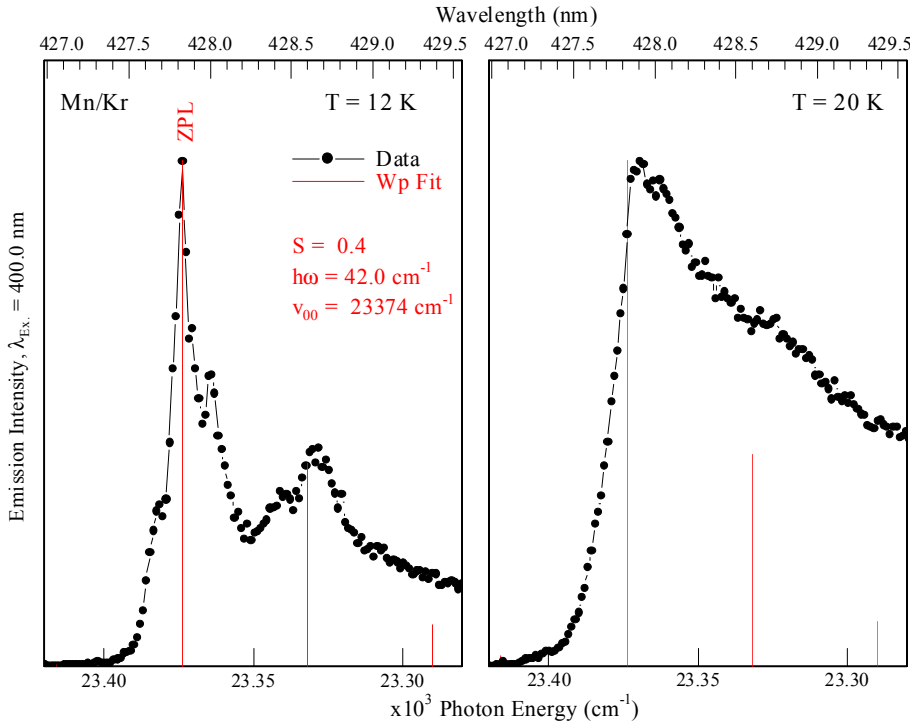

Figure VII.54 **The Wp lineshapes calculated with Equation III.4 for the resolved emission features observed in solid Kr at 12 K and 20 K produced with site specific pulsed laser excitation at 400 nm corresponding to the $z^6P_{5/2} \leftarrow a^6S_{5/2}$ transition from 2° site. The location of the zero phonon line is indicated as ZPL and $\nu_{0,0}$ in wavenumber units.**

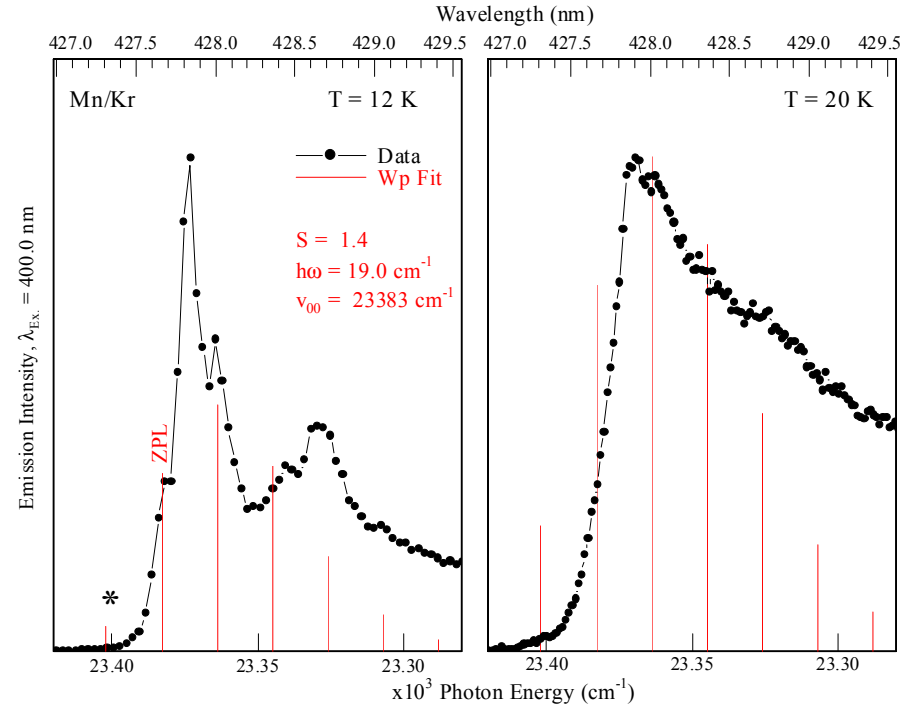

Figure VII.55 **The second Wp lineshapes calculated with Equation III.4 for the resolved emission features observed in solid Kr at 12 K and 20 K produced with site specific pulsed laser excitation at 400 nm corresponding to the $z^6P_{5/2} \leftarrow a^6S_{5/2}$ transition from 2° site. The location of the zero phonon line is indicated as ZPL and $\nu_{0,0}$ in wavenumber units.**

An assessment of the overall quality of the fits completed is presented in Figure VII.56, where Gaussian functions exhibiting linewidths of 5.4 cm^{-1}, corresponding to the linewidth of the ZPL identified at 23374 cm^{-1} are shown. The fitted Gaussian functions have been substituted for the Wp positions and are scaled to reflect the intensity distribution at 12 K. This analysis shows that both intensity distributions (Wp Fit 1 and 2) are required to simulate the band profile observed at 12 K. This analysis succeeds in reproducing the high-energy features corresponding to the positions of the ZPL's. In addition, the simulation predicts the weak features located at 428.45 and 428.65 nm. However, the simulation is unable to reproduce the broad underlying low energy feature. This feature is attributed to a residual amount to the thermally unstable 431.7 nm band, which exhibits a broad Gaussian lineshape as shown in Figure VII.53.

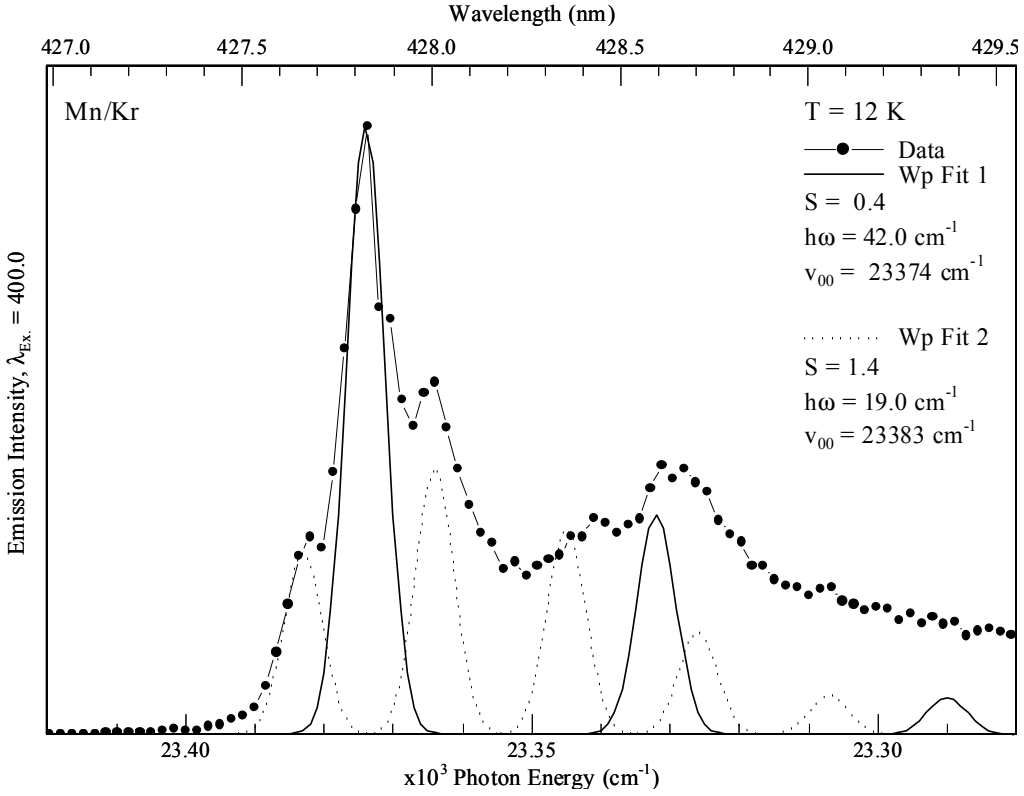

Figure VII.56 Simulation of the emission band profile generated using Gaussian lineshapes (*fwhm* 5.6 cm^{-1}) for both of the Wp distributions identified as described in the text. The parameters and the positions of the two ZPL's ($\nu_{0,0}$) identified are indicated.

Table VII.11 summarises the results of the Wp lineshape analysis completed. Overall, the Mn/Kr Wp analysis strongly resembles that done for Mn/Ar (Section VII.2.II.II), which also showed that the high temperature emission band profile was

dominated by the component with the larger phonon frequency. The spectral separation between the two ZPL's identified is attributed to a crystal field effect generated by the site of isolation. This indicates a crystal field splitting of 9.0 cm^{-1} for the a^4D state of atomic manganese in solid Kr.

Table VII.11 The location of the ZPL's extracted in the Wp lineshape analyses of the emission assigned to the $a^4D_{7/2} \rightarrow a^6S_{5/2}$ transition in solid Kr.

Transition	*ZPL*, $\nu_{0,0}$ (cm^{-1})	*S*	$h,^{-}\omega$ (cm^{-1})
$a^4D_{7/2} \leftrightarrow a^6S_{5/2}$ - Wp Fit 1	23374	0.4	42
$a^4D_{7/2} \leftrightarrow a^6S_{5/2}$ - Wp Fit 2	23383	1.4	19

The decay profile recorded monitoring the most intense resolved emission feature centered at 427.84 nm (corresponding to the *ZPL* identified from the primary Wp lineshape function) at 12 K is presented in Figure VII.57. An adequate fit of the decay profile was achieved using a double exponential trial function that allowed the extraction of two excited state lifetime values of 23.97 msec and 12.49 msec. The longer decay component of 23.97 msec, dominated at 12 K and is identified as the observed lifetime. This excited state lifetime is consistent with assignment of the observed emission to that of the $a^4D_{7/2} \rightarrow a^6S_{5/2}$ phosphorescent transition of atomic Mn isolated in Kr matrices, as the transition is both spin and parity forbidden. The same analysis was applied to the emission feature observed at 428.66 nm. The decay profile recorded at 12 K (shown in Figure VII.58) exhibited increased complexity and required the use of a triple exponential function to provide an adequate fit. The dominant decay component had a lifetime of 11.9 msec. This component compares well to the second short decay component extracted from the analysis of the 427.86 nm feature. As such this shortening of the observed decay time is assigned to the enhancement $a^4D_{7/2} \rightarrow a^6S_{5/2}$ transition from a selection rule relaxation induced by local phonon interaction. The additional third component (τ_3 = 5.0 msec) observed in the decay profile of the 428.66 nm feature of Figure VII.58 originates from spectral overlap with the broad 431.7 nm emission. This is confirmed by decay times of 26.4, 9.9 and 2.2 msec which were extracted monitoring the 431.7 nm emission feature fitted with a triple exponential trial function.

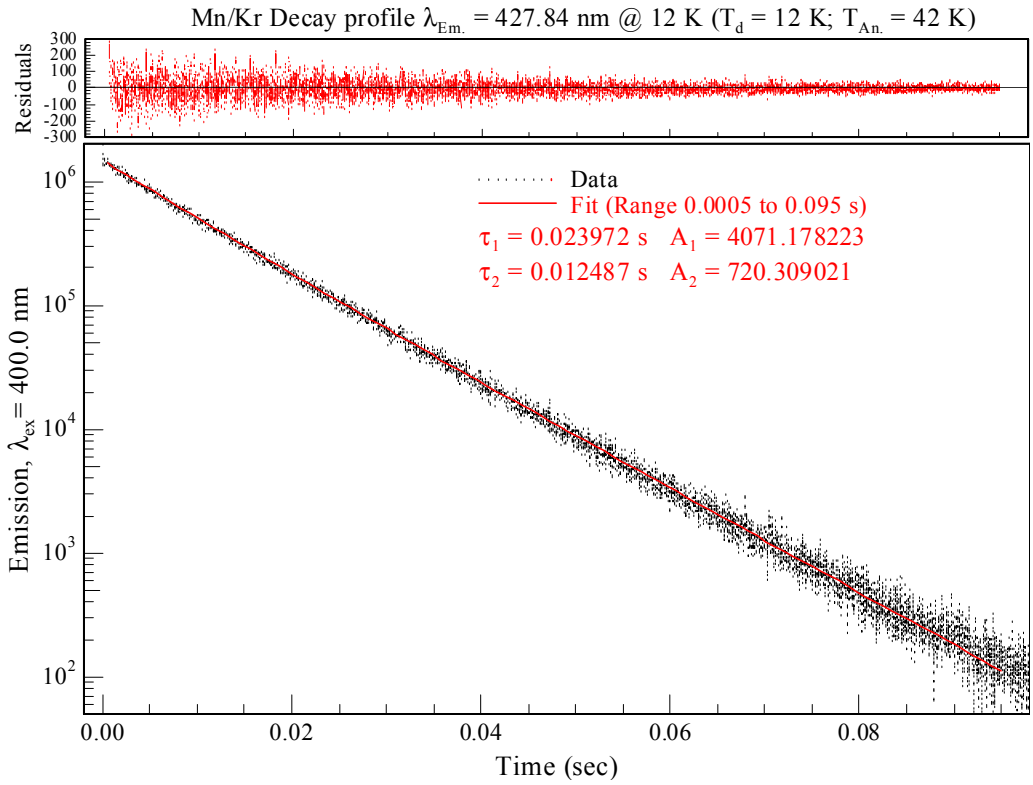

Figure VII.57 **Decay profile of the 427.84 nm emission feature recorded at 12 K using TCSPC following pulsed laser excitation at 400 nm.**

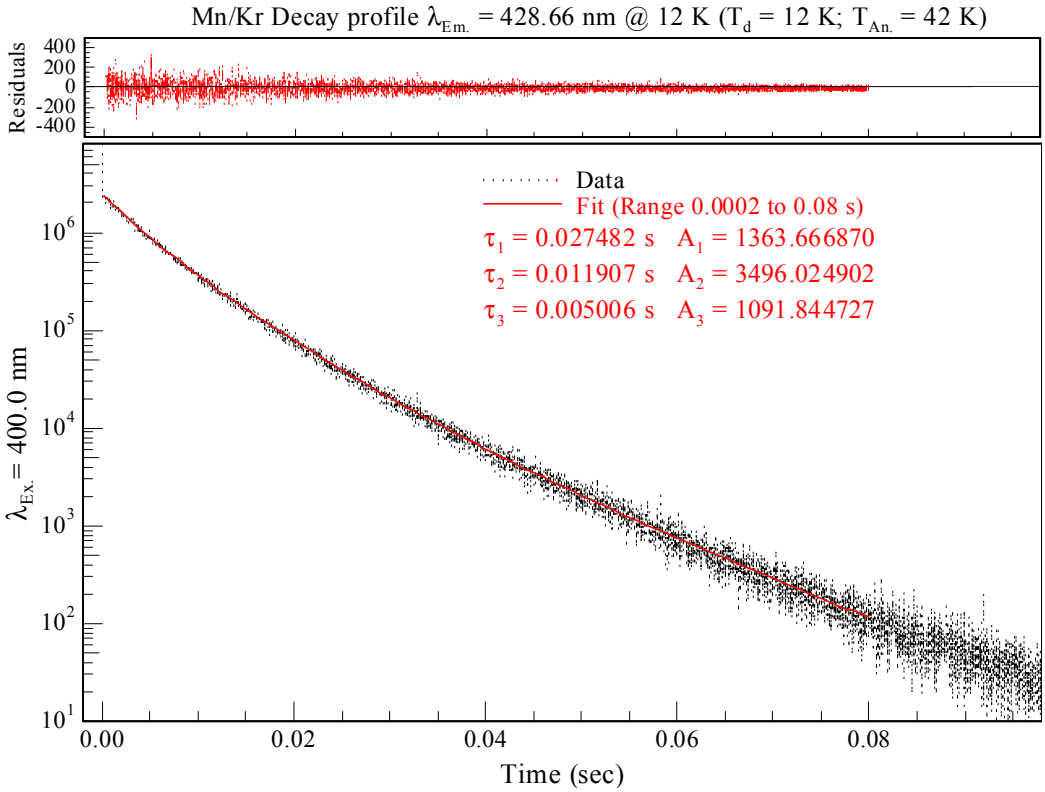

Figure VII.58 **Decay profile of the 428.66 nm emission recorded at 12 K using TCSPC following pulsed laser excitation at 400 nm. The residuals present the difference between the triple exponential fit and the decay recorded.**

The excited state lifetime identified for the pure electronic $a^4D_{7/2} \rightarrow a^6S_{5/2}$ transition (ZPL) in solid Kr is 24 msec. However, the decay times were observed to be temperature dependent at 12 K hence the radiative lifetime of the $a^4D_{7/2}$ excited state has not been identified.

Table VII.12 **Excited state decay components (τ) and amplitudes (A) extracted using exponential functions to fit to the decay curves recorded monitoring the 427.86 nm corresponding to the ZPL identified in Wp fit 1 and the phonon sideband at 428.66 nm at 12 K following pulsed laser excitation at 400 nm. Note the dominant decay contribution is presented in bold.**

$\lambda_{Em.}$ (nm)	Fit Range (msec)	A_1	τ_1 (msec)	A_2	τ_2 (msec)	A_3	τ_3 (msec)
427.84	0.5 – 95.0	**4071.2**	**23.97**	720.3	12.49	-	-
428.66	0.2 – 80.0	2363.7	27.48	**3496.0**	**11.91**	1901.8	5.0

The resolved emission features centered at 428 nm in solid Kr following red (2°) site excitation at 400 nm are assigned to ZPL's and phonon side-bands of the $a^4D_{7/2} \rightarrow a^6S_{5/2}$ transition of atomic Mn. These assignments were based on the spectral and temporal characteristics presented in the previous sections. A comparison of the observed matrix lifetimes (solid Ar and Kr) reveals the similarity in the relaxation time of the pure electronic transitions assigned. In solid Ar and Kr the observed lifetimes for the $a^4D_{7/2} \rightarrow a^6S_{5/2}$ transitions are 25.28 and 23.97 msec respectively. The decay times recorded were temperature dependent so these lifetimes are not identified as the radiative lifetimes of the $a^4D_{7/2} \rightarrow a^6S_{5/2}$ transition of atomic Mn. Moreover, the gas phase lifetime for the $a^4D \leftrightarrow a^6S$ transition which is both electric-dipole and electric-quadrupole forbidden is unknown.

Mn(z^6P)/Kr - 2° Site - $\lambda_{Em.} \approx$ 585.8 nm

The second, narrow emission present at 585.8 nm (17070 cm^{-1}) as a result of red (2°) site excitation is shown in the top panel of Figure VII.40. This feature is blue shifted of the atomic Mn gas phase $a^6D_{9/2} \leftrightarrow a^6S_{5/2}$ transition[1] (586.43 nm, 17052 cm^{-1}) by only 18 cm^{-1}. High-resolution emission spectra recorded in this spectral region at 12 K employing pulsed laser excitation are indicated by the solid line in Figure VII.59. A clear asymmetry in the emission band profile is evident. Recording the emission at temperatures in excess of 12 K, resulted in the reduction of the intensity of sharp feature relative to the broad sideband, as shown in Figure VII.59. The temperature

dependence exhibited was completely reversible, an effect characteristic of phonon structure on the emission profile. Therefore, the *ZPL* is assigned to 585.8 nm (17070 cm^{-1}) with the phonon sideband occurring to lower energy at 588 nm (17007 cm^{-1}).

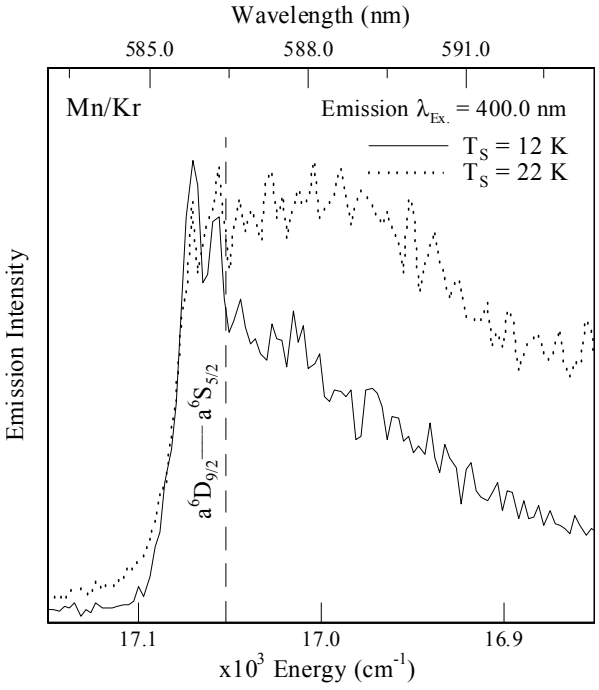

Figure VII.59 Mn/Kr time-resolved emission spectra produced with red (2°) site pulsed laser excitation ($\lambda_{Ex.}$ = 400 nm) at 12 K and 22 K, following annealing to 42 K.

Fitting the decay profile recorded at 12 K monitoring the *ZPL* at 585.8 nm, using a double exponential fitting function, allowed the extraction of the excited state decay characteristics as shown in Figure VII.60. The two decay components extracted are 287 and 147 μsec[12].

No temperature dependent decay profiles were recorded. Therefore, at present the dominant temporal component τ = 287 μsec is assigned as the observed lifetime for the electronic transition. However, this value is substantially shorter than the lifetime of 3.4 sec calculated[3] for the $a^6D_{9/2} \leftrightarrow a^6S_{5/2}$ transition of atomic manganese in the gas phase. Based on the spectral location of the band and the temperature dependence exhibited, the 585.8 nm emission is assigned to the $a^6D_{9/2} \rightarrow a^6S_{5/2}$ transition of atomic Mn. The assignment of this emission feature is discussed in greater depth in the next Chapter following the presentation of the luminescence of the a^6D state produced with direct dye laser excitation of the forbidden $a^6D \leftarrow a^6S$ transition.

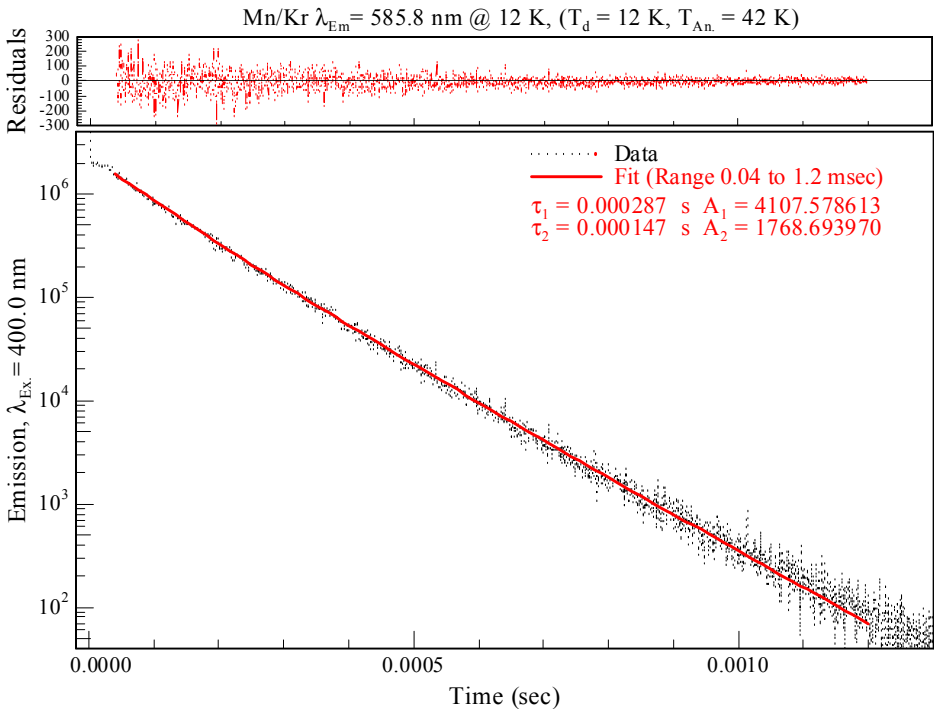

Figure VII.60 **Decay profile of the 585.9 nm emission recorded at 12 K using TCSPC following pulsed laser excitation at 400 nm. Note the early portion of the decay profile not accounted for by the double exponential fit[12] and therefore truncated at ≈ 40 μsec. This was required due to pulse-pile up in emission.**

VII.2.III.IV Discussion - Mn(z^6P)/Kr

A summary of all the luminescence spectroscopy resulting from excitation of the $z^6P_{5/2} \leftrightarrow a^6S_{5/2}$ transition of atomic Mn isolated in solid Kr is presented in Figure VII.61. The relative positions of the gas phase transitions of atomic Mn are indicated by the vertical lines and the emission features produced by excitation of the thermally unstable 3° site are indicated by an asterisk. The emission features resultant from blue (1°) and red (2°) site-specific excitation are labelled with arrows to indicate the assigned electronic transition. The emission features at 416, 440 and 626.8 nm produced by $z^6P_{5/2}$ excitation of Mn atoms isolated in the dominant (blue) site of isolation are shown in the bottom right of Figure VII.61. The photophysical properties and where possible, the electronic transitions assigned to the observed matrix emission bands, are presented in Table VII.13. In the following section, the mechanisms leading to the production of the observed features are discussed and the site specificity of the emission spectroscopy is highlighted.

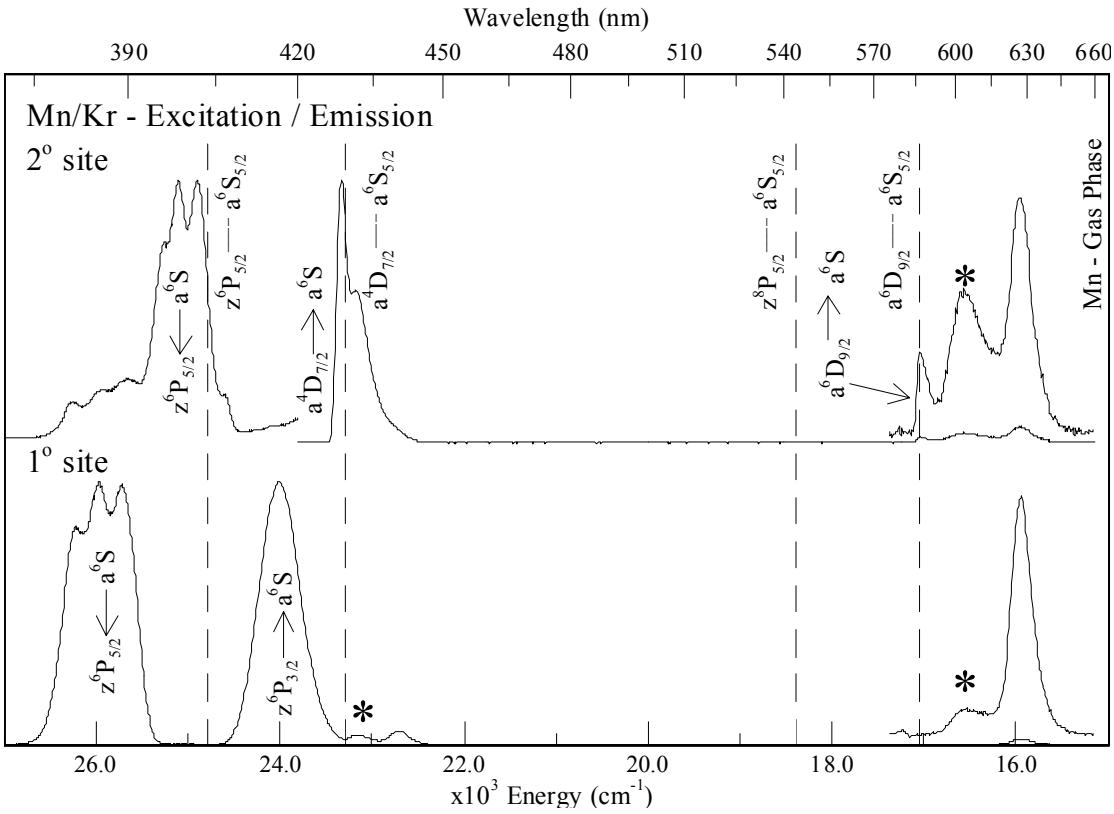

Figure VII.61 **Emission spectra recorded at 12 K for the Mn/Kr system with site-selective lamp excitation of the Mn $z^6P_{5/2} \leftarrow a^6S_{5/2}$ transition. The excitation spectra (1° and 2° site), were recorded by monitoring emission at 428.4 (top) and 416 / 626 nm (bottom) for the 1° and 2° sites respectively are shown by the dash-dot trances left. Spectra were recorded following Mn/Kr sample deposition at T_d= 12 K and matrix annealing to $T_{An.}$ >32 K. The spectral positions of the gas phase transitions of atomic Mn are shown by the dashed vertical lines. The observed Mn/Kr matrix absorption and emission bands assigned are indicated. Note * indicates the emission band is produced by excitation of the thermally unstable 3° site as the excitation band profile overlaps both the 1° and 2° sites see Figure VII.39.**

Firstly, site-specific emission features are clear from inspection of Figure VII.61 as reflected in the excited states assigned. The blue (1°) site produces resonance $z^6P_{3/2} \rightarrow a^6S_{5/2}$ fluorescence at 416 nm - an assignment which is strong due to the close agreement between the gas phase lifetime, $\tau_{G.P.}$ = 66.1 ± 1.4 nsec[9] and the matrix radiative lifetime τ_{Rad} = 55.3 nsec identified. However, the 440 nm emission that exhibits a linewidth of 280 cm^{-1} is unassigned due to the conflicting spectral and temporal data available.

The 626.8 nm emission feature also remains unassigned. Like the 440 nm emission, the linewidth observed and the spectral position alone do not allow a definitive state assignment of this feature. Moreover, multiple non-radiative channels are believed to be involved in the production of the 626.8 nm band following z^6P

excitation involving more than one low lying excited state, all of which lead to the complex cascade kinetics suggested by the temperature dependence observed in the decay profiles

Table VII.13 **Photophysical characteristics and excited state assignments of the emission features produced following excitation of the $3d^54s4p\ z^6P_{5/2} \leftarrow 3d^54s^2\ a^6S_{5/2}$ transition of matrix – isolated atomic manganese isolated in the high energy 1° site centered at 385 nm (25974 cm^{-1}). λ_{Em} indicates the emission band-centre in nm units. The full-width at half-maximum intensity of the emission features is denoted by Δ_{AV} and the matrix shift by δ - both in wavenumber (cm^{-1}) units. The excited state lifetimes (decay characteristics) are presented (τ) the subscripts Rad. and Cor indicate the radiative lifetime of the excited state and the lifetimes corrected for the effective field. $\tau_{Obs.}$ indicates the dominant decay characteristic at 12 K.**

Mn Gas Phase	**Mn/Kr Matrix (1° site)**			
Transition nm / cm^{-1}	Assignment	$\lambda_{Em.}$ (nm) / Δ (cm^{-1})	δ (cm^{-1})	Decay time
$z^6P_{3/2} \leftrightarrow a^6S_{5/2}$ 403.56 / 24779	$z^6P_{3/2} \rightarrow a^6S_{5/2}$	416 / ≈ 505	-740	τ_{Rad} = 55.3 nsec
$z^6P_{3/2} \leftrightarrow a^6S_{5/2}$ 403.56 / 24779 $a^4D_{7/2} \leftrightarrow a^6S_{5/2}$ 429.25 / 23297	(?)	440.0 / ≈ 280	-2052 -570	$\tau_{obs.}$ = 0.1 sec
$z^8P_{5/2} \leftrightarrow a^6S_{5/2}$ 543.40 / 18402 $a^6D_{9/2} \leftrightarrow a^6S_{5/2}$ 586.43 / 17052	(?)	626.8 / ≈ 235	-2448 -1097	$\tau_{1\ Obs.}$= 564 μsec

The low energy (2°) site centered at 398.3 nm leads to the production of excited state emission bands at 428.4 and 585.8 nm as shown in the top panel of Figure VII.61. The photophysical characteristics of these emission features are presented in Table VII.14. Both of these emission features show narrow linewidths and occur relatively unshifted from the gas phase positions of the $a^4D_{7/2}$ and $a^6D_{9/2} \leftrightarrow a^6S_{5/2}$ transitions of atomic Mn. As a result, these bands have been assigned to the $a^4D_{7/2}$ and $a^6D_{9/2}$ states produced via an inter system crossing (ISC) mechanism. The production of the 428.4 nm emission feature is 100% efficient from the $z^6P_{5/2}$ state accessed in absorption. In addition, the lifetime measurements indicate the forbidden nature of the transition leading to the 427.8 nm band as the observed lifetime is 23.97 msec. The 585.8 nm emission feature produced with red (2°) site excitation was assigned based on the spectral location and the asymmetric lineshape to the $a^6D_{9/2} \rightarrow a^6S_{5/2}$ transition. The dominant decay component extracted for the 585.8 nm

emission was 287 μsec, suggesting a direct $z^6P \Rightarrow a^6D$ feeding mechanism leading to the production of the observed $a^6D_{9/2}$ state emission.

Table VII.14 **Photophysical characteristics and excited state assignments of the emission features produced following excitation of the $3d^54s4p\ z^6P_{5/2} \leftarrow 3d^54s^2\ a^6S_{5/2}$ transition of matrix – isolated atomic manganese isolated in the low energy 1° site centered at 400 nm (25000 cm^{-1}). λ_{Em} indicates the emission band-centre in nm units. The full-width at half-maximum intensity of the emission features is denoted by Δ and the matrix shift by δ both in wavenumber (cm^{-1}) units. The excited state lifetimes (decay times) presented are those corresponding to the dominant decay characteristic at 12 K.**

Mn Gas Phase	Mn/Kr Matrix (2° site)			
Transition nm / cm^{-1}	Assignment	$\lambda_{Em.}$ (nm) / Δ (cm^{-1})	δ (cm^{-1})	Decay time
$a^4D_{7/2} \leftrightarrow a^6S_{5/2}$ 429.25 / 23297	$a^4D_{7/2} \rightarrow a^6S_{5/2}$	427.8 / ≈ 5.4	+78	23.97 msec
$a^6D_{9/2} \leftrightarrow a^6S_{5/2}$ 586.43 / 17052	$a^6D_{9/2} \rightarrow a^6S_{5/2}$	585.3 / ≈ 65	+18	287 μsec

VII.3 Discussion Mn(z^6P)/RG luminescence

In this section, the luminescence spectroscopy recorded with excitation of the $z^6P_{5/2} \leftarrow a^6S_{5/2}$ transition of atomic Mn isolated in solid Ar, Kr and Xe is summarised in terms of site occupancy. Figure VII.62 and Figure VII.63 present the luminescence excitation and emission spectroscopy from the blue and red sites of isolation assigned to the $z^6P_{5/2} \leftrightarrow a^6S_{5/2}$ transition. The spectral positions of the gas phase transitions are indicated for comparison purposes.

The excitation spectra presented in Figure VII.62 for the blue site of isolation show an increasing shift away from the gas phase position for the $z^6P_{5/2} \leftrightarrow a^6S_{5/2}$ transition from Xe to Ar. The matrix shift is blue in all cases with values of 1531, 1187 and 500 cm^{-1} for Ar, Kr and Xe respectively. A decrease in the linewidth of the excitation band profile is exhibited from Ar to Xe, as shown in Figure VII.62. This effect is also exhibited by the red sites occupied by Mn atoms in solid Ar and Kr as shown in Figure VII.63.

All the excitation spectra shown exhibit Jahn-Teller threefold split patterns indicative of atomic isolation in highly symmetric environments. Given that a single site of isolation exists for Mn atoms in solid Xe and the trend in the Ar and Kr matrix shifts, evident in Figure VII.62, the blue site of isolation is assigned to a single substitutional site in each rare gas. Mn atoms isolated in solid Ar exhibit dominance

of the lower energy (red site) suggesting a preference for isolation in a larger, multi-vacancy type site.

The emission spectroscopy that is observed is very site–specific. Indeed the emission features produced with blue site excitation for Mn/Ar and Mn/Kr exhibit marked similarities, as shown in Figure VII.62. Thus both systems produce emission features assigned to $z^6P_{3/2}$ fluorescence occurring at 413 and 416 nm for Mn/Ar and Mn/Kr respectively exhibiting similar Stokes' shifts of 2106 and 1936 cm^{-1} and linewidths of 465 to 505 cm^{-1}. The radiative lifetimes of 57.5 and 55.3 nsec were extracted for the $z^6P \rightarrow a^6S$ transitions in solid Ar and Kr at 12 K. In contrast Mn/Xe exhibits no resonance z^6P fluorescence at all. This indicates that non-radiative relaxation processes occur for this state in Xe on a timescale faster than the nanosecond fluorescence observed in Ar and Kr.

Two emission features located at 438 and 440 nm in Ar and Kr matrices cannot at this stage be assigned to electronic transitions of atomic Mn due to the conflicting spectral and temporal data available. However, these features exhibit similar Stokes' shifts of 1948 and 2052 cm^{-1} and linewidths of 230 and 280 cm^{-1} in Ar and Kr respectively. They are discussed in Chapter VIII following further analysis of their associated features at 625 and 626.8 nm in Ar and Kr respectively. The aforementioned red features observed in Ar and Kr at 625 and 626.8 nm respectively are still unassigned. The following Chapter presents the luminescence recorded following excitation of both the z^8P and a^6D excited states in an attempt to definitively assign these red emission features. In solid Xe the single thermally stable emission feature at 620 nm is assigned to the $a^6D_{9/2} \rightarrow a^6S_{5/2}$ transition due to more efficient curve crossing processes occurring within the blue site which is thought to correspond to substitutional site occupancy. The topic of site occupancy will be discussed in Chapter IX.

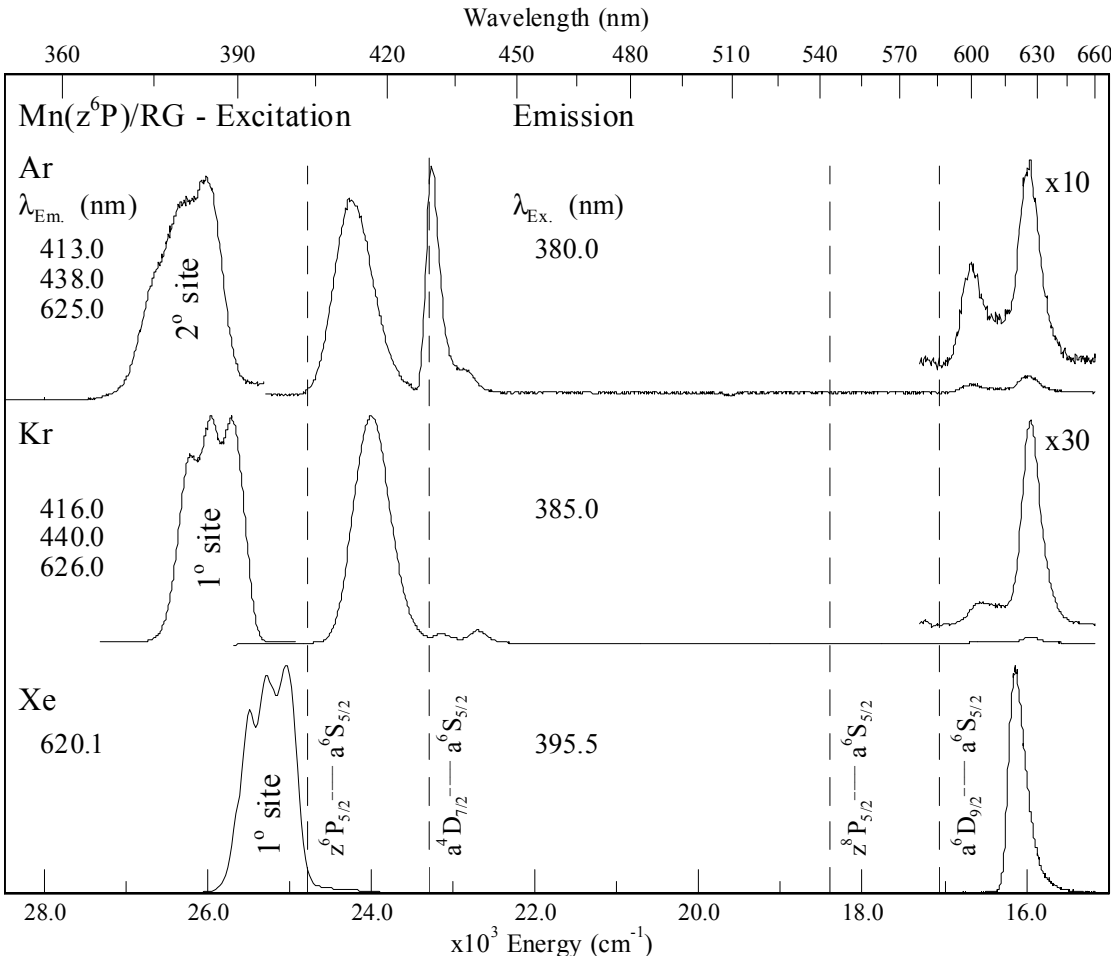

Figure VII.62 Emission spectra recorded at 12 K for atomic Mn/Ar, Mn/Kr and Mn/Xe systems with site-selective lamp excitation of the high energy blue site corresponding to the Mn $z^6P_{5/2} \leftarrow a^6S_{5/2}$ transition. The excitation wavelengths used are shown (centre) as $\lambda_{Ex.}$ (nm). The excitation spectra shown (left), were recorded by monitoring emission bands as indicated by $\lambda_{Em.}$ in wavelength units. All spectra were recorded following Mn/RG sample deposition at T_d= 12 K and matrix annealing. The spectral positions of the gas phase transitions of atomic Mn are shown by the dashed vertical lines.

The emission features produced in Ar and Kr at 428 nm with red site excitation are assigned to the $a^4D_{7/2} \rightarrow a^6S_{5/2}$ transition occurring with 100% efficiency via $z^6P \Rightarrow a^4D$ intersystem crossing. Wp lineshape analyses completed on each system allowed the identification of two ZPL's for the $a^4D_{7/2} \rightarrow a^6S_{5/2}$ transition in each system. The splitting between the ZPL's was identified as 9.0 and 10.0 cm^{-1} for Ar and Kr respectively. Low energy emission bands centered at 590 and 585.3 nm were assigned to the $a^6D_{9/2} \rightarrow a^6S_{5/2}$ transition of atomic Mn produced via an ISC mechanism from the a^4D state. This assignment accounted for the complex kinetics observed, a topic that is discussed further in the next Chapter.

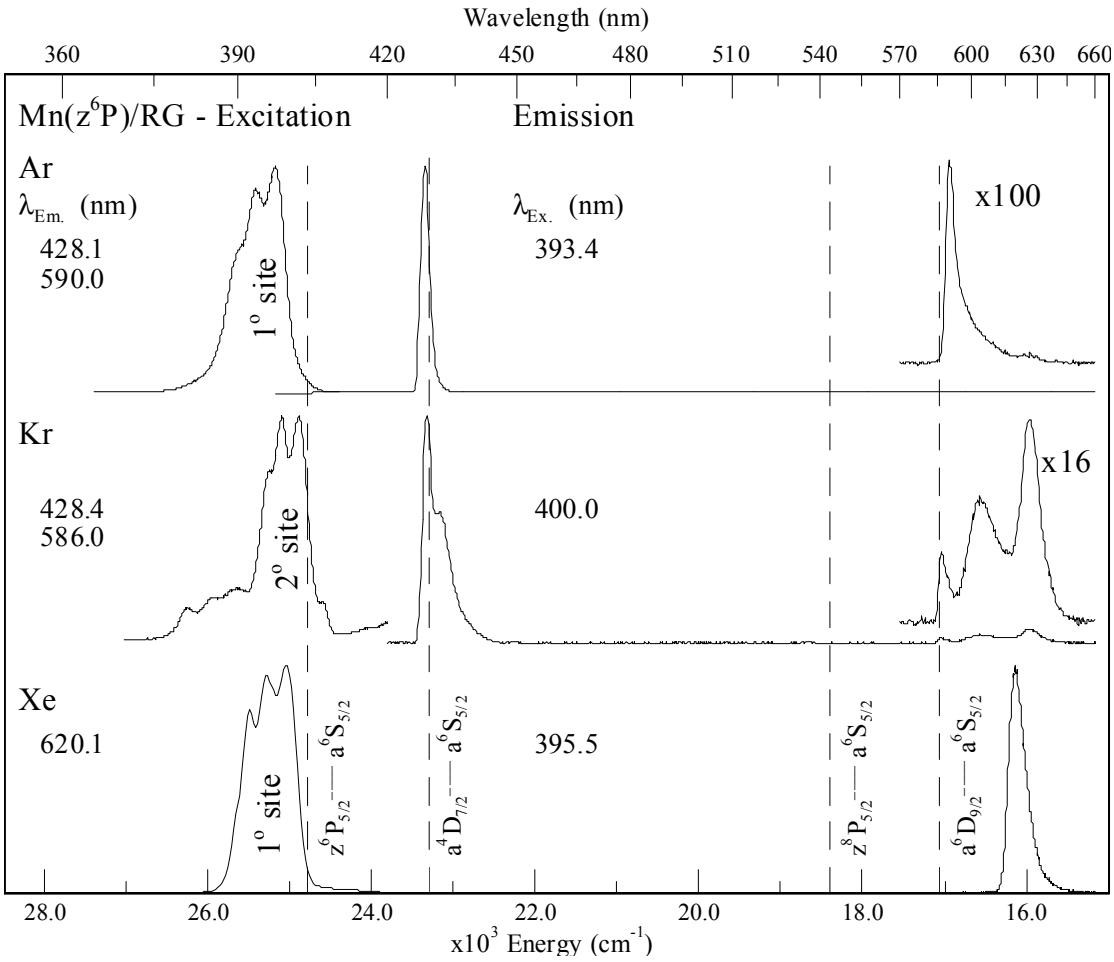

Figure VII.63 **Emission spectra recorded at 12 K for atomic Mn/Ar, Mn/Kr and Mn/Xe systems with site-selective lamp excitation of the low energy red-site corresponding to the Mn $z^6P_{5/2} \leftarrow a^6S_{5/2}$ transition in Ar and Kr and the thermally stable site in solid Xe. The excitation wavelengths used are shown (centre) as $\lambda_{Ex.}$ (nm). The excitation spectra shown (left), were recorded by monitoring emission bands as indicated by $\lambda_{Em.}$ in wavelength units. All spectra were recorded following Mn/RG sample deposition at T_d= 12 K and matrix annealing. The spectral positions of the gas phase transitions of atomic Mn are shown by the dashed vertical lines.**

VII.4 Conclusion

The luminescence spectroscopy observed for the excited z^6P state of atomic Mn isolated in solid Ar, Kr and Xe allowed the identification of multiple sites of isolation of Mn atoms in Ar and Kr and a single site in solid Xe. The excitation-emission spectra reported for each Mn/RG system allowed the deconvolution of the complicated absorption spectra reported in Chapter VI into separate site contributions. The steady-state and time-resolved emission spectroscopy (TRES) reported allowed the definitive assignment of two very site-specific relaxation

channels in the Mn/Ar and Mn/Kr systems giving rise to $z^6P \rightarrow a^6S$ fluorescence and $a^4D \rightarrow a^6S$ phosphorescence from the blue and red sites respectively. Excited state lifetime measurements definitively assigned $z^6P \rightarrow a^6S$ fluorescence at 413 and 416 nm in Ar and Kr respectively. In addition, a lifetime is reported for the first time for the forbidden $a^4D \rightarrow a^6S$ transition to be approximately 25 msec in both matrices. Currently, no experimental gas phase lifetime data is available for this transition. The results of lineshape analyses of the emission features assigned to the $a^4D \rightarrow a^6S$ transition allowed the identification of zero phonon lines and sidebands and the relative lifetimes of each. Also the requirement of two sets of phonon frequencies allowed the tentative assignment of the crystal field splitting parameter for the a^4D state of Mn atoms isolated in the red sites in Ar and Kr to be approximately 10 cm^{-1}. In solid Xe, no emission features were assigned to either the $z^6P \rightarrow a^6S$ or the $a^4D \rightarrow a^6S$ transitions of atomic Mn. The luminescence spectroscopy reported in the previous sections highlights the importance of the site of atomic isolation in determining the resulting excited state relaxation processes. Trends observed in the spectral analysis and knowledge of the site sizes available within the hosts, suggests single substitutional site occupancy in Xe, whereas Mn/Ar and Mn/Kr solids exhibit a combination of thermally stable sites that are tentatively assigned to substitutional and multi-vacancy type sites. A preference for the larger site was observed to increase from Kr to Ar. A definitive assignment of the site symmetries is not possible at present, as no data exists for the corresponding Mn·RG van der Waals complexes. The discussion of the site occupancy is postponed until Chapter IX.

References

1 N.I.S.T. Atomic Spectra Database, Website: http://physics.nist.gov/cgi-bin/AtData/display.ksh?/XXE0qMnqIXXP-15XXT2XXS, (Last accessed 4th February 2004).

2 S. M. Younger, J. R. Fuhr, G. A. Martin and W. L. Wiese, *J. Phys. Chem. Ref. Data* Vol. **7**, No. 2, 495, 1978.

3 A. A. Radzig and B. M. Smirnov, *Reference Data on Atoms, Molecules and Ions*, Springer-Verlag, Berlin, 1985.

4 The Mn/Ar 3° site identified by monitoring emission at 434 nm, red of the band maximum at 431 nm to avoid complication due to site overlap with the 428.3 nm feature. This third site is identified as the origin of the atomic Mn $z^6P_{5/2}$ absorption leads to the 600 nm emission band.

5 The relative intensity of the 427.5 nm and 590 nm emission features produced for Mn/Ar with site selective excitation at $\lambda_{Ex.}$ = 393.4 nm (1° Site) cannot be extracted from the emission spectra reported Figure VII.11, as the resolution used to record each is not comparable.

6 The linewidth identified for the ZPL of 6.6 cm^{-1} is greater than the spectral resolution of the ARC SpectraPro 500i monochromator used to monitor emission known to be 5.4 cm^{-1} at 438.5 nm, (Table II.6).

7 Intuitively it would be expected that the feeding rate from the a^4D state should produce a risetime on the 590 nm band. This is true only for the situation that the emission decay rate of the 590 nm band is slower than the rate at which the level is fed. Identification of the radiative decay rate of the 590 nm emission is attempted in Chapter VIII following laser excitation of the forbidden $a^6D_{5/2} \leftarrow a^6S_{5/2}$ at 573 nm

8 G. A. Martin, J. R. Fuhr and W. L. Wiese, Atomic Transition Probabilities Scandium through Manganese, *J. Phys. Chem. Ref. Data,* Vol. 1**7**, No. 3, 1, 1988.

9 R. Schnabel, A. Bard and M. Kock, *Zeitschrift für Physik D*, **34**, 223, 1995.

10 The index of refractive used for solid Ar at 233 nm is 1.32 at 6 K, (P. Gürtler, *unpublished results*, 1996).

11 The index of refractive used for solid Kr at 241 nm is 1.428 at 12 K, (P. Gürtler, *unpublished results*, 1996).

12 The fit completed to the decay profile recorded monitoring the 585.8 nm emission feature produced with red (2°) site excitation at 400 nm shown in Figure VII.60 is truncated at early time ≈ 40 μsec. This was required due to pulse-pile up in emission.

Chapter VIII

Direct laser excitation of the 'forbidden' $z^8P \leftrightarrow a^6S$ and $a^6D \leftrightarrow a^6S$ transitions of atomic Mn/RG solids, (RG = Ar, Kr and Xe)

VIII.1 Introduction

The luminescence spectroscopy resulting from $z^6P_{5/2}$ excitation of atomic manganese isolated in solid Ar, Kr and Xe presented in Chapter VII, yielded complex kinetics and only tentative assignment of both the $z^8P_{5/2} \rightarrow a^6S_{5/2}$ and $a^6D_{9/2} \rightarrow a^6S_{5/2}$ transitions to emission bands in the red region of the spectrum. The requirement of obtaining simpler kinetics and more definitive spectral assignments prompted an investigation of the excitation spectroscopy in the regions of the forbidden $3d^54s4p$ $z^8P_{5/2} \leftrightarrow 3d^54s^2$ $a^6S_{5/2}$ and $3d^64s$ $a^6D_{5/2} \leftrightarrow 3d^54s^2$ $a^6S_{5/2}$ transitions at 543.4 and 573 nm, (18402.46 and 17451.52 cm^{-1}) respectively in the gas phase[1]. The weak oscillator strengths of the spin forbidden $z^8P_{5/2}$ and parity forbidden $a^6D_{9/2}$ transitions from the ground state $a^6S_{5/2}$ state required the use of a high intensity excitation source. Hence a nanosecond pulsed laser was employed. The relative weakness of these forbidden transitions versus the allowed $3d^54s4p$ $z^6P_{5/2} \leftrightarrow 3d^54s^2$ $a^6S_{5/2}$ transition, is revealed in the recorded matrix absorption spectra where none of these forbidden transitions were detected. This behaviour correlates with the long radiative lifetimes of 149.3 μsec and 3.4 sec calculated for the gas phase $z^8P \leftrightarrow a^6S$ and $a^6D \leftrightarrow a^6S$ transitions[2,3,4] respectively as presented in Figure VIII.1.

Prior to the presentation of the results of the luminescence spectroscopy produced with direct $z^8P_{5/2}$ and $a^6D_{5/2} \leftrightarrow a^6S_{5/2}$ excitations, a short review of the spectral assignments made, the questions posed and the trends evident in the emission spectroscopy reported in Chapter VII is given.

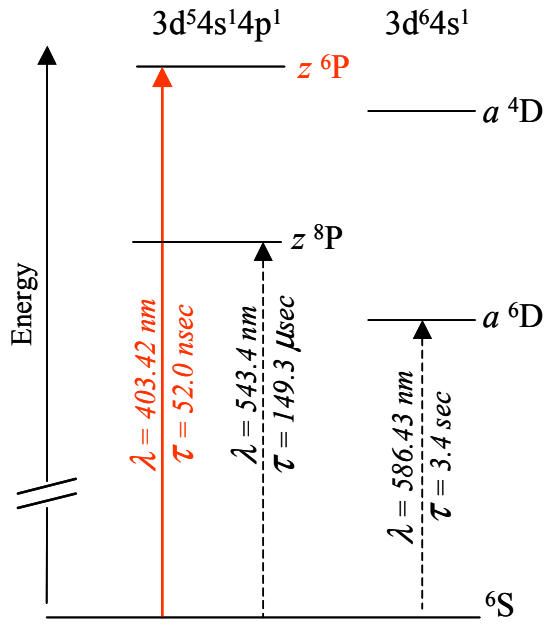

Figure VIII.1 **Schematic representation of the energy levels of gas phase atomic manganese. The $z^6P_{5/2}$; $z^8P_{5/2}$ and $a^6D_{5/2} \leftrightarrow a^6S_{5/2}$ transitions occur at 24788 cm^{-1} (403.42 nm); 18402 cm^{-1} (543.40 nm) and 17451 cm^{-1} (573.03 nm)[1]. The arrows indicate the difference between the allowed (solid) and forbidden (broken) optical transitions. The known gas phase radiative lifetimes[2-4] (τ) for these transitions are indicated.**

Mn/Xe was observed to be the simplest of the rare gas systems as only a single thermally stable site of isolation was identified in absorption spectra, blue-shifted with respect to the gas phase position of the $z^6P_{5/2} \leftarrow a^6S_{5/2}$ transition. A single emission band located at 620 nm (16129 cm^{-1}) with a linewidth (*fwhm*) of 240 cm^{-1} was tentatively assigned to the $a^6D_{9/2} \rightarrow a^6S_{5/2}$ transition, corresponding to a red matrix-shift of 926 cm^{-1}, as shown in Figure VII.2. Emission lifetime measurements recorded at various temperatures revealed long-lived but complex decay kinetics for the observed 620 nm emission band. The spectral position, the asymmetric emission profile and the extracted decay times suggested an assignment of the 620 nm feature to the $a^6D_{9/2} \rightarrow a^6S_{5/2}$ transition. However, the absence of $z^8P_{5/2}$ state emission bands and the moderately broad 620 nm lineshape did not completely preclude this alternative assignment. Therefore, definitive assignment of the 620 nm emission feature required an investigation of the luminescence spectroscopy of Mn/Xe with direct excitation of the forbidden $a^6D \leftarrow a^6S$ and $z^8P \leftarrow a^6D$ transitions.

The luminescence recorded with excitation of the Mn atom $z^6P_{5/2} \leftarrow a^6S_{5/2}$ transition in solid Ar and Kr was indicative of features due to the $z^8P_{3/2}$ and $a^6D_{9/2} \rightarrow a^6S_{5/2}$ transitions of atomic manganese. The high-energy blue sites lead to emission

bands at 413 and 416 nm (shown in Figure VII.64) definitively assigned to the $z^6P_{3/2} \rightarrow a^6S_{5/2}$ fluorescence in both matrices. However, the red spectral features at 625 and 626.8 nm that exhibited matrix shifts of 2002 and 2448 cm^{-1} and linewidths of approximately 260 and 235 cm^{-1} in Ar and Kr respectively, were not assigned to either the $z^8P_{5/2} \rightarrow a^6S_{5/2}$ or the $a^6D_{9/2} \rightarrow a^6S_{5/2}$ transitions.

The emission spectroscopy observed following red site excitation in solid Ar and Kr led to the tentative assignment of the narrow bands at 590 and 585.8 nm respectively to the $a^6D_{9/2} \rightarrow a^6S_{5/2}$ transition of atomic Mn. However, this assignment also presents an inconsistency, because although the emission bands show a clear asymmetry and small matrix shifts from the gas phase position, the 585.8 nm feature in Kr is blue of the assigned features in Ar and Xe. Definitive assignment of the emission features to the $a^6D_{9/2} \rightarrow a^6S_{5/2}$ transition following direct a^6D excitation would allow a discussion of possible reasons for this observation. Therefore analysis of the luminescence spectroscopy resulting from direct excitation of the forbidden $a^6D_{9/2} \leftarrow a^6S_{5/2}$ and $z^8P_{5/2} \leftarrow a^6S_{5/2}$ transitions of atomic Mn will provide simpler kinetics and thereby more definitive state assignments. The excitation spectra recorded for both of these forbidden transitions also allows a critical comparison of the absorption characteristics of Mn atoms undergoing P $\leftarrow$ S or D $\leftarrow$ S transitions.

This Chapter is structured as follows; firstly the excitation spectroscopy recorded by monitoring the red emission features identified in the previous chapter are presented for each Mn/RG system. Secondly, following an assessment of the sites of isolation, the excitation band profiles are analysed to extract detail on the excited state interaction within the specific sites of isolation. Thirdly, time-resolved emission spectra (TRES) and excited state lifetime measurements, recorded with pulsed dye laser excitation tuned to $a^6D_{5/2}$ and $z^8P_{5/2} \leftarrow {}^6S_{5/2}$ matrix transition energies, are employed to state assign the observed emission. Temperature dependent measurements are reported to provide insight into the non-radiative excited state dynamics and ISC processes leading to the observed emission. The luminescence results are presented first for excitation into the lowest energy level of atomic Mn, the metastable a^6D state. The same analysis is then applied to the $z^8P_{5/2}$ state. This allows an assessment of the extent of interaction between the z^8P and the a^6D states in determining the kinetics of the site-specific emission. Finally, the spectral and

temporal characteristics of the site-specific emission features assigned to transitions of atomic Mn resulting from a^6D, z^8P and z^6P excitation are presented.

VIII.2 Results Mn(a^6D)/RG luminescence

Chapter VII presented the luminescence spectroscopy resulting from excitation of the $z^6P_{5/2} \leftrightarrow a^6S_{5/2}$ transition of atomic manganese isolated in solid Ar, Kr and Xe. Analysis of the emission features produced and monitored using both time-integrated and time-resolved methods lead to possible assignment of the red emission bands in Ar and Kr at 590 and 585.8 nm (16949 and 17070 cm^{-1}) respectively, to the $a^6D_{9/2} \rightarrow a^6S_{5/2}$ transition. As shown in Figure VII.65 these emission bands are produced with red-site excitation only. The photophysical characteristics of the Mn/Ar and Mn/Kr emission features at 590 and 585.8 nm respectively are presented in Tables VII.6 and VII.13. In solid Xe, the single emission feature observed at 620 nm (16129 cm^{-1}) following $z^6P_{5/2}$ excitation, was tentatively assigned to the $a^6D_{9/2} \rightarrow a^6S_{5/2}$ transition. The following sections present excitation spectra recorded in the vicinity of the gas phase position[1] of the $a^6D_{5/2} \leftrightarrow a^6S_{5/2}$ transition at 573.03 nm (17451 cm^{-1}) using tuneable dye laser excitation. Rhodamine 590 was the laser dye material employed. It is tuneable over the spectral range 555 to 580 nm (Chapter II, Table II.IX, middle panel).

VIII.2.I Mn(a^6D)/Xe

Figure VIII.2 presents the laser excitation spectra recorded for Mn/Xe in the region of the gas phase $a^6D_{5/2} \leftrightarrow a^6S_{5/2}$ transition of atomic manganese monitoring the thermally stable and unstable emission features at 620 nm and 656 nm respectively. The excitation spectra shown have not been corrected for the wavelength response of the dye material, Rhodamine 590. Inspection of Figure VIII.2 reveals three resolved excitation features at 563.4, 565.4, 569.1 and a partially resolved band centered at 574 nm, monitoring the 620 nm emission. The excitation band profile recorded by monitoring the 656 nm feature is more diffuse, showing little resolved structure but is most intense at 572 nm. The spectral overlap in the excitation profiles recorded by monitoring the 620 and 656 nm bands is greatest at 572 nm.

The observation that the excitation band profiles remain relatively unshifted from the gas phase position of the $a^6D_{5/2} \leftrightarrow a^6S_{5/2}$ transition is indicative of a weak interaction between the a^6D excited state Mn atom and the immediate environment within the host matrix.

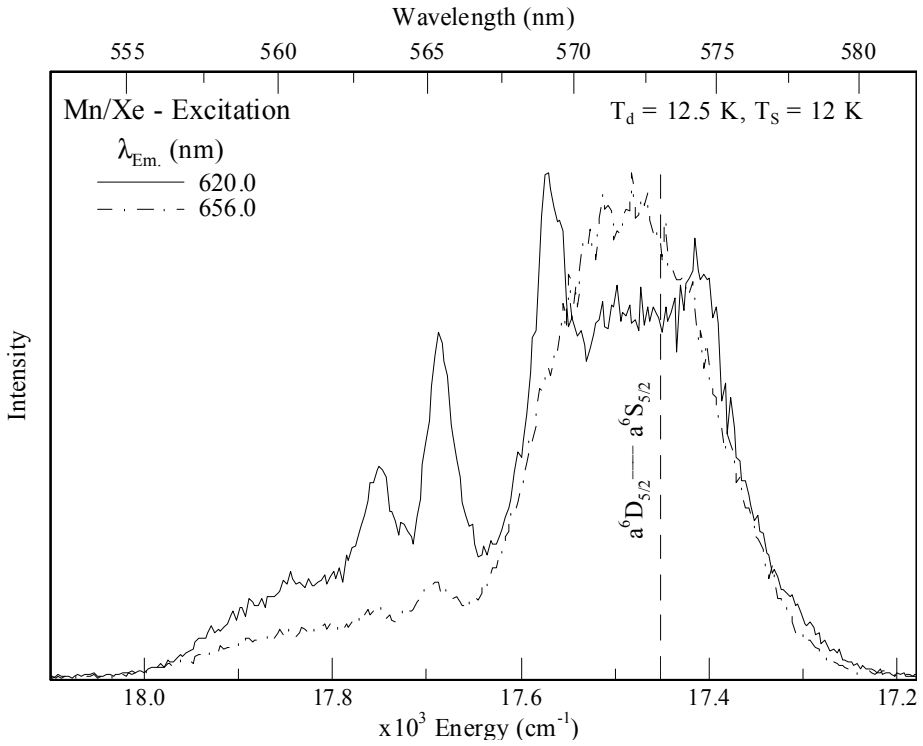

Figure VIII.2 Dye laser excitation spectra recorded at 12 K, in the vicinity of the $a^6D_{5/2} \leftrightarrow a^6S_{5/2}$ gas phase transition (dashed vertical line) monitoring the red emission features in solid Xe. The spectra recorded monitoring the thermally stable 620 nm emission and thermally unstable 656 nm emission bands are shown by the solid and dash-dot traces respectively.

Emission spectra recorded following laser excitation at wavelengths corresponding to the excitation features identified in Figure VIII.2 are presented in Figure VIII.3. It is evident from the emission features produced that irradiation at wavelengths corresponding to the resolved excitation features, blue of the gas phase $a^6D_{5/2} \leftrightarrow a^6S_{5/2}$ transition, efficiently produce the 620 nm feature. The 656 nm band is produced with excitation in the range 570 – 575 nm.

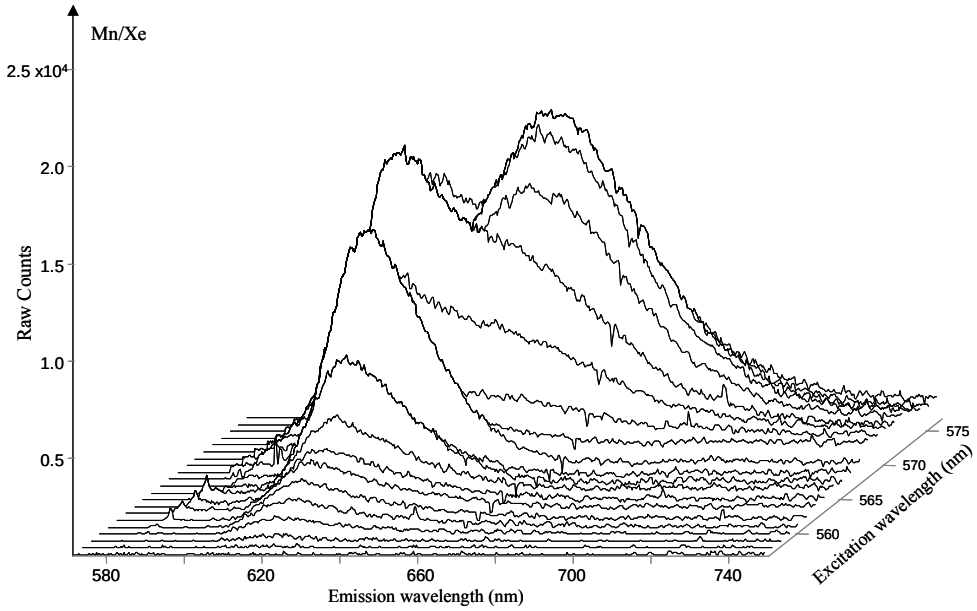

Figure VIII.3 Time-integrated emission spectra recorded in Mn/Xe with iCCD detection following dye laser excitation at various wavelengths within the range shown in Figure VIII.2.

The spectral overlap of the excitation band profiles recorded monitoring the 620 and 656 nm bands coupled with the previously identified thermal instability of the 656 nm band, (Figure VII.II) allows the subtraction of the 656 nm component from the excitation spectrum recorded for the 620 nm feature. The corrected excitation spectrum is presented in Figure VIII.4. Comparison of the raw excitation spectrum, Figure VIII.2 (solid trace), to that corrected for the presence of the overlapping 656 nm component Figure VIII.4, leads to the enhancement of lowest energy feature centered at 574.6 nm (17402 cm^{-1}). The correction procedure therefore allows clear identification of four narrow excitation features located at 563.38, 565.35, 569.12 and 574.6 nm.

A comparison of the observed matrix band positions with the gas phase transition energies[1] from the ground $a^6S_{5/2}$ state to the individual a^6D_J spin-orbit levels, J = $^9/_2$, $^7/_2$, $^5/_2$, $^3/_2$ and $^1/_2$ reveals the same splitting pattern. The splittings between the observed excitation bands are 62, 117 and 169 cm^{-1}, (Table VIII.1), while the gas phase splittings between the adjacent spin-orbit levels of the a^6D_J state are 69, 116, 170 and 230 cm^{-1}, for the $^1/_2 \leftrightarrow ^3/_2$; $^3/_2 \leftrightarrow ^5/_2$; $^5/_2 \leftrightarrow ^7/_2$; and $^7/_2 \leftrightarrow ^9/_2$ levels respectively. Based on this favourable comparison, the resolved excitation features are assigned as transitions to the individual spin-orbit levels of the a^6D excited state of atomic Mn. From the observed splittings, the four resolved features are assigned

to the Mn($a^6D_J \leftarrow a^6S_{5/2}$)/Xe transitions for J = $^1/_2$, $^3/_2$, $^5/_2$, and $^7/_2$. While the $a^6D \leftrightarrow a^6S$ transition is electric-dipole forbidden it is an electric-quadrupole allowed[5,6] E2 type transition, governed by the selection rules $\Delta J = 0, \pm1, \pm2$ and $\Delta L = 0, \pm1, \pm2$ for $\Delta S = 0$. These conditions are fulfilled by the $a^6D_J \leftrightarrow a^6S$ transitions therefore, transitions to each of the J = $^1/_2$, $^3/_2$, $^5/_2$, $^7/_2$ and $^9/_2$ excited state spin-orbit levels from the ground J = $^5/_2$ level should be observed.

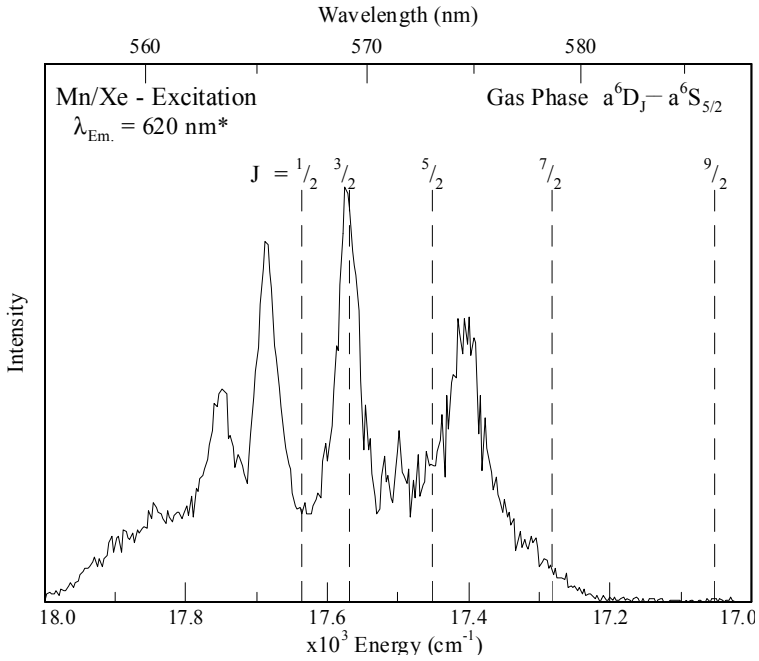

Figure VIII.4 Dye laser excitation spectrum recorded at 12 K, monitoring the 620 nm emission feature. The excitation spectrum presented has been corrected (*) for the spectral overlap of the thermally unstable 656 nm emission band. The dashed vertical lines indicate the spectral locations of the individual $a^6D_J \leftrightarrow a^6S_{5/2}$ transitions in the gas phase[1].

However, the transition to the lowest energy $a^6D_{9/2}$ spin-orbit level is not discernible in the excitation spectrum shown in Figure VIII.4. Given the gas phase spin-orbit splitting pattern is maintained in the solid, this transition is predicted to occur at 582.34 nm (17172 cm^{-1}). However, the dye response in this region is weak and it is likely the $a^6D_{9/2} \leftarrow a^6S_{5/2}$ transition is outside the tuning range of Rhodamine 590 from 555 to 580 nm, (Table II.9, middle panel). As the spectra reported have not been corrected for intensity output of the laser dye material, the intensities observed reflect the tuning range. Thus it is proposed that the $a^6D_{9/2} \leftarrow a^6S_{5/2}$ transition was not observed in excitation for experimental reasons.

Table VIII.1 **The transitions assigned and the photophysical characteristics of the resolved excitation features recorded monitoring the 620 nm emission. The spectral positions of the observed features and the gas phase transition energies[1] for the individual $a^6D_J \leftrightarrow a^6S_{5/2}$ are indicated in nm and wavenumber units (cm^{-1}). Δ indicates the splitting between successive spin-orbit levels in the gas phase (G.P.) and Xe matrix environment (Mn/Xe). The matrix-shift (δ) observed for the assigned transition is presented in wavenumber units.**

Mn Gas Phase		**Mn/Xe Excitation**		
Transition (nm / cm^{-1})[1]	$\Delta_{G.P.}$ (cm^{-1})[1]	Assignment (nm) / (cm^{-1})	$\Delta_{Mn/Xe}$ (cm^{-1})	δ (cm^{-1})
$a^6D_{1/2} \leftrightarrow a^6S_{5/2}$ 566.98 / 17637		$a^6D_{1/2} \leftarrow a^6S_{5/2}$ 563.38 / 17750		+113
	69		62	
$a^6D_{3/2} \leftrightarrow a^6S_{5/2}$ 569.21 / 17568		$a^6D_{3/2} \leftarrow a^6S_{5/2}$ 565.35 / 17688		+120
	116		117	
$a^6D_{5/2} \leftrightarrow a^6S_{5/2}$ 573.03 / 17452		$a^6D_{5/2} \leftarrow a^6S_{5/2}$ 569.12 / 17571		+119
	170		169	
$a^6D_{7/2} \leftrightarrow a^6S_{5/2}$ 578.63 / 17282		$a^6D_{7/2} \leftarrow a^6S_{5/2}$ 574.65 / 17402		+120
	230			
$a^6D_{9/2} \leftrightarrow a^6S_{5/2}$ 586.43 / 17052				

The assigned $a^6D_J \leftarrow a^6S_{5/2}$ transitions all exhibit a matrix shift (δ) of approximately +120 cm^{-1} from the gas phase positions (Table VIII.1). The observation that the gas phase splittings between the individual spin-orbit states is maintained in the solid, infers that the observed matrix shift arises predominantly from stabilisation of the $a^6S_{5/2}$ ground state in its site of isolation in Xe. Figure VIII.5 shows the effect of subtracting the matrix shift (δ = +120 cm^{-1}) from the spectrum recorded. Employing the matrix shift reveals how well the gas phase spin-orbit splitting of the a^6D state is maintained for Mn atoms isolated in the thermally stable site in solid Xe. This reinforces the assignments made and the conclusion that the observed matrix shift results from the stabilisation occurring on the ground state.

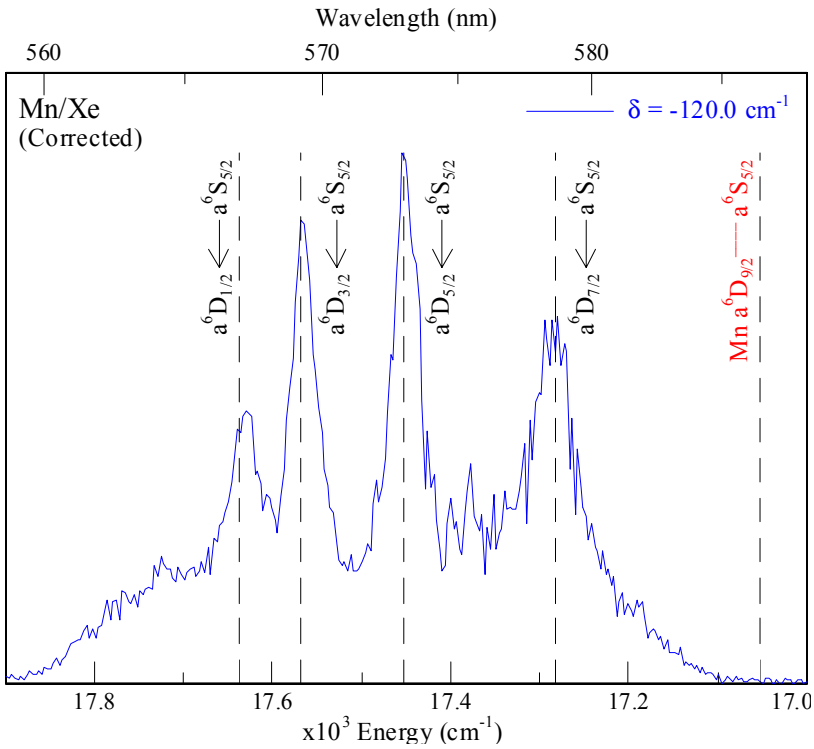

Figure VIII.5 **Corrected dye laser excitation spectrum recorded by monitoring the 620 nm emission band at 12 K. The correction procedure red shifts the excitation spectrum (Figure VIII.4) by the observed matrix shift (δ) of 120 cm^{-1}. The dashed vertical lines indicate the gas phase positions of the individual $a^6D_J \leftrightarrow a^6S_{5/2}$ transitions[1] and the labels indicate the transitions assigned to occur in solid Xe.**

In Chapter VII the Mn/Xe emission spectroscopy produced with resonance z^6P excitation revealed a single thermally stable band at 620 nm, (see Figure VII.2). As shown in Figure VIII.3 and Figure VIII.6 this thermally stable emission feature is also produced with a^6D excitation. It is red shifted from the $a^6D_{9/2} \leftrightarrow a^6S_{5/2}$ gas phase position by 923 cm^{-1}. The luminescence spectra were recorded following annealing ($T_{An.}$ = 38 K) of the Mn/Xe sample deposited at 12 K. However, the true emission lineshape of the 620 nm feature produced with $a^6D \leftarrow a^6S$ excitation is difficult to access due to the overlap of the 656 nm band and further complicated by the presence of two weak features at 600 and 700 nm[7] due to contaminants. The equivalent intensities of the thermally stable 620 nm band and 'unstable' 656 nm emission feature is attributed to the enhancement of the $a^6D \leftarrow a^6S$ transition in the thermally unstable site. This observation contrasts with those made in Chapter VII (Figure VII.II) as the annealing procedure lead to the reduction in the emission intensity at 656 nm (resulting from z^6P excitation) corresponding to site removal.

This effect is discussed in more detail following the presentation of the results obtained on the Mn/Ar and Mn/Kr systems.

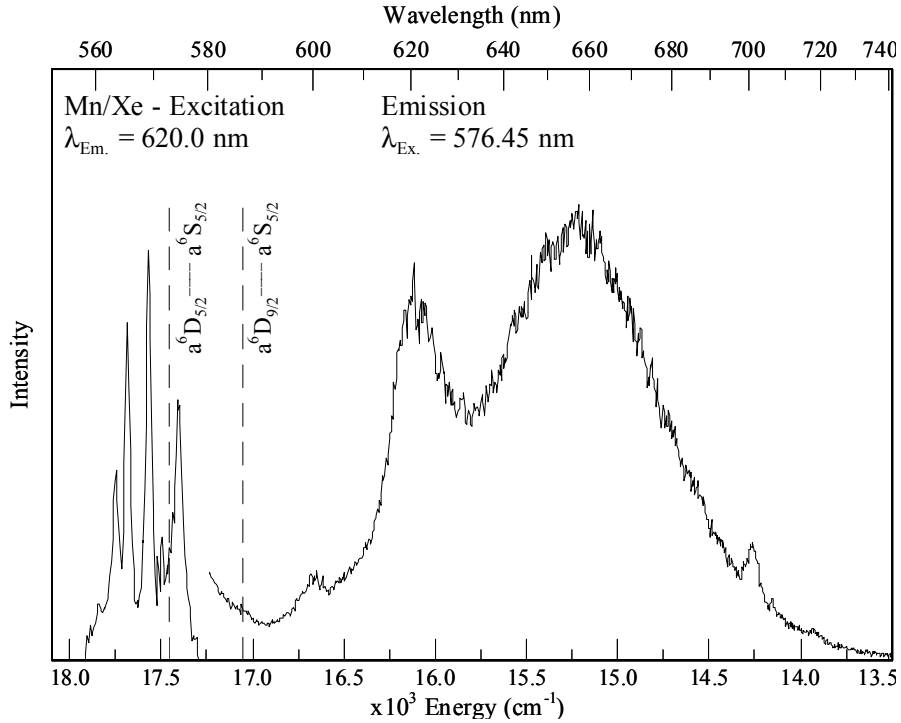

Figure VIII.6 **Dye laser excitation spectrum recorded monitoring the observed emission band at 620 nm, shown left, in the vicinity of the gas phase $a^6D_{5/2} \leftrightarrow a^6S_{5/2}$ transition of atomic Mn at 573.03 nm upon sample deposition at 12.5 K and subsequent annealing to 38 K. Emission spectra recorded (shown right) upon excitation into the low energy shoulder assigned to the $a^6D_{7/2} \leftarrow a^6S_{5/2}$ transition. The dashed vertical lines indicate the positions of the $a^6D_{5/2}$ and $a^6D_{9/2} \leftrightarrow a^6S_{5/2}$ transitions in the gas phase[1].**

Excited state lifetime measurements were made using the TCSPC technique. Figure VIII.7 presents the decay profile of the 620 nm feature produced with pulsed laser excitation of the $a^6D_{3/2} \leftarrow a^6S_{5/2}$ transition at 565.55 nm. An adequate fit of the decay profile was achieved using a trial function containing three exponential components, as shown by the residuals presented. The three decay times identified are 1.34 msec, 346 μsec and 25 μsec. Inspection of the relative amplitudes of the decay components reveals that the shortest, (25 μsec) component dominated at 12.5 K. However, the substantial amplitude extracted for the 346 μsec component reveals its importance. Recording the decay profile of the 620 nm band at temperatures above 12.5 K revealed very little changes in the emission decay characteristics.

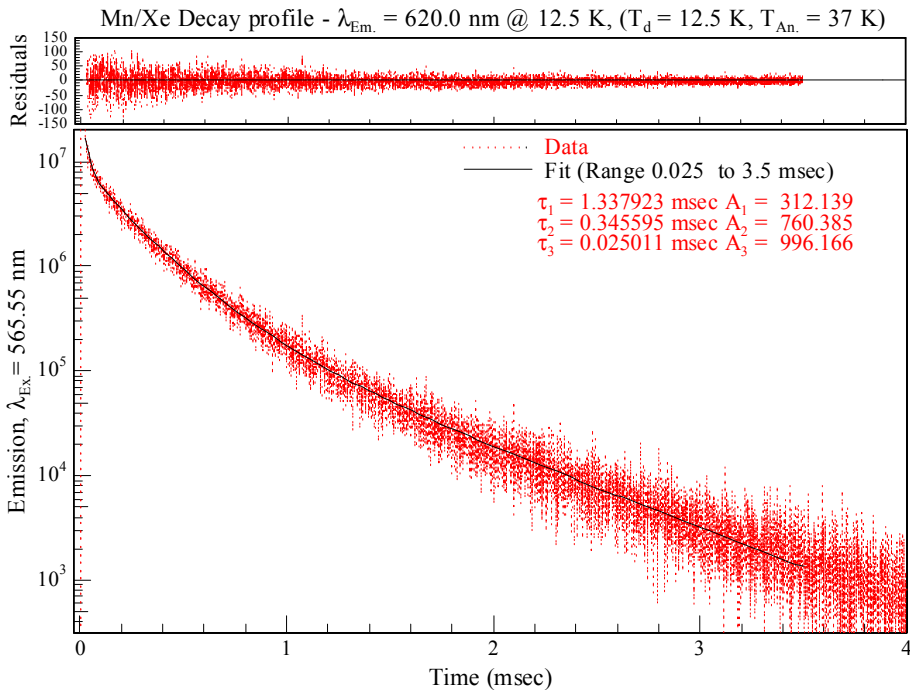

Figure VIII.7 **Decay profile of the 620 nm emission recorded at 12 K using TCSPC following pulsed laser excitation at 565.55 nm, corresponding to the excitation feature assigned to the $a^6D_{3/2} \leftarrow a^6S_{5/2}$ transition of atomic Mn isolated in solid Xe.**

Table VIII.2 **Decay characteristics, components and amplitudes (A) extracted from non-linear least squares analysis of the temporal profiles recorded monitoring the 620 nm emission at different temperatures, (T_s) following pulsed laser excitation at 565.55 nm. Note the dominant decay contribution is presented in bold.**

$T_{s.}$ (K)	Fit Range (msec)	A_1	τ_1 (msec)	A_2	τ_2 (μsec)	A_3	τ_3 (μsec)
12.5	0.025 – 3.5	312	1.34	760	346	**996**	**25.0**
15.0	0.025 – 3.5	594	1.21	1278	307	**2340**	**20.0**
18.0	0.025 – 3.5	545	1.18	1218	309	**1720**	**23.5**
22.0	0.025 – 3.5	874	1.11	1859	301	**2404**	**23.5**
27.0	0.025 – 3.5	493	1.11	**1139**	**329**	810	26.2

The decay times extracted monitoring the emission at 620 nm are believed to represent a combination of the temporal characteristics from the 620 and 656 nm features due, as shown in Figure VIII.6 to their considerable spectral overlap. Although further analysis of the excited state lifetimes is required, an assessment of the extent of the spectral overlap in Figure VIII.6 shows a 50/50 relationship of the two bands at 620 nm. A comparison to the relative amplitudes extracted from the decay profile in Figure VIII.7 reveals the same relationship between the short microsecond component (A_3 = 996) and the sum of the amplitudes of the two millisecond decay times, (A_1 + A_2 = 1072). The presence of the two long-lived

components (1.34 msec and 346 μsec), significantly longer than the 149.3 μsec lifetime of the $z^8P \leftrightarrow a^6S$ transition suggests assignment of the 620 nm emission to the $a^6D_{9/2} \rightarrow a^6S_{5/2}$ transition. The different linewidths displayed by the 620 (asymmetric) and 656 nm (Gaussian) suggest radiative transitions from the $a^6D_{9/2}$ and $z^8P_{5/2}$ excited states respectively. The broad linewidth exhibited by the 656 nm emission feature is indicative of a P → S type electronic transition. The presence of the short 25 μsec decay time suggests assignment of the 656 nm band to the $z^8P_{5/2} \rightarrow a^6S_{5/2}$ transition.

Thus the lifetime measurements made with direct $a^6D \leftarrow a^6S$ excitation still does not allow a definitive identification of the unperturbed lifetime for the ($a^6D_{9/2} \rightarrow a^6S_{5/2}$ transition) emission at 620 nm. Given the complex decay characteristics extracted for the 620 nm band, the observed excited state lifetime is thought to lie in the range 346 μsec to 1.34 msec at 12.5 K. Table VIII.3 presents the photophysical characteristics of the 620 nm band now assigned to the $a^6D_{9/2} \rightarrow a^6S_{5/2}$ transition but shifted by more than 900 cm^{-1} from its gas phase value.

Table VIII.3 **Photophysical characteristics and excited state assignment of the emission feature produced following excitation of the $a^6D_J \leftarrow a^6S_{5/2}$ transition. λ_{Em}, indicates the emission band-centre in nm and wavenumber units. The matrix shift for the transition is indicated δ in wavenumber (cm^{-1}) units. The decay characteristics of the emission feature is also presented at 12.5 K.**

Mn Gas Phase	**Mn/Xe Matrix – *Emission***			
Transition[1] nm / cm^{-1}	Assignment	$\lambda_{Em.}$ (nm) / (cm^{-1})	δ (cm^{-1})	Decay Characteristic ($\tau_{Obs.}$)
$a^6D_{9/2} \leftrightarrow a^6S_{5/2}$ 586.43 / 17052	$a^6D_{9/2} \rightarrow a^6S_{5/2}$	620 / 16129	-923	τ_1 = 347.0 μsec τ_2 = 1.34 msec

VIII.2.II Mn(a^6D)/Kr

In Chapter VII, emission spectra recorded following site-selective excitation of the $z^6P_{5/2} \leftrightarrow a^6S_{5/2}$ transition of Mn isolated in Kr revealed bands centered at 585.8 and 626.8 nm. The asymmetric band shape of the emission at 585.8 nm (17070 cm^{-1}) produced with red (2°) site excitation, (Figure VII.63, top panel) was tentatively assigned to the $a^6D_{9/2} \rightarrow a^6S_{5/2}$ transition in solid Kr. The broad 626.8 nm (15954 cm^{-1}) emission produced with blue (1°) site excitation remains unassigned, (Figure VII.63, bottom panel). In addition to these thermally stable emission features, the 3°

site of isolation identified for Mn/Kr solids produced a broad thermally unstable emission band centered at 603.8 nm.

Excitation spectra recorded in the region of the $a^6D_{5/2} \leftrightarrow a^6S_{5/2}$ gas phase transition with dye laser scans are presented in Figure VIII.8 monitoring the 587, 600 and 626.7 nm emission bands. Inspection of the excitation spectrum recorded by monitoring the 587 nm emission feature (presented in Figure VIII.8) shows four resolved components at 566.18, 568.44, 572.54 and 578.27 nm. Excitation recorded monitoring the 626.7 nm emission revealed the same structured bands with a broad underlying feature, centered near the $a^6D_{5/2} \leftrightarrow a^6S_{5/2}$ gas phase transition at 573.03 nm (17452 cm^{-1}). The excitation spectrum recorded monitoring the thermally unstable 600 nm emission exhibits a broad band-profile centered also at 572 nm. In general the excitation spectra shown in Figure VIII.8, exhibit different lineshapes but remain spectrally unshifted with respect to each other, indicating the minor effect of the site of isolation on the $a^6D_J \leftarrow a^6S_{5/2}$ transition energy.

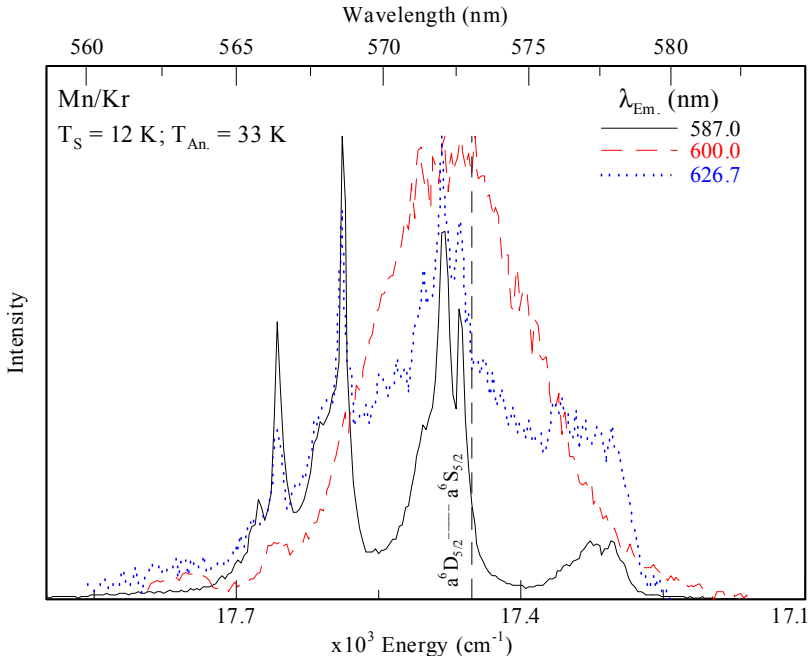

Figure VIII.8 **Dye laser excitation spectra recorded at 12.5 K (following matrix annealing to 33 K), in the vicinity of the $a^6D_{5/2} \leftrightarrow a^6S_{5/2}$ gas phase transition monitoring the red emission features observed in Chapter VII with $z^6P_{5/2} \leftarrow a^6S_{5/2}$ excitation. The sample deposition was completed at 12 K.**

A comparison of the signal-to-noise in the excitation spectra recorded monitoring the 587 and 626.7 nm features, shown by the solid and dotted traces in Figure VIII.8 respectively, reveals the 587 nm band dominates the emission. This

represents an apparent reversal of the site dominance observed in the $z^6P_{5/2}$ state absorption spectra reported in Chapter VI for Mn/Kr. However, the tentative assignment of the 587 nm and the 626.7 nm emissions to site-specific relaxation of the $a^6D_{9/2}$ state, where the $a^6D \leftrightarrow a^6S$ transition is enhanced in one site, provides a plausible reason for this observation. Therefore, it is proposed that the broad 626.8 nm feature results from the emitting a^6D level undergoing a stronger interaction with the matrix in a distinct site of isolation which results in broadening and shifting the $a^6D \rightarrow a^6S$ transition. If the site-specificity of the z^6P state emission is maintained for the a^6D state, the observation that the excitation spectra recorded for the 587 and 626 nm emission bands are in the same narrow spectral range indicates the site occupancy has only a small influence on the $a^6D_J \leftarrow a^6S_{5/2}$ transition energy. These proposals are consistent with the unshifted positions of the excitation bands observed.

An analysis of the excitation spectrum recorded monitoring the 587 nm emission allows the assignment of the observed features to electronic transitions between the ground $a^6S_{5/2}$ state and the spin-orbit levels of the a^6D_J excited state atomic Mn for J = $^1/_2$, $^3/_2$, $^5/_2$, and $^7/_2$ respectively. This is revealed in Table VIII.4 by comparing the splittings recorded for the resolved matrix excitation features ($\Delta_{Mn/Kr}$) at 566.18, 568.44, 572.54 and 578.27 nm with the gas phase spin-orbit splittings, (Δ_{GP}). The transitions identified in solid Kr occur to higher energy than the gas phase positions[1] by 15 cm^{-1}. This effect is attributed to a weak stabilisation of the $a^6S_{5/2}$ ground state of atomic Mn isolated in Kr. As presented for Mn/Xe in the previous section, a transition to the $a^6D_{9/2}$ level was not observed in excitation. On the basis of the conserved spin-orbit splittings, the $a^6D_{9/2} \leftrightarrow a^6S_{5/2}$ transition is predicted to occur at 586.06 nm (17063 cm^{-1}) in solid Kr.

Emission spectra recorded at 12.5 K are shown in Figure VIII.9 resulting from $a^6D_{5/2}$ excitation at 572.46 nm following Mn/Kr sample deposition at 12.5 K and subsequent annealing to 34 K. The spectra presented show three emission features located at approximately 587, 604 and 628 nm. The spectra have been normalised, so a comparison of the relative intensities of the observed features, before and after matrix annealing, reveals the thermally instability of the 604 nm emission feature and the enhancement of the 587 nm feature by the annealing procedure.

Table VIII.4 **The transitions assigned and the photophysical characteristics of the resolved excitation features recorded by monitoring the emission at 587 and 626.8 nm. The spectral positions of the observed excitation features and the gas phase transition energies for the individual $a^6D_J \leftrightarrow a^6S_{5/2}$ are indicated in nm and wavenumber units (cm^{-1}) for the individual spin-orbit levels. Δ indicates the splitting between successive spin-orbit levels in the gas phase (G.P.)[1] and Kr matrix environment (Mn/Kr). The matrix-shift (δ) observed for the assigned transition is presented in wavenumber units.**

Mn Gas Phase		Mn/Kr Excitation		
Transition (nm / cm^{-1}) [1]	$\Delta_{G.P.}$ (cm^{-1})[1]	Assignment (nm) / (cm^{-1})	$\Delta_{Mn/Kr}$ (cm^{-1})	δ (cm^{-1})
$a^6D_{1/2} \leftrightarrow a^6S_{5/2}$ 566.98 / 17637		$a^6D_{1/2} \leftarrow a^6S_{5/2}$ 566.18 / 17662		+25
	69		70	
$a^6D_{3/2} \leftrightarrow a^6S_{5/2}$ 569.21 / 17568		$a^6D_{3/2} \leftarrow a^6S_{5/2}$ 568.44 / 17592		+24
	116		126	
$a^6D_{5/2} \leftrightarrow a^6S_{5/2}$ 573.03 / 17452		$a^6D_{5/2} \leftarrow a^6S_{5/2}$ 572.54 / 17466		+14
	170		173	
$a^6D_{7/2} \leftrightarrow a^6S_{5/2}$ 578.63 / 17282		$a^6D_{7/2} \leftarrow a^6S_{5/2}$ 578.27 / 17293		+11
	230			
$a^6D_{9/2} \leftrightarrow a^6S_{5/2}$ 586.43 / 17052				

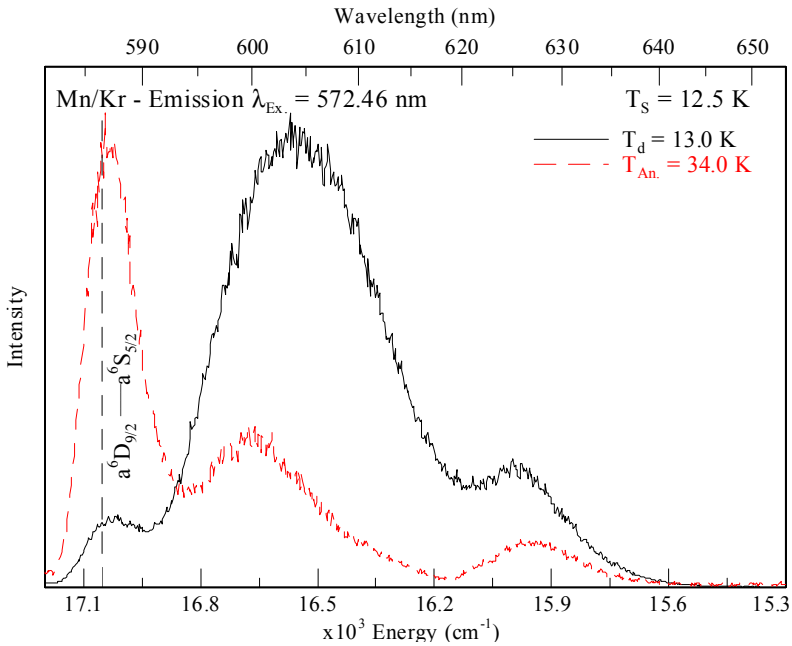

Figure VIII.9 **Emission spectra recorded with dye laser excitation at 572.46 nm corresponding to the $a^6D_{5/2} \leftarrow a^6S_{5/2}$ transition assigned. The dashed vertical line indicates the gas phase position[1] of the $a^6D_{9/2} \leftrightarrow a^6S_{5/2}$ transition of atomic Mn.**

High-resolution emission spectra recorded at 12.6 and 15 K with excitation at 568.4 nm (corresponding to the $a^6D_{3/2} \leftarrow a^6S_{5/2}$ transition), are shown in Figure

VIII.10. At 12.6 K the emission band shows a clear asymmetry and exhibits a band maximum at 585.75 nm (17072 cm^{-1}). At a higher temperature (15 K) the intensity of the band maximum is reduced relative to the low energy wing. This temperature dependence was completely reversible allowing the assignment of the 585.75 nm (17072 cm^{-1}) band as the band origin ($\nu_{0,0}$) of the pure $a^6D_{9/2} \rightarrow a^6S_{5/2}$ electronic transition. Excitation of the remaining J levels in the four possible $a^6D_J \leftarrow a^6S_{5/2}$ transitions produced the same 585.75 nm feature but with no additional emission bands. This behaviour indicates efficient IMR amongst the J levels, which populates the lowest energy J level. Given the slow radiative decay rate, the IMR rate must greater than 10^3 sec^{-1}.

A summary of the high-resolution excitation and emission spectroscopy corresponding to the electronic transitions to the a^6D_J states is presented in Figure VIII.11.

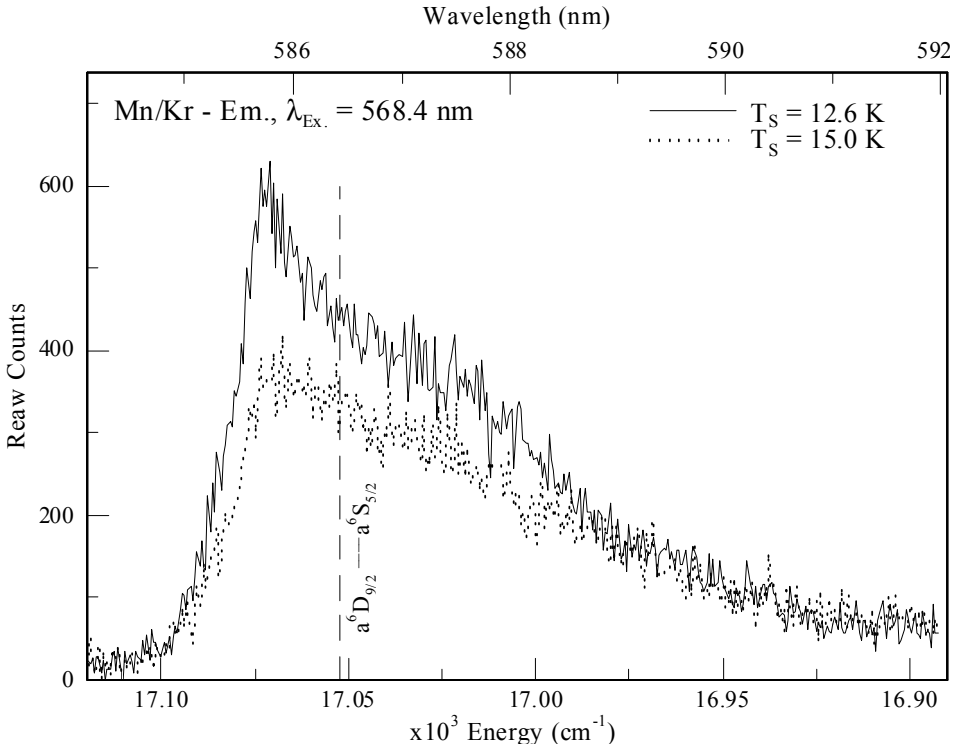

Figure VIII.10 High-resolution emission spectra recorded at T_S (Kelvin) upon excitation at 568.4 nm (17593 cm^{-1}) corresponding to the $a^6D_{3/2} \leftarrow a^6S_{5/2}$ transition assigned.

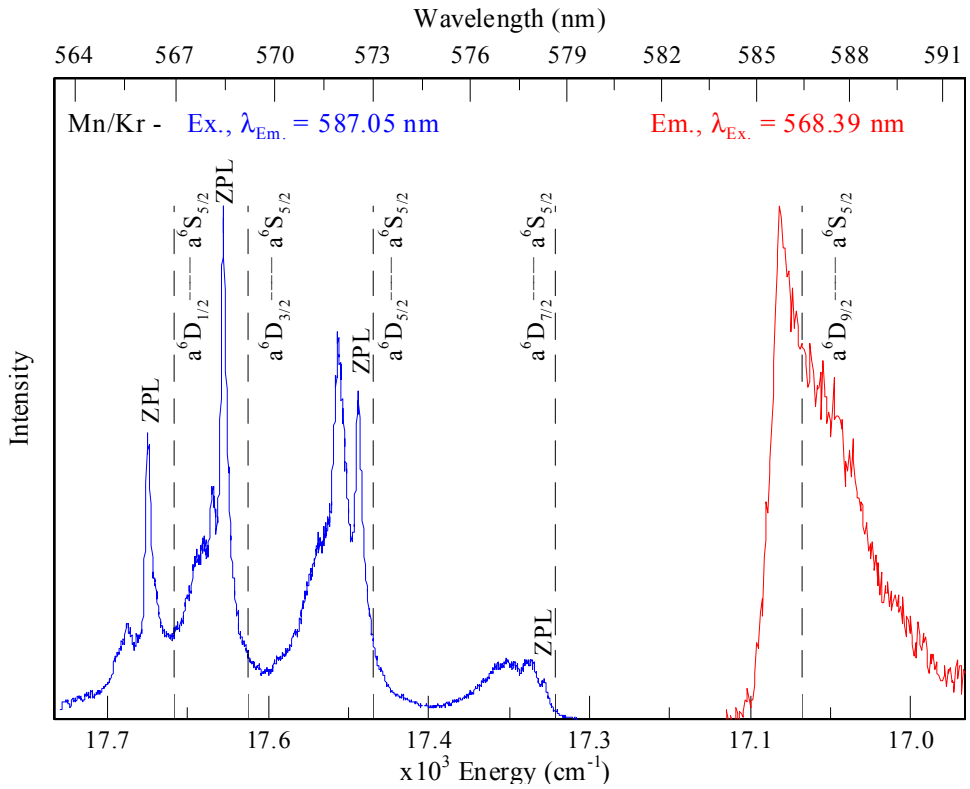

Figure VIII.11 High resolution excitation spectrum recorded monitoring emission at 587.05 nm assigned to the $a^6D_{9/2} \rightarrow a^6S_{5/2}$, shown left, and emission recorded with excitation at 568.39 nm assigned to the $a^6D_{3/2} \leftarrow a^6S_{5/2}$ transition of atomic Mn in solid Kr at 12.5 K. The dashed vertical lines indicate the gas phase positions of the $a^6D_J \leftrightarrow a^6S_{5/2}$ transitions. The band origins, zero phonon lines (ZPL) assigned for the $a^6D_J \leftarrow a^6S_{5/2}$ transitions observed in solid Kr are indicated.

To further analyse the excitation spectrum shown on the left of Figure VIII.11 and identify the origin of the lineshapes assigned to the transitions to the individual spin-orbit levels of the a^6D excited state, excitation spectra were recorded at temperatures in excess of 12.6 K. Figure VIII.12 presents the temperature dependence recorded for the 566.18 nm (17662 cm^{-1}), 568.44 nm (17592 cm^{-1}) and 572.54 nm (17466 cm^{-1}) excitation features assigned in Table VIII.4 to the $a^6D_{1/2}$; $a^6D_{3/2}$ and $a^6D_{5/2} \leftarrow a^6S_{5/2}$ transitions of atomic Mn. Inspection of the right hand panel of Figure VIII.12 reveals evidence for the presence of a zero-phonon line in excitation as the relative intensity of the bands at 572.54 nm (17466 cm^{-1}) and 572.05 nm (17481 cm^{-1}) changes with increasing temperature. Although both features are diminished at higher temperatures (18 K) the rate at which this process occurs is different.

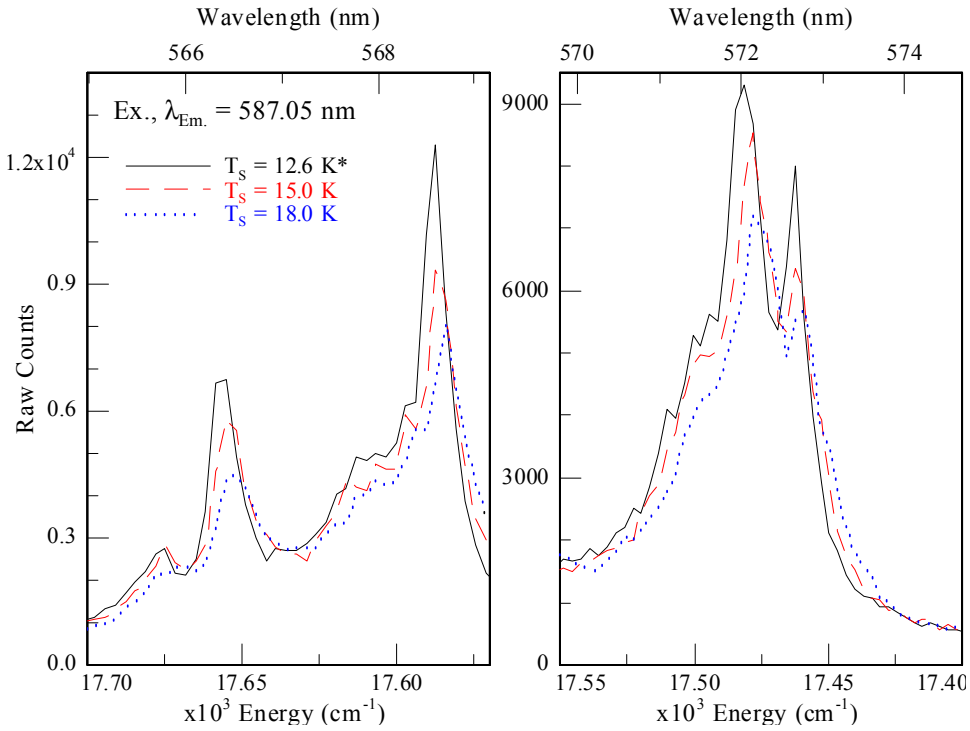

Figure VIII.12 Excitation spectra recorded at sample temperatures T_S (Kelvin) monitoring the emission at 587.05 nm assigned to the $a^6D_{9/2} \rightarrow a^6S_{5/2}$ transition of atomic Mn isolated in solid Kr. The excitation features assigned to the $a^6D_{1/2}$ and $a^6D_{3/2} \leftarrow a^6S_{5/2}$ transitions at 566.18 nm (17662 cm^{-1}) and 568.44 nm (17592 cm^{-1}) are shown left. The feature assigned to the $a^6D_{5/2} \leftarrow a^6S_{5/2}$ at 572.54 nm (17466 cm^{-1}) and the resolved but unassigned 572.05 nm (17481 cm^{-1}) feature, shown right.

Increasing the sample temperature from 12.6 K (solid) to 15 K (dashed) results in an immediate reduction in the intensity of the sharp 572.54 nm feature while the intensity of the 572.05 nm feature is only slightly reduced. This allows the assignment of the 572.54 nm (17466 cm^{-1}) feature as the band origin of the $a^6D_{5/2} \leftrightarrow a^6S_{5/2}$ transition ($\nu_{0,0}$). The broader band at 572.05 nm (17481 cm^{-1}) is then assigned to the phonon sideband. In addition to this effect, all the excitation features manifest a decrease in intensity and a shift to lower energy.

Following the identification of the zero-phonon line ($\nu_{0,0}$) for the $a^6D_{5/2} \leftrightarrow a^6S_{5/2}$ transition at 17481 cm^{-1}, the matrix shift (δ) for the transition is then +15 cm^{-1}. Subtracting this matrix shift from the recorded excitation spectrum monitoring the $a^6D_{9/2} \rightarrow a^6S_{5/2}$ emission, and the high-resolution emission spectrum allows a critical assessment of the transitions assigned. Comparison of the location of the resolved excitation features corrected for the matrix-shift (δ = + 15 cm^{-1}) with the gas phase positions in Figure VIII.13 reveals how good the agreement is. Slight deviation in the location of the features assigned to the $a^6D_{1/2}$ and $a^6D_{3/2} \leftarrow a^6S_{5/2}$ transitions at

566.18 nm and 568.44 nm (17662 and 17592 cm^{-1}) is also revealed. The linewidths of the $a^6D_J \leftarrow a^6S_{5/2}$ bands at 566.18, 568.44, 572.54 and 578.27 nm assigned to the J = $^1/_2$, $^3/_2$, $^5/_2$ and $^7/_2$ levels increase, as is evident upon inspection of Figure VIII.13, with increasing J. This behaviour may arise from the partial removal of the level degeneracy leading to band profiles broadening as 2J+1.

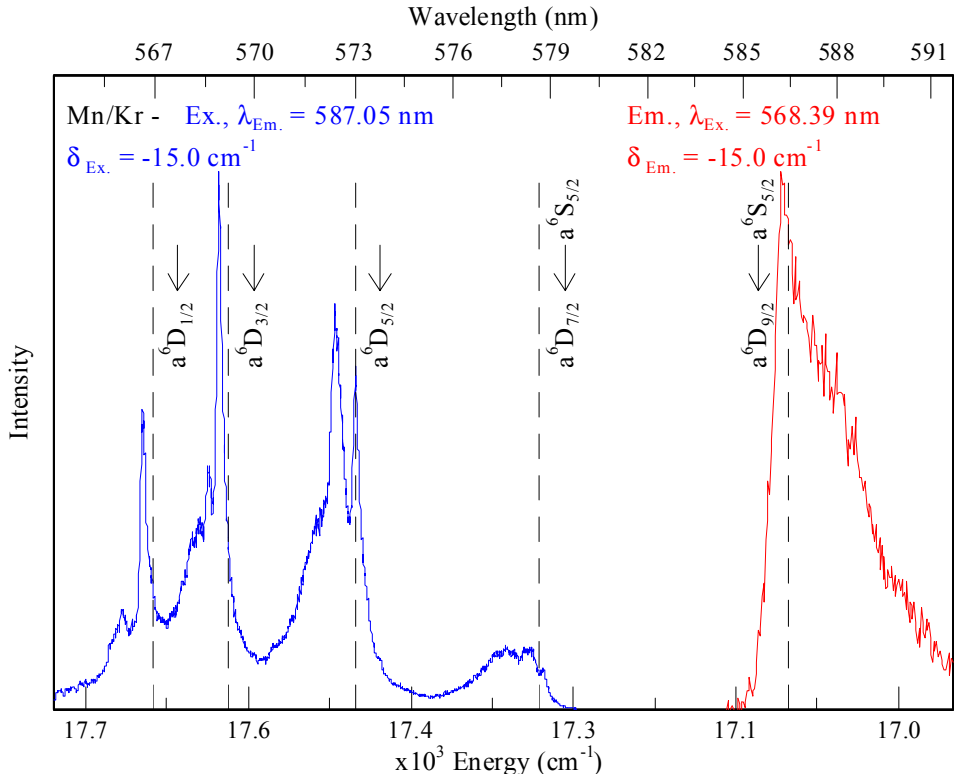

Figure VIII.13 High resolution excitation spectrum recorded monitoring, $\lambda_{Em.}$ = 587.05 nm corrected by subtraction of the matrix-shift (δ) of 15 cm^{-1} calculated from the position of the ZPL assigned to the $a^6D_{5/2} \leftarrow a^6S_{5/2}$ transition, shown left. The emission spectrum recorded with excitation at 568.39 nm assigned to the $a^6D_{3/2} \leftarrow a^6S_{5/2}$ transition of atomic Mn in solid Kr at 12.5 K following correction for the matrix-shift (shown right). The dashed vertical lines indicate the gas phase positions of the $a^6D_J \leftrightarrow a^6S_{5/2}$ transitions to the excited state spin-orbit levels[1].

From its spectral position, the single emission band observed for atomic Mn isolated in solid Kr at 585.75 nm (17072 cm^{-1}) is assigned to the $a^6D_{9/2} \rightarrow a^6S_{5/2}$ transition. The correction of the emission spectrum for the matrix-shift identified in excitation also succeeds in accounting for the *ZPL* assigned in emission. A decay profile recorded with the TCSPC technique by monitoring the 585.7 nm emission feature at 12.5 K is presented in Figure VIII.14. An adequate fit was achieved employing a double exponential trial function. Decay times of 227 and 26.5 μsec were extracted. The longer microsecond component dominated the decay profile

recorded at 12.5 K. Recording the decay profile at higher temperatures showed only minor temperature dependence, Table VIII.5. Therefore the observed 227 μsec lifetime at 12.5 K is assigned as the radiative lifetime of the electric quadrupole $a^6D_{9/2} \rightarrow a^6S_{5/2}$ transition of atomic manganese in solid Kr.

Table VIII.5 **Decay characteristics, components and amplitudes (A) extracted from double exponential fits of the temporal profiles recorded monitoring 585.7 nm emission feature at different temperatures, (T_s) following pulsed laser excitation at 567.55 nm. Note the dominant decay contribution is presented in bold.**

T_s. (K)	Fit Range (msec)	A_1	τ_1 (μsec)	A_2	τ_2 (μsec)
12	0.005 – 0.8	**380**	**227**	172	26.5
14	0.005 – 0.8	**217**	**224**	111	22.6

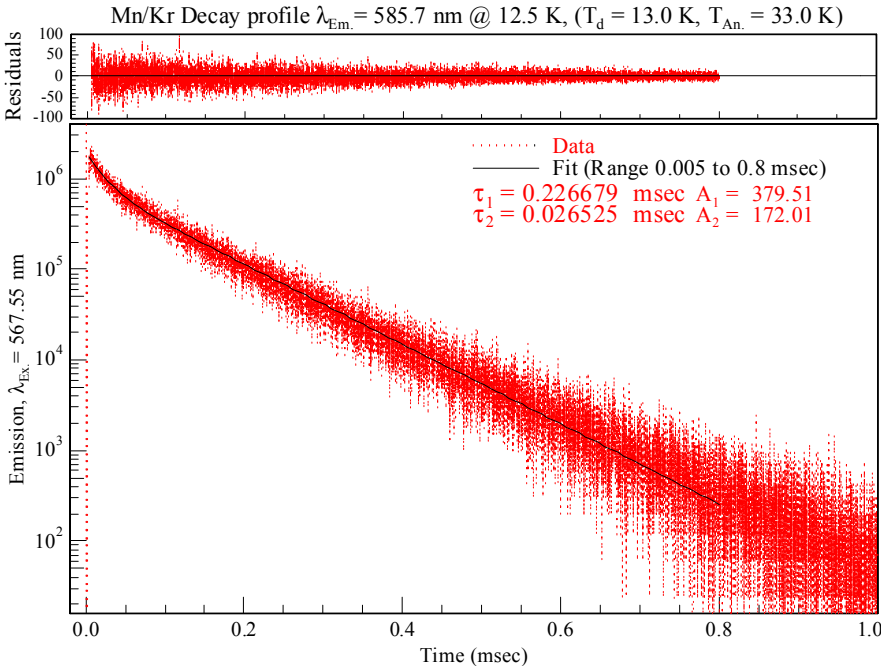

Figure VIII.14 **Decay profile recorded by monitoring the 585.7 nm emission feature at 12 K using TCSPC following pulsed laser excitation at 567.55 nm.**

The resolved features assigned to the transitions to the a^6D state spin-orbit levels are also present in the excitation spectra recorded monitoring the emission feature centered at 626.7 nm, Figure VIII.8. Analysis of the excitation spectra recorded monitoring the 585.7 and 626.7 nm features shows the spectral overlap of the bands. However, the different linewidths indicate that the site specificity in emission is maintained with direct a^6D excitation but less than that observed with $z^6P_{5/2}$ excitation.

A time-resolved emission spectrum (TRES) recorded monitoring the emission features at 626.7 nm and 585.7 nm is presented in Figure VIII.15 following pulsed laser excitation of the $a^6D_{5/2} \leftarrow a^6S_{5/2}$ transition at 572 nm. This figure shows the intensity of the 585.7 nm feature, assigned to the $a^6D_{9/2} \rightarrow a^6S_{5/2}$ phosphorescence, decreasing on a microsecond timescale. This behaviour is in agreement with the TCSPC measurements presented earlier in this section, in which the observed radiative lifetime of the $a^6D_{9/2}$ state in the matrix that was identified as 227 μsec. In contrast, the intensity of the 626.7 nm feature is observed, (as shown in Figure VIII.15) to increase on this timescale. The TRES spectrum in Figure VIII.15 also reveals the presence of an emission feature centered at 603 nm corresponding to the thermally unstable red emission feature that is, as reported in Chapter VII, produced with $z^6P_{5/2}$ 3° site excitation. The broad emission is not completely removed by the annealing procedure and therefore may be the origin of the 23.5 μsec component present in the decay time recorded monitoring the 585.7 nm emission feature presented in Table VIII.5. This allows a correlation of this band to the 656 nm feature observed in solid Xe and strengthening the argument that the Mn/Xe 25 μsec component results from the $z^8P_{5/2} \rightarrow a^6S$ transition.

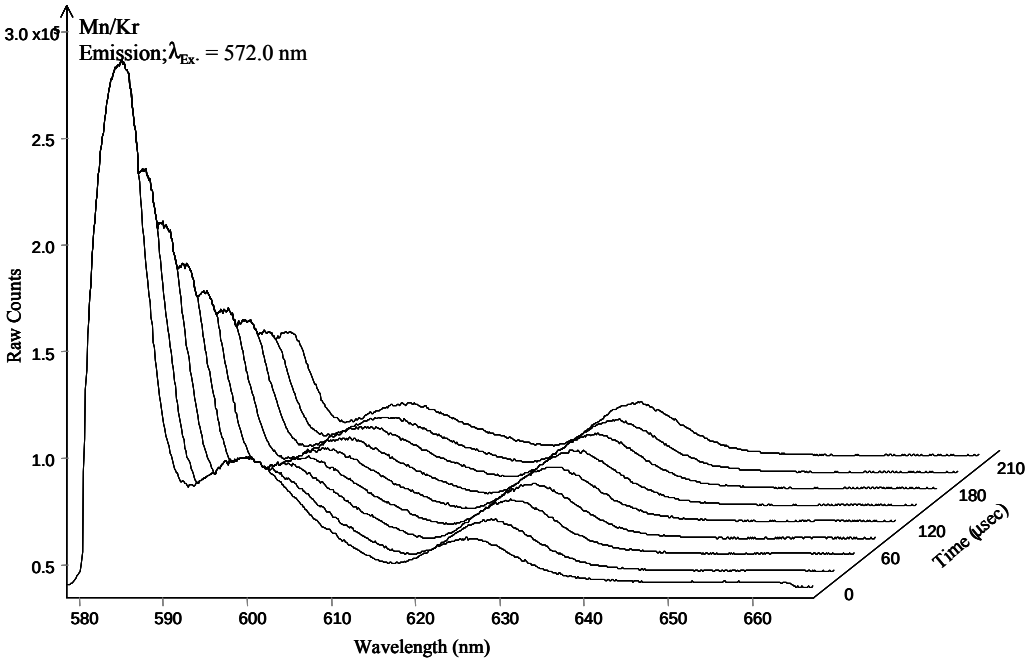

Figure VIII.15 Time-resolved emission spectra recorded monitoring the red features (at 12 K) following pulsed dye laser excitation at 572 nm ($a^6D_{5/2} \leftarrow a^6S_{5/2}$). The temporal step and width used was 30 μsec with a delay time of t_d = 0.0 nsec. Mn/Kr sample deposition was completed at 12.5 K and subsequently annealed.

Figure VIII.16 presents a decay profile recorded at 12.5 K for the 626.7 nm emission feature using TCSPC. First inspection of the recorded decay profile reveals a rising portion at short time, indicating the presence of the feeding step. This was also observed in the time-resolved emission spectra, (TRES) presented in Figure VIII.15 in which the 626.7 nm intensity increased on the microsecond timescale shown. A trial function consisting of three exponential components allowed an adequate fit of the temporal profile as shown by the residuals. Two decay components 2.19 and 1.61 msec and a rising component of 108 μsec were extracted.

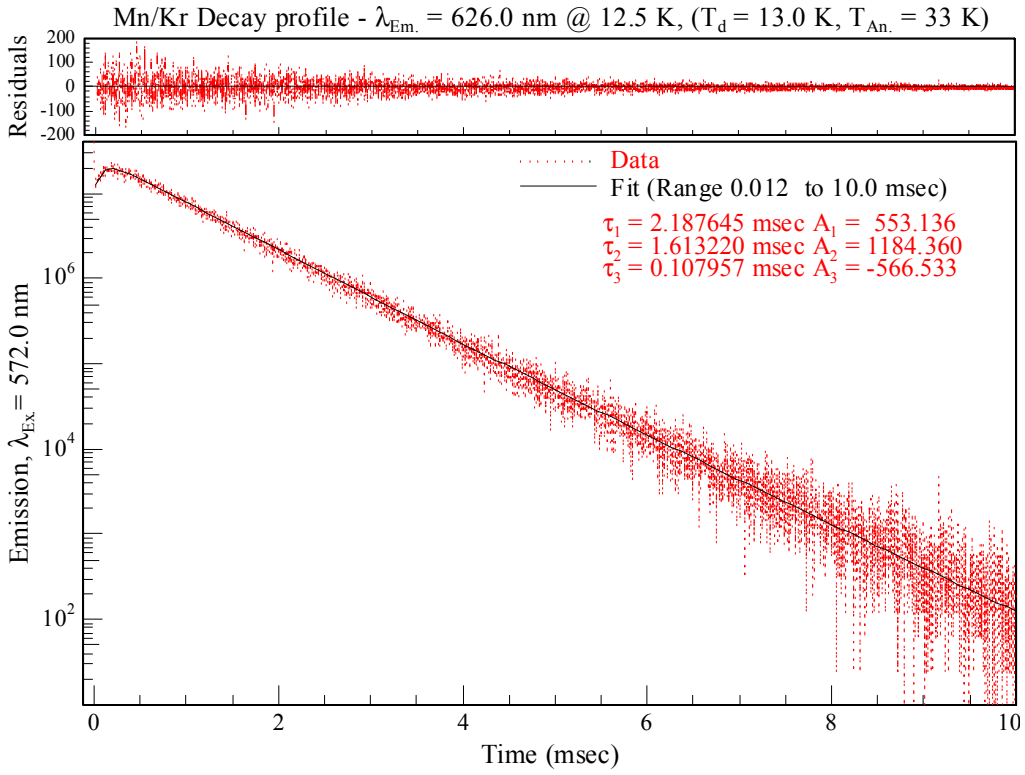

Figure VIII.16 Decay profile of the 626 nm emission feature recorded at 12.5 K using TCSPC following pulsed laser excitation of the $a^6D_{5/2} \leftarrow a^6S_{5/2}$ transition identified in Kr to occur at 567.55 nm. The residuals present the difference between the triple exponential fit completed and the decay recorded. Note the negative amplitude A_3 indicates the presence of a feeding step or rising portion in the decay profile recorded.

Analysis of the decay profiles was also done at 14 K. The decay characteristics extracted from the analysis of the decay profiles at 12 and 14 K are presented in Table VIII.6. Comparison of the excited state lifetime components extracted at each temperature reveals that all the components are temperature sensitive over the small temperature range. Therefore the radiative lifetime for the 626.8 nm feature has not been observed. The relaxation mechanism involved and the

state assignment of the 626.7 nm emission are discussed in detail at the end of this Chapter following a presentation of the luminescence spectroscopy recorded with direct laser excitation of the z^8P excited state.

Table VIII.6 **Decay characteristics, components and amplitudes (A) extracted from non-linear least squares analysis of the temporal profiles recorded monitoring emission at 626 nm at different temperatures, (T_s) following pulsed laser excitation at 572 nm. Note the dominant decay contribution is presented in bold.**

T_s. (K)	Fit Range (msec)	A_1	τ_1 (msec)	A_2	τ_2 (msec)	A_3	τ_3 (μsec)
12	0.012 – 10.0	553	2.19	**1184**	**1.61**	-567	108
14	0.005 – 8.0	**605**	**2.09**	542	1.29	-228	124

Table VIII.7 **Photophysical characteristics and excited state assignments of the emission feature produced following excitation of the $3d^64s\ a^6D_J \leftarrow 3d^54s^2\ a^6S_{5/2}$ transitions of matrix – isolated atomic manganese isolated in solid Kr. λ_{Em}, indicates the emission band-centre in nm and wavenumber units. The matrix shift (δ) for the transitions are presented in wavenumber (cm^{-1}) units. The positions of the band origins (ZPL) identified are presented in wavenumber units.**

Mn Gas Phase[1]	**Mn/Kr Matrix – *Emission***			
Transition Nm / cm^{-1}	Assignment	$\lambda_{Em.}$ (nm) / (cm^{-1})	δ (cm^{-1})	Decay Characteristic
$a^6D_{9/2} \leftrightarrow a^6S_{5/2}$ 586.43 / 17052	$a^6D_{9/2} \rightarrow a^6S_{5/2}$	585.75 / 17072 *ZPL* = 17072	+20	τ_{Rad} = 227.0 μsec
$z^8P_{5/2} \leftrightarrow a^6S_{5/2}$ 543.4 / 18402	(?)	628.7 / 15906	-2496	$\tau_{Obs.}$ = 1.61 msec (τ_{Rise} = 108 μsec)
$a^6D_{9/2} \leftrightarrow a^6S_{5/2}$ 586.43 / 17052			-1146	

VIII.2.III Mn(a^6D)/Ar

The luminescence spectroscopy of the $z^6P_{5/2}$ excited state of atomic Mn isolated in solid Ar, presented in Chapter VII, identified three site specific emission features at 590, 625 and 604 nm produced with 1° red, 2° blue and 3° site excitation respectively. The 590 nm emission feature resulting from red (1°) site excitation, shown Figure VII.41, was tentatively assigned to the $a^6D_{9/2} \rightarrow a^6S_{5/2}$ transition. Table VII.6 presents the photophysical characteristics of this emission feature. Blue (2°) site excitation produced emission at 625 nm, which has not been state assigned. Finally, careful annealing experiments showed the 604 nm feature to be a thermally unstable site for Mn isolated in solid Ar.

Figure VIII.17 presents high-resolution excitation spectra recorded in the region of the $a^6D_{5/2} \leftrightarrow a^6S_{5/2}$ gas phase transition[1] of atomic manganese at 573.03 nm (17452 cm^{-1}). Inspection of the spectra recorded monitoring the 590 (solid line) and 625 nm (dashed line) features reveals similar broadband excitation profiles, overlapping the gas phase $a^6D_J \leftrightarrow a^6S_{5/2}$ transitions for J = $^1/_2$; $^3/_2$; $^5/_2$ and $^7/_2$ spin-orbit levels. The most resolved excitation band profile was recorded monitoring the 590 nm emission, showing components at 567.5, 569.6, 573 and 578.2 nm. The excitation profile (dotted line) recorded monitoring the 604 nm emission feature is broad with a main band at 573 nm and an unresolved shoulder at 570 nm, Figure VIII.17.

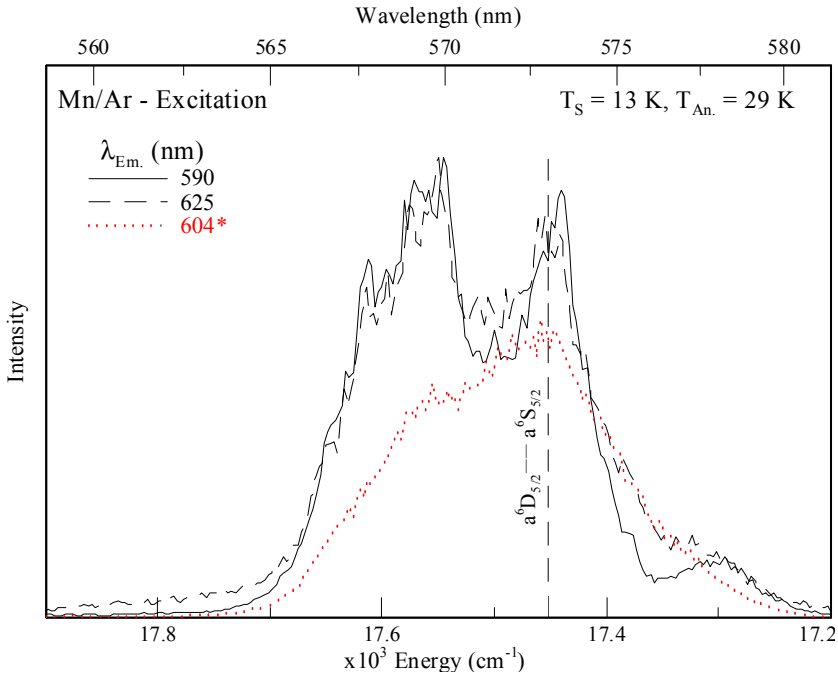

Figure VIII.17 Dye laser excitation spectra recorded at 12.5 K, in the vicinity of the $a^6D_{5/2} \leftrightarrow a^6S_{5/2}$ gas phase transition monitoring the red emission features.

An overlap of the excitation spectrum recorded monitoring the 590 nm emission with the gas phase transitions from the ground state to the individual spin-orbit levels of the a^6D_J state is presented on the left side of Figure VIII.18. The close agreement evident in Figure VIII.18 between the gas phase spin-orbit levels and the partially resolved excitation features allows a definitive assignment of Mn/Ar bands as transitions to the individual spin-orbit states of the excited a^6D_J states, Table VIII.8. The narrow features are red shifted in the Ar matrix by approximately 23 cm^{-1} from the gas phase positions. The right panel of Figure VIII.18 shows the good agreement between the gas phase transitions and the observed matrix bands following the

correction for the matrix-shift. The poorer resolution in Mn/Ar originates from the wider bandwidths of the transitions compared to those in Xe but especially in Kr.

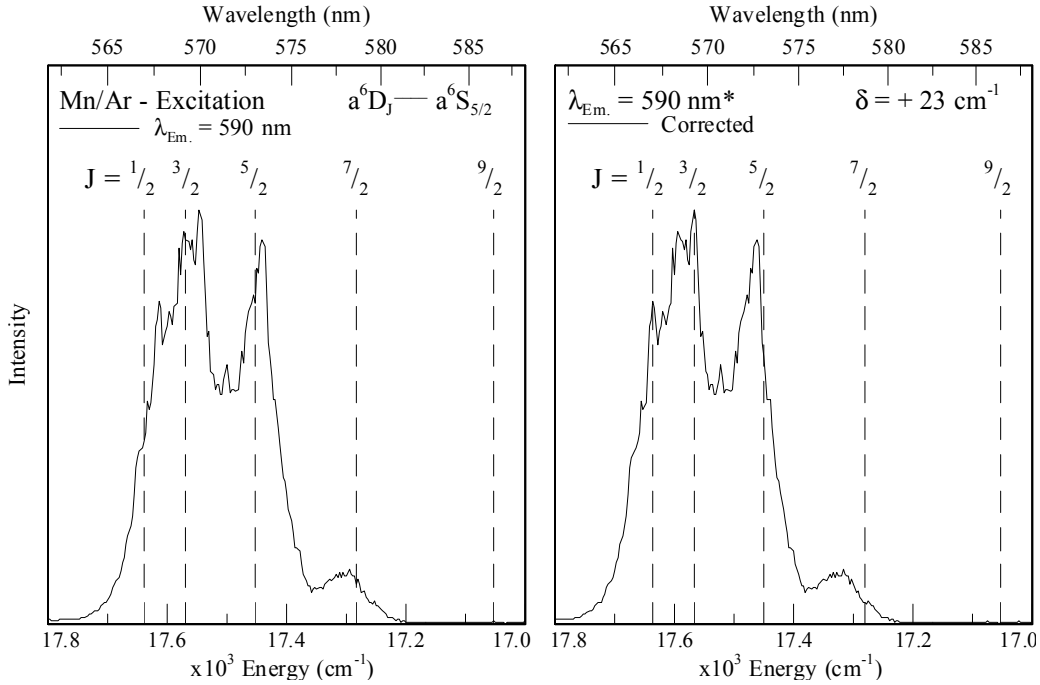

Figure VIII.18 **Dye laser excitation spectrum recorded by monitoring emission at 590 nm, shown left. Excitation spectrum corrected by a blue matrix shift of 23 cm^{-1} is presented right. The dashed vertical lines indicate the gas phase positions of the $a^6D_J \leftrightarrow a^6S_{5/2}$ transitions to the excited state spin-orbit levels[1].**

Table VIII.8 **The transitions assigned and the photophysical characteristics of the resolved excitation features recorded by monitoring the emission at 590 nm. The spectral positions of the observed excitation features and the gas phase transition energies[1] for the individual $a^6D_J \leftrightarrow a^6S_{5/2}$ are indicated in nm and wavenumber units (cm^{-1}) for the individual spin-orbit levels. Δ indicates the splitting between successive spin-orbit levels in the gas phase (G.P.) and Ar matrix environment (Mn/Ar). The matrix-shifts (δ) observed for the assigned transitions are presented in wavenumber units.**

Mn Gas Phase		**Mn/Ar Excitation**		
Transition[1] (nm / cm^{-1})	$\Delta_{G.P.}$ (cm^{-1}) [1]	Assignment (nm) / (cm^{-1})	$\Delta_{Mn/Ar}$ (cm^{-1})	δ (cm^{-1})
$a^6D_{1/2} \leftrightarrow a^6S_{5/2}$ 566.98 / 17637		$a^6D_{1/2} \leftarrow a^6S_{5/2}$ 567.7 / 17615		-22
	69		71	
$a^6D_{3/2} \leftrightarrow a^6S_{5/2}$ 569.21 / 17568		$a^6D_{3/2} \leftarrow a^6S_{5/2}$ 570.0 / 17544		-24
	116		104	
$a^6D_{5/2} \leftrightarrow a^6S_{5/2}$ 573.03 / 17452		$a^6D_{5/2} \leftarrow a^6S_{5/2}$ 573.4 / 17440		-12
	170		192	
$a^6D_{7/2} \leftrightarrow a^6S_{5/2}$ 578.63 / 17282		$a^6D_{7/2} \leftarrow a^6S_{5/2}$ 579.8 / 17248		-34
	230			
$a^6D_{9/2} \leftrightarrow a^6S_{5/2}$ 586.43 / 17052				

The right hand side of Figure VIII.19 presents a high-resolution emission spectrum recorded with excitation at 569.9 nm corresponding to the excitation band of maximum intensity, (shown left). The emission band centered at 590 nm exhibits a linewidth of 100 cm^{-1} and is red shifted from the $a^6D_{9/2} \leftrightarrow a^6S_{5/2}$ gas phase position by 103 cm^{-1}.

Excited state decay profiles recorded for the 590 nm emission feature reveals complex kinetics even for the direct a^6D excitation. Figure VIII.20 presents a decay profile monitoring the 590 nm feature produced with pulsed laser excitation at 572.9 nm corresponding to the $a^6D_{5/2} \leftarrow a^6S_{5/2}$ transition. Inspection of the residuals shown in the top panel of Figure VIII.20 reveals an adequate fit of the decay profile was achieved using a triple exponential function. This analysis allowed the identification of the largest contribution to the excited state lifetime as 1.09 msec at 12 K. However, the two other decay components extracted, with lifetimes of 302 and 36 μsec, both have substantial amplitudes.

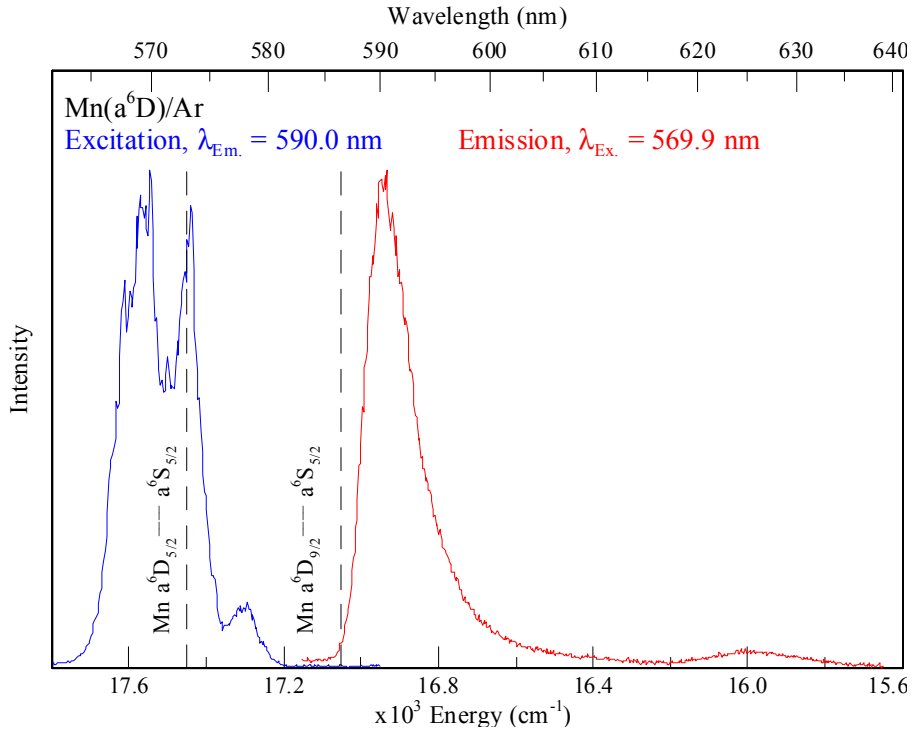

Figure VIII.19 Dye laser excitation spectrum recorded by monitoring the 590 nm emission feature, shown left. Emission recorded with excitation at 569.9 nm, (shown right). The dashed vertical lines indicate the gas phase positions of the $a^6D_{5/2}$ and $a^6D_{9/2} \leftrightarrow a^6S_{5/2}$ transitions.

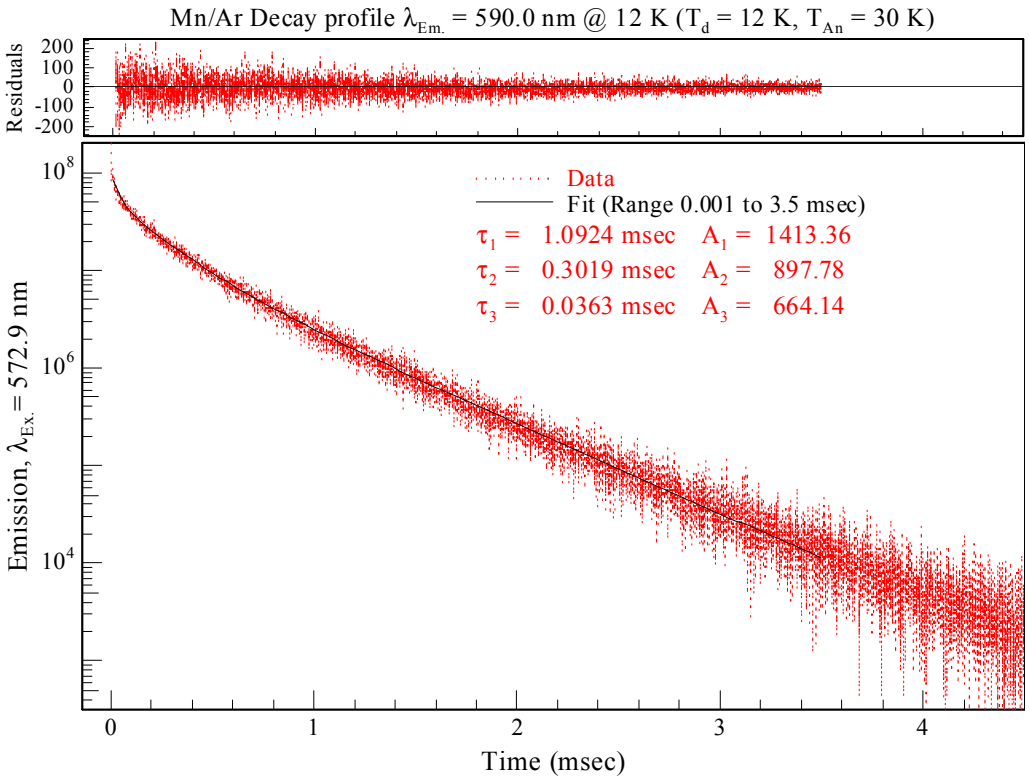

Figure VIII.20 Decay profile recorded for the 590 nm emission feature at 12 K using TCSPC following pulsed laser excitation at 572.9 nm.

The observed lifetime of the 590 nm emission feature is identified as 1.09 msec at 12 K. Decay profiles recorded at temperatures between 12 and 25 K exhibit, as shown in Figure VIII.21, a dependence on the acquisition temperature. Therefore the radiative lifetime of the transition has not been observed at 12 K the lowest temperature attainable in the present experiment. The excited state lifetime components extracted from fits of the decay profiles are presented in Table VIII.9. Inspection of the decay components identified shows that the millisecond component dominates at all temperatures. Based on the spectral proximity of the 590 nm emission band in Ar to the $a^6D_{9/2} \leftrightarrow a^6S_{5/2}$ gas phase transition and the asymmetric lineshape exhibited, this band is assigned to the $a^6D_{9/2} \rightarrow a^6S_{5/2}$ transition of atomic Mn. The lifetime of this transition is taken as 1.09 msec at 12 K.

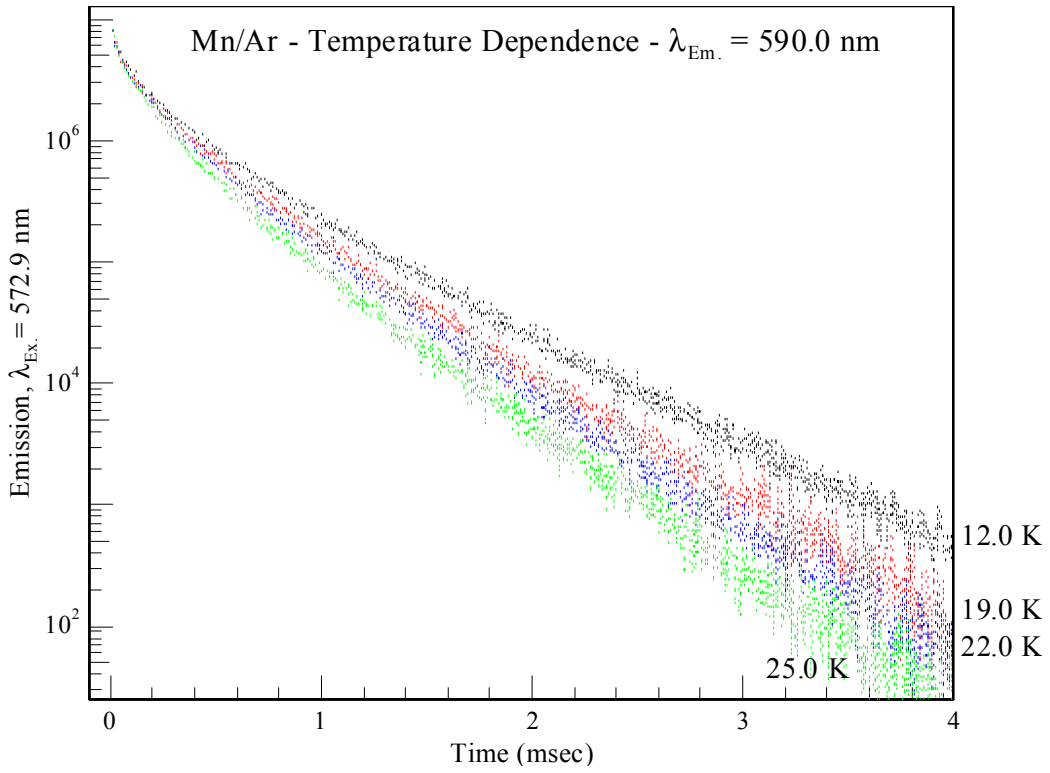

Figure VIII.21 **Decay profiles recorded for the 590 nm emission feature following pulsed laser excitation at 572.9 nm at various temperatures as indicated right in Kelvin, following sample deposition at 12.5 K and matrix annealing to 30 K.**

Table VIII.9 **Decay characteristics, components and amplitudes (A) extracted from non-linear least squares analysis of the temporal profiles recorded by monitoring the 590 nm emission at different temperatures, (T_s) following pulsed laser excitation at 572.9 nm. Note the dominant decay contribution is presented in bold.**

T_s. (K)	Fit Range (msec)	A_1	τ_1 (msec)	A_2	τ_2 (μsec)	A_3	τ_3 (μsec)
12	0.001 – 3.5	**1413**	**1.09**	898	302	664	36
19	0.01 – 3.5	**1169**	**0.93**	749	253	580	25
22	0.01 – 3.5	**1484**	**0.86**	971	236	622	28
25	0.01 – 3.0	**1013**	**0.78**	774	207	518	24

Figure VIII.19 presents a summary of the luminescence spectroscopy of the a^6D state of atomic Mn isolated in solid argon. The emission feature at 625 nm was not state assigned in Chapter VII. Fitting the 625 nm decay profile with a triple exponential trial function allowed the extraction of 1.08 msec, 425 and 124 μsec lifetime components. The intermediate component dominates the emission decay profile recorded, so the observed excited state lifetime is identified as 425 μsec at 12 K. Like the Mn/Kr system, presented in the previous section, the high resolution laser excitation spectra recorded by monitoring the 590 and 625 nm emission features

exhibit different linewidths but are spectrally unshifted with respect to each other. Considering these two characteristics indicates that the 625 and 590 nm emissions result from different sites of isolation where the $a^6D_J \leftarrow a^6S_{5/2}$ transition energy is independent of the matrix environment.

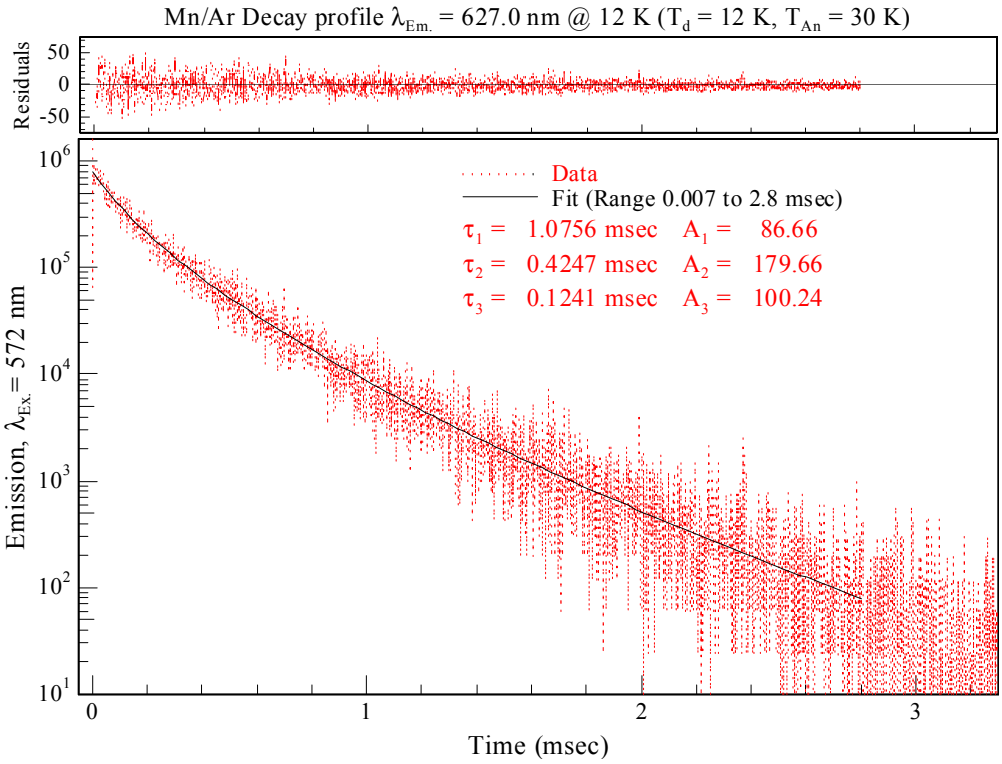

Figure VIII.22 **Decay profile recorded for the 627 nm emission feature at 12 K using TCSPC following pulsed laser excitation at 572 nm. The residuals present the difference between the triple exponential non-linear least squares fit completed and the decay recorded.**

Table VIII.10 **Photophysical characteristics and excited state assignments of the emission feature produced following excitation of the $3d^64s$ $a^6D_J \leftarrow 3d^54s^2$ $a^6S_{5/2}$ transitions of matrix – isolated atomic manganese isolated in solid Ar. λ_{Em}, indicates the emission band-centre in nm and wavenumber units. The matrix shift for the transition is indicated δ in wavenumber (cm^{-1}) units.**

Mn Gas Phase	**Mn/Ar Matrix – *Emission***			
Transition[1] nm / cm^{-1}	Assignment	$\lambda_{Em.}$ (nm) / (cm^{-1})	δ (cm^{-1})	Decay Characteristic
$A^6D_{9/2} \leftrightarrow a^6S_{5/2}$ 586.43 / 17052	$a^6D_{9/2} \rightarrow a^6S_{5/2}$	590 / 16949	-103	$\tau_{Obs.}$ = 1.09 msec
$Z^8P_{5/2} \leftrightarrow a^6S_{5/2}$ 543.40 / 18402 $a^6D_{9/2} \leftrightarrow a^6S_{5/2}$ 586.43 / 17052	(?)	625 / 16000	-2402 -1052	$\tau_{Obs.}$ = 424 µsec

VIII.3 Discussion - Mn(a^6D)/RG luminescence

In this section, the observed luminescence of the $a^6D_J \leftrightarrow a^6S_{5/2}$ transition of atomic Mn isolated in solid Ar, Kr and Xe is summarised and some trends evident in the recorded excitation and emission spectroscopy are presented.

VIII.3.I Mn(a^6D)/RG Excitation spectroscopy

The excitation spectra recorded in the region of the gas phase $a^6D_{5/2} \leftrightarrow a^6S_{5/2}$ transition, monitoring the red emission features tentatively assigned in Chapter VII to the $a^6D_{9/2}$ state of atomic Mn isolated in solid Ar, Kr and Xe, are presented in Figure VIII.23. All the excitation spectra exhibit resolved features, some with very narrow linewidths, and on the basis on the splitting exhibited and their proximity to the gas phase energies are assigned to transitions to the individual spin-orbit levels of the a^6D state from the ground $a^6S_{5/2}$ state. The assignments made to the individual resolved features are presented in Table VIII.1, Table VIII.4 and Table VIII.8 for Mn/Ar, Mn/Kr and Mn/Xe systems respectively. The excitation bands recorded for different sites in a given rare gas matrix overlap indicating that the energy of the a^6D state does not shift significantly with different site occupancy in the matrices from the gas phase. Hence, the site of isolation plays only a minor role in the observed excitation spectroscopy. In the next section the role of host in determining the excitation spectroscopy is discussed.

As evidenced in Figure VIII.23, a progressive shift to higher energy is observed for the a^6D levels from Ar to Xe matrices. The matrix-shift was calculated to be -23, +15 and +120 cm^{-1} for Ar, Kr and Xe respectively. As the relative splitting between spin-orbit levels is maintained in all three solids, the observed matrix shift is ascribed to the manifestation of the extent of ground state stabilisation for the Mn atom isolated in a given site of isolation within a particular host solid. The comparison of the Mn/Kr high-resolution excitation spectra to the gas phase transition energies and the temperature dependence observed, allowed the assignment of the *ZPL's* for the a^6D_J ($J = {}^1/_2, {}^3/_2, {}^5/_2$ and ${}^7/_2$) $\leftarrow a^6S_{5/2}$ transitions in solid Kr.

It is significant that the excitation spectra recorded here do not conserve the site dominance identified in the previous Chapter with resonance z^6P excitation. In Chapter VII the excitation spectra allowed the identification of specific sites of isolation (1°, 2°, red, blue etc) in the vicinity of the resonance $z^6P_{5/2} \leftrightarrow a^6S_{5/2}$ gas

phase transition of atomic Mn. However, in the a^6D case the luminescence data suggests that although the site-specific emission features, identified in Chapter VII, are present, the emission features produced with blue site ($z^6P_{5/2}$) of isolation at 625 and 627 nm are much weaker with direct a^6D excitation. This effect was most evident in solid Xe where the emission intensity for the thermally unstable 656 nm feature persisted after annealing and was observed to have an equivalent intensity as the 620 nm band. As the 620 nm band is the only Mn/Xe thermally stable emission feature reported to date, the weak emission intensity observed with direct a^6D excitation must be attributed to the site of isolation. The sites of isolation are discussed in greater detail in Chapter IV where the blue sites are assigned to single substitutional site occupancy in Ar, Kr and Xe. However, the blue site only allows the $a^6D \leftarrow a^6S$ transition to occur efficiently in Xe, whereas the red sites in Ar and Kr allow an enhancement of the transition. This effect may owe its origin to either the site size or the site symmetry.

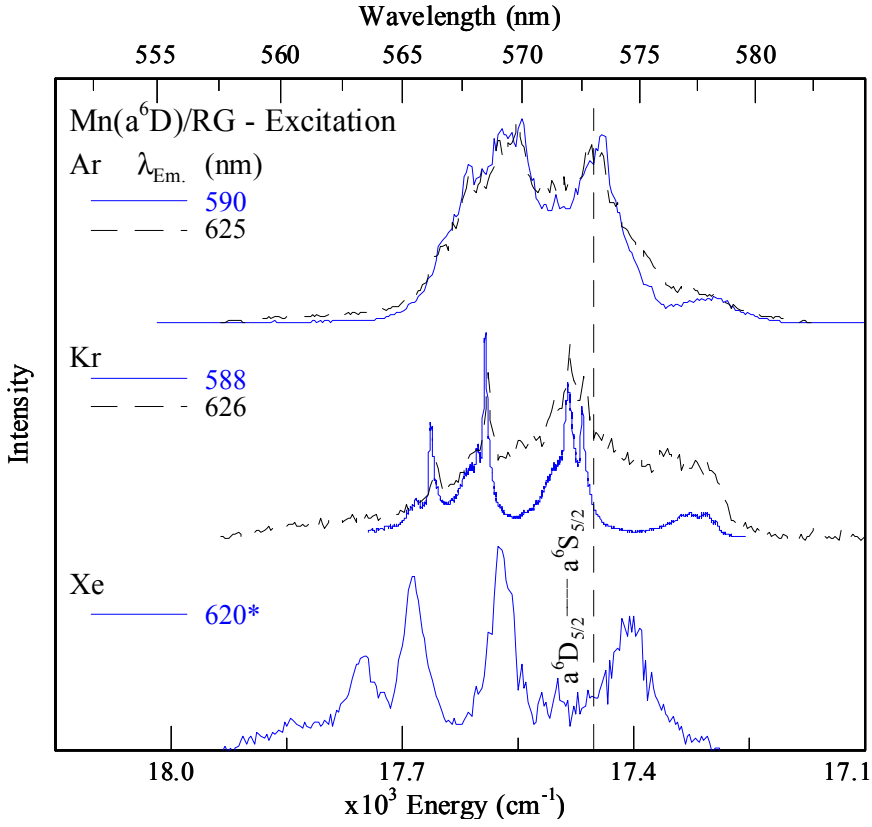

Figure VIII.23 **Dye laser excitation spectra recorded monitoring the red emission features as indicated in wavelength units at 12 K for all the Mn/RG systems, in the vicinity of the Mn $a^6D_J \leftarrow a^6S_{5/2}$ transition. All spectra were recorded following Mn/RG sample deposition at 12 K and matrix annealing. The dashed vertical line indicates the position of the $a^6D_{5/2} \leftarrow a^6S_{5/2}$ gas phase transition of atomic Mn at 573.03 nm (17452 cm^{-1}) [1].**

VIII.3.II Mn(a^6D)/RG Emission spectroscopy

The emission spectroscopy reported in the previous sections following excitation of the $a^6D \leftrightarrow a^6S$ transitions is summarised in Figure VIII.24. The transitions assigned and photophysical properties of the observed emission features are presented in Table VIII.10, Table VIII.7 and Table VIII.3 for Mn/Ar, Mn/Kr and Mn/Xe respectively. The emission spectroscopy reported here allowed a more definitive assignment of the emission features observed at 590, 587 and 620 nm (presented in Chapter VII following $z^6P_{5/2}$ excitation) in Ar, Kr and Xe to the $a^6D_{9/2} \rightarrow a^6S_{5/2}$ phosphorescent transition of atomic Mn. The most definitive assignment was achieved for the 587 nm band in the Mn/Kr system. Temperature dependence observed in the emission intensity of the 587 nm band of Mn/Kr allowed the assignment of the *ZPL* for the band to be at 585.75 nm (17072 cm^{-1}) blue shifted from the gas phase $a^6D_{9/2} \leftrightarrow a^6S_{5/2}$ position[1] by +20 cm^{-1}. The blue shift observed correlates well with the matrix-shift of +15 cm^{-1} extracted from excitation of the a^6D_J (J = $^1/_2$; $^3/_2$; $^5/_2$;and $^7/_2$) $\leftarrow a^6S_{5/2}$ transitions. Inspection of the middle panel of Figure VIII.24 shows the agreement achieved and the effect of increased resolution on the emission band profile observed.

The emission features assigned to the $a^6D_{9/2} \rightarrow a^6S_{5/2}$ transition of Mn isolated in solid Ar, Kr and Xe at 590, 585.75 and 620 nm show uncharacteristic matrix-shifts of –103, +20 and –923 cm^{-1} respectively. This effect is attributed to the Frank Condon accessible region in excitation for certain site types in the rare gases. In the previous Chapter, Mn isolated in the red sites (identified on the $z^6P_{5/2}$ transition) in Ar and Kr lead to the production of the 590 and 585.75 nm features which are now assigned to the emission of the $a^6D_{9/2}$ state (shown Figure VII.65). However the 620 nm feature assigned to the same electronic transition was observed to occur from the blue site equivalent. It is suggested that the site size available in Kr allows access to the minimum of the excited state potential energy surface, by allowing the observation of the *ZPL* for the $a^6D_{9/2} \rightarrow a^6S_{5/2}$ transition. In solid Xe, the Mn atom occupies a different site type and the site size does not allow coincidence of the minima of the ground and excited state. Subsequent interaction with the matrix host results in the broadening of the emission lineshapes and in the matrix-shifts observed.

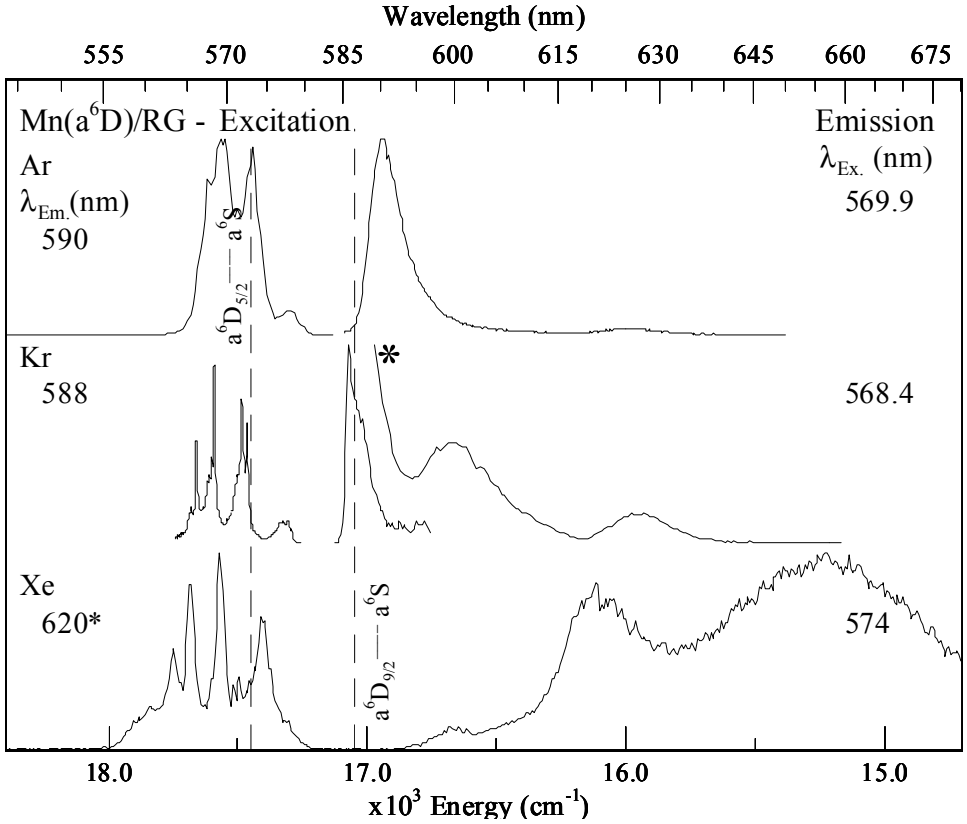

Figure VIII.24 Emission spectra (shown right) recorded at 12 K for all the Mn/RG systems investigated produced with laser excitation in the vicinity of the Mn a^6D ← $a^6S_{5/2}$ transition. The excitation wavelengths used are shown (right) as $\lambda_{Ex.}$ (nm). The excitation spectra shown (left), were recorded by monitoring emission bands as indicated by $\lambda_{Em.}$ in wavelength units. All spectra were recorded following Mn/RG sample deposition at 12 K and matrix annealing. The dashed vertical lines show the spectral locations of the gas phase transitions of atomic Mn. The asterix indicates that the Mn/Kr emission presented was recorded at lower spectral resolution over this range.

VIII.4 Conclusion Mn(a^6D)/RG luminescence

The excitation spectra recorded monitoring the emission features in the region of the gas phase $a^6D_{5/2} \leftrightarrow a^6S_{5/2}$ transition are presented in Figure VIII.23 for Mn atoms isolated in solid Ar, Kr and Xe. The observation of the individual spin-orbit levels in excitation is attributed to weak coupling of the a^6D excited state of Mn to the solid-state environment provided by the site of isolation. This contrasts with the excitation spectra recorded monitoring the same emission features, in the vicinity of the gas phase $z^6P_{5/2} \leftrightarrow a^6S_{5/2}$ and $z^8P_{5/2} \leftrightarrow a^6S_{5/2}$transitions, in the previous Chapter VII and later in this Chapter. The P ← S excitation spectra show characteristic Jahn-Teller threefold splitting pattern and large shifts from the gas phase positions. The comparison indicates the stronger interaction of the $z^6P_{5/2}$ excited state with the

matrix environment, highlighted by the observation of different matrix shifts for particular sites of atomic isolation.

The conservation of the gas phase spin-orbit splittings on the a^6D state in the solid allows the identification of the matrix shift observed for the $a^6D_{5/2} \leftrightarrow a^6S_{5/2}$ transition in all RG hosts, to the extent of ground state stabilisation for the Mn atom isolated in a given site of isolation within a particular host. The temperature dependence in the recorded spectra allowed the first observation of a *ZPL* for a matrix-isolated metal atom in excitation. This is best illustrated for the $a^6D_{5/2} \leftarrow a^6S_{5/2}$ transition for the Mn/Kr system.

The spectroscopy recorded following direct a^6D_J excitation allowed a definitive assignment of the 585 nm emission to the $a^6D_{9/2} \rightarrow a^6S_{5/2}$ transition in the Mn/Kr system. In Ar and Xe such a definitive assignment was not possible but the 590 and 620 nm emission bands in these solids are attributed to the a $a^6D_{9/2}$ state. The emission features observed at 625, 626.7 and 656 nm in Ar, Kr and Xe matrices remain unassigned.

VIII.5 Results Mn(z^8P)/RG luminescence

The following sections present the luminescence spectroscopy produced with direct laser excitation of the $z^8P_{5/2}$ excited state of atomic Mn isolated in solid Ar, Kr and Xe. Excitation spectra recorded in the vicinity of the gas phase position[1] of the $3d^54s4p\ z^8P_{5/2} \leftrightarrow 3d^54s^2\ a^6S_{5/2}$ transition at 543.4 nm (18402 cm^{-1}) allow the identification of the $z^8P_{5/2} \leftarrow a^6S_{5/2}$ transition in each RG host.

Time-resolved emission spectra and excited state lifetime measurements following pulsed laser excitation are used to attempt state assignments of the red emission bands reported at 625 and 627 nm in solid Ar and Kr respectively. These measurements also serve as a probe of the excited state relaxation mechanisms leading to the observed emission. This secondary role is of great importance in assessing the relaxation paths, which produce the emission features assigned to the $a^6D_{9/2} \rightarrow a^6S_{5/2}$ transitions produced from the higher lying $z^6P_{5/2}$ state, the luminescence spectroscopy of which was presented in Chapter VII.

The dye material used for direct z^8P state laser excitation was Coumarin 500. This is tuneable over the spectral range 485 to 535 nm (Chapter II, Table II.IX,

bottom panel) and exhibits a fluorescence maximum at 504 nm when pumped with the third harmonic of the Nd:YAG laser at 355 nm.

VIII.5.I Mn(z^8P)/Xe

In Section VIII.2.I the emission at 620 nm produced with $a^6D_{7/2} \leftarrow a^6S_{5/2}$ excitation at 574.65 nm was cautiously (Figure VIII.6) assigned to the relaxation of the $a^6D_{9/2}$ state. Figure VIII.3 showed that the 620 nm emission was separable from the thermally unstable 656 nm feature, identified in Chapter VII, Figure VII.2. Figure VIII.25 now presents high-resolution excitation spectra recorded in the vicinity of the gas phase $z^8P_{5/2} \leftrightarrow a^6S_{5/2}$ transition by monitoring the 621 (solid line) and 650 nm (dotted line) emissions. Inspection of the 621 nm excitation spectrum reveals two well-resolved features at 521.24 and 527.31 nm and a third weaker feature at 533.21 nm. The overall band shape is characteristic of Jahn-Teller threefold splitting of the $z^8P_{5/2} \leftarrow a^6S_{5/2}$ transition of atomic Mn, exhibiting a blue matrix-shift of 562 cm^{-1} from the gas phase position[1] at 543.4 nm, (18402 cm^{-1}). The average linewidth observed for the threefold split components is 192 cm^{-1}. The weak intensity of the lowest energy threefold component is due to the intensity drop-off of the Coumarin 500 dye curve at 535 nm.

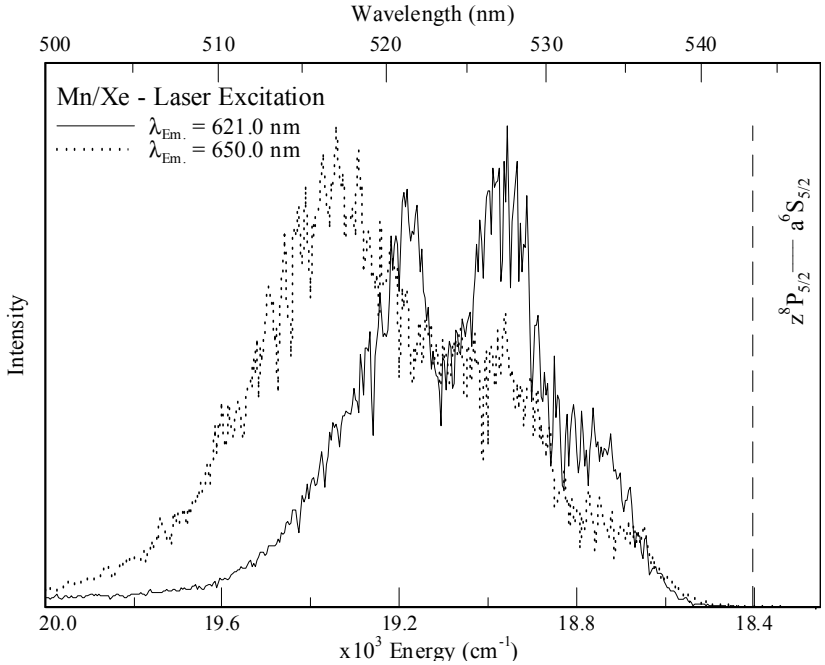

Figure VIII.25 Mn/Xe dye laser excitation spectra recorded at 12 K, in the vicinity of the $z^8P_{5/2} \leftrightarrow a^6S_{5/2}$ gas phase transition (dashed vertical line).

The most striking feature evident in the spectra presented in Figure VIII.25 is the presence of the threefold splitting pattern. This is attributed to the P ← S nature of the electronic transition involved and indicates a strong interaction of the excited state Mn atom with the matrix environment. Earlier in this Chapter the excitation spectra recorded for the a^6D excited state, allowed the identification of electronic transitions to the individual spin-orbit (J) levels. This occurred due to the weak guest-host interaction in the a^6D excited state of atomic Mn. In the z^8P case, the gas phase splitting between the spin-orbit levels[1] ($^5/_2 \leftrightarrow {}^7/_2$ and $^7/_2 \leftrightarrow {}^9/_2$) is 130 and 173 cm^{-1}. The observed splittings between the threefold components identified in the solid are 221 and 210 cm^{-1}. From this comparison it is evident that the observed matrix splittings exceed the gas phase spin-orbit splittings[1]. Moreover, the broad linewidth and the constant splitting further reinforces the assignment of the three observed bands as arising from Jahn-Teller interaction between the degenerate z^8P state and the matrix environment.

Following the identification of the z^8P state in excitation, emission spectra were recorded with z^8P ← a^6S excitation at 529.4 nm. The emission spectrum recorded is shown in Figure VIII.26 – it exhibits no additional features to those observed previously.

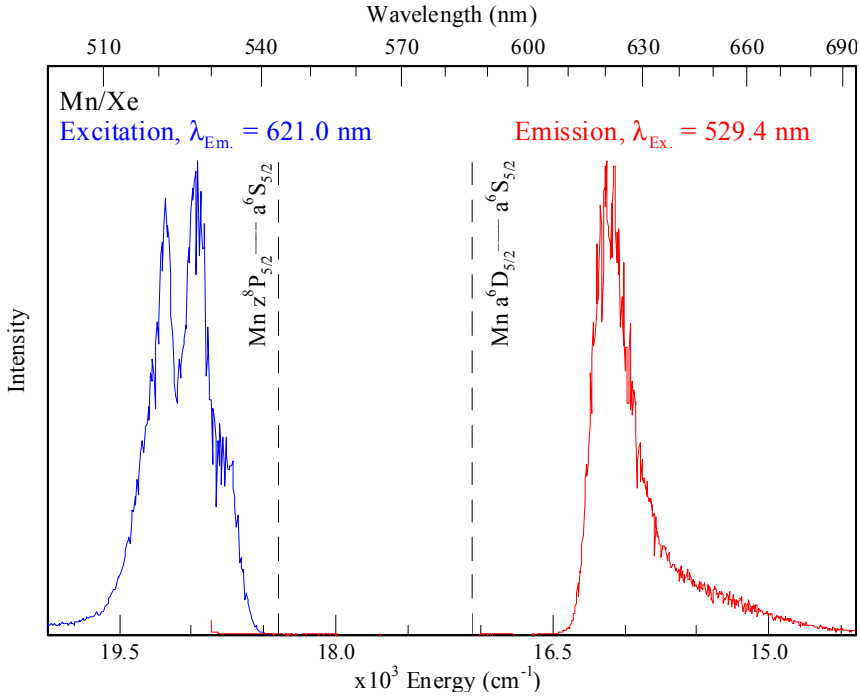

Figure VIII.26 Emission spectrum (shown right) recorded at 12.5 K following pulsed laser excitation at 529.4 nm, corresponding to the central threefold split component identified in excitation (shown left). Sample deposition was completed at 12.5 K and subsequently annealed to 37 K.

Table VIII.11 **Photophysical characteristics of excitation and emission bands assigned to the $3d^54s4p$ $z^8P_{5/2} \leftarrow 3d^54s^2$ $a^6S_{5/2}$ transition and emission features produced following $z^8P_{5/2} \leftarrow a^6S_{5/2}$ excitation of atomic manganese isolated in solid Xenon. λ_{Ex} / λ_{Em} indicates the position of an individual threefold excitation feature and emission band-centre in nm units respectively. The full-width at half-maximum intensity of the excitation/emission features is denoted by Δ and the gas phase to matrix frequency shifts (δ) are presented for the assigned absorption and emission features are presented in wavenumber (cm^{-1}) units. The decay characteristics extracted for the observed emission feature at 12.7 K are also presented.**

Mn Gas Phase	**Mn/Xe Matrix – *Excitation***			
Transition[1] nm / cm^{-1}	Assignment	$\lambda_{Ex.}$ (nm) / Δ (cm^{-1})		δ (cm^{-1})
$z^8P_{5/2} \leftrightarrow a^6S_{5/2}$ 543.4 / 18402	$z^8P_{5/2} \leftarrow a^6S_{5/2}$	521.24 527.31 / ≈ 192 533.21		+562
	Mn/Xe Matrix – *Emission*			
	$\lambda_{Em.}$ (nm) / Δ (cm^{-1})		Decay (msec)	δ (cm^{-1})
$a^6D_{9/2} \leftrightarrow a^6S_{5/2}$ 586.43 / 17052	$a^6D_{9/2} \rightarrow a^6S_{5/2}$	620.0 / ≈ 240	τ_{Obs} = 1.75	-926

Figure VIII.27 presents the decay profiles recorded for the 620 nm emission band at 12.7, 14, 22 and 27 K. It is clear from Figure VIII.27 that the radiative decay of the excited state has not been identified, as the decay profile observed is sensitive to temperature, even over the range 12.7 to 14 K. Figure VIII.28 presents a fit of the decay profile recorded by monitoring the 620 nm emission at 12.7 K. Therefore, the observed lifetime of the 620 nm emission is identified as 1.75 msec. The results of the fit of the decay profiles recorded at various temperatures (Table VIII.12) show that the relative contributions of the three temporal components were constant over the range investigated. However, all three decay characteristics decrease with increasing temperature. The temperature dependence observed is consistent with the assignment of the emission feature to the $a^6D_{9/2} \rightarrow a^6S_{5/2}$ transition of atomic Mn, as the observed excited state lifetime τ_{Obs} ($\lambda_{Ex} = z^8P_{5/2}$) of 1.75 msec is longer than that observed with direct $z^6D_{5/2}$ excitation where a microsecond excited state lifetime dominated, as shown in Table VIII.3. Therefore, the temperature dependence exhibited by the decay profiles presented in this section is a manifestation of the efficiency of the $z^8P \Rightarrow a^6D$ inter system crossing (ISC) process leading to the observed emission. Accordingly, no $z^8P_{5/2}$ state emission features are identified in the spectra resulting from direct $z^8P_{5/2}$ excitation in solid Xe.

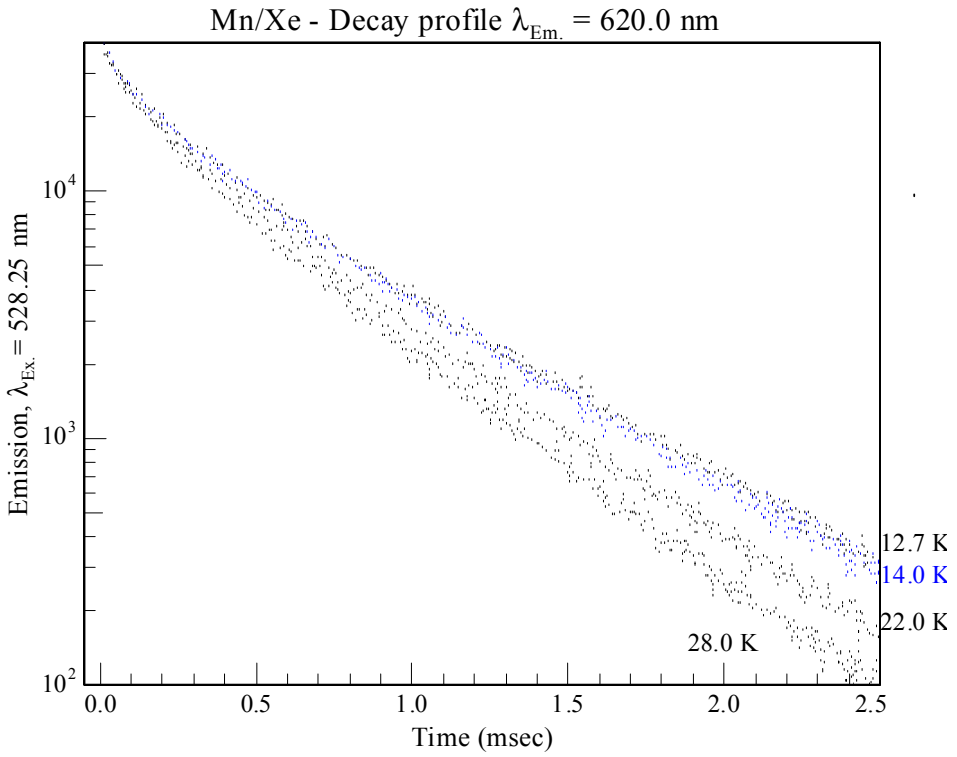

Figure VIII.27 **Decay profiles recorded monitoring the 620 nm emission recorded at various temperatures as indicated, following pulsed laser excitation at 528.25 nm.**

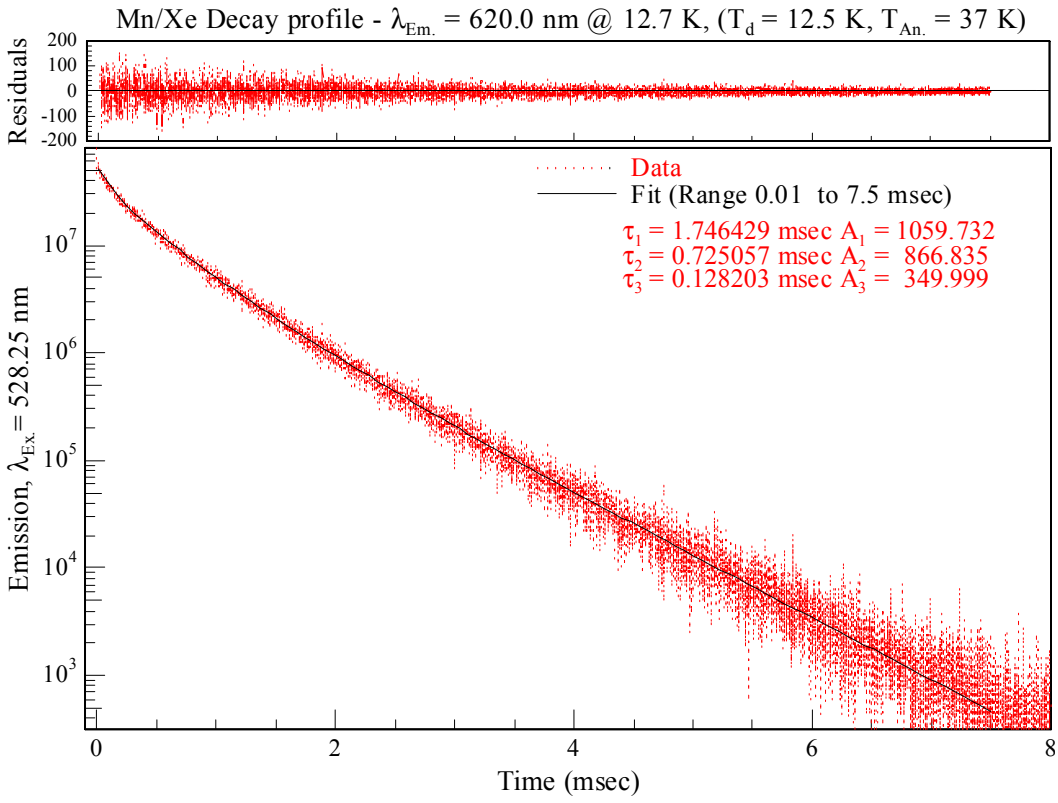

Figure VIII.28 **Decay profile of the 620 nm emission recorded at 12.7 K using TCSPC following pulsed laser excitation at 528.25 nm. The residuals presented allow an assessment of the fit quality as they represent the difference between the triple exponential fit completed and the decay recorded.**

Table VIII.12 **Decay characteristics, components and amplitudes (A) extracted from non-linear least squares analysis of the temporal profiles recorded monitoring emission at 620 nm at different temperatures, (T_s) following pulsed laser excitation at 528.25 nm. Note the dominant decay contribution is presented in bold.**

T_s. (K)	Fit Range (msec)	A_1	τ_1 (msec)	A_2	τ_2 (μsec)	A_3	τ_3 (μsec)
12.7	0.01 – 7.5	**1060**	**1.75**	867	725	350	128
14.0	0.01 – 7.5	**876**	**1.67**	677	632	261	72.0
18.0	0.01 – 7.5	**869**	**1.59**	810	724	322	124
22.0	0.01 – 6.0	**1263**	**1.39**	784	569	342	85.6
25.0	0.01 – 6.0	**1010**	**1.34**	733	592	283	81.2
28.0	0.01 – 4.7	**994**	**1.21**	503	460	233	75.3

VIII.5.II Mn(z^8P)/Kr

The luminescence spectroscopies resulting from z^6P state excitation (presented in Chapter VII), and resulting from a^6D state excitation, presented earlier in this Chapter, have shown the complexity of the Mn/Kr system, where multiple sites of atomic isolation and emission features have been identified. The emission feature produced to lower energy than the $z^8P_{5/2} \leftrightarrow a^6S_{5/2}$ gas phase transition[1] of atomic Mn at 585.75 has been definitively assigned to the $a^6D_{9/2} \rightarrow a^6S_{5/2}$ transition. However the 626.8 nm emission band has not been state assigned. The production of the broad 626.8 nm emission was only observed with blue (1°) site excitation of the $z^6P_{5/2}$ state, Figure VII.63. The temperature dependence observed in the steady-state and decay time measurements indicated a complex inter-system crossing (ISC) process leads to the production of the emission feature. The complexity of the relaxation process involved serve to make direct $z^8P_{5/2}$ resonance excitation important in deciphering the relaxation processes leading to the observed emission.

High-resolution excitation spectra recorded with a dye laser monitoring the thermally stable 628.3 and 589.4 nm and unstable 605.2 nm emission features are presented in Figure VIII.29. These excitation restore the site-specific nature of the emission features previously observed for the $z^6P_{5/2}$ excited state luminescence, Chapter VII; Figure VII.43. The dominant 1° site is located to higher energy and exhibits resolved threefold splitting. The excitation spectrum obtained monitoring the 589.4 nm emission is located at lower energy (2° site) and manifests two resolved features and a weaker, low energy feature[8]. The excitation spectrum recorded

monitoring the thermally unstable emission at 605.2 nm exhibits the broadest excitation lineshape, behaviour consistent with the results achieved for the $z^6P_{5/2}$ state, Chapter VII; Figure VII.43. The photophysical characteristics of the excitation spectra shown in Figure VIII.29 are collected in Table VIII.13.

The recorded excitation spectra allowed the assignment of the blue (1°) and red (2°) sites of isolation of Mn atoms. Emission spectra recorded with 1° and 2° site excitation at 513.8 and 531.8 nm respectively are shown in Figure VIII.30. Blue (1°) site excitation leads to the production of three broad emission features centered at 565.2 nm (17693 cm^{-1}), 605 (16529 cm^{-1}) and 627.4 nm (15938 cm^{-1}) with linewidths of 523, 430 and 262 cm^{-1} respectively. The higher energy 565.2 nm feature was not observed with any of the previous excitation methods used in this study.

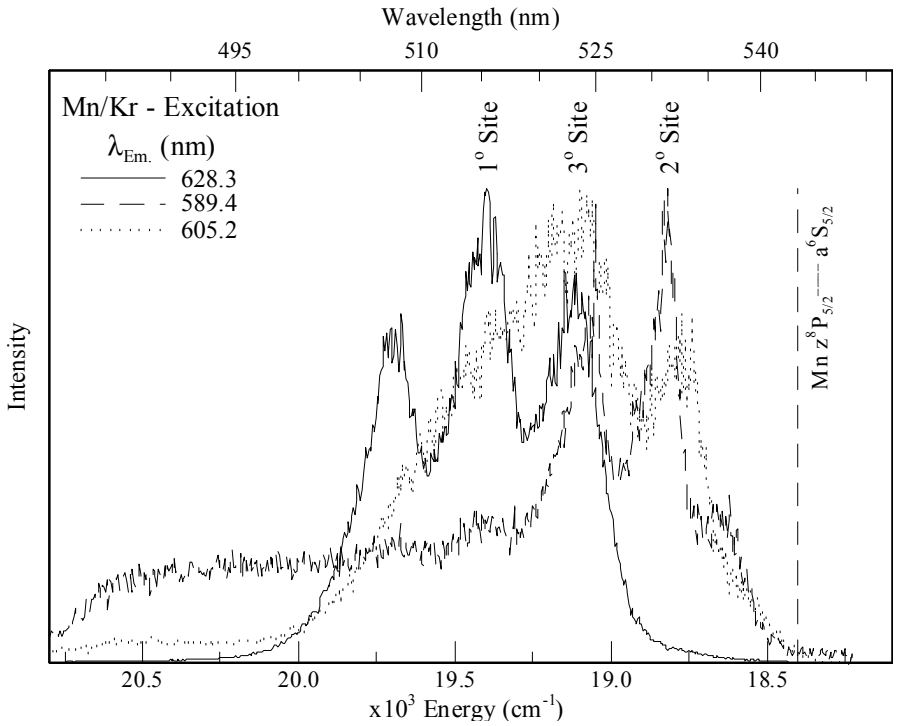

Figure VIII.29 Mn/Kr high-resolution excitation spectra recorded at 12.5 K, in the vicinity of the $z^8P_{5/2} \leftrightarrow a^6S_{5/2}$ gas phase transition (dashed vertical line) by monitoring the emission features as indicated. Sample deposition was completed at 12.5 K.

Inspection of Figure VIII.30 shows that red (2°) site excitation at 531.8 nm leads to the 586 nm emission feature assigned earlier in this Chapter to the $a^6D_{9/2} \rightarrow a^6S_{5/2}$ transition. In addition the 605 and 627 nm emission features are present due to the spectral overlap. No further analyses of the 586 nm emission band, or excited state lifetime measurements are reported for the $a^6D_{9/2} \rightarrow a^6S_{5/2}$ transition.

Table VIII.13 **Photophysical characteristics of the 1°, 2° and 3° sites of isolation $3d^54s4p$ $z^8P_{5/2}$ ↔ $3d^54s^2$ $a^6S_{5/2}$ transition of atomic manganese. The spectral position and average full width at half maximum (*fwhm*) denoted as Δ_{AV} of the three components identified in Gaussian lineshape analyses for the three–fold split excitation spectra are presented in wavenumber units. Gas phase to matrix frequency shifts (δ) are presented for the atomic Mn $z^8P_{5/2}$ ← $a^6S_{5/2}$ transition (G.P.: 18402 cm^{-1}) in wavenumber units. Note the frequency shifts are calculated with respect to the central feature of the observed three-fold pattern.**

Mn/Kr Site	E (cm^{-1})	Δ_{AV} (cm^{-1})	δ (cm^{-1})
1°	19696 19397 19114	≈ 223	+ 995
2°	19081 18822 18648	≈ 150	+ 420
3°	19408 19129 18778	≈ 360	+ 727

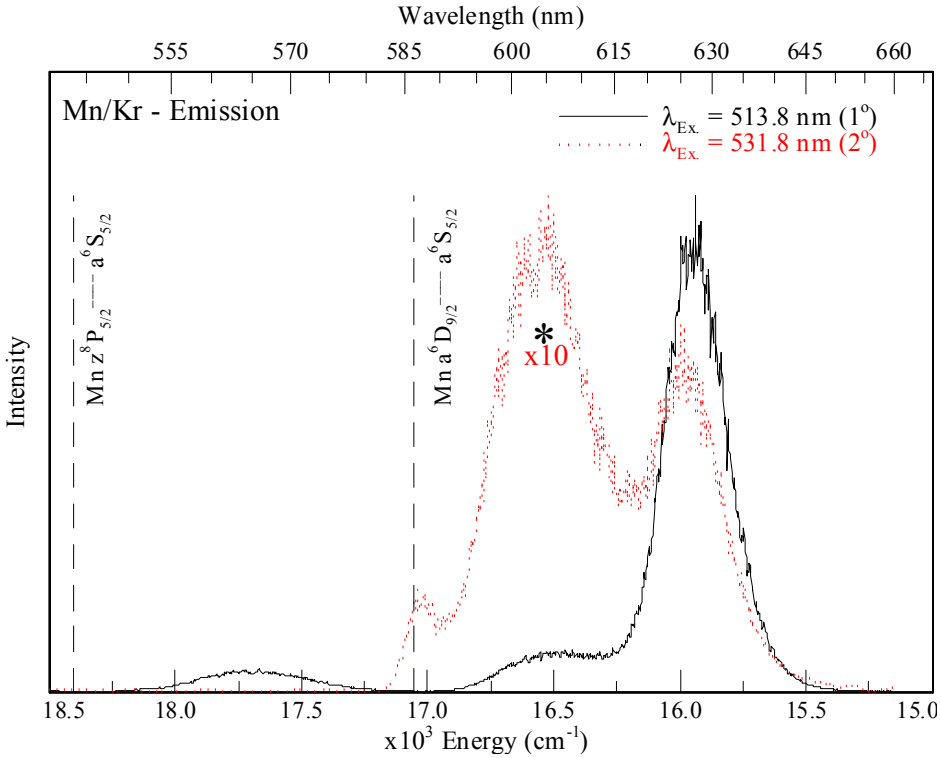

Figure VIII.30 **Emission spectra recorded at 12.5 K produced with site-selective laser excitation of the 1° (513.8 nm) and 2° (531.8 nm) sites assigned to the Mn $z^8P_{5/2}$ ← $a^6S_{5/2}$ transition on deposition at 12.5 K. The spectra have been normalised and the scaling factors are shown. Note the asterix denotes the presence of thermally unstable emission. The positions of the $z^8P_{5/2}$ ↔ $a^6S_{5/2}$ and $a^6D_{9/2}$ ↔ $a^6S_{5/2}$ gas phase transitions are indicated.**

VIII.5.II.I Mn(z^8P)/Kr - 1° site luminescence

This section presents time-resolved emission spectra, excited state lifetime measurements and the temperature dependence of the two site-specific emission features observed at 565.2 and 627.4 nm. Figure VIII.31 presents time-resolved emission recorded with iCCD detection following $z^8P_{5/2} \leftarrow a^6S_{5/2}$ excitation of Mn atoms isolated in the blue (1°) site at 513.8 nm. It is evident from Figure VIII.31 that the excited state lifetimes of the emission features are very different.

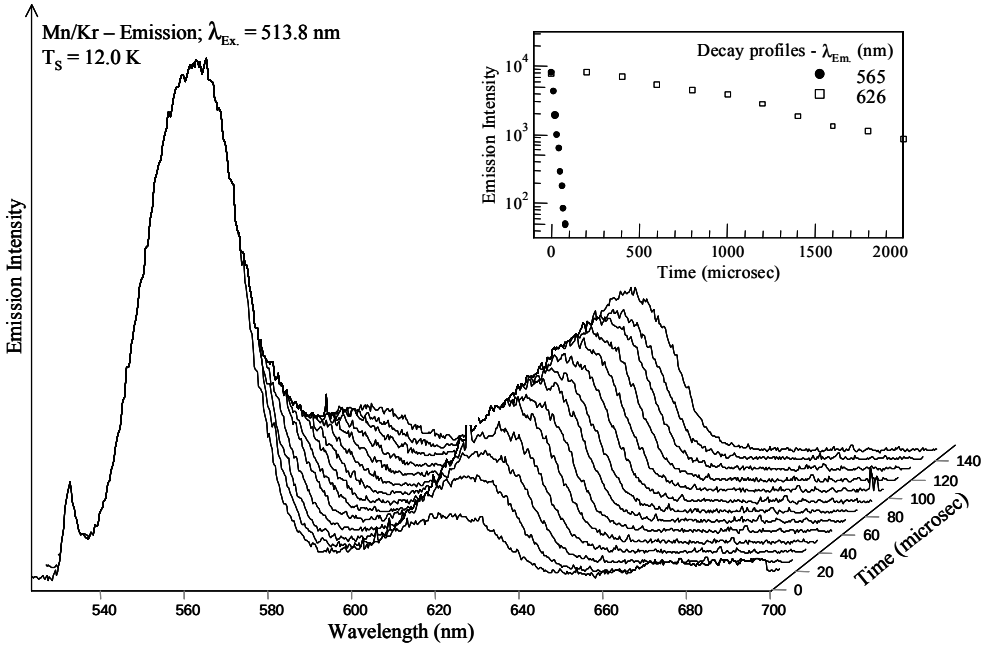

Figure VIII.31 Time-resolved emission spectrum recorded monitoring emission at 565 and 626 nm (at 12 K) following pulsed laser excitation at 513.8 nm. The temporal step and width used was 15 μsec with a delay time of t_d = 0.0 nsec. The excited state decay profiles extracted for the emission features are presented (Inset).

Thus the 565.2 nm feature is observed to decrease in intensity over the 0 to 150 microsecond timescale shown, whereas the intensity of the 627 nm band is still increasing in this time interval. Decay profiles extracted from the time-resolved measurement are shown in the inset of Figure VIII.31. Comparison of the decay curves shows that the 565.2 nm emission occurs on a microsecond timescale, and the 627 nm feature requires milliseconds to decay. The rising portion of the 627 nm band is observed over the same timescale as the 565.2 nm decay. A fit of the decay profile recorded for the 565 nm feature using a single exponential trial function allowed the extraction of an excited state lifetime of 43.4 μsec. The temperature dependence in the 565 nm decay profile is shown in Figure VIII.32 revealing that the radiative

lifetime of the feature has not been observed. This is evident from the change in the decay profiles measured in the small temperature range 12.6 to 13.5 K. Excited state lifetimes of 43.4, 29.3 and 20.1 μsec were extracted at temperatures of 12.6, 13.5 and 16 K respectively.

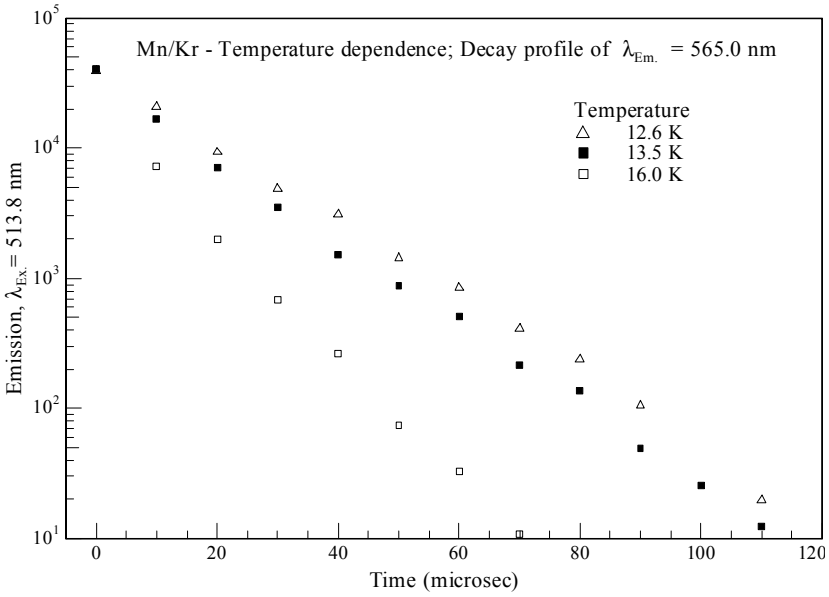

Figure VIII.32 Decay profiles recorded monitoring the 565 nm emission recorded at various temperatures as indicated, following pulsed laser excitation at 513.8 nm. The excitation wavelength chosen corresponds to the central threefold excitation feature identified.

As the radiative lifetime for the transition has not been identified, the observed lifetime at 12.6 K is taken to be 43.4 μsec. Correction of the observed lifetime for the effective field of the Kr solid is achieved using Equation III.1, given the refractive index of Kr is 1.428[9]. Applying the effective field correction yields a corrected excited lifetime of 112.4 μsec a value which compares well with the known gas phase lifetime[2] for the $z^8P_{5/2} \leftrightarrow a^6S_{5/2}$ transition of 149.3 μsec. This value in conjunction with the spectral location, see Figure VIII.30, allows a convincing assignment of the observed 565.2 nm emission feature to the $z^8P_{5/2} \rightarrow a^6S_{5/2}$ phosphorescence of atomic Mn. Emission spectra recorded following blue (1°) site $z^8P_{5/2} \leftarrow a^6S_{5/2}$ excitation at 513.8 nm were recorded at various temperatures. The emission spectra showed that the emission intensity of the 565.2 nm feature decreased to zero over the temperature range 12 to 24 K. The 565.2 nm feature was not observed at temperatures above 22 K.

Figure VIII.33 presents the decay profiles extracted for the 627 nm emission feature from time-resolved spectra. The decay profile exhibits a rising portion

indicative of a complex relaxation process where the final relaxation step may be faster than the initial feeding step. Inspection of Figure VIII.33 also reveals that the 626 nm decay profiles recorded with $a^6D_{5/2}$ (567.55 nm) and $z^8P_{5/2}$ (513.8 nm) state excitation are similar. Figure VIII.16 presented a triple exponential fit of the decay profile recorded monitoring 627 nm emission (at 12.5 K) following pulsed laser excitation of the $a^6D_{5/2} \leftarrow a^6S_{5/2}$ transition. Three excited state lifetime components of 2.19, 1.61 and 0.11 msec were extracted. The dominant component corresponded to τ_2 and the rise time was identified as τ_3, Figure VIII.16. Earlier in this Chapter the decay profile recorded monitoring the 626.7 nm band was observed to show a rise time with a^6D excitation, (Figure VIII.16).

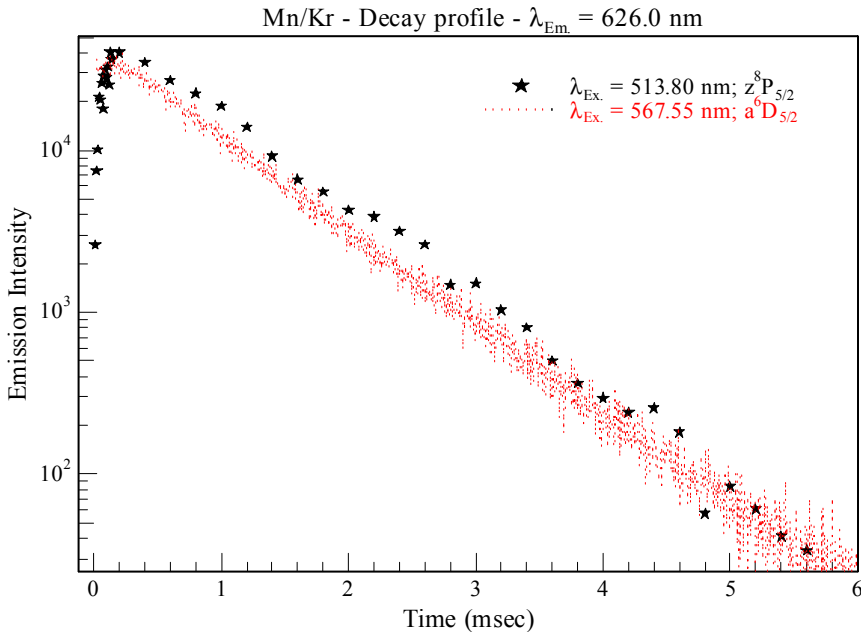

Figure VIII.33 Comparison of the decay profiles recorded monitoring the 626 nm emission feature recorded following pulsed laser excitation at 513.8 and 567.55 nm corresponding to the blue (1°) site $z^8P_{5/2} \leftrightarrow a^6S_{5/2}$ and the $a^6D_{5/2} \leftrightarrow a^6S_{5/2}$ transitions of atomic Mn isolated in solid Kr.

The observation of site specificity with z^8P excitation and the presence of approximately the same rise time (108 μsec) indicated the site-specific emission is maintained with $a^6D \leftarrow a^6S$ excitation, even though the spectra were unshifted. This suggests the 626.7 nm emission results from the relaxation of the a^6D state via direct feeding from the z^8P with the rise time representing the efficiency of the $z^8P \Rightarrow a^6D$ ISC. However, the broad emission lineshape and the large matrix shift observed do not favour this assignment. These mechanisms are discussed at the end of this

Chapter following the presentation of the Mn(z^8P)/Ar luminescence in tandem with a review of the site-specific relaxation mechanisms reported for the z^6P and a^6D excited states of atomic Mn in the RG solids. The site-specific luminescence spectroscopy of the $z^8P_{5/2} \leftrightarrow a^6S_{5/2}$ transition of atomic Mn isolated in solid Kr is summarised in Figure VIII.34. The photophysical characteristics and the transitions assigned to the emission features observed are collected in Table VIII.14. Overall the site-specificity reported in Chapter VII for Mn(z^6P)/Kr luminescence is conserved by the $z^8P_{5/2}$ state. The excitation spectra reported showed the presence of multiple sites of isolation; two thermally stable and a single thermally unstable site were identified. The blue (1°) site produced emission at 565 nm assigned from lifetime measurements to the z^8P excited state phosphorescence. The low energy emission at 627 nm remains unassigned due to the complexity of the dynamic processes leading to the observed feature. The red (2°) site leads to the production of the 587 nm emission band, assigned earlier in the analysis of the a^6D state luminescence. In this case the relaxation occurred via a $z^8P \Rightarrow a^6D$ ISC process of 100% efficiency[10].

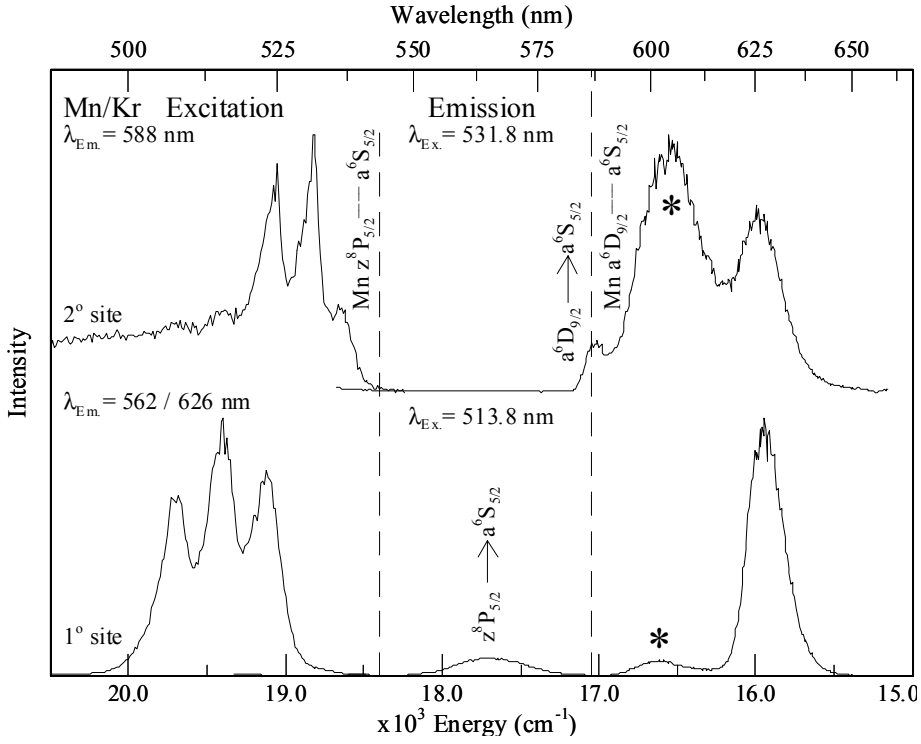

Figure VIII.34 Emission spectra recorded with site-selective pulsed laser excitation of the Mn $z^8P_{5/2} \leftarrow a^6S_{5/2}$ transition. The excitation spectra (1° and 2° site), were recorded by monitoring emission at 588 (top) and 565 / 626 nm (bottom), shown left. The spectra were recorded following sample deposition at 12 K and annealing to 32 K. The dashed vertical lines show the spectral positions of the gas phase transitions of atomic Mn. Note the asterix indicates the spectral location of thermally unstable emission features.

Table VIII.14 Photophysical characteristics and excited state assignments of the emission feature produced following site-specific $3d^54s4p$ $z^8P_{5/2}$ excitation. $\lambda_{Em.}$ indicates the emission band-centre in nm and wavenumber units. The matrix shift (δ) for the transitions are indicated in wavenumber (cm^{-1}) units.

Mn Gas Phase	**Mn/Kr Matrix – *Emission* (1° Site)**			
Transition[1] nm / cm^{-1}	Assignment	$\lambda_{Em.}$ (nm) / (cm^{-1})	δ (cm^{-1})	Decay Characteristic
$z^8P_{5/2} \leftrightarrow a^6S_{5/2}$ 543.40 / 18402	$z^8P_{5/2} \rightarrow a^6S_{5/2}$	565.2 / 17693	-709	$\tau_{Obs.}$ = 43.4 μsec
$z^8P_{5/2} \leftrightarrow a^6S_{5/2}$	(?)	627.4 / 15938	-2464	$\tau_{Obs.}$ = 1.61 msec
$a^6D_{9/2} \leftrightarrow a^6S_{5/2}$			-1114	τ_{Rise} = 108 μsec
	Mn/Kr Matrix – *Emission* (2° Site)			
$a^6D_{9/2} \leftrightarrow a^6S_{5/2}$ 586.43 / 17052	$a^6D_{9/2} \rightarrow a^6S_{5/2}$	586.75 / 17043	-9	

VIII.5.III Mn(z^8P)/Ar

In this section the luminescence spectroscopy of the $z^8P_{5/2} \leftrightarrow a^6S_{5/2}$ transition is presented for Mn isolated in solid Ar. Chapter VII; Section VII.2.II and Section VIII.2.III of this chapter presented the luminescence of the $z^6P_{5/2}$ and a^6D excited states of atomic Mn. The three emission features reported at 590, 605 and 625 nm, occurred to lower energy than the $z^8P_{5/2} \leftrightarrow a^6S_{5/2}$ gas phase position[1] at 543.4 nm (18402 cm^{-1}). The Mn($z^6P_{5/2}$)/Ar spectroscopy identified multiple sites of isolation, and subsequently attributed the emission features at 590 and 625 nm as resulting from distinct sites of isolation. Results from direct a^6D state excitation allowed the 590 nm emission band to be assigned to the $a^6D_{9/2} \rightarrow a^6S_{5/2}$ transition, Figure VII.41. However, the 625 nm emission feature has not been assigned to either the $a^6D_{9/2} \rightarrow a^6S_{5/2}$ or $z^8P_{5/2} \rightarrow a^6S_{5/2}$ transitions of atomic Mn in solid Ar.

Dye laser excitation spectra recorded monitoring the thermally stable 590 and 625 nm and unstable 605 nm emission features are presented in Figure VIII.35. These excitation spectra exhibit the same site-specific characteristics previously observed in excitation spectra of the $z^6P_{5/2}$ state, in Chapter VII. The low energy, red site dominates (1° site) and exhibits very well resolved threefold splitting and a blue matrix shift (δ) of 636 cm^{-1} from the gas phase transition[1]. Resolved threefold splitting was also recorded monitoring the 625 nm feature. This corresponds to the blue (2°) site of isolation identified for the $z^6P_{5/2}$ transition. The excitation spectrum

recorded monitoring the thermally unstable emission at 605 nm shows a broad lineshape consistent with that obtained for the $z^6P_{5/2}$ state, Chapter VII; Figure VII.12. The photophysical characteristics of the excitation spectra are shown in Figure VIII.35 and presented in Table VIII.13.

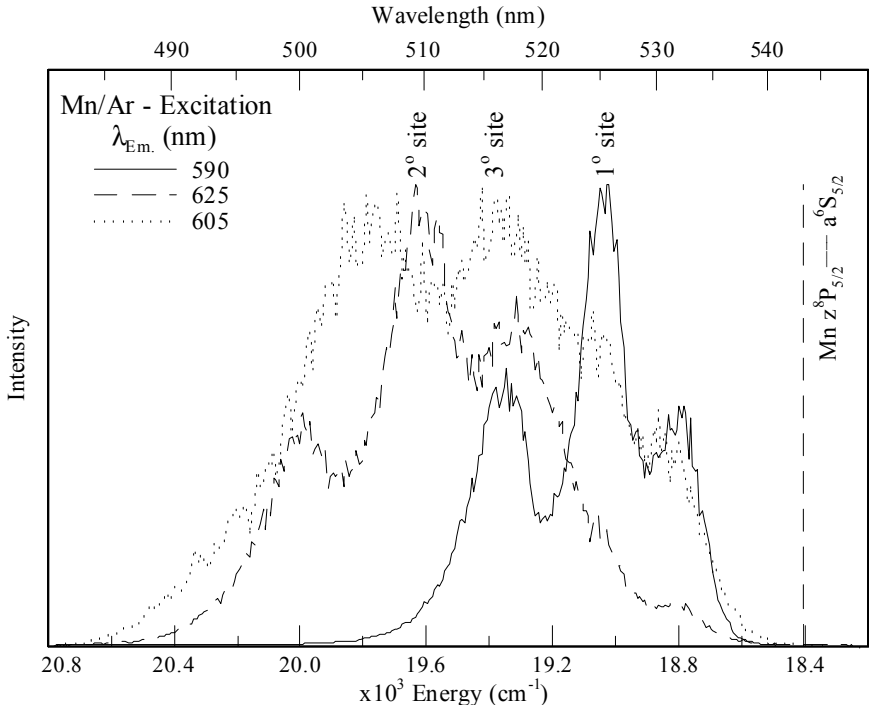

Figure VIII.35 Mn/Ar high-resolution excitation spectra recorded at 12.5 K by monitoring the emission features as indicated. The dashed vertical lines indicates the spectral location of the $z^8P_{5/2} \leftrightarrow a^6S_{5/2}$ gas phase transition[1].

Table VIII.15 Photophysical characteristics of the 1°, 2° and 3° sites of isolation $3d^54s4p\ z^8P_{5/2} \leftrightarrow 3d^54s^2\ a^6S_{5/2}$ transition of atomic manganese. The spectral position and average full width at half maximum (*fwhm*) denoted as Δ_{AV} of the three components identified in Gaussian lineshape analyses for the three–fold split excitation spectra are presented in wavenumber units. Gas phase to matrix frequency shifts (δ) are presented for the atomic Mn $z^8P_{5/2} \leftarrow a^6S_{5/2}$ transition[1] (G.P.: 18402 cm^{-1}) in wavenumber units. Note the frequency shifts are calculated with respect to the central feature of the observed three-fold pattern.

Mn/Ar Site	E (cm^{-1})	Δ_{AV} (cm^{-1})	δ (cm^{-1})
1°	19354 19038 18798	≈ 193	+ 636
2°	19989 19617 19315	≈ 320	+ 1215
3°	19773 19346 18982	≈ 428	+ 944

Emission spectra recorded with site-specific excitation at 528.8 nm (1°); 508.8 nm (2°) and 515.8 nm (3°) are shown in Figure VIII.36. The emission spectra shown reveal the red (1°) site excitation at 528.8 nm leads to the production of the 590 nm emission feature previously assigned to the $a^6D_{9/2} \rightarrow a^6S_{5/2}$ transition. Blue (2°) site excitation at 508.8 nm produced the 625 nm emission previously identified. However, unlike the 565 nm band in the Mn(z^8P)/Kr system, no emission feature with a small Stokes' shift is observed in Ar with direct $z^8P_{5/2} \leftarrow a^6S_{5/2}$ excitation. The sections that follow present a detailed analysis of the site-specific emission spectroscopy observed following $z^8P_{5/2}$ excitation, focussing on the excited state lifetime measurements conducted in an attempt to identify the excited state dynamics leading to the observed emission features.

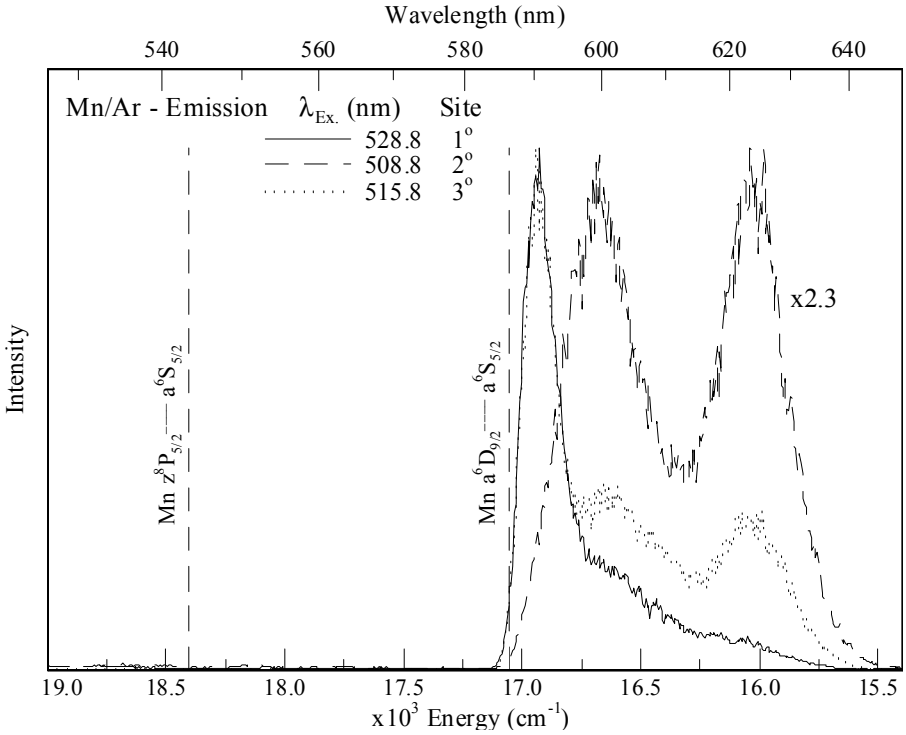

Figure VIII.36 Mn/Ar emission spectra recorded at 12.5 K produced with site-selective laser excitation of the 1°, 2° and 3° sites assigned to the Mn $z^8P_{5/2} \leftarrow a^6S_{5/2}$ transition on deposition at 12.5 K. The spectra have been normalised and the scaling factors are shown. The dashed vertical lines indicate the positions of the $z^8P_{5/2} \leftrightarrow a^6S_{5/2}$ and $a^6D_{9/2} \leftrightarrow a^6S_{5/2}$ gas phase transitions[1].

VIII.5.III.I Mn(z^8P)/Ar - 1° site luminescence

As shown in Figure VIII.36, laser irradiation at 528.8 nm corresponding to excitation of the red (1°) site, leads to the production of the 590 nm emission feature assigned in

Section VIII.2.III to the $a^6D_{9/2} \rightarrow a^6S_{5/2}$ transition. Figure VIII.37 presents the decay profile recorded monitoring the 590.5 nm feature at 12 K. The decay times extracted using a trial triple exponential function are dominated by two long lived components of 1.28 and 0.51 msec. These long-lived millisecond components dominate for all temperatures in the range 12 to 24 K.

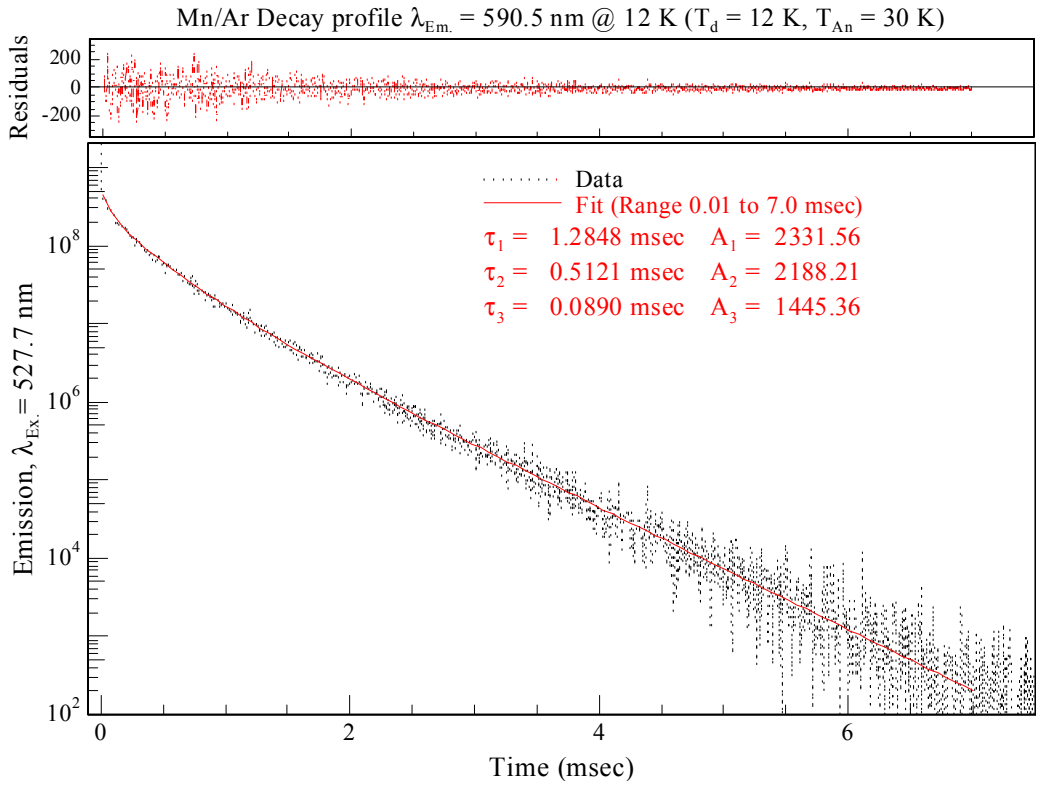

Figure VIII.37 Decay profile of the 590.5 nm emission feature recorded at 12 K using TCSPC following pulsed laser excitation at 527.7 nm. The residuals present the difference between the triple exponential non-linear least squares fit completed and the decay recorded.

Comparison of the decay times extracted at all temperatures following pulsed laser excitation of the $z^8P_{5/2} \leftarrow a^6S_{5/2}$ transition in Table VIII.16 can be made with those presented in Table VIII.9 following $a^6D_{5/2} \leftarrow a^6S_{5/2}$ excitation. This reveals that the excited state decay characteristics are slightly longer with $z^8P_{5/2}$ excitation than with a^6D_J. This therefore suggests that the relaxation occurs by an efficient $z^8P \Rightarrow a^6D$ ISC process which is 100% efficient with red (1°) site excitation as no rise times (non-radiative feeding rates) are evident in the decay profiles recorded.

Table VIII.16 **Decay characteristics, components (τ) and amplitudes (A) extracted from non-linear least squares analysis of the temporal profiles recorded by monitoring emission at 590 nm at different temperatures, (T_s) following pulsed laser excitation at 528.8 nm. Note the dominant decay contribution is presented in bold.**

T_s. (K)	Fit Range (msec)	A_1	τ_1 (msec)	A_2	τ_2 (μsec)	A_3	τ_3 (μsec)
12.7	0.01 – 7.0	**2332**	**1.28**	2188	512	1445	89.0
15.0	0.01 – 5.0	**1054**	**1.08**	641	330	464	55.2
18.0	0.01 – 5.0	**1482**	**0.99**	916	288	581	41.9
21.0	0.01 – 5.0	**1414**	**0.91**	908	240	574	21.8
24.0	0.01 – 5.0	**1781**	**0.83**	1201	216	740	21.9

VIII.5.III.II Mn(z^8P)/Ar - 2° site luminescence

Emission spectra recorded with blue (2°) site excitation at 508.8 nm yielded the single thermally stable emission centered at 625 nm. Unlike Mn/Kr, presented in the previous section, no feature in the 560 nm region was observed in solid Ar, Figure VIII.36. However, the strong temperature dependence observed for the 565.2 nm band in Kr, suggests that the minimum temperature accessible of 12 K, may not allow the production of an emission feature due to fast non-radiative relaxation of the z^8P excited state. Therefore experiments below 12 K are suggested but cannot be realised using the current cryogenic apparatus.

Decay profiles recorded monitoring the 625 nm emission band show no indications of a rise time component unlike that present in the 627 nm feature in solid Kr. Analysis of the decay profiles recorded monitoring the 625 nm emission required a triple exponential function, Figure VIII.38 at 12 K. The dominant millisecond decay components extracted at all temperatures are presented in Table VIII.17.

The conflicting spectral and temporal characteristics of the 625 nm emission feature preclude a definitive assignment to either the $z^8P_{5/2} \rightarrow a^6S_{5/2}$ or the $a^6D_{9/2} \rightarrow a^6S_{5/2}$ transitions of atomic Mn isolated in Ar. Specifically, the broad symmetric lineshape is indicative of a P → S type transition, while the long decay time (980 μsec) and the spectral location suggest an assignment to the $a^6D_{9/2} \rightarrow a^6S_{5/2}$ transition. The assignment of this emission band is discussed further at the end of this Chapter.

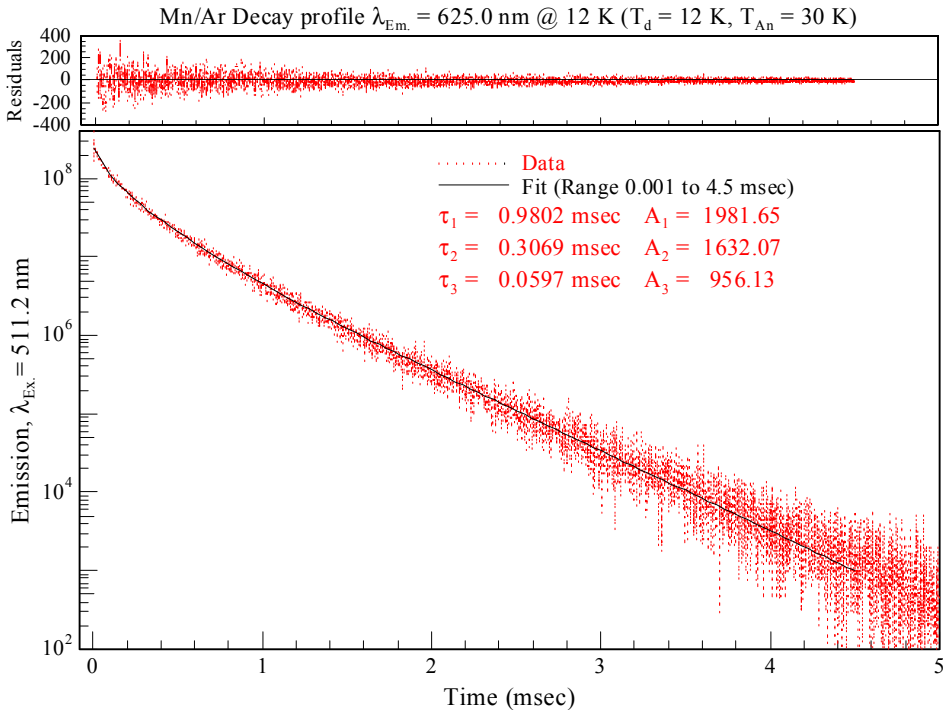

Figure VIII.38 **Decay profile of the 625 nm emission feature recorded at 12 K using TCSPC following pulsed laser excitation at 511.2 nm. The residuals present the difference between the triple exponential non-linear least squares fit completed and the decay recorded.**

Table VIII.17 **Decay characteristics, components and amplitudes (A) extracted from non-linear least squares analysis of the temporal profiles recorded monitoring $\lambda_{Em.}$ = 625 nm at different temperatures, (T_s) following pulsed laser excitation at 511.2 nm. Note the dominant decay contribution is presented in bold.**

$T_{s.}$ (K)	Fit Range (msec)	**A_1**	**τ_1 (μsec)**	A_2	τ_2 (μsec)	A_3	τ_3 (μsec)
12.7	0.001 – 4.5	**1982**	**980**	1632	307	956	59.7
15.0	0.001 – 4.0	**711**	**961**	641	290	369	39.7
18.0	0.001 – 4.0	**909**	**960**	852	324	470	63.5
25.0	0.001 – 4.0	**1032**	**854**	827	270	564	40.9

The site-specific luminescence spectroscopy of the $z^8P_{5/2} \leftrightarrow a^6S_{5/2}$ transition of atomic Mn isolated in solid Ar is summarised in Figure VIII.39. The photophysical characteristics and the transitions assigned to the observed emission features are presented in Table VIII.18.

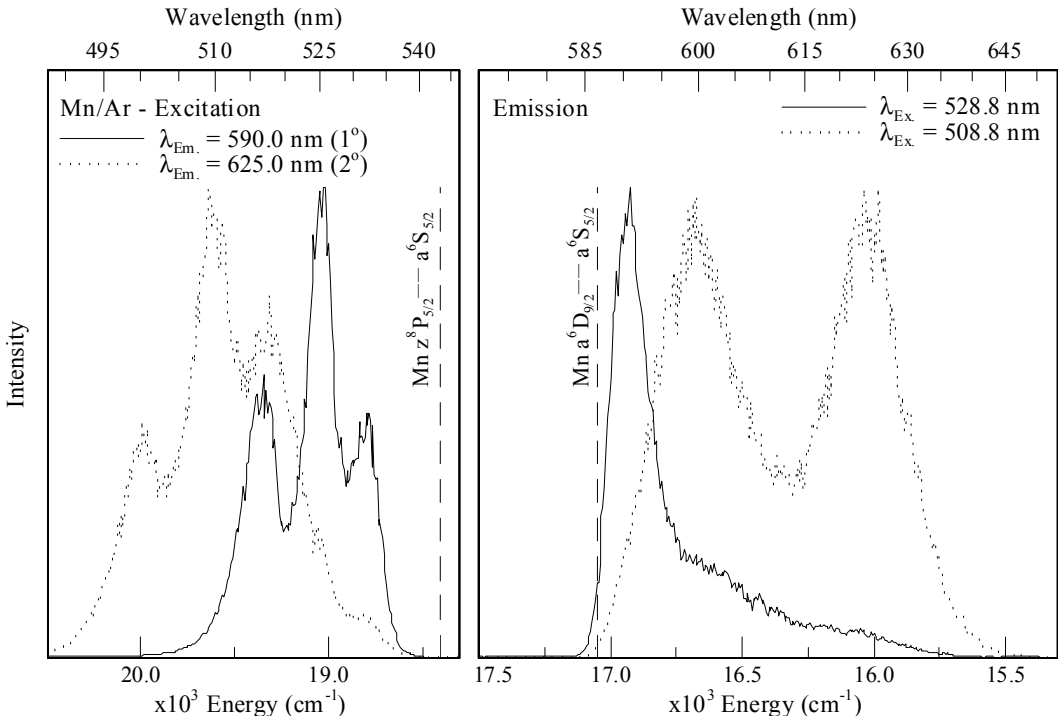

Figure VIII.39 **Emission spectra recorded at 12.5 K with site-selective pulsed dye laser excitation of the Mn $z^8P_{5/2} \leftarrow a^6S_{5/2}$ transition (right). The excitation spectra (1° and 2° site) were recorded by monitoring emission at 590 (solid trace) and 625 nm (dotted trace), shown left. Sample deposition was completed at 12 K and subsequently annealed to 28 K. The dashed vertical lines show the spectral positions of the relevant gas phase transitions[1] of atomic Mn. The 600 nm emission band results from excitation of the thermally unstable 3° site. The photophysical characteristics of the excitation and emission features are presented in Table VIII.15 and Table VIII.18 respectively.**

Table VIII.18 **Photophysical characteristics and excited state assignments of the emission features produced following site-specific $3d^54s4p$ $z^8P_{5/2}$ excitation. λ_{Em}, indicates the emission band-centre in nm and wavenumber units. The matrix shift for the transition is indicated δ in wavenumber (cm^{-1}) units. The observed excited state lifetimes are also presented as $\tau_{Obs.}$ at 12 K. Note additional decay times extracted of substantial amplitude are also presented.**

Mn Gas Phase	**Mn/Ar Matrix – *Emission* (1° Site)**			
Transition[1] nm / cm^{-1}	Assignment	$\lambda_{Em.}$ (nm) / (cm^{-1})	δ (cm^{-1})	Decay Characteristic
$a^6D_{9/2} \leftrightarrow a^6S_{5/2}$ 586.43 / 17052	$a^6D_{9/2} \rightarrow a^6S_{5/2}$	590 / 16949	-103	$\tau_{Obs.}$ = 1.28 msec 512 µsec
	Mn/Ar Matrix – *Emission* (2° Site)			
$z^8P_{5/2} \leftrightarrow a^6S_{5/2}$ 543.40 / 18402	(?)	625 / 16000	-2402	$\tau_{Obs.}$ = 1.03 msec 360 µsec
$a^6D_{9/2} \leftrightarrow a^6S_{5/2}$ 586.43 / 17052			-1052	

VIII.6 Discussion Mn(z^8P)/RG luminescence

In this section, the observed luminescence spectroscopy of the $z^8P_{5/2} \leftrightarrow a^6S_{5/2}$ transition of atomic Mn isolated in solid Ar, Kr and Xe is summarised and some trends evident in the excitation and emission spectroscopy are presented.

VIII.6.I Mn(z^8P)/RG Excitation spectroscopy

A summary of the excitation spectra recorded by monitoring the red emission features of Mn isolated in solid Ar, Kr and Xe in the region of the gas phase $z^8P_{5/2} \leftrightarrow a^6S_{5/2}$ transition is presented in Figure VIII.40. In all matrices and for all the sites, the excitation spectra exhibit resolved threefold split excitation patterns. The photophysical characteristics of the sites of isolation identified from the excitation spectra are collected in Table VIII.15, Table VIII.13 and Table VIII.11 for Mn/Ar, Mn/Kr and Mn/Xe respectively. Of particular note in the excitation spectra is the occurance of threefold splitting patterns indicating the strong interaction of the $z^8P_{5/2}$ excited state with its matrix environment. This contrasts the excitation spectra recorded for the $a^6D \leftarrow a^6S_{5/2}$ transition (Section VIII.3.I) in which the individual spin-orbit levels were identified reflecting the weak coupling of the a^6D excited state to the local solid-state environment. The sites of isolation identified with z^8P state are spectrally well separated like those of the z^6P, exhibiting large matrix shifts (100's of cm^{-1}). It will be remembered that the excitation spectra of the a^6D state all occurred within the same narrow spectral range. Both of these observations support the conclusion that the interaction of the Mn atom within the site is much stronger for the z^8P state than the a^6D state. In the next section the emission spectroscopy resulting from z^8P excitation is discussed, highlighting the role of the site of isolation in determining excited state relaxation processes.

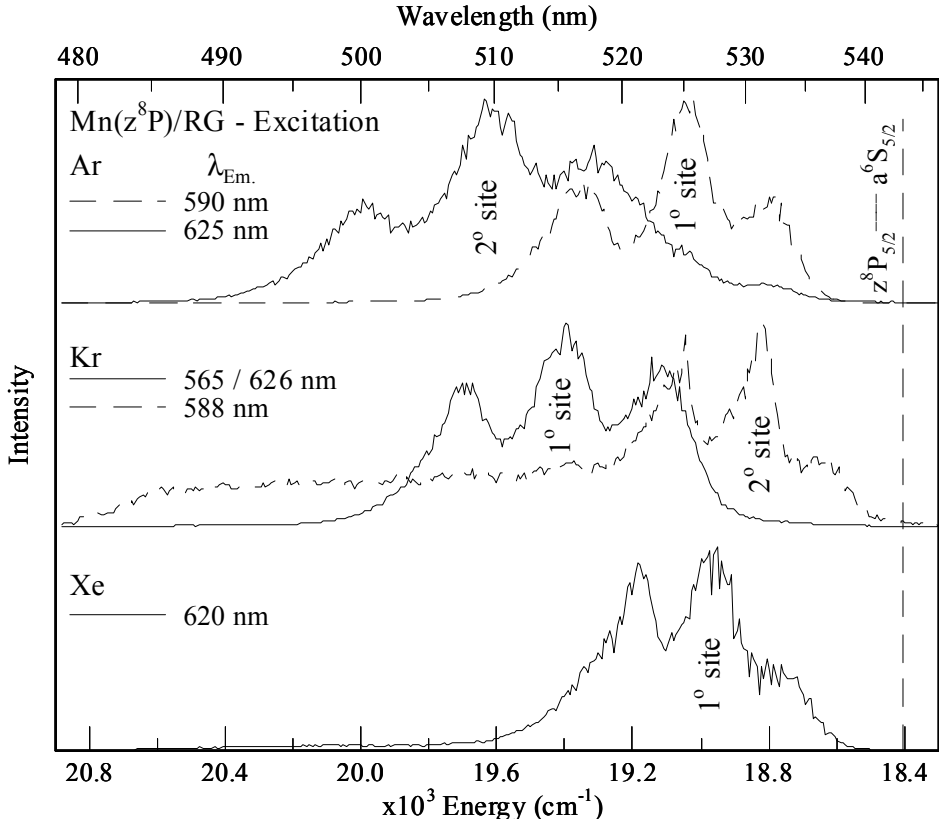

Figure VIII.40 Mn/RG excitation spectra recorded at 12 K for all the Mn/RG systems investigated produced with laser excitation in the vicinity of the Mn $z^8P_{5/2} \leftarrow a^6S_{5/2}$ transition. The spectra shown were recorded monitoring emission bands as indicated by $\lambda_{Em.}$ (left) in wavelength units. All spectra were recorded following Mn/RG sample deposition at 12 K and matrix annealing. The dashed vertical line indicates the position of the $z^8P_{5/2} \leftarrow a^6S_{5/2}$ gas phase transition[1] of atomic Mn at 543.3 nm.

VIII.6.II Mn(z^8P)/RG Emission spectroscopy

The emission spectroscopy presented in the previous sections with excitation of the $z^8P_{5/2} \leftarrow a^6S_{5/2}$ transition is summarised in Figure VIII.41. The transitions assigned and photophysical properties of the observed emission features are collected in Table VIII.18, Table VIII.14 and Table VIII.11 for Mn/Ar, Mn/Kr and Mn/Xe respectively. The Mn/Kr system provided an additional emission feature (shown centre, Figure VIII.41) at 565.2 nm (17693 cm^{-1}) with blue (1°) site excitation at 513.8 nm. This band represents the only emission feature observed which has been definitively assigned to the phosphorescence of the $z^8P_{5/2}$ excited state. This assignment was made on the basis of the excitation spectra recorded, the excited state lifetime measured and the spectral location of the emission. This band was observed earlier in Moskovits' work[11] on Mn/Kr in which a fixed frequency Ar ion laser at 514.8 nm

was used as the excitation source. Based on the presence of dimer bands at 667 and 690 nm in the absorption spectra it was assumed in this earlier work that the 565 nm band was also related to Mn_2. The data recorded for this band in the present study clearly indicates the atomic origin of the 565 nm emission in Mn/Kr.

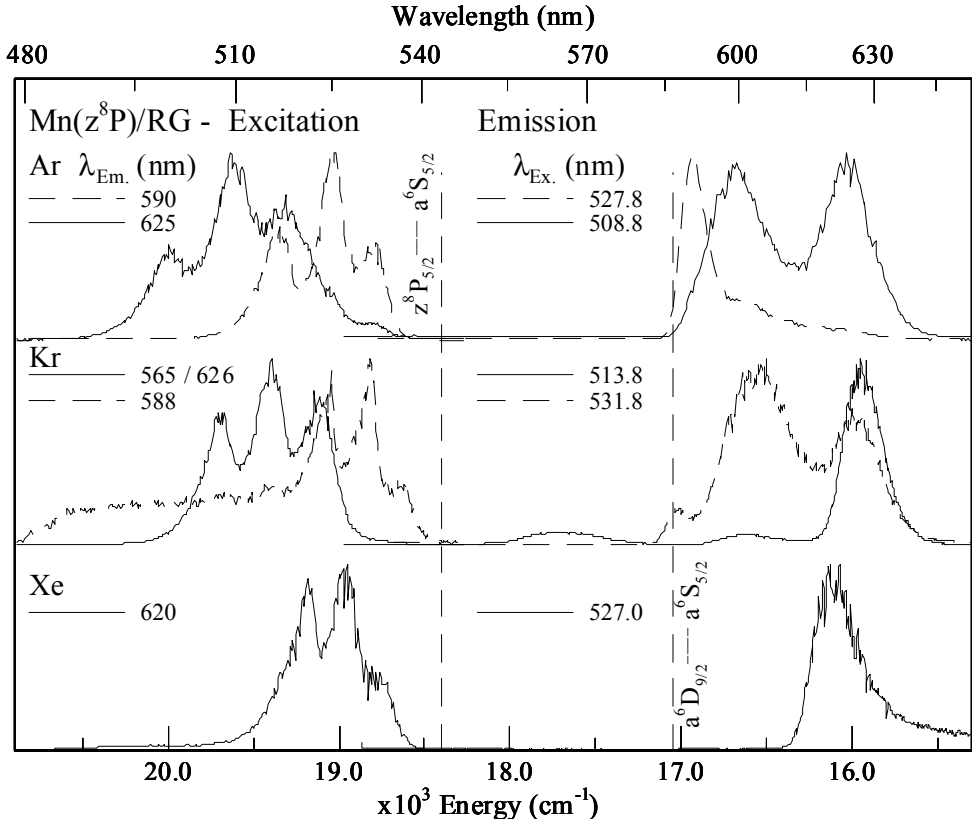

Figure VIII.41 Mn/RG site-specific emission spectra (shown right) recorded at 12 K for all the Mn/RG systems investigated produced with laser excitation corresponding to the $z^8P_{5/2} \leftarrow a^6S_{5/2}$ transition. The excitation wavelengths used are shown (centre) as $\lambda_{Ex.}$ (nm). The excitation spectra shown (left), were recorded by monitoring emission bands as indicated (left) by $\lambda_{Em.}$ in wavelength units. All spectra were recorded following Mn/RG sample deposition at 12 K and matrix annealing. The dashed vertical lines show the spectral positions of the gas phase transitions[1] of atomic Mn.

Excited state lifetime measurements and the temperature dependence observed in the emission spectra recorded, have not allowed a definitive assignment of the 627 nm or the 625 nm emissions in Kr and Ar respectively. The possible state assignments of these emission features are discussed at the end of this Chapter.

The spectroscopy recorded with specific 1° site excitation in Ar and Xe and 2° site excitation in solid Kr revealed the emission features at 590, 620 and 585.8 nm respectively, shown in Figure VIII.41. These features were assigned to the $a^6D_{9/2} \rightarrow a^6S_{5/2}$ transition of atomic Mn earlier in this chapter. These assignments are

suggested by excited state lifetime measurements made following $z^8P_{5/2}$ excitation, as the emission lifetimes extracted were longer than those recorded with direct a^6D excitation. Therefore, a $z^8P \Rightarrow a^6D$ ISC process can efficiently produce the emission features assigned to the $a^6D_{9/2} \rightarrow a^6S_{5/2}$ transition.

VIII.7 Conclusion Mn(z^8P)/RG luminescence

The excitation spectroscopy reported and assigned in the previous sections to the $z^8P_{5/2} \leftarrow a^6S_{5/2}$ transition of Mn atoms isolated in solid Ar, Kr and Xe showed threefold split bands. The multiple sites of isolation identified in Chapter VII from an analysis of the Mn(z^6P)/RG luminescence were also identified here for the $z^8P \leftarrow a^6S$ transition. The emission spectroscopy revealed the presence of an additional atomic feature at 565.2 nm in solid Kr, which was assigned to emission of the $z^8P_{5/2}$ state following direct dye laser excitation. Moskovits and co-workers[11] previously observed this emission feature in Mn/Kr samples but assumed it was manganese dimer. Excitation spectroscopy and lifetime measurements reported here indicate conclusively this band is emission of the z^8P excited state of atomic manganese. Moreover, the Mn/RG samples prepared in this work with electron bombardment contain little manganese dimer.

VIII.8 Mn/RG Discussion – Blue site-specific luminescence

The following section reviews the emission spectroscopy reported for the unassigned features resulting from blue site excitation of the $a^6D \leftarrow a^6S$, $z^8P \leftarrow a^6S$ and $z^6P \leftarrow a^6S$ transitions of atomic Mn isolated in solid Ar and Kr. These unassigned bands occur at 438 and 626.7 nm in solid Kr and 438 and 625 nm in Ar. Earlier in this Chapter, blue (1°) site excitation of the $z^8P \leftarrow a^6S$ matrix transition in Kr produced two emission features located at 565.2 and 627.4 nm exhibiting linewidths of 519 and 260 cm^{-1} and matrix shifts of 709 and 2464 cm^{-1} respectively as shown in Figure VIII.41, middle panel. In solid Ar, blue site excitation produced the 625 nm feature with a linewidth of 260 cm^{-1} located 2402 cm^{-1} lower in energy than the gas phase $z^8P_{5/2} \leftarrow a^6S_{5/2}$ transition, (Figure VIII.41, top panel). The Mn/Kr 565.2 nm emission feature was confidently assigned to the phosphorescence of the $z^8P_{5/2}$ excited state

based on its spectral location and the observed excited state lifetime. Decay profiles recorded for the 626.7 nm emission (Figure VIII.33) with z^8P state excitation showed a rise time component (108 μsec) indicative of direct feeding of the emitting level from the z^8P state accessed in excitation. The observed decay time extracted at 12 K was 1.61 msec, (Table VIII.14). Such a long decay time suggests the assignment of the 626.7 nm feature to the forbidden $a^6D_{9/2} \rightarrow a^6S_{5/2}$ transition of atomic Mn whose gas phase lifetime is calculated to be 3.4 sec[4]. However, the broad (Gaussian) lineshape and substantial matrix shift of 1114 cm^{-1} from the gas phase position of the D ↔ S transition are at variance with this assignment. In addition, the emission spectroscopy recorded with red (2°) site $a^6D_J \leftarrow a^6S_{5/2}$ excitation in Kr (Figure VIII.24) allowed definitive assignment of the 586.75 nm (587 nm) asymmetric emission band to the $a^6D_{9/2} \rightarrow a^6S_{5/2}$ transition.

Dye laser excitation spectra recorded in the vicinity of the $a^6D_{5/2} \leftrightarrow a^6S_{5/2}$ transition monitoring both the 587 and 626.7 nm bands showed resolved features in the same spectral region but with very different linewidths, (Figure VIII.8). This observation indicated that the two emission features were specific to the site of isolation in agreement with the results achieved for the $z^8P_{5/2} \leftarrow a^6S_{5/2}$ and $z^6P_{5/2} \leftarrow a^6S_{5/2}$ transitions. The site specificity is shown in Figure VII.62 (z^6P) and Figure VIII.30 (z^6P) where the 587 and 626.7 nm features are produced only with selective excitation of the red (2°) and blue (1°) sites identified. Emission decay times recorded with a^6D excitation revealed the same decay characteristics, as shown by the comparison made in Figure VIII.33. The observed 1.61 msec decay time allows the tentative assignment of the 626.7 nm feature to the $a^6D_{9/2} \rightarrow a^6S_{5/2}$ transition. Therefore, the rise time observed with z^8P excitation may reflect an interaction of the excited state with the site of isolation, such as a structural rearrangement of the site of isolation by the $a^6D_{9/2}$ excited state Mn atom, prior to emission.

Further evidence for this is provided by the comparison of the photophysical characteristics (*fwhm* and Stokes' shifts) exhibited by the 626.7 nm and the unassigned 440 nm emission in Mn/Kr produced with $z^8P \leftarrow a^6S$ and $z^6P \leftarrow a^6S$ excitation respectively. Inspection of these bands in Figure VIII.42 reveals that the linewidths of both of the unassigned features are approximately half of those assigned to the direct z^6P fluorescence (416 nm) and z^8P phosphorescence (565.2 nm) transitions.

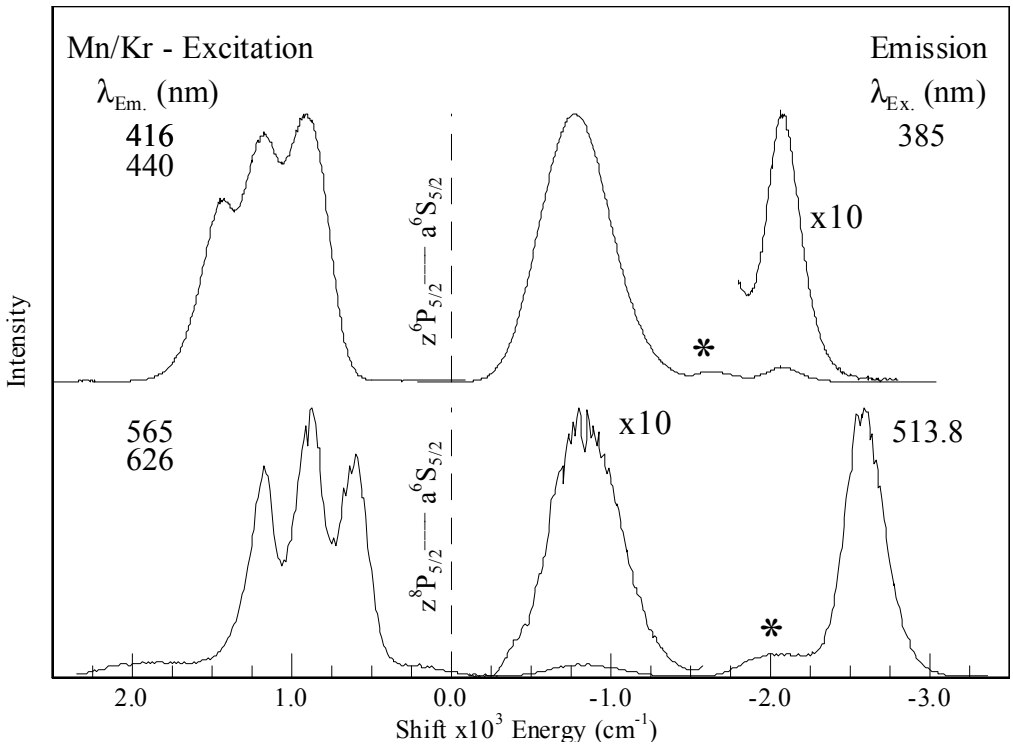

Figure VIII.42 A comparison of the emission spectra produced with blue site selective z^6P ← a^6S and z^8P ← a^6S excitation in solid Kr, shown top and bottom respectively. Note the thermally unstable emission is indicated using an asterix.

In addition the Stokes' shifts observed on the $a^6D_{9/2} \rightarrow a^6S_{5/2}$ transition are 1029, 1110 and 1043 cm^{-1} for 625, 626.7 and 620 nm bands using the matrix-shifts observed in excitation for the $a^6D_{5/2} \leftarrow a^6S_{5/2}$ transition in Ar, Kr and Xe solids respectively. Figure VIII.41 presents the emission features produced with z^8P excitation for Mn/Ar, Mn/Kr and Mn/Xe allowing a direct assessment of the photophysical properties of the emission bands. Inspection of the gas phase energy level diagram for atomic Mn in Figure VIII.43 reveals that the splitting between the $z^8P_{5/2}$ and the $a^6D_{9/2}$ levels is 1350 cm^{-1}. This value is greater than the observed Stokes' shifts of the tentatively assigned $a^6D_{9/2} \rightarrow a^6S_{5/2}$ transitions in all matrices and suggests that the large shift observed results from an increased interaction between the $a^6D_{9/2}$ and the site of isolation due to the size and symmetry of the blue matrix sites.

Extension of these arguments to the 438 and 440 nm features reported following z^6P ← a^6S excitation in Ar and Kr suggests an assignment of these bands to the $a^4D_{7/2} \rightarrow a^6S_{5/2}$ transitions, given the linewidths are 230 and 280 cm^{-1}

respectively. These features exhibit matrix shifts of 466 and 570 cm^{-1} from the $a^4D_{7/2}$ $\leftrightarrow$ $a^6S_{5/2}$ gas phase transition[1] in Ar and Kr. The energy separation between the

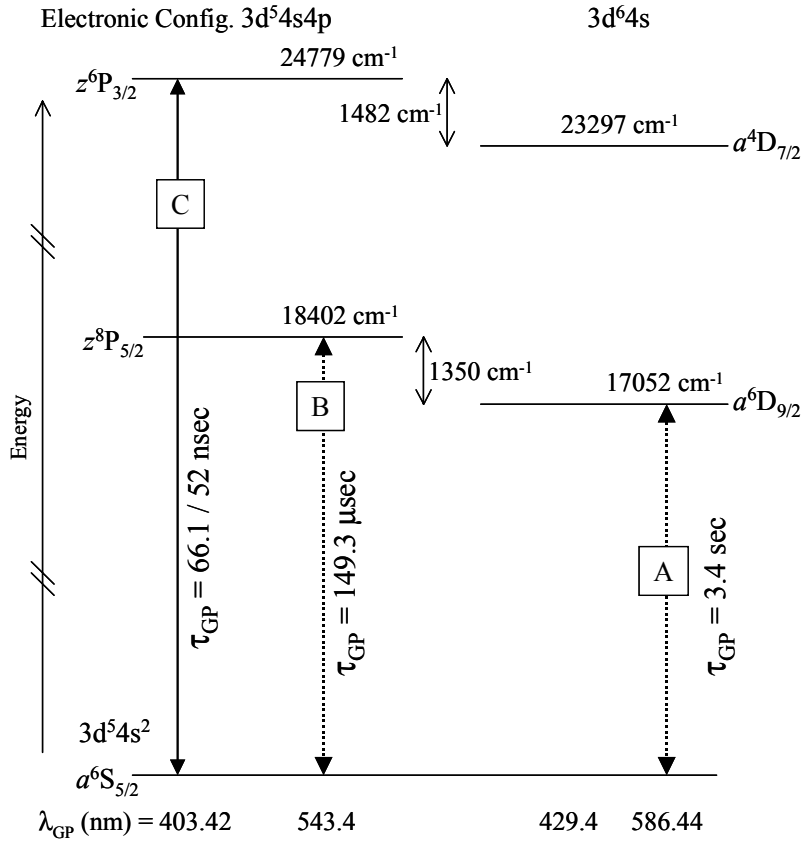

Figure VIII.43 Summary of the three transitions of atomic manganese used for excitation of the Mn/RG thin films. The solid line represents the fully allowed $z^6P \leftrightarrow a^6S$ transition, whereas the dotted lines show the spin forbidden $z^8P \leftrightarrow a^6S$ and the parity forbidden $a^6D \leftrightarrow a^6S$ transitions. The latter transition is electric quadrupole allowed. Particularly noteworthy is the roughly similar gaps between the z^6P/a^4D levels and the z^8P/a^6D levels of 1428 and 1350 cm-1 respectively.

assigned matrix $z^6P_{3/2} \rightarrow a^6S_{5/2}$ fluorescence at 413 nm and the 438 nm bands is 1382 cm^{-1} in Ar. A corresponding splitting of 1310 cm^{-1} exists between the 416 nm z^6P fluorescence and the 440 nm band in Kr. As shown in Figure VIII.43, the gas phase splitting between the $z^6P_{3/2}$ and the $a^4D_{7/2}$ levels is 1482 cm^{-1}. Thus, the qualitative agreement with the gas phase splitting and the matrix emission features suggest the 438 and 440 nm features in Ar and Kr are a^4D state emission. Therefore, the broad emission bands in Ar at 438 and 625 nm are tentatively assigned to emission from the a^4D and a^6D states respectively. Accordingly the bands at 440 and 626.7 nm in Kr have the same spectral assignments. These emission are blue site specific and are

produced by $z^6P \Rightarrow a^4D$ and $z^8P \Rightarrow a^6D$ ISC processes. In the Chapter, which follows, the blue and red sites of isolation are identified as matrix substitutional and tetravacancy sites respectively; therefore stronger interactions for Mn D-state atoms within cramped Ar and Kr substitutional sites is the likely cause of the broadened and shifted D → S emissions.

Assuming the assignment of the red emission features at 625, 626.7 and 620 nm in Ar, Kr and Xe to the $a^6D_{9/2} \rightarrow a^6S_{5/2}$ transition of atomic Mn, the asymmetric lineshape in Xe represents a decrease in the electron-phonon coupling. The site of isolation is again considered the origin of the observed Gaussian lineshapes in Ar and Kr where the substitutional site of isolation maintains the same symmetry but decreases in size. Overall the linewidths may result from an increased electron-phonon coupling strength in the cramped sites of isolation. In addition, inspection of Figure VIII.41 reveals the matrix shifts of the red emission bands do not exhibit a specific trend. This may also owe its origin to Mn atom occupancy in cramped sites of isolation where the minimum on the excited state potential energy surface does not coincide with that of the ground state for the blue site. Mn atoms isolated in the larger red sites can access a region where there is a concurrence of the ground and excited state minima, producing more asymmetric emission lineshapes. This is discernable for the larger red sites by comparison of the 590 and 587 nm bands in Ar and Kr, assigned to the $a^6D_{9/2} \rightarrow a^6S_{5/2}$ transition. A broad (*fwhm* = 100 cm^{-1}) matrix shifted (103 cm^{-1}) feature was observed in Ar but the ZPL was assigned in solid Kr.

VIII.9 Conclusion Mn(a^6D and $z^8P \leftrightarrow a^6S$)/RG

Laser excitation scans of Mn/RG emission features in the red spectral region reveals their atomic origin as they can be produced with excitation of the forbidden $a^6D \leftarrow a^6S$ and $z^8P \leftarrow a^6S$ transitions. These emission bands were recorded in an earlier study of matrix-isolated manganese but assigned to dimer emission bands. The reason for this mis-assignment is not clear from the published data[11] but appears to be due to the presence of dimer absorption bands in their Kr samples, and the assumed negligible oscillator strength of the electric-dipole forbidden $z^8P \leftarrow a^6S$ and the electric-quadrupole allowed $a^6D \leftarrow a^6S$ transition. The excitation spectra recorded in

the present work proves conclusively the atomic origin of these features. This is confirmed by lifetime measurements.

The laser excitation scans reveal very different spectral behaviour for the z^8P and a^6D excited states. Thus, the former is typical of P ← S transitions with broad, threefold split profiles shifted considerably from the gas phase positions while the latter reveal narrow lines with spin-orbit splittings almost identical to the gas phase values. Assignments of the red spectral features to emission of the metastable a^6D state has been made. The quality of these assignments ranges from confident for the narrow 586 and 590 nm features in Kr and Ar respectively to only tentative for the broad 625/627 nm bands. A plausible explanation for the broad 625/627 nm linewidths is presented on the basis of the cramped substitutional sites occupied by the 'blue-site' atoms producing this emission. In contrast the 'red-site' atoms, thought to originate from tetravacancy site occupancy, produce very narrow, unshifted D-state emission. The case of Mn/Xe is intermediate between these two extremes where the observed band is asymmetric but shifted because its occupied substitutional site is considerably larger than those in Ar and Kr.

References

1 N.I.S.T. Atomic Spectra Database, Website: http://physics.nist.gov/cgi-bin/AtData/display.ksh?/XXE0qMnqIXXP-15XXT2XXS, (Last accessed 4th February 2004).

2 R. Schnabel, A. Bard and M. Kock, *Zeitschrift für Physik D*, **34**, 223, 1995.

3 G. A. Martin, J. R. Fuhr and W. L. Wiese, Atomic Transition Probabilities Scandium through Manganese, *J. Phys. Chem. Ref. Data,* Vol. 17, No. 3, 1, 1988.

4 A. A. Radzig and B. M. Smirnov, *Reference Data on Atoms, Molecules and Ions*, Springer-Verlag, Berlin, 1985.

5 A. Corney, *Atomic and Laser Spectroscopy*, Clarendon Press and Oxford University Press, 1977.

6 W. C. Martin and W. L. Wiese, *Atomic Spectroscopy, A Compendium of Basic Ideas, Notation and Formulas* in *Atomic, Molecular, and Optical Physics Handbook*, National Institute of Standards and Technology, Gaithersburg, MD, Website: http://physics.nist.gov/Pubs/AtSpec/ (Last accessed 12th July 2004).

7 The narrow emission features centered at 600 and 700 nm (shown in Figure VIII.6) were produced with fixed wavelength ($\lambda_{Ex.}$ = 576.45 nm) pulsed dye laser excitation. These bands are assigned to sample contaminants (non atomic species) as they are not present in the emission spectra recorded using CCD detection following excitation at various wavelengths in the vicinity of the a^6D $\leftrightarrow$ a^6S gas phase transition as shown in Figure VIII.3.

8 The excitation band-profile is due to the weak emission intensity of $\lambda_{Em.}$ 589.4 nm, confirmed by the marked baseline to higher energy, due to the Coumarin 500 dye response.

9 The index of refractive used for solid Kr at 241 nm is 1.428 at 12 K, (P. Gürtler, *unpublished results*, 1996).

10 The excitation spectrum recorded by monitoring the 587 nm emission band and the emission spectra presented have been normalised. The additional emission bands evident in Figure VIII.34 at 603 and 626 nm are due to spectral overlap of the 1° and 3° sites with the 2° site, which produces the 587 nm emission.

11 A. D. Kirkwood, K. D. Bier, J. K. Thompson, T. L. Haslett, A. S. Huber and M. Moskovits, *J. Phys. Chem.*, **95**, 2644 (1991).

Chapter IX

Sites of manganese atom isolation in RG solids, RG = Ar, Kr and Xe

IX.1 Introduction

The absorption and luminescence spectroscopy of atomic Mn isolated in solid Ar, Kr and Xe, reported in Chapters VI to VIII, identified multiple trapping sites and highlighted the importance of metal atom site occupancy in determining the excited state luminescence. In addition emission bands recorded for the resonance $z^6P_{5/2} \leftrightarrow a^6S_{5/2}$, the 'forbidden' $z^8P_{5/2} \leftrightarrow a^6S_{5/2}$ and the quadrupole $a^6D \leftrightarrow a^6S_{5/2}$ transitions for the Mn/Ar, Mn/Kr and Mn/Xe systems yielded high-resolution excitation spectra that permitted the extraction of the photophysical properties of the trapping sites present but not resolved in absorption. Although, the spectral and temporal characteristics observed allowed the assignment of many of the features to the emission from specific atomic levels, a complete analysis has not been possible due to the presence of multiple intersystem crossing (ISC) and intermultiplet relaxation pathways (IMR) in each Mn/RG system. Therefore, knowledge of the site of isolation occupied would provide great insight into the interactions occurring between the matrix cage and the excited state Mn atom that allow the radiative and non-radiative processes identified.

This Chapter collects the information extracted from the observed absorption and luminescence excitation spectroscopy and presents an analysis of these results to assign the sites occupied by Mn atoms in the RG solids. Overall, the two thermally stable blue and red sites of isolation of atomic Mn in solid Ar and Kr are assigned to substitutional site and multi-vacancy (tetra-vacancy) sites respectively. The single thermally stable site identified for Mn isolated in Xe is assigned to a substitutional site. The assignments completed are based on the application of the polarizability model of Laursen and Cartland[1] (L&C) to the $z^6P_{5/2} \leftarrow a^6S_{5/2}$; $z^8P_{5/2} \leftarrow a^6S_{5/2}$ and $y^6P_{5/2} \leftarrow a^6S_{5/2}$ electronic transitions of atomic Mn. This model allows the association of certain site types occupied by metal atoms in the rare gas solids from an analysis of the gas phase to RG matrix frequency shifts observed for P ← S type electronic transitions. The required condition being a linear correlation of the matrix shifts with rare gas polarizability for those metal atoms 'trapped' in a particular site type. As discussed in Chapter I, (Introduction), atomic Mn has a spherically

symmetric a^6S ground state and therefore will favour isolation in spherical sites of the lattice. Trends, such as the preference for Mn occupancy in certain sites of isolation in the rare gases (Ar, Kr and Xe), as evident from the absorption spectroscopy, are used to assess the trapping environment. These trends, coupled with polarizability arguments form a major part of the sections which follow, as currently no information is available on the simpler Mn·RG 1:1 complexes from gas phase or *ab initio* studies. Instead, the similarities between atomic manganese, which exhibits an ns^2 ground state electronic configuration and the M/RG systems (M = Zn[2], Cd[3], Hg[4,5] and Mg[6]) where the solid-state and gas phase[7] spectroscopy has been studied in detail are exploited. The spectroscopic parameters such as the ground state bond lengths for these known systems are used to tentatively assess the sites occupied by atomic Mn. The comparison between these M(P ← S)/RG (M = Zn, Cd and Hg) and the Mn/RG systems allows the extraction of finer details regarding the ground and excited state interactions of Mn with the host matrix.

To achieve these goals this Chapter has the following structure. Firstly, the absorption results and luminescence excitation results obtained for the P ← S transitions presented in the previous Chapters are reviewed and details specific to site occupancy are highlighted. Secondly, the L&C polarizability model is applied to the excitation spectra recorded in the vicinity of the $z^6P_{5/2} \leftrightarrow a^6S_{5/2}$ gas phase transition. Thirdly, as UV absorption spectra recorded for Mn/RG samples provided information on the multiple sites of isolation on the $y^6P_{5/2} \leftrightarrow a^6S_{5/2}$ transition, excitation spectra recorded by monitoring the atomic emission features assigned in Chapter VII are presented for the first time. This therefore allows a comparison of the matrix shifts observed for the 'singlet – like' $y^6P_{5/2} \leftrightarrow a^6S_{5/2}$ and 'triplet – like' $z^6P_{5/2} \leftrightarrow a^6S_{5/2}$ transitions and an assessment of the extent of the Mn atom matrix interaction for these different excited states. The results of this comparison are directly comparable to the ns^2 metal atom $^1P_1$ and $^3P_1 \leftarrow {}^1S_0$ transitions discussed by L&C[1]. The analysis is extended by showing the relationship of the different 'triplet – like' excited state interactions that are manifest in the different matrix shifts observed for the $z^6P_{5/2} \leftarrow a^6S_{5/2}$ and $z^8P_{5/2} \leftarrow a^6S_{5/2}$ transitions.

Overall the application of the polarizability model to the P ← S type transitions of atomic Mn in RG solids allowed the correlation of the high-energy blue sites in Ar and Kr with the single site in solid Xe and the subsequent assignment of this site to

Mn atoms in single substitutional sites. The analysis also allowed the grouping of the low energy red sites in Ar and Kr and their assignment to Mn atoms isolated in matrix tetra-vacancies. This was achieved numerically using a comparison of the Mg·RG ground state bond lengths assuming the transference of the known Mg·RG parameters to the Mn·RG systems. The site dominance showed that Mn atoms in solid Ar exhibit a preference for trapping in tetra-vacancy sites whereas single substitutional site occupancy is preferred in Kr, while this site is the single thermally stable site in solid Xe.

IX.2 Site Analysis Mn(z^6P ← a^6S)/RG

The UV/Vis absorption spectroscopy recorded near the gas phase $z^6P_{5/2} \leftrightarrow a^6S_{5/2}$ transition[8] of atomic Mn isolated in Ar, Kr and Xe (see Chapter VI, Figure VI.8) allowed the identification of multiple thermally stable features to the $z^6P_{5/2}$ transition in solid Kr only. Table VI.2 presented the spectral positions of the sites assigned as the blue (1°) and red (2°) sites. In solid Ar the occurrence of multiple site occupancy was indicated by the apparent loss of the linear correlation between the observed matrix shifts in absorption. Consideration of this effect predicted the existence of a secondary site of atomic isolation in solid Ar. The results of the Mn(z^6P)/Ar excitation spectroscopy reported in Chapter VII, revealed the presence of the weak blue (2°) site. Therefore two thermally stable sites of isolation were identified in solid Ar and Kr but with intensity reversals. In solid Xe absorption spectra recorded following sample deposition at various temperatures and/or matrix annealing following deposition at 12 K allowed the identification of only a single thermally stable trapping site.

The high resolution excitation spectra recorded by monitoring the atomic emission features produced with steady-state excitation of the $z^6P_{5/2} \leftarrow a^6S_{5/2}$ transition for all Mn/RG systems investigated are presented in Figure IX.1. The excitation spectra shown, reveal the presence of threefold split excitation patterns for each of the sites identified in all the RG gas solids. The splitting observed is attributed to the Jahn Teller effect indicative of Mn atom occupancy in highly symmetric matrix environments.

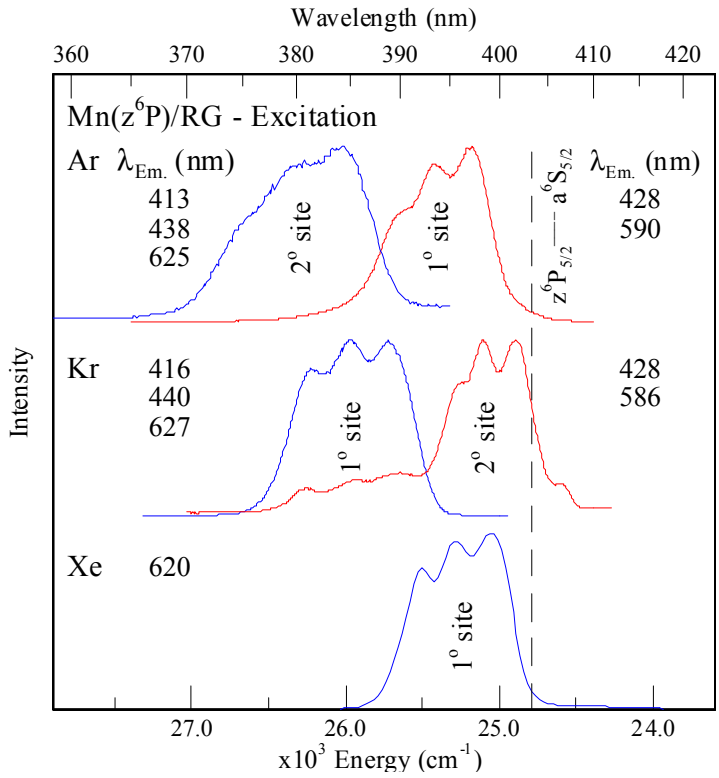

Figure IX.1 **Excitation spectra recorded by monitoring the emission features as indicated reported in Chapter VII (at 12 K) resulting from $z^6P_{5/2} \leftarrow a^6S_{5/2}$ excitation for the atomic Mn/Ar, Mn/Kr and Mn/Xe systems. The excitation spectra shown were recorded following Mn/RG sample deposition at T_d= 12 K and matrix annealing. The dashed vertical line shows the spectral location of the gas phase transition.**

Because of its spatial symmetry, the a^6S ground state of atomic manganese will favour isolation in spherical sites of isolation. Therefore, as discussed in the Chapter I, (Introduction) only spherically symmetric trapping sites within the RG *fcc* lattice are considered for atomic Mn isolation. The simplest matrix system, with respect to site occupancy, is Mn/Xe as only a single thermally stable site was identified in absorption and excitation spectra of annealed samples. This provides the starting point for this site analysis as Xe represents the ideal matrix host for atomic isolation due to the increased site sizes available as shown by the numerical analysis presented in Table I.1, Chapter I. The similarity between the energetics of the ^{1}P and ^{3}P $\leftrightarrow$ ^{1}S gas phase transitions of atomic Mg and those of the y^6P and z^6P $\leftrightarrow$ a^6S transitions of Mn is clearly evident from the diagram presented in Figure I.5. The Mg·RG (RG = Ar and Xe) diatomic ground state bond lengths, known from 1:1 complexes prepared in supersonic expansions[7], are believed to be a good approximation to those of the Mn·RG systems. The Mg atom exhibits a $3s^2$ ground state electronic configuration

while that of Mn is $3d^5 4s^2$. The presence of the half filled $3d^5$ shell and the small difference in energy to the 4s orbital makes the correlation with the $3s^2$ Mg ground state feasible. The known Mg·RG (RG = Ar and Xe) ground state bond lengths (r_e) are presented in Table IX.1. Comparison of the ground state bond lengths with the available site sizes reveals either isolation of Mg (and therefore Mn) in deformed substitutional sites or tetra-vacancy sites in solid Xe. The presence of a single thermally stable site of isolation in solid Xe shows the preference for the Mn atoms for a particular site type. However, an assignment is not possible based solely on application of the Mg·Xe ground state bond length to the Mn system, as the comparison reveals the possibility of multiple site occupancy.

Table IX.1 **Site sizes[9] in angstrom units (Å) for specific spherically symmetric site types in the solid rare gases. The details of these sites was presented in Chapter I, Introduction. In addition, the polarizability of the solid rare gases and the known Mg($^1S_0$)·RG diatomic ground state bond lengths are also presented.**

RG Solid	*ss* (Å)	T_{Vac} (Å)	RG Polarization (Å^3)[10]	Mg·RG, r_e (Å)[7]
Ar	3.756	4.404	1.640	4.49
Kr	3.991	4.679	2.485	
Xe	4.335	5.083	4.050	4.56

Therefore, trends shown by Mn atoms isolated in solid Ar and Kr are used to strengthen any assignment of site occupancy. In solid Ar, the red site dominates the z^6P state excitation spectra. However, the dominant site of isolation in solid Kr is as shown in Figure IX.1 the blue site. This difference represents a reversal of the dominance of a particular site type from Mn/Ar to Mn/Kr. To identify the trends in the site occupancy and the relationship of thermally stable sites of isolation in each RG solid, the polarizability model[1] is employed. This is achieved by plotting the gas phase to matrix frequency shifts for the $z^6P_{5/2} \leftarrow a^6S_{5/2}$ transition, calculated from the central threefold split component for each of the thermally stable sites in the solid RG's (observed in the excitation spectroscopy and shown in Figure IX.1), against host RG polarizability data given in Table IX.1. The polarizability analysis is presented in Figure IX.2 and it is evident that a linear correlation exists between RG polarizability and the matrix shifts (δ, cm^{-1}) observed for the high-energy sites identified in Ar and Kr and the single site Xe. An extrapolation of the red site Ar and

Kr data (triangles) in Figure IX.2 clearly does not include the single site present in the Xe system.

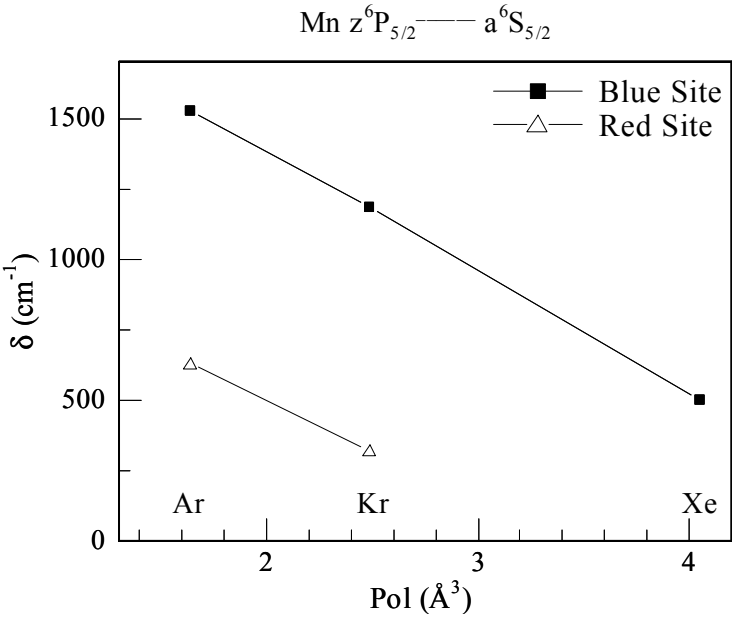

Figure IX.2 **A plot of the gas phase to Mn/RG matrix frequency shifts (δ cm^{-1}) observed for the blue and red sites identified for the $z^6P_{5/2} \leftarrow a^6S_{5/2}$ transition of atomic manganese versus the RG host polarizabilities. The squares (connected by the solid line) highlights the linear correlation between the frequency shifts and rare gas polarizability observed for the Mn $z^6P_{5/2} \leftarrow a^6S_{5/2}$ transition occurring within the blue sites of isolation.**

The red site, which dominates the Mn/Ar solid-state spectroscopy, is correlated with the red but minor site identified in Kr. The site dominance is reversed from red to blue from Mn/Ar to Mn/Kr and there is a correlation between the blue sites identified in all three rare gas hosts. The red/blue site dominance is attributed to the preference for a different site type in the heavier RG solids. A comparison of the Mg·Ar ground state bond length (4.49 Å) with the site size available for the tetra-vacancy in solid Ar (4.404 Å) and the substitutional site (3.756 Å) reveals a favourable match with the former site. Therefore the red sites of atomic Mn isolation identified in solid Ar and Kr are assigned Mn atom trapping in tetra-vacancy sites. The preference for a single site in solid Xe, and the correlation of the matrix-shifts observed for the blue sites, allows the assignment of the blue sites to the trapping of Mn atoms in single substitutional sites of these matrices.

In the following section the results of excitation spectroscopy recorded in the vicinity of the $y^6P_{5/2} \leftarrow a^6S_{5/2}$ transition are presented for the first time and the

polarizability model is applied to these results and those achieved in Chapter VIII for the $z^8P_{5/2} \leftarrow a^6S_{5/2}$ transition, to check the trends with respect to site occupancy evident for the $z^6P_{5/2} \leftarrow a^6S_{5/2}$ transition. In addition some trends in the photophysical characteristics of the excitation bands observed for the P ← S type transitions related to the site occupancy are discussed. The 'singlet' vs. 'triplet' nature of the excited state transitions are discussed with respect to the excited state matrix interactions leading to the observed matrix shifts.

IX.3 Site Analysis Mn(y^6P and z^8P ← a^6S)/RG

IX.3.I Mn $y^6P \leftarrow a^6S$ Excitation spectroscopy

The UV absorption features recorded for Mn/RG solids in the vicinity of the $y^6P_{5/2} \leftrightarrow a^6S_{5/2}$ gas phase transition[8] and presented in Chapter VI provided more direct information on the atomic trapping sites than the corresponding $z^6P_{5/2} \leftrightarrow a^6S_{5/2}$ transition. This is in part due to the increased oscillator strength of the 'singlet' like $y^6P_{5/2} \leftarrow a^6S_{5/2}$ over the 'triplet' like $z^6P_{5/2}$ transition but also the better separation on the former transition. This is clear upon inspection of the Mn/RG absorption spectra shown in Figure VI.7 where the $y^6P_{5/2}$ absorption bands dominate the spectra. In solid Xe, the ratio of the absorption intensity for the $y^6P_{5/2}$ and $z^6P_{5/2} \leftarrow a^6S_{5/2}$ $I_{Abs}(y^6P) : I_{Abs}(z^6P)$ was found to be 14:1 providing a measure of the relative oscillator strengths. The absorption bands assigned to the $y^6P_{5/2}$ state exhibited a red-shift of the band maximum from Ar to Kr to Xe which deviate from linearity, consistent with the reversal of red dominant / blue minor sites of isolation from Ar to Xe observed on the $z^6P_{5/2} \leftarrow a^6S_{5/2}$ transition. In solid Ar, the two thermally stable $y^6P_{5/2} \leftarrow a^6S_{5/2}$ absorption features were identified occurring to higher energy than the gas phase transition at 273 and 278.1 nm. These bands were assigned to the blue (2°) and red (1°) sites of isolation respectively. In Kr the 1° Mn/Kr absorption feature at 279.9 nm overlaps the gas phase transition and the 2° site occurred to lower energy. In solid Xe high temperature deposition and matrix annealing experiments allowed the definitive identification of the band located at 288.2 nm to a single site. Tables VI.I to VI.III present the details of the transition energies for the sites of isolation identified on the $y^6P_{5/2} \leftarrow a^6S_{5/2}$ transition of atomic Mn occurring in solid Ar, Kr and Xe respectively.

High-resolution excitation spectra recorded in the vicinity of the $y^6P_{5/2} \leftarrow a^6S_{5/2}$ transition monitoring the site-specific atomic emission features produced with $z^6P_{5/2}$ excitation in the Chapter VII allowed the identification of the sites of isolation. Figure IX.3 presents the UV excitation spectra recorded. These all show resolved threefold split patterns indicative of Mn occupancy in high symmetry matrix sites for all the Mn/RG systems. The photophysical characteristics of the 1° and 2° sites extracted from the excitation spectra shown in Figure IX.3 are presented in Table IX.2.

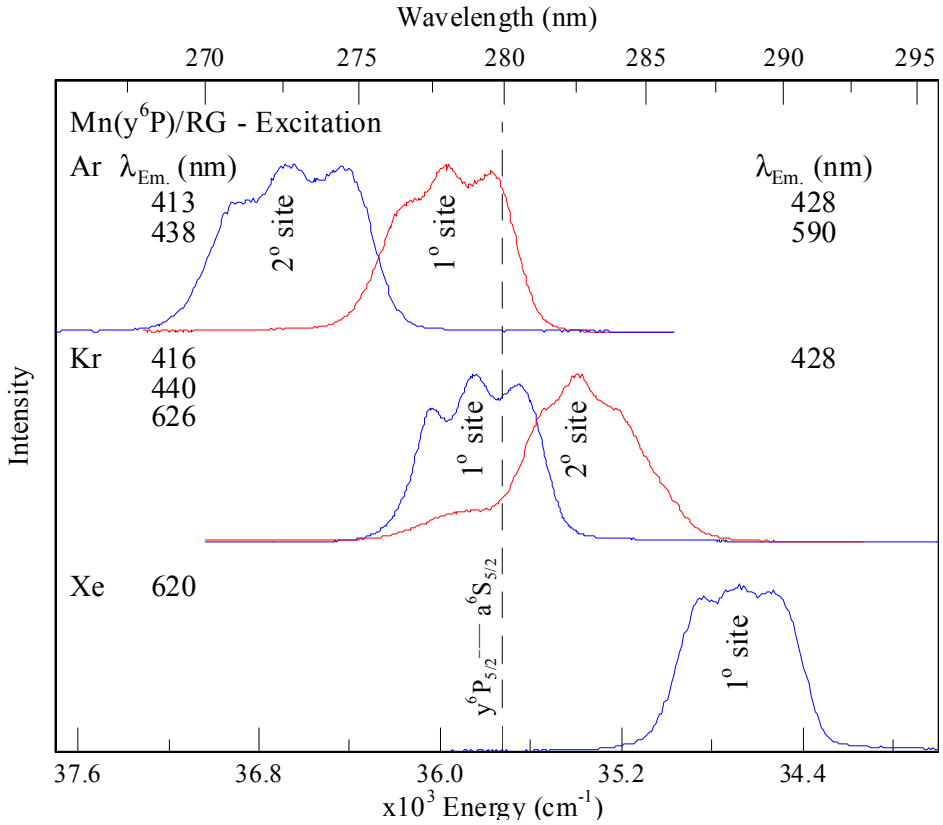

Figure IX.3 **Excitation spectra recorded in the vicinity of the $y^6P_{5/2} \leftrightarrow a^6S_{5/2}$ gas phase transition by monitoring the emission bands reported in Chapter's VII and VIII (at 12 K) to result from z^6P; z^8P and a^6D excitation for each of the Mn/RG systems investigated. Mn/RG sample deposition was completed at 12 K and matrix annealing. The dashed vertical lines show the spectral position of the gas phase transition. The photophysical properties of the sites of isolation identified are presented in Table IX.2.**

As observed in the absorption spectroscopy, the $y^6P_{5/2} \leftarrow a^6S_{5/2}$ transition occurring for Mn atoms isolated in the 1° site of solid Kr overlaps the gas phase transition (indicated by the vertical line in Figure IX.3), while the Mn/Ar and Mn/Xe the bands occur at higher and lower energies respectively. It is noteworthy that the matrix

excitation spectra of the $z^6P_{5/2}$ state are blue of the gas phase transition for all three hosts. This observation is attributed to the spin 'singlet' characteristic of the $y^6P_{5/2}$ state and 'triplet' nature of the $z^6P_{5/2}$ state. Comparison of the $y^6P_{5/2}$ state excitation spectra presented in Figure IX.3 reveals the same site specificity as observed with excitation of the $z^6P_{5/2}$ state shown in Figure IX.2.

Table IX.2 **Photophysical characteristics of the sites of isolation (1° and 2°) revealed in the excitation spectra of the $3d^54s4p$ $y^6P_{5/2} \leftrightarrow 3d^54s^2$ $a^6S_{5/2}$ transition of atomic manganese. Where possible the spectral position and average linewidth (full width at half maximum, *fwhm*) is denoted as Δ_{AV} of the three components identified in Gaussian lineshape analyses for the threefold split excitation spectra are presented in wavenumber units. Gas phase to matrix frequency shifts are presented for the atomic Mn $y^6P_{5/2} \leftarrow a^6S_{5/2}$ transition[8] (G.P.: 35726 cm^{-1}), δ in wavenumber units. Note the frequency shifts are calculated with respect to the central feature of the observed threefold pattern.**

Mn/RG Site	Component	E (cm^{-1})	Δ_{AV} (cm^{-1})	δ (cm^{-1})
Argon	1	36138		
Red (1°)	2	35978	≈ 215	+252
	3	35778		
Blue (2°)	1	36879		
	2	36676	≈ 265	+950
	3	36438		
Krypton	1	36030		
Blue (1°)	2	35851	≈ 200	+125
	3	35656		
Red (2°)	1	-		
	2	35386	≈ 115*	-340
	3	35231		
Xenon	1	34841		
(1°)	2	34692	≈ 206	-1034
	3	34540		

IX.3.II Mn $z^8P \leftarrow a^6S$ Excitation spectroscopy

A summary of the site-specific excitation spectra recorded by monitoring the red emission features of Mn isolated in solid Ar, Kr and Xe in the region of the gas phase $z^8P_{5/2} \leftrightarrow a^6S_{5/2}$ transition is presented in Figure IX.4. The excitation spectra presented were recorded monitoring atomic emission bands produced with direct dye laser excitation. It is evident in Figure IX.4 that all the sites exhibit excitation spectra with resolved threefold split excitation patterns in all matrices. Chapter VIII presents the specific details of each system and comments on the effect of the intensity

distribution of the dye material on the observed spectra. Significantly all the $z^8P_{5/2} \leftarrow a^6S_{5/2}$ transitions are blue-shifted from the gas phase position and exhibit a progressive red shift from Ar to Xe. The blue shifts observed, similar to that reported for the $z^8P_{5/2} \leftarrow a^6S_{5/2}$ transition, is attributed to the 'triplet' like nature of both the z^8P and z^6P excited states. The photophysical characteristics of the sites of isolation identified from the excitation spectra are collected in Tables VIII.15, VIII.13 and VIII.11 for Mn/Ar, Mn/Kr and Mn/Xe respectively.

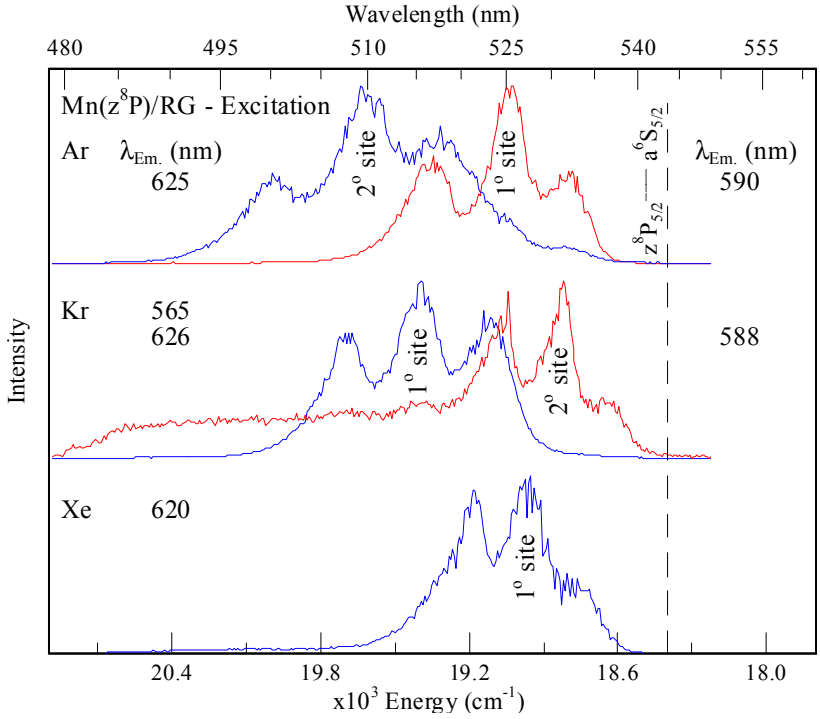

Figure IX.4 **Mn/RG excitation spectra recorded at 12 K for all the Mn/RG systems investigated produced with laser excitation in the vicinity of the Mn $z^8P_{5/2} \leftarrow a^6S_{5/2}$ transition. The spectra shown were recorded monitoring emission bands as indicated by $\lambda_{Em.}$ in wavelength units. The dashed vertical line indicates the position of the $z^8P_{5/2} \leftarrow a^6S_{5/2}$ gas phase transition of atomic Mn at 543.3 nm (18402 cm^{-1})[8].**

Earlier in this Chapter, application of the matrix polarizability model allowed the assignment of the red and blue sites on the $z^6P_{5/2} \leftrightarrow a^6S_{5/2}$ transition to two different sites types. Furthermore trends evident in the dominance of the red and blue sites in solid Ar, Kr and Xe allowed the assignment of the blue and red sites to Mn atoms trapped in single substitutional sites (*ss*) and matrix tetra-vacancy sites ($T_{Vac.}$) respectively. When the polarizability model is applied to all the blue (substitutional) sites identified on the $z^6P \leftarrow a^6S$, $y^6P \leftarrow a^6S$ and $z^8P \leftarrow a^6S$ transitions, the results

shown in Figure IX.5 are obtained. It is evident from the linear relationship between the matrix shifts and the host polarizability, that all the blue sites correspond to the same matrix-trapping environment. The similarity in the matrix shifts and the slopes of the polarizability plots for both the $z^6P \leftarrow a^6S$ and $z^8P \leftarrow a^6S$ transitions is also of particular note and revisited in the discussion section which follows.

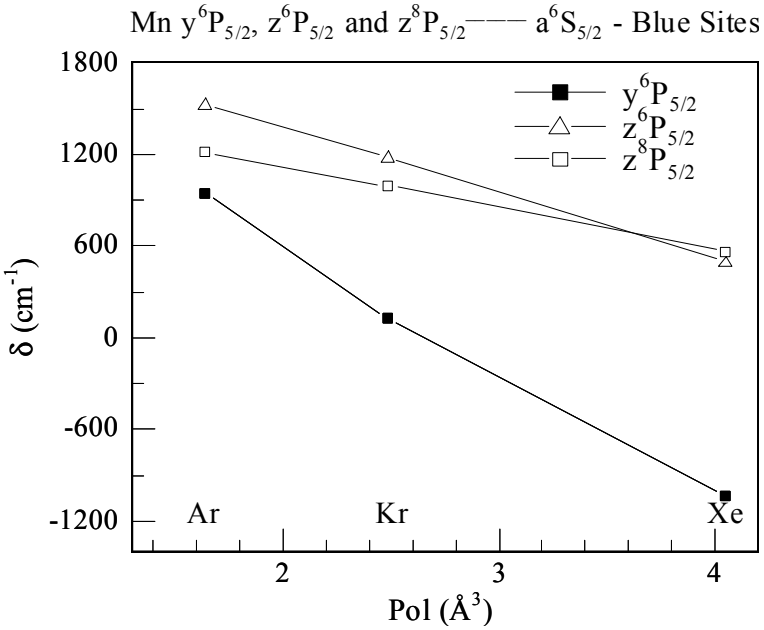

Figure IX.5 **A plot of the gas phase to Mn/RG matrix frequency shifts (δ cm^{-1}) observed for the blue sites identified for the all the P ← S transitions of atomic manganese investigated. The matrix shifts are plotted versus the RG host polarizability.**

IX.4 Discussion

Figure IX.6 provides a plot of the matrix shifts observed on all the sites for the $y^6P \leftarrow a^6S$, $z^6P \leftarrow a^6S$ and $z^8P \leftarrow a^6S$ transitions with RG polarizability. The observed matrix shifts represent the relationship between the absolute frequency of the matrix absorption and the gas phase transition energy. Since the ground state (a^6S) is common to all the transitions investigated, this shift depends on the Frank Condon (FC) accessible region in the three excited states. Essentially it is controlled by the shape of the excited state potential energy surface as controlled by the relative contributions of the Π and Σ interactions occurring between the excited state Mn atom and the matrix environment. The transition energy occurring to lower energy than the gas phase results from a dominance of the attractive excited state Π metal atom RG interaction. However a blue shift is observed if the repulsive Σ excited state

dominates the FC region accessed. Therefore the extent of the Π and Σ excited state interactions occurring over the FC region governs the direction and magnitude of the observed shift. The linear correlation between the observed matrix shift and the polarizability of the RG host arises from the Σ/Π interplay as the Π excited state binding energies are higher and dominate for metal atoms interacting with the heavier rare gases.

Laursen and Cartland's application of the polarizability model to the Group 12 metal atoms[1] Zn, Cd and Hg undergoing $^1P_1 \leftarrow {}^1S_0$ and $^3P_1 \leftarrow {}^1S_0$ transitions revealed that the frequency shifts of the absorption bands were approximately linear with the RG polarizability. This has also been shown to be the case for the P ← S type electronic transitions of atomic Mn.

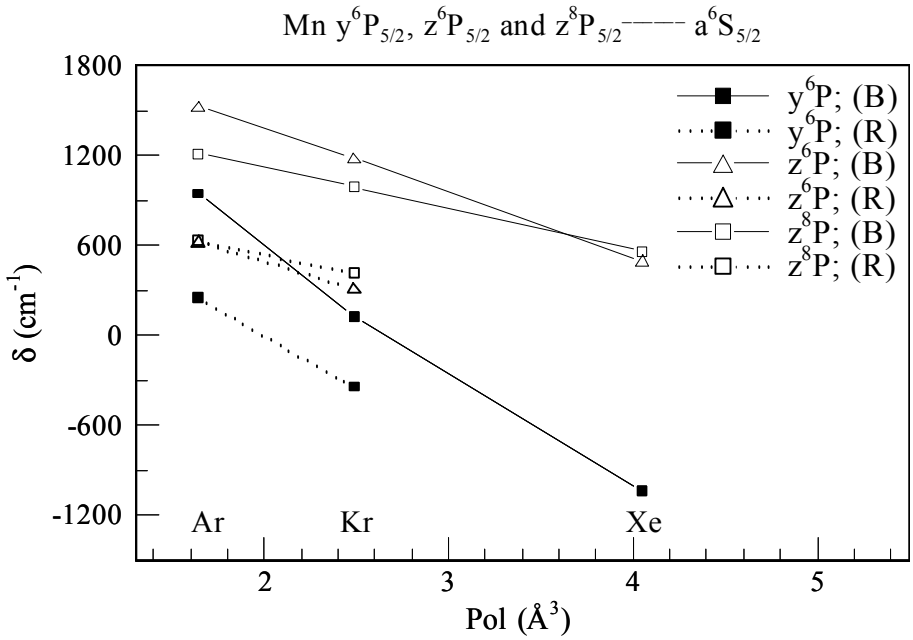

Figure IX.6 **A summary plot of the gas phase to Mn/RG matrix frequency shifts (δ cm^{-1}) observed for all the sites identified corresponding to the P ← S transitions of atomic manganese investigated. The matrix shifts for the red and blue sites (as indicated by the dashed (B) and solid (R) lines used respectively) are plotted versus the RG host polarizability..**

This was achieved in the previous sections by the correlation of the blue and red sites. However L&C also observed that the slope of the linear relationship of the matrix shifts was dependent on the multiplicity of the excited state. This is also observed for Mn/RG solids because, as shown in Figure IX.5, the slope of the 'singlet' like y^6P state is much greater than the 'triplet' like z^6P and z^8P states. This effect is attributed

to the different Π and Σ excited state interactions occurring for the Mn atom in a particular site of isolation. The blue site for the y^6P state transition occurs to higher and lower energy than the gas phase transition from Ar to Xe respectively, whereas the $z^6\text{P} \leftarrow a^6\text{S}$ transition occurs to higher energy than the gas phase in all hosts. The 'triplet' like nature of the $z^8\text{P} \leftarrow a^6\text{S}$ transition is also evident in Figure IX.6 as the transition energy occurs to higher energy than the gas phase in all Mn/RG systems. The difference in the matrix shifts observed for the P ← S type transitions is most pronounced in solid Xe where the y^6P transition is red shifted while both the z^6P and z^8P transitions exhibit a blue matrix shift as shown in Figure IX.7.

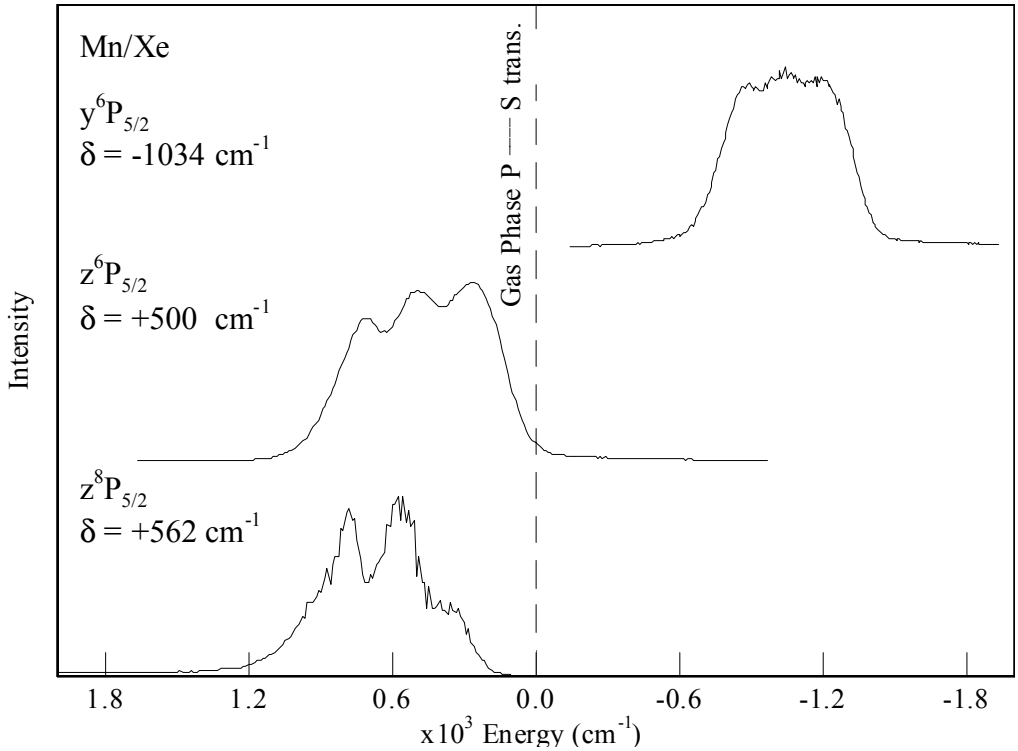

Figure IX.7 **Excitation spectra recorded by monitoring the 620 nm emission feature observed in solid Xe to result from $y^6\text{P}_{5/2}$; $z^6\text{P}_{5/2}$ and $z^8\text{P}_{5/2}$ excitation. Note the excitation spectra are shown relative to the appropriate gas phase transition where the zero position represents the gas phase transitions involved.**

This effect is attributed to the dominance of the $^1\Pi$ like interaction over the $^1\Sigma$ like occurring in the FC accessible region of the y^6P excited state. In the z^6P and z^8P excited states the repulsive $^3\Sigma$ like interaction dominates the weaker attraction of the $^3\Pi$ state, resulting in the observed blue matrix shift. It is also evident that in Xe matrices the difference in the matrix shifts observed for both the z^6P and $z^8\text{P} \leftarrow a^6$S transitions is only 62 cm^{-1}. This effect is manifest in Figure IX.6 where the slopes of

the polarizability plots are in close agreement. This suggests that the excited $^3\Pi$ and $^3\Sigma$ interactions occurring in the Frank Condon region of both z^6P and z^8P states are similar.

The analysis of the absorption and excitation spectroscopy of the $z^6P_{5/2} \leftarrow a^6S_{5/2}$ transition of atomic Mn isolated in solid Ar, Kr and Xe revealed the presence of two types of thermally stable sites of atomic isolation in the lighter RG's Ar and Kr and a single site in Xe matrices. The application of the polarizability model[1] in conjunction with an analysis of the trends regarding the observed site dominance established a connection between the high energy blue sites in Ar and Kr and the single site in Xe and allowed the identification of the same matrix vacancy in all solids. The polarizability model also allowed the grouping of the low energy red sites in Ar and Kr. A comparison of the Mg·RG ground state bond lengths allowed a comparison of the sites of Mn atom isolation assuming the transference of the known Mg·RG bond lengths to the Mn·RG systems. Overall the blue sites were assigned to substitutional site occupancy of Mn in RG solids and the red sites to matrix tetra-vacancy occupancy. Therefore Mn atoms in solid Ar show a preference for trapping in tetra-vacancy sites whereas in solid Kr and Xe single substitutional sites are preferred.

The site-specificity observed in the luminescence spectroscopy of Mn atoms can be interpreted in terms of the freedom of the Mn atom to traverse regions of the excited state potential energy surface provided by the interaction of the excited state metal atom in the site of isolation. The emission spectroscopy of the z^6P excited state of atomic Mn reported in Chapter VII assigned two different relaxation pathways for the excited state populations. Firstly the blue sites identified in Ar and Kr allowed direct $z^6P \rightarrow a^6S$ fluorescence whereas the red sites produced emission assigned to the $a^4D \rightarrow a^6S$ phosphorescence via a $z^6P \Rightarrow a^4D$ intersystem crossing mechanism that is 100% efficient. The preference for phosphorescent transitions of Mn atoms isolated in the red (tetra-vacancy) sites is attributed to the existence of energetically accessible $^6P/^4D$ excited state curve crossings on the more extensive excited state potential energy surfaces afforded to the Mn atoms in the larger tetra-vacancy sites in Ar and Kr matrices. This curve crossing is not favoured or does not occur efficiently for Mn atoms isolated in the more restricted substitutional sites.

IX.5 Conclusion

Analysis of the site occupancy has allowed the assignment of Mn atom isolation in substitutional and tetra-vacancy sites in solid Ar, Kr and Xe, with a preference for the larger site increasing from the heaviest rare gas host, Xe to the lightest Ar. The application of the polarizability model to the $y^6P \leftarrow a^6S$, $z^6P \leftarrow a^6S$ and $z^8P \leftarrow a^6S$ transitions of atomic Mn showed the same overall trends as the ns^2 metal atom systems investigated by Laursen and Cartland[1] insofar as the behaviour evident on the $y^6P \leftarrow a^6S$ and $z^6P \leftarrow a^6S$ matrix shifts mirrored those reported for the $^1P \leftarrow {}^1S$ and $^3P \leftarrow {}^1S$ transitions of Zn, Cd and Hg[1]. This highlighted the differences in the relative contributions from the Π and Σ excited states in the Frank Condon accessible regions to the observed matrix shifts. The importance of the excited state multiplicity on the observed shifts was evident in comparison of the 'singlet' like $y^6P \leftarrow a^6S$ and 'triplet' $z^6P \leftarrow a^6S$ and $z^8P \leftarrow a^6S$ transitions. In addition the analysis of the of $z^6P \leftarrow a^6S$ and $z^8P \leftarrow a^6S$ transition energies reflected the similarity of the excited state interactions for these states.

References

[1] S. L. Laursen and H. E. Cartland, J. Chem. Phys., **95**, 4751, (1991).

[2] V. A. Braken, P. Gürtler and J. G. McCaffrey, J. Chem. Phys., **107**, 5290 (1997).

[3] B. Healy and J. G. McCaffrey, *J. Chem. Phys.*, **110**, 3903 (1999).

[4] C. Crepin and A. Tramer, *J. Chem. Phys.*, **97**, 4772 (1992).

[5] M. A. Collier and J. G. McCaffrey, *J. Chem. Phys.*, **119**, 11878, (2003).

[6] J. G. McCaffrey and G. A. Ozin, *J. Chem. Phys.*, **101**, 10354 (1994).

[7] W. H. Breckenridge, C. Jouvet and B. Soep, *Advances in Metal and Semiconductor Clusters*, edited by M. A. Duncan (JAI, Greenwich, 1995), Vol. III.

[8] N.I.S.T. Atomic Spectra Database, Website: http://physics.nist.gov/cgi-bin/AtData/display.ksh?/XXE0qMnqIXXP-15XXT2XXS, (Last accessed 4th February 2004).

[9] H. E. Hallam, *Vibrational Spectroscopy of Trapped Species*, Wiley – Interscience, New York, 1973.

[10] T. M. Miller, *Handbook of Chemistry and Physics*, edited by D. R. Lide, 73rd ed. (CRC, Boca Raton, 1991-1993).

Chapter X
Conclusions

IX.1 Hg/RG

Hg/RG absorption and excitation spectra recorded in the vicinity of the gas phase $6s^1 6p^1\ ^3P_1 \leftarrow 6s^2\ ^1S_0$ transition revealed bands at 245.9, 248.9 and 253.6 nm in Ar, Kr and Xe respectively. Spectra were obtained with a deuterium lamp following matrix deposition at 22, 25 and 35 K for Ar, Kr and Xe. The progressive red-shift of the excitation bands from Ar to Xe was accompanied with decreasing linewidths but with better resolved threefold splitting. Excitation into the recorded absorption bands produced emission features centered at 250.3, 254.1 and 273 nm in Ar, Kr and Xe respectively. These features all showed nanosecond emission lifetimes and from temperature dependent studies of the recorded decay curves, are identified as the matrix radiative lifetimes of the Hg atom $^3P_1 \rightarrow\ ^1S_0$ transition. The emission bands exhibited an increased Stokes' shift and linewidth from Ar to Xe - results in good agreement with those reported earlier by Crepin and Tramer. At higher temperatures the linewidth of the Hg($^3P_1 \rightarrow\ ^1S_0$)/Xe band increases but the band maximum blue shifts – an effect which is completely reversible. Gaussian lineshape analysis showed three components are required to reproduce the emission bands in Ar, Kr and Xe. They also revealed that the reduced intensity of central, 273 nm component is the origin of the blue shift observed in the Mn/Xe system at high temperature. The multi-component nature of the $^3P_1$ state emission is shown from excitation spectroscopy not to arise from solid-state effects such as multiple site trapping. Its origin is examined with a pair-potential method in which the energetics of excited state vibronic modes are calculated for Hg($^3P_1$)/RG_{18} clusters. The multi-component emission bands were identified as arising from the stabilisation of several 'waist' and 'body' type vibronic interactions occurring for the excited $^3P_1$ state Hg atom isolated at single substitutional sites in each rare gas host.

Time-gated emission spectra recorded following Hg $^3P_1 \leftarrow\ ^1S_0$ excitation revealed the presence of weak, narrow linewidth features at 258.9, 260.8 and 265.1 nm respectively in Ar, Kr and Xe. The millisecond decay times measured for these emission bands allowed their assignment to the forbidden $^3P_0 \rightarrow\ ^1S_0$ transition of

atomic mercury. The maximum contribution of this band to the time integrated emission intensity is found in Xe where it is only 0.5%, indicating the inefficiency of intramultiplet $^3P_1 \rightarrow {}^3P_0$ relaxation compared with radiative decay of the $^3P_1$ excited state. The efficiency of the intramultiplet relaxation increases only very slightly at higher temperatures. The presence of resolved fine structure on the Hg $^3P_0 \rightarrow {}^1S_0$ emission in Xe (and partly in Kr) matrices and the temperature dependence exhibited, allowed the identification of a resolved zero phonon line and a phonon side band. This assignment is confirmed in the lineshape simulation conducted with the Wp function yielding small S values (1.3 and 2.2 in Xe and Kr respectively), which represent weak electron-phonon coupling. The close match between the excited Hg·RG($^3P_0$) $\tilde{a}^3 0^-(^3\Sigma)$ and ground X Hg·RG($^1S_0$) $^1 0^+(^1\Sigma)$ state bond lengths is identified as the origin of the very weak electron-phonon coupling in the Hg($^3P_0$)/RG matrix system. This represents the first observation of a resolved zero-phonon line for an electronic transition of a matrix isolated metal-atom.

From the close agreement found with observed absorption energies, simulations based on the localised, pair-potentials approach developed by the *Maynooth Group* to Hg($^3P_1 \leftrightarrow {}^1S_0$)/$RG_{18}$ indicated that atomic mercury occupies essentially undistorted substitutional sites in solid Ar, Kr and Xe. The Hg·RG_{18} calculations predict the spectral location of the pure $^3P_1 \leftarrow {}^1S_0$ electronic transition to occur red of the observed band maxima but within the observed band profile in all cases. These calculations also succeeded in predicting multiple emission energies for Hg/Ar and Hg/Kr revealing that three vibronic modes lead to emission in these matrices. Of the stabilised modes, the 6-atom 'waist' mode, Q_5, is expected to dominate the low temperature spectra as it has the steepest stabilization gradient. In Hg/Ar matrices, this mode predicts emission in good agreement with the observed bands, but in Hg/Kr, it is slightly to the red of the observed band. Excited state calculations showed the importance of the site of isolation in determining the solid-state luminescence, as Stokes' shifted emission is only predicted for 'waist' vibronic modes. In the waist mode the RG atoms move with respect to the fixed Hg atom at the centre of a substitutional site. The 'body' modes, involving internal motion of the excited state Hg atom from the substitutional site, do not lead to an excited state minimum in Ar and Kr. However, for Hg/Xe calculations indicate that emission can arise from both 'body' and 'waist' modes to give a total of six stabilised modes. The

2–atom 'body' $Q_6(p_y)$ mode leads to emission which most closely matches the observed band centre at 273 nm. This mode involves motion of the Hg(p_y) atom to one of the 12 nearest neighbour Xe atoms and corresponds to excimer type behaviour that Crepin and Tramer proposed was the origin of the emission in Hg/Xe. The solid-state calculations show, however, that to achieve stabilization, the excimer type interaction is specific to one orbital orientation. Tetragonal calculations, namely the 4–atom 'waist' (Q_3) and the 4–atom 'body' modes (Q_2), predict emission at 377.73 and 358.74 nm respectively. However, no Hg/Xe emission features have been observed in the 350-400 nm spectral region. A mechanism by which these modes are quenched was identified in the calculations, involving the crossing of these strongly bound excited state vibronic states by the repulsive ground state potential. This crossing does not occur in the Hg/Ar and Hg/Kr systems.

$Hg(^3P_1)\cdot Ne_{18}$ pair-potential simulations showed good agreement between the calculated and observed absorption energies for atomic Hg occupying distorted (relaxed) single substitutional sites in solid neon. This accounts for the observation that the Hg 6p $^3P_1 \leftarrow$ 6s $^1S_0$ transition occurs to lower energy than that predicted by an extrapolation of the polarizability model. A radial expansion of 0.293 Å of the 1st co-ordination sphere surrounding the Hg atom occurs to allow the isolation of the ground state Hg atom in a single substitutional site. The metal atom induced site deformation, calculated with the ground state 'breathing' mode (Q_1) for the $Hg(^1S_0)\cdot Ne_{18}$ cluster, represents a 9.29% expansion of the nearest neighbour distance. The observed emission spectroscopy can only be predicted with simulations based on relaxed substitutional site occupancy for Hg in neon as no excited state stabilisation giving rise to substantially Stokes' shifted emission is found for rigid site occupancy. It is observed that the excited state lattice reorganisation is dependent on I) the lattice energy and II) the stabilisation of the metal atom excited state. Solid neon provided an ideal system to probe the effect of ground and excited state solvation as the cramped lattice site allowed an investigation of the lattice contribution to the overall excited state cluster stabilisation. In emission the best agreement is achieved using the 6-atom 'waist + limited stretch' mode, (Q_8^*) for the p_z orbital orientation. The stabilization arises from the 'in-phase' contraction of the six close packed Ne atoms towards the metal atom, a motion which allows half the Ne·Ne interactions to regain their equilibrium lattice positions. Therefore, the simulations highlight the

importance of restoring the equilibrium lattice in producing the observed luminescence for metal atoms isolated in cramped sites. The role of the metal atom is revealed as Q_8^* is stabilised for the p_z orbital orientation, thus maximising the attractive pure-Π Hg·Ne interaction. The 6-atom 'stretch' contributes to the overall energy of the Hg $^3P_1$ excited state by reducing the Σ interaction. Overall, 'waist' type vibronic modes are more important than 'body' modes in producing excited state stabilisation of metal atoms located in cramped lattice sites, as internal motion of the metal atom is not feasible under these circumstances.

The pair-potential approach was also used to simulate the recorded Hg($^3P_0 \rightarrow {}^1S_0$)/RG spectroscopy. The simulations predict excited state absorption and emission energies for an excited state 'breathing' mode (Q_1^*), with small Stokes' shifts consistent with the observation of zero-phonon lines for the transition in Ar, Kr and Xe. The calculated emission energies do not show good agreement with the observed matrix emission bands. A comparison reveals the emission energies calculated are progressively red-shifted of the observed band maxima. The red shift discrepancy is attributed to a breakdown in the pure Hund's Case–*c* coupling of the Hg ($^3P_0$) state in the solid. In addition, the Hg($^3P_0$)·RG diatomic potentials are not available experimentally for any of the Hg·RG pairs except Ar. As such the [$^3P_0$ (0) $\tilde{a}$] potentials used were calculated from the known [A $^3\Pi$ ($^30^+$)] and [B $^3\Sigma$ (^{31})] states of the Hg($^3P_1$)·RG diatomics. Overall the pair-potential calculations conducted during the course of this work demonstrate that given accurate Metal (M)·Rare Gas (RG) interaction potentials, available from spectroscopic studies or *ab initio* calculations, the M·RG$_{18}$ localised cluster model succeeds in identifying the sites of metal atom isolation and provides insight into the ground and excited state interactions which lead to the observed solid-state luminescence.

IX.2 Mn/RG

Absorption spectra were recorded in the vicinity of the gas phase $3d^54s4p$ $y^6P \leftrightarrow 3d^54s^2$ a^6S; $3d^54s4p$ $z^6P \leftrightarrow 3d^54s^2$ ^6S and $3d^64s^1$ $x^6P \leftrightarrow 3d^54s^2$ ^6S transitions of atomic manganese at 279.91, 403.42 and 221.45 nm respectively, with deuterium and tungsten lamps. The simplicity of the absorption spectra reported and the spectral location of the bands observed allowed easy assignment of the matrix equivalent of

these atomic P ← S type transitions. The Mn/RG samples prepared during the course of this work were more 'atomic' than those reported in previous studies. This was due to the increased control of the Mn vaporisation afforded by localised heating of Mn via electron bombardment compared to the bulk heating of Knudsen cells used in previous works. As a result, the samples prepared under low Mn concentrations showed only small amounts of Mn aggregate absorptions and the spectra recorded in this study allowed easy distinction of Mn atom and Mn_2 transitions.

Multiple thermally stable sites of atomic isolation were identified in solid Ar and Kr whereas single site occupancy is indicated in solid Xe. The Mn($y^6P_{5/2} \leftarrow a^6S_{5/2}$)/RG transitions were observed to occur at 273 / 278.1; 279.3 / 284.9 and 288.2 nm in Ar, Kr and Xe respectively. A progressive red shift was observed from Ar to Xe with respect to the gas phase $y^6P \leftrightarrow a^6S$ transition energy for the Mn atom. The red site at 278.1 nm dominated only in Mn/Ar. The features assigned to the $z^6P_{5/2} \leftarrow a^6S_{5/2}$ transition occur at 397.4, 385.5 / 401.9 and 395.5 nm in Ar, Kr and Xe respectively all of which are blue of the gas phase transition. A progressive red-shift from Ar to Xe is not observed for the $z^6P_{5/2} \leftarrow a^6S_{5/2}$ transition as the absorption band in Mn/Kr appears to higher energy than the Mn/Ar band. The presence of a secondary site (corresponding to the 273 nm band on the y^6P), blue-shifted from the assigned 397.4 nm absorption in Ar, (identified in excitation spectra) rationalized the behaviour exhibited by the matrix shifts for the $z^6P_{5/2} \leftarrow a^6S_{5/2}$ absorption. This allowed a linear correlation between the gas phase-matrix shift and host matrix polarizability. The $x^6P_{5/2} \leftarrow a^6S_{5/2}$ transition was also identified in absorption spectra and occured blue-shifted of the gas phase transition energy by approximately 2000 cm^{-1} for all Mn/RG systems investigated.

The luminescence spectroscopy observed for the z^6P excited state of matrix-isolated atomic Mn confirmed the presence of multiple sites of isolation of Mn atoms in Ar and Kr and a single site in solid Xe. The excitation-emission spectra recorded for each Mn/RG system allowed the deconvolution of badly overlapped absorption bands into separate site contributions. The steady-state and time-resolved emission spectroscopy (TRES) allowed the identification of two very site-specific relaxation channels in the Mn/Ar and Mn/Kr systems giving rise to $z^6P \rightarrow a^6S$ fluorescence and $a^4D \rightarrow a^6S$ phosphorescence from the blue and red sites respectively. The a^4D state emission occurs by $z^6P \Rightarrow a^4D$ intersystem crossing a process which is 100%

efficient. Excited state lifetime measurements definitively assigned $z^6P \rightarrow a^6S$ fluorescence at 413 and 416 nm in Ar and Kr respectively. In addition, the matrix lifetime for the forbidden $a^4D \rightarrow a^6S$ transition is reported for the first time to be approximately 25 msec in both matrices. Currently no experimental gas phase lifetime data is available for this transition which is both electric-dipole and electric-quadrupole forbidden. The results of lineshape analyses of the very narrow emission features assigned to the $a^4D \rightarrow a^6S$ transition allowed the assignment of zero phonon lines and phonon sidebands with distinct lifetimes of 25 and 10 msec. Also the requirement of two sets of phonon frequencies allowed the identification of a small (10 cm^{-1}) crystal field splitting parameter for the a^4D state of Mn atoms isolated in the red sites in Ar and Kr. In solid Xe, no emission features were observed in the 400 – 600 nm spectral range so neither the $z^6P \rightarrow a^6S$ nor the $a^4D \rightarrow a^6S$ transitions of atomic Mn occur in this host.

High-resolution dye laser excitation spectra were recorded in the region of the gas phase $a^6D_{5/2} \leftrightarrow a^6S_{5/2}$ transition by monitoring Mn emission features present in the red spectral region for solid Ar, Kr and Xe with z^6P excitation but not definitively assigned. The excitation spectra revealed that the gas phase spin-orbit splittings were maintained in all three solids. The temperature dependence exhibited allowed the assignment of zero phonon lines for the excited state J = $^1/_2$, $^3/_2$, $^5/_2$ and $^7/_2$ levels of the $a^6D_J \leftarrow a^6S_{5/2}$ electric-quadrupole transition in Mn/Kr. This represents the first report of zero phonon lines observed in excitation for metal atoms isolated in RG solids. Their occurrence is attributed to weak coupling of the a^6D excited state of Mn to the solid-state environment provided by the site of isolation. In addition, an enhancement of the transition was observed to occur for Mn atoms in the larger, red sites of isolation. However, different excitation lineshapes were observed monitoring Mn atoms located in high symmetry sites in Ar and Kr but the excitation spectra recorded by monitoring site specific emission features showed no relative shifts. This behaviour, different to P ← S transitions, occurs due to the weak coupling of the a^6D state with different environments within the same matrix host. The emission spectroscopy recorded following a^6D state excitation allowed the definitive assignment of emission to the relaxation of the $a^6D_{9/2}$ state in the Mn/Kr system. A comparison of the matrix radiative lifetime (227 μsec) to the calculated gas phase lifetime for the $a^6D \leftrightarrow a^6S$ transition (3.4 sec) shows the extent of the enhancement

of this forbidden transition in the matrix environment. Selective excitation of the individual levels assigned to the a^6D state in Kr resulted in the production of only the $a^6D_{9/2}$ emission due to efficient intermultiplet relaxation. The $a^6D_{9/2} \rightarrow a^6S_{5/2}$ transition occurs with direct a^6D red site excitation in Ar at 590 nm. In this case the electronic transition occurs to lower energy than in solid Kr with a substantially longer lifetime (1.09 msec). These observations are attributed to the smaller site size available in solid Ar. In solid Ar and Kr, no rise times are observed in the decay profiles for the a^6D emission bands suggesting direct feeding processes lead to the observed emission bands. Blue site a^6D excitation also produces direct phosphorescence emission features at 625, 626.7 and 620 nm in Ar, Kr and Xe matrices. The emission bandbands are Gaussian in Ar and Kr and asymmetric in Xe, but linewidths of approximately 260 cm^{-1} are observed in all cases. These bands were assigned to the $a^6D_{9/2} \rightarrow a^6S_{5/2}$ transitions from the long lifetimes recorded, (1 msec) and a comparison of the gas phase splittings between the z^8P/a^6D pair that is maintained in emission for Mn atoms isolated in cramped matrix environments. The lifetimes recorded (1 msec) are substantially longer than the radiative lifetime extracted for the a^6D state emission at 586 nm in solid Kr following red site excitation. The long decay times and the substantial Stokes' shifts observed for these bands arise due to size and symmetry reasons in the cramped substitutional site which for does not allow the enhancement of the transition like the red tetravacancy site.

The excitation bands recorded for the forbidden $z^8P_{5/2} \leftarrow a^6S_{5/2}$ transition of Mn atoms isolated in solid Ar, Kr and Xe showed well resolved threefold splittings, behaviour evident in the Mn z^6P state absorption and excitation spectra. Moreover, the $z^8P_{5/2} \leftarrow a^6S_{5/2}$ transition reveals multiple Mn atom trapping sites consistent with the z^6P and y^6P states. Emission spectra recorded with $z^8P_{5/2} \leftarrow a^6S_{5/2}$ excitation allowed the identification of $z^8P_{5/2}$ state emission at 565 nm in solid Kr only. Moskovits and co-workers previously observed this emission feature with fixed wavelength excitation at 514 nm using an Ar^+ laser but assigned it to Mn_2. The excitation spectroscopy and the lifetime measurements recorded here indicate, however, that the 565 nm band is emission of the z^8P excited state of atomic manganese. As observed with z^6P excitation, the smaller, blue site in Mn/Kr leads to direct z^8P state emission whereas the larger, red site leads to the a^6D emission via an $z^8P \Rightarrow a^6D$ ISC process of 100% efficiency. Overall, the luminescence and excited

state lifetime measurements reported allowed the definitive assignment of emission from all the excited states of Mn, which occur below the z^6P state.

Mn atoms are isolated in single substitutional and tetra-vacancy sites in solid Ar, Kr and Xe, with a preference for the larger site increasing from the heaviest rare gas host, Xe to the lightest, Ar. The application of the polarizability model to the $y^6P \leftarrow a^6S$, $z^6P \leftarrow a^6S$ and $z^8P \leftarrow a^6S$ transitions of atomic Mn showed the same overall trends as the ns^2 metal atom systems investigated by Laursen and Cartland insofar as the behaviour evident on the $y^6P \leftarrow a^6S$ and $z^6P \leftarrow a^6S$ matrix shifts mirrored those reported for the $^1P \leftarrow {}^1S$ and $^3P \leftarrow {}^1S$ transitions of Zn, Cd and Hg. This highlighted the differences in the relative contributions from the Π and Σ M·RG excited state interactions in the Frank Condon accessible regions of the excited states. The importance of the excited state spin multiplicity on the observed matrix shifts was evident in comparison of the 'singlet' like $y^6P \leftarrow a^6S$ and 'triplet' $z^6P \leftarrow a^6S$ and $z^8P \leftarrow a^6S$ transitions. In addition, the analysis of the z^6P and z^8P excited state energies reflected the spin triplet nature of these two states.

IX.3 Summary

The luminescence spectroscopy reported here for Hg and Mn isolated in rare gas matrices have shown that the solid state environment provides an ideal environment to study the interactions of the ground and excited state metal atoms. It allows the extraction of information on long-lived electronic transitions (> 100 μsec) which cannot be observed in gas phase experiments. The solid state simulations have shown that given accurate potentials, the interactions between the metal atom and the solid RG environment can provide information on the vibronic modes leading to the observed luminescence. The results of the Mn/RG experimental work have shown that the site of isolation critically governs the excited state guest/host interactions. This observation therefore would allow the extension of this work to investigate site selective excited state reactions with reagents such as CH_4, CH_3F, NH_3 and H_2 doped RG matrices. In addition studies of Mn/G matrices (G = CH_4, CF_4 and N_2) are suggested. However, the most pertinent information to allow a complete analysis of the Mn/RG luminescence reported would be the simulation of the solid state using diatomic pair–potentials which are unavailable at present for the Mn·RG 1:1 van der Waals complexes from either spectroscopic studies or *ab initio* calculations.